School of Computer, Science and Engineering

Petroleum & Gas Engineering

A study into the mapping of an induced fracture in a fine grained sediment in biaxial & triaxial stress formations.

Submitted by

Stuart Phillip Penketh

In fulfilment for a PhD in Petroleum & Gas Engineering

2018

Contents

Appendices

List of Figures

List of Tables

Dedication

To Karen, thank you.

Acknowledgments

During the course of my investigation I relied on a number of people and I would like to extend my thanks to each and every single one of them.

To my wife Karen, I cannot put in words how grateful I am to her for her patience, her forbearance and her ability to use her own doctorate to help me see the wood as well as the trees.

My family, namely my Grandmother and her generous nature, my mother and step father for their encouragement.

My supervisors Professor Nasr for his time and effort, Dr Martin Burby, for not only his close supervision, but also for his unique sense of humour. My technician, Mr Alan Mappin, always surprising me with his ability to work up a solution to a problem. Also I would like to thank Dr Levingshan Augusthus-Nelson & Dr Lawrence Weekes for helping to evaluate the design of the rig.

To David Milton-Tayler at Frac tech, if it wasn't for him and his generosity I don't think I would have survived the first year nor would I have got the samples I needed to carry out this experiment.

To my late friend and colleague Jordan who actually identified the build error when I couldn't get the acoustic software to work. A brilliant and selfless physicist, who at 20, was taken too soon.

My friends at university who have worked with, or suffered me, depending on your opinion, MK, Kabiru and my fellow fraccing leper Suzanne.

My friends who I worked with in Subway, firstly for giving me a job and secondly for helping me relive my student days without feeling like an old man and for showing me new experiences, though I still contend the music was better in my day. My boss Stu, my supposed boss Ken, Abby (keeping Karen sane), Kev, my fellow Salfordian scientist Shan, Suz, my fellow geologist Ayrton, Chloe, Meg and Les.

Finally, my thanks to the 503 STRE of the 170th Royal Engineers a specialist group of petroleum engineers. Thanks for accepting an ex Sailor and thank you for all the advice and pointers.

Nomenclature

σ_H	Principle stress (psi)
σ_{max} or σ_m	Maximum vertical stress (Mpa)
σ_{min}	Minimum horizontal stress applied (Mpa)
σ_o	Nominal applied stress to the crack tip (Mpa)
σ_{ij},	Cauchy stresses (Mpa)
σc	Fracture constant
σ^1	Vertical/Greatest load (Mpa)
σ^2	Intermediate load (Mpa)
σ^3	Minimum load (Mpa)
θ	The angle with respect to the plane of the crack.
∅	Porosity
F_{ij}	Variable function
ρ_t	Radius of the curvature of the crack tip (in.)
α	Length of the surface crack (ft.)
c_r	Rock compressibility
E	Young's Modulus (psi)
G	Strain energy release rate.
k	Permeability (md)
K_i	Stress Intensity
K_t	Stress concentration
K_c	Fracture toughness
r	Distance from the crack tips (in.)
r_w	Wellbore radius (in.)
T	Tensile strength of the rock (psi)
T_o	Rock toughness
$T_{o,i}$	Fracture toughness at the point of propagated fracture intersecting natural fracture
υ	Poisson's ratio
W	Strain energy density
W_w	Width of fracture at its widest point (in.)
AE	Acoustic Emission
J	Joules
µsec	Microsecond

ρVs	Or ρV-Sec, Signal Strength based on the PAC system but independent of gain and calculated over the Entire AE signal dynamic range, (1 μsec x 1.05 μV = 1.05 ρVs)
C.T.	Computerised tomography
mm	Millimetre
bar	Measure of pressure = 100kPa
μA	Micro Amps
V	Volts
W	Watts

Abstract

Unconventional hydrocarbon extraction has increased in the last twenty years due to the post-industrial west needing to increase energy security. This has meant tapping into hydrocarbon resources that are trapped within impermeable sediments. Shale hydrocarbon reservoirs have a permeability of less than 0.01mD, therefore to extract hydrocarbons the shale has to be fractured to release the trapped fluid.

The ability to predict when a fracture will occur and what the resulting shape of that fracture will be has recently become increasingly important in engineering, and, in particular the petroleum industry. This has been done previously using the fracture growth equation for brittle material with additional modifications for ductile materials. A number of pseudo 3D equations have been developed which are used by these software simulations to try and predict the dimensions of a fracture so that reservoir engineers can calculate the volume of fluid expected to be produced by any drilling well. However, the simulations provide only a reasonable prediction of fluid flow and can be under or overestimated by up to 60% of returns. Previous fraccing experiments carried out to determine how the models could be improved have relied on data whereby reservoir rocks have been placed under bi-axial pressure, (two forms of pressure acting perpendicular to each other) rather than tri-axial ($\sigma^1\sigma^2\sigma^3$) which would more adequately reflect the pressures acting on in-situ shale formations.

The present investigation has focused on building a pressure rig that allows rock samples to be placed under tri-axial pressure. To this end a concrete rig structure has been built to house three flat jacks which place a 100mm^3 rock sample under pressure of up to 120 bars (12MPa) in three different directions, to represent rock at in situ depths. In conjunction with the flat jacks, 6 acoustic sensors can be placed around the rock sample to allow 3D mapping of the acoustic emissions occurring during the drilling and fracturing phase.

10 different shale samples were scanned (using the GE Phoenix v|tome|xs CT scanner) and their images reconstructed to show 3-D visualisations of any pre-existing fractures or structures. 9 of those samples were then drilled and fractured and scanned again. Using reconstruction software each drilling fracture was mapped and the dimensions measured at regular intervals in order to provide a more accurate picture of how the fracture developed when the rock is subjected to tri-axial loading.

Two types of shale rock were tested, samples from the Westbury Shale Formation and samples from the Accrington Mudstone Formation. Two Accrington and one Westbury were fractured under bi-axial conditions and two Accrington and four Westbury under tri-axial pressure.

The Accrington Mudstones formed a fracture that was almost elliptical in shape with ultra-thin extended tips along both the top and bottom of the fracture. There was a direct correlation between fracture width and height, those fractures that narrowed along the half-length increased in height, whilst fracture half-

lengths that didn't narrow resulted in a reduced height. The Westbury Shales, which are more organic rich, had a more distorted shape due to fractures opening up along the weaker bedding planes helping to disperse the pressure from the fracturing fluid. The acoustic sensors accurately picked up and located the fracture inducement, proving that they opened instantaneously and also revealing damage that occurred during drilling at a small distance (2mm ±1mm) below the position of the drill tip. The acoustic data also revealed existing fractures and planes of weakness that the induced fracture would follow.

1 Introduction

Oil and gas production has evolved significantly over the last hundred years or so that large-scale petroleum and gas production has been carried out. The advanced industrial nations of the West have heavily depleted hydrocarbon reserves held in conventional plays. These are reservoirs in which the permeability is greater than 0.01mD; i.e. reservoirs in which fluid can flow relatively easily and which are extracted in the conventional manner. The political stances of those countries who account for large scale oil production has forced the West to look at newer and more secure sources of fuel in recent years. It is estimated that the UK has sufficient hydrocarbon reserves to account for only 30% of Britain's total energy needs for the next fifty years (British Geological Survey, 2013) and this is forcing energy companies to look at geological formations with high organic content but low permeability for new hydrocarbon sources. Shale is a fine grained, organic rich sedimentary rock that has very low permeability due to its fine-grained structure. In order to get the hydrocarbons out of the shale, the shale has to be broken up (to increase the permeability) and this is usually done by injecting a fluid at high pressure to open up micro fractures in the shale – fracture induction. This 'ripping' apart of the sediment releases the fluid held inside the formation.

In order to ascertain how much oil a well would produce petroleum companies rely on three dimensional (3D) and pseudo 3D fracture simulation software. These software programmes model the various geomechanical aspects of an induced fracture to determine the volume of oil likely to be extracted. However, there have been relatively few studies which have experimentally replicated the exact conditions that a shale sample would be subjected to in a reservoir formation: i.e. the sample being fractured whilst under tri-axial compression with pressures high enough to duplicate the overburden pressures at depth. Therefore, little is known about the progression of fracture propagation through a shale once a fracture has been induced. This lack of knowledge to accurately define how the fracture evolves means that an accurate 3D model of the fracture cannot be developed. Due to this lack of knowledge these estimates are often widely inflated from what is achieved in the field. This deviation between the modelled output and the reality in terms of barrels produced presents a number of issues not least of which is a lack of efficiency in the removal of hydrocarbons from the shale plays resulting in hugely increased operating costs or reduced income to hard pressed unconventional oil operating companies.

Therefore, being able to identify the path and visualise any correlations from the point of inducement of the fracture through to the edge of a sample under triaxial pressure using acoustic sensors and CT scanning equipment will increase the understanding of the properties of an induced fracture in shale. This will then allow the formulation of more accurate equations which can be used in the fracture simulation software to facilitate a more precise 3D reconstruction to be built when placing a fracture. This, in turn, will improve the accuracy of the prediction of hydrocarbon returns than is currently

possible and save the industry money by providing more efficient recovery of unconventional hydrocarbon resources.

1.1 Aims and Objectives

AIMS

The aims of this investigation are to:

- Track and analyse the path of an induced fracture within different shale samples by measuring the parameters of a fracture from the start of the inducement to the end.
- Assess any changes in the differing areas of a fracture to give a more accurate understanding of typical fracture behaviour throughout the whole of the fracture half length.
- Evaluate the effectiveness of 3D acoustic software to show the evolution of the fracture from inducement to the end.

OBJECTIVES

- Shale rock samples from different formations will be placed under tri-axial conditions at pressures similar to those that exist at depth in unconventional reservoirs and then a fracture will be induced. For this reason, the rig will be designed to simulate pressures of up to 120Mpa. The rig will be enclosed so that an inert viscous fluid can be injected into the void space to mimic fluid pressure.
- Samples will need to be characterised before fracture induction and then examined in detail post fracture. As shale is well known for its friability the non-destructive technique of CT scanning has been chosen that will allow a full 3D reconstruction and facilitate measurements of the fracture plane along the different sections of the fracture half-lengths.
- Acoustic sensors will surround each sample which will be linked to the 3D acoustic software in order to map the evolution of a fracture from inducement to its end point. The sensors will also be used to trace the drilling of the sample before the fracture is induced. If the drilling can be accurately tracked, then the results of the mapping of the fracture inducement can also be interpreted as reliable. The use of the sensors during the drilling of the borehole will also show where the greatest amount of damage occurs to the shale formation when drilling.

1.2 Thesis Overview.

This thesis comprises of 5 chapters.

- Chapter 1 sets out the aims and objectives of this work.
- Chapter 2 contains the literature review which gives an overview of unconventional hydrocarbon reservoirs and fracture induction, the history and evolution of fracture mechanics,

complex fracture behaviour and modelling of fractures. The history of acoustic emissions and how they can be used to trace an emissions source is also explained.

- Chapter 3 covers the apparatus design procedure and method of data processing and describes the evolution of the design process and data collection.
- Chapter 4 presents and discusses the commissioning test results for the acoustic data, the pre and post fracture CT scans with post fracture measurements and the acoustic emission data from the drilling and fracturing events.
- Chapter 5 is the conclusion and recommendations of this investigation for future study.

2 Literature review

2.1 Overview

This literature review covers the importance of unconventional hydrocarbon deposits and their significance to industrialised and post industrialised nations. It summarises the history and evolution of fracture mechanics and the inefficiency of the current fracture inducement models along with the recent introduction of acoustic emission detection and location placement and their current role in the oil industry. The review also emphasises the current lack of knowledge and the need to improve the understanding and accurate prediction of fracture behaviour.

2.2 Unconventional Hydrocarbon Deposits.

Unconventional hydrocarbon deposits usually refer to shale deposits or other tightly packed sedimentary deposits with a permeability of < 0.01mD. The definition of unconventional hydrocarbon is somewhat limited in that it does not give any consideration to fluid properties and the impact on hydrocarbon deposit classification. These deposits have had a major impact on global energy plans. The United States (US) became the first country to realise the potential of exploiting these reserves and since the advent of unconventional drilling technology brought these shale reservoirs into play US gas reserves have increased by 35% (Potential Gas Committee, 2009).

2.2.1 Formation of oil & gas in unconventional reservoirs

Formation of oil and gas in an unconventional reservoir is just the same as in a normal reservoir where 90% is produced from kerogen. Kerogen is a complex geopolymer formed by the diagenesis of organic matter. This matter is made up of hydrates, lignin, proteins and lipids; lipids are the closest in composition to that of kerogen. There are four types of kerogen which give differing propensities of oil and gas and hydrocarbon densities as the kerogen matures (Tucker, 1991); Type I – liptinite, type II – extinite, type III – vitirinite and type IV - inertinite. Rising temperatures as burial depths increase cause kerogen to mature, when the heat reaches between 60-120ºC, the oxygen/carbon ratio and the hydrogen/carbon ratio will decrease at the same time. The greater the decrease in the ratios the lighter the hydrocarbon will be. This is shown in the form of a Vann Krevelen Diagram, Figure 2-1.

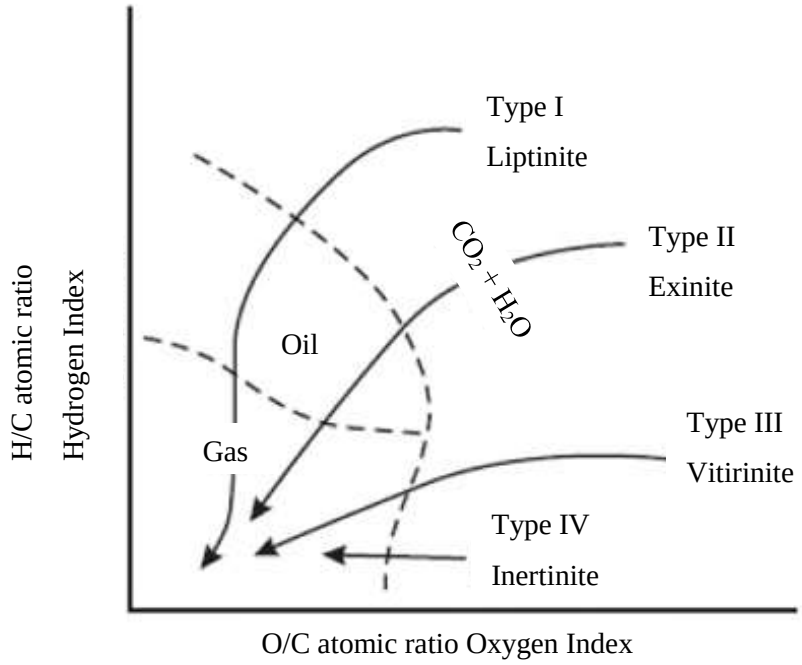

FIGURE 2-1: Van Krevelen Diagram showing maturation of Kerogen into Oil and Gas.

In order for an economically exploitable amount of gas and oil to form in shale a number of conditions must be met;

- The total organic carbon (TOC) content must be greater than 2%.
- It must contain sufficient active TOC (that is kerogen in groups I to III in Fig. 2-1) compared to inactive TOC (this is generally oxidised and recycled kerogen found in group IV in Fig. 2-1).
- There must be sufficient heat for a significant period of time to allow the maturation of the kerogen in each family (allowing it to reach either the oil or gas phase).

2.3 The Process of Hydraulic Fracturing

The modern form of hydraulic fracturing can be traced back to 1947 with the first commercial use of a vertical hydraulic fracturing process carried out by the Pan American Petroleum Corp in the Hugoton field, Kansas, (Montgomery & Smith, 2010). This procedure was also exploited to obtain water in arid areas with a low water table. Whilst the primary use of hydraulic fracturing was to obtain hydrocarbons, In 2003 hydraulic fracturing proliferated massively in the United States. This was due to Energy Companies based in the maturing field areas of Texas and Pennsylvania actively searching for gas deposits in the shale formations of concession areas that they already controlled. This expansion was further reinforced when the Environmental Protection Agency (EPA) published a study confirming that the hydraulic process did not contaminate drinking water (Environmental Engineering and Contracting, Inc, 2010).

Energy Companies have used the hydraulic fracturing process to improve productivity in maturing wells by, in effect, increasing the permeability and thus increasing the flow of material to the well. This process has also been used to exclusively unlock potential gas and oil deposits in reservoirs that have, hitherto, remained un-exploitable due to their low permeability.

Hydraulic fracturing, or fraccing, is where a hydraulic fluid is used to apply force to a rock formation. This load initiates and then propagates a fracture. The process is started by drilling a wellbore into the formation, the wellbore is cased, and perforations are created at the end of the wellbore (or wherever the engineer deems the most productive placement of fractures will be) by strategically placed explosive charges along the casing. Once a perforation is created the proppants are pumped in at high pressures to initiate new fractures and force existing fractures to open up. The perforations will also allow the hydrocarbons to enter into the wellbore.

There are four stages during the hydraulic fracturing process:

Stage 1 - the Pad; this is where a clean fluid is pumped into the formation at high pressure to force the fractures to open wide enough to allow the proppant to enter.

Stage 2 – Proppant stage; this is where the proppant is injected down the well at high pressure but will keep the fracture open even at low pressures.

Stage 3 – Flush; a volume of clean fluid then pumps the well clear of proppant.

Stage 4 – Recovery; fracture fluid is recovered as it flows back to the well, it will now contain the dissolved minerals from the shale and excess proppant.

When all four stages have been carried out the hydrocarbons will then flow from the fractures into the well head as shown in the following Figure 2-2 to Figure 2-3. Figure 2-3 shows how the proppant then maintains the increased permeability created in the newly formed fracture as pressure is reduced allowing the hydrocarbons and fracture fluid to return through the perforation to the surface.

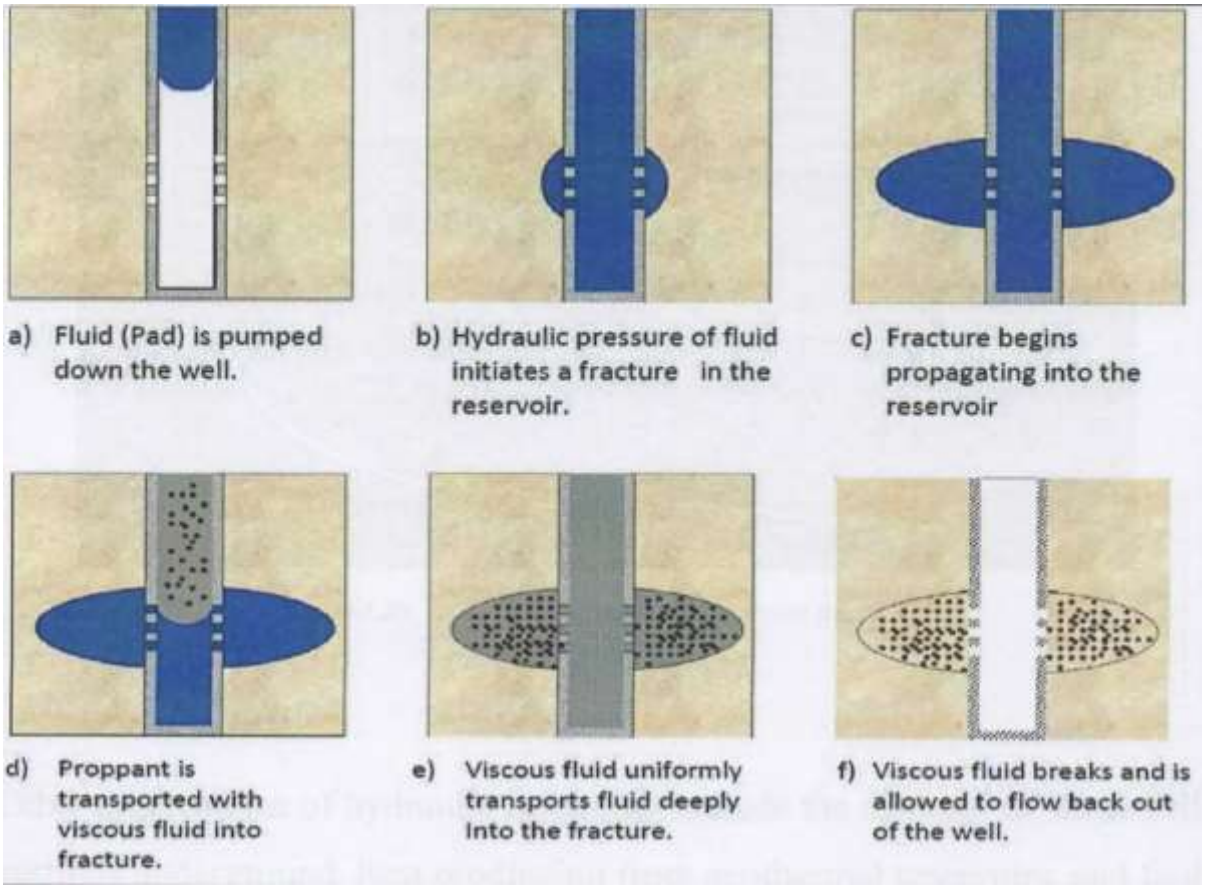

FIGURE 2-2: Process involved in hydraulic fracturing.

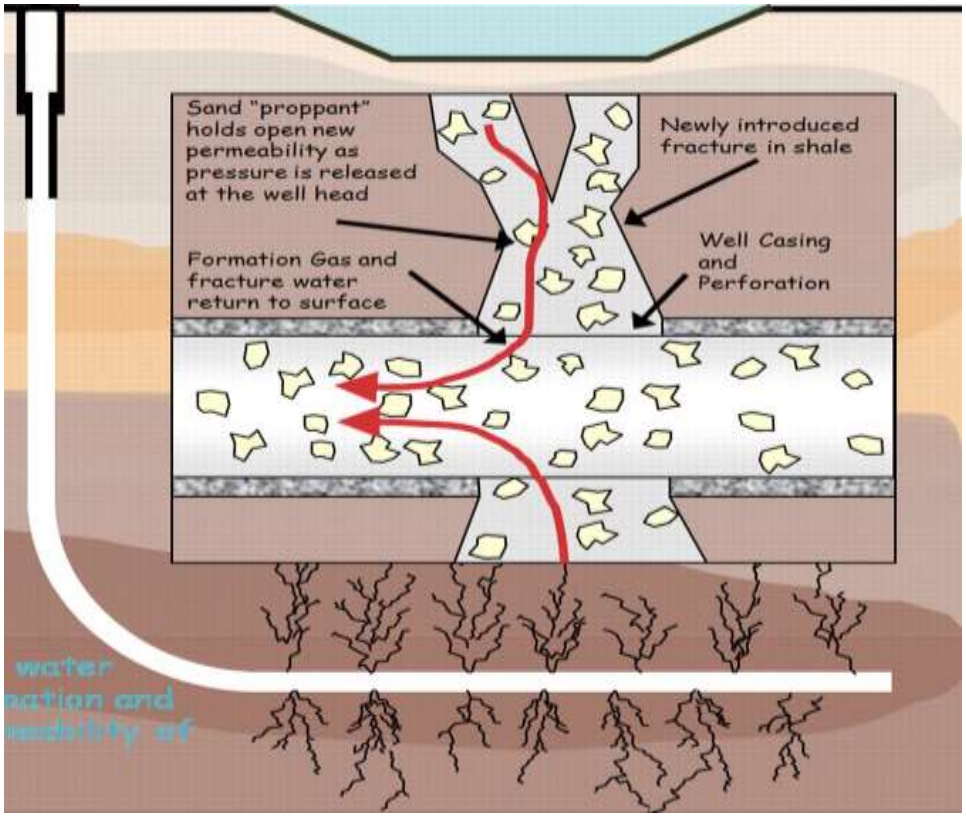

FIGURE 2-3: Gas extracted following the processes shown in Figure 2-2.

2.4 Geomechanical Factors Affecting the Productivity of a Hydrocarbon Field

Simulating how a fractured reservoir will behave is complicated by the introduction of the rock mechanics into the model. The geomechanics at play in a reservoir will affect the fracture length, height and width and, in turn, these factors will affect the rate of flow into a well.

To fully understand the geomechanics in play in a reservoir the following issues need to be considered:

2.4.1 Young's Modulus (E);

This is a measure of the ability of a material to resist deformation whilst that material is under a load. I.e. when under stress what is the ability of the body to resist strain (a change in the body's dimensions). It can be calculated simply by 2-1;

$$\mathrm{E} = \frac{\text{Tensile Stress}}{\text{Extensional Strain}} \qquad \textbf{2-1}$$

2.4.2 Poisson's Ratio (υ);

This is a dimensionless ratio, it measures the change of the dimension. When a stress is applied to a rock the negative ratio of the strain on the transverse to the axial strain gives Poisson's Ratio as shown in 2-2;

$$\nu = \frac{\mathrm{d}\varepsilon_{\mathrm{trans}}}{\mathrm{d}\varepsilon_{\mathrm{axial}}} \qquad \textbf{2-2}$$

Stresses and their effects on a reservoir

Underground formations are subjected to three principle stresses, (Nolen-Hoeksema, 2013);

- σ_v This is the vertical/overburden stress, it is the stress derived from the overburden - it is the maximum vertical stress, the overburden determines the minimum and intermediate pressure.
- σ_{Hmax} is the maximum principle stress, this is the maximum stress perpendicular to the σ_v & is often referred to as the intermediate stress.
- σ_{Hmin} is the minimum horizontal stress applied, perpendicular to the σ_v & is often referred to as the minimal stress.

The application of which is shown in Figure 2-4. These stresses are usually compressive, non-homogenous and anisotropic. This means that they will not be equal and the magnitude applied to the formation will vary. In order for a fracture to occur:

- In-situ earth stresses have to be overcome
- The tensile strength of the rock has to be overcome. This only needs to happen once, as once the strength has been overcome, the rock will break.

Whilst to extend a fracture the stresses applied have to:

- Overcome frictional pressures down fracture
- Exceed the minimum fracture propagation requirements

The created fracture plane is perpendicular to the minimum principle stress

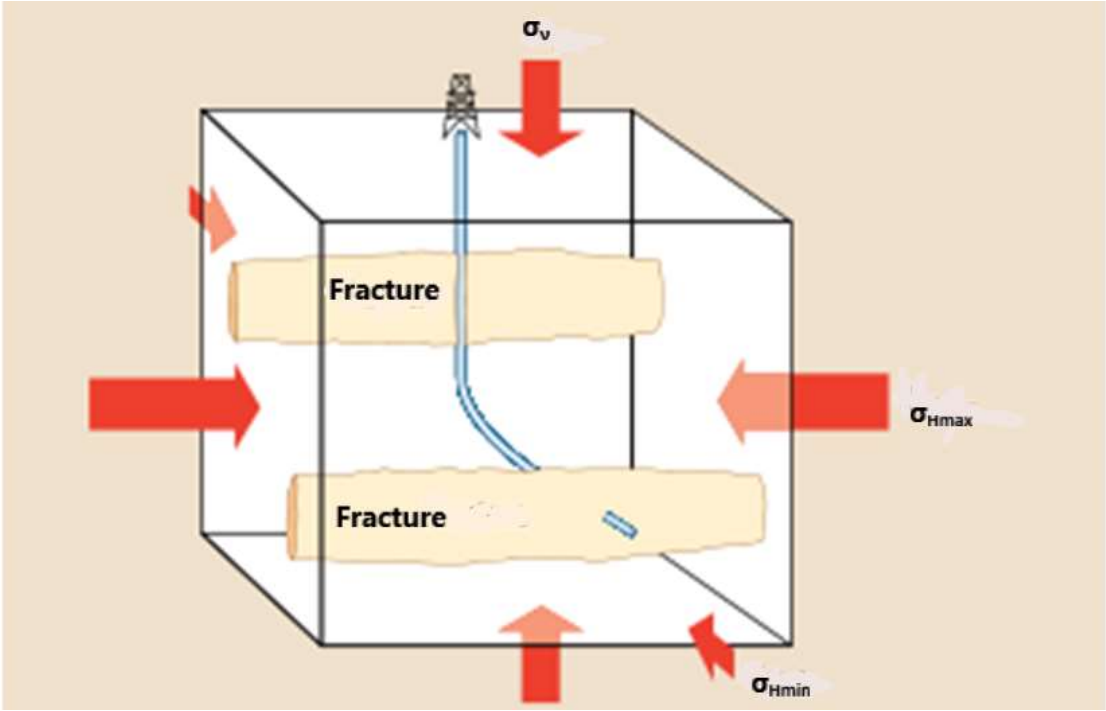

FIGURE 2-4: In-situ stresses applied to a formation.

2.5 Process of Fracturing and Fracture Propagation

As described in Section 2.2 the process of hydraulic fracturing centres on a hydraulic fluid acting as a propagant. The fluid is pumped into a well until the pressure builds up in the desired strata, as this pressure exceeds the fracture toughness of the strata, the strata fractures. This is referred to as tensile failure. This tensile failure of the rock is required to propagate the fracture. During the process of the fracturing of a rock, like most materials the rock displays elastic properties. Elastic properties can be defined as "one for which a strain energy density $W=W(\varepsilon_{mn})$ exists as a single strain space,". (Rice, 1968).

Shown in equation 2-3;

$$W = W(\epsilon_{mn}) = \int_0^{\epsilon_{mn}} \sigma_{ij}\, d\epsilon_{ij} \qquad \textbf{2-3}$$

Where:

σ^{ij} is the stress at a point in the sample where the fracture will occur.
$d\epsilon_{ij}$ is change of the strain in the rock along a point of the fracture.

This will mean typically that the rock will exhibit an elastic deformation at low confining stresses i.e. deformation will distort the rock, however, when the stress is relieved the rock will return to its normal

state. At high confining stress rates, that is when the stress exceeds the fracture stress level, the rock will undergo a brittle/ductile change where any deformation due to strain will be permanent and the original form of the rock is never recovered.

Tensile failures fall into one of three categories as shown in Figure 2-5;

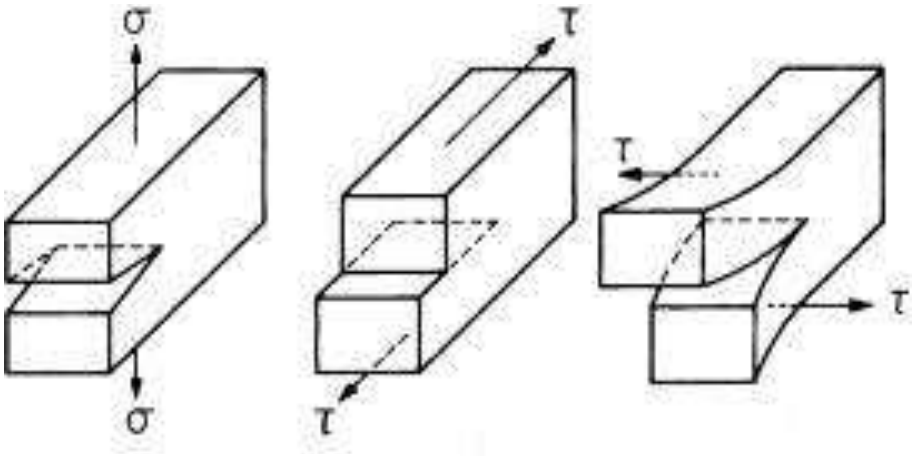

FIGURE 2-5: Tensile Fracture types.

Mode 1: Where the tensile strength is normal to the plane of the fracture (i.e. the fracture will open at 90^o to the direction of the stress which is being applied in a divergent way at 180^o from each other). This is referred to as **Opening Mode**

Mode 2: A shear stress acts in parallel to the plane of a crack and is perpendicular to the crack front. This is referred to as a **Sliding Mode.**

Mode 3: Shear stress acts in parallel to the plane of a crack and the crack front also, referred to as **Tearing Mode**.

2.6 Fracture Analysis

Analysis of the fracture is used to determine the critical stress that is required to allow a fracture to propagate. The stress at which this occurs is called the fracture stress; the typical stress for a brittle/elastic rock is approximately *E*10, where *E* is the modulus of elasticity, i.e. typically ten times its own strength. (Farkas, 2000).

If the assumption is made that the shape of a grain is ellipsoid with the applied stress perpendicular to the major stress then the maximum stress at the crack tip is said to be represented as;

$$\boldsymbol{\sigma_m = 2\sigma_o \left(\frac{\alpha}{\rho_t}\right)} 1/2 \qquad \textbf{2-4}$$

Where:

σ_m= maximum stress at the crack tip
σ_o = nominal applied stress to the crack tip
ρ_t = radius of the curvature of the crack tip
α = the length of the surface crack.

Only when this maximum stress value is exceeded can the fracture propagate. When stress is applied to a rock, the stress will be amplified at the tip of the crack. Therefore, the ratio of σ_m/σ_o is the stress concentration (K_t), (Farkas, 2000), seen in 2-5.

$$K_t = \frac{\sigma_m}{\sigma_o} = 2\left(\frac{\alpha}{\rho_t}\right)^{1/2} \quad \textbf{2-5}$$

2.6.1 Modern fracture mechanics and Griffith's criterion

Albert Griffith (Griffith, 1921) noted that bulk glass materials had very low fracture resistance compared with the theoretical resistance required to break the atomic bonds. He conducted experiments that showed that fracture stress increased as the fibre diameter decreased. He, therefore, concluded that the glass he was testing must have microscopic defects (such as crack tips etc) in the bulk material.

In order to test his theory Griffith (1921) introduced a large flaw into a specimen and placed it in a grip with divergent force introducing stress onto the bulk material as represented in Figure 2-6, below. (Griffith 1921) Griffiths model of energy release is shown below (Alves & De Lacerda, 2012).

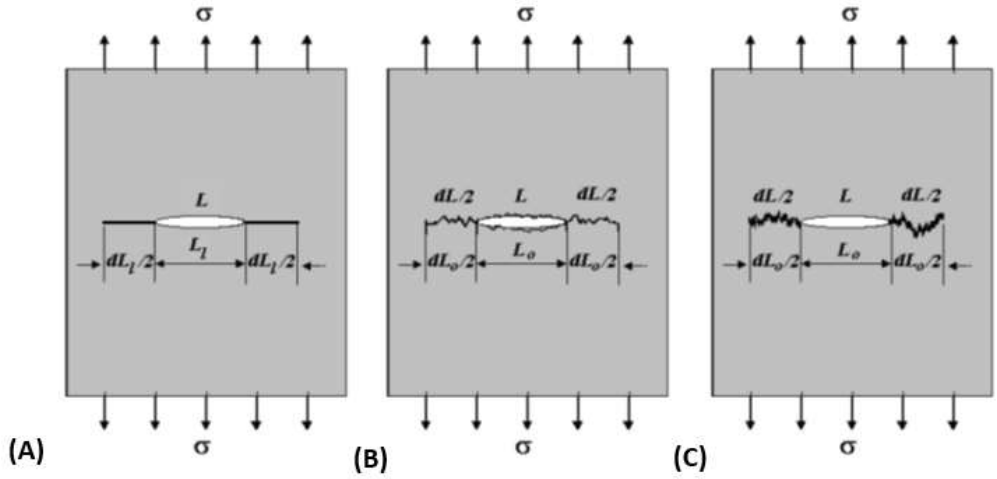

FIGURE 2-6: Griffith model for crack growth introduced in a plate under σ stress: A) Flat crack and initial length l1 increasing to length dl1 B) Rugged crack at its initial length L increasing to length dL. C) Fractural crack, showing increase to dL in fracture length. (Griffith, 1920).

These experiments showed that the product of the square root of the flaw length (α) and the stress at the fracture were constant (σ_c) as shown in 2-6 (Griffith, 1921);

$$\boldsymbol{\sigma_f\sqrt{\alpha} = \sigma_c} \quad \textbf{2-6}$$

Where a growing fracture length introduces two new surfaces, this increases the surface energy. An expression was then devised for the constant (*c*) in terms of the surface energy of the crack as in 2-6 (Griffith, 1921);

$$\boldsymbol{\sigma_c = \sqrt{\frac{2E\gamma}{\pi}}}$$

2-7

2.6.2 Irwin's Modification to the Griffith theory

Irwin (1957) designated the left-hand side of Griffith's equation the energy release rate, this he termed, G. G represents the energy per unit new crack area available for infinitesimal crack extension. Irwin designated the right-hand side of the equation the crack resistance, R, the surface energy increase per unit crack area that would occur owing to infinitesimal crack extension. Thus, G needs to be greater than R for crack growth to occur. Assuming a laboratory specimen is a thin rectangular shape with a crack/flaw perpendicular to the stress applied 2-5 becomes 2-8

$$\boldsymbol{G = \frac{\pi\sigma^2\,\alpha}{E} > G_c = R = 2\gamma_e}$$

2-8

Where:

E = Youngs Modulus

σ = Stress load

α = crack length

G = the strain energy release rate. George Irwin (1957) modified Griffith's original work to incorporate more ductile materials when it was revealed that plasticity had a significant effect on the fracturing of ductile materials. The plastic zone develops around the crack in ductile material. As the stress being applied to the material increases, the plastic zone at the tip also increases until the crack grows; the material behind the crack tip then unloads and this unloading leads to the dissipation of energy in the form of heat. Irwin realised that Griffith's original energy balance term had to have a dissipative term added creating 2-9. (Irwin, 1957).

$$\boldsymbol{\sigma_f\sqrt{\alpha} = \sqrt{\frac{EG}{\pi}}}$$

2-9

Irwin also noted that the asymptotic expression for the stress field around the crack was given as 2-10:

$$\boldsymbol{\sigma_{ij} \approx \left(\frac{k}{\sqrt{2\pi r}}\right) f_{ij}(\theta)}$$

2-10

Where σ_{ij} is the Cauchy stresses, r is the distance from the crack tips and θ is the angle with respect to the plane of the crack. F_{ij} is a variable function. (Irwin, 1960).

2.6.3 Strain energy release rate

Irwin speculated that if the plastic zone around a crack is small compared to the size of the crack a purely elastic solution can be applied to the specimen to calculate energy available in the system for propagating a fracture. This led to 2-11 which is applicable to mode 1 cracking;

$$\mathbf{G = G_i = \begin{cases} \frac{K_1^2}{E} & \textbf{Plane Stress} \\ \frac{(1-v^2)K_1^2}{E} & \textbf{Plane Strain} \end{cases}} \qquad \textbf{2-11}$$

From Irwin's work on 2-9 and 2-10 the strain energy release rate was replaced by the stress intensity and surface weakness energy was replaced by the term fracture toughness leading to 2-12 to 2-14; (Isida, 1966) (Rooke & Cartwright, 1976).

$$\mathbf{K_i = \sigma\sqrt{\pi\alpha}} \qquad \textbf{2-12}$$

Where K_i is the stress intensity
K_c is the fracture toughness

$$\mathbf{K_c = \sqrt{EG_c}} \qquad \textbf{2-13}$$

for Plane Stress

$$\mathbf{K_c = \sqrt{\frac{EG_c}{1-\upsilon^2}}} \qquad \textbf{2-14}$$

for Plane Strain

2.7 Issues with Modelling Fractures

The main areas of concern in fracture analysis, i.e. the main avenues of rock failure, are either tensile or shear, "in direct compression, it is found that, on the micro- and meso-level, the fracturing is essentially a tensile phenomenon" (Tang & Hudson, 2010). The main issue is that complete stress-strain curve results from experimental data are very rare. This is due to the difficulty in conducting an experiment with an un-notched rock to establish a complete stress-strain curve. Then, when they have been produced, the effects of the gripping devices still influence the readings. However, although the experimental data has flaws the curves obtained do show important features and can be considered to show accurate effects of stress on rock causing a tensile failure (Tang & Hudson, 2010). This investigation does not produce a stress strain curve, but, due to the placement of pressure that remains steady, in a tri-axial arrangement, along with a non-destructive scan, we can assess whether the process is essentially either a tensile or a shear phenomenon.

2.8 Shale Fracture Development

There are many factors that will influence the ability of a shale rock to fracture and control the distribution of those fractures. Unlike many other rocks, a Total Organic Content (TOC) rich shale with

highly plastic behaviour will exhibit some common features. These can be split into non-tectonic and tectonic conditions (Ding, et al., 2012).

2.8.1 Non-tectonic factors

These factors include lithology and mineral composition, rock mechanics, TOC content, abnormally high pressure, shale thickness, dehydration and the ductile properties of the clay minerals. Each reservoir will have varying conditions that the shale is subjected to which will affect its propensity to fracture. For example, it has been found that quartz cementation can impact the fracture propensity of sandstones (WalderHaug, 1994), whilst the speed of the change could affect the properties of the rock. If the propagation period is too long the mechanical properties of the rock could change as minerals leach out of the fracture (Olson, et al., 2007). Having multiple specimens and different shale and mudstone types should, therefore, counter the non-tectonic factors.

2.8.2 Tectonic factors

Tectonic factors are the other important source of rock rupture. Higher plasticity shale zones under local/regional tectonic stress will cause the shale to experience ductile shear ruptures. The fractures are termed tectonic fractures and have formed by shear and tension shear and tend to be high angled (Ding, et al., 2012). This investigation will not be able to answer this problem.

2.9 Fracture Complexity

A simple fracture is a single tear in the rock whilst a complex fracture is an amalgamation of multiple tears/fractures with a more complicated nature than that shown by a) in Figure 2-7 (Clarkson, 2011).

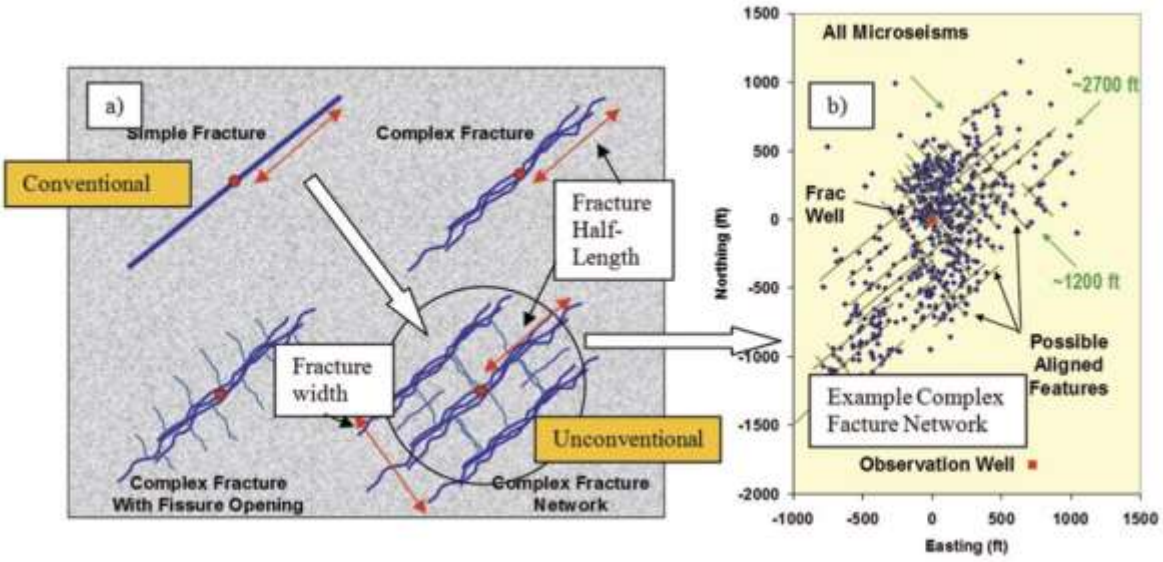

FIGURE 2-7: Simple and complex fractures.

The complexity of the fracture will be affected by the direction that the fracture is initiated from the wellbore. If the fracture is initiated at an alignment parallel to the sediment's bedding then the fracture will be increasingly complex (Bhattacharya, 2011). Due to the ability of complex fractures to increase the reservoir contact to the wellbore they are usually beneficial, though, unlike simple fractures, they provide less cumulative conductivity. The ability to detect the fractures using the non-destructive CT scan technique used in this study will show any complexity of the fractures induced in the different specimen types.

Once the hydraulic fracture has been propagated, gas and oil accumulation will begin along the naturally occurring fractures. Experiments were conducted (Lamont & Jensen, 1963) to model the interactions between naturally forming and hydraulically placed fractures. Typical shale reservoir rocks were cut and then placed in a brace whilst hydraulic fluid was forced through it. In 66% of the experiments the induced fracture was able to cross the simulated natural fracture. As the natural fractures allow the welling and concentration of gas to occur, crossing of these fractures by the induced fractures caused by the hydraulic pressure will thereby increase the amount of gas extracted from the shale. (Lamont & Jensen, 1963). Later studies by Blanton (1982) showed that high differential pressures at a high angle of approach were required to force hydraulic fractures to cross existing fractures, otherwise they were diverted or arrested by the existing fracture (Blanton, 1982). Recent studies by Stanchits, et al. (2011) show that textural complexity in heterogeneous low permeability reservoir rocks, like shale, create more complex fractures. Therefore, the more complex the textures are such as bedding unconformities, veins and boundaries, the higher the likelihood becomes of forming a complex fracture geometry. (Stanchits, et al., 2011). The use of more texturally complex shales as well as more homogenous mudstones that is intended in this project will compliment previous work and will either confirm or modify the results of those previous investigations.

When a hydraulic fracture intersects with a natural fracture the pressure at the intersection point is lower than the pressure required to create the natural fracture. Only if the hydraulic fracture pressure is lower than that of the natural fracture will the hydraulic fracture cross the natural fracture. This is represented by equation 2-15; (Li, et al., 2012).

$$\mathbf{P > \sigma_3 + T_{o,i}} \qquad \textbf{2-15}$$

Scanning the samples from this study before inducing a fracture will show whether any pre-existing fractures are present. If pre-existing fractures are present in the samples then this will allow this investigation to confirm these findings.

2.9.1 Flow through complex hydraulic and natural fracture joints

The more natural fractures present in a shale, the more complex the fracture geometry. This complex geometry can affect the flow of gas and oil, particularly as the fluid becomes more viscous. Bends and kinks in the fractures and where they join will act as choking points causing proppant blockages. Injection pressures of the proppant will decrease until the hydraulic fracture intersects a natural fracture. Upon opening a natural fracture the injection pressure will increase and will only decrease again upon the start of propagation of the fracture itself (Sesetty & Ghassemi, 2012), Figure 2-8.

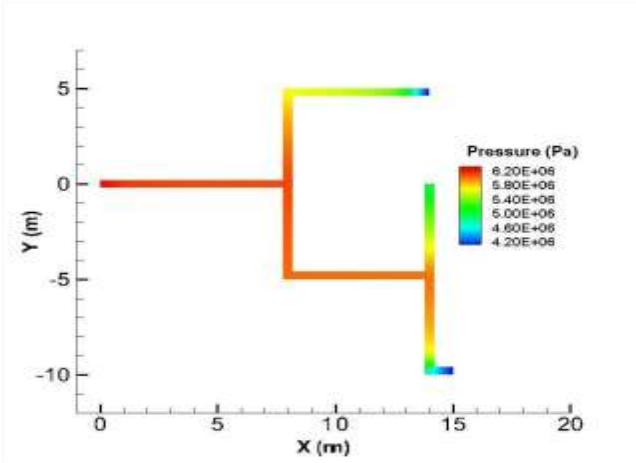

FIGURE 2-8: Contour plot of fracture pressures at 35 seconds.

2.10 Fracture Geometries

Early research into fractured rock assumed that the plane stress was vertical to the orientation of the sediments; therefore, the width would not change for vertical fractures (Kristianovic, 1955). This meant that the width of the fracture could be assumed to be constant (Howard & Fast, 1957) enabling a model to be made that allowed engineers to calculate the fracture area based on leak-off characteristics. This model worked on the principle that the geometry of the fracture would be simple bi-wing planar geometry. This condition was further compounded by the observation that a fracture occurred perpendicular to the weakest of the three principle stresses.

TWO DIMENSIONAL (2D) MODELS

2D models evolved as one of the dimensions always remained fixed. The Howard and Fast model proposed in 1957 was 2D but was later supplanted by revised newer models that were more suited to the individual conditions experienced in the reservoir.

2.10.1 Perkins-Kern-Nordgren (PKN) model (T. K. Perkins, 1961)

This model was used when the fracture length was greater than the vertical height of the fracture, thus the fracture length could be used as the non-varying parameter. This model gave an elliptical shape, as shown in Figure 2-9, and used the formula shown in 2-16, although this equation and model did not

deal with fluid leak off or the fracture volume change as it travelled further from the point of the fracture initiation, it did give an approximation of a long fracture and its dimensions.

$$W = 0.38\left[\frac{Q\mu L}{E}\right]^{\frac{1}{4}}$$

2-16

Where:

Q = injection rate, L^3/t
μ = fluid viscosity, m/Lt
L = fracture half length

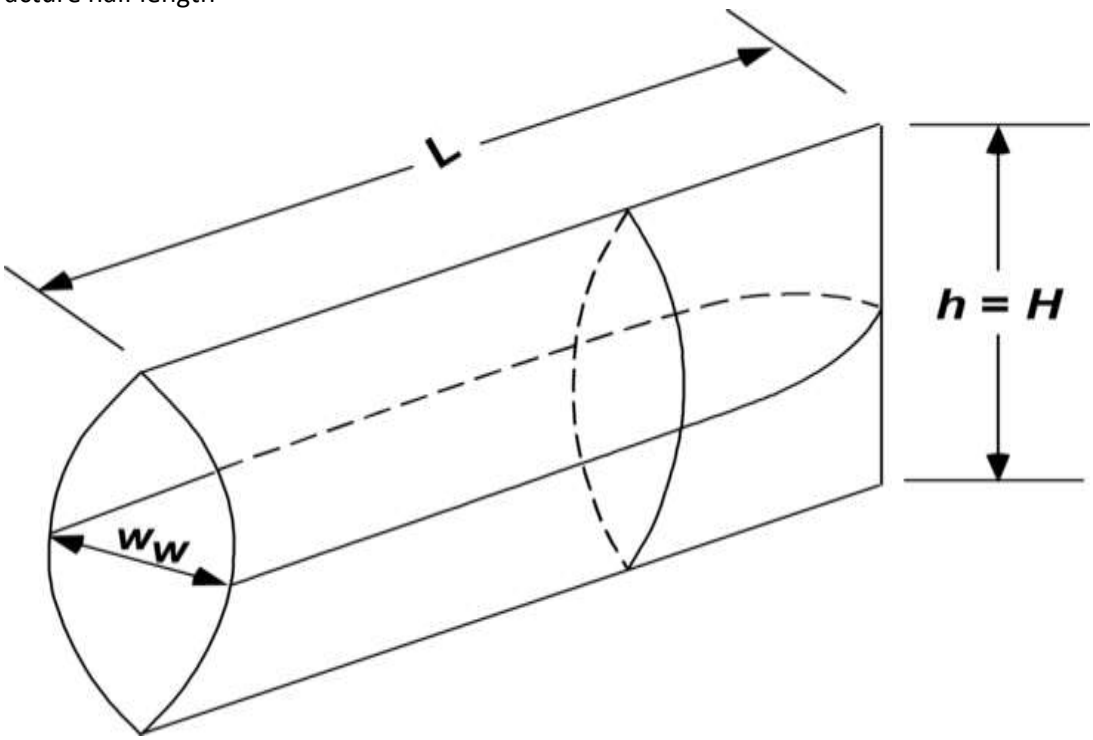

FIGURE 2-9: PKN Model.

$$\frac{\delta\Delta p}{\delta x} = \frac{64}{\pi} - \frac{q\mu}{Hw^3}$$

2-17

Where:

δΔp = change in net pressure in the fracture, m/Lt^2
∂x = incremental distance down the fracture, L

2-17 was used to calculate the pressure distribution along the fracture for any given combination of injection rate, fracture fluid viscosity, fracture height and fracture width.

2.10.1.1 Nordgren Modification to the PKN

Further modifications were made to the PKN model to take into account the fluid leak-off and fracture volume change as shown in 2-18 (Nordgren, 1972).

$$W(0,t) = 4\left(\frac{2(1-\nu)\mu q_i^2}{\pi^3 GCh}\right)t^{\frac{1}{8}}$$

2-18

Where:

G = Shear modulus, m/L3

2.10.2 Kristonovich-Geertsma-Daneshy (KGD) 2D Model

Originally proposed by Kristonovich (1955) and later modified by Geertsma and De Klerk (1969). This model was created for circumstances when the fracture height was greater than the fracture length, this is particularly useful when a 'short/fat frac' is required. For example, in conventional fields where fractures are used instead of gravel packing to control sand ingression into the wellbore. This 2D model will not provide a completely realistic dimension but will provide a guide. The designer fixes a dimension, usually the height or width, and from that creates a model. By comparing the model to the actual results the designer can then rectify the model for future fractures/stimulation effects in that reservoir, though this is an iterative process and not a perfect model. This model works by incorporating a basic fluid loss, of the fracturing fluid, in the fracture model and proposing a simple equation to decide the width of the fracture. See 2-19 and Figure 2-10. (Geertsma & F. De Klerk, 1969)

$$W_w = 2.1x^4\sqrt{\frac{\mu QL^2}{Gh}}$$

2-19

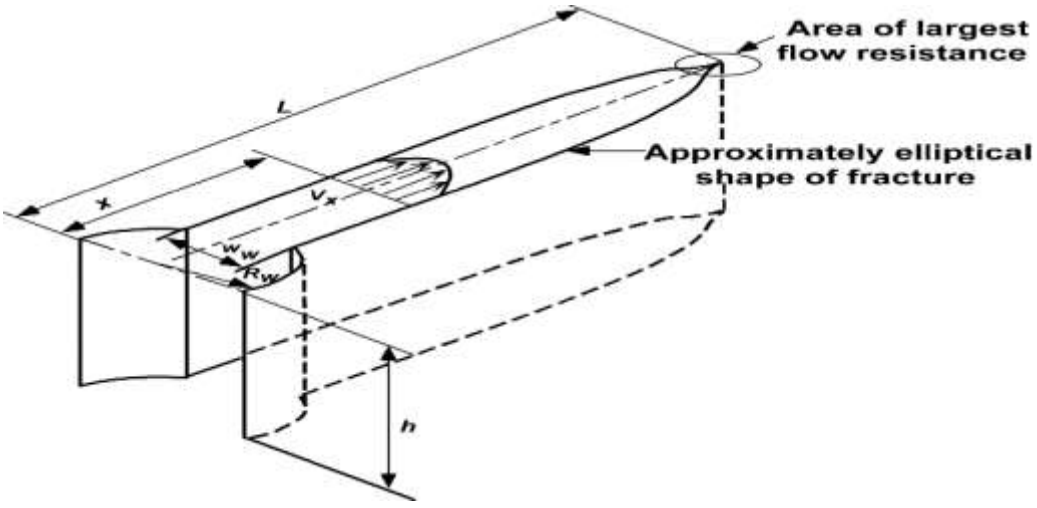

FIGURE 2-10: A typical KGD model.

2.10.3 Three dimensional (3D) models

The advent of computers has facilitated more accurate and detailed pseudo 3D and 3D models to be formulated and used. The computer models utilize the complicated data and variables from each reservoir to produce more accurate fracture propagation predictions by using complex algorithms.

These programs can calculate the fracture height, width and length distribution using all the geological data collected from surveys.

The complex algorithms used to derive the 3D fracture propagation models were theorised and initiated in 1989 (Gidley, et al., 1989). These simulations made use of the data by integrating the interactions of the geomechanics from each individual reservoir to calculate more accurate and realistic fracture geometry – these evolutions are described in more detail in Section 2.11. As computer processing power has increased so too has the accuracy of the simulation models as more and more data can be incorporated. The accuracy of a model relies heavily on the amount of data that is used in the simulation; more data ensures greater accuracy as reservoir conditions can be more precisely replicated. This helps the designer to develop the most accurate well.

2.11 Geomechanics; Their Evolving Role in Simulation Modelling

Historically, when conducting a simulation an engineer would make use of the time invariant rock compressibility (c_r). Initially to create a more realistic model engineers would incorporate an arbitrary spatial variation but this did not take into account how the geomechanics of the reservoir were coupled to the fluid flow. The following section describes the evolution of the fracture model towards a more accurate reflection of the variable parameters encountered in a reservoir. Whilst some of these parameters are not being explored during this study they have been included for completeness.

2.11.1 Pore-volume coupling

Traditionally porosity (φ) was regarded as a function of the pressure (P) exerted due to the rock compressibility, as shown in 2-20.

$$\boldsymbol{\phi = f(p) = (\phi + c_r[p - P^0])} \quad \textbf{2-20}$$

Therefore, change in pore volume was given as 2-21.

$$\boldsymbol{V_p = V_b^0 \phi} \quad \textbf{2-21}$$

However, the change in pore volume is due to complex interactions of pore pressure, stresses that are applied to the rock, and temperature. A combination of stresses and pressure changes results in the rock being deformed. This deformation changes the bulk volume of the rock (V_b), as shown in 2-22.

$$\boldsymbol{V_b = V_b^0(1 - \varepsilon_v)} \quad \textbf{2-22}$$

This will allow the true value of the porosity to be given by 2-23.

$$\boldsymbol{\phi = V_p/V_b} \quad \textbf{2-23}$$

As both pore volume and bulk volume are variables, true porosity and pore volumes are functions of pressure, temperature and stress as shown in 2-24,

$$\boldsymbol{\emptyset = V_p/V_b = f \cdot (p \cdot T \cdot \sigma) \cdot V_p = g \cdot (p \cdot T \cdot \sigma)}$$

2-24

thus, demonstrating the relationship between fluid flow and geomechanics. (Darve, 1990). This is referred to as stress modelling; where porosity & volumetric strain changes are derived from two complex constitutive relations of the material.. This gives the definition of stress-strain behaviour and also that of the volumetric behaviour. (Darve, 1990) showed that for pressure changes to be determined accurately in a simulation it is essential that pore volume is changed to reflect the values calculated. This is known as the volume coupling arrangement. There are two main ways to carry this out on 3D and pseudo 3D computer models but in both cases the coupling of the stress-strain solution replaces the treatment of porosity by rock compressibility that was originally used.

2.11.2 Coupling of flow properties

This coupling arrangement relies on the dependence of permeability upon the stresses applied and is shown in 2-25 (Lorenz, 1999).

$$\mathbf{k} = \mathbf{f}(\boldsymbol{\sigma}_{\mathbf{eff}}) = \mathbf{f}\left(\boldsymbol{\sigma}_{\mathbf{avg}} - \mathbf{p}\right), \boldsymbol{\sigma}_{\mathbf{avg}} = (\boldsymbol{\sigma}_{\mathbf{x}} + \boldsymbol{\sigma}_{\mathbf{y}} + \boldsymbol{\sigma}_{\mathbf{z}})/\mathbf{3}$$

2-25

This equation works on the principle that changes of stress in any of the directions of loaded stress would cause a change in the porosity. This coupling arrangement was derived for cases where the permeability has decreased to less than < 1 mD hence it can be used primarily on fractured shales and other reservoirs that require stimulation to improve their productivity. The fracture aperture is stress dependent so creating fractures causes large anisotropic changes. The above coupling arrangement deals specifically with this issue where tensor character of permeability may be important in these applications. Lorenz (1999) also found that this arrangement was suited to soft or unconsolidated formations. These formations deform easily on the application of stresses and strains as the pores dilate (widen/lengthen) and thus will increase in permeability. However, there is a time lag between the formations undergoing reloading of stresses to increasing in permeability. These changes in permeability are a function of some measure of effective stress.

2.11.3 Reservoir compaction and dilation

It is important to model compaction in soft and thick reservoirs where compaction may produce a large scale volumetric change in the production rates, or ground subsidence or even a well failure. To model compaction a modification to the reservoir model was incorporated and numerical additions were made to an existing model of a reservoir (Finol & Farouq Ali, 1975). This was expounded throughout the 1970's and 1980's with modifications taken from observations made in Venezuela's Basin (Merle & Kentie, 1976). In 1981 further effects of compaction on petroleum production (Rattia & Ali, 1981) were investigated in association with uplift procedures whereby the efficiencies of the steam lift on production were simulated. In 1989 new technology was used to assess the effects of compaction due to the fluid extraction from the reservoir. This made use of hysteresis caused by the limited rebound of steam injection and was made more realistic by incorporating the effects of the creep (relaxation time of the stresses applied). (Chase & Dietrich, 1989). The original solution and subsequent modifications

and additions enabled the calculation of the porosity change by modifying the reservoirs compressibility as a function of pressure, using only conversion tables based on observations of a particular reservoir. The unifying feature of all these reports was that they used a model that treated compaction in one dimension. This assumed that only vertical strain occurred, and that each vertical column of formation blocks would deform independently of each other. Using a table meant ignoring the contribution of stress as shown in equation 2-24. In 1998 a solution to this problem was suggested by coupling the simulator of the reservoir with the stress-strain solution, by using an iterative coupling (Settari & Mourits., 1998). This made use of combining the multiphase flow in the reservoir and elastic plastic solution of deformations. This meant a much larger area could be included than previously used so the simulation could take into account the whole reservoir as well as the reservoir's side, under and overburdens, to produce a much more realistic model.

2.11.4 Evolution of stress-dependent flow properties

This mainly deals with modelling the effects of permeability; as equation 2-25 shows this is dependent on effective stresses. Modelling this property was based on using tables of pressure versus permeability. In 1984 simulation modelling was attempted to account for the fracture mechanics, fluid flow and heat transfer of the fracture and reservoir and these results were published (Settari & Price, 1984). The model endeavoured to incorporate physical features that had previously been ignored including the stress related changes of permeability. The model achieved good results for the particular reservoir the simulation was based on, but only for that reservoir, this showed that local constraints needed to be added to the pressure tables.

In 1992 the first attempt at coupling the stress-strain solution using only the flow properties was employed to study permeability changes in the North Sea (Heffer, et al., 1992). This study was then expanded to show that coupling allowed the prediction of permeability changes in the reservoir due to fracture opening or dilation of the joints (Stephansson, 1996). Attempts to make even more accurate models led to the simulations that could account for the differences in the rock formation (anisotropy) which causes fracture orientation, and it was recognised that this would require a full transmissibility tensor into the flow model. In 1998 this was successfully shown for the first time (Koutsabeloulis & Hope, 1998). Using the same principles, a model was successfully devised to show how hydraulically induced fractures can grow in the future. This was achieved by having the fractures represented by dynamically changing transmissibility multipliers, the effect of which was placed in the model in the area identified as the potential fracture plane (Settari, 2000). Although this investigation will not look at the porosity or compaction of the shale, the rig as designed will allow future investigation to accurately model those parameters.

2.11.5 Fracture conductivity in different parts of a fracture

Suare-Rivera (2013) investigated the differences between the fracture conductivity of a fractured rock and then concluded that when a rock is propped four different regions of the fracture can be assigned:

1) Wellbore - found to have the lowest surface area contact but highest level of proppant and highest fracture conductivity.

2) Wellbore/fracture connector – choke point of proppant area.

3) Near wellbore fracture.

4) Far wellbore fracture network – highest surface area but lowest connectivity due to the low proppant concentration being low. This affects the productivity of well, with an area that can be improved.

The ability to scan the sample using a non-destructive technique will allow this investigation to see if these four different regions exist in a non-propped rock, or if a similar pattern along the half-fracture can be seen. Although the rig has been built to accommodate the use of a proppant there was not sufficient time in this study to incorporate that objective.

2.12 Principles of Acoustic Monitoring

An acoustic emission is the release of an elastic wave through a solid material due to the redistribution of stress. Kishinouye (1937) published what would later become the first study into acoustic emission testing anywhere in the world when he looked at wood that was bent by stress deformation that had a steel needle attached to a phonograph. This was done to try and mimic rocks during an earthquake (Kishinouye, 1937). This study relied on the same principle that had been observed for a number of years previously during the failure of rocks and metals. The principle relies on stress being placed on a body which leads to a strain displacement of said body. The strain displacement induced by stress causes a realignment of the atomic planes, which is referred to as a dislocation and which, in turn, forms microcracks. This microcracking releases elastic waves, in the form of AE, that propagate through the material and are picked up by the sensor which then converts the energy into an electronic signal, (Ohtsu, 1995) Figure 2-11 a principle that will be made use of in this investigation, when using acoustic emission software to detect the speed and position of the fracture propagation.

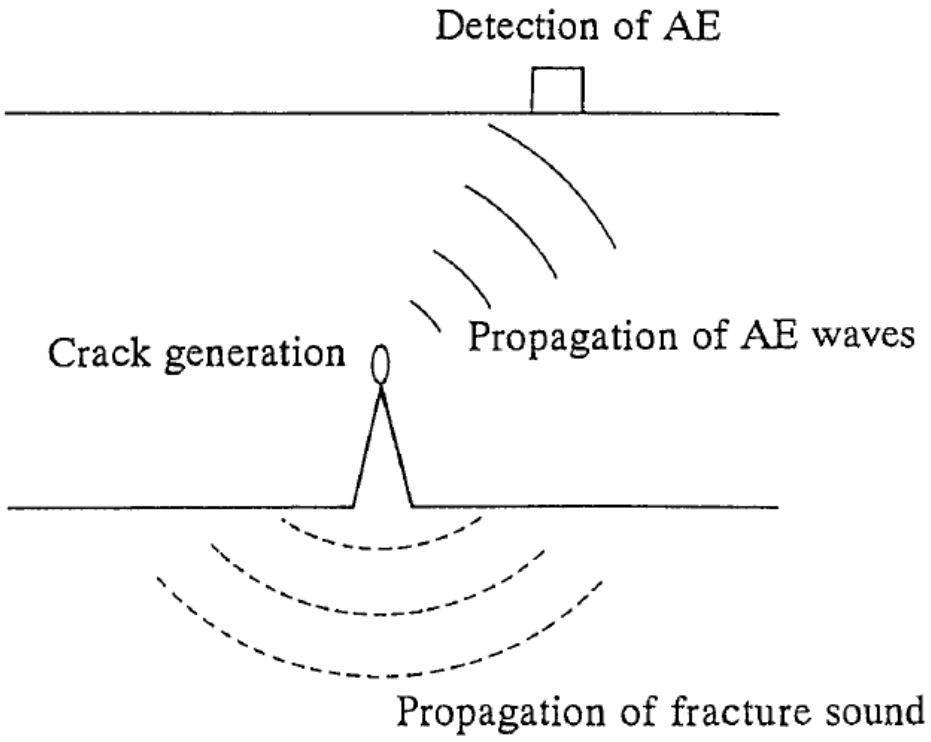

Figure 2-11: Acoustic emission generation.

The importance of acoustic emissions in engineering was investigated in the late 1940's by Joseph Kaiser, his findings (Kaiser, 1950) were based on the observation that prior to the catastrophic failure of metal, pressure vessels were reported to emit sounds. The acoustic recordings showed a peak occurring at the same time as the yield strength of the metal being tested, shown in Figure 2-12 (Kaiser, 1950). Kaiser's study revealed that when a load placed on a sample was removed the sample did not emit a noise until a new load was reapplied that had surpassed the previous load – this became known as the Kaiser effect. He also suggested that by identifying the load at which an acoustic emission is first detected tells the observer what load has previously been applied to that specimen. Kaiser's work (1950) centred on the acoustic emissions detected by a microphone when a load was placed on different metals.

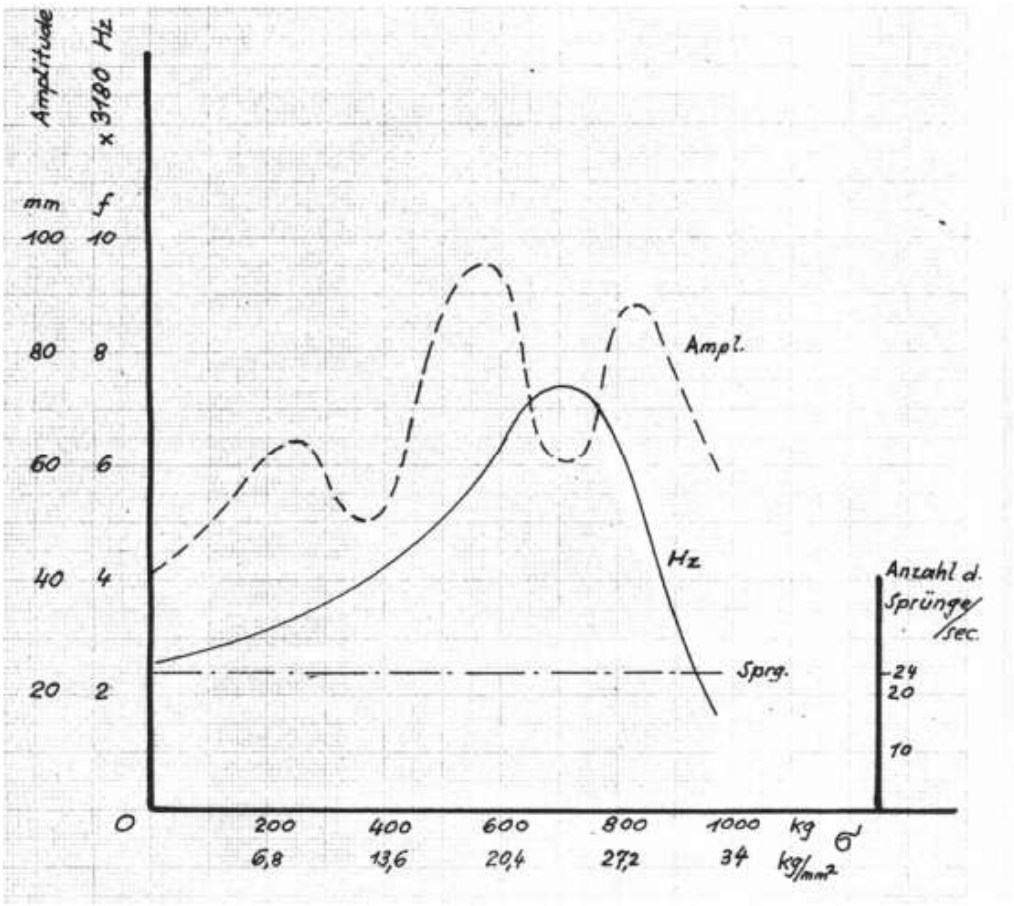

FIGURE 2-12: Joseph Kaiser's original findings showing acoustic emissions correlated to yield strength.

The early years of acoustic emission testing was directed primarily towards aeronautical, ship building and pressure vessel design and largely involved research in metals. Bradford Schofield (1963) coined the term acoustic emission (AE) when he studied the effects of surface oxides on single crystals of aluminium under pressures in different directions. He noted that the impurities aided the creation of a fracture that could create a high frequency acoustic emission that could be detected by sensors (Schofield, 1963), Figure 2-13.

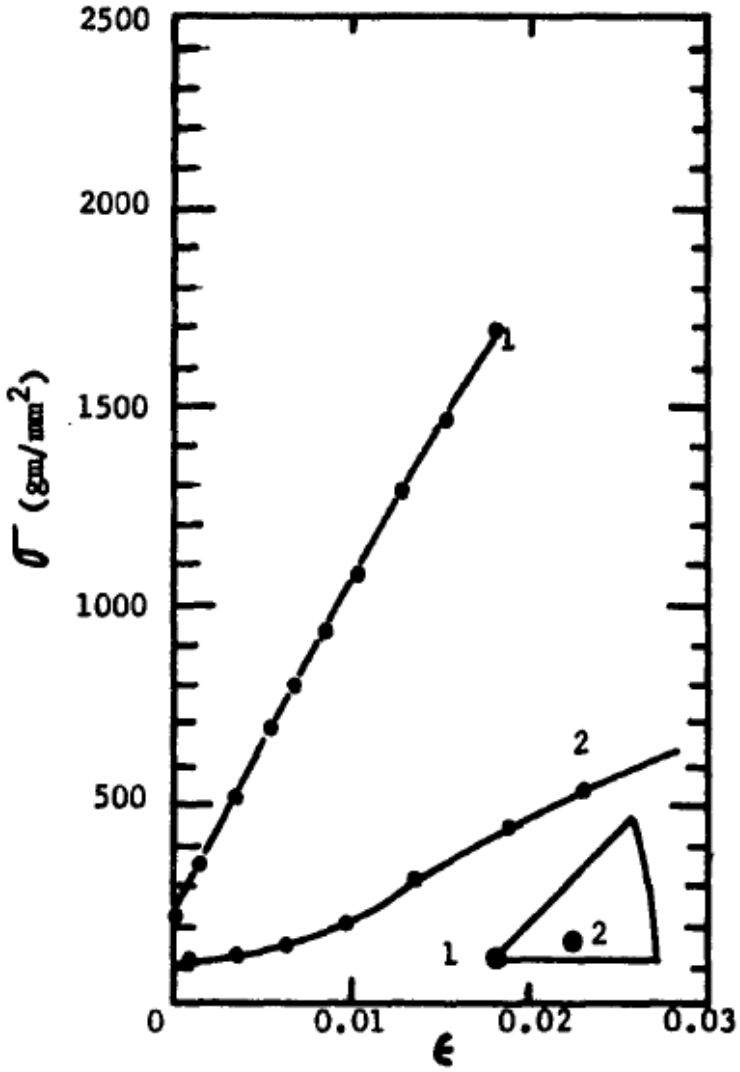

FIGURE 2-13: **Stress-Strain Curves and axial orientations of aluminium single crystal test specimens.**

2.12.1 Felicity Effect

Until the 1970's it had been assumed that the 'Kaiser effect', whereby an AE was created when stress was added to an object, would mean that a further acoustic emission could not be emitted once that stress was released, until the initial stress levels were surpassed, Figure 2-14. However, during the 1970's this assumption was determined to be incorrect when vessels made of glass fibre reinforced thermoset plastics (FRP) suffered from catastrophic failures during use. One study showed that wave propagation could occur when the area was under less stress than that previously applied (Pollock & Cook, 1976) whilst a study by Adams (1982) put FRP under flexural tests and concentrated on the emissions during a static pressure test focussing on the amplitude and frequency of the returns. The graphical representation of some of this effect on laminated products is shown in Figure 2-14 and is known as the Felicity effect. Originally this effect was deemed a curious anomaly, it was only later that

the implications for fracture mechanics were realised. The Kaiser effect was originally observed in boilers made of nearly pure metal, whereas the Felicity effect was noted in materials that were not of a uniform construct. The Kaiser effect occurs in materials of uniform structure and composition and the Felicity effect occurs in materials made of different components and of varying structural composition. As shale is complex in its structure and composition, while mudstone is relatively more homogenous, though not completely homogenous, this study will utilise this knowledge to determine the location the acoustic emission is emanating from within the sample.

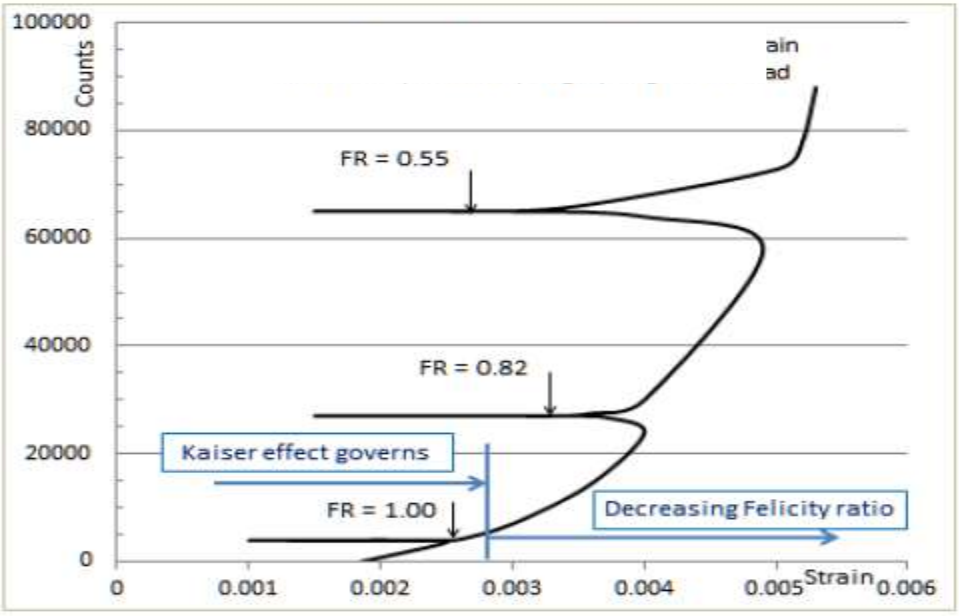

FIGURE 2-14*: The felicity effects in graphical form showing the effects on different laminate products used in Aircraft*.

2.12.2 The importance of AE in detecting failure and microcracks

As it was the FRP industry that initially investigated the Felicity effect, the relevant companies agreed to form the Committee on Acoustic Emission from Reinforced Plastics (CARP) in order to draft a procedure on the AE testing of FRP materials. This study was finally achieved by Adams (1982) as mentioned above but prior to this study CARP continued the assessment of AE with Thomas Crump (Crump & Droge, 1979) testing FRP samples that had been corroded by a 5% sodium hydroxide solution for periods of up to a year. The samples were then loaded, and AE was recorded showing a positive correlation between increased loss of strength of the FRP with increased duration of exposure to the solution (Crump & Droge, 1979). The wavering lines of the results presented in Figure 2-15 shows again the importance of AE in detecting failure and microcracks/fractures before they are visible.

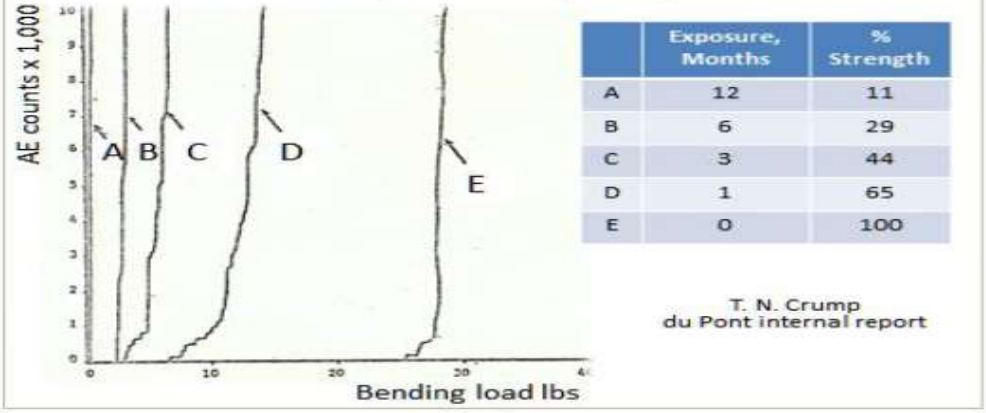

FIGURE 2-15*:* T.N Crump report on degradation of FRP as proved using AE.

The same principle for detecting failure was then applied to brittle elastic rock with more impurities than a relatively homogenous material structure such as steel or concrete. The technique of mapping using AE was first tried in 1986 to map the fracture faces of a dense granite (Halcomb & Costin, 1986). The fact that a granite is a very dense heterogeneous material proved that the propagation waves could still be detected with a high degree of precision. In 1989 Wang et al. lead a team which investigated geothermal fractures caused by heating a small granite rock sample and inducing stress to create a fracture. Using a series of digital sensors Wang et al. (1989) were able to present the first reasonable attempt to map the initiation of a fracture in a rock (Wang, et al., 1989). As the equipment evolved and became more sophisticated the ability to map and pin-point fractures became greater.

2.12.3Concrete Testing

Acoustic Emission detection has long been used by engineers to test concrete material designs and structures. Concrete is another dense material and can be non-homogenous as shown in (Murakami, et al., 1991).when the slow and delicate growth of a fracture due to freeze thaw weathering was mapped. While the ability of the emission detection sensors were proven to be able to not only pick up the shock wave of these fractures as they grew but also to detect the variations of the amplitude and their frequency which then allowed a greater understanding of when the speed and effect of the fracture growth was greatest in the freeze thaw period (Ohtsu, 1995), Figure 2-16.

A

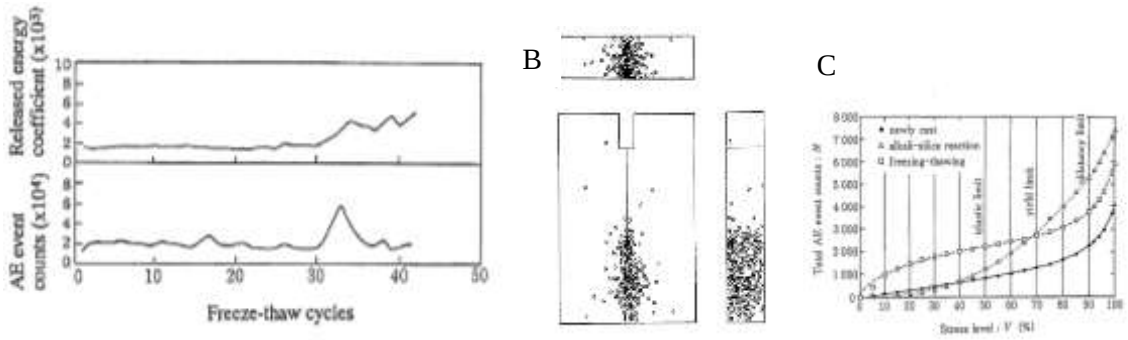

Figure 2-16: Plots showing A) the freeze/thaw cycle the concrete was subjected to; B) the location of the emission source; C) the total AE event count versus stress level in the concrete sample.

2.13 Chapter summary

The literature review describes the importance of unconventional reservoirs and the need to efficiently extract the hydrocarbons contained therein. The process of fracture induction and the ability to accurately model the volume of oil likely to be produced is determined by the depth of understanding of how a fracture evolves in complex heterogeneous materials complicated by geomechanical interaction. For this reason, the history of fracture modelling and application of geomechanical factors has also been reviewed. This investigation will add actual experimental data to the results of the models to further the understanding of fracture propagation under reservoir conditions by applying triaxial stress to different shale samples and monitoring the fracture growth. Acoustic emissions are an integral part of this study as acoustic sensors will be used to detect the fracture and map the evolution of fracture growth.

The next chapter will describe the process in which the fracturing rig was designed and built, along with a detailed methodology of the experimental procedure and a comprehensive description of the equipment used.

3 Apparatus Design

3.1 Structure of the investigation

AS THIS STUDY INVOLVED A NUMBER OF COMPLEX RE-DESIGNS, REBUILDS AND AMENDMENTS THE STRUCTURE OF THE INVESTIGATION HAS BEEN LAID OUT AS DETAILED IN

Figure 3-1. To make the process easier to follow the flow chart shows the breakdown of the structure of this report and the structure of the investigation as carried out.

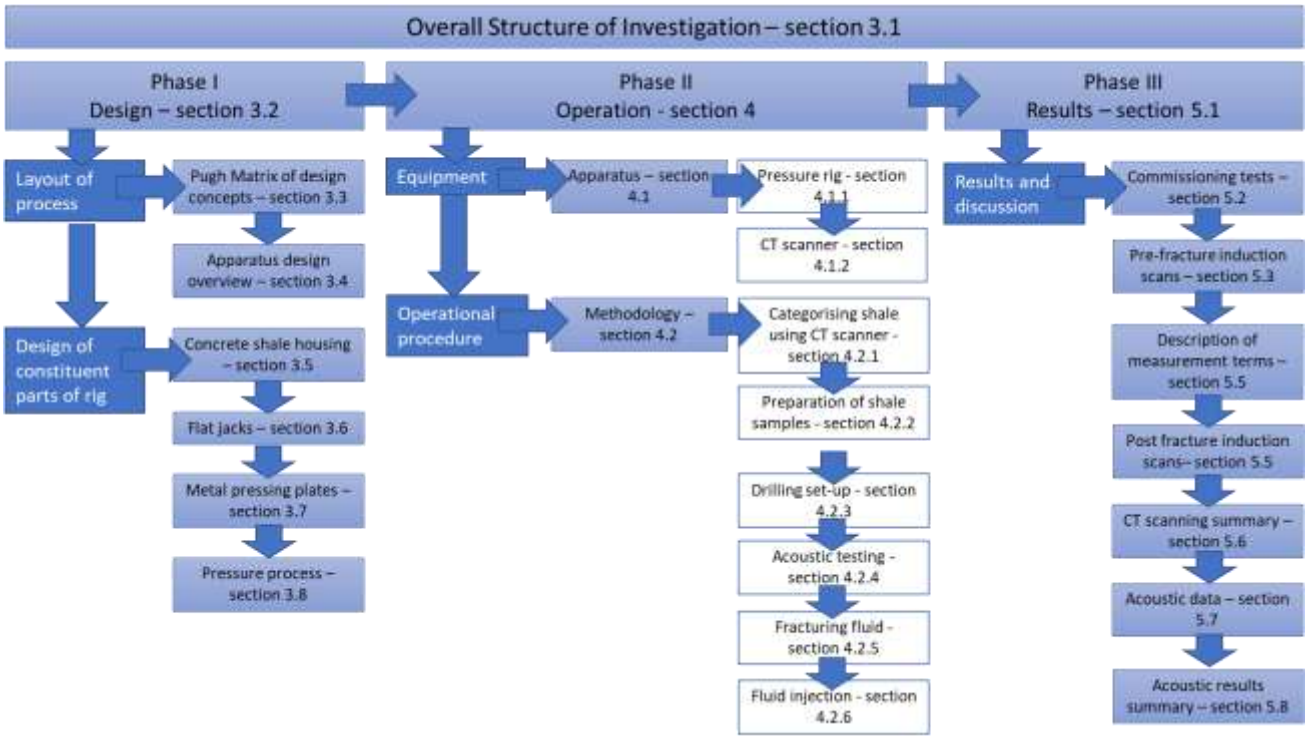

FIGURE 3-1: Flow diagram of the breakdown of the investigation.

3.2 Design (Phase I)

When designing such a complicated structure, the process inevitably involves a number of iterations. In order for these iterations to flow smoothly and to ensure that the design is completed effectively it is important to show the clear progression and evolution of the design, build and testing. Figure 3-2 shows the process that was used when designing the rig that is central to this investigation.

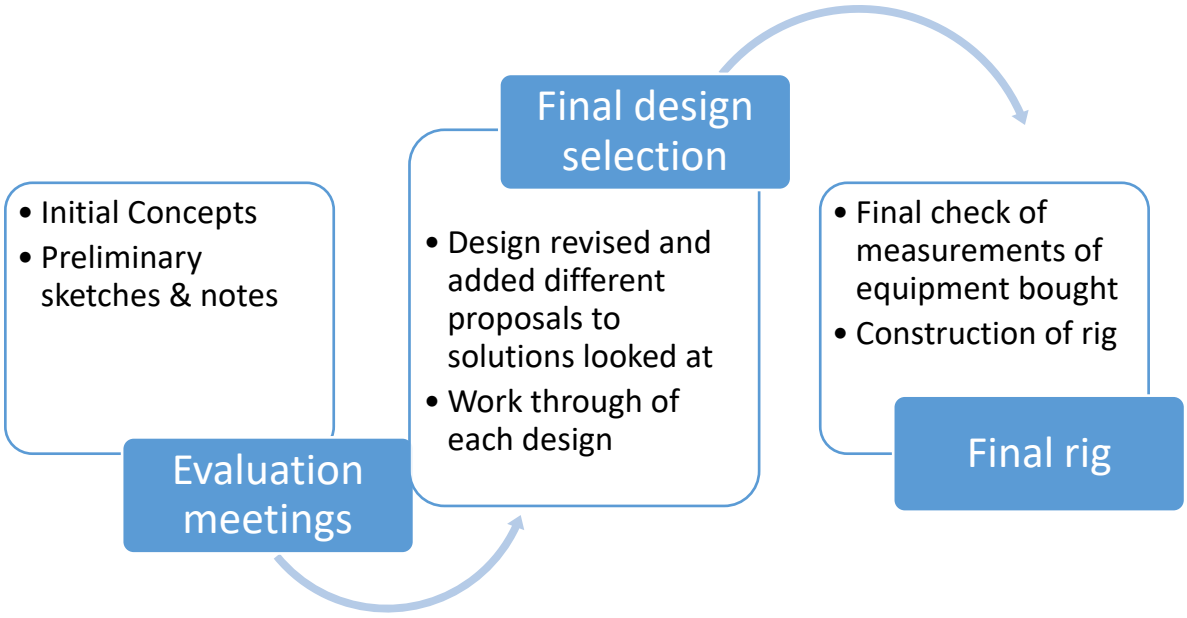

FIGURE 3-2: Flow chart showing the design evolution process.

The flowchart, Figure 3-2, shows the process that was followed when designing the apparatus needed to carry out the experiment. This report provides the detail of the progression of how the design evolved from the initial brainstorming through to the build and ensuring that each part marries easily into the next and that all the processes are workable. Finally, this design section then shows the approved, as built, final design and construction of the rig and the methodology process. To assess which plan would be taken through the design process all initial concepts were processed through a Pugh matrix to evaluate which would be the most beneficial and effective.

3.3 Pugh Matrix of the Design Concepts

At the start of the investigation there were four basic design concepts. To move on to the final design stage each concept was first measured against the others using a Pugh matrix. The concept scoring the highest was then taken further with each stage being designed from the initial concept through to the preliminary design before the final design was settled upon. The four concepts that were assessed are presented below.

Concept 1; A reinforced concrete structure would be constructed. This structure would have a square void housing a cubic shale sample with flat jacks positioned on all faces of the sample thus allowing a

true tri-axial pressure arrangement to be made. This concrete structure would then be placed inside a metal poly axial stress container to provide increased safety.

Concept 2; This concept was the same as concept 1 but with the concrete structure being constructed out of metal instead as this would be more hardwearing and it would make it easier to contain fluid.

Concept 3; A shale core sample would be placed within a concrete structure but with a cylindrical void housed inside the top half to allow shaped pistons to apply pressure. However, this concept would only involve the sample being subject to bi-axial stresses.

Concept 4: Similar to concept 3 however the concrete structure would be replaced by a strengthened steel structure.

The Pugh matrix evaluation of these concepts is presented below in Table 3-1, where:

+ = the option scores a positive

- = thee option scores a negative

S = the option is neutral

Key Criteria	Weighting	Concept 1	Concept 2	Concept 3	Concept 4
Costings	2	+	-	+	-
Abilty to reduce size of the sample	1	S	S	-	-
Risk to services reduced	3	+	+	+	+
Abilty to take live acoustics	5	+	+	+	+
Reduce movement of samples	4	S	S	S	S
Abiltity to Easily replicate Tri-axial arrangement	6	+	+	-	-
	Sum of all positives	16	14	10	8
	Sum of all negatives	0	-2	-7	-9
	Total	16	12	3	-1

TABLE 3-1: Pugh diagram, charting the strengths and weaknesses of the different concepts.

As shown in the Pugh diagram the first concept is the idea that scores the highest. Therefore, this was the concept that was chosen to be the main feature, with each separate stage being subject to the design evolution shown in Figure 3-2.

3.4 Apparatus Design Overview

In order to investigate the fracturing process of a shale core under tri-axial pressure conditions a rig needed to be designed and built that would allow the shale sample to be subjected to the same conditions that would be experienced in an in-situ shale formation i.e. tri-axial - the directions of forces applied to a rock are shown in Figure 3-3. To briefly summarise a concrete structure was devised to work in partnership with a high-grade steel frame that would act as a poly axial stress frame. The concrete to be used was C60 grade, a high strength concrete, selected for its ability to withstand huge pressures, whilst simultaneously being able to house the flat jacks, steel plates, metal plates and acoustic sensor that surrounded the shale sample. As the project has progressed the design has been amended and refined but a number of characteristic elements have remained the same throughout the project, these are described below

.

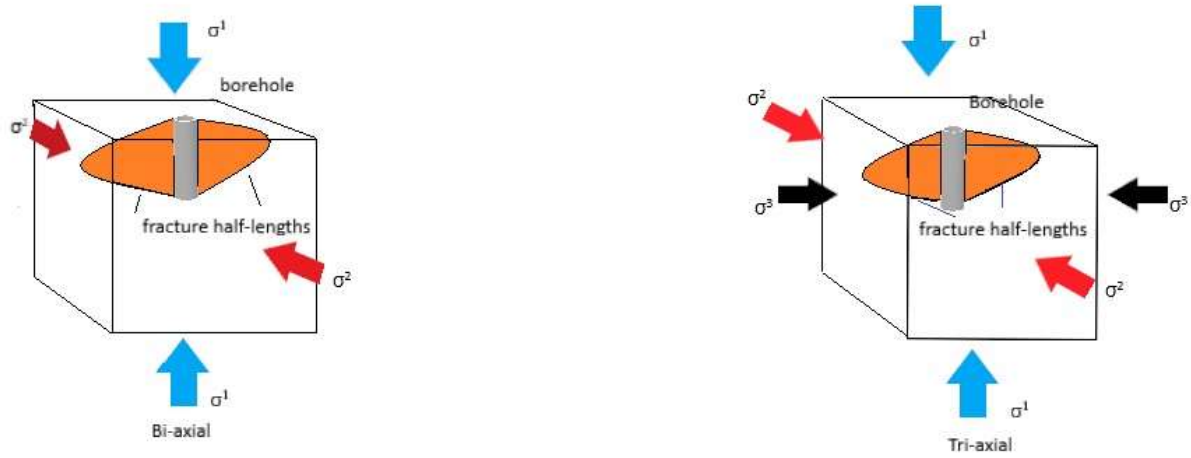

FIGURE 3-3: Pressure arrangements placement.

3.5 Concrete Shale Housing

3.5.1 Concrete stress frame and reservoir simulation

INITIAL CONCEPT

The experiment relies on the placement of a shale sample surrounded by the flat jacks, metal plates, load cells and the power and electrical wires. The plates are to ensure that the pressure applied to each face of the shale sample is equal. The plates also house the acoustic sensors protecting them from being crushed whilst, simultaneously, allowing the detector to rest on the face of the shale to detect the emissions from the subtle pressure changes as the fracture evolves. A void had to be designed that would allow for all of the above and yet maximise the width of the concrete, which would be needed to take the immense pressures involved. This necessitated the design of a void that was based around a central cuboid shape, but which had thin arms that would protrude from each corner to house the in-flow and outflow hydraulic pipes of the flat jacks. The original design is shown below in Figure 3-4.

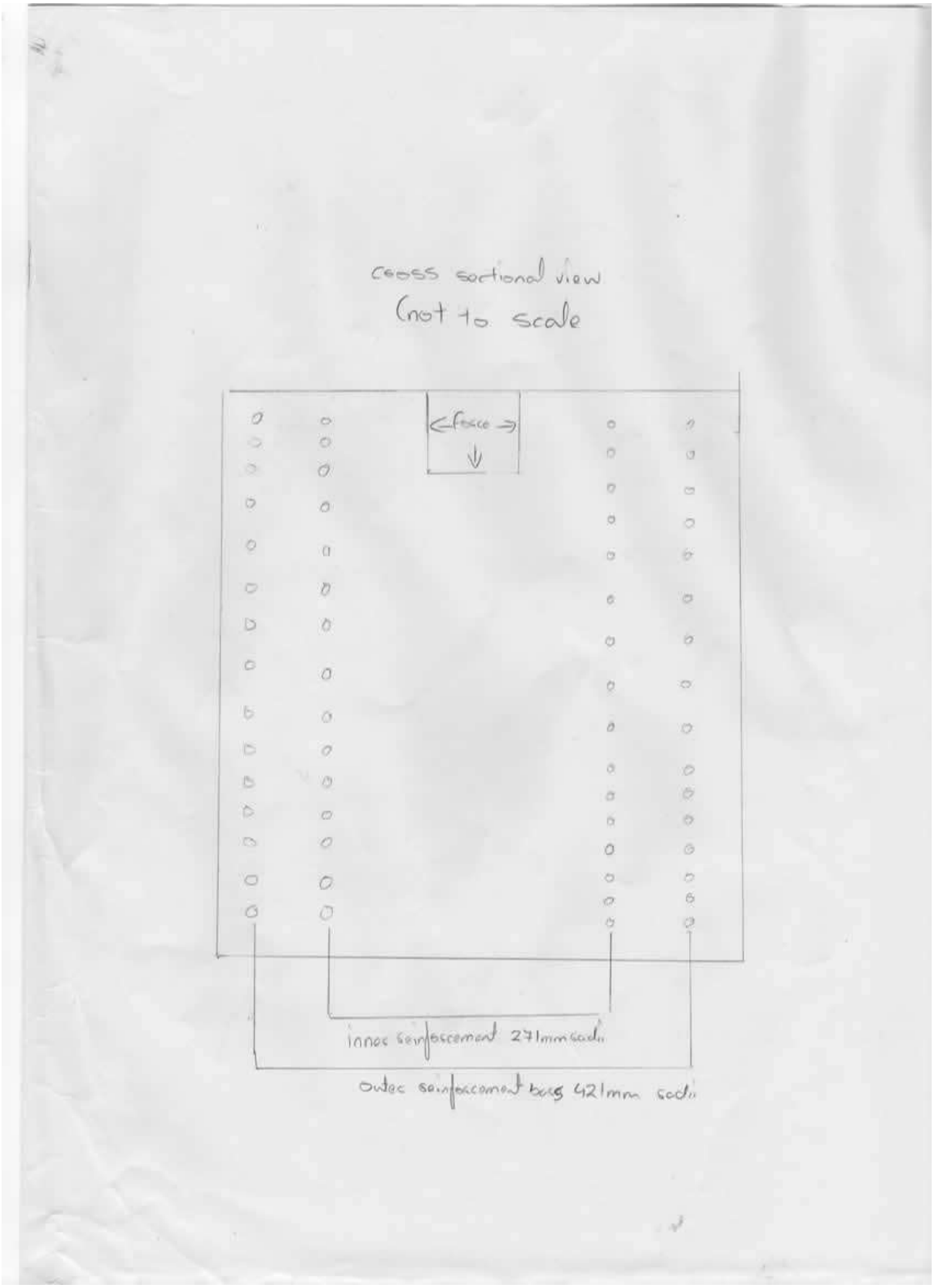

FIGURE 3-4: Concept sketch to show concrete void.

PRELIMINARY DESIGN

In the initial design stage a load cell of 100mm diameter was settled on to measure the loads applied to the shale. However, whilst working on the design it became obvious that space taken up by the load cell would restrict the ability to place hydraulic lines and sensors within the void. Therefore, in order to calibrate the flat jacks and ensure that they were exerting the same pressure as that shown on the pressure gauge, the flat jacks were placed in pairs and then subjected to a pressure measuring device. These results were then compared to the pressures recorded on the pressure gauge.

During the final discussion stages concern was raised that the excessive void size would create difficulties when holding the fluid at pressure within the void space. For this reason, the void size was reduced by removing the space intended for the load cells. The arms of the flat jacks were also too long so they too were reduced in order to fit within the smaller void. The updated design work is shown at full scale in drawing 12 in Appendix B and the main design evolution, as calculated with the support of the civil engineering department, is presented in Appendix C. The preliminary design is shown overleaf, in Figure 3-5.

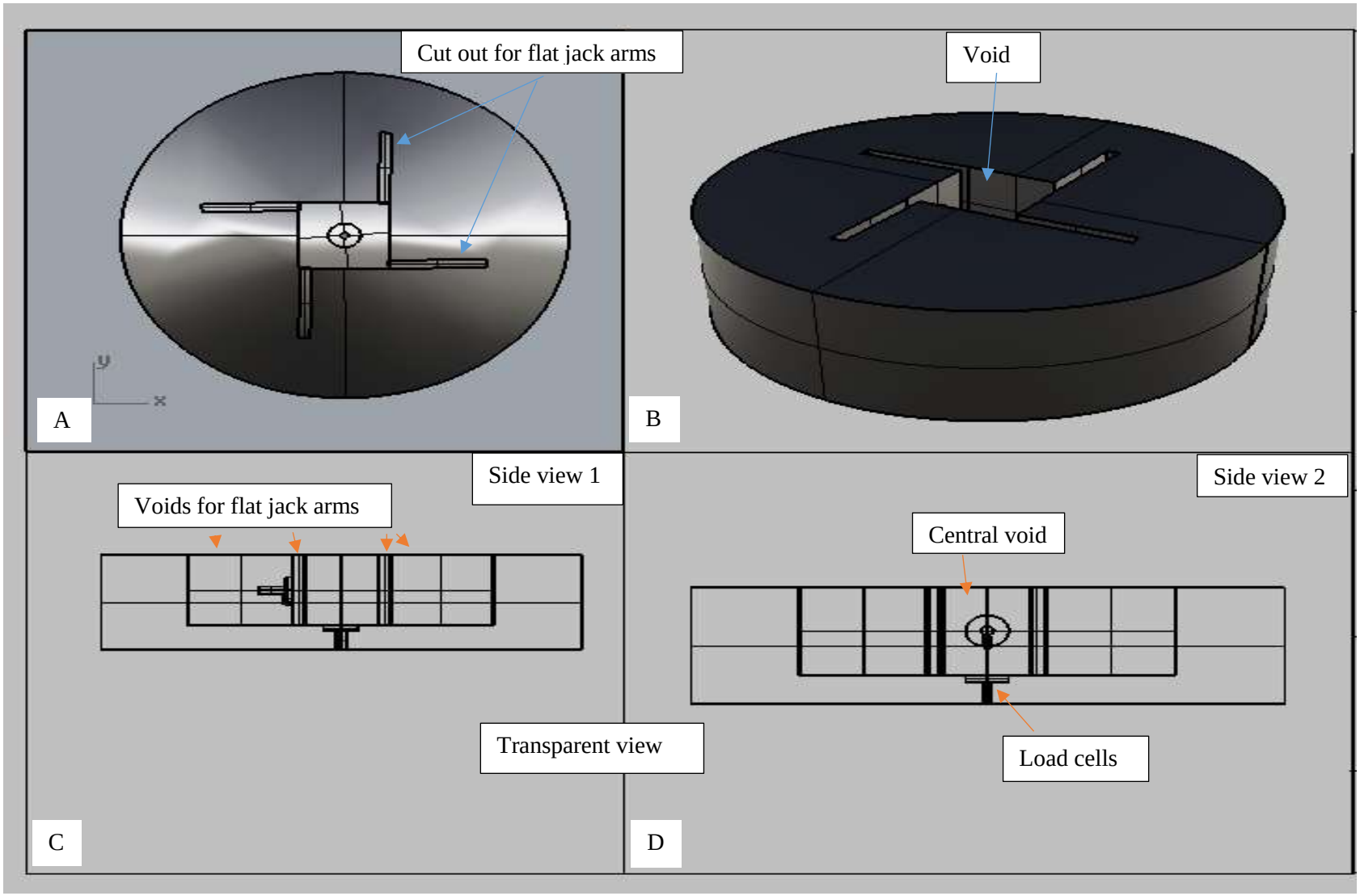

FIGURE 3-5: Preliminary concrete void design. A) Plan view showing the void set within the concrete structure. B) 3-D view to show the shape of the void. C) Side view 1. D) Side view 2.

3.5.2 Original stress calculations of the concrete and forces applied to the metal lid and sides

The original plan was to exert a maximum pressure of 120 bar on the shale samples in the concrete void using flat jacks and to pressurise the fluid to 40 bar to represent loaded rock. The calculations to prove the concrete could withstand the pressure of the fluid that surrounds the shale sample are shown below:

In order to calculate whether the rig has been designed to an adequate standard the pressures that are being exerted and applied to the surrounding concrete must also be calculated.

First the shortest distance between the concrete void and the steel face of the stress face was calculated. The longest face of the rectangular concrete void is used, as this would be the face that would have the shortest distance between the internal radius and external radius, thus would be under the greatest loading;

Internal radius of

R_i=220mm

External radius (distance from the of centre of the void to the stress frame);

R_o = 675mm

Maximum internal and external pressures are as follows:

Internal pressure

P_i = 0.6 N mm-2 (4 bar x 1.5 factor of safety)

External pressure

P_o= 0 N mm^{-2}

3.5.2.1 Lame's Equation

Lame's Equation can be used to measure the pressures exerted on a thick-walled cylinder, one in which the ratio diameter/thickness < 20. The thick-walled cylinder equation is used because the dissipation of stress at the inner and outer walls behaves very differently. The various components of Lame's equation are shown in 3-1 to 3-2.

Radial Stress:

$$\sigma_r = \frac{r_i^2 \cdot p_i - r_1^2 \cdot p_o}{\left(r_o^2 - r_i^2\right)} - \frac{(p_i - p_o) \cdot r_i^2 \cdot r_o^2}{\left(r_o^2 - r_i^2\right) \cdot r^2}$$

3-1:

Hoop stress

$$\sigma_h = \left[\frac{r_i^2 \cdot P_i - r_o^2 \cdot P_o}{(r_o^2 - r_i^2)} + \frac{(P_i - P_o) \cdot r_i^2 \cdot r_o^2}{(r_o^2 - r_1^2) \cdot r^2}\right]$$

3-2:

Where: P_i + inner pressure, P_o is outer pressure r_i is inner radius and r_o is outer radius.

Simplifying the straight edges into a thick-walled cylinder means that Lame's equation can be used. The use of Lame's equation to work out the required thickness's are presented in Appendix A.

3.6 Flat Jacks

The flat jacks that were used to apply a tri-axial load were supplied by Freysinet Bridge Bearings ltd. The Freysinet Sz15 flat jack (150mm∅) as shown in Figure 3-6 was selected. The dimensions of the jacks with their operating specifications are presented in Appendix D.

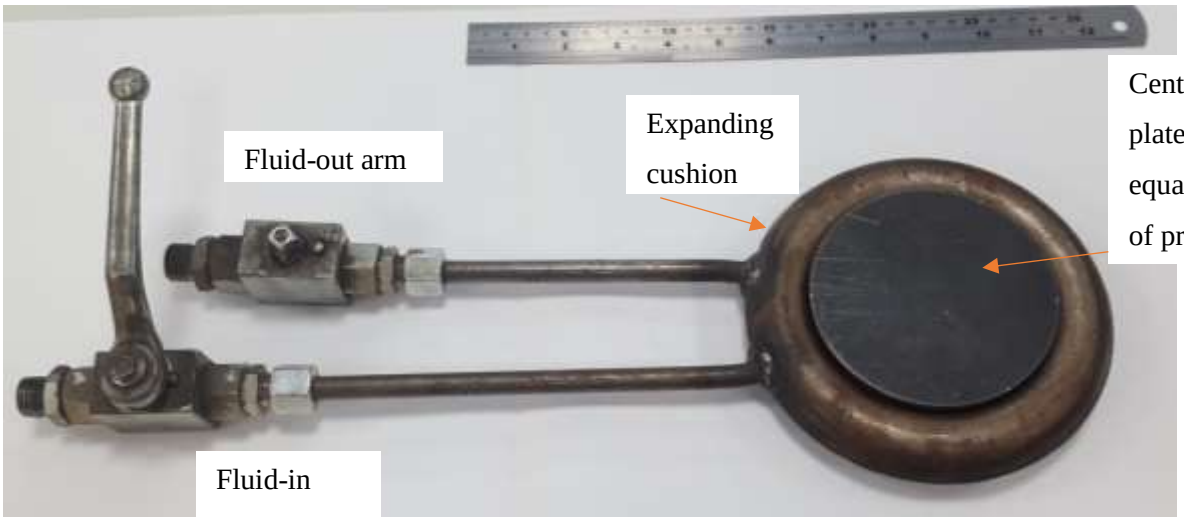

FIGURE 3-6: Flat Jack, 150mm diameter.

The flat jack is a thin circular concave cushion, which has two steel press plates in each concave position in order to press against the body being subjected to the pressure and also to protect the flat jack. Upon the injection of hydraulic fluid, the cushion expands pushing the two metal disks outwards.

Originally it was intended to have the flat jacks acting on all faces, however, it was later decided that this would potentially cut off the service holes. In order to simulate the pressures acting on all the faces the pressure would be jacked up on the ventral face and the dorsal face would sit flush against the metal lid.

The reduction in the length of the flat jack arms (previously mentioned) will help to keep the reservoir fluid at a constant pressure and also to mitigate against potential leaks in the system.

3.7 The Metal Pressing Plates

These plates, shown in Figure 3-8, are 30mm thick and made out of S355 grade steel. They are designed to have pressure exerted onto them by the flat jacks to ensure that there is an even distribution of that pressure on to shale sample. These plates also hold the acoustic sensors which are placed in a void in the corner of the plate which has been named the acoustic housing. The top of the plate, which presses against the shale sample, has a concentric ring surrounding this void, to house the 'O' ring that will form a waterproof seal around the acoustic sensor. It is essential that the seal is used to protect the sensors from being crushed by the reservoir fluid. In order to ensure the acoustic housing is completely waterproof a Swagelok 'O' ¼ inch NPT seal has been used where the sensor wires come out of the metal plates. This seal screws into the metal plate and joins on to ¼ inch Swagelok piping which will allow the sensor electronics to transmit the data in a waterproof environment.

In order for the surrounding fluid to be able to flow through the shale it must be in contact with the sample itself. If the surface of the plate is smooth and uncut, there will be no route for the fluid to access the shale as the plate will be pressing directly onto the shale, therefore, channels have been cut into the surface. 8 channels of 5mm width by 5mm depth by 145mm long and 4 channels of 5mm width, 5mm depth and 85mm long were used in the following equations to calculate the surface area open to the fluid, shown below.

$$\Sigma\text{surface area} = 8(5 \cdot 145) + 4(5 \cdot 85) = 7300\text{mm}^2$$

While the flow area in cubic mm that the plate can allow is:

$$\Sigma\text{free flow area} = 8(5 \cdot 145) \cdot 5 + 4(5 \cdot 85) \cdot 5 = 37500\text{mm}^3$$

The relationship between the flat jacks and the metal plates is show in Figure 3-7.

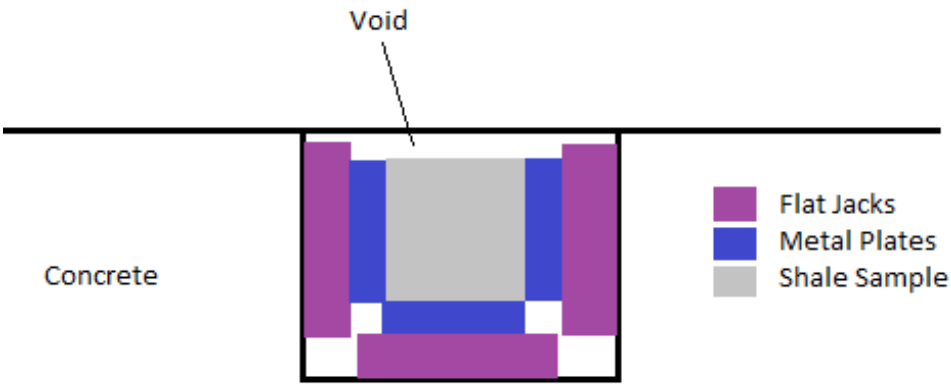

FIGURE 3-7: Relationship between the flat jacks, metal plates and shale sample in the void of the concrete rig.

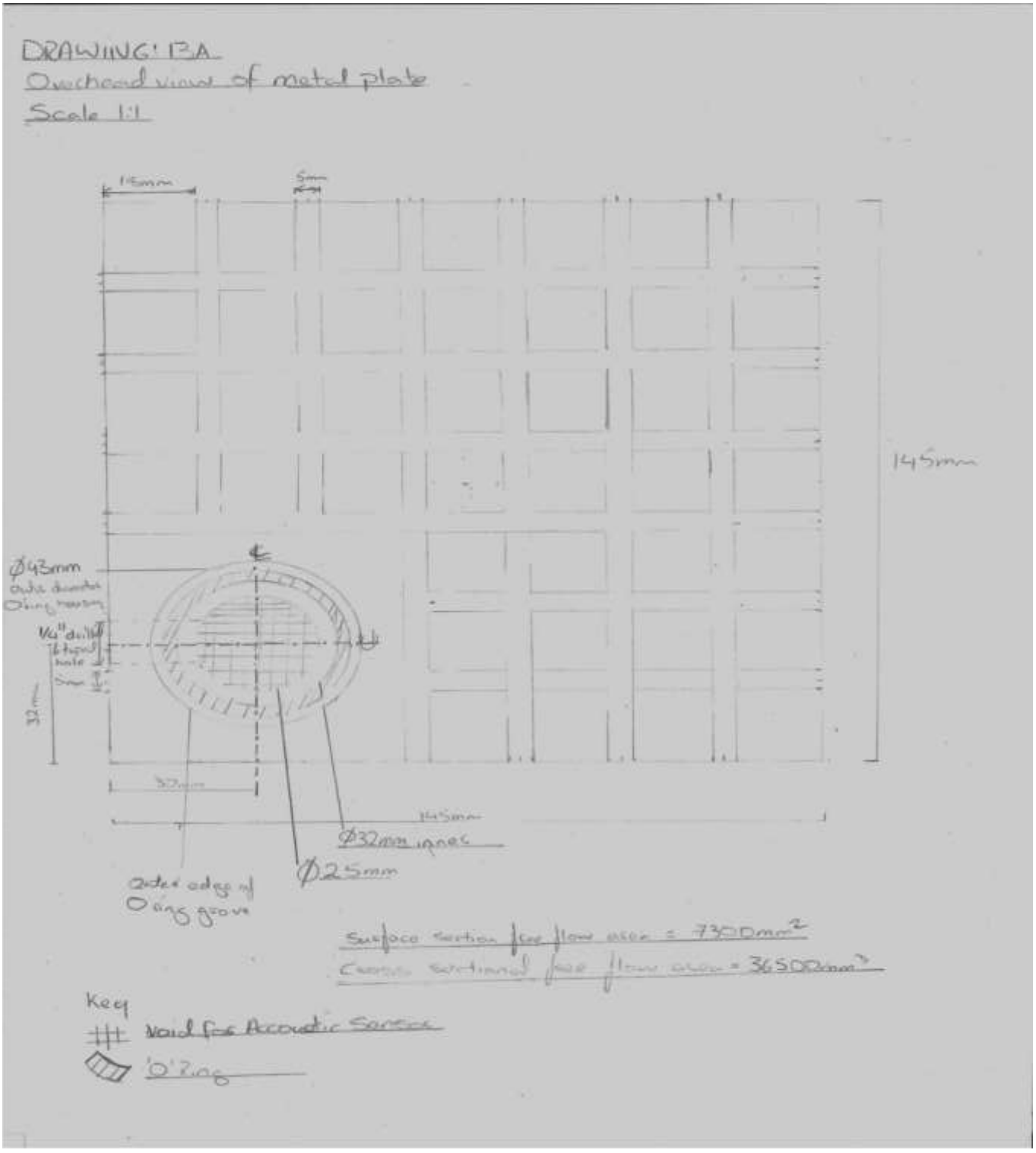

FIGURE 3-8: Design of the metal pressing plates with acoustic sensor housing (overhead view).

3.8 The Pressure Process

3.8.1.1 Fluid injection - initial concept.

This section of the experiment is the most important as it deals with the complex problem of introducing fluid into the rock sample at a relatively small but steady flow rate whilst the rock is still under tri-axial pressure. Two plans were drawn up to deal with this issue before one would be finally chosen as the best option, both are summarised below.

1) British Standard Pipe (BSP) fittings attached to a 50mm thick metal plate above the shale sample connected via a hydraulic pipe to a BSP fitting embedded in the shale.

This method involves drilling a 6.35mm (dia.) hole through the middle of the shale sample to a depth of 75mm. Followed by a further hole drilled at 11.2mm dia. in the same location of the dorsal face to a depth of 50mm, this creates a graduated borehole that mimics the effect of an actual borehole. A 6.35mm (i/d) BSP pipe end is fitted down the entire length of the 50mm depth of the 11.2mm dia. hole with the internal diameter aligned perfectly with the 6.35mm borehole. The void between the 15mm (o/d) and the BSP is filled in with epoxy resin, thus keeping the fracture fluid from back flowing whilst allowing the fluid to concentrate in the base of the void inducing a fracture to form.

A metal plate with an 11.2mm diameter hole drilled through the middle and an 11.8mm tap screw is placed into the outer diameter. A BSP fitting is screwed into this hole. The two BSP fittings, the one in the metal plate and the one in the shale, are then connected by a hydraulic pipe with an internal diameter of 6.35mm. This is shown below in Figure 3-9.

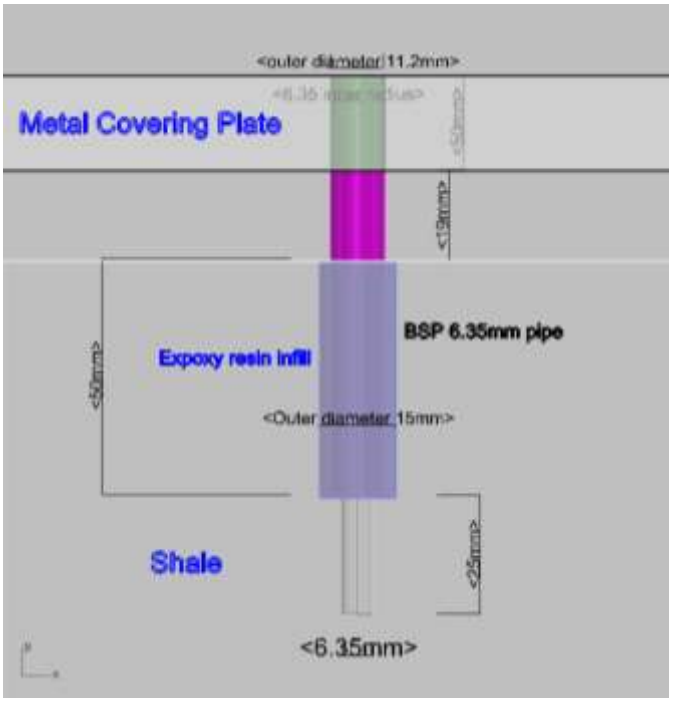

FIGURE 3-9: BSP fitting placed in the shale to secure the pipe.

2) A hydraulic pipe alone is placed in the shale.

In this option a 6.35mm (dia.) hole is drilled into the centre spot of the dorsal face of the shale to a depth of 75mm, whilst an overlapping hole of 15mm (o/d) is drilled to a depth of 50mm from the top of the shale. A piece of hydraulic pipe is then fitted into the entirety of the 11.2mm (dia.) hole. The void between the outer diameter of the hydraulic pipe and the 11.2mm diameter hole is then filled with an epoxy resin. Like method 1 a BSP fitting is drilled into the metal plate and the hydraulic pipe is then connected to the BSP fitting in the shale, this is shown in Figure 3-10.

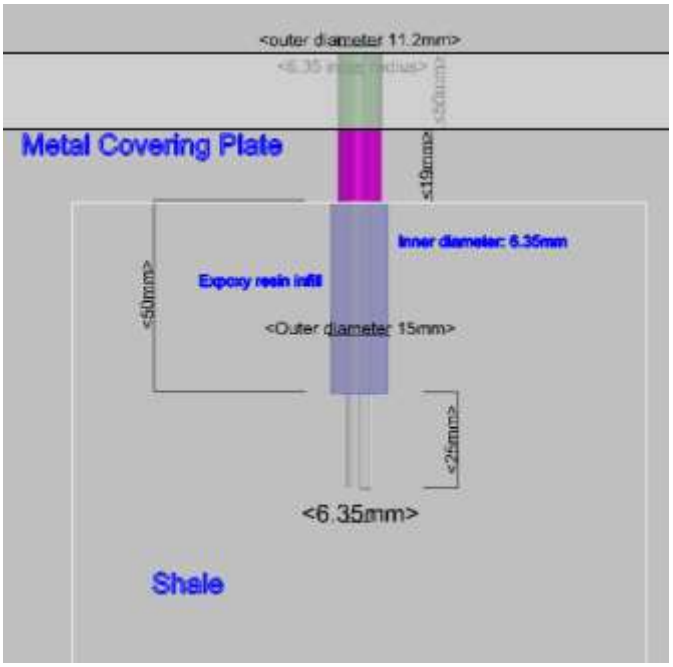

FIGURE 3-10: **Epoxy resin used to hydraulically fracture the shale.**

In both scenarios a hydraulic pipe would be attached to the other side of the pipe connector and would lead out of the rig to a regulator which itself is connected to a pump. The regulator would ensure a constant stream of 30ml/min.

During this part of the design process a number of attempts were made to replicate this design using a concrete block, not in the rig – just free standing with a pipe leading into the concrete in order to evaluate the ability of the pipe to stay in the sample and allow a pressure head to build up to induce the fracture. However, none of these attempts were successful and it was impossible to keep the pipe secured in the borehole, thus, the initial concept designs were rejected.

3.8.1.2 Fluid injection - final design.

A metal nozzle with a rubber gasket placed over it, would be more likely to stay in place, form a seal and thus allow a pressure head to form. A normal metal pipe was selected to run into this nozzle so that the pipe would be less likely to move and break the seal. A preliminary design was drawn up and a

model was made, this design successfully fractured a freestanding concrete block with a borehole drilled into it. As this test was successful this design was accepted and is presented in Figure 3-11.

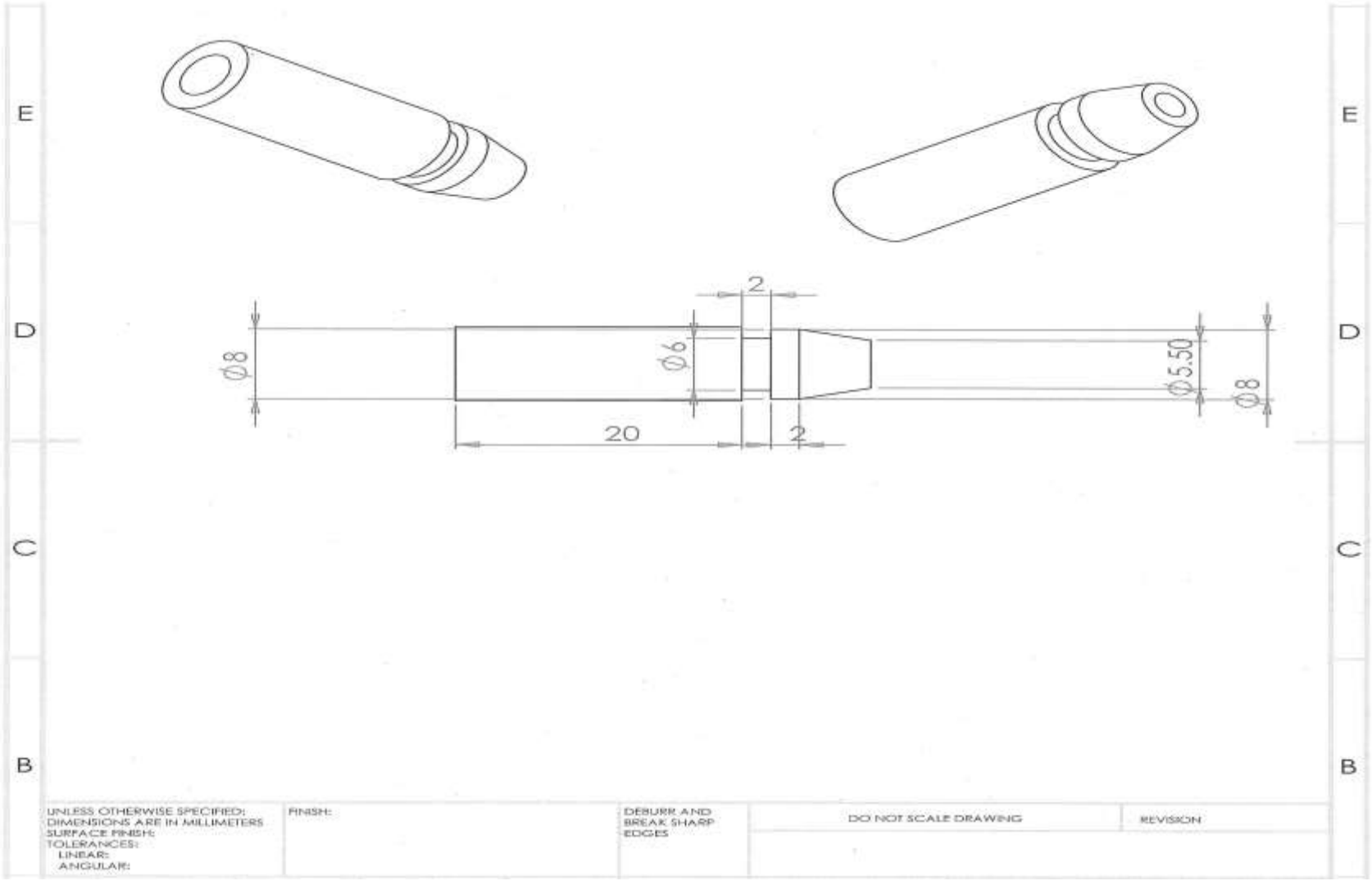

FIGURE 3-11: Preliminary and final design for fluid injector.

3.8.2 Reservoir simulation

In order to simulate the reservoir, the shale was to be placed in a bath of viscous inert fluid - glycerol, which is a safer alternative to petroleum or dissolved gas. The fluid would be pumped into the void under pressure. The pressure differential created by the glycerol being pumped into the void and the borehole drilled into the now fracked shale would then mean that the fluid should pass through the shale into the borehole to be taken out of the rig, as long as the pressure of the glycerol is kept at a greater pressure than atmospheric pressure.

3.8.2.1 Initial concept

The original plan for this investigation was to have a tri-axial force exerted on to the shale by having force applied by the hydraulic flat jacks on each face of the sample. These flat jacks would press on to a metal plate, which held the acoustic sensors, which would in turn press on to the shale sample, as shown in Figure 3-12. The shale would be situated within the void in the middle of the concrete structure which would encompass all bar the dorsal side of the shale sample, the dorsal side would abut to the metal lid. The shale sample would sit in the void that was shaped in a Catherine wheel style arrangement, as shown in Figure 3-13. The protruding arms within the void structure would house the arms of the flat jacks. Figure 3-13 shows that the central block that makes up the void, with one width larger, at 440mm, than the others, 280mm, was to make room for installing two load cells into the arm with the larger width.

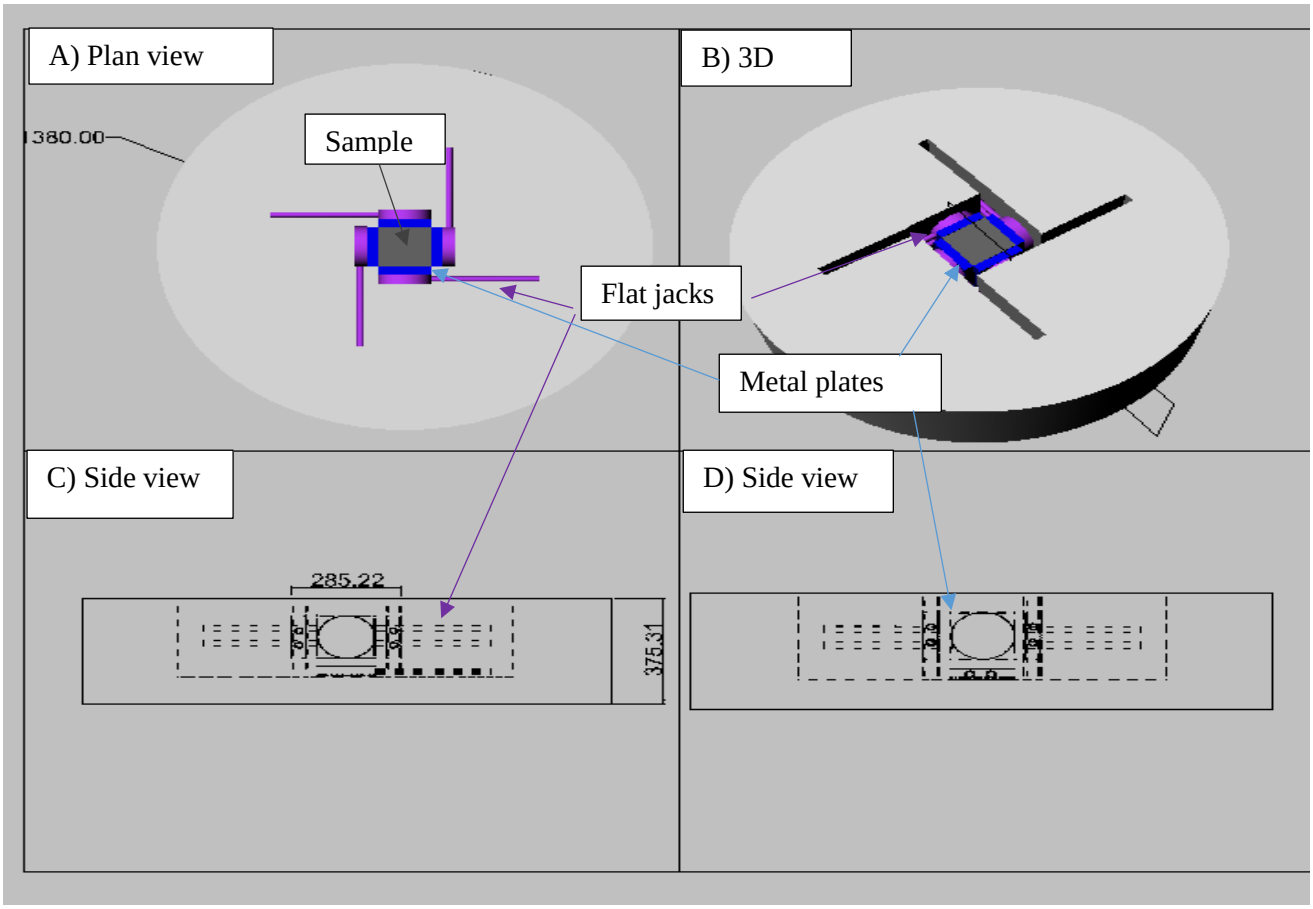

FIGURE 3-12: Original concrete and flat jack, metal plate and shale placement. A) Plan view. B) 3-D view. C) Side view 1. D) Side view 2.

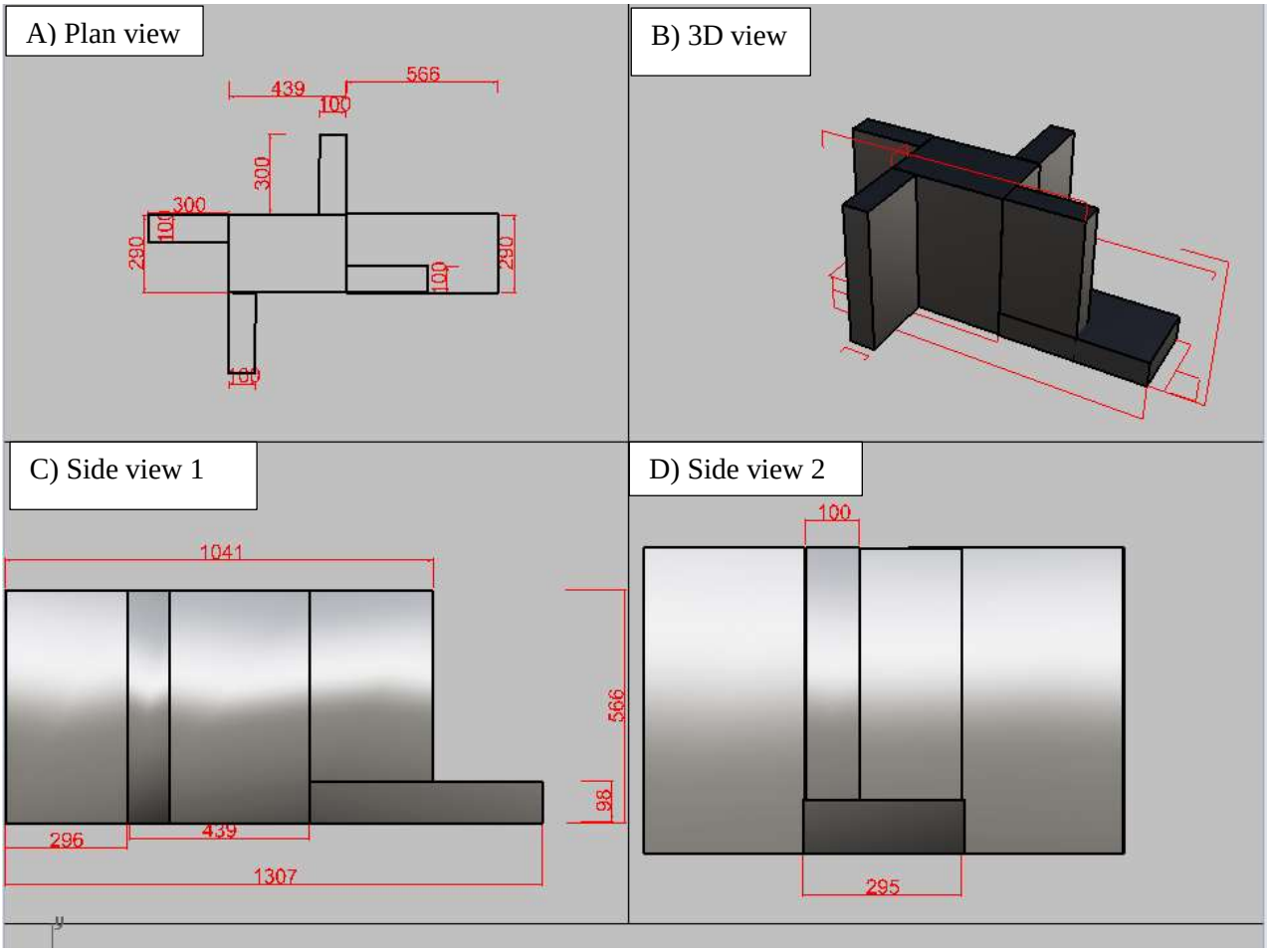

FIGURE 3-13: Void design with shortened protruding arm dimensions. A) Plan view. B) 3-D view. C) Side view 1. D) Side view 2.

3.8.2.2 The Universal Beam Modification

The pressure exerted by a flat jack or the fluid onto the metal lid would require a lid of 50mm thickness covering the area of the shale housing and reservoir void that could be detachable from the rest of the lid. As such this detachable part would have been too expensive and incredibly cumbersome to use. The plate would take up too much space and be a potential risk to the services that would be destroyed by any slight movement of the flat jack. It was also noted that if a flat jack was to be placed on the top face of the shale this would block the route of the drill into the shale which would mean that the shale could not be fractured. The original plan therefore had to be modified.

In order to reach a value of 12MPa on the σ^1 scale faces, the author changed the design. The flat jack on the ventral side will be the sole source of the σ^1/σ_{max} pressure, this will have the effect of pushing the sample upwards. This pressure will be countered by four universal 'I' beams that will absorb this force and will be anchored into the concrete to allow access to the ventral side of the shale sample. Thus, allowing the sample to be drilled into via the metal plate that houses the acoustic sensors, and which also allows the force to be spread evenly over the shale sample, thereby allowing the author to

be able to induce a hydraulic fracture into the shale. Figure 3-14 shows the cross-sectional views of the universal beam selection with dimensions of 100 x 55 x 8.1KG S275JR IPE100.

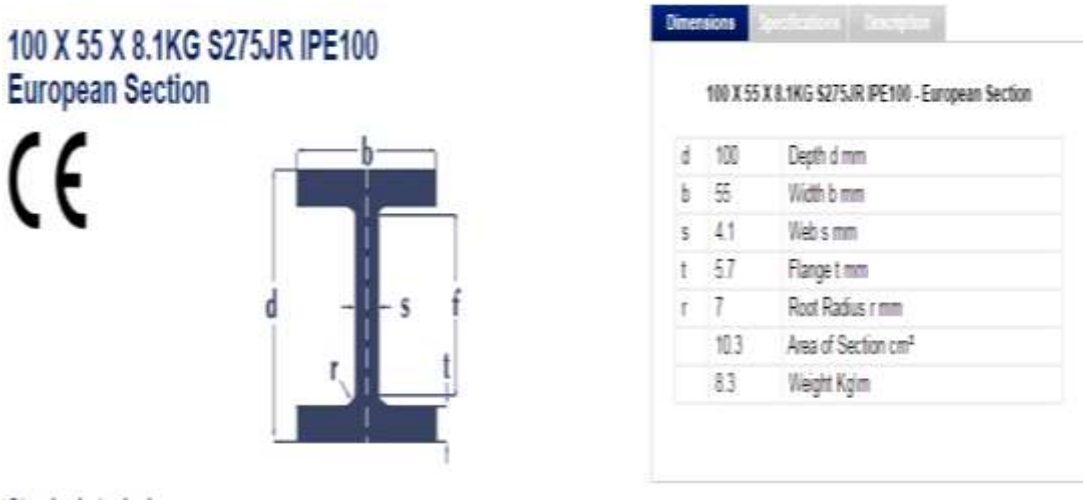

FIGURE 3-14: Dimensions of the universal beam (PARKER & SON LIMITED, 2016).

The cross beam is made to BS standard BS EN 10025: S275JR (43A/B) and has a yield strength of 275N/mm^2. In order to see whether this will be able to take the pressures involved it is imperative to calculate the moment of inertia in the beam; this is shown below, Equation 3-3.

$$I_x = \frac{1}{12}(55)\cdot(100)^3 - 2\left(\frac{1}{12}(25.45)\cdot(88.6)^3\right) = 4580635.393\text{mm}^4$$

3-3

Equation 3-12 is used to show how the maximum stress is placed in the beam. The force applied, 12Mpa, is uniform and shared between two bars that are situated equidistant over the void, equation 3-4.

$$\sigma = \frac{y\ q\ L^2}{(8\ I)}$$

3-4

Where σ= the maximum stress in the beam

y = Distance of extreme point off neutral axis (mm)
q = uniform load per length unit (N/mm^2)
L = length of beam (mm)
I = moment of Inertia (mm)

$$\sigma = \frac{49.41\ \cdot 6\ \cdot 310^2}{8\ \cdot 4580635.393} = 0.0777\text{N/mm}^2$$

EN 10025: PART 2: 2004 NON-ALLOY STRUCTURAL STEELS

Comparison between grades in EN 10025: part 2: 2004 and nearest equivalent versions in EN 10025 : 1993 and BS 4360 : 1990.

Comparison between grades in EN 10025: part 2: 2004 and nearest equivalent versions in EN 10025 : 1993 and BS 4360 : 1990						
EN 10025 : part 2 : 2004					EN 10025 : 1993	BS 4360 : 1990
Grade	Yield (Reh) min	Tensile (Rm)	Charpy V-notch longitudinal		Grade	Grade
	Strength at t=16mm (Mpa)		Temp (°C)	Energy (J) t=16mm		
S185	185	290/510	-	-	S185	-
-[1]	235	340/470	-	-	S235	40A
S235JR [2]			20	27	S235JRG1/G2	40B
S235J0			0	27	S235J0	40C
S235J2			-20	27	S235J2G3/G4	40D
-[1]	275	410/560	-	-	S275	43A
S275JR[2]			20	27	S275JR	43B
S275J0			0	27	S275J0	43C
S275J2			-20	27	S275J2G3/G4	43D
-[1]	355	490/630	-	-	S355	50A
S355JR[2]			20	27	S355JR	50B
S355J0			0	27	S355J0	50C
S355J2			-20	27	S355J2G3/G4	50D
S355K2			-20	40	S355K2G3/G4	50DD
E295	295	470/610	-	-	E295	-
S335	335	570/710	-	-	S335	-
E360	380	650/830	-	-	E360	-

1 MPa = 1N/mm^2

TABLE 3-2: Table showing British standard strengths of I beams.

As shown in Figure 3-14 and taken with the information supplied on Table 3-2 four beams, placed two across and two more sat perpendicular to the bottom two, would be enough to absorb the stress of the

bottom flat jack exerting vertical pressure. However, this would create a huge void that would be subject to the reservoir fluid pressures. This large void could lead to potential complications in the operation of the rig by exposing the edges of the top plate to huge pressures as constant removal of the lid would affect the rubber edges that provide the high-pressure seal. Also, this particular arrangement provides a greater area over which sensitive equipment is exposed to high pressures and despite the protection could lead to a greater risk of a leak and thus a greater risk of damaged equipment.

3.8.3 The metal plate design initial concept

Figure 3-15 shows a lip in the concrete surrounding the shale where a 50mm S335 grade steel plate would be inserted. This plate would be able to take the pressure exerted vertically by the flat jack placed on the bottom of the void to mitigate the increased risk mentioned above and the arms of the rig would be exposed allowing fluid to be injected away from any of the equipment. However, this would still leave a greater area than necessary exposed to the high-pressure fluid so it was decided, therefore, that the whole concrete void would have to be covered. To cover the void and reduce the area under fluid pressure, the protruding arms of the design were shortened to form a void with the general concept shape of the concrete shown in Figure 3-16.

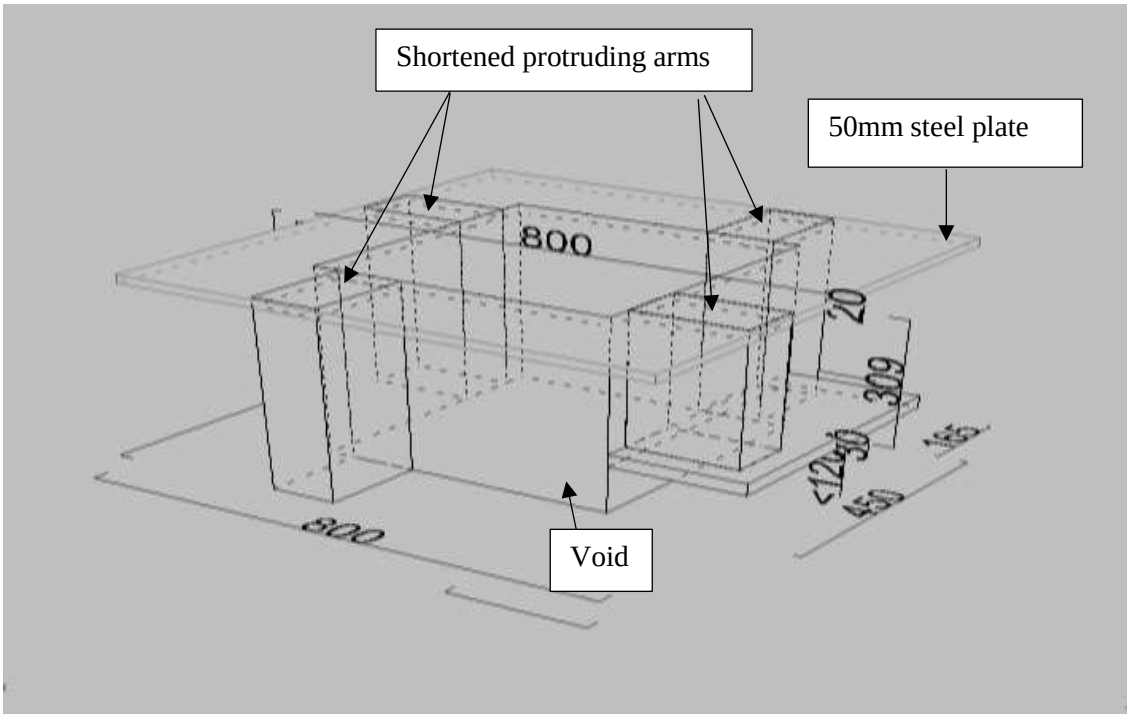

FIGURE 3-15: Modified design, plate covering the whole void and the shortened protruding arms.

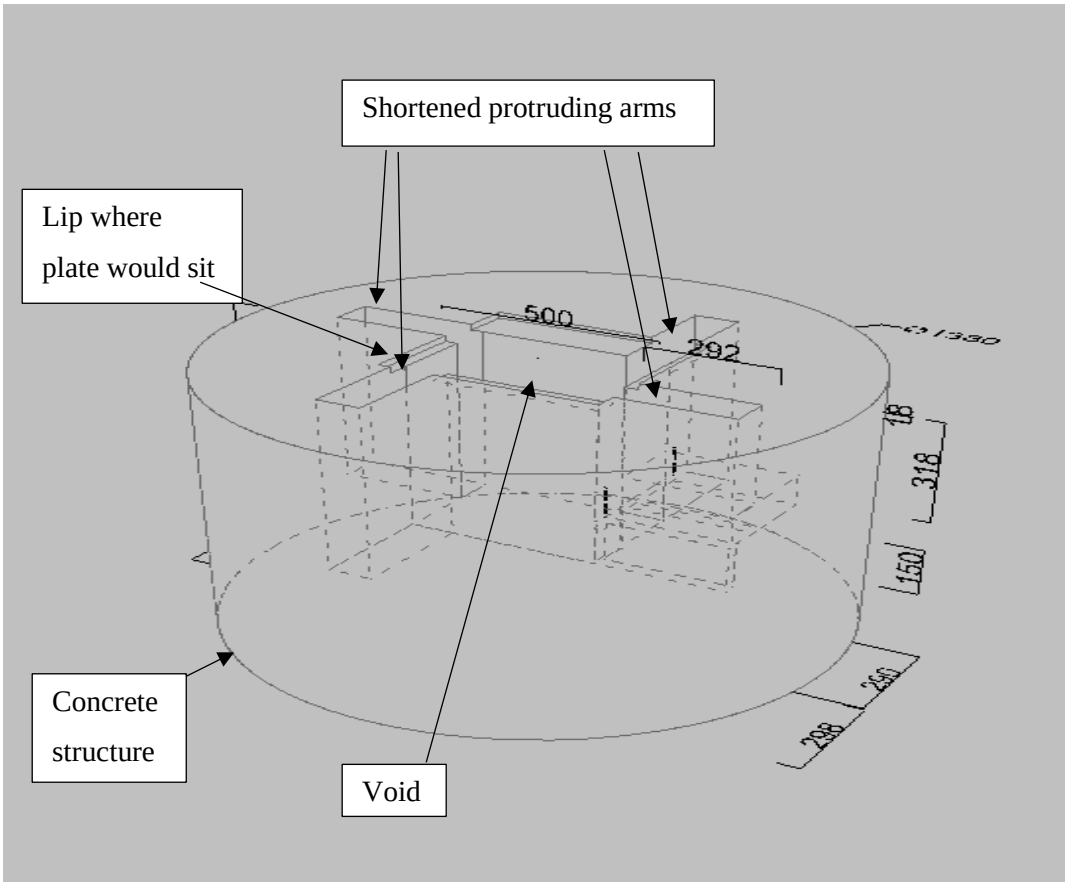

FIGURE 3-16: Modified void showing where the concrete lid would sit in relation to the void.

3.8.4 The finalised version

For the final version the protruding arms of the flat jacks were removed to stay within budget. The approved drawings for the concrete structure are shown in Appendix B - Drawings 11 & 12.

The cross-sectional design of the rig shows the wires from the acoustic sensors protected from the high-pressure fluid with ¼ inch diameter Swagelok piping which leads from the metal plate to the concrete. In order to keep a waterproof seal an S355 grade steel bar will be used with a bulkhead fitting screwed into the bar to stop the fluid from following the Swagelok into the concrete and thus flowing back into Swagelok piping.

The piping leads to the metal pressing plates, the design of which is shown in the two drawings, Figure 3-8, these in turn are held in place by the plate supports as shown in Figure 3-21.

The original plans for the metal plates had to be amended when the sample size was reduced from 150mm^3 to 100mm^3. This amendment occurred after the plates had been manufactured and delivered which meant that 50mm from the two outer sides opposite the sensor housing had to be removed.

As shown in Appendix C the structural calculations required a top plate of 50mm thickness. The author finalised the design of the plate, a small copy of which is presented in Figure 3-19, it is also presented in Appendix B labelled as drawing 16. The top plate consists of a centre hole drilled and tapped as a ¼

inch BSP. This means that a sealed pipe can be placed into the shale sample to induce a fracture, whilst also allowing the reservoir pressure to be maintained. This central hole is surrounded by four service holes along a pitch circle diameter (PCD) of 250mm. The service holes have been designed to be drilled and tapped to a ¼ inch BSP fitting so that the holes can be blocked off if needed. These extra holes were included so that if further access is required, these holes can be utilised. There are also 12 holes along a PCD of 692mm, these holes are smooth bored for an M20 bolt and match with the corresponding holes in the bottom plate. The top plate also features 8 holes on the outer edge, grouped into two sets of four which follow a straight line 100mm from the edge of the middle axis line. These additional holes are also smooth bored and are the access holes for the Swagelok piping that contains the acoustic sensor wires from the void. As the Swagelok piping will pass through a watertight bulkhead and then concrete there will be no need for these holes to be closed off. Finally, the top plate also contains three lifting eyes which are used for lifting the lid. The top plate can also be seen in Figure 4-2 before the fittings are attached.

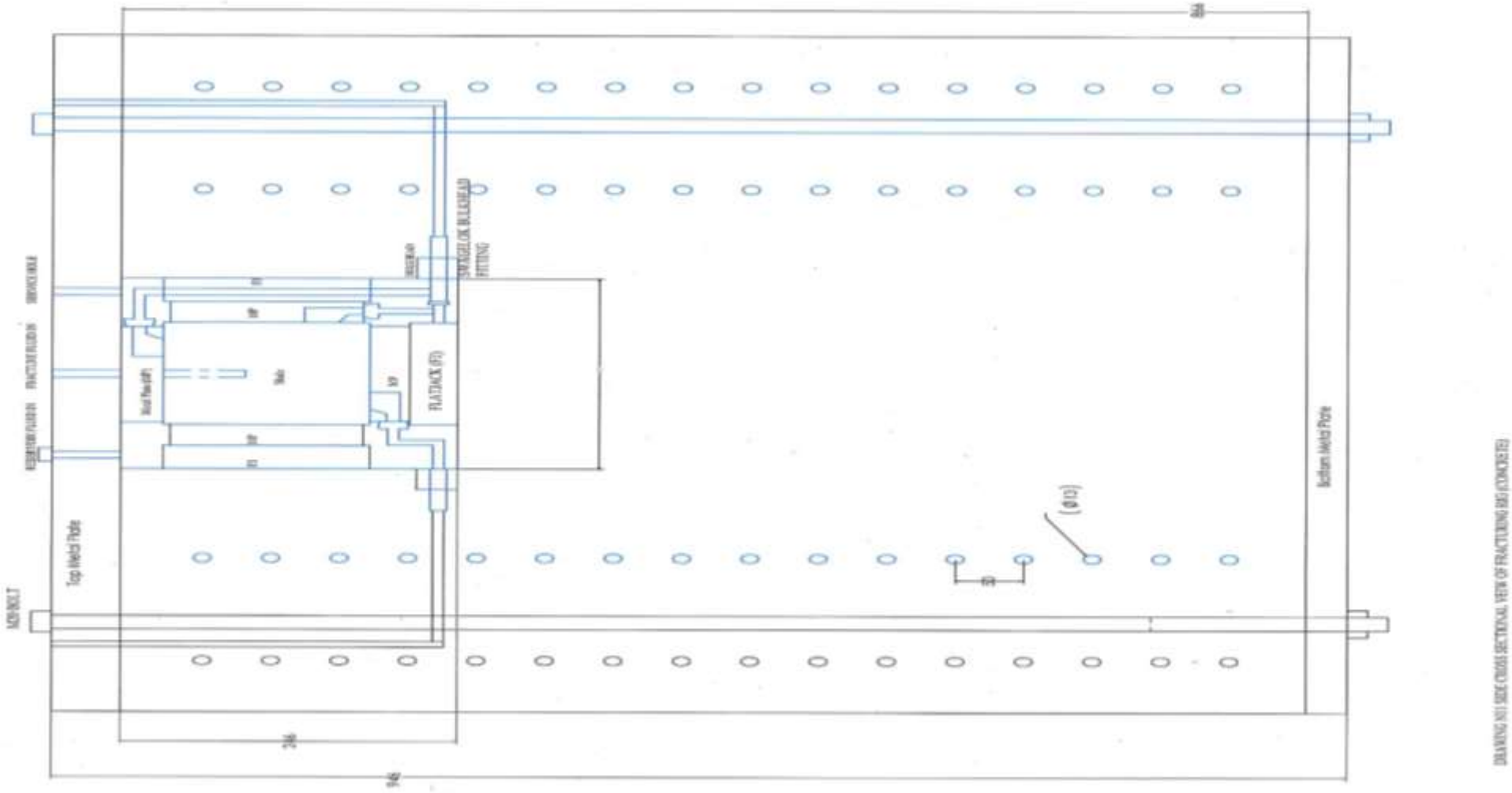

FIGURE 3-17: Finalised concrete and void design, cross-sectional view.

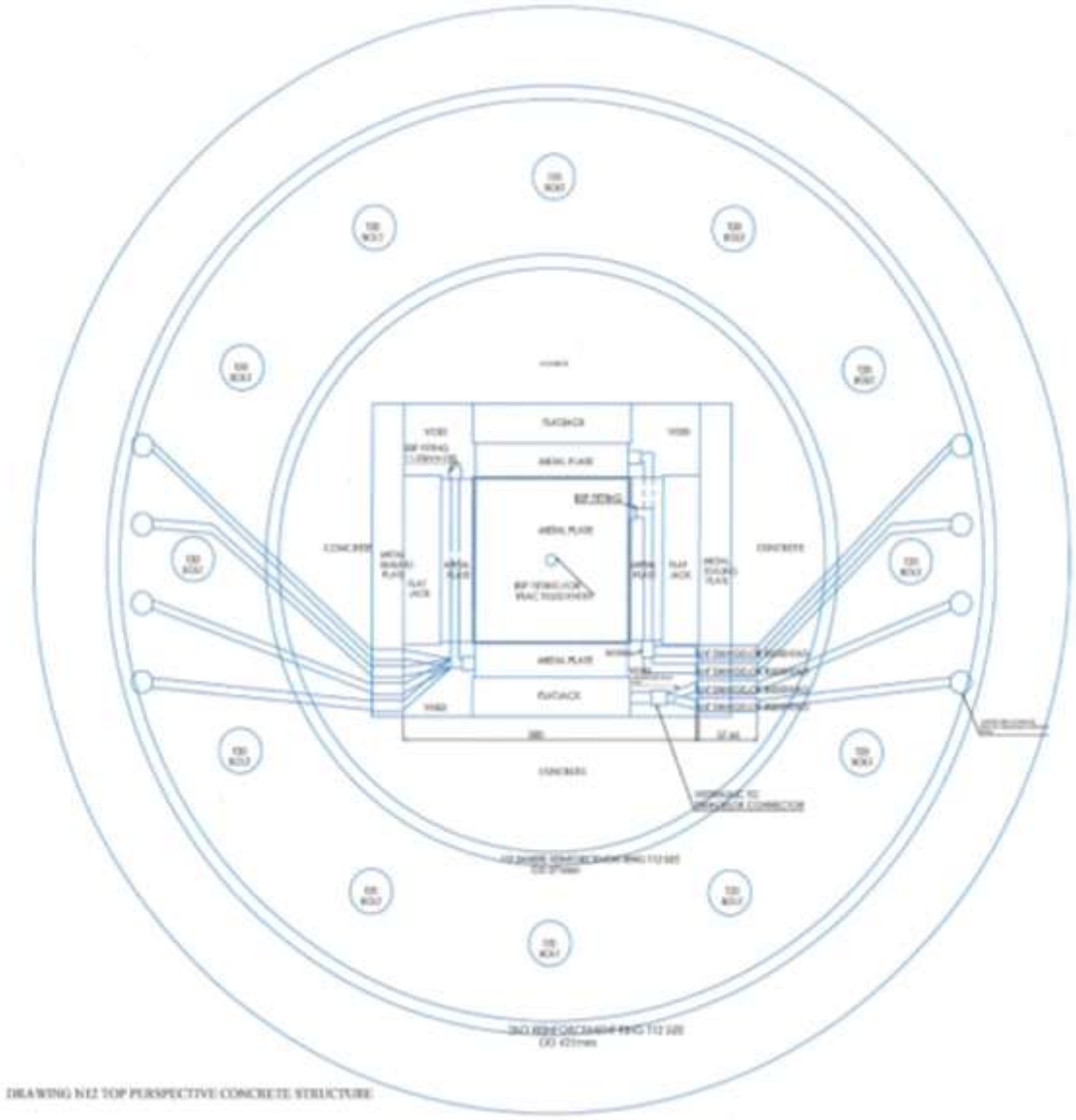

FIGURE 3-18: Finalised design of concrete and void structures, overhead view.

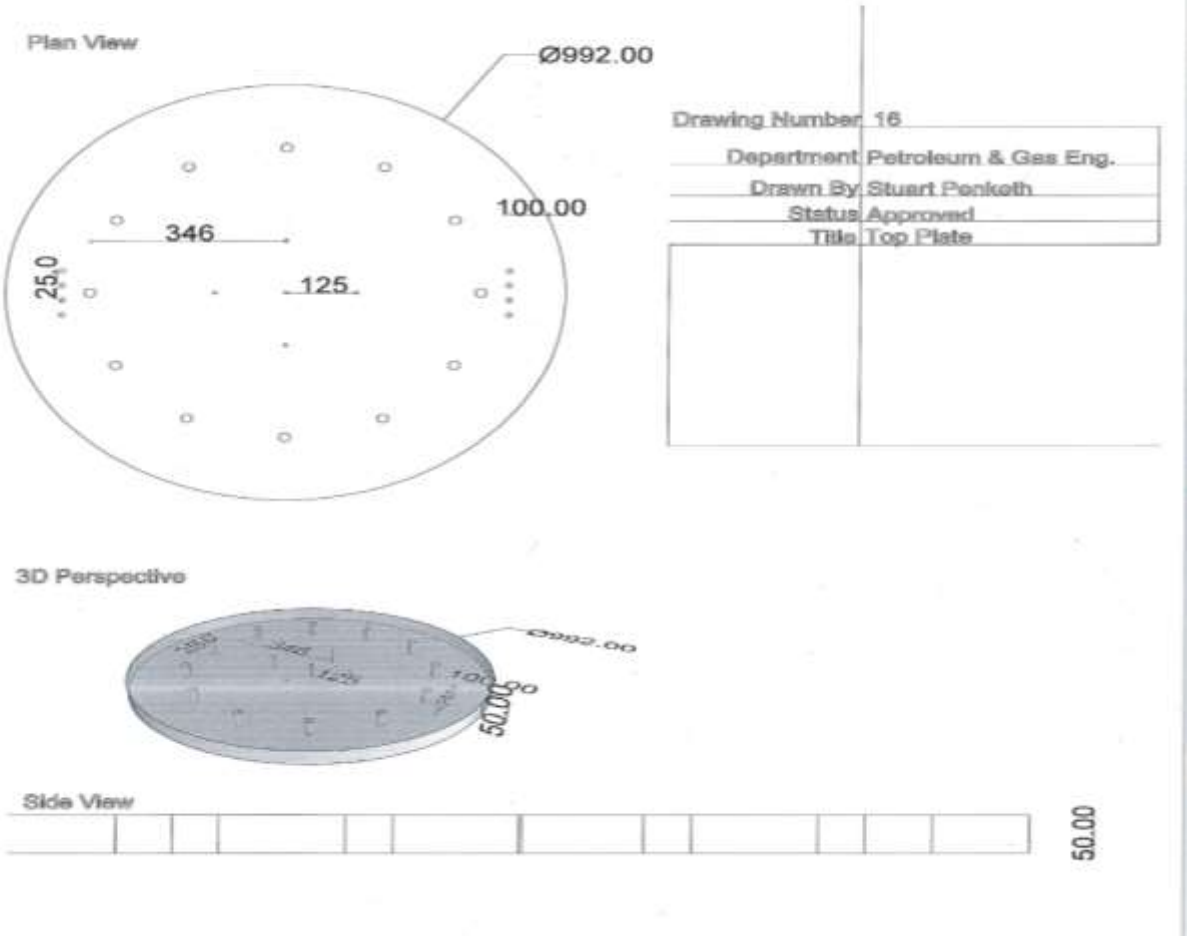

FIGURE 3-19: Design of the top plate.

The bottom plate, pictured in Figure 3-20 and numbered 17 in Appendix B, is only 30mm thick, as opposed to the 50mm thick top plate. This is because the bottom plate is separated from the majority of the pressure exerted by the flat jacks and fluid by over 500mm of S60 high strength concrete which absorbs the majority of the stress caused by the expansion of the flat jacks. Indeed, the primary stress acting on the bottom plate is from the bolts, as the M20 bolt is forced upward by the pressure exerted on the top plate from the bottom plate.

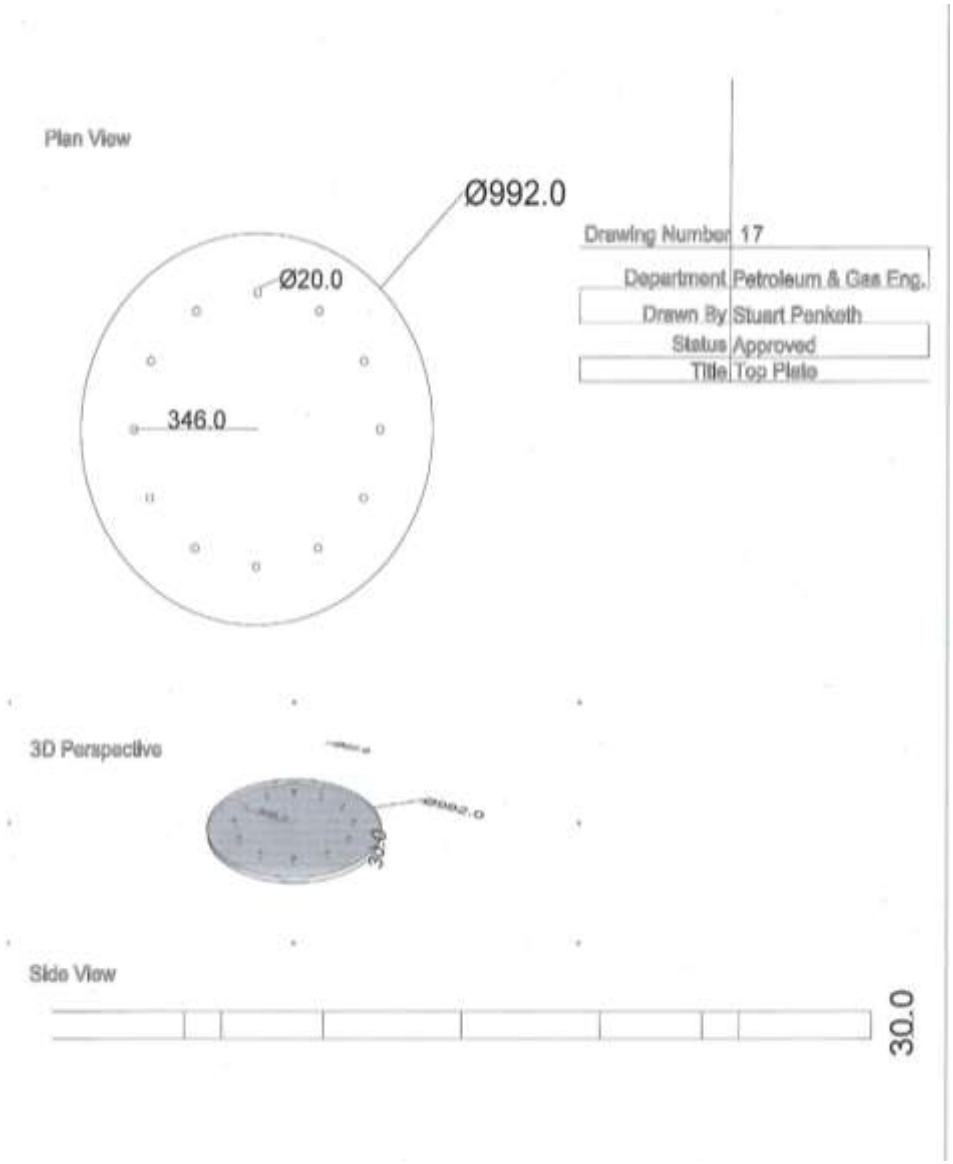

FIGURE 3-20: Bottom plate design.

In order for the sample to be placed in the void correctly and remain stable two types of support were needed for both the flat jacks and the metal plates that are acting on each of the four side faces. Due to the confined space it is essential that the supports not only hold the heavy materials in place but also help to better utilise the space, thus both of the designs follow that of an arched bridge shape. This allows pipe work to be directed under the flat jacks, while the long side is arched reducing the amount of material needed and thus reducing costs. This provided access to the pipework without having to move the hydraulically operated flat jack once it is connected to the hydraulic system. This design is similar to that used for the metal plates housing the acoustic sensors. These are both shown in Figure 3-21 & Figure 3-22.

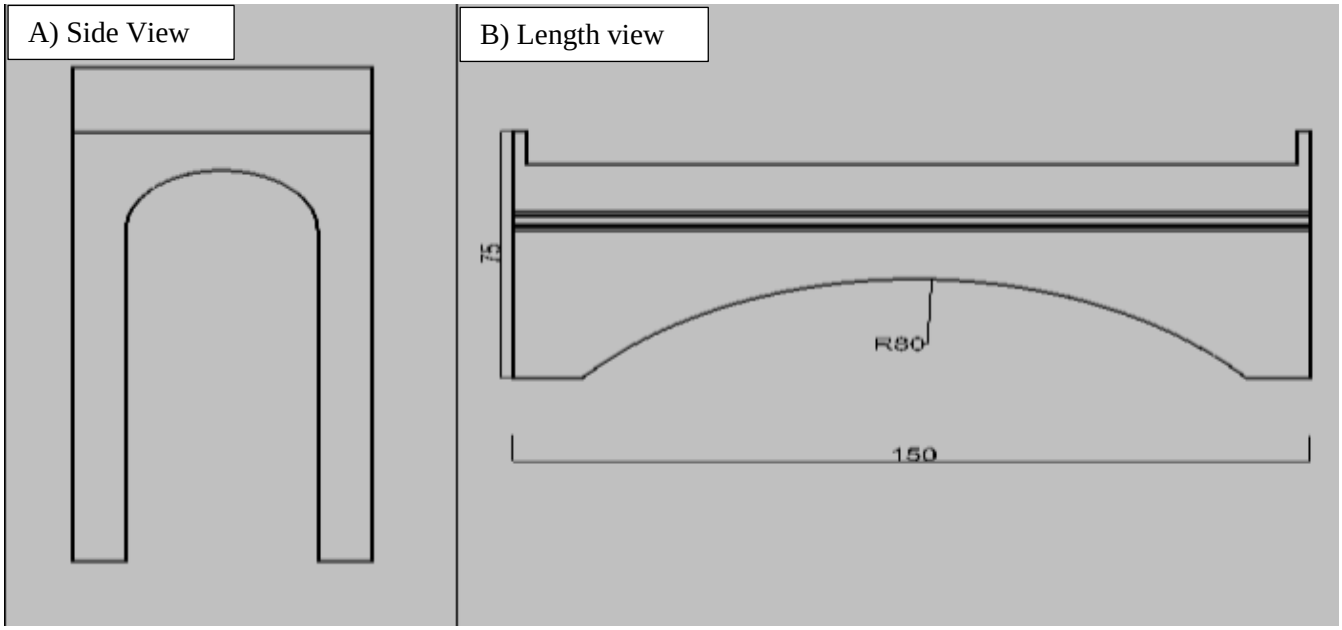

FIGURE 3-21: Metal pressing plates support design.

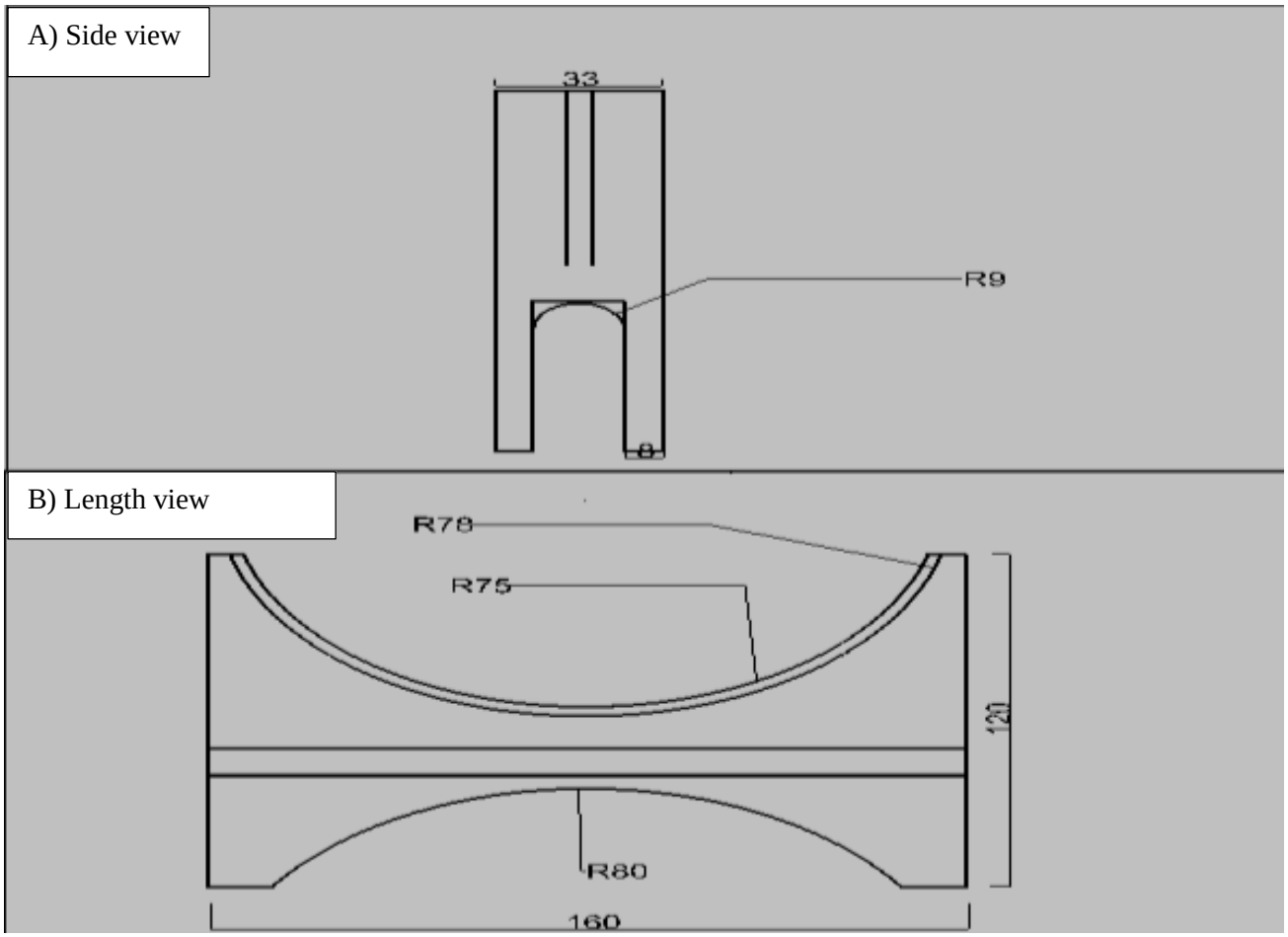

FIGURE 3-22: Flat jack supports.

The 'as built' concrete structure is shown in **Figure 3-23**. The figure shows the concrete just after the foam was removed.

Figure 3-23: Concrete structure, as built, being removed from its foam.

4 Operation of Equipment (Phase II)

The following sections describe the equipment used in this study which details the pressure rig as built with accompanying apparatus and the CT scanner used for the x-ray imaging. Also described is the methodology followed which details the general operation of the CT scanner, the protocol for mapping the fractures and calculating porosity as well as the sample preparation, drilling and acoustic testing. The final section then describes and discusses the problems encountered during initial operation and testing and what decisions were taken to fix those issues.

4.1 Apparatus

4.1.1 Pressure rig

The pressure rig (as shown in Figure 4-1) consists of a concrete pressurised reservoir vessel containing twelve metal type M20 rods of 1300mm length located in a circle around the rig and designed to withstand the pressure applied by the hydraulic presses (flat-jacks). The rig also has a central void for the placement of the shale samples, flat jacks and acoustic sensors.

FIGURE 4-1: Concrete reservoir pressure simulator.

The top plate was constructed from 50mm thick type S355 steel with a diameter of 992mm and is shown in Figure 4-2.

FIGURE 4-2: Top plate. A) M20 bolt holes. B) 20mm lifting eyes. C) Acoustic sensor entry port. D) Service points.

A 30mm thick type S355 steel metal plate with a diameter of 992mm was cut for the bottom of the concrete vessel. A simpler model than the top plate as previously explained in Section 3.8.4 because the majority of stress will be absorbed by the 500mm of S60 high strength concrete. The M20 metal rods contained within the concrete vessel (Figure 4-1) and their corresponding bolts also have a secondary purpose of securing the top and bottom plates to the rig.

As shown in Figure 4-3: six metal plates are used to place equalised stress on each face of the shale sample contained within the central void of the rig. The 25mm diameter holes shown in the bottom right hand corners house the acoustic sensors which are sealed from the well pressure by a gasket seal.

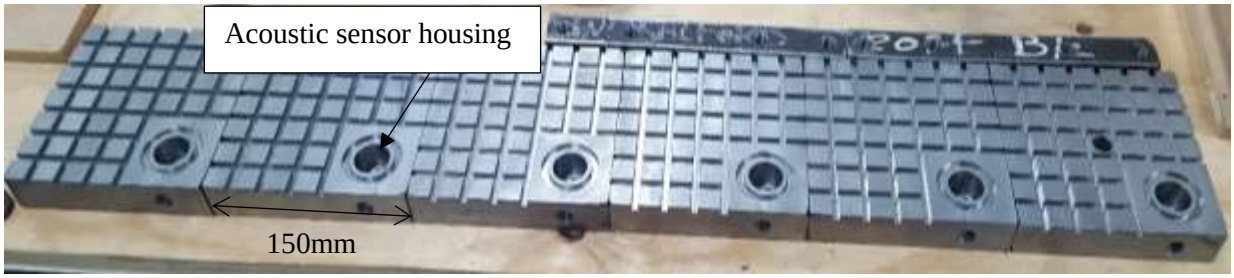

FIGURE 4-3: Metal plates and bulkheads as originally built.

The metal plates were originally designed for a sample of 150mm^3, however, as will be explained in Section 5.2.2.1, the sample size is later reduced to 100mm^3 which meant that the outer edges of these plates had to be reduced to match.

Error! Reference source not found. shows one of the three flat jacks which are used to apply the biaxial and, later, the triaxial pressures. Also shown in Figure 3-6 is one of the thin hydraulic press plates with a diameter of 150mm diameter which is used in combination with the flat jack. The flat jack uses a hydraulic system to inflate the cushion which then applies pressure to the metal plate (Figure 4-3:) this then compresses the shale sample.

The arms of the flat jacks were cut short in order to allow the lid to be placed on the rig. **Error! Reference source not found.** shows the flat jacks as they were used with the shortened arms. Each flat jack can apply 150 bars of pressure and so meet with the top limit of 120 bars required for this experiment. The fracturing fluid used in this experiment consisted of 50 ounces of Guam polymer to produce a 5cp viscous fluid.

FIGURE 4-4: Fluid injector.

Also required was a fluid injector shown in Figure 4-4. This device was designed by S Penketh and A Mappin, the design is shown in Figure 3-11. It is used to direct the fracturing fluid into the borehole and to act as a seal to prevent back flow, thus allowing a sufficient pressure head to build to induce fracturing.

4.1.2 The CT scanner

The instrumentation used to obtain the CT images of the shale samples pre and post fracture inducement was the Phoenix v/tome/x s CT scanner by GE, Figure 4-5.

FIGURE 4-5: Phoenix v/tome/x s CT scanner.

Pictured above in Figure 4-5 is the Phoenix v/tome/x s CT scanner manufactured by General Electric for the University of Salford. The reconstruction software used was the accompanying VGstudio MAX 2.2 software. The method of operation of the CT scanner and parameters used during the study are discussed in the methodology section (3.11).

4.2 Methodology

The process of collecting the data followed the path shown in Figure 4-6.

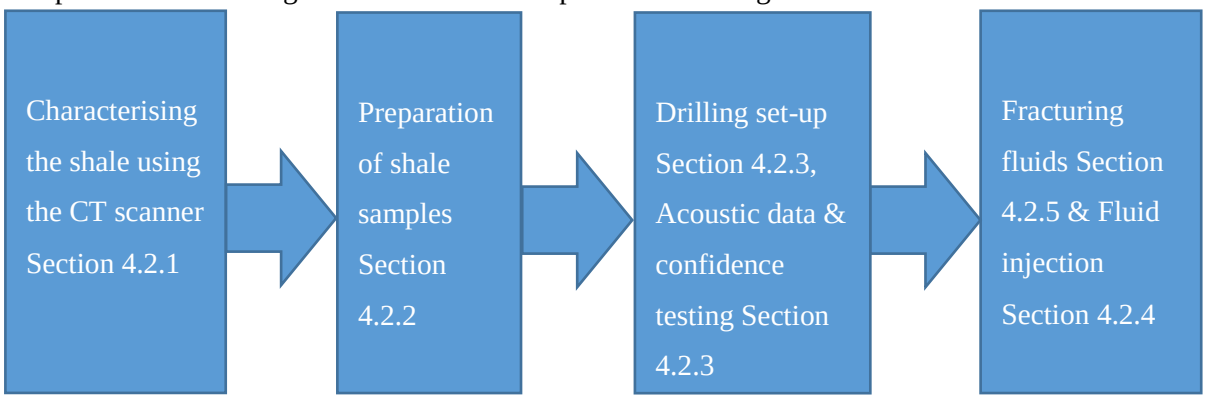

FIGURE 4-6: Flow chart showing the various stages of the data collection.

4.2.1 Categorising the Shale using the CT scanner.

In order to accurately map the hydraulically induced fracture it is essential that the existing fractures and pores of the shale samples are mapped and characterised prior to fracture induction. To this end 15 samples were scanned in the Phoenix v/tome/x s CT scanner. The images of the samples from the Bowland Shale, Westbury Shale and Accrington Mudstone were then reconstructed to reveal the internal structure and any faults thus, allowing for accurate mapping.

(i) General operation and handling of the CT scanner

The Phoenix v/tome/x s CT scanner emits a series of x rays along designated planes which pass through an object and are then received by the collector. These individual planar images, the number of which determines the resolution of the reconstruction and is set by the operator, can then be stitched together to form a solid image. This reconstructed image then shows the internal structure of an object allowing any defects or micro structures within the sample to be seen. The correct operation of the apparatus is, therefore, fundamental not only to the safe running of the instrument but also for the accurate representation of the scanned samples.

When the CT scanner is first switched on it will run through a self-check routine, this is done before placing the sample inside the X-ray chamber. The CT scanner has an internal calibration for the settings which are used to calculate the maximum, minimum and mean values of the grey scales for use during the scan. It is essential that the pixel mask is checked at this point otherwise the detector plate will not calculate the correct minimum grayscale settings to determine the object that is being scanned. Once a power setting has been selected the CT scanner has to be attuned for that power setting so that the sample and detector are not under or over saturated with x rays. By using the auto calibration option both the offset and the gain are calibrated together. It can be done individually, though this can lead to the gain and the offset being slightly off from each other. If the offset and gain setting are not calibrated

properly then the scan will have poor definition and the finer scale structures (fractures) will not be seen. In this case a gain and offset of at least 50 frames is selected. Two points are then selected; more points can be used but will have no noticeable effect on the scan and will only subject the target to more power, which in turn means that the target plate needs to be moved on a more regular basis. The calibration is then set to run. Once all the settings have been checked filters can be placed on the detector to reduce background scatter. The max, mean and minimum grey scale numbers will now have changed slightly from before the calibration, but they will now be the correctly calibrated greyscale numbers. Running these calibrations allows the scan to be accurate to 0.6μm.

The relevant settings selected for each scan are as shown in Table 4-1.

Sample type	Voltage kV	Current uA	Power W	Timing ms	Average	Skip	Binning	Sensitivity	Vsensor	Focus	Image
AMS1	210	450	94.5	1000	1	0	1x1	2.00	2	Std	1000
AMS2	210	450	94.5	1000	1	0	1x1	2.00	2	Std	1000
AMS3	210	450	94.5	1000	1	0	1x1	2.00	2	Std	1000
AMS4	210	450	94.5	1000	1	0	1x1	2.00	2	Std	1000
WBS1	190	400	76	1000	1	1	1x1	2.00	2	Std	1000
WBS2	190	400	76	1000	1	1	1x1	2.00	2	Std	1000
WBS3	190	400	76	1000	1	1	1x1	2.00	2	Std	1000
WBS4	190	400	76	1000	1	1	1x1	2.00	2	Std	1000
WBS5	190	400	76	1000	1	1	1x1	2.00	2	Std	1000
WBS6	190	400	76	1000	1	1	1x1	2.00	2	Std	1000

TABLE 4-1: **Settings used on the CT scanner for each shale sample.**

The timing refers to the milliseconds (ms) that the detector takes to capture each image, the longer the setting, the higher the contrast levels. A high contrast is required between the sample and the background as the shale is a relatively dense material. A minimum grey scale value needs to be set to at least 200 (the minimum value represents the material) whilst the maximum value represents the background material (air) and typically needs to be within 2 to 20 times the value of the minimum. The high contrast necessary was typically found on the 1000 or 2000ms settings. As the timings relate to the amount of time that the detector takes to capture and calculate each image, this means that if, for example, 1000 images have been selected for the scan at 1000ms, then each one of the thousand images will take 1,000 milliseconds to capture.

In order to keep computational time to a minimum, '1' should be selected for the average number of images to be paired. This process helps to keep the image well defined by ensuring that pictures at complimentary rotation angles are matched.

Sensitivity also affects the contrast levels and should be kept as low as possible, for the main sample sizes this was kept to between 0.500 and 2.000.

Once the scan is completed the relevant file is opened in the GE phoenix datosx 2 acq srv software. The file looks like the screen shot shown below in Figure 4-7 when opened.

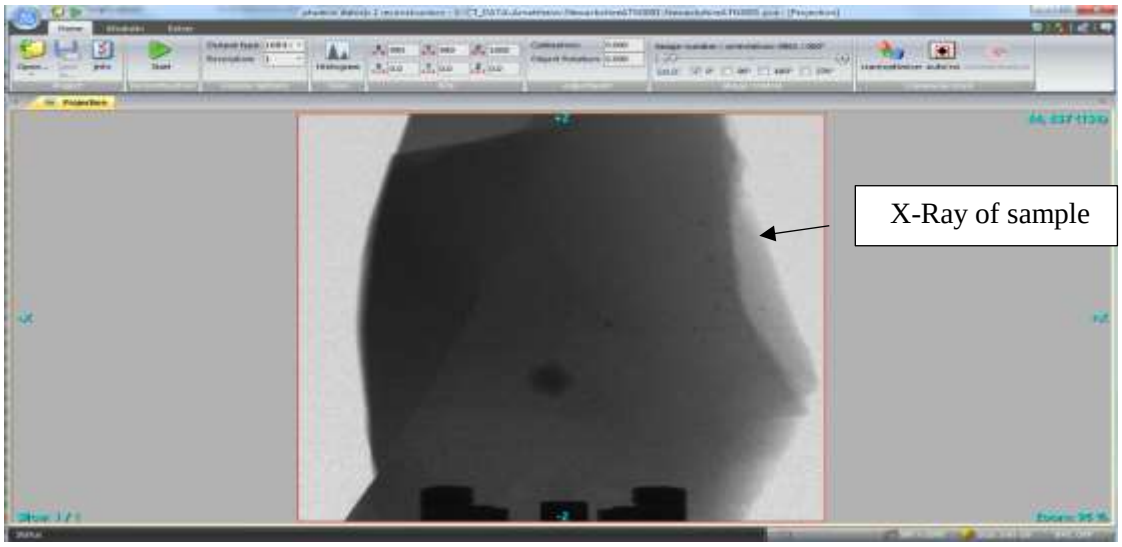

FIGURE 4-7: Datosx 2 acq srv software loaded up with scan.

At this point the scan optimiser is then used, this removes imperfections and corrects any variations that may have occurred during the scan (see Figure 4-8). The auto-roi option (Figure 4-9), allows the software to check the correct axis point and remove soft materials that would otherwise cause a loss of definition.

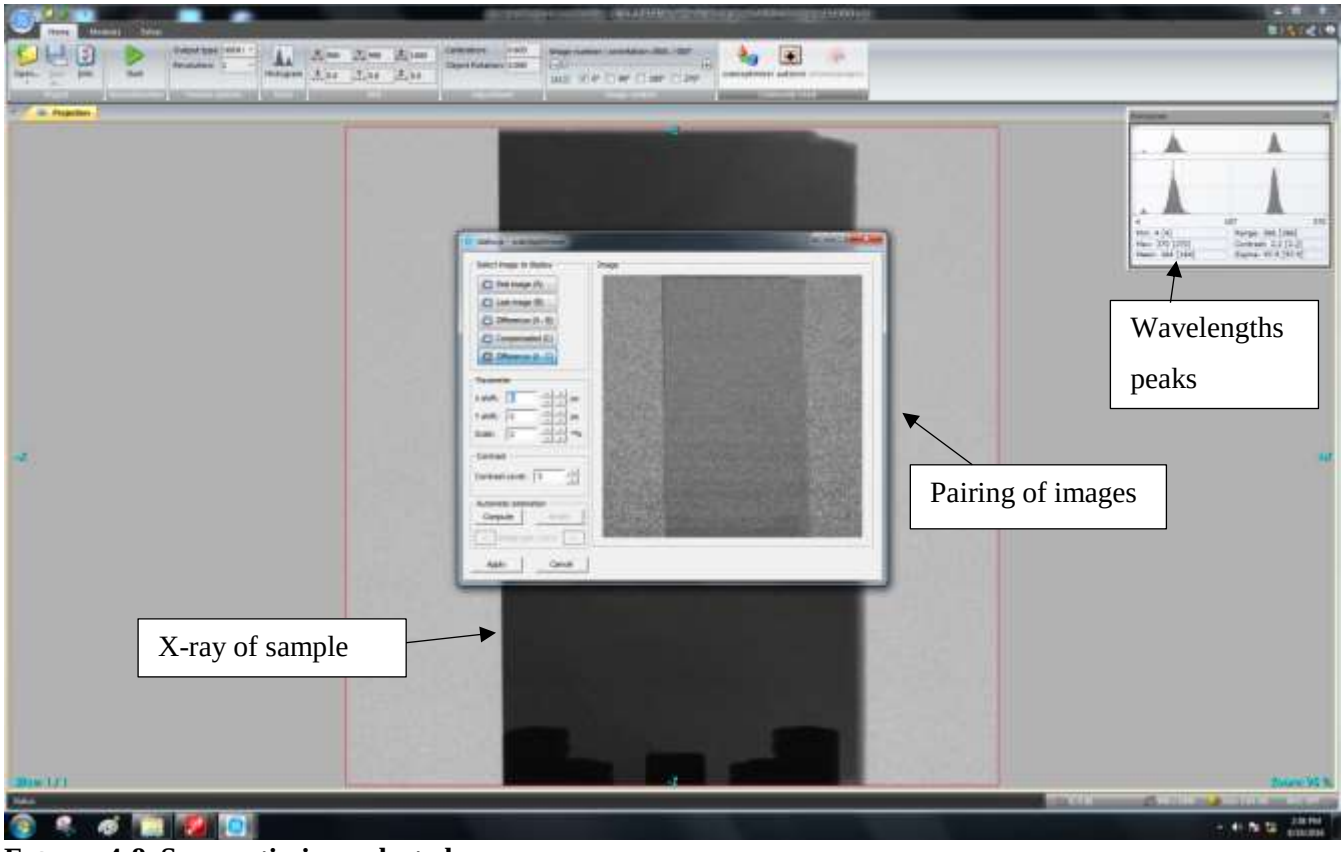

FIGURE 4-8: Scan optimiser selected.

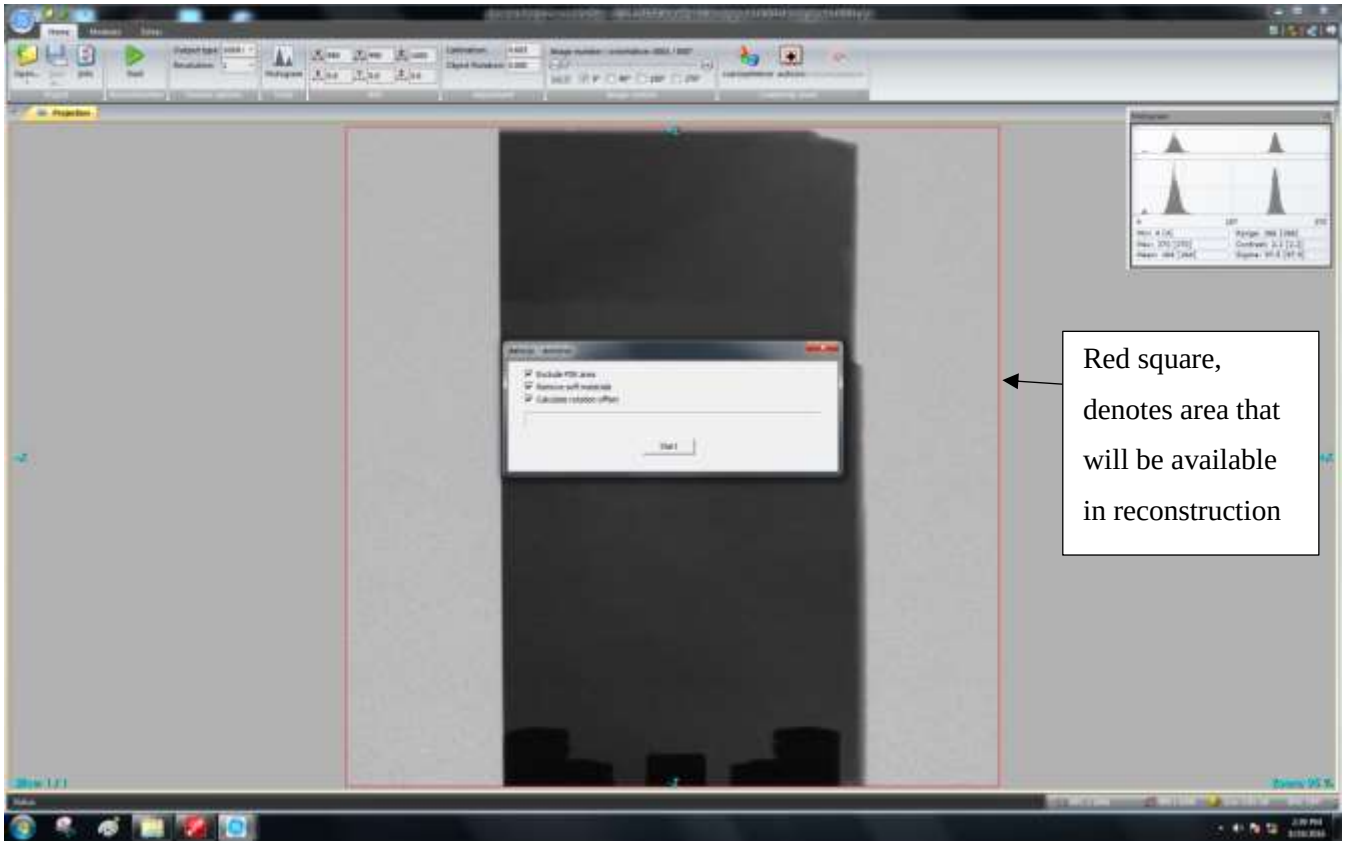

FIGURE 4-9: **Auto-roi selected.**

A manual check is then done on the rotation effect to ensure that the axis is correctly placed. The volume analyser then loads up the reconstruction page showing a three-planar view of the scan and a 3D reconstruction of the area, as shown in Figure 4-10. However, before the 3D reconstruction can take place, a surface definition must be set so that the software can determine which part of the image is the surface. To this end the surface determination protocol is the next step. To get a more accurate surface 'manual definition' is selected then the background area and then the area of the scan representing the actual scan object.

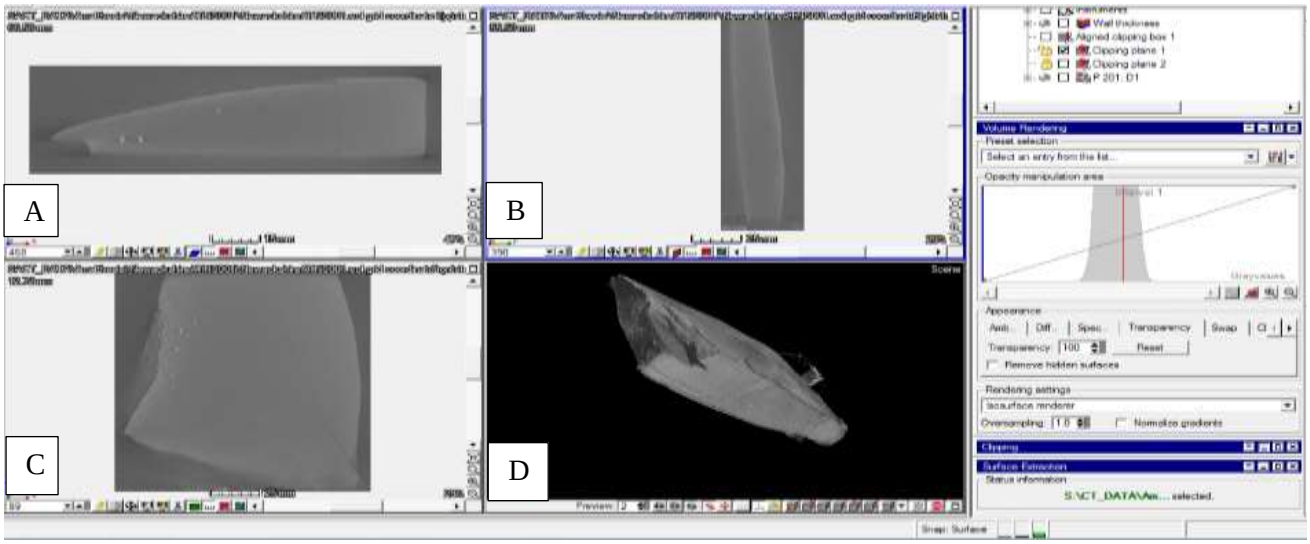

FIGURE 4-10: Scan of reconstruction prior to surface determination, A) Planar view, B) Side View 1, C) Side view 2, D) 3D reconstruction.

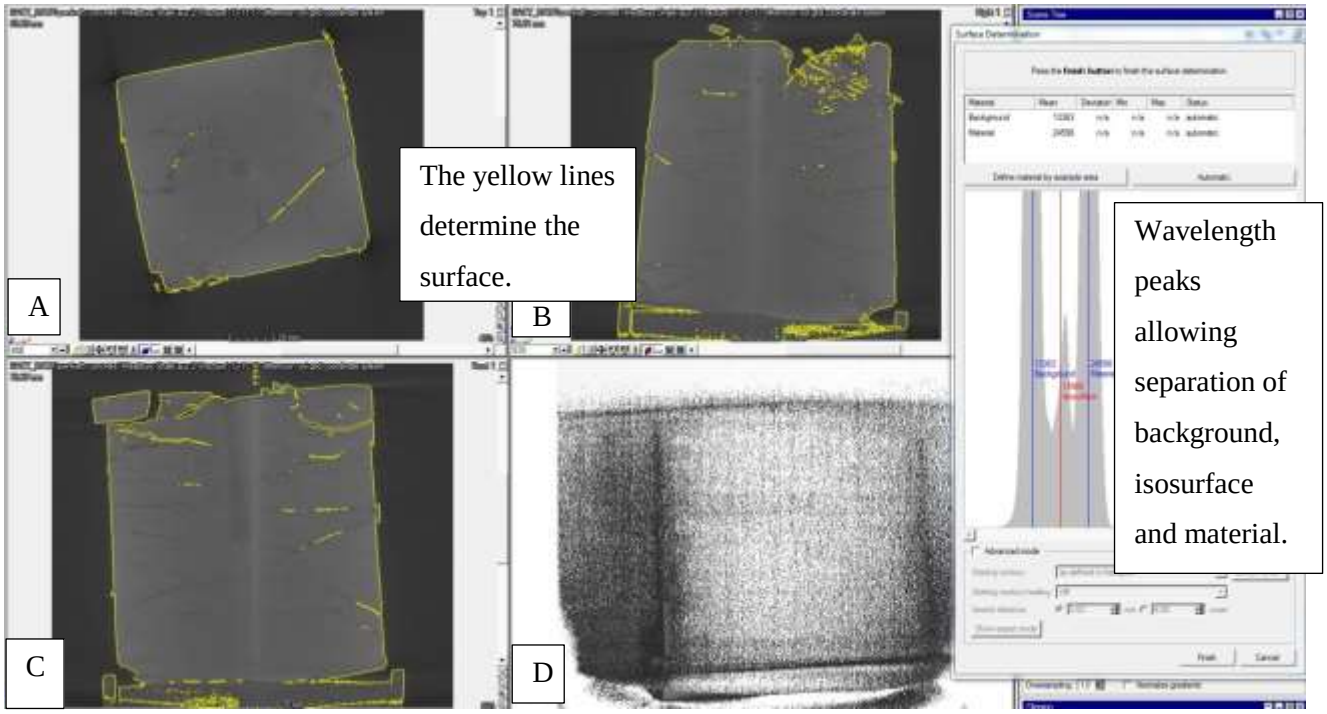

FIGURE 4-11: Surface determination A) Overview, B) Sideview 1, C) Sideview 2, D) 3D reconstruction prior to accepting surface determination.

It is important that the surface is determined accurately (Figure 4-11) as the calculations used to determine any defects, porosity and/or wall thickness all rely on the correct surface determination and accurate iso-surface being made. Failure to determine the iso-surface correctly will result in either a hollow object or an overly dense object, both of which would affect any porosity readings.

(ii) Mapping fractures

Mapping of the fractures can only take place once the surface determination has been made. In order to characterise and map the existing fractures one of the plane views is scrolled through so that each structure can be noted. Each plane view is a full x ray image of that slice, rather like a medical x ray, which allows the user to see the internal structures. When a crack or fracture in the shale is observed it is relatively easy to highlight, as shown by A and B in Figure 4-12.

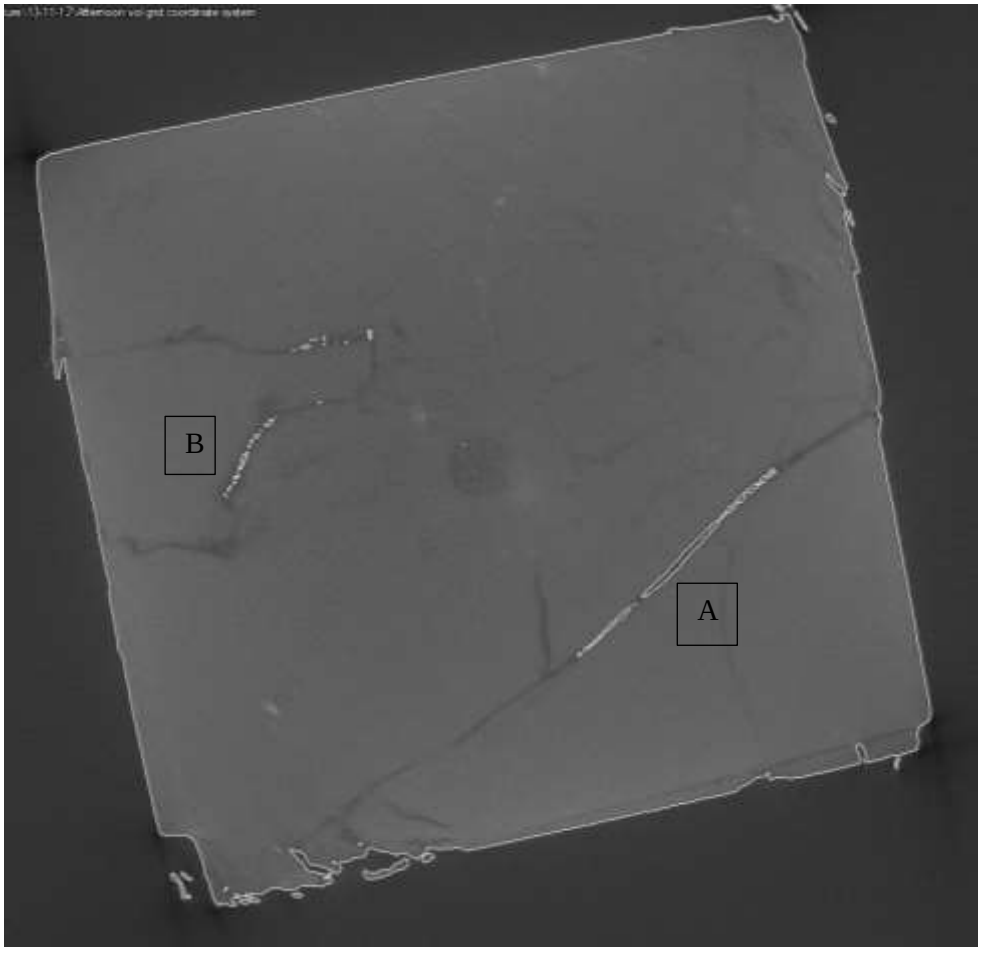

FIGURE 4-12: Planar view of a fracture (overhead planar view), A)and B) show cracks & fractures highlighted.

When a fracture has been identified the drawing tool is selected with a small diameter point, typically 0.6 to 0.3mm, to trace the fracture and cover the shale on either side, an action called 'seeding'. This 'seeding' needs to be carried out over two distinct areas of a fracture/fractures within the same plane (two areas in two separate planar views could be selected but this would slow down the analysis drastically). This action means the software can recognise which areas to compare the grey scales to. The crack segmentation icon is selected and loaded. Once loaded a red box will surround the area of the seeding. The red box is then expanded to cover the entire area, thus instructing the computer that any crack segmentation should be calculated for the entire sample area.

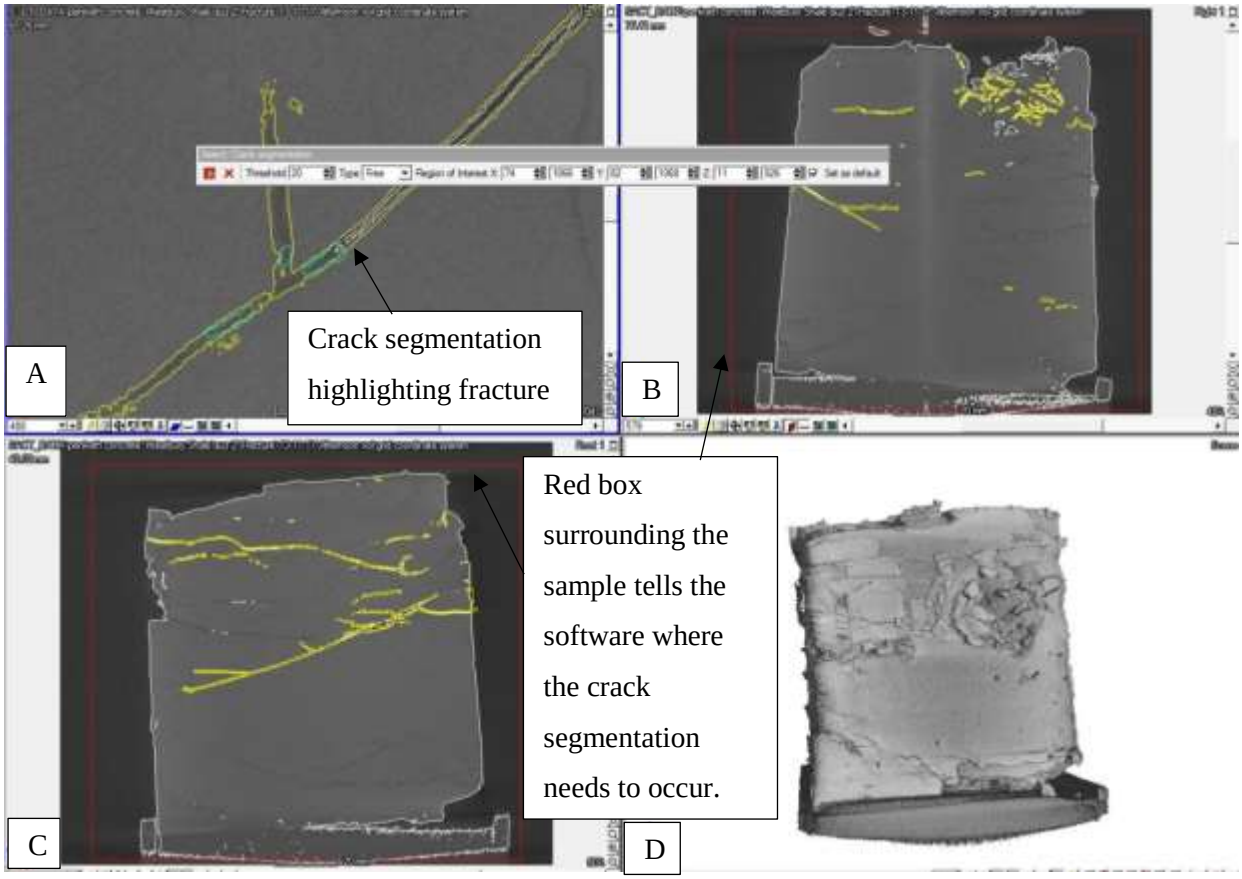

FIGURE 4-13: Crack segmentation. A) Planar view, B) Side view 2 C) Side view 3 D) 3D reconstruction.

The seeded area should then show yellow lines, Figure 4-13, indicating which areas the computer has calculated to be the fracture. If the full length of the fracture has not been picked out by the yellow lines, then the threshold level can be increased. This threshold level uses an algorithm to calculate the differences of the grey scales and work out the probability of whether the greyscale represents a fracture or not. Great care is required here as any expansion which then includes the full length of the fracture may also contain sections that are instead coherent shale and not just fracture. It is, therefore, prudent to keep a low threshold level of between 0 and 2 to ensure this does not occur. Once the optimum width is created, Figure 4-14, a transparency much greater than that of the sample is selected. Typically, each main sample has the transparency set at 10% allowing it to be translucent whilst the region of interest is set at 100% so that the fracture can be clearly seen, Figure 4-15.

This process is repeated until all the visible fractures have been mapped. Once the fractures are mapped the measuring tools can be used to measure the various widths, height and lengths of the fracture along the half-length plane.

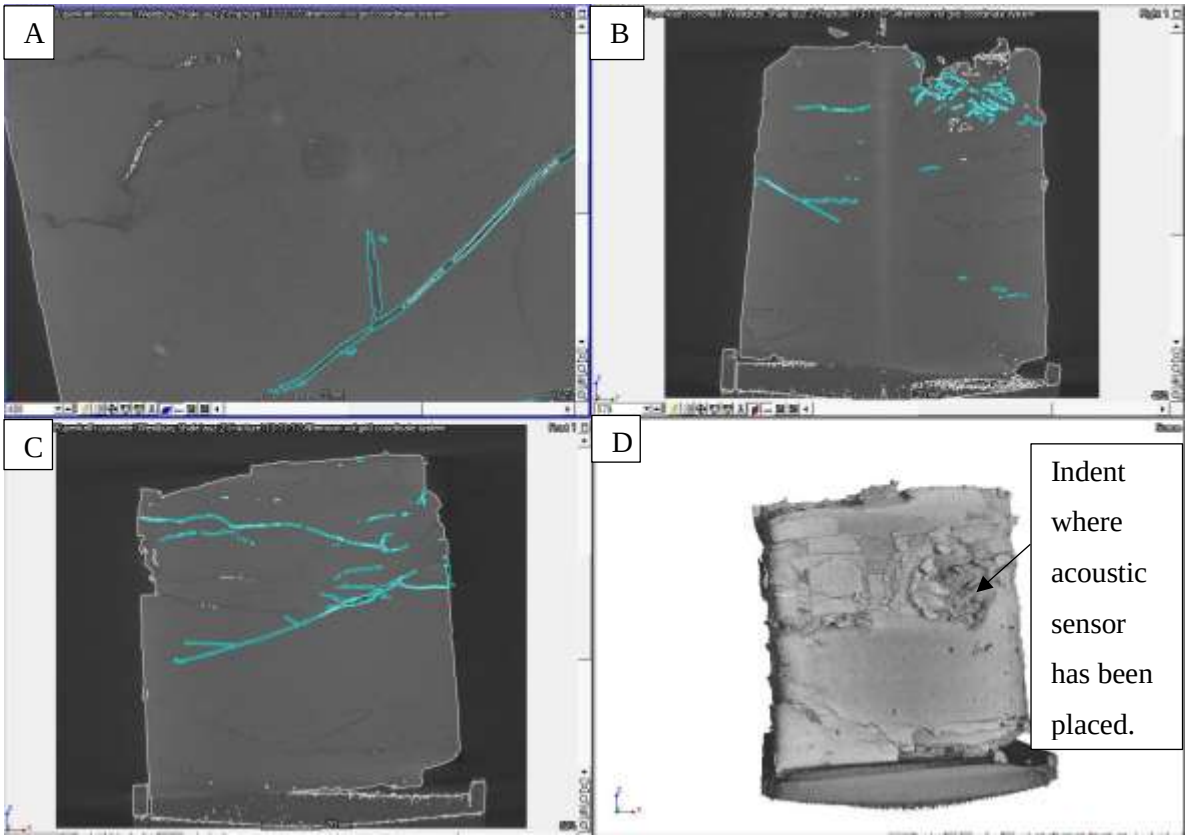

FIGURE 4-14: Mapping the fractures. A) Planar View, B) Side view 1, C) Side view 2 D) 3D Reconstruction.

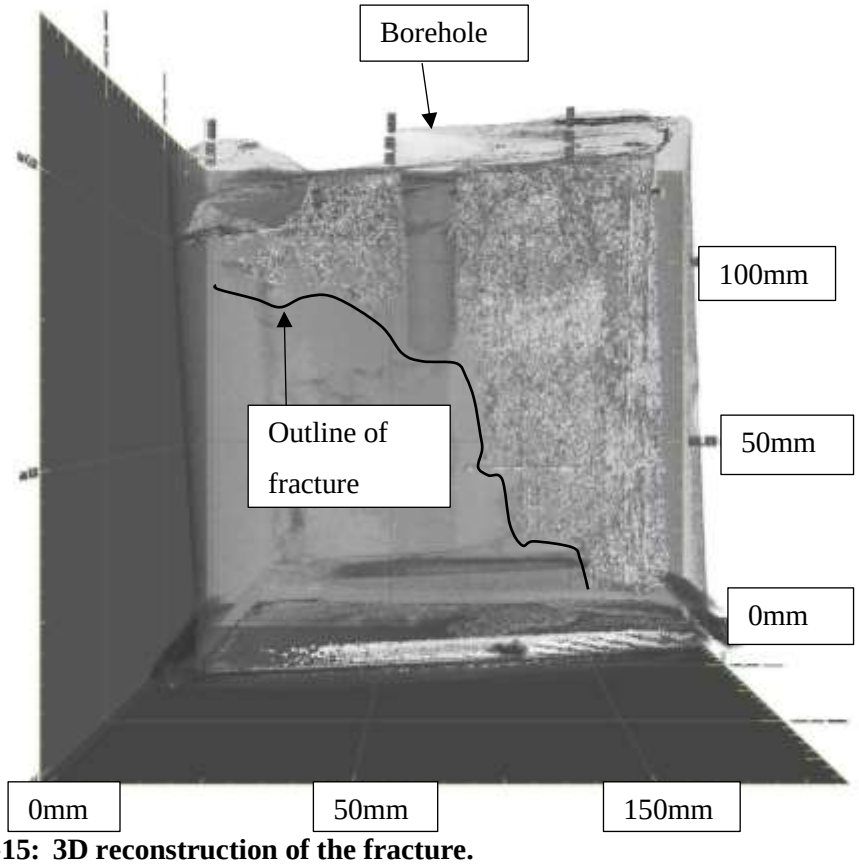

FIGURE 4-15: 3D reconstruction of the fracture.

(iii) Calculation of porosity

The porosity of a sample is measured using a new tool that has been added to version 2.0 of VGStudio max, the 'New P201' function. This function calculates and displays the pores in the selected plane of view. The P201 function calculates the voids in the sample by taking the thin section of whichever of the three planes (top, right, front) has been selected and comparing the speed of the x-rays as they cut through the sample.

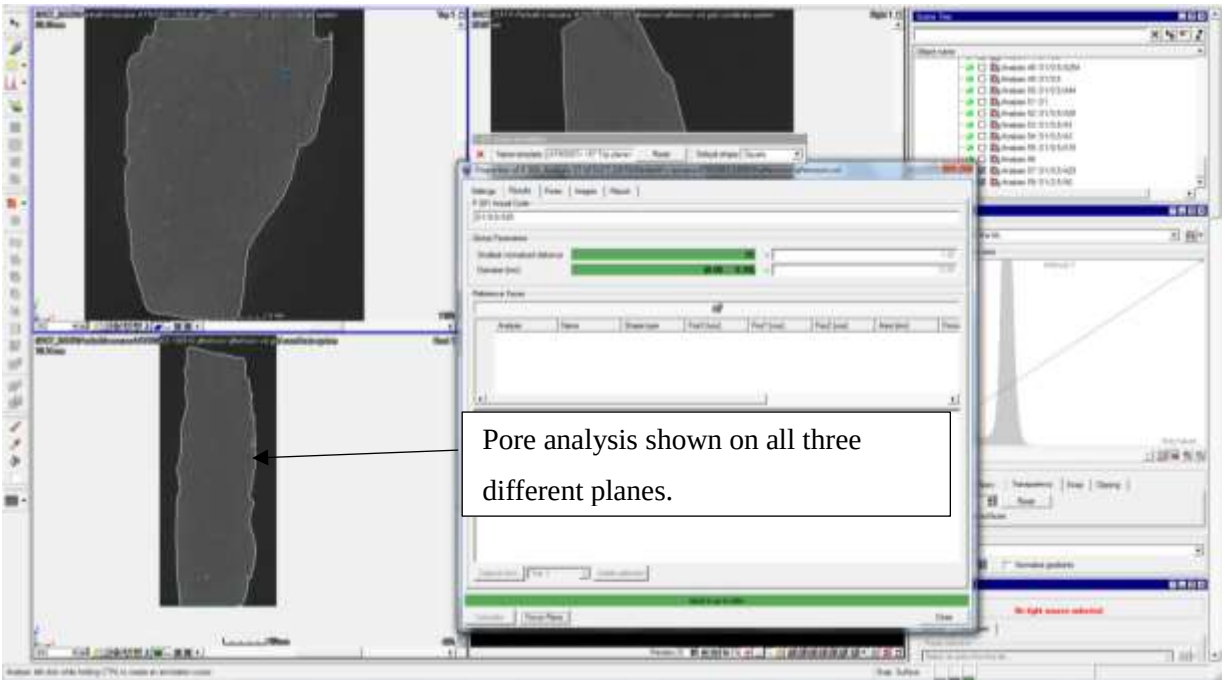

FIGURE 4-16: P201 function working.

The threshold bar sets the border between the sample and background which is marked with orange to show the areas of void. If the orange background pixels show inside the sample, then lower the threshold number gradually until the background is orange but the sample is not. The volume of pores present can then be calculated and placed into the 3D reconstruction and viewed by reducing the transparency of the construction. For this study the transparency has been typically reduced to 4 percent. However, this function can be time consuming and dense samples can require a large amount of computational time for each plane selected. This would mean that to select each of the 1,000 planes in each of the 3 directional planes (top, right or front) would take weeks for each sample. Therefore, for each section 6 planes were taken so a representative sample of the porosity could be determined.

(iv) Issues encountered with the large size of the sample

During the commissioning phase it was discovered that the CT scanner could not fully penetrate some of the denser samples as the scanner was losing the grey scale settings part way through the scan. This meant that it was impossible to differentiate between the different internal structures which made tracing

the fracture impossible from a depth greater than 20mm. The GE acquisition team believed this was due to the machine operating at the high edge of its abilities for too long. After discussing this with the supervising team, it was decided that the sample size would be reduced from 150mm^3 to 100mm^3. However, the predrilled samples of Accrington Mudstone, being composed of a less dense material were able to be fully resolved at the original sample size of 150mm^3.

Due to the sample size reduction from 150mm^3 to 100mm^3 the metal pressing plates also had to be reduced to 95mm^2 in order to ensure that when the plates were compressed they would not connect with each other and thus not fully compress the sample.

4.2.2 Preparation of shale samples.

The fracturing rig was originally designed to fit a sample of 150mm^3. However, as just discussed in the previous section the sample size was reduced to 100mm^3. To achieve a sample size of 100mm^3 a sample was selected and cut using a concrete saw to dimensions just smaller than 100mm^3, Figure 4-17.

FIGURE 4-17: Shale sample cut to just short of 100mm^3.

In order to make up the small difference of a few millimetres to ensure that all sides had flat equal faces a high strength plaster was added. Cassini plaster was selected for this purpose and a ratio of 30:100 water to plaster was used. The plaster was subjected to a test prior to being used with the shale samples to ensure that it was fit for purpose whereby a small 100mm^3 sample of plaster was made then left to set. After 3 days the plaster was placed under a pressure. The plaster failed at 12KN, failing in an apple core pattern as shown in Figure 4-18. Though this strength is lower than expected it is still reasonably close to the strength of the weak shale samples that would be used and was, thus, deemed as adequate.

FIGURE 4-18: Apple core failure of the high strength plaster.

The shale samples were then placed in a 100mm^3 mould (Figure 4-19) and the plaster was added to ensure the exact dimensions were formed. It was then allowed to set for 3 days.

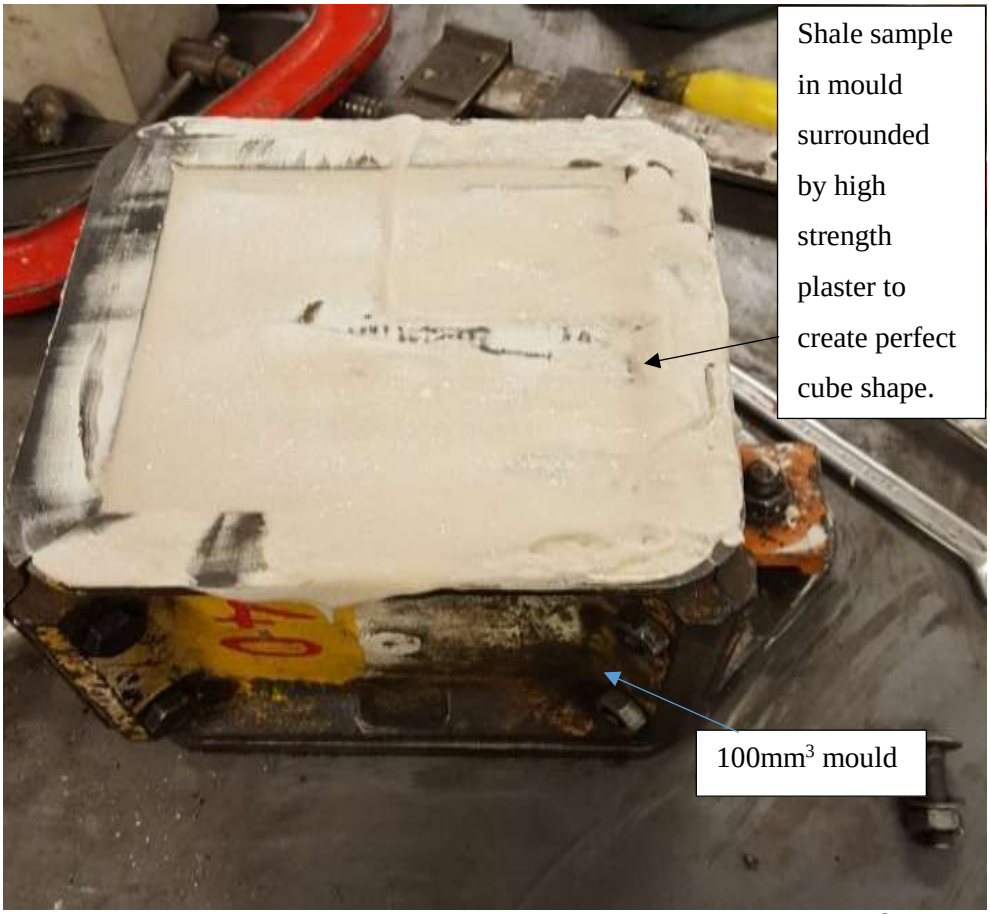

FIGURE 4-19: Shale prepared with high strength plaster added to make 100mm^3.

4.2.3 Drilling set-up.

The bottom flat jack is secured in place and its inflow is attached to a service port. In biaxial mode this flat jack is not pressurised but as the sample sizes and supports have been calculated to provide a tight fit once installed the flat jack is left in place.

The bottom sensor housing plate is then placed on the bottom flat jack. The sensor inside the plate has standard exterior window sealant pasted to it to ensure that there is a smooth and continuous grip between the sensor and the sample. Placing the sensor without a viscous substrate would mean that there could be microscopic gaps between the sensor and the sample which would hinder the acquisition of acoustic data. The sample is carefully loaded onto the plate, taking care to ensure that the sensor attaches and sticks on to the sample itself and not to any of the plaster.

The wires from the sensors are fed through another service port. The combined flat jack and sensor housing plate supports were put in place on all four sides to surround each side of the sample. The sensors have a small drop of sealant placed on them and, like the bottom sensor, are attached to the shale. Flat jacks are placed on two of the sides of the sample perpendicular to each other – in order to allow the sensors to perform the function of σ^2 and σ^3 stresses when the rig is operating in tri-axial mode and σ^1 & σ^2 when the rig is in biaxial mode. A metal plate is placed between the sensor housing plates and the flat jacks to ensure that the pressure is shared equally across the whole of the diameter of the flat jack and to ensure that there is a solid metal plate that the jack can press upon. Any unequal pressure could force the flat jack cushion to balloon and pop. For the same reason a solid metal plate is also placed behind the flat jack, again covering the whole of the face. Behind this is more metal packing to ensure that the flat jack is pressing against a solid surface from the wall to the sample as shown below in Figure 4-20.

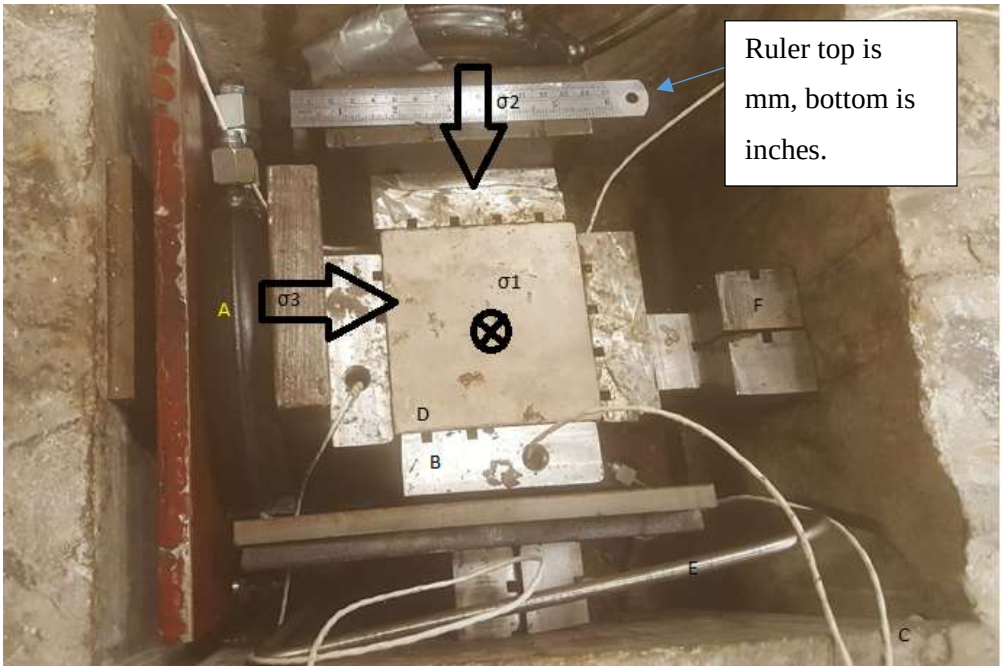

FIGURE 4-20: Sample set up with acoustic sensor inside metal plates - the top plate is not in place to show how the sample fits in. A = Flat jack, B = Metal plates, C = Sensor Wires, D = Sample, E = Hydraulic pipe feeding the flat jacks, F = Packing. Arrows show the direction of different stress directions.

The acoustic emission software is then set up and the positions of the sensors are checked against the position registered manually on the computer. The relevant material selection is made in the software and the system is ready to acquire. The two side flat jacks are then pumped up to relevant pressures. One exerting at least 60 bar (6MPa -σ^3) and the other exerting at least 65 bar (6.5MPa - σ^2). These pressures represent σ^2 & σ^3 and as with normal rock formation σ^2 is always a greater value than σ^3.

When the rig is performing under tri-axial conditions the lid is then placed on top of the concrete structure and is securely fastened using the high strength bolts and screws. The bottom flat jack is then pumped to a pressure of no more than 120 bar (12MPa), this will provide σ^1 reflecting the overburden pressures that a sediment is subjected to.

Through the central hole in the lid a drill is then placed which is marked every 10 mm along its length as the drilling is carried out in 10mm increments. This software only allows for 26 groups of acoustic events to be made so if the drilling to the centre of the sample is carried out in one go there would be too much data to accurately group any of events, i.e. data points would be clearly clustered but not grouped together. In addition, too much data would be visible making it impossible to track the acoustic waves chronologically. Therefore, if the acoustic emissions from the drilling of the shale are collected on an incremental basis, a much clearer picture of the progression of damage and microfracture growth from around the borehole will be obtained, as shown in Figure 4-21. Each individual grouping is given a letter so that it can be identified.

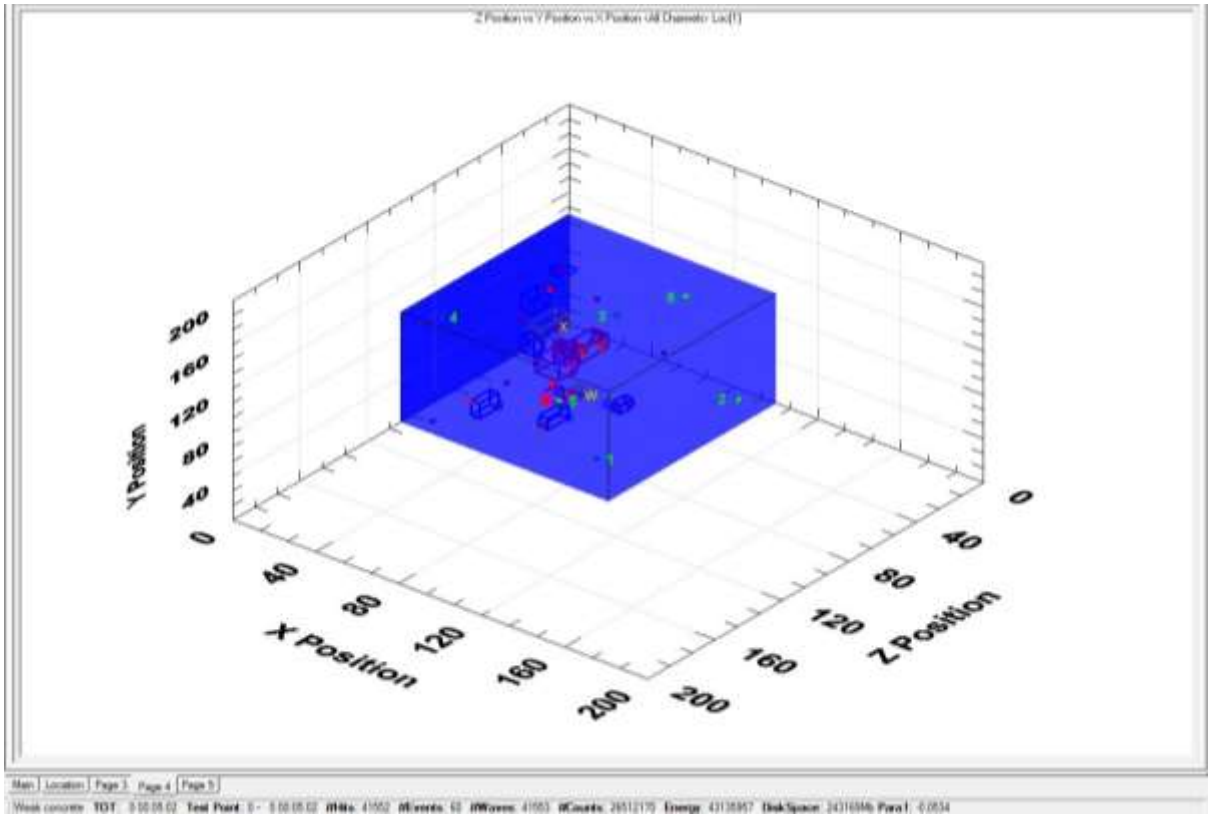

FIGURE 4-21: Grouping of acoustic events, the numbers show the position of the sensors and the letters denote the individual emission groupings.

Once the drill has reached 50mm. The fluid injection nozzle is inserted into the borehole and the fracturing fluid is pumped into the borehole. Upon the sample fracturing, identified when the pressure gauge (measuring the fracturing fluid pressure) drops, the pressure is released in the bottom flat jack. The lid of the rig is then removed and the pressure released from the side flat jacks. This allowed the sample to be removed and scanned. The measurements of the fracture were taken and compared to acoustic maps.

4.2.4 Acoustic testing

The Acoustic software works on the basis that each individual sensor contains a crystal. When an acoustic emission, a pressure wave, hits a sensor the crystal forms an electrical current. These currents travel to the computer which records the time of arrival, then compares the timing of that current with arriving signals from the other sensors. To create a 3D placement the software needs signals from at least 3 sensors. The software uses algorithms to place the source of the emission based on the timing of the signal arrivals and the placements of the sensors on the sample, the locations of which are input into the software before starting. The software spatially locates the signal hits received by using that same signal received by at least three sensors thus triangulating its placement. This placement derives from the input of a wave velocity (WV). The strength of the signal and its reverberation are based on the strength of the pressure wave. This allows for the various types of signal to be differentiated by the system.

A sample of concrete was cut to 150mm^3 and placed into the void in the concrete frame. The concrete void was filled, as shown Figure 4-22. On the side of each face a flat jack support followed by a metal plate support was placed. The flat jacks were placed on their supports on each side wall of the void, Figure 4-22.

FIGURE 4-22: Sample placed for acoustic confidence testing, this time with the top metal plate attached.

An acoustic emission sensor was placed into the hole in the metal plate, while an 'o' ring Swagelok fitting was screwed into the BSP fitting, in the metal plate, and the wires led out of the concrete fitting, Figure 4-23.

FIGURE 4-23: Acoustic sensor fitted in to the metal plate.

The concrete sample was then placed next in the sequence; the ordering sequence is shown in Figure 4-24.

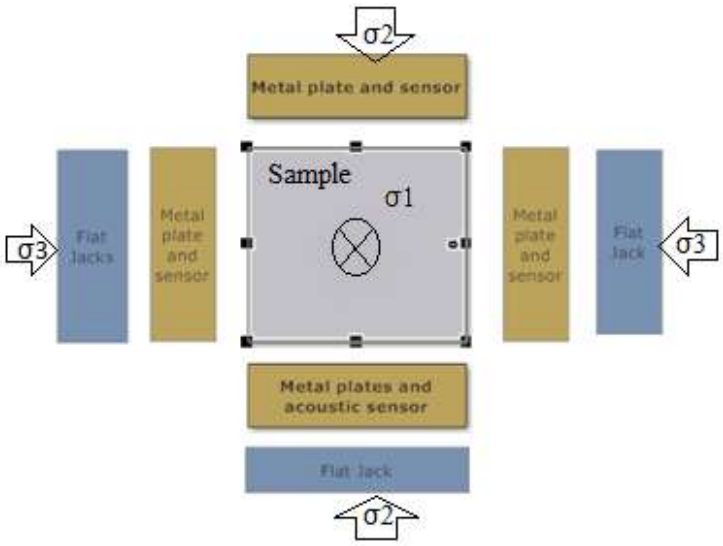

FIGURE 4-24: Ordering sequence of the plates in relation to the sample in planar view.

The acoustic monitoring system was turned on and the position of each sensor was entered onto the computer, this ensured that the software could accurately place each acoustic emission if there were at least 3 sensors detecting it. To test this system would work, a 20mm drill bit was drilled into the middle of the top face of the sample through the hole in the top metal plate. Once the hole was drilled into the sample, a 20mm diameter metal rod, with a 30^{o} tip and 150mm in length was then placed into the drilled

hole. This metal rod was hit once with a 20lb lump hammer in order to induce a fracture into the concrete. The live view screens were observed to see where the acoustic sensor picked up the acoustic emissions. This data was then used to fine tune the software, where, through a series of iterative steps, the wavelength was determined for a sample under stress loading. Once the correct position was detected the correct loading pattern was secured. Before this was carried out the software picked up noise emissions and placed the detected emissions in the centre of the concrete block no matter where the noise was initiated from. As shown in Figure 4-25 it was determined that the threshold, the point above which the computer would analyse and place the emissions, was set too low at 45dB. The wave velocity was also set too low which meant that anything below this threshold was being ignored. The wave velocity is the speed at which the acoustic emission travels through an object. The denser the material the slower the wave travels.

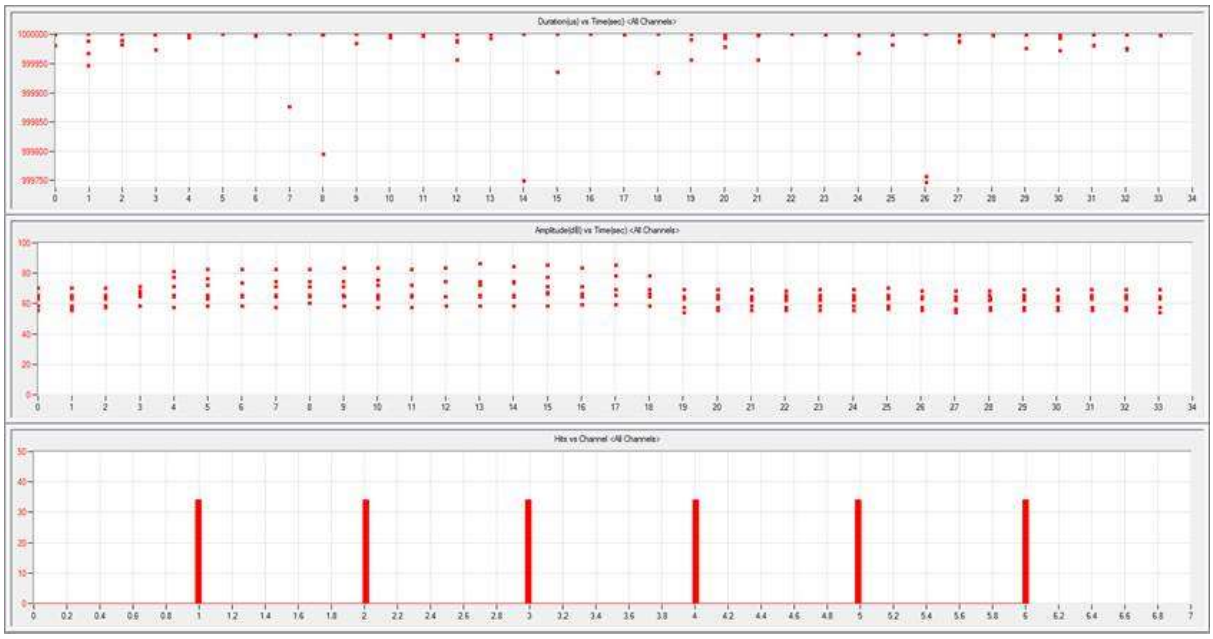

FIGURE 4-25: Graphs showing the saturated noise emissions within the concrete.

This created two main problems that needed to be resolved. First the low wave emissions that were detected meant that the system was saturated with too much noise. This left the system unable to accurately pinpoint the placement of the concrete block as shown in Figure 4-26.

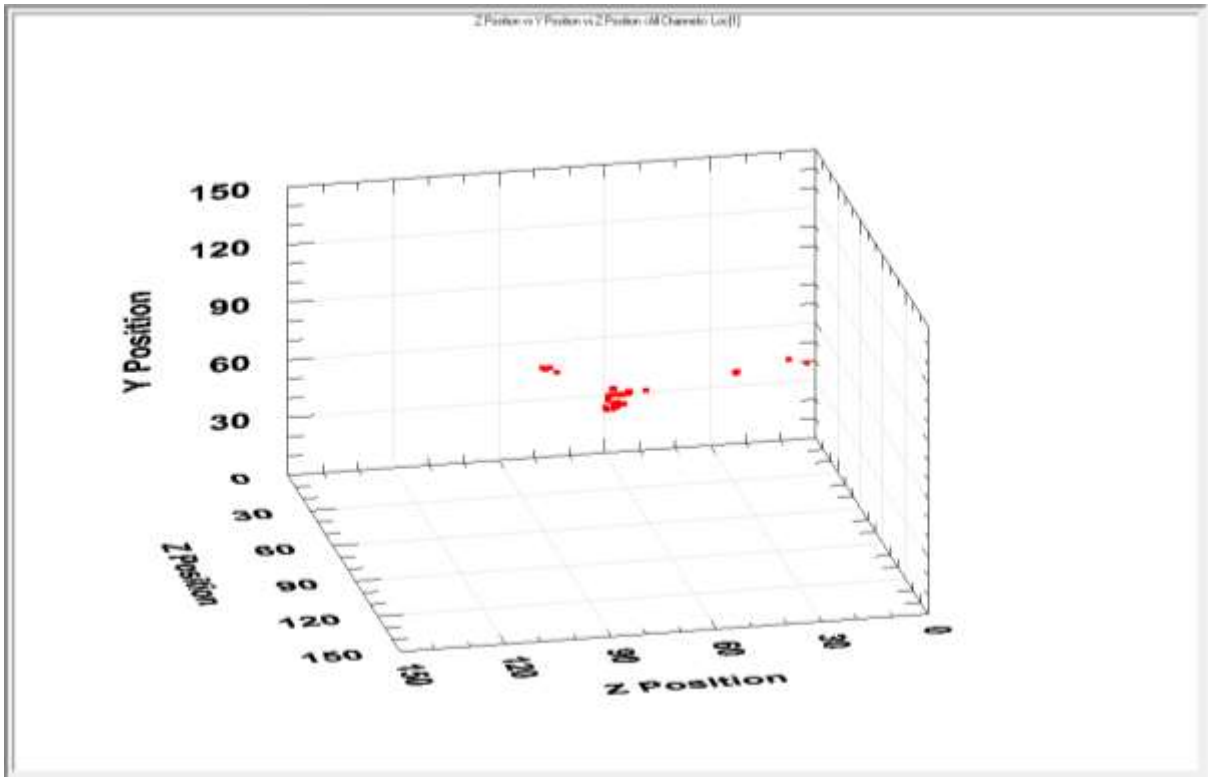

FIGURE 4-26: Overly saturated noise emissions detected in the middle of the concrete, the red dots represent detected events.

Secondly, the wave velocity was too low which meant that the computer sensors were calculating the emission at a reduced speed. If the sample was homogenous, like manufactured steel, it would be possible to calculate the speed accurately but as the concrete and shale samples (to be analysed later) are not homogenous the author had to start by using velocities typical of that material and then refine the data. The first concrete sample had no aggregate and was just composed of a sand and cement mix so was more like a sandstone, therefore, typical sandstone wave velocities were used. This improved the accuracy of locating the source of the acquired waves.

After the first concrete was scanned, planer images were produced. These images were tracked and compared to the placement of acoustic hits detected in accordance to their placing on the three-dimensional graphs.

PROBLEMS ENCOUNTERED

During the initial testing it was found that the acoustic emissions were scattered and chaotic. A number of concrete samples were tested at this time, but the results were still the same. In order to solve this issue, the sensors were taken off the sample and tested individually by breaking a pencil on the sensor, a HB pencil break next to a sensor registers as 100Db. Originally each sensor picked up the noise, however, when placed back on the sample it became clear that some of the sensors were either not

picking up acoustic signals or were picking up signals when no acoustic event had taken place. To prevent this from occurring the connections for the wires were re-soldered and then the sensors were re-tested.

During this period, it was also noted that sensors 6 and 2 were still registering 'ghost' acoustic events where none had been initiated but when the sensors were placed outside of the metal plate the sensor registered no acoustic events. Therefore, the metal plates would be removed for the initial testing period. Fortunately, at this point it was discovered that the factory settings for the acoustic sensor software had been set incorrectly so that instead of running at 28volts it was only running at 3 volts. This was corrected immediately and the trials were run again with no further problems encountered.

4.2.5 Fracturing fluids

A fracturing fluid was made up using the Guar polymer. The project required a fracturing fluid that was between 3 to 5.5cp. Three 150ml samples were made up using 3g, 5.5g and 8g of guar added to the water, respectively. The samples were mixed using a fast mixer for 20 minutes.

4.2.6 Fluid injection

During the initial testing of the fluid injection system, the sample was set up as shown below in Figure 4-28. A hydraulic pipe with an outer threaded part was fixed to a metal channel with a 6 mm connector. This was in order to keep the pipe fixed whilst allowing it to be placed securely within the borehole and lowering the risk of movement when pressure is applied as fluid is pumped into the borehole. This also stops the injector being forced out by the increase in fluid pressure during this phase. The injector nozzle, shown in Figure 3-11, was screwed onto the end of a tapped hydraulic pipe and inserted directly into the borehole forming a water tight seal. The injection system was then screwed on to the hydraulic pipe, as shown in Figure 4-27. The injector system sits on top of the metal plate and the metal train is careful tightened in order for the blow out preventer to form a perfect seal and prevent any rush of fluid flowing into it.

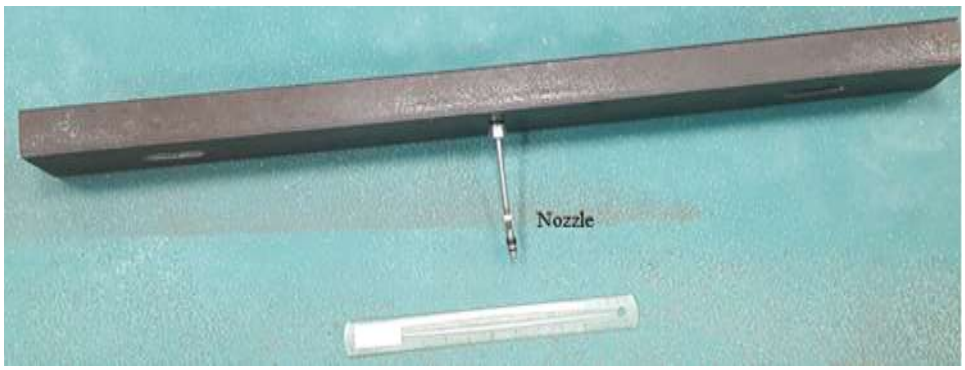

FIGURE 4-27: Fluid injection system set up.

FIGURE 4-28:: Fluid injection system set up and in place

EXPERIMENTAL ISSUES DERIVED FROM INJECTING FLUID

(i) ***No seal inside the borehole*.**

In this design the top metal pressing plate had two 3D printed plastic packing pieces, lower than the height of the grooves which surround the central hole in the pressing plate, placed to a depth of 3 mm, Figure 4-29. A 3mm thick rubber was then placed on the plastic packing (Figure 4-30). In theory this would provide a seal around the central hole in the top metal plate through which the pipe is inserted into the borehole. In conjunction with the fluid blowout preventer this should have sealed the top of the plate so that a large pressure head could be built in the bore hole. Tightening the blowout preventer onto the metal plate would then tightly force the metal plate onto the face of the sample. Once secured the fracturing fluid was pumped into the hole and the pressure gauge was observed. The top of the sample was also observed to watch for fluid leakage. A number of initial attempts were made to screw down the plates and the blowout preventer tighter onto the sample but none of these registered an increase in the fluid pressure in the borehole. With each repetition water leaked out from under the

plate. It was later determined that the small surface defects in the sample meant a watertight seal could not be achieved using this technique.

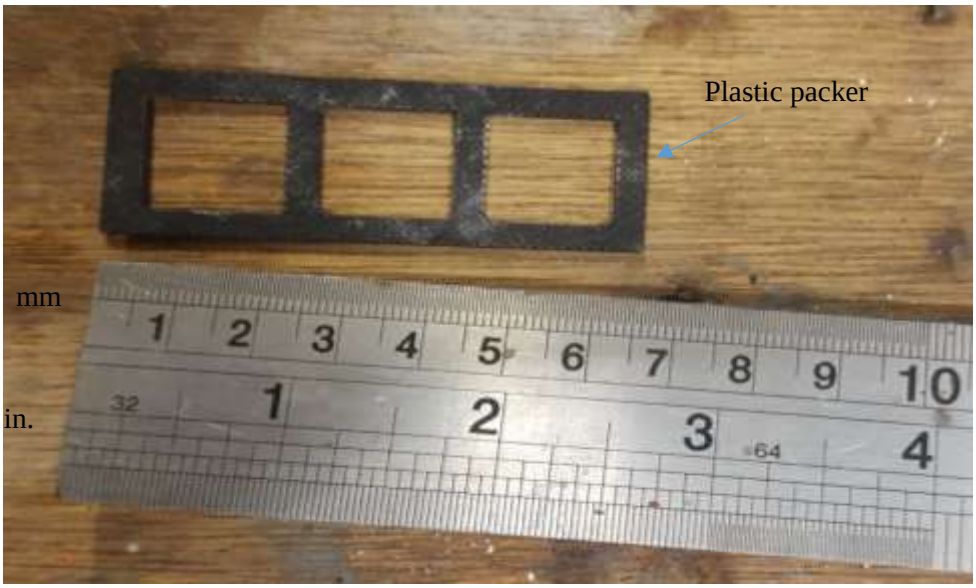

FIGURE 4-29: Plastic packer.

FIGURE 4-30: Plastic packer and rubber seal placed on the metal plate.

(ii) Bung placed on the end of the injection piece.

The failure of previous attempts to use a seal in the metal plate showed the importance of forming and keeping the fluid pressure head within the borehole. To this end a rubber bung was screwed into the tapped end of the injection device with 'o' rings placed underneath it, Figure 4-31.

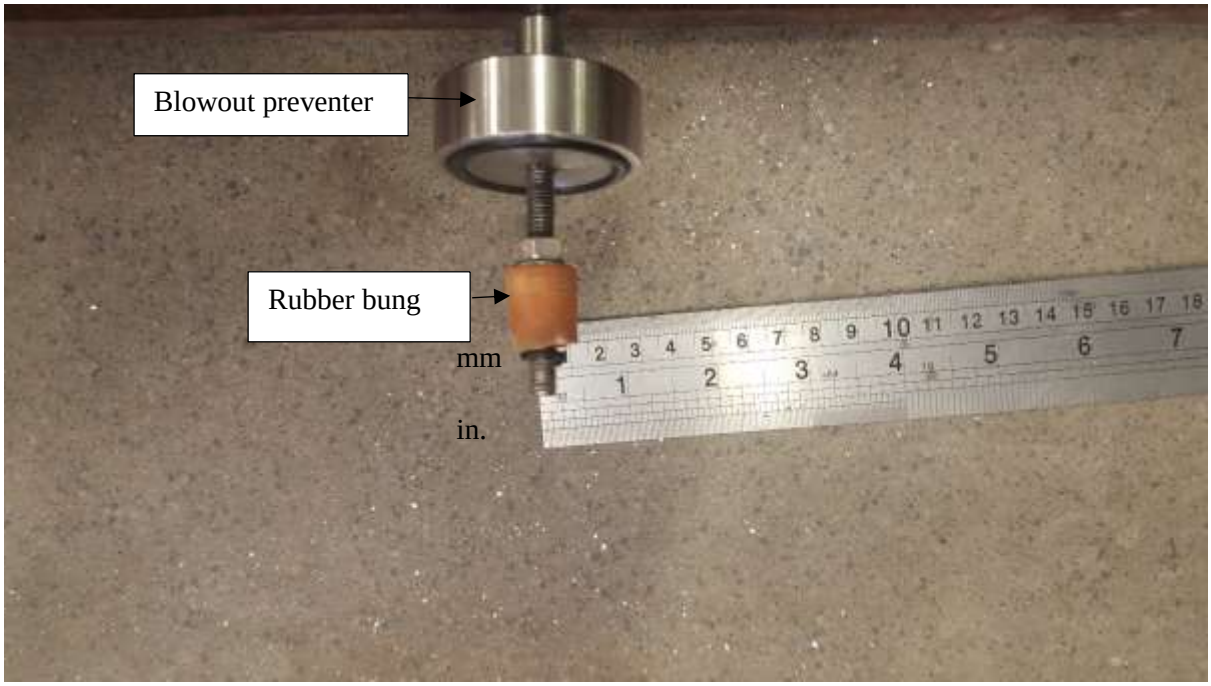

FIGURE 4-31: Rubber bung attached on to the fluid injection pipe.

The fluid injection system was placed into the borehole and the channel screwed down slowly, ensuring the blowout preventer was resting snuggly on the metal plate. This ensured the bung was slowly squeezed into the borehole, giving a fully water tight seal. Fracturing fluid was pumped through the injection system into the borehole. With this procedure it was possible to reach 1,000 psi before the seal broke and 2 acoustic emissions were recorded showing a micro fracture had formed. However, upon reaching 1,000 psi the seal would break and fluid would slowly leak out of the borehole onto the top plate. Upon removal of the fluid injection system it was noted that the bung was deformed due to the high pressure it had been subjected to and that this deformation was breaking the water tight seal and causing the drop in water pressure.

4.3 Chapter Summary

In this chapter the apparatus used in the experiment has been listed and the evolution of the design of the apparatus has been described; including how the concrete rig structure has evolved from housing a complex void shape to being revaluated in the design process to make the void space a simple cube. This chapter has also looked at the problems encountered in getting accurate acoustic and x-ray image data and getting the fracturing fluid to pressurise to a sufficiently high pressure to induce a fracture in a sample.

This chapter also shows how the apparatus has been assembled and how the experiment has been carried out. It describes how the samples are scanned before the experiment to see if there are pre-existing fractures, setting up the sample and applying pressure whilst taking acoustic readings, and then the

drilling and fracturing process. A 5cp guar based fracturing fluid was prepared and injected into the drilled sample.

5 Results and discussion

5.1 Introduction (Phase III)

The results and discussion section presents both the results (CT scan images and acoustic emission data) gained during this experiment and the discussion and analysis of those results. The results of the CT scanner, i.e. the placement and location of fractures, are used to validate the results of the acoustics. However, as this experiment includes the design of a brand new rig which has not been used previously, it is important to understand how the results were obtained. Therefore, this section also covers the commissioning tests and the confidence testing of the both the acoustic data and CT scanner.

The structure of this section is shown in the flow diagram Figure 5-1.

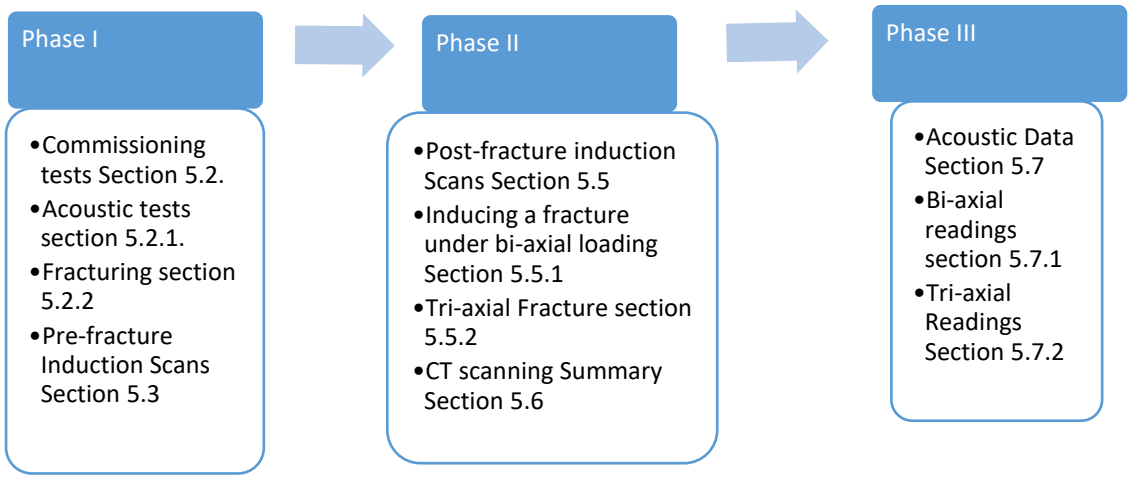

FIGURE 5-1: Flow chart showing progress of the results section.

5.1.1 Methods of Data Processing

In this investigation the data processing is split into three distinct areas;

1. Geomechanical data: Pressures applied to the sample and fluid pressures obtained in the borehole when the sample is fractured.

2. Fracture measurements: Dimensions of the fractures once the fracture has been induced within the samples.

3. Acoustic Data: Data of drilling damage and fracture inducement in the sample.

The geomechanical data of each sample was recorded from the calibrated pressure gauges used along the pressure lines and then presented in a simple spread sheet. This spread sheet is combined with the

fracture measurements and the settings used on the CT scanner for each setting. These fracture measurements are taken from the CT scan of the samples, the plane that is perpendicular to the length of the fracture were used to take measurements on and four distances from the borehole are taken on each fracture half length, shown in Figure 5-2. The following measurements were taken for each plane; distance from the borehole, full height of the fracture, the maximum width, 30% of the maximum width for the top and bottom halves of the fracture, 10% of the maximum width for top and bottom halves of the fracture, distance from the maximum width and to both the 10% and 30% max widths.

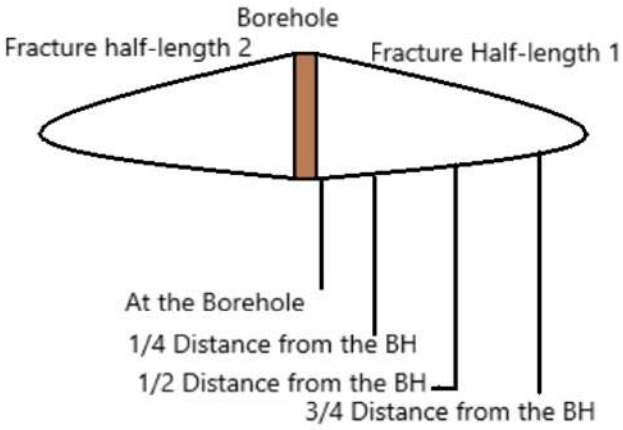

FIGURE 5-2: DESCRIPTION SCHEME FOR MEASURING INDUCED FRACTURES

Acoustic data was collected by the acoustic software. The software placed the locations and energy data that were derived from the sensor returns. This data was then recalled onto graphs with pictorial representation to show where the acoustic events had taken place.

5.1.2 Potential for Error in Data

In this investigation there are two separate areas that could cause a potential error in the results.

(i) CT scanning

Errors can occur during both the mapping and the measuring of the fracture parameters. While mapping a fracture it is possible to zoom into the planar view and still be able to make out the graduation of grey changes that mark the boundary of a fracture to 0.01mm which equates to 0.5mm on the scale bar. As the human eye can clearly distinguish to a point of 0.25mm this would mean each side of the fracture could have an error of 0.005mm which gives an overall error of ±0.01mm for the fracture. Whilst measuring the fracture the same discrepancy can occur again giving a potential error of ±0.01mm on the fracture parameters. Taken together this would give a potential error of ±0.02mm.

(ii) Acoustics

The acoustic software can locate the source of an acoustic emission using the signals received by a minimum of three sensors to triangulate from. Any possible errors other than those based on the timing of the signal arrival could be caused by the operator when inputting the original placement data for the sensors, by a change in medium or by using the incorrect wave velocity for the medium being analysed. These issues are discussed throughout the acoustic data results section. Accuracy can be improved by ensuring that the sensor is in direct contact with the shale sample and by using six sensors rather than three. The more sensors used for picking up the signal the more accurate the placement of the acoustic source. Using three sensors the software can place the source within ±1mm, by increasing that to six reduces the error to ±0.5mm.

(iii) Pressure Gauge

The pressure gauges that were used to set the load on the flat jacks and for injecting the fracturing fluid are accurate to 1% full scale, which equates to 0.1378 Bar.

5.2 Commissioning Test Results

5.2.1 Acoustic tests

Prior to commencing full scale testing on the rig, it was essential to run a series of tests to ascertain whether the rig was running correctly and to ensure that all systems were working effectively. To this end several preliminary tests were carried out on concrete cubes in order to save valuable shale samples. A sample was scanned, then drilled then scanned and drilled again before a hydraulic fracture was induced, after which the sample was scanned for a third time. This was so that it could be established if the acoustic emissions aligned with any fractures that were picked up in the scans to promote confidence in the acoustic emission software. Two concrete samples were processed this way before beginning on the Accrington Mudstone samples. The two concrete samples were comprised of a basic sandy concrete containing no aggregate, but one was much denser than the other to cover both conditions when testing the scanning capabilities of the CT scanner.

As described previously, the acoustic software can only work if the user inputs a wave velocity in the sample, this is done reiteratively by applying a wave velocity to a file breaking a pencil at a known place within the sample. With no pressure applied to a sample the wave velocity of an acoustic emission is usually measured in its 100,000's range. The increase in pressure meant the wave velocity of an acoustic emission was quite low, instead of being in the hundreds of thousands the WV stands in the hundreds. The wave velocities are presented below, in Table 5-1.

Sample	Drilling interval mm	Wave velocity	Sample	Drilling interval mm	Wave velocity
AMS1	80-70	50	**WS1**	100-80	1000
	60-55	900	**WS2**	100-70	1000
	55-50	100		fracture	1000
	fracture	100	**WS3**	70-60	800
AMS2	80-70	550		60-50	300
	70-60	550		fracture	1000
	60-50	300	**WS4**	80-70	400
AMS3	100-90	1000		60-50	1000
	90-80	950		fracture	500
	80-70	600	**WS5**	100-90	50
	70-60	250		80-70	310
	60-50	250		60-50	60
	fracture	1000	**WS6**	100-90	70
AMS4	100-90	500		90-80	83
	90-80	1000		80-70	190
	80-70	1000		70-60	100
	70-60	100		60-50	100
	60-50	510		fracture	300
	fracture	500			

TABLE 5-1: Wave velocities used at each drilling interval.

5.2.1.1 Sandy concrete – drilling results

The results shown in Figure 5-3 to Figure 5-5 for the sandy concrete are the acoustic hits recorded for the final 5mm of drilling down to the middle of the sample. The previous 45mm of drilling was used to fine tune the acoustic software so the results were not recorded. The graph shown in the top left (A) represents the acoustic recordings spatially on the Y axis. the top right plot (B) & the bottom left plot (C) shows the locations of the acoustic hits in 3-D space and the bottom right graph (D) is the exact position of each recorded hit in graph form. The blue field in the top right plot denotes the actual sample.

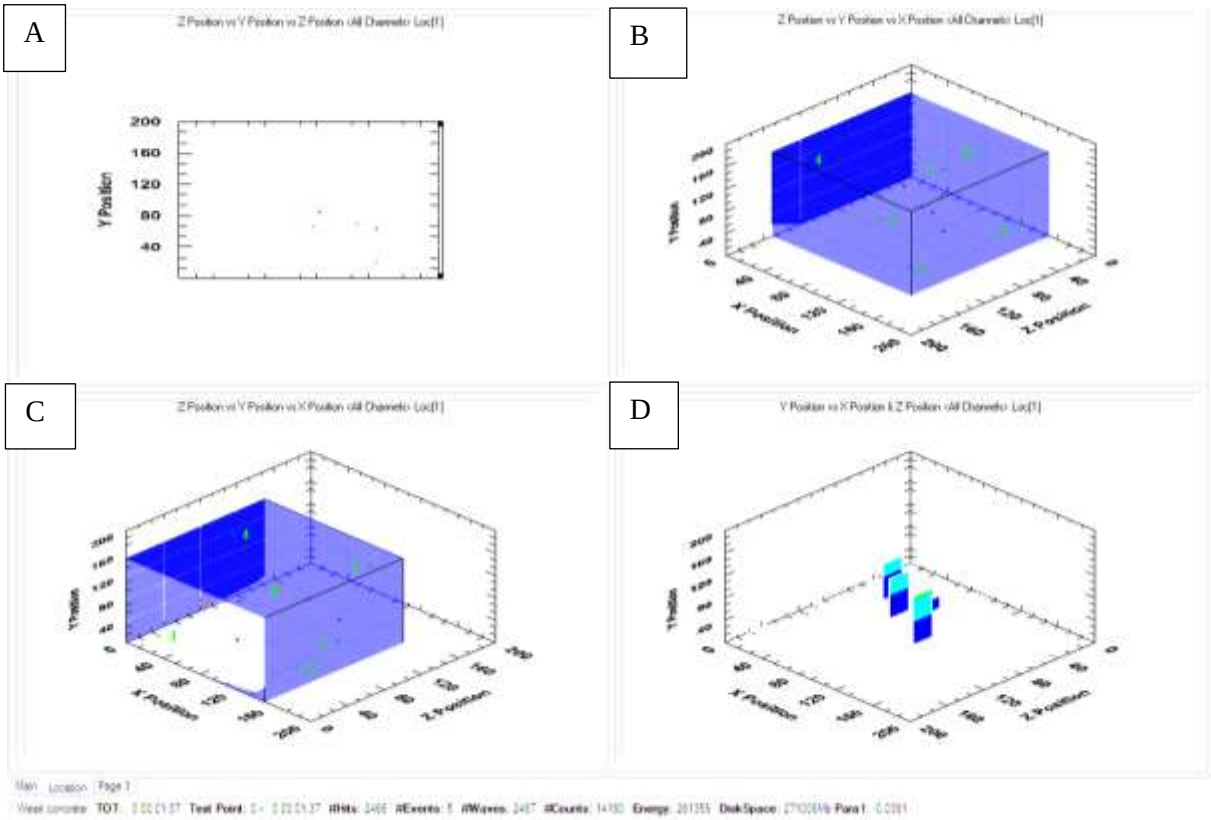

FIGURE 5-3: Concrete sample 1 showing first recorded acoustic emissions; A) Y position Axis, B) 3D view 1, C) 3D view 2, D) Graph positioning of the events

Figure 5-3 records the acoustic waves received from the first concrete sample showing a series of 5 events from 2466 hits (acoustic emissions detected by the sensors) within seconds of each other, extending in a diagonal direction downwards and away from the bottom of the borehole. These hits were aligned with some fractures (shown circled in Figure 5-6) found during the CT scan and equate to the drill hitting the bottom of the hole.

These drilling interval depths do not specifically correspond to depths in the reservoir, as the pressure of the rock is already set at a load that is representative of a depth – in this case the sample is unloaded so will represent a depth of zero, whilst other samples in the investigation will be loaded to represent a rock at depth. These drilling intervals are instead designed to ensure the acoustic data received is not cluttered and therefore more readable.

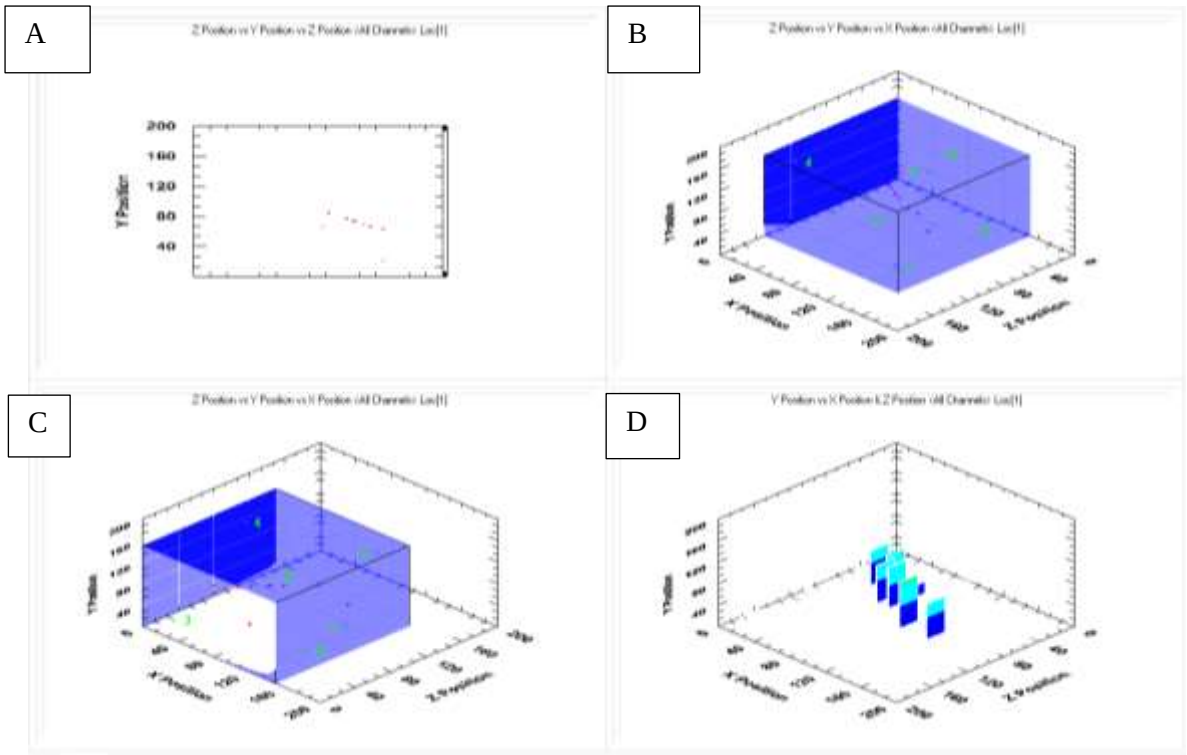

FIGURE 5-4: Concrete 1 second wave of acoustic emissions detected; A) Y position Axis, B) 3D view 1, C) 3D view 2, D) Graph positioning of the events

As the drilling progressed, the recorded hits (Figure 5-4) continued in the same direction as those shown in Figure 5-3and they appear to coincide with the large fracture shown in the CT scan Figure 4.5, which follows the same linear formation as that recorded by the hits.

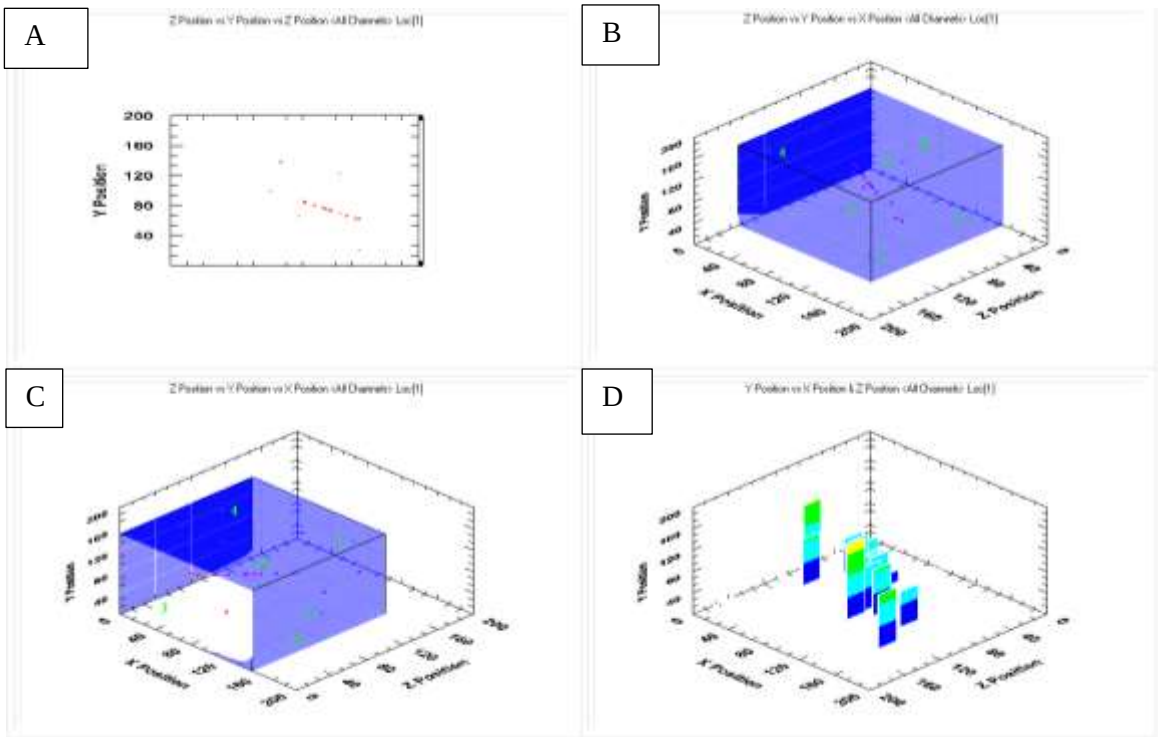

Figure 5-5: Concrete sample 1, acoustic emissions recorded when drilling stopped; A) Y position Axis, B) 3D view 1, C) 3D view 2, D) Graph positioning of the events.

Figure 5-5 then shows a number of acoustic hits recorded higher up from the bottom of the borehole, which goes down to approximately 85mm. These acoustic emissions are reasonably close to the borehole and show that even though the tip of the borehole has passed that point, the rapid rotation of the drill bit can cause vibrations which can reverberate in pre-existing voids or fractures. These additional vibrations would occur as acoustic emissions. The groupings of the acoustic emissions recorded away from the borehole closely coincide with these voids and can be seen in Figure 5-6. Figure 5-6 shows fractures emanating diagonally away from the bottom of the borehole.

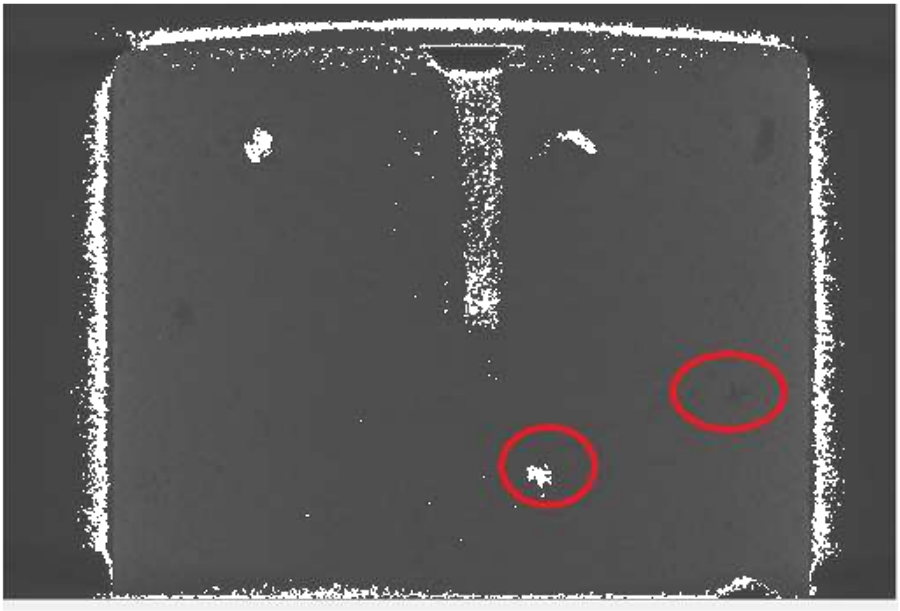

FIGURE 5-6: **Concrete 1 CT scan showing, locations of fractures corresponding to acoustic emission hits**.

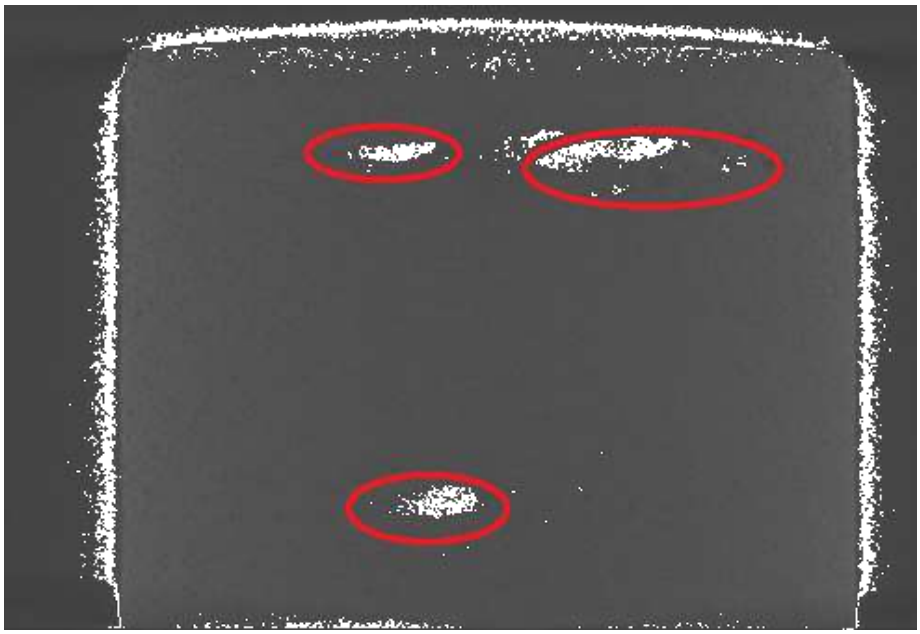

FIGURE 5-7: **Concrete 1 CT scan showing fractures that correspond to the acoustic hits partway down the borehole.**

In Figure 5-7 the scan image is rotated 180º from Figure 5-6 and shows a large void/fracture present slightly to the side and below the borehole, again showing agreement with the acoustic data.

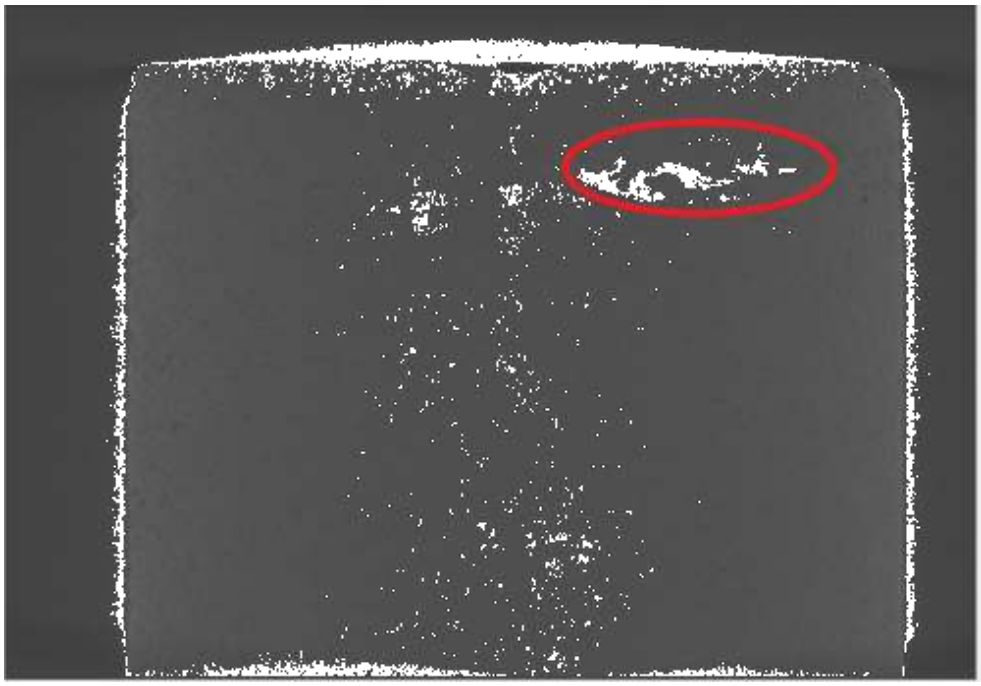

FIGURE 5-8: Concrete 1 CT scan showing extent of fracture width recorded at the side of the borehole.

As discussed during the methodology section, the CT scan is made up of hundreds of planar images. Figure 5-8 shows that as these subsequent planar views are revealed closer towards the back of the concrete sample it becomes more apparent that the fracture recorded to the left of the borehole is very wide as well as long.

5.2.1.2 Second concrete sample – drilling results

The results of the second concrete sample follow the complete drilling phase from the surface of the sample to the base of the bore hole at the centre of the sample. The results are presented below in Figure 5-9 through to Figure 5-14. Second test drilling was carried out from the top of the sample (corresponding to a height just below 145mm on the Y axis - the drill was placed where a number of calibration hits had previously been taken) and taken to a depth of approximately 80mm on the Y axis – a total depth of 65mm. The drill was started on the slowest speed setting on hammer mode before being switched to intermediate, then progressing to the fastest speed setting before finally reverting back to the intermediate setting again. After assessment of the drill speed it was found that a low number of hits were recorded when the speed setting was on slow, however when the drill was set to high speed the acoustic emissions became too clustered to read, therefore, the intermediate setting was chosen to be the optimum setting for the remainder of the project.

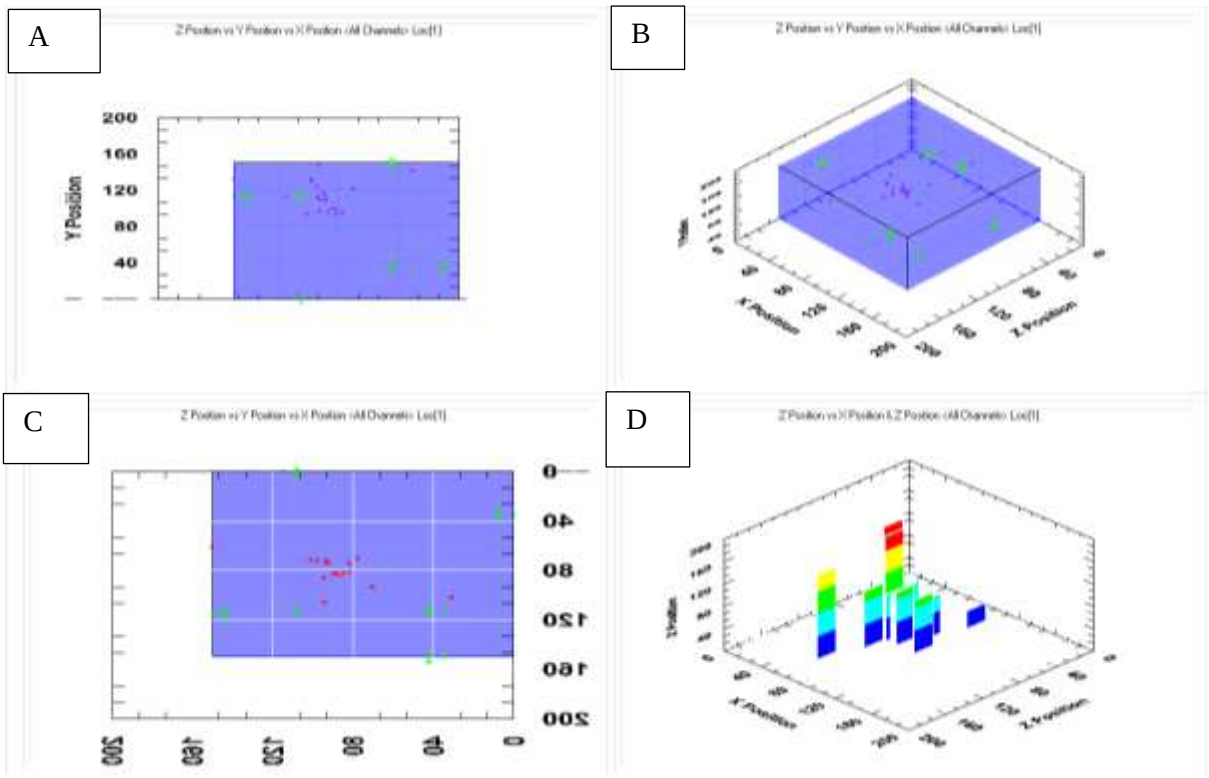

FIGURE 5-9: Concrete 2 acoustic emissions detected at the start of drilling, with the drill speed at its slowest setting 135mm to 80mm. A) Y position view, B) 3D view C) overhead view D actual placements in graph form

Figure 5-9 shows that the first couple of events, (red dots) where the software has placed the hits received, coincide with where the drill strikes at the top of the concrete sample. This is immediately followed by events placed below this location from approximately 135mm down to approximately 95mm, (shown in the top left hand graph in Figure 5-9). The bottom left graph shows the positions of the recorded emissions on the X and Z axes. These two plots show a clear clustering of hits around the borehole location and indicate the continuation of micro fractures that have been induced with the calibration hits.

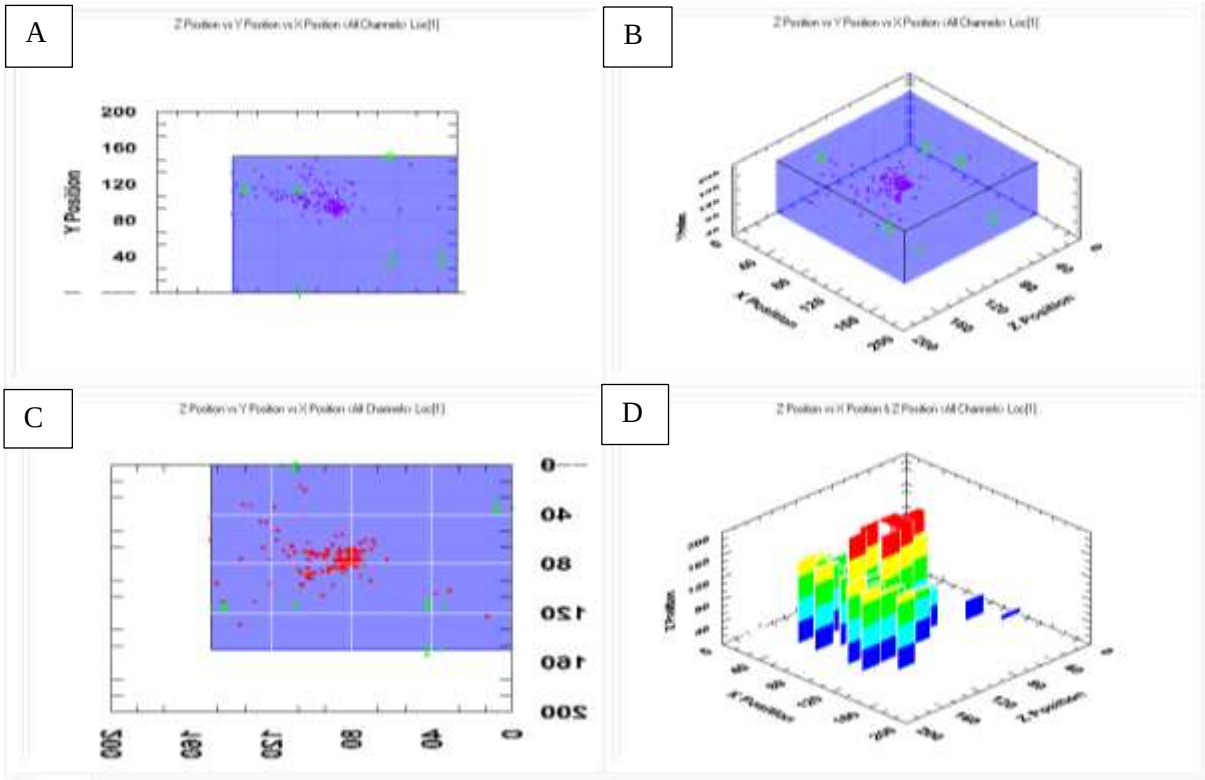

FIGURE 5-10: Concrete 2 acoustic emission as drilling progresses with the slowest speed setting of the drill from 135mm to 80mm. A) Y position view, B) 3D view C) overhead view D actual placements in graph form.

Figure 5-10 shows the progression of the drill, the majority of the events are still reasonably centred, however as the drill advances further into the centre of the sample, the detected emissions begin to advance in a north westerly direction on the plot (as shown in the A and B graph in Figure 5-10). This is to be expected as micro fractures begin to connect, or form a plane of weakness, thereby 'break' evolving along a vector in the direction of least stress applied (i.e. the north-westerly direction). The emissions detected on the left-hand side, top right graph in Figure 5-10, correspond to the author holding the sample to alleviate a vibration problem during drilling. In summary this was deemed to further confirm the accuracy of the acoustic software, as the software was able to accurately plot where my fingers had touched the sample from the small acoustic events this created.

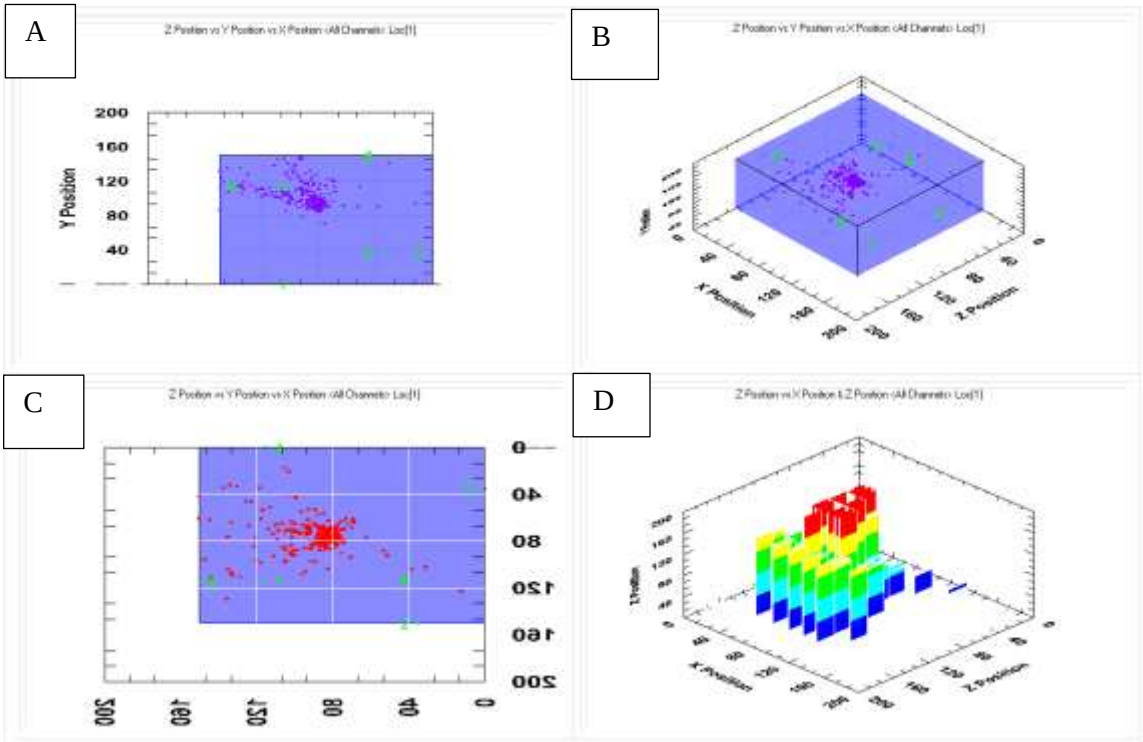

FIGURE 5-11: Concrete 2 acoustic emission hits as drilling progresses 135mm to 80mm. A) Y position view, B) 3D view C) overhead view D actual placements in graph form.

Figure 5-11 shows the emissions, which are now deemed to reflect the microfractures, continuing to be induced during the drilling with the greatest concentration directly below the borehole. As it is the tip of the fracture that causes the emission, this would explain why the hits are now some distance from the drill point seen in A, B and C. The other area of acoustic emission continuing on the left hand side of the borehole is also considered to be microfracture growth. Figure 5-12 to Figure 5-13 show the amplitude and energy emitted by the acoustic hits.

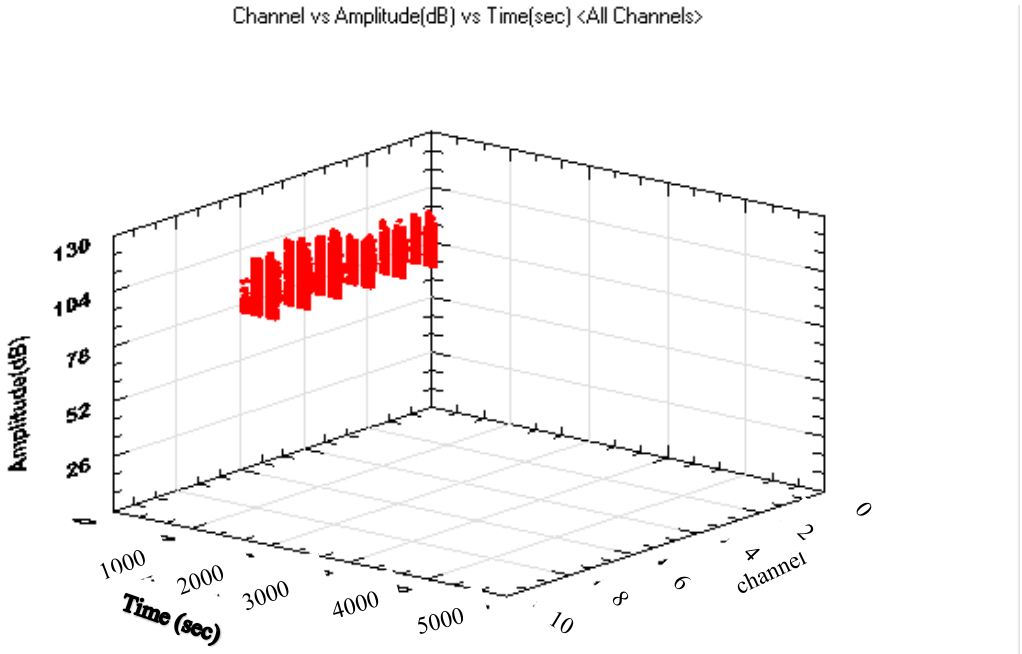

FIGURE 5-12: Concrete 2 showing amplitude levels.

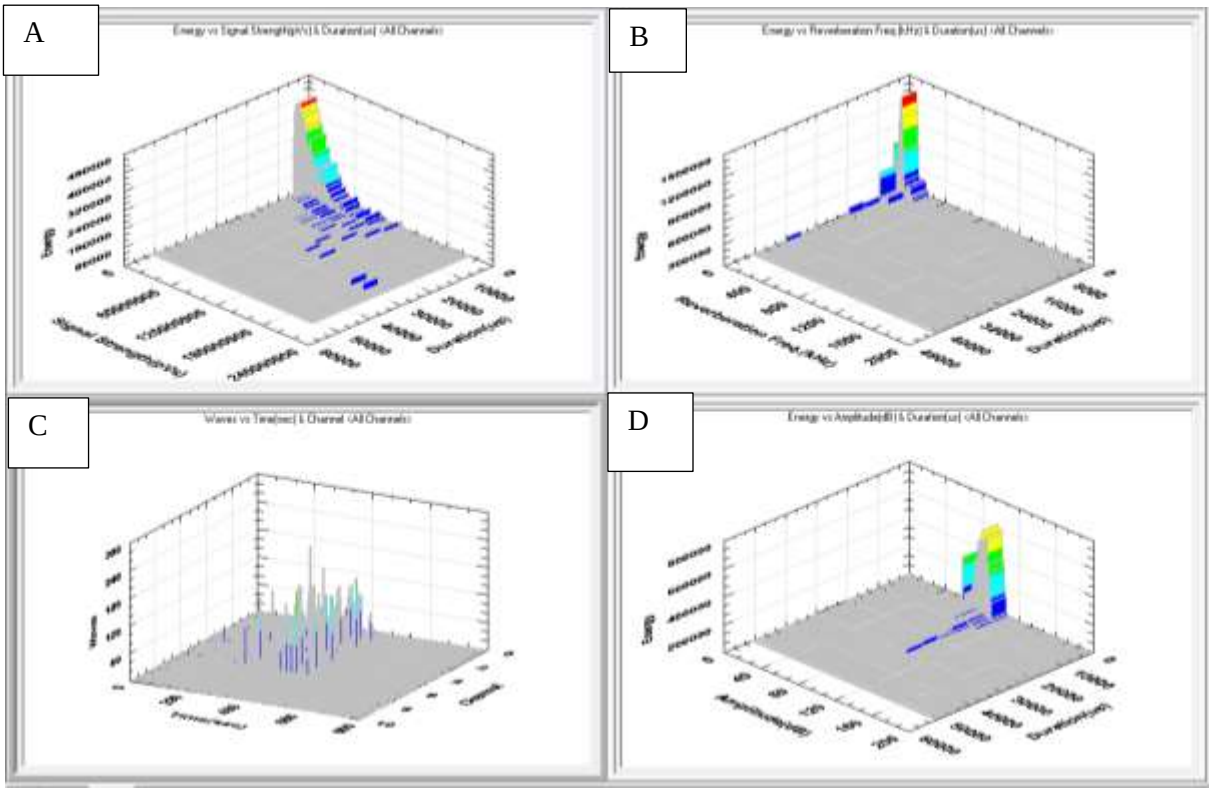

FIGURE 5-13: Concrete 2 energy levels recorded during drilling. A) Energy vs Signal Strength and direction B) Energy Vs Reverberation and Duration C) Wave vs Time (sec) and channel D) Energy vs amplitude and Duration

To more accurately analyse the acoustic emissions, placed as events, the author was able to group the hits of similar acoustic events with a similar waveform in areas of equal size. This could then show the progression of the acoustic hits away from the borehole as the drill continued to penetrate the sample. These groupings show the volume of acoustic hits in each event and the location of the grouping in relation to sample. The result is shown pictorially in Figure 5-14.

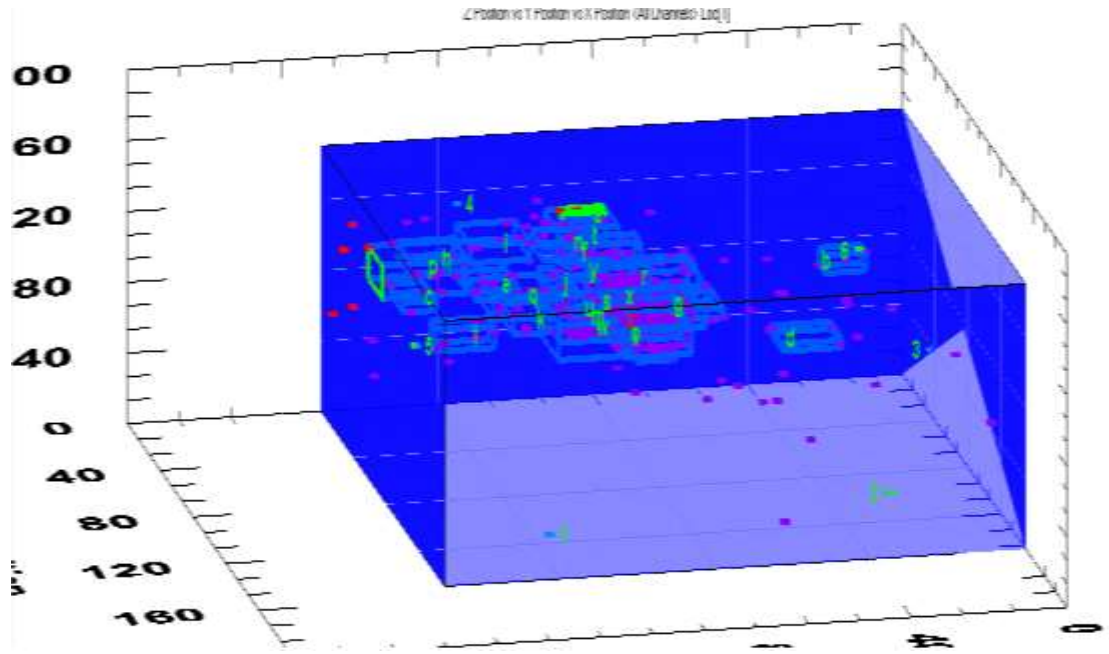

FIGURE 5-14: **Concrete 2 grouping progression.**

Figure 5-14 shows that the largest grouping is located in the area directly below the borehole, while smaller groupings extend from the edge of the borehole to the outer edge of one side of the sample.

5.2.1.3 Accrington Mudstone sample 1

This sample was cut to approximately 148mm^3 and placed in a 150mm^3 concrete cube mould to which plaster was then added to ensure the sample would be exactly 150mm^3 in size. This sample was drilled in the centre of the dorsal face to a depth of 95mm. The drilling was split into 2 sections, the first from 150mm to 135mm and then 135mm to 95mm. These values correspond to the values shown on the Y axis on the top left plots of these acoustic emission graphs. Due to the nature of the mudstone water was added to help smooth the drilling. The acoustic recordings of the two drilled sections are presented in Figure 5-15.

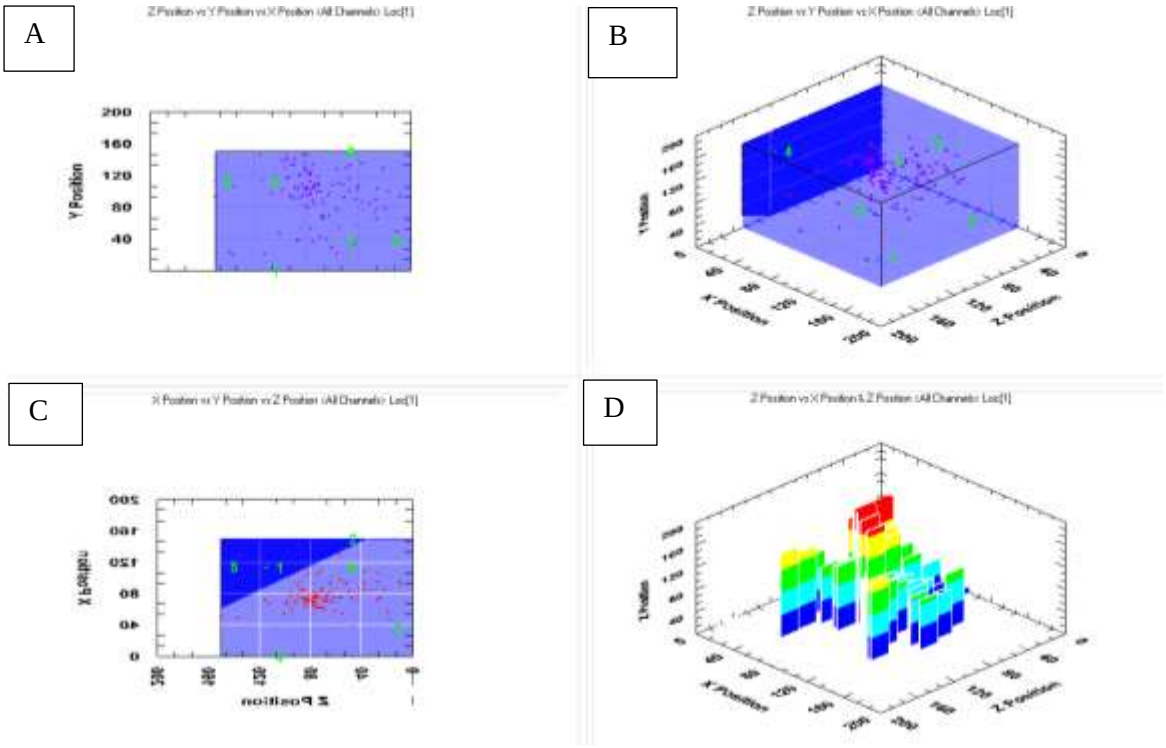

FIGURE 5-15: Accrington Mudstone 1 acoustic emissions detected from 150mm to 135mm. A) Y position view, B) 3D view C) overhead view D) actual placements in graph form.

Figure 5-15 shows the events placed linked to the acoustic emissions from drilling from 150 to 135mm along the Y axis, with the majority of the hits located around the central area of the borehole then developing along one direction. As the section only covers 15mm the sample area is not overly crowded, which shows how the acoustics hits are continuously emitted as the drill progresses.

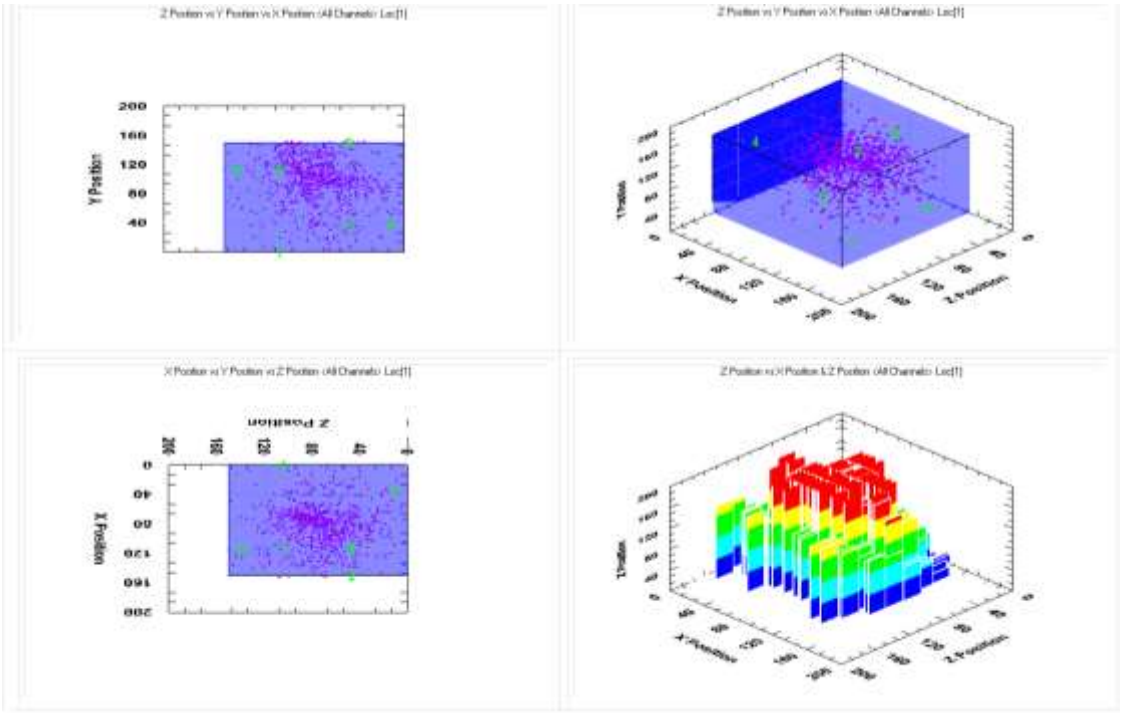

FIGURE 5-16: Accrington Mudstone 1 acoustic emissions detected drilling from 135mm to 95mm. A) Y position view, B) 3D view C) overhead view D) actual placements in graph form.

Figure 5-16 records the drilling event from 135mm to 95mm, drilling from the top downwards i.e. as recorded on the Y axis, showing the acoustic emissions detected over a 45mm drilling depth range. This reveals a more crowded image with a still greater concentration of hits surrounding the borehole. The plot shows the clear progression of the emissions from micro fractures being created below the tip of the drill bit then as drilling progresses so too does the large group of emissions detected approximately 25 to 30mm below the drill tip. The drilling stopped at 95mm (on the Y axis) but a discrete large grouping of emissions can be seen at approximately 60mm on the Y axis. There is also a discernible break in the direction of the face holding the number 2 sensor, this is also the face subjected to the least amount of pressure.

As previously explained it is easier to analyse these placings if each acoustic hit is placed within a grouping. The groupings used are presented below;

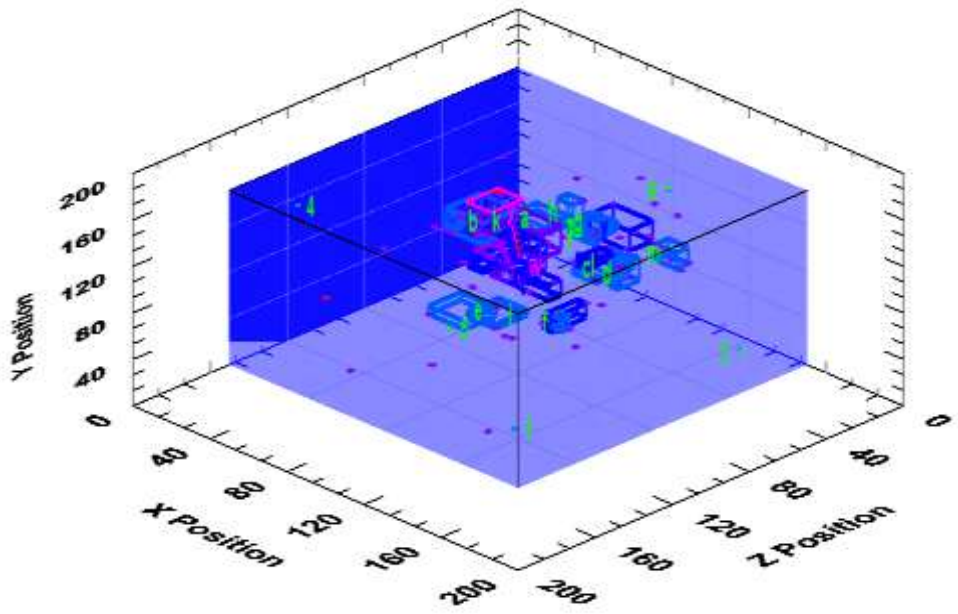

FIGURE 5-17: Accrington Mudstone 1 acoustic emission groupings drilling from 150 to 135mm.

As can be seen in Figure 5-17 which shows the majority of groupings (displayed as labelled boxes in the diagram) are found near and around the borehole, with a few random events that are not within any of the clusters. The breakaway groups of emissions, forming boxes c, l, d, f and m, show a clear progression moving away from the central borehole as the drill reaches further down in the sample.

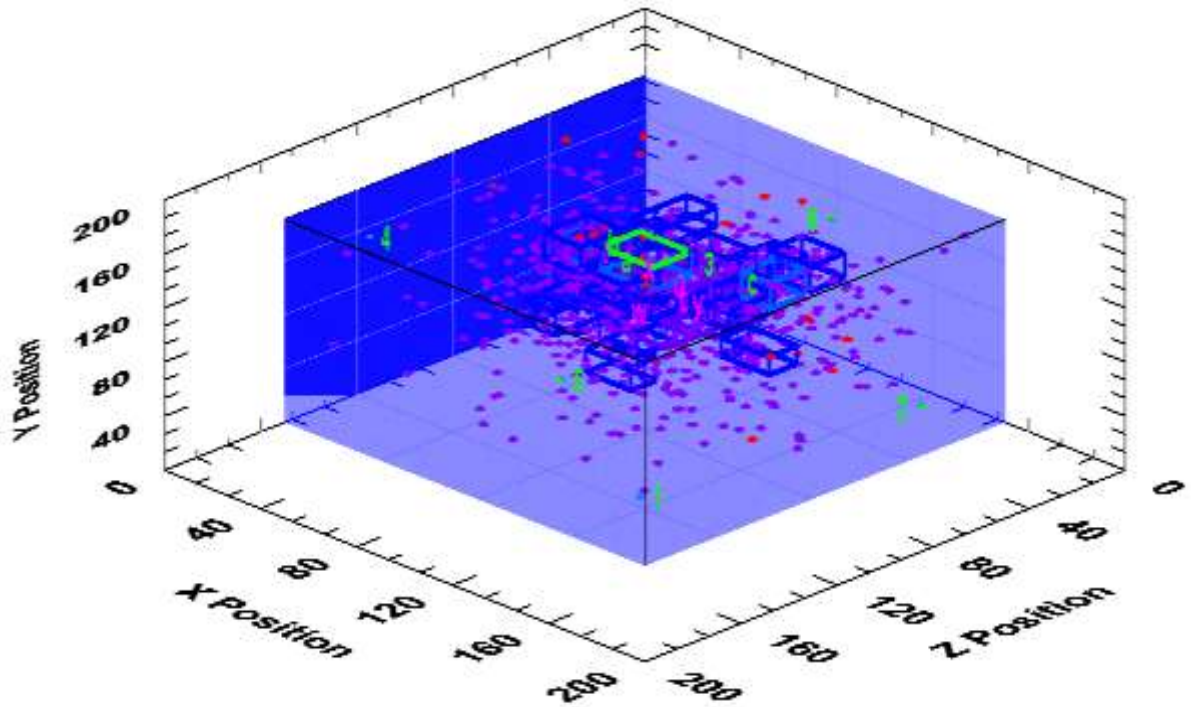

FIGURE 5-18: Groupings of acoustic data from drilling 135mm to 95mm.

The groupings in Figure 5-18 now show that although a much greater number of events are now placed outside of the groupings, those that are grouped still follow a similar pattern as observed in the previous figure, Figure 5-17 in that as the drilling progresses deeper into the sample the acoustic emissions are detected further away from the borehole. The data from the groupings is presented below in Table 5-2;

Cluster	ID	Points	Energy	Counts	Amplitude	X	avg. Y	avg. Z	min	Xrange max	min Y	range max	min Z	range max_
z	2	15	820	422	1067	68.23	103.71	78.01	61.72	75.95	95.18	112.96	70.23	84.11
y	1	8	481	190	550	74.96	142.4	89	69.35	82.28	133.62	150.33	79.78	96.27
x	3	7	315	169	493	79.81	122.74	76.65	73.02	93.24	108.49	129.76	70.88	81.85
w	10	7	307	103	462	76.96	84.8	75.47	68.69	81.33	79.95	89.79	66.93	83.87
v	7	5	167	61	324	87.45	91.5	30.05	75.12	95.43	86.13	103.41	25.73	37.88
u	6	4	78	36	273	70.79	68.28	66.61	69.56	73.46	65.31	70.11	62.9	68.81
t	19	4	294	89	259	97.96	98.91	89.67	91.47	108.67	91.48	104.69	86.63	92.66
s	4	3	190	108	221	72.71	121.25	83.08	64.84	84.26	119.8	122.17	78.92	85.29
r	8	3	138	40	198	96.44	94.85	59.46	94.1	100.6	93.12	97.87	51.5	64.33
q	13	3	168	55	210	80.75	104.13	76.48	77.03	86.45	97.95	110.89	71.51	81
p	18	3	83	52	203	70.75	92.92	87.06	65.73	73.92	91.23	93.94	83.34	92.21
o	25	3	72	36	221	75.96	26.8	54.02	74.4	78.95	21.33	33.34	43.49	61.57
n	5	2	103	16	128	63.67	76.06	23.75	56.86	70.48	73.25	78.86	19.49	28.01
m	9	2	118	15	127	124.35	108.96	44.51	119.04	129.66	102.18	115.74	41.22	47.81
l	11	2	58	10	126	80.41	61.88	34.63	73.39	87.43	58.56	65.19	26.96	42.31
k	12	2	353	101	149	65.35	125.84	84.73	56.02	74.68	117.37	134.31	75.43	94.02
j	14	2	132	36	135	77.07	90.36	42.79	70.45	83.68	89.8	90.92	42.66	42.91
i	15	2	164	45	148	67.34	41.2	78.2	59.92	74.77	39.55	42.84	69.82	86.58
h	16	2	79	38	133	79.5	120.31	52.56	75.53	83.46	111.08	129.53	49.72	55.39
g	17	2	159	43	133	86.09	107.98	46.29	79.66	92.52	107.32	108.63	40.24	52.33
f	20	2	115	41	134	84.64	35.05	62.64	82	87.29	29.64	40.46	60.55	64.74
e	21	2	227	113	150	63.73	50.87	92.55	54.33	73.13	47.42	54.31	84.19	100.92
d	22	2	222	53	137	138.63	131.57	83.83	136.18	141.09	121.86	141.28	78.28	89.37
c	23	2	90	23	134	90.96	75.03	46.97	84.54	97.39	74.47	75.6	37.09	56.84
b	24	2	22	17	133	66.3	134.63	98.06	64.44	68.17	129.8	139.46	97.09	99.04
a	26	2	136	37	133	66.01	104.83	54.38	57.46	74.57	101.61	108.05	47.88	60.89

TABLE 5-2: Acoustic grouping data from 150mm to 135mm.

Table 5-2 lists the data for each grouping (labelled here as cluster). The counts are the number of events, acoustic emissions, and for each group the amplitude, energy and the location are given.

This data shows that whilst the acoustic emissions are relatively light the greatest proportion of combined amplitude is in the cluster marked Z which is underneath the drill bit. A similar picture can be seen in the grouping data for 135 to 95mm shown in Table 5-3. Clusters V, U & T have the greatest amounts of combined amplitude and their placings on the X, Y and Z axes show that they are directly under the borehole showing a clear progression as the borehole deepened.

Cluster	ID	Points	Energy	Counts	Amplitude	X	avg. Y	avg. Z	min	Xrange	min Y	range max	min Z	range max_
v	1	19	9346	2296	1374	69.26	131.03	91.54	55.96	77.49	122.45	140.35	82.14	100.27
u	5	18	90012	10246	1307	93.53	107.63	70.48	84.62	101.27	99.82	119.89	59.97	79.59
t	12	16	861	178	1042	82.92	90.15	56.04	72.47	91.69	71.91	98.12	45.99	70.84
s	6	15	14210	2642	1115	74.83	123.81	68.47	65.51	81.93	115.06	134.01	60.59	76.21
r	24	13	675	239	878	69.14	90.98	75.97	61.98	74.91	83.03	95.78	70.3	82.56
q	28	13	705	200	877	68.29	96.41	94.99	60.85	73.75	89.26	106.32	87.48	111.03
p	29	13	794	146	860	86.43	84.31	47.65	79.54	92.94	77.29	91.1	38.79	55.37
o	47	13	60680	12495	913	72.28	67.9	74.64	63.68	79.31	57.4	75.06	67.13	82.58
n	20	12	751	180	776	76.96	100.65	43.95	65.55	82.63	93.54	107.27	38.33	52.19
m	2	10	715	241	657	95.45	97.25	28.86	86.39	104.06	89.28	107.54	21.01	35.06
l	14	10	66698	18386	715	91.58	114.46	90.94	84.82	100.5	109.81	121.89	87.11	97.79
k	19	10	4800	715	726	71.01	145.15	94.96	62.03	77.46	132.08	152.15	86.11	104.05
j	80	9	2582	519	640	86.64	131.3	100.17	80.39	98.79	124.51	141.01	92.47	107.34
i	9	8	632	141	527	80.02	84.39	27.63	72.84	86.98	78.34	92.56	19.07	33.15
h	16	8	1015	248	543	110.54	111.5	77.5	102.42	118.4	105.67	118.47	64.63	83.64
g	18	8	404	98	528	137.3	112.48	93.68	131.34	151.59	106.91	120.1	88.1	99.79
f	23	8	2397	487	589	76.88	141.27	67.17	69.71	82.2	134.69	147.89	52.25	75.43
e	44	8	30048	2044	614	59.63	84.86	84.86	52.21	68.54	76.12	94.45	78.49	96.91
d	100	8	884	346	561	63.97	36.21	73.53	53.53	72.48	24.12	41.13	67.61	78.1
c	3	7	952	306	496	115.2	121.23	63.92	111.58	123.65	115.58	134.44	57.09	71.27
b	15	7	7394	737	531	55.81	124.4	79.4	51.32	64.88	116.71	131.03	71.15	87.99
a	33	7	722	231	472	87.9	141.4	89.82	81.01	102.61	133.92	151.08	83.11	99.26

TABLE 5-3: Acoustic emission groupings at depths drilling 135mm to 95mm.

The scan of the Accrington Mudstone sample 1 after drilling is shown below in Figure 5-19 and shows that the borehole is clearly detectable whilst the rate of penetration is quite good. This scan confirms that the interpretation of the acoustic data is accurate, and that the software can be used to accurately and confidently track fractures induced by drilling. Figure 5-19 to Figure 5-20 show possible damage around the borehole in the same locations that the acoustic emissions were detected.

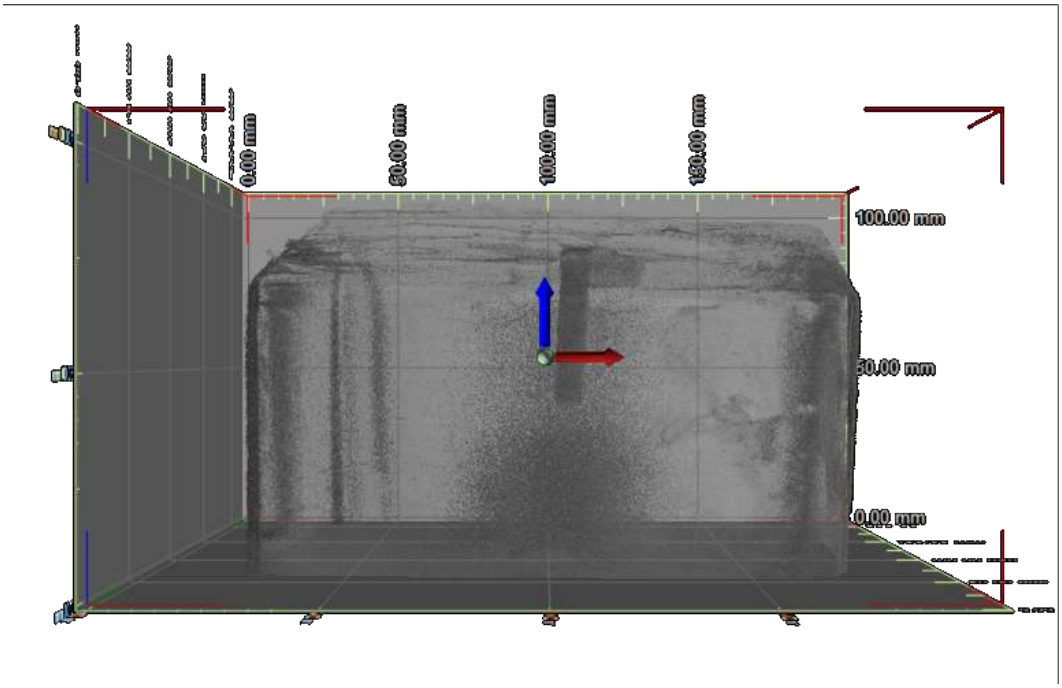

FIGURE 5-19: Accrington Mudstone 1 Scan of top half, note the darkened borehole in the centre.

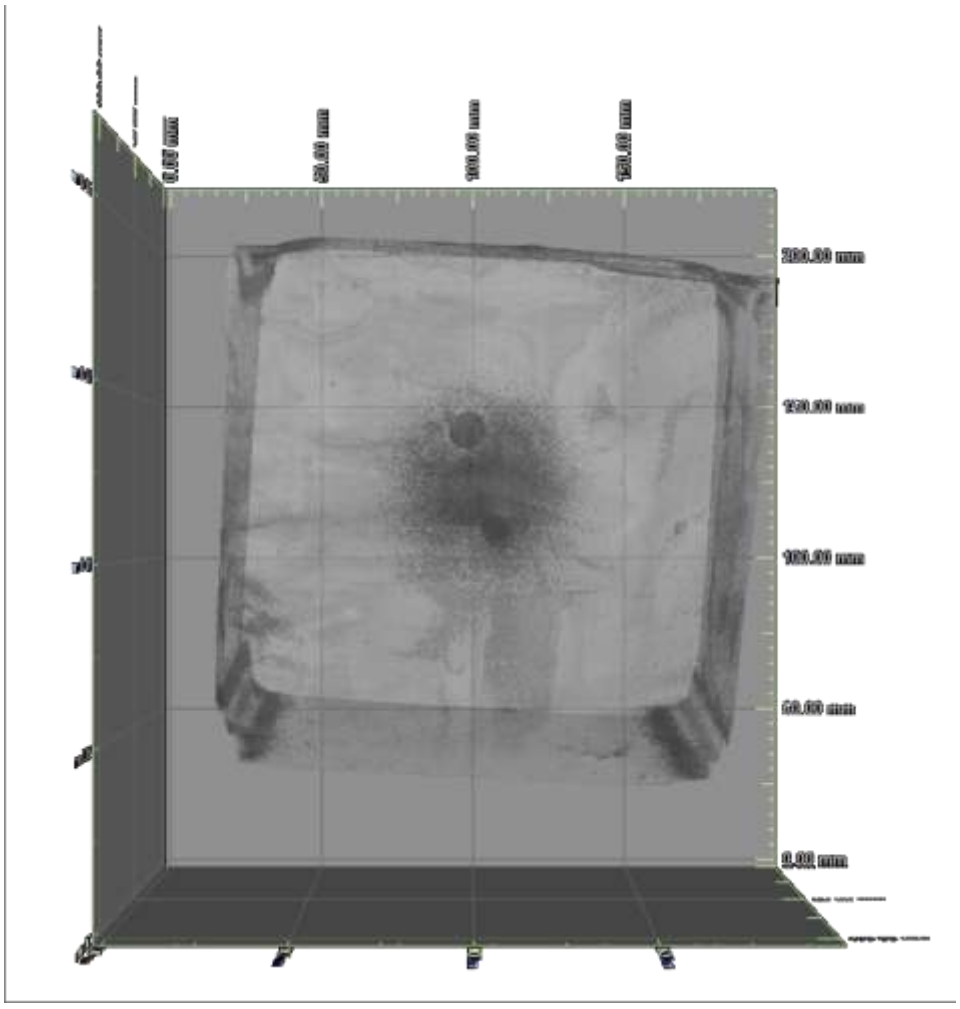

FIGURE 5-20: Accrington Mudstone 1 overhead view.

5.2.2 Fracturing.

5.2.2.1 Aggregate concrete sample 1

A test sample of aggregate concrete was fractured at a pressure of 1,500 psi using a 99.9% water 0.1% hydraulic oil mix to make a crude approximation of a fluid within the borehole. After fracturing the sample was re-scanned. Unfortunately, due to the previously mentioned limitations of the CT scanner caused by the size and density of the concrete sample, the grey values required to fully penetrate through the sample would gradually decrease throughout the scan, meaning that it was impossible to fully penetrate the sample in order to trace the fracture.

After consultation with the acquisition department of GE oil and gas division, it was decided that sample sizes of 100mm^3 would have to be used instead to address this issue.

5.3 Pre-Fracture Induction Scans

5.3.1 Accrington Mudstone 100mm^3 samples

PREDRILL

Prior to fracturing all of the Accrington Mudstone (AM) 100mm^3 samples were prepared and scanned. Preparation for these re-sized samples was similar to before, samples were cut to around 97 - 98mm^3 and then placed in a 100mm^3 mould. High strength plaster was then introduced into the mould to ensure a uniform sample size of 100mm^3 giving the sample sharper, flatter surfaces than could be achieved by attempting to cut 100mm^3 samples straight from the source rock. Thus, ensuring a more equal distribution of force across the whole of each face. After the sample was removed from the mould the placings for the sensors were located and the plaster was carefully removed in order to present only mudstone to the sensor so that the sensor would not be affected by the sudden change in substrate.

5.3.1.1 AMS S1

The predrill scan of this sample is presented in Figure 5-21 to Figure 5-23. As can be seen in the side views and top view, the only collection of visible pores are around the edges of the samples and in the plaster, very few pores are detected in the shale and those that do exist are spaced randomly. The large grey area along the bottom of the sample is the angled table that was used to ensure all the sides of the sample are fully penetrated and thus preventing any of the samples from suffering from any ‘Feldkamp’ issues, this is where a flat surface will lead to a blurring of the top and bottom edges of a sample as the scatter of the microwaves are unable to directly hit the top or bottom sides, leaving the top and bottom edges poorly defined. Due to the angle of the wooden and plastic table it was not possible to crop this out of the scan without removing a large section of the sample. The circled area, Figure 5-21, is just the corner of the sample.

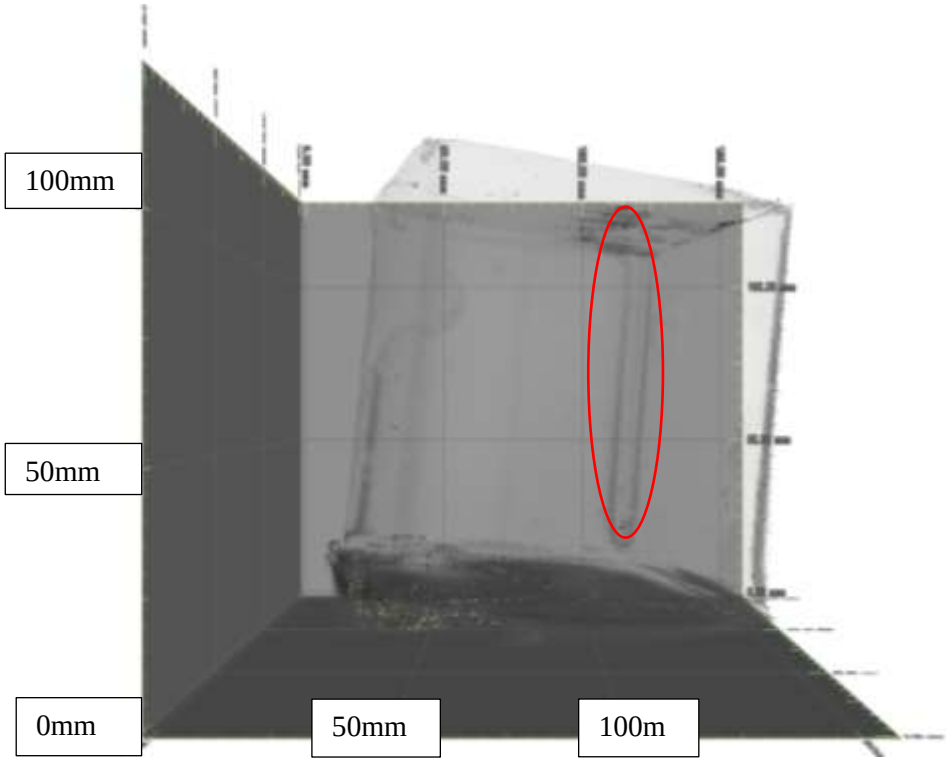

FIGURE 5-21: AMS 1 Side 1 view.

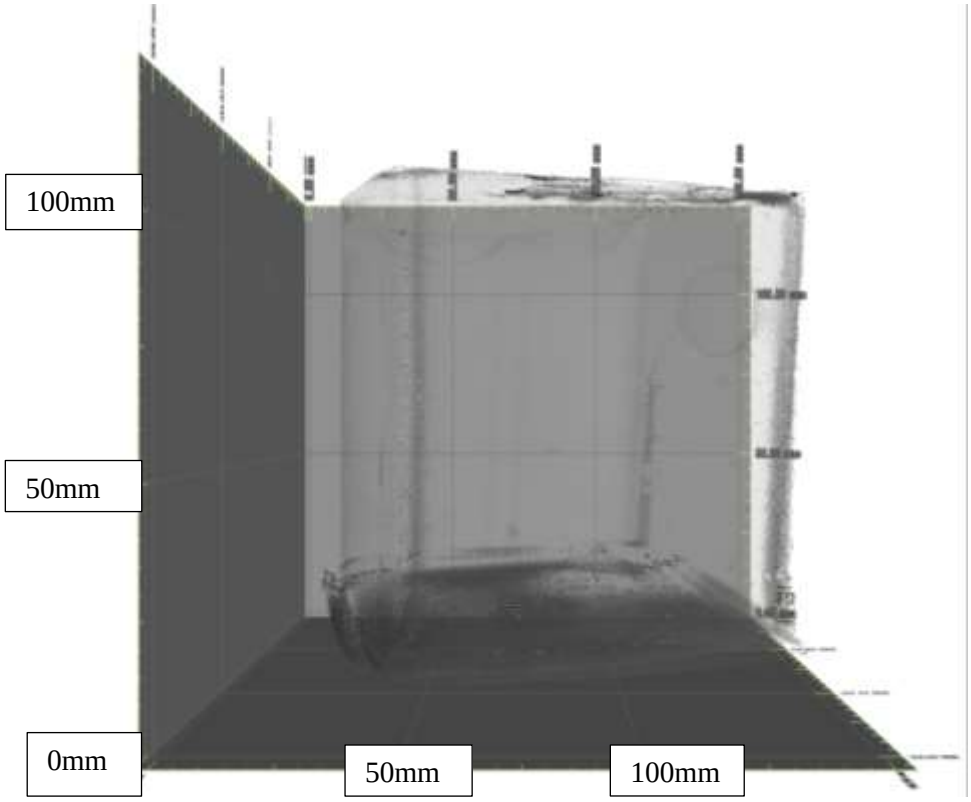

FIGURE 5-22: AMS 1 side 2 view.

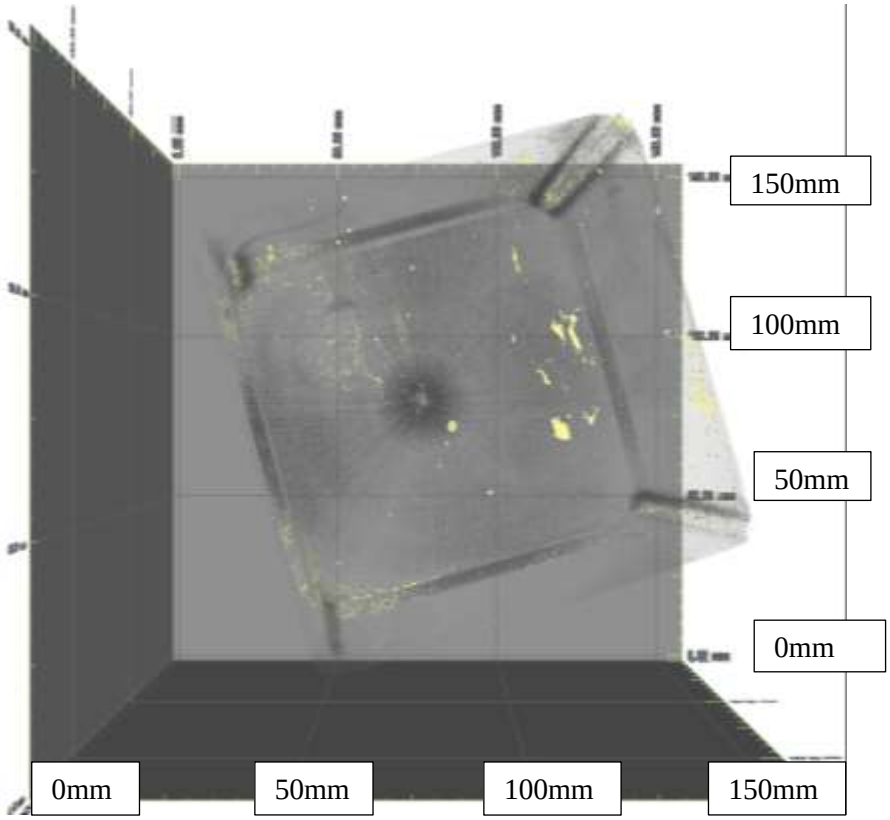

FIGURE 5-23: AMS1 overhead view.

5.3.1.2 AMS S2

The scans of this sample are presented in Figure 5-24 to Figure 5-26. In this sample, like AMS S1 the majority of pores are found in the high strength plaster with only a couple found sporadically and randomly in the actual shale. However, a small pre-existing fracture was found in this sample and is highlighted by the red circle in Figure 5-24. This small fracture was close to one of the walls, near sensor 4 measuring approximately 1.09mm in width at its maximum width, 16.32mm in height and 8.44mm in depth.

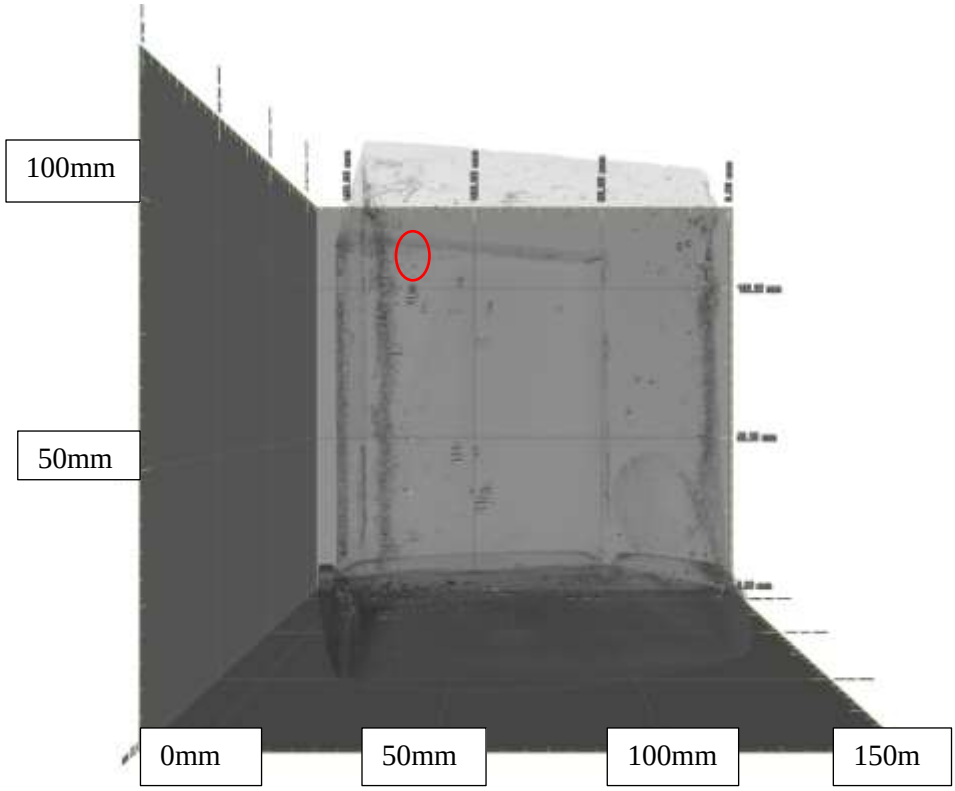

FIGURE 5-24: AMS2 side 1.

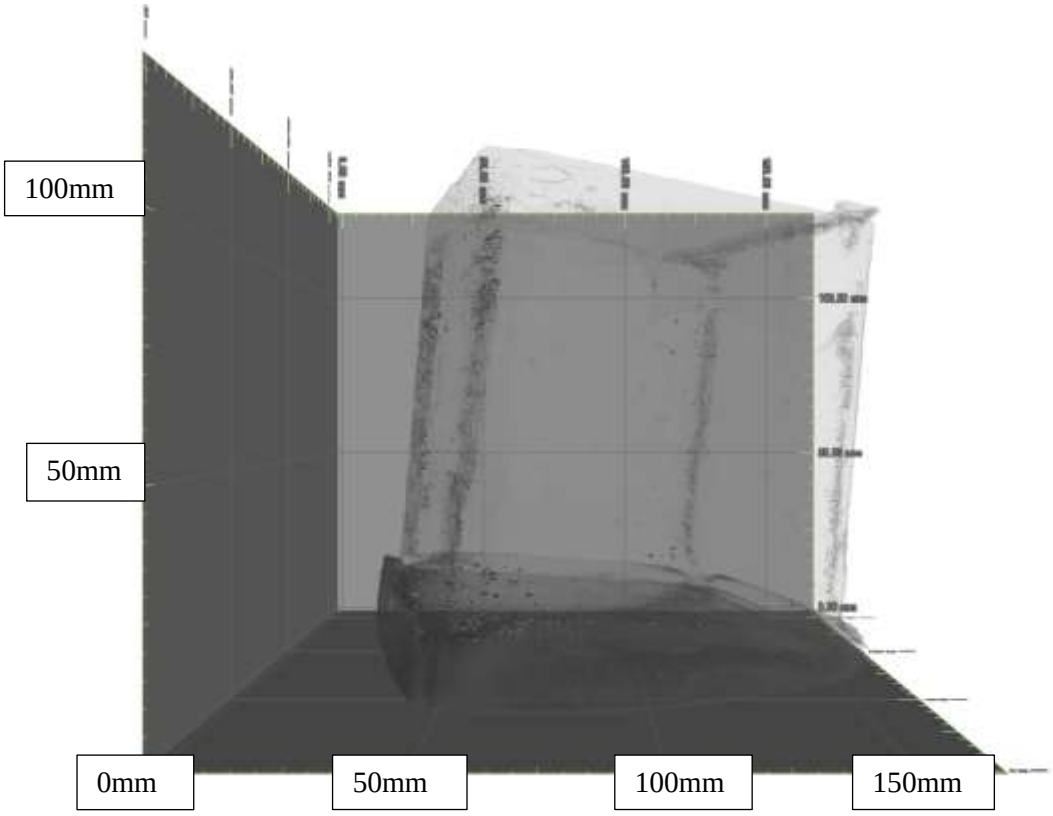

FIGURE 5-25: AMS2 side 2.

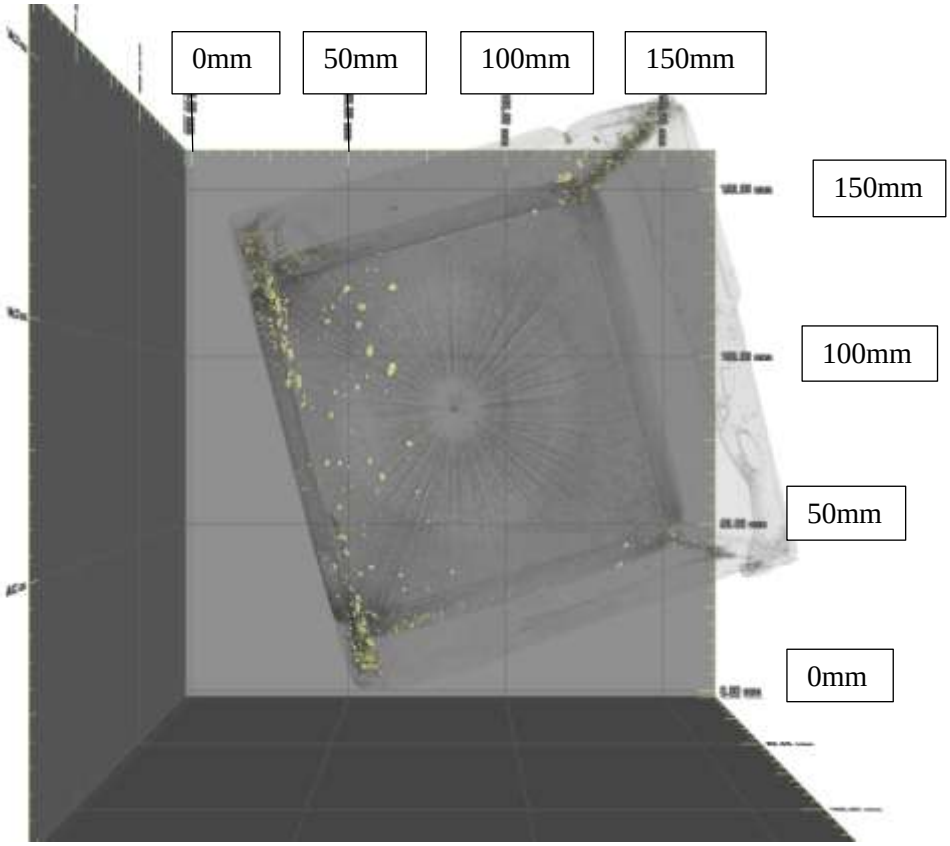

FIGURE 5-26: AMS2 overhead view.

5.3.1.3 AMS S3

Sample AMS3 is shown in Figure 5-27 to Figure 5-29. Figure 5-29 shows small groupings of pores clustered exclusively in the plaster at the corners of the sample and along the line marking the delineation of the mudstone and the plaster. Pores in the mudstone itself are sparse and sporadically placed, typically less than 0.5mm in diameter. However, this sample does have a large thin pre-existing fracture that cuts up through the base of the sample (Figure 5-28) near the middle almost through to the other end before ending, blade like, between halfway and three quarters of the way up the sample. The fracture has no great concentration of pores surrounding it. The fracture is shaped as one would expect and would appear to be a break along a bedding plane. On closer inspection this plane was different from other planes and probably indicates a temporary change in the depositional environment in the form of a storm or a landslide event. The fracture height at its greatest is 54.47mm whilst in the middle the fracture decreases in height to 45.74mm. It loses further height as the fracture cuts into the sample, to 11.70mm. The fracture is at 69.49mm into the sample and has a thickness of 1.09mm.

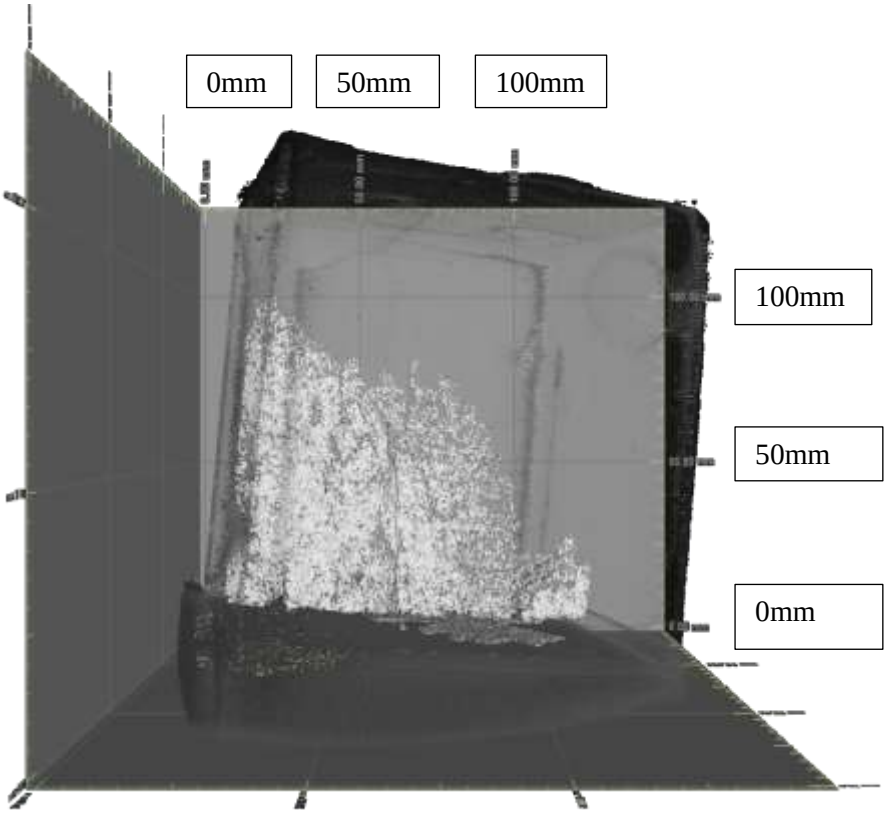

FIGURE 5-27: AMS3 side view 1.

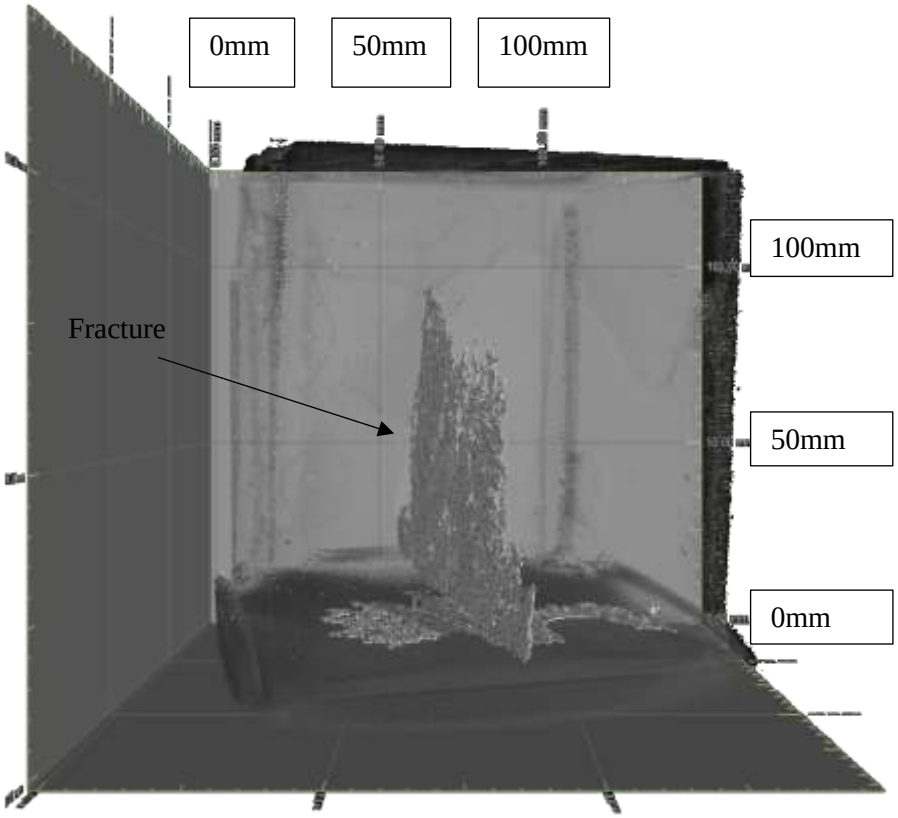

FIGURE 5-28: AMS3 side view 2.

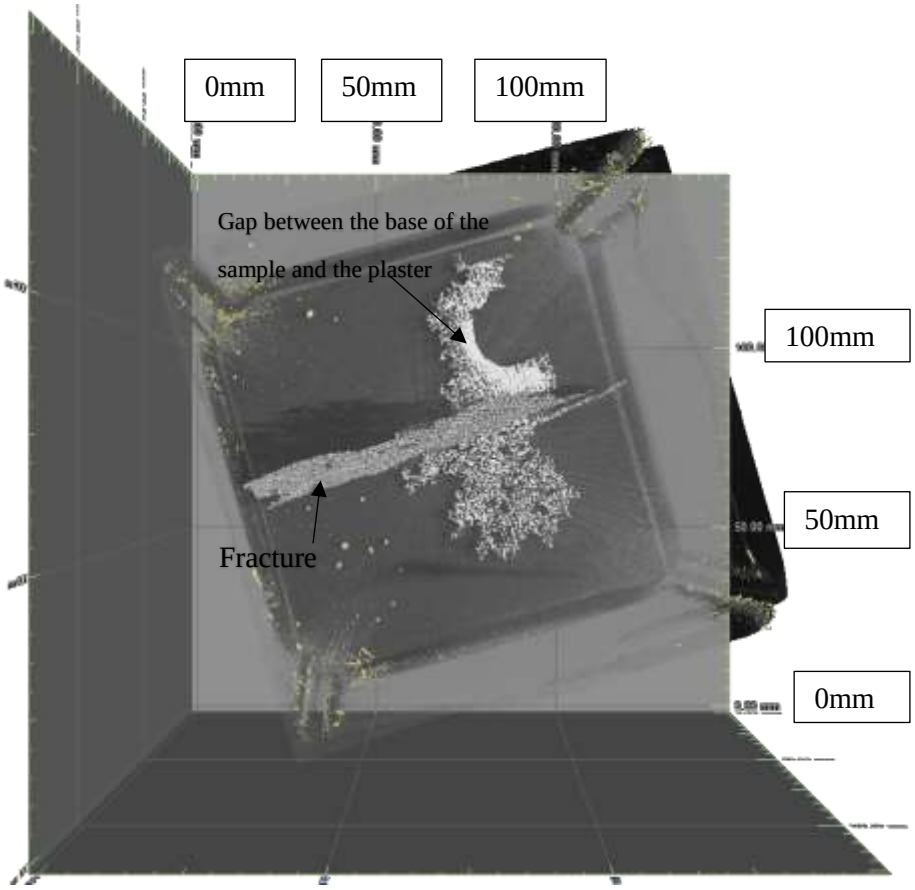

FIGURE 5-29: AMS3 Overhead view.

5.3.1.4 AMS4

AMS4 is presented in Figure 5-30 to Figure 5-32. This sample displayed many pores within the plaster as shown in the overhead view Figure 5-32, highlighted in gold. The sample did have two small pores in the actual shale towards the edge of the sample which can be seen most clearly in Figure 5-30. These are the only faults recorded in this sample and as the pores are away from the central area where the borehole would be drilled they are, therefore, unlikely to have any negligible effect on any fracture propagation pattern.

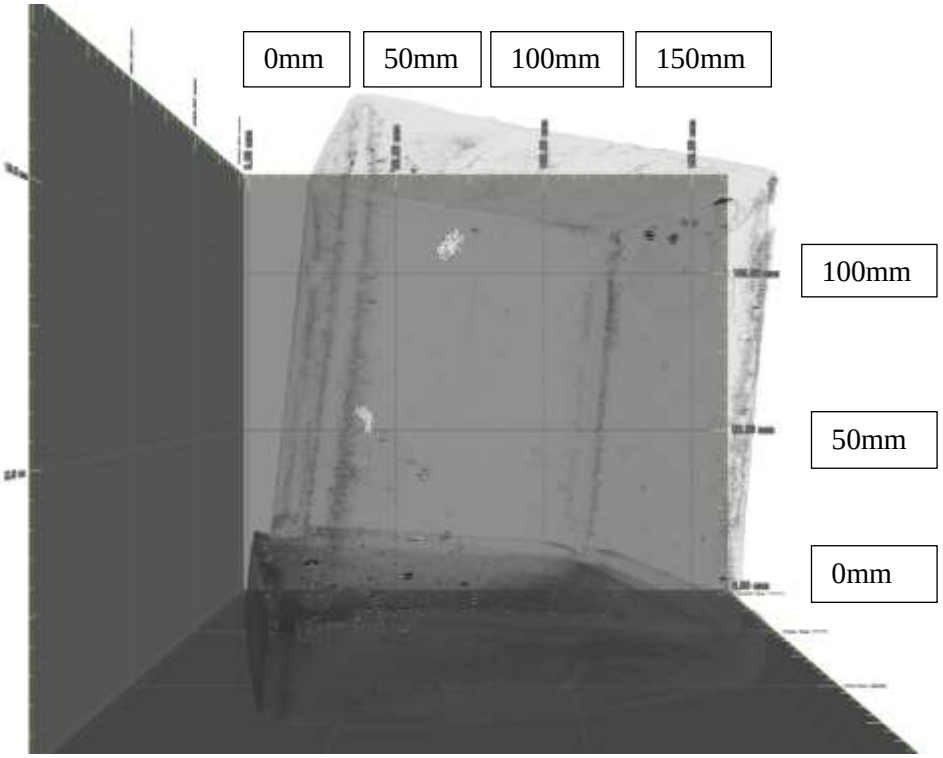

FIGURE 5-30: AMS4 side view 1.

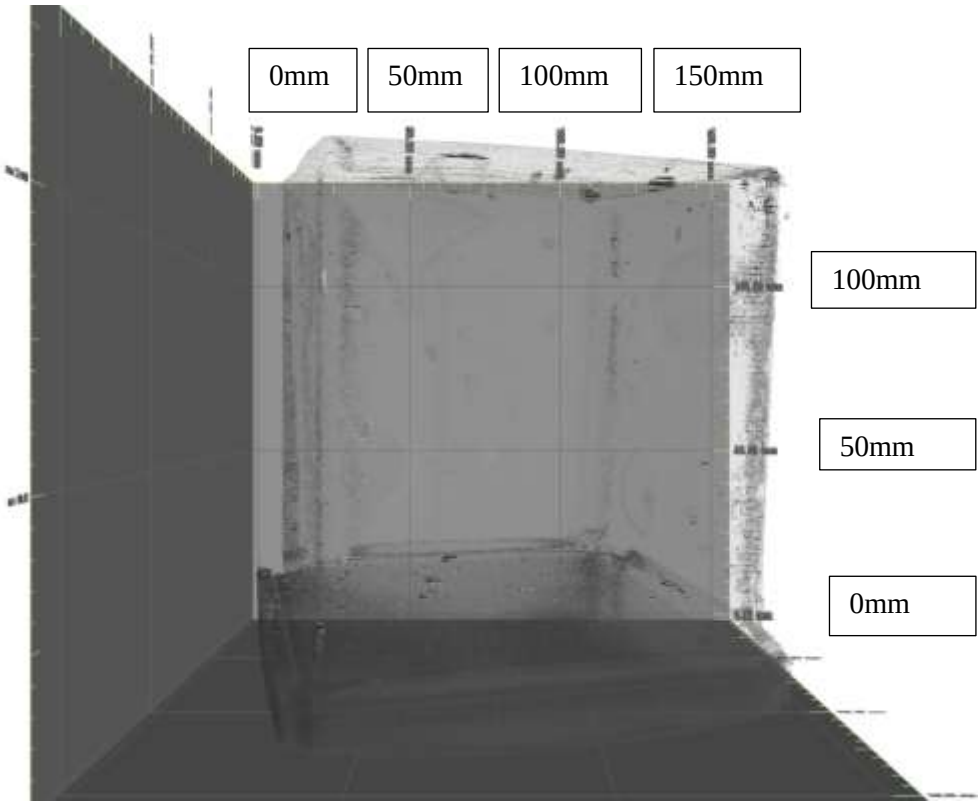

FIGURE 5-31: AMS4 side view 2.

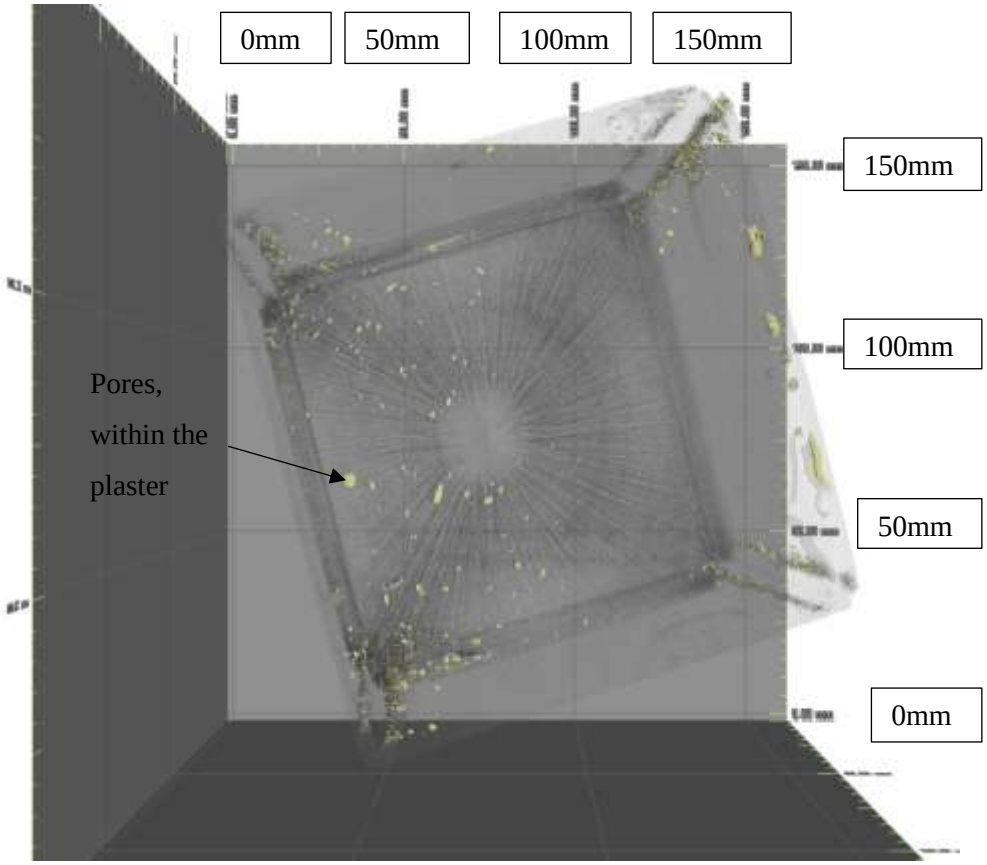

FIGURE 5-32: AMS4 Overhead view.

5.3.2 Westbury Shale

5.3.2.1 WBS1

The Westbury Shale (WBS) sample WBS1 is presented in Figure 5-33 to Figure 5-35, this sample has a number of pores in the interface between the high strength plaster and the shale, circled, and there was a little splitting around the edges of the shale, following the bedding planes. As can be seen in the images, there is no detectable pre-existing fracture within the central section of the actual shale sample. Only at the edges of the sample is there a small volume of splitting, this will produce an area of weakness with the potential to break into the centre of the sample, though with careful handling the sample should be good to use.

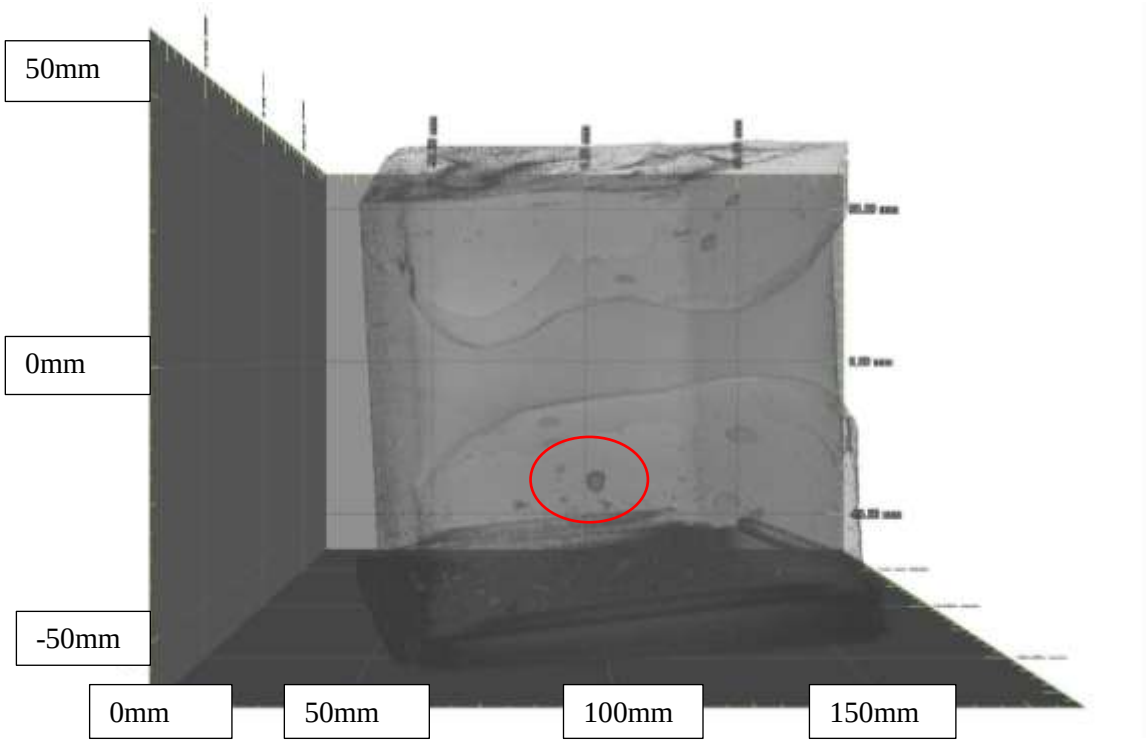

FIGURE 5-33: WBS1 Side view 1 predrill scan.

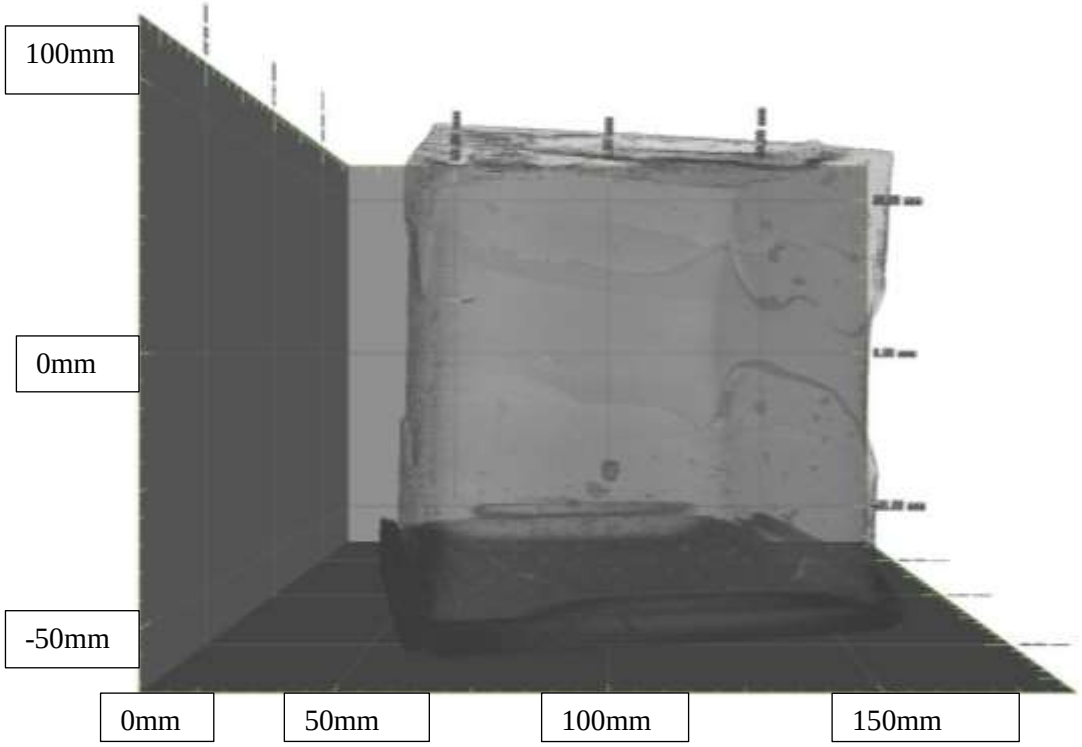

FIGURE 5-34: WBS1 Side view 2 Predrill Scan.

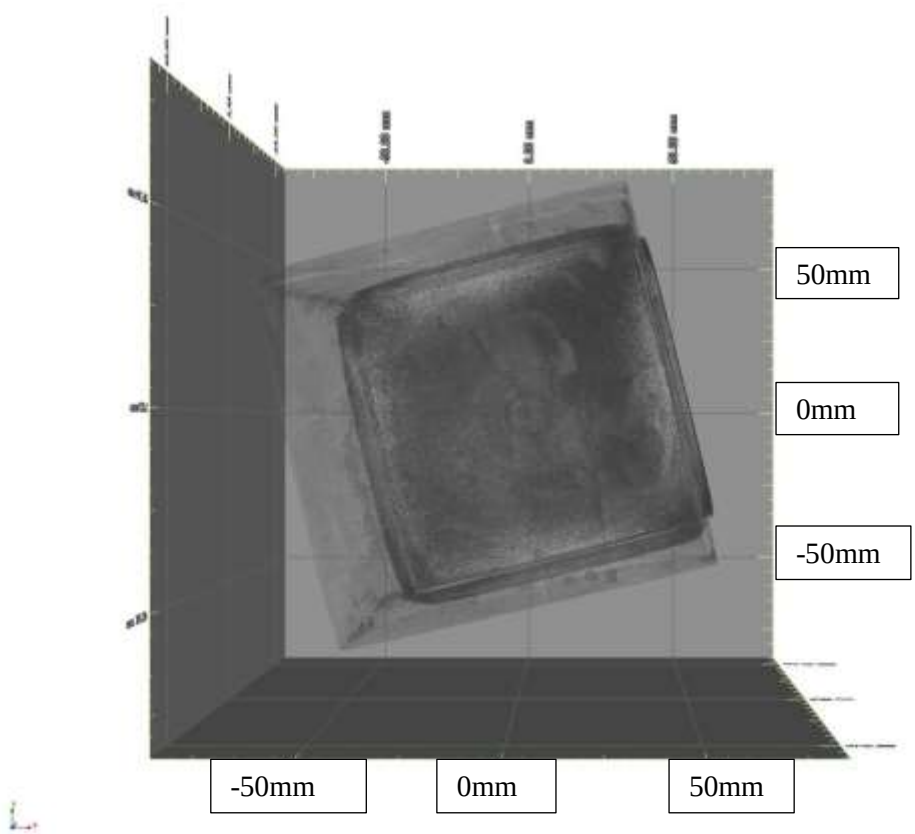

FIGURE 5-35: WBS1 Planview Predrill scan.

5.3.3 WBS2

The WBS2 sample is presented in Figure 5-36 to Figure 5-38. There are a couple of small fractures that follow the bedding plane but they are not extensive and do not extend into the middle of the sample, circled in red in Figure 5-36. Thus, the risk of the borehole cutting through them is reduced, unless the drilling instigates the growth of these pre-existing fractures. However, the fact that the placement of the fracture is so far away from the centre mitigates against this. There are some random poorly sorted pores but again these are situated in the interface between the shale and plaster.

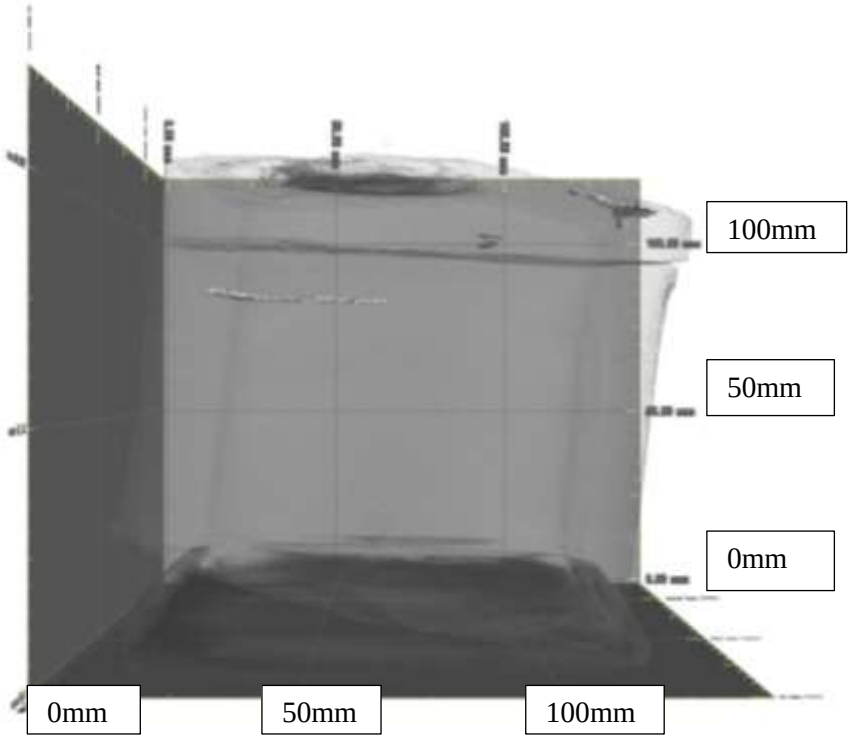

FIGURE 5-36: WBS2 Side view 1 Predrill Scan.

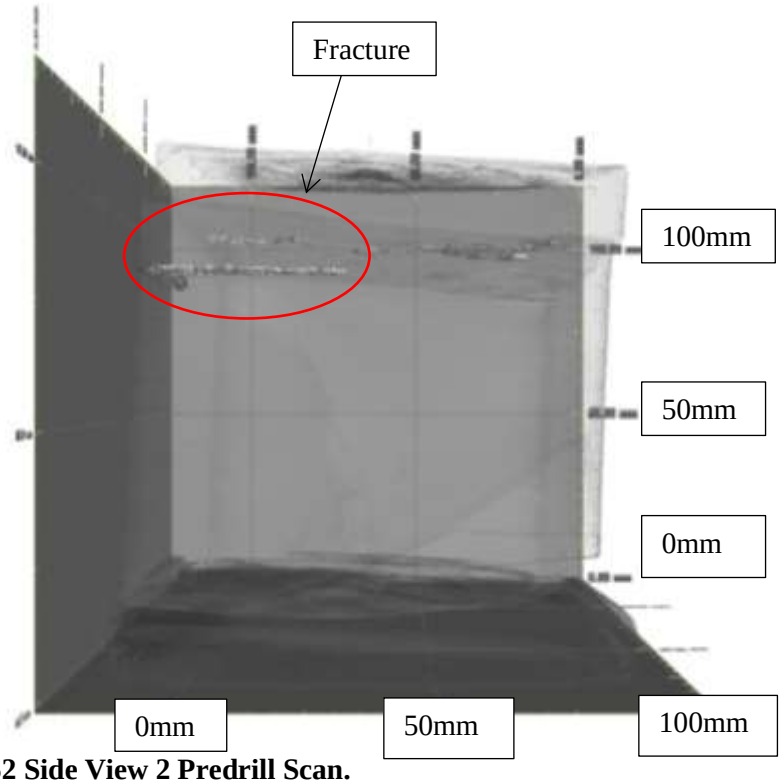

FIGURE 5-37: WBS2 Side View 2 Predrill Scan.

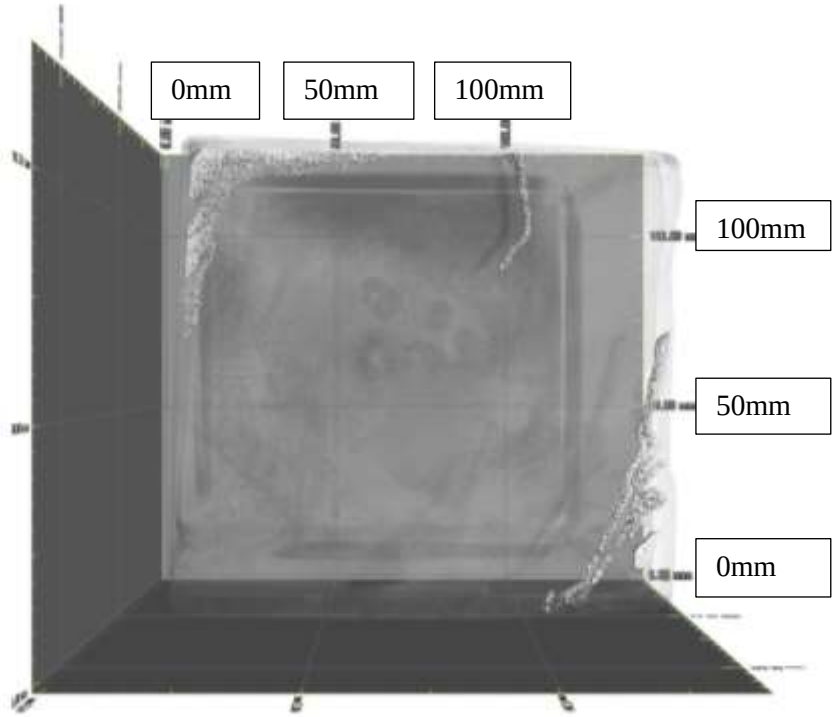

FIGURE 5-38: WBS2 Plan View Predrill Scan.

5.3.4 WBS3

The WBS3 shale sample is presented in Figure 5-39 to Figure 5-41. This sample has one fracture along the bedding plane cutting through the middle of the sample just below the point of where the borehole will end. Due to the nature of the shale and the lack of samples it has been decided that this sample will still be used. Otherwise there are some random pores at the interface between the shale and plaster mediums.

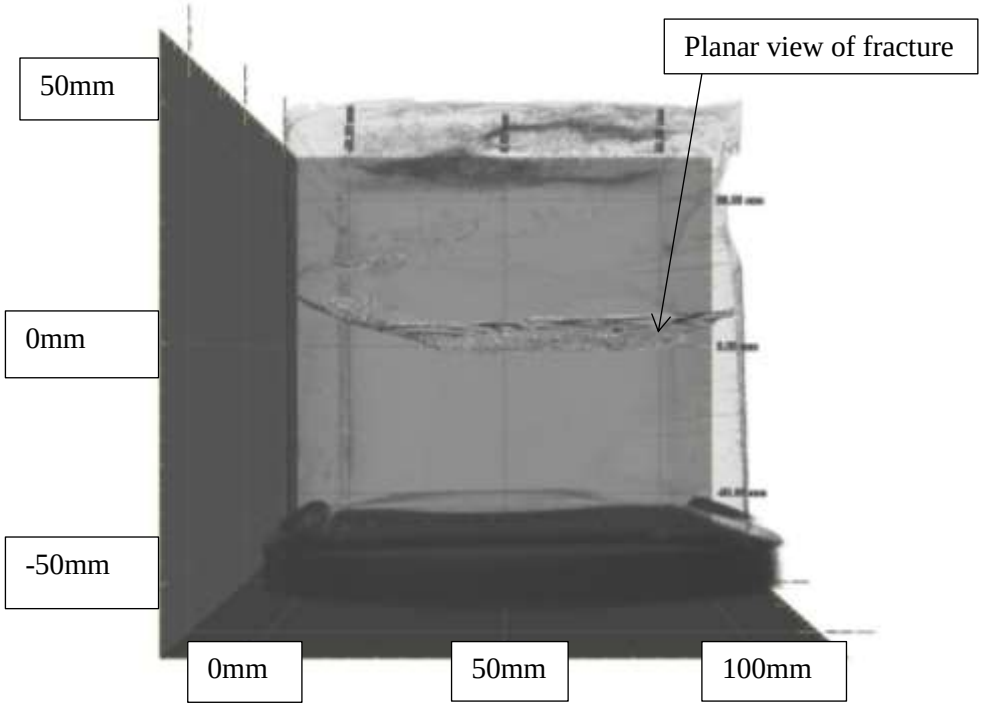

FIGURE 5-39: WBS3 Side view 1 Predrill Scan.

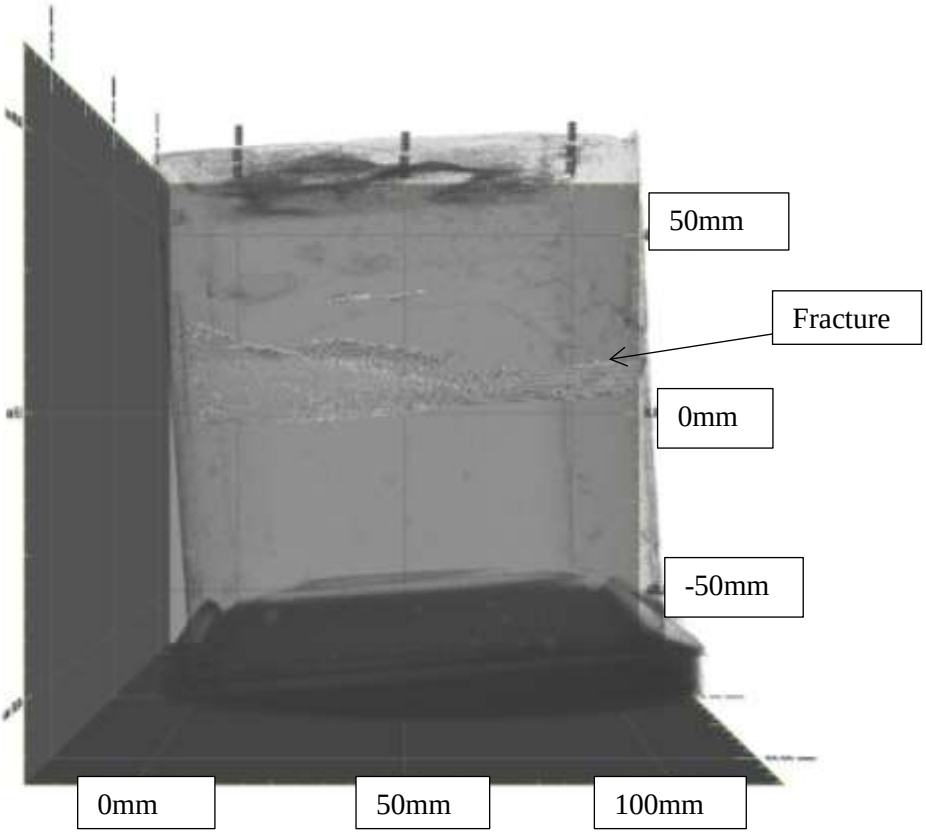

FIGURE 5-40: WBS3 Side View 2 Predrill Scan.

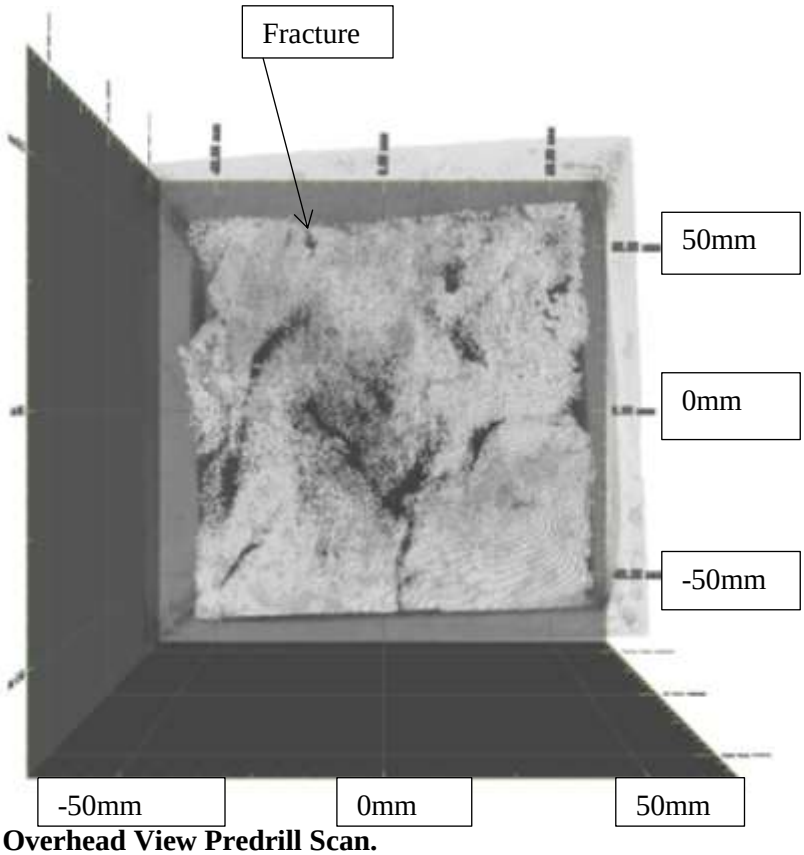

FIGURE 5-41: WBS3 Overhead View Predrill Scan.

5.3.5 WBS4

The WBS4 sample is presented in Figure 5-42 to Figure 5-44. Three medium sized fractures can be seen with the top and middle fracture following the bedding planes but not cutting through the path of where the borehole will be located. The third pre-existing fracture follows the interface between the plaster and the shale and is likely to be due to a large air bubble forming when the shale was placed in the mould. Despite tapping the mould to displace any air when adding the plaster, the air was not completely dissipated. This can lead to the plaster separating from the shale when placing the sample under pressure. However, as this sample is being compressed, this should not affect the surface of the shale and the pressure applied to each face should still be equal.

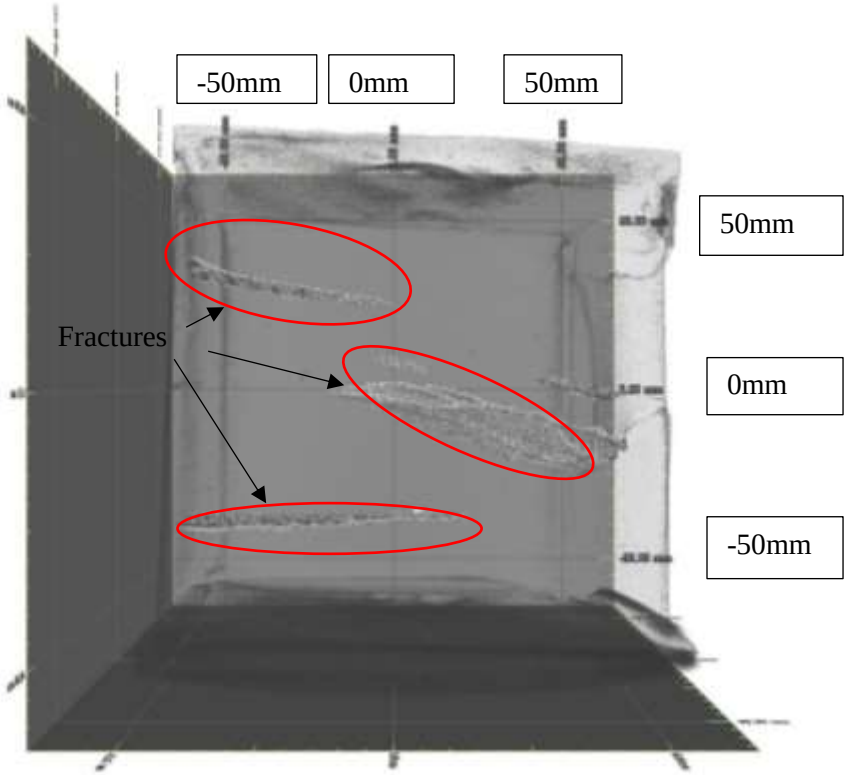

FIGURE 5-42: WBS4 Side View 1 Predrill Scan.

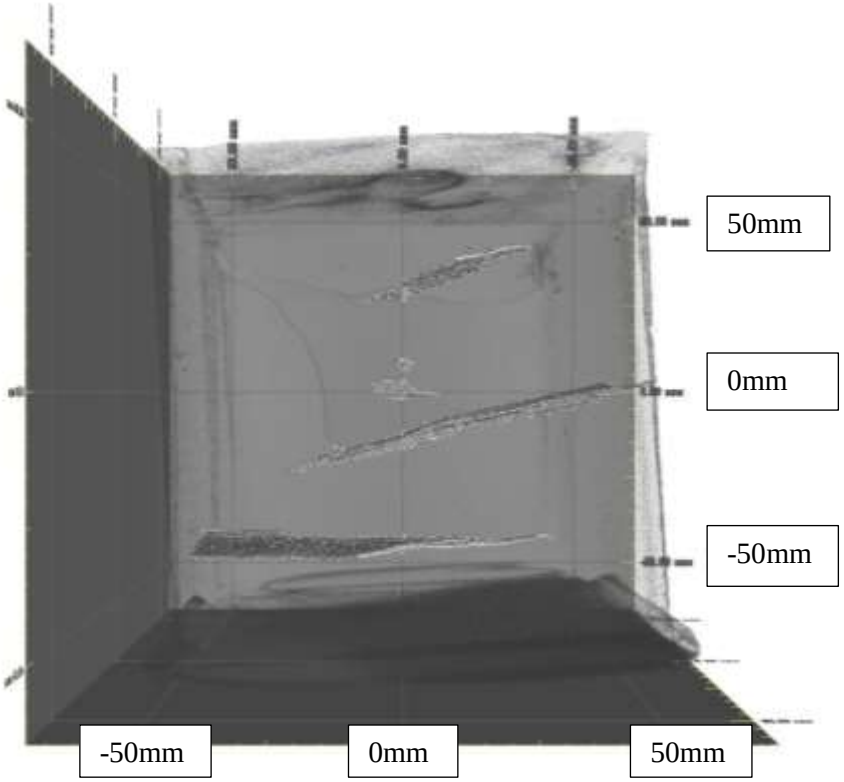

FIGURE 5-43: WBS4 Side View 2 Predrill scan.

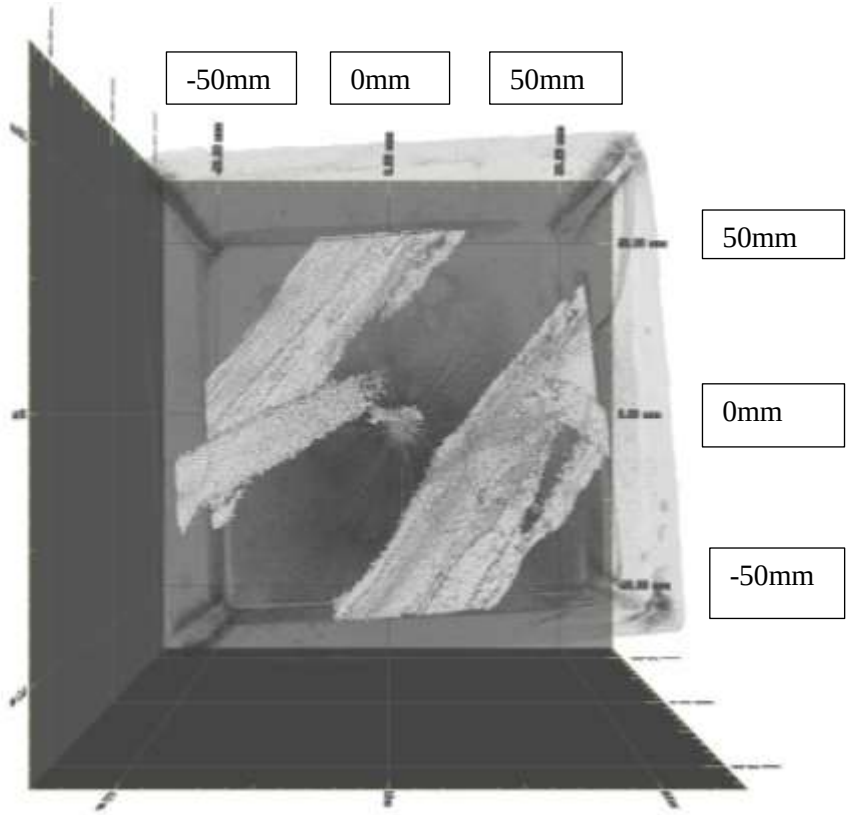

FIGURE 5-44: WBS4 Overhead View Predrill Scan.

5.3.6 WBS5

The WBS5 sample is presented in Figure 5-45 to Figure 5-47. As shown there are no detected fractures and very few pores by the outer edges where the shale meets the high strength plaster.

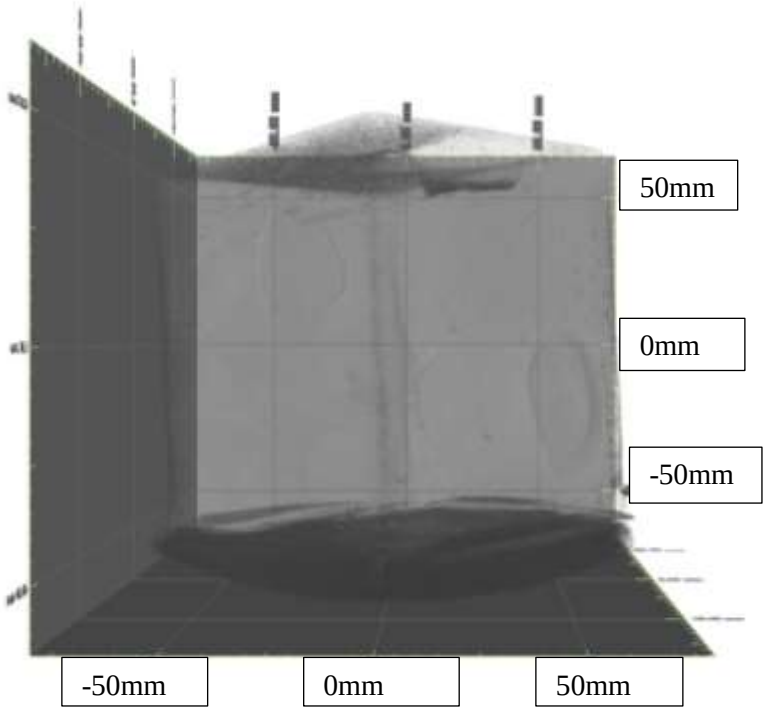

FIGURE 5-45: WBS5 Side View 1 Predrill Scan.

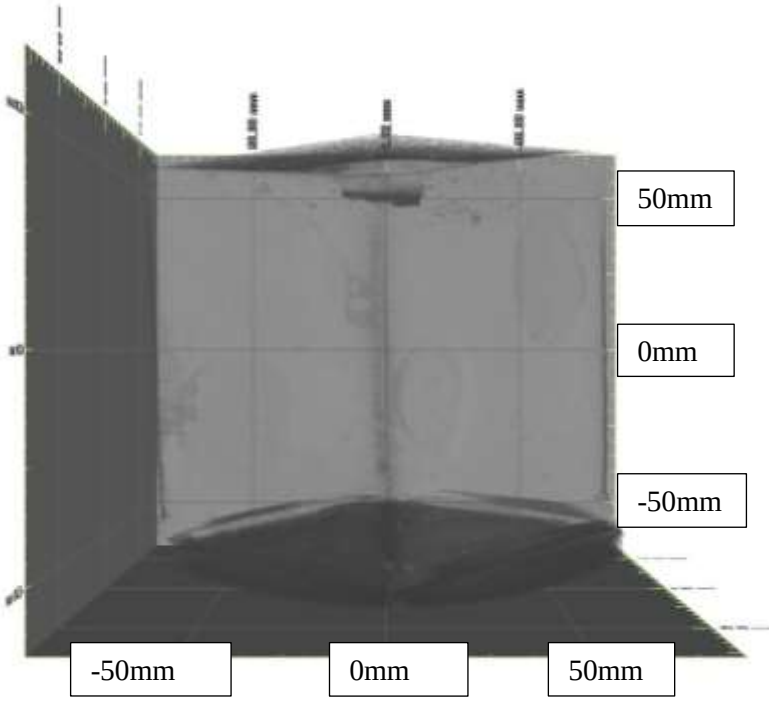

FIGURE 5-46: WBS5 Side View 2 Predrill Scan.

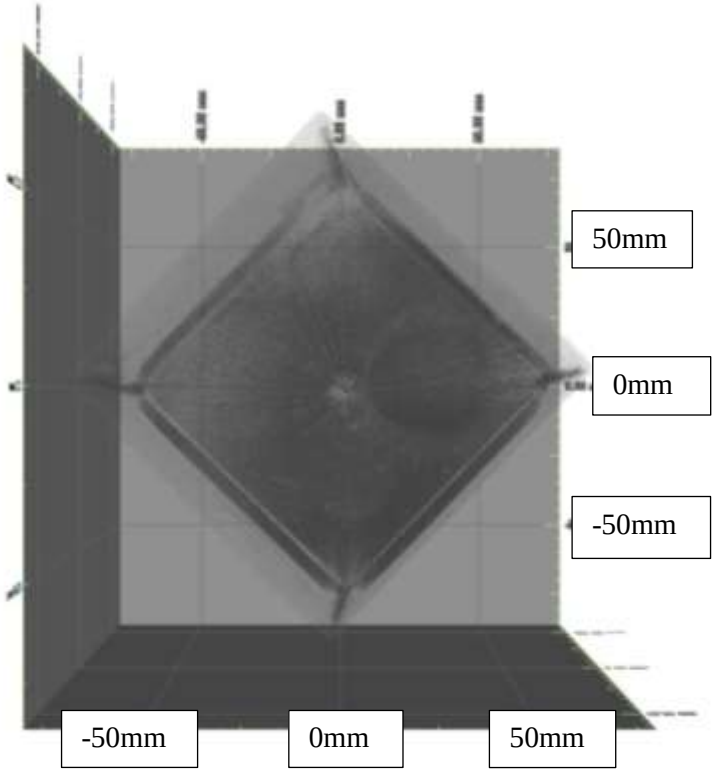

FIGURE 5-47: WBS5 Overhead View Predrill Scan.

5.3.7 WBS6

The WBS6 Shale sample is presented in Figure 5-48 to Figure 5-50. As in WBS5 previously, only a few pores on the interface between the two mediums are detected and there are no fractures.

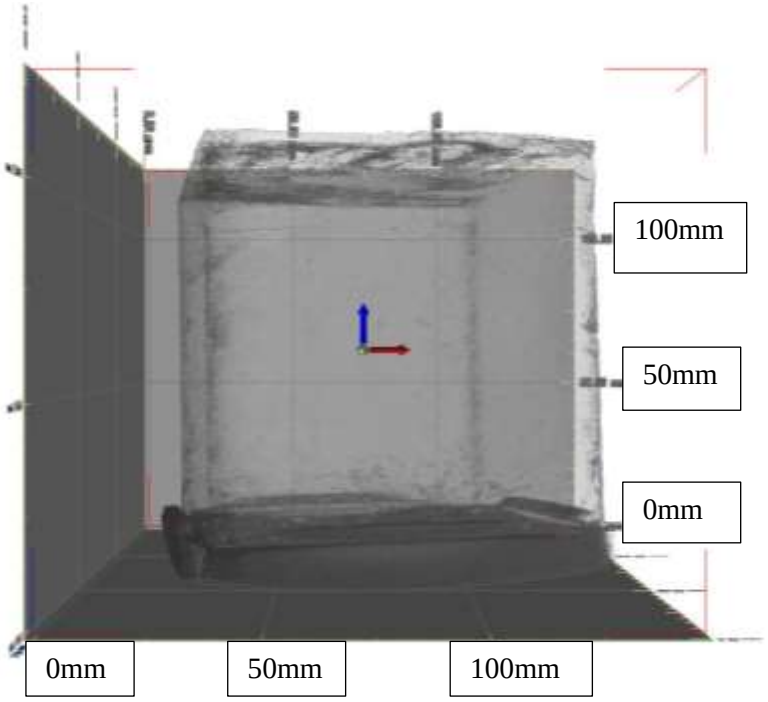

FIGURE 5-48: WBS6 Side view 1 Predrill scan.

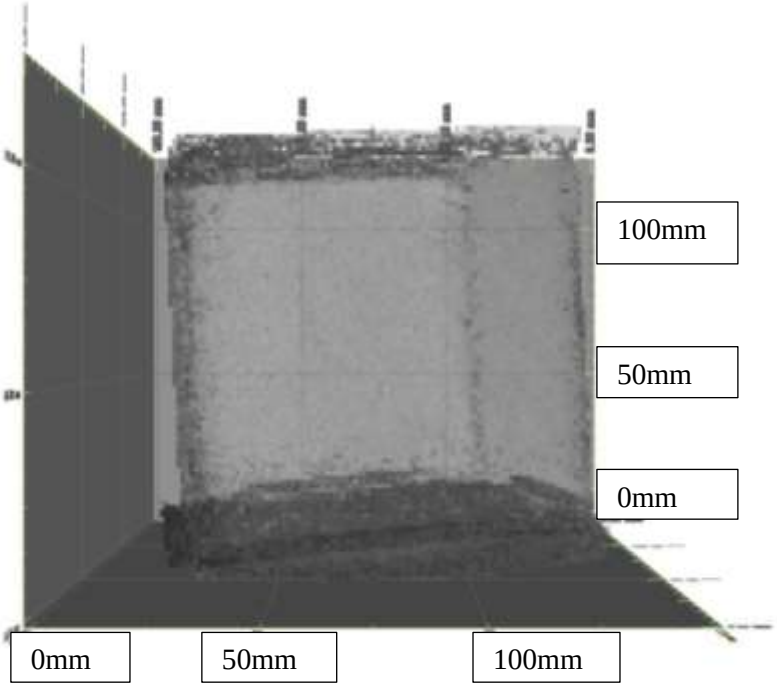

FIGURE 5-49: WBS6 Side View 2 Predrill Scan.

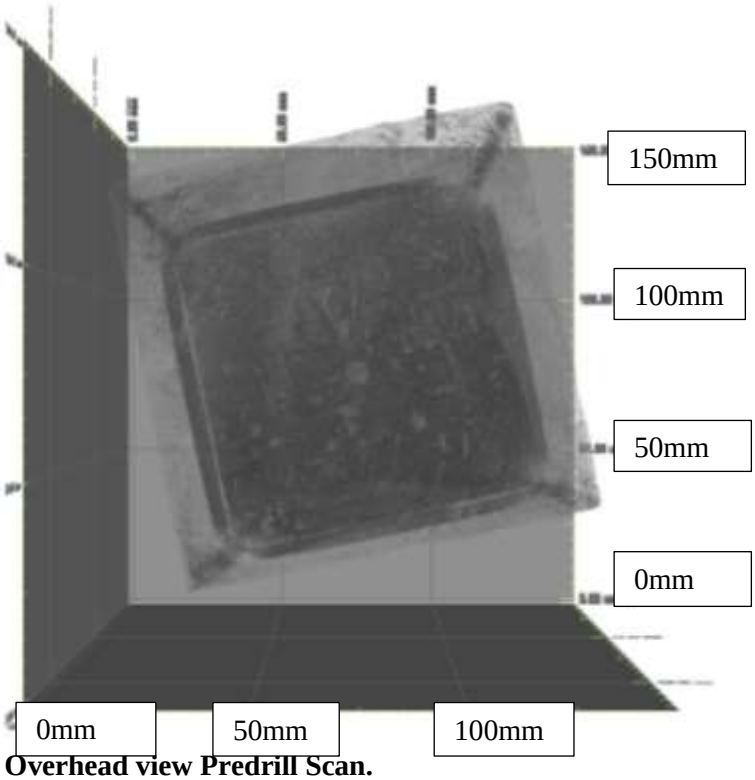

FIGURE 5-50: WBS6 Overhead view Predrill Scan.

5.4 Description of fracture measurement terms

Four areas of a fracture were identified in this study in a similar vein to Suare-Rivera's work (2013), each half length of the fracture was analysed and where the planar view showed a visible change in the dimensions of the fracture, the fracture parameters were measured as previously discussed and shown in Figure 4 50 and Figure 4 51.

The fracture was noted to be almost completely elliptical in shape but to contain a middle section that would gradually narrow. This narrowing occurred from a maximum width point with a top and bottom section that behaved the same as each other (where the fracture would narrow rapidly from the middle section but broadly maintain its narrow width to the end of the fracture), from where it would narrow rapidly to form an elongated, ultra-thin crack to bottom and top edges of the sample.

To ensure that all induced fractures can be considered in equal terms the samples will be described according to the following diagrams, Figure 5-51 and Figure 5-52. Each fracture will be split into half-length 1 and 2 from the borehole as shown below in Figure 5-51 and the fracture width will be measured horizontally from the centre of the borehole, ¼ distance from the borehole, ½ the distance from the borehole and ¾ the distance from the borehole. The measuring distances that are shown in Figure 5-51 are used & shown throughout the results section.

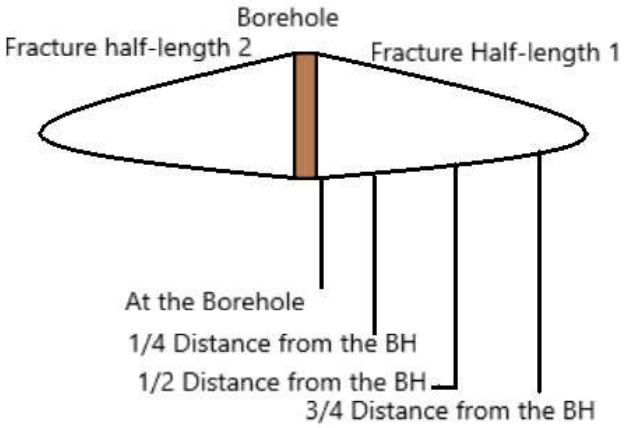

FIGURE 5-51 Description scheme for measuring induced fractures.

During this investigation it was noted that the fractures often had a wide middle section which would narrow to a thin section at the top and bottom of the fracture cross section. Quite often this would be too narrow to differentiate between the different grey scales used to take an accurate reading of the fracture thickness. Thus, a further two widths were taken above and below the maximum width of the fracture cross section as shown in Figure 4-50 below. A width of 30% and 10% of the 'maximum width' were taken to help define the shape and also to work out the percentage of the height of the 'wide section' of the fracture (taken from the maximum width and the top and bottom 30% of the max width) against the total height of the fracture in the plane that was measured. The productive parts of induced fractures are often taken as the area between top and bottom 10% of max width.

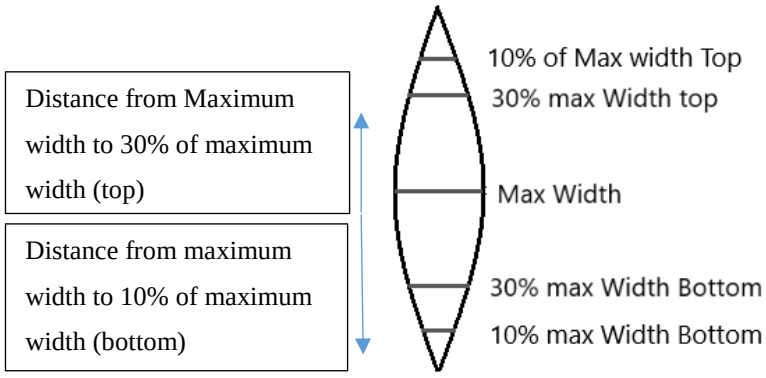

FIGURE 5-52 Measuring cross sectional fracture width at Max Width (mid fracture) and at 10% and 30% of Max width.

5.5 Post-fracture Induction Scans

Below is Table 5-4 showing the pressures that were applied to each of the samples along with the pressure of the fluid when the sample fractured. Due to some of the samples starting to show signs of

breaking under the loads applied some of the tri-axially loaded samples had lower loads applied to them otherwise the samples were at risk of disintegration and therefore no results would have been obtained.

Sample	σ^1 (Bar)	σ^2 (Bar)	σ^3 (Bar)	Fracturing pressure (psi)
AMS1	50	45	-	2,580
AMS2	75	70	-	2,690
WBS1	80	75	-	-
WBS2	80	75	-	1,750
AMS3	100	85	80	3,500
AMS4	100	85	80	2,990
WBS3	100	80	75	1,750
WBS4	100	85	80	1,600
WBS5	70	65	60	1,350
WBS6	70	65	60	1,350

TABLE 5-4: Pressures applied and fluid pressure at the point of fracture.

5.5.1 Inducing a fracture under biaxial loading

ACCRINGTON MUDSTONES

5.5.1.1 AMS1

The AMS1 sample shows one clear fracture cutting across the sample with fracture half-length 1 increasing in height to extend to the full height of the sample by the outer edges, while the other half-length (fracture half-length 2) gradually decreases in height further away from the borehole. The CT reconstructions of the sample after fracturing are presented in Figure 5-53 to Figure 5-55.

Figure 5-53 to Figure 5-55 reveal two fracture half lengths emerging from the borehole through to the edge of the sample. Figure 5-53 and Figure 5-54 show that fracture half-length 1 extends in height the full length of the borehole then continues to increase in height until it is the full height of the sample just as it reaches the edge of the sample. Whilst fracture half-length 2 is the exact opposite with the fracture starting at the borehole at a height just short of the borehole length. The height of this fracture half-length then decreases further away from the borehole and by the time the fracture reaches the edge of the sample the fracture height is approximately half the borehole depth.

The dimensions of the fracture half lengths are presented in Table 5-5 & are explained previously in Figure 5-51 & Figure 5-52.

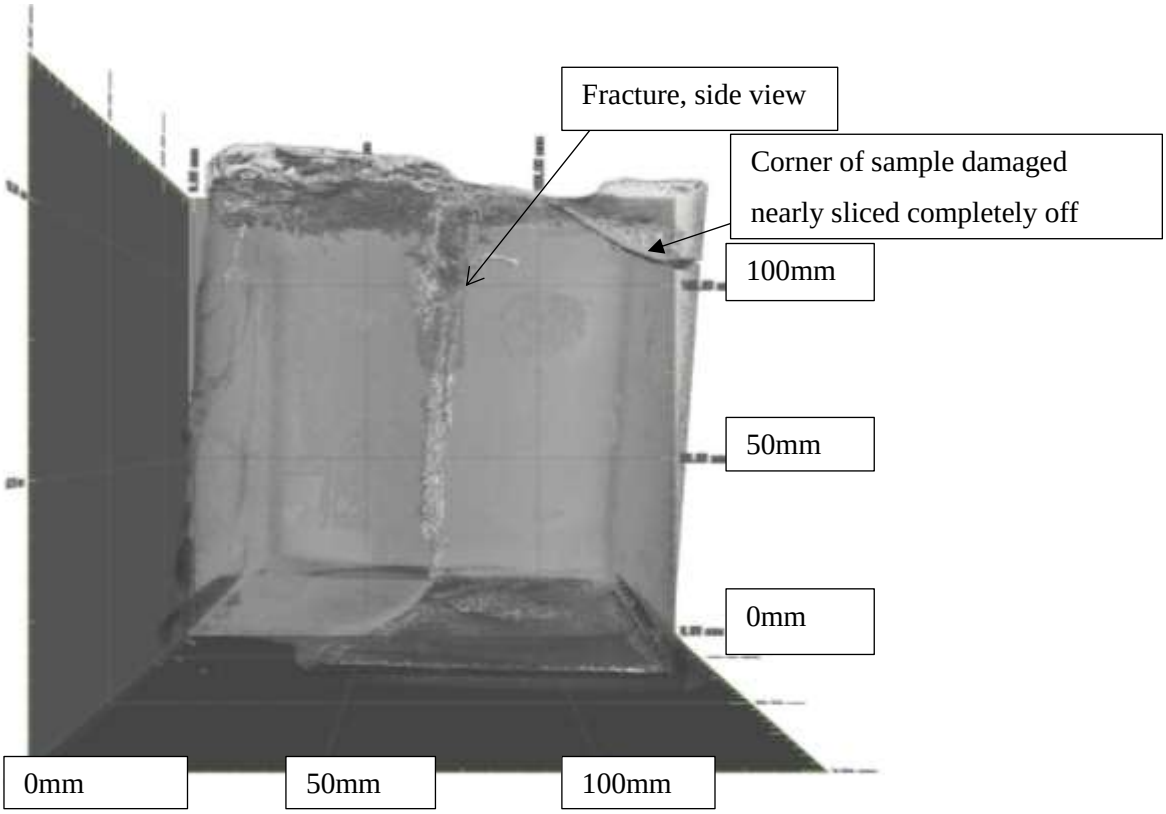

FIGURE 5-53: AMS1 Side view 1.

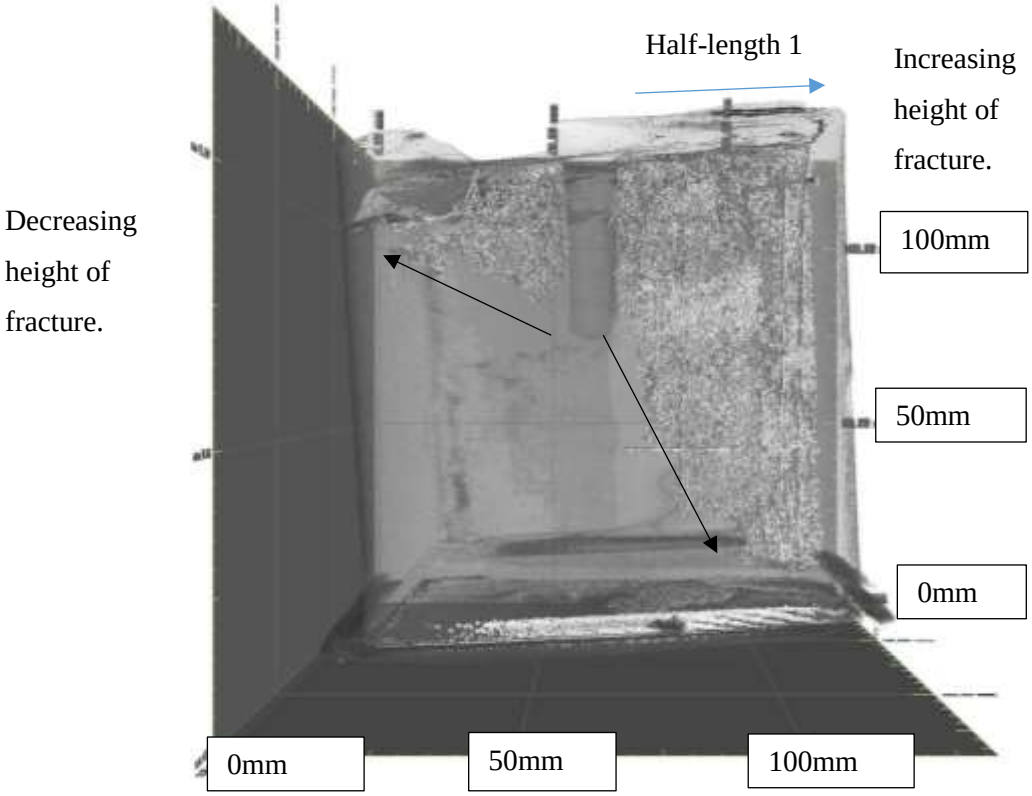

FIGURE 5-54: AMS1 side view 2.

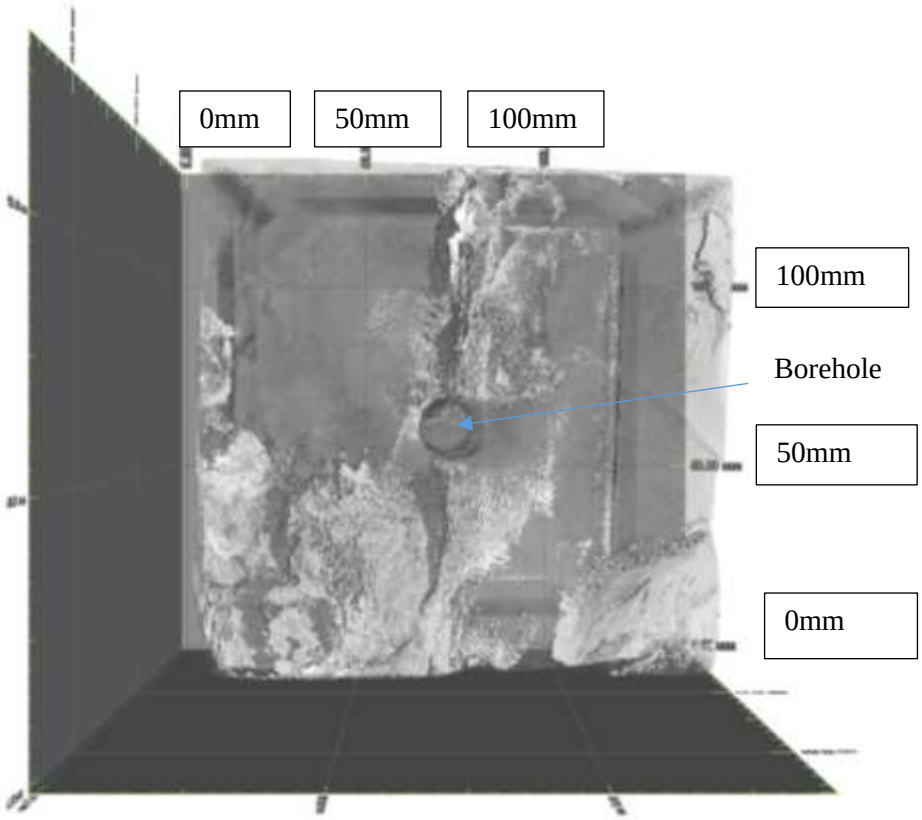

FIGURE 5-55: AMS1 Overhead view.

Sample name: AMS1											
Position to Borehole	Distance from borehole (mm)	Fracture length (mm)	Distance from Max width to the 10% max width at the top (mm)	Distance from maximum width to the 10% max width at the bottom (mm)	Maximum width (mm)	Top narrowing width (mm)	Bottom narrowing width (mm)	30% max width top	30% max width bottom	Distance from max width to 30% max top	Distance from max width to 30% max bottom
Half-length 1											
At the borehole	1.69	34.72	23.03	7.00	0.27	0.03	0.03	0.09	0.09	22.95	3.67
Near Borehole	6.83	65.83	31.11	11.35	0.44	0.04	0.04	0.12	0.12	35.16	6.41
Halfway from borehole	17.98	78.49	26.83	22.96	0.25	0.03	0.03	0.08	0.08	25.41	18.17
Three quarters way from borehole	29.80	94.97	27.46	43.78	0.23	0.02	0.02	0.07	0.07	27.44	42.63
Half-length 2											
At the borehole	0.51	26.74	12.82	7.14	0.41	0.04	0.04	0.12	0.12	12.66	5.34
Near borehole	9.28	29.36	14.27	9.03	0.23	0.02	0.02	0.07	0.07	11.11	7.93
Halfway from the borehole 1	15.88	25.10	11.13	9.82	0.23	0.02	0.02	0.07	0.07	11.05	9.80
Three quarters way from the borehole	28.28	25.72	10.85	4.78	0.23	0.02	0.02	0.07	0.07	10.84	4.75

TABLE 5-5: AMS1 fracture half-length measurements.

The relative positions of the fracture are shown in Figure 5-52.

Fracture half-length 1; the maximum width shows a discrepancy from the start, starting at the borehole the width was 0.27mm but increased by 63.0% to 0.44mm. Progressing ½ way along the fracture half-length from the borehole the maximum width had decreased to 0.25mm and by ¾ point along the fracture half-length the width had decreased to 0.23mm. The widest part of the fracture would normally be expected by the borehole with the width decreasing as the fracture travels away from the borehole.

On fracture half-length 1 the height of the fracture greater than 10% of the max width was 30.03mm compared to a full fracture height of 34.72mm and accounted for 86.5% of the fracture. The widest part of the fracture (wider than 30% of the max width of the fracture) accounts for 76.7% of the fracture length. At a quarter way along the fracture half-length the fracture greater than 10% of the max width accounts for 64.5% of the total fracture height, whilst the widest part of the fracture accounts for 55.6%. Halfway along the proportion drops to 63.43% and 55.5% for widths greater than 10% of the maximum width and greater than 30% respectively, whilst ¾ along the fracture half-length from the borehole the fracture is 75.0% and 73.8% for widths greater than 10% and 30% of the maximum width respectively. It is interesting to note that the proportion of the widest part of the fracture decreases in comparison to the fracture length the further away from the borehole, with the exception of the measurements taken ¾ away from the sample. No obvious faults were seen in the sample before fracturing, though areas did show hummocky bedding, including on the side of the sample that fracture half-length 1 broke out from. A possible explanation for this result could be an existing plane of weakness that the fracture had taken advantage of during propagation which may have helped to release the pressure built up by the fluid.

Fracture half-length 2; the maximum width starts at 0.41mm but then decreases and remains steady at 0.23mm throughout. This corresponds to the fracture half-length decreasing in height as it was propagated further away from the borehole as opposed to increasing in height as observed in half-length 1 and other samples. The lack of further reduction in width suggests that what has been traded for as a loss of height in the fracture as it propagates has been made up for in maintaining the fracture width as the absence of further narrowing means that there was a lower requirement to dissipate pressure from the fracturing fluid and thus an increase in the fracture height was unnecessary. This can be seen by the negative correlation when the fracture height is plotted against the width, Figure 5-56, where, barring one anomalous result, there is a clear negative correlation of decreasing width against increasing height. With an equation of $y=-1506.2x+445.96$ and an r^2 value of 0.94 the trend line is close fit for the three points.

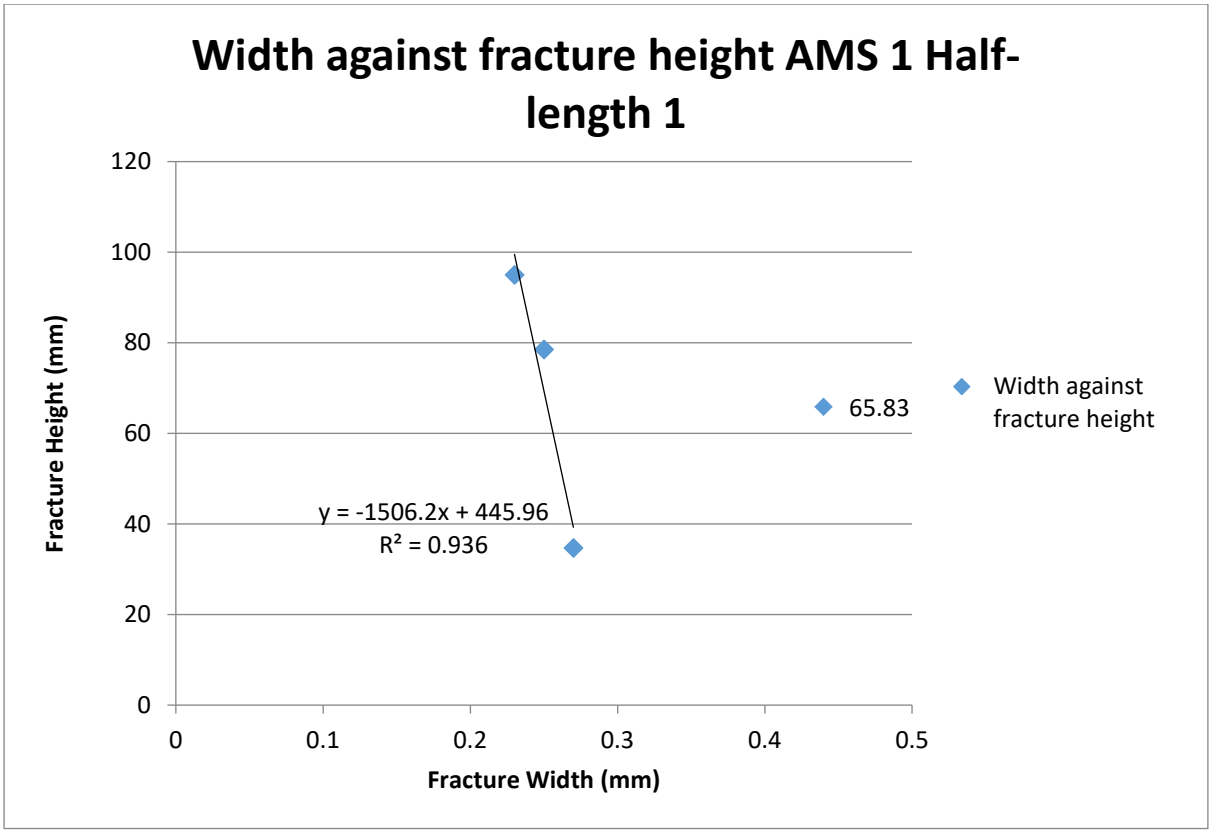

FIGURE 5-56: Graph showing width against fracture height fracture half-length 1

Conversely, the widest part of fracture half-length 2 did not follow the pattern set by half-length 1. At the borehole the proportion of the fracture that was above the 10% maximum width and the proportion that made up the wide section of the fracture was 74.6% & 67.3% respectively. At ¼ of the way along the half-length it had become 79.4% and 64.9% respectively. By ½ way along the fracture half-length the proportion of the fracture wider than 10% of the maximum width had reached 83.5% but the proportion of the fracture that was made of the wide section was 83.1%. At ¾ along the half-length the proportions had become 60.8% & 60.6% respectively. This shows a disparity where there was not a gradual decrease but a steady increase in the area of the fracture greater than 10% of the maximum thickness along with the fracture half-length until it reached ¾'s of the way whilst the widest section of the fracture followed no noticeable pattern, first decreasing then slowly increasing until dropping drastically at ¾ along the fracture half length. This could be explained again by the lack of a decrease in the width of the fracture. A decreasing fracture height has led to the need to dissipate the pressure in the fracture by increasing the proportion of the fracture greater than 10% of the maximum thickness when compared to other samples.

This can be seen in the graph, presented in Figure 5-57, where, again as previously in Figure 5-56 there is one anomalous result, but three of the results show a clear trend. In this example however, the trend shows a vertical line where the fracture width stays the same as the height decreases. y=128x + 32.

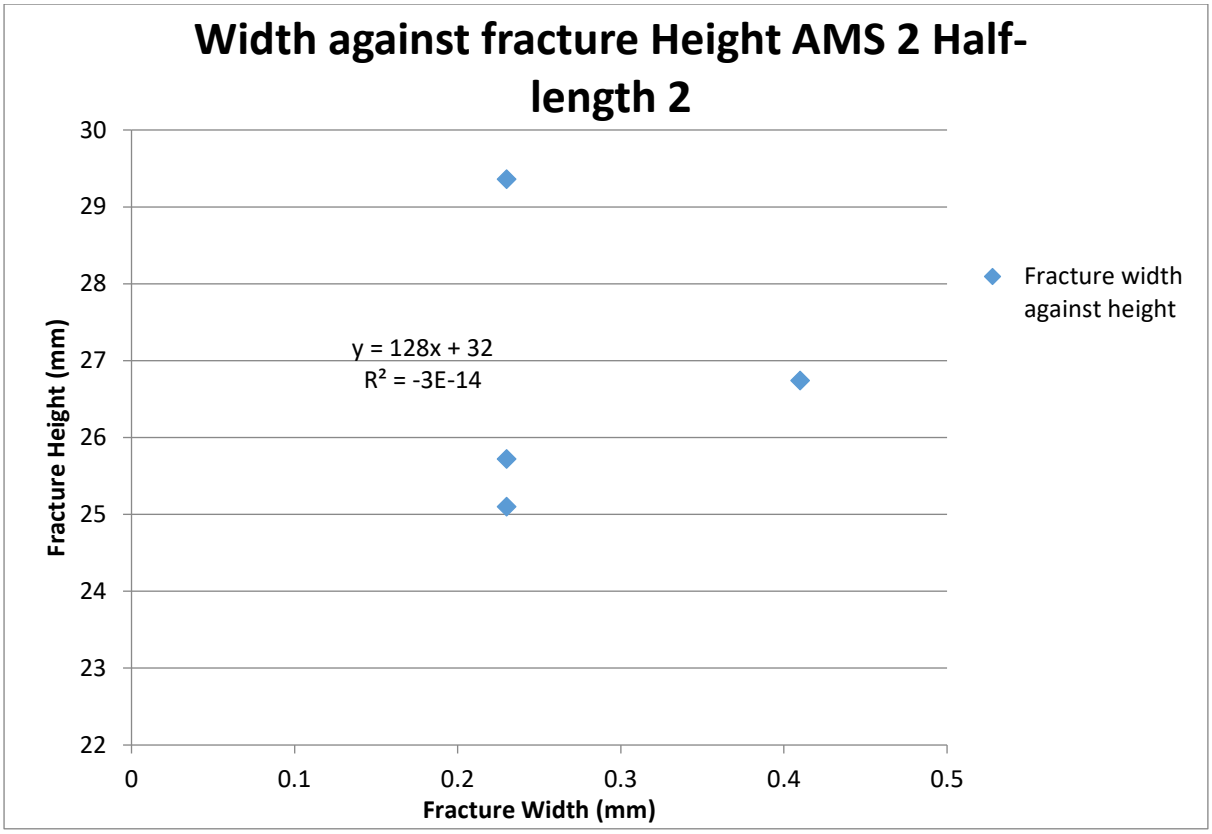

FIGURE 5-57: Graph showing width against fracture height fracture half-length 2

The variation of proportions in the wide section could be explained by something similar though the decrease in the area to a ¼ along the fracture half-length is only 3.6% which to all intents is staying the same before a large increase occurs by the time it reaches ½ way along the fracture half-length. The fracture is forming more of an elliptical cross-sectional shape as there is a lack of fracture length to dissipate the pressure in the fluid to form the long thin sections that follow on the top and bottom of the fractures. This points to a strong area of resistance along this fracture half-length that does not allow the fracture to grow further away from the borehole, as seen by half-length 1. This lack of fracture progression, albeit thin extensions to the height of the main fracture, forces a wider bodied fracture than compared to what is seen in fracture half-length 1. The planar view of each fracture at the point measurement is presented in Figure 5-58 to Figure 5-59.

The relative position of the fracture measurements, in relation to the positions distance from the borehole, are shown in Figure 5-51 while the measurements taken in the planar view of the fracture, that make up the labelling of these figures are presented in Figure 5-52.

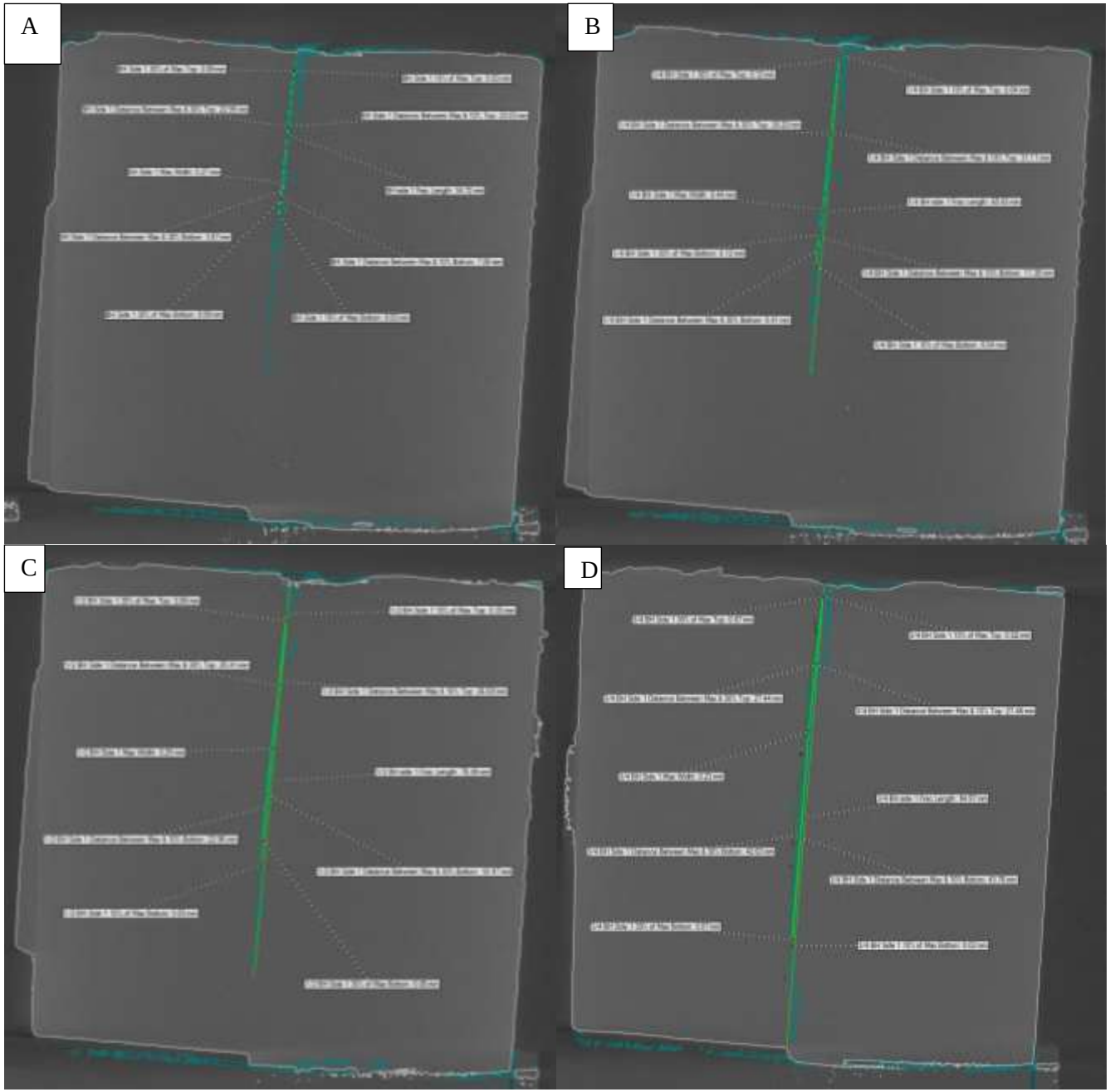

FIGURE 5-58: AMS 1 Fracture half-length 1, A) At the borehole, B) Near the borehole, C) Halfway along the half-length, D) ¾ along the half-length.

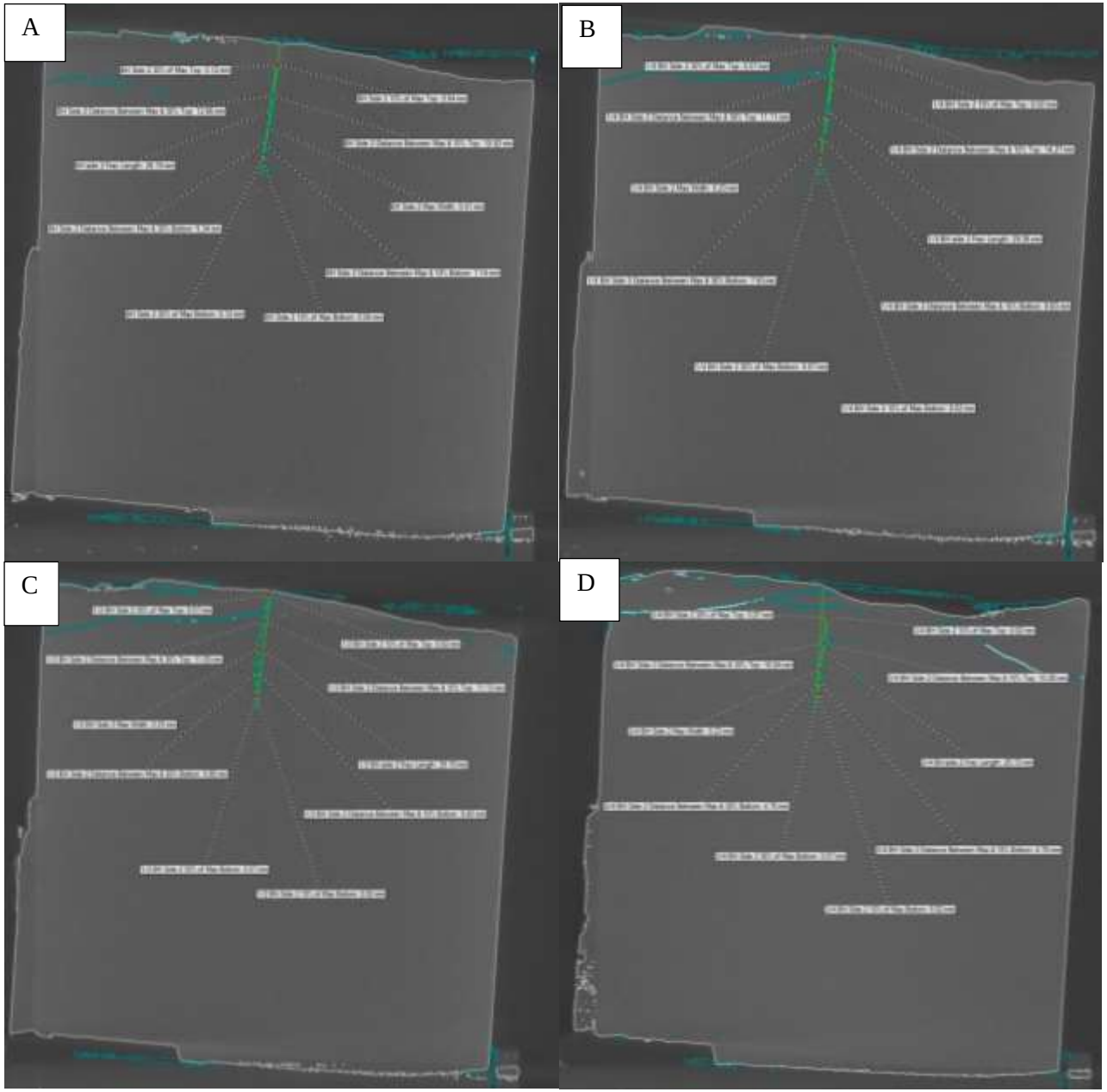

FIGURE 5-59: AMS1 Fracture half-length 2, A) At the borehole, B) Near the borehole, C) Halfway along the half-length, D) ¾ along the half-length.

5.5.1.2 AMS2

The AMS2 sample fractured during drilling. The scan of the sample after the drilling is presented in Figure 5-60 to Figure 5-61.

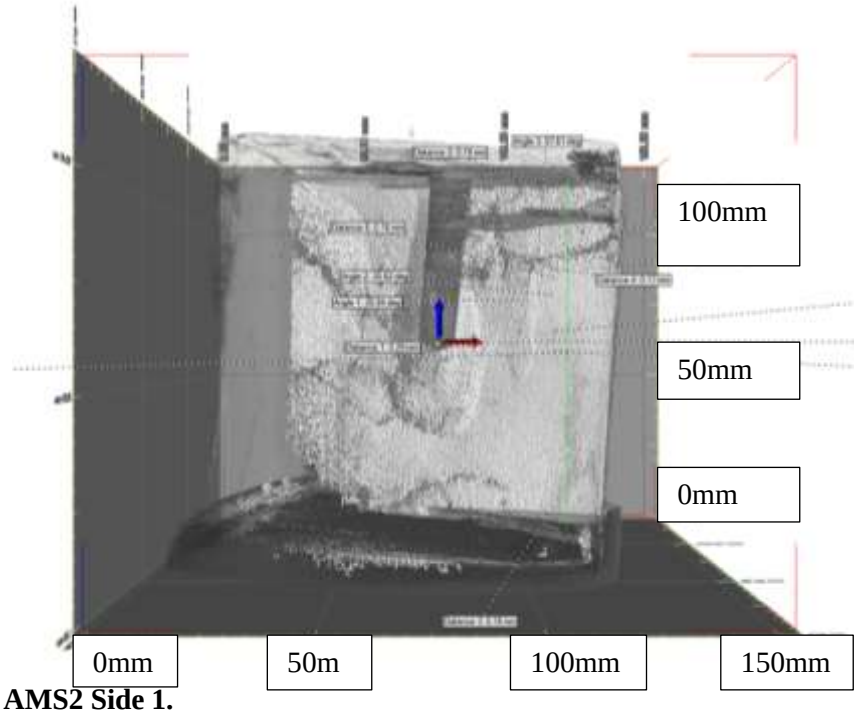

FIGURE 5-60: AMS2 Side 1.

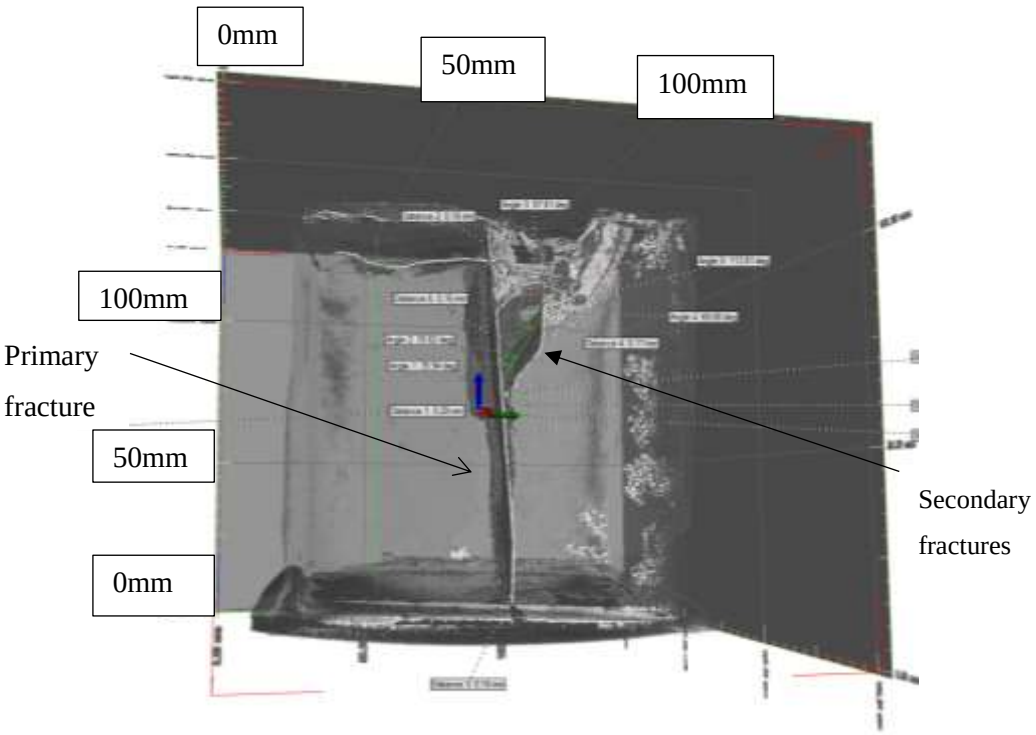

FIGURE 5-61: AMS2 side 2.

As shown in Figure 5-60 the main fracture cuts directly from the middle of the borehole and through to the extremities of the sample. Furthermore, a secondary fracture has evolved from the main fracture and follows a path to the top of the sample, as can be seen in Figure 5-61. It is of interest to note that the secondary fracture appears only in the top half of the sample and that it starts just above the base of the borehole where the main fracture initiated whilst drilling. The interaction between the main fracture and the secondary fracture changes as both fractures progress further away from the borehole. The secondary fracture forms towards the bottom of the borehole, as shown in Figure 5-62. As the fracture progresses away from the borehole, towards the edge of the sample it joins with the main fracture, in an area termed the intersection area. Close to the borehole the fracture forms an acute angle of 47.42^{o} with the main fracture, as seen in Figure 5-62, which is a side profile x ray slice of the fractures. The fracture forms at the point of initiation creating a reasonably straight line with only two slight changes in angle. These angles, or changes in direction of the fracture, range from 146.07^{o} and 111.13^{o} and are relatively obtuse. They probably reflect the fact that the energy release rate (G) described by Irwin (1957) is greater than the crack resistance (R) leading to the acute angle where the secondary fracture and the main fracture join each other and the relatively small amounts of deviation of the secondary fracture as the fracture contains enough energy to overcome the surface energy of all but the strongest components of the sample. These angles were measured using the reconstruction software tools to ensure an accurate reading between the two identified arms of the angle.

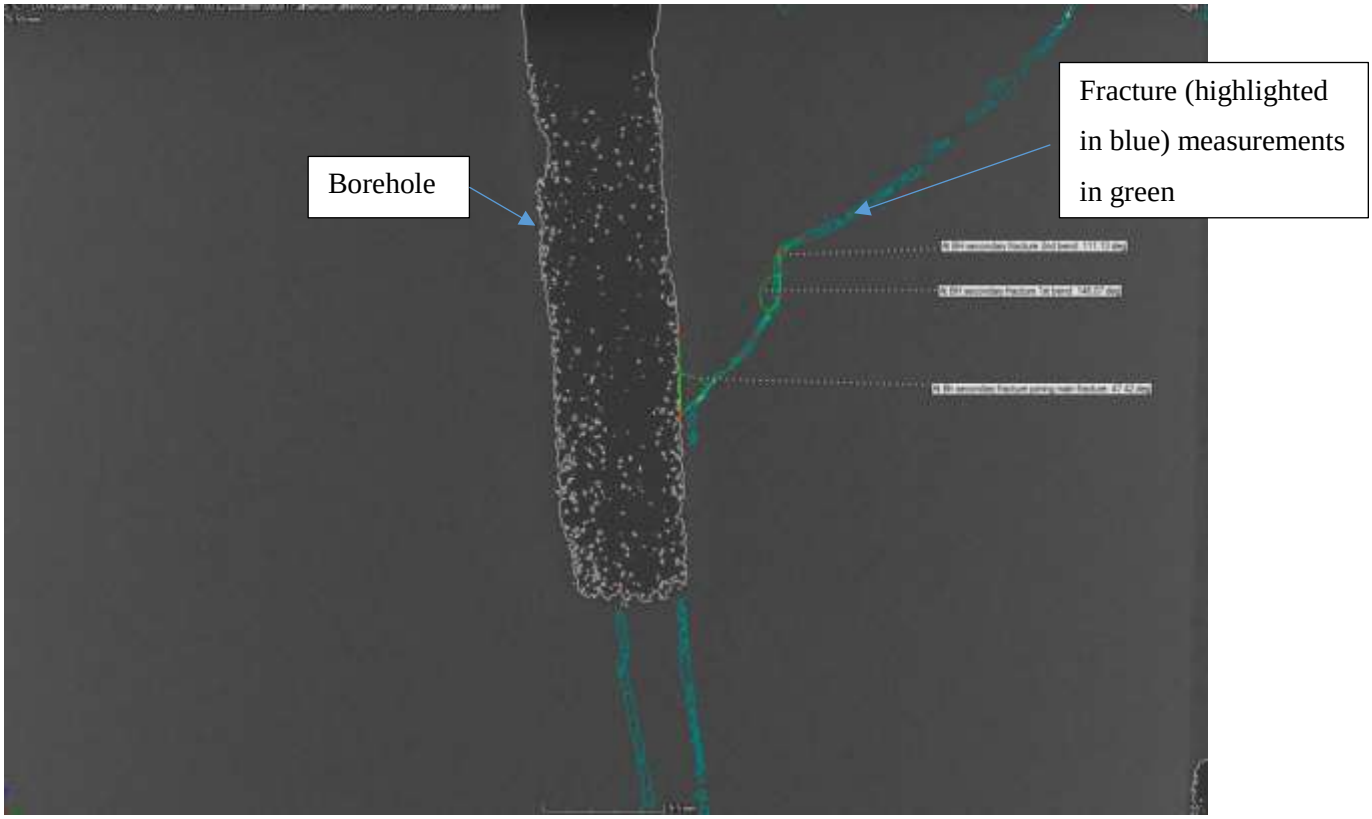

FIGURE 5-62: AMS2 tortuosity in the secondary fracture, taken at the borehole, leading to the dorsal.

Further away from the borehole the secondary fracture shows more tortuosity, in the area around the junction of the two fractures. Moving to a distance of 13.73mm from the borehole, this junction between the two fractures has increased in tortuosity with 4 turns in the junction area, with angles ranging from 138.87° to 150.37° as seen in Figure 5-63, as the fracture looks to release the potential energy inside it by finding the weakest parts of the bed rock. This can be explained by noting that the energy behind the inducement of a fracture was greatest at the borehole and would provide the fracture with enough energy to overcome the structural integrity of the sediment.

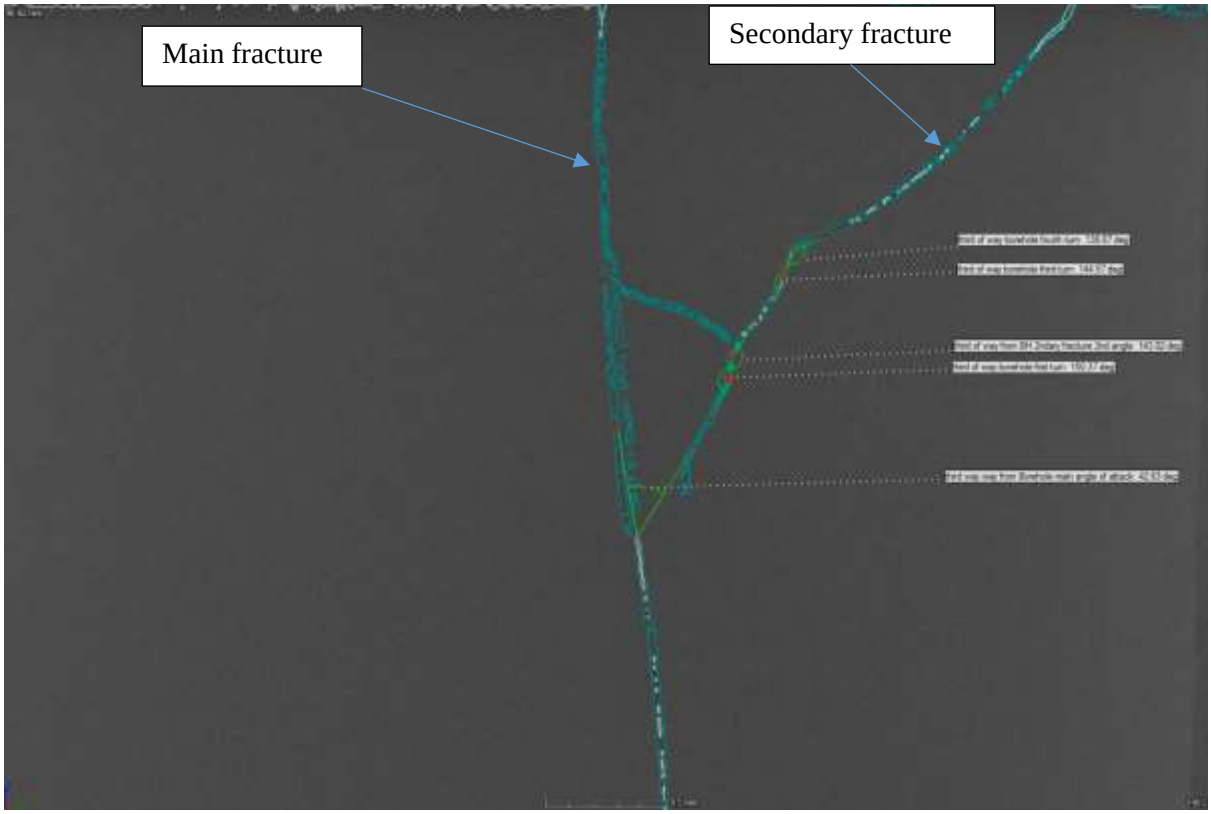

FIGURE 5-63: Increased tortuosity of the secondary fracture taken 1/4 along the fracture half length.

Along the fracture half length, at a distance of 21.12mm from the borehole, the intersection area of the secondary fracture shows a noted increase in the tortuosity with 14 angles forming along the path of the fracture ranging from 116.39° to 172.19°. The angle between the secondary and main fracture has also increased to 67.27°, as seen in Figure 5-64. This large increase in the tortuosity along the pathway of the secondary fracture gives further evidence that as the fracture progresses from its point of inducement the dissipation of energy crack growth rate, G, means it is unable to overcome the crack resistance of stronger components in the sediment, yet still has enough energy to force the crack to extend along weaker planes.

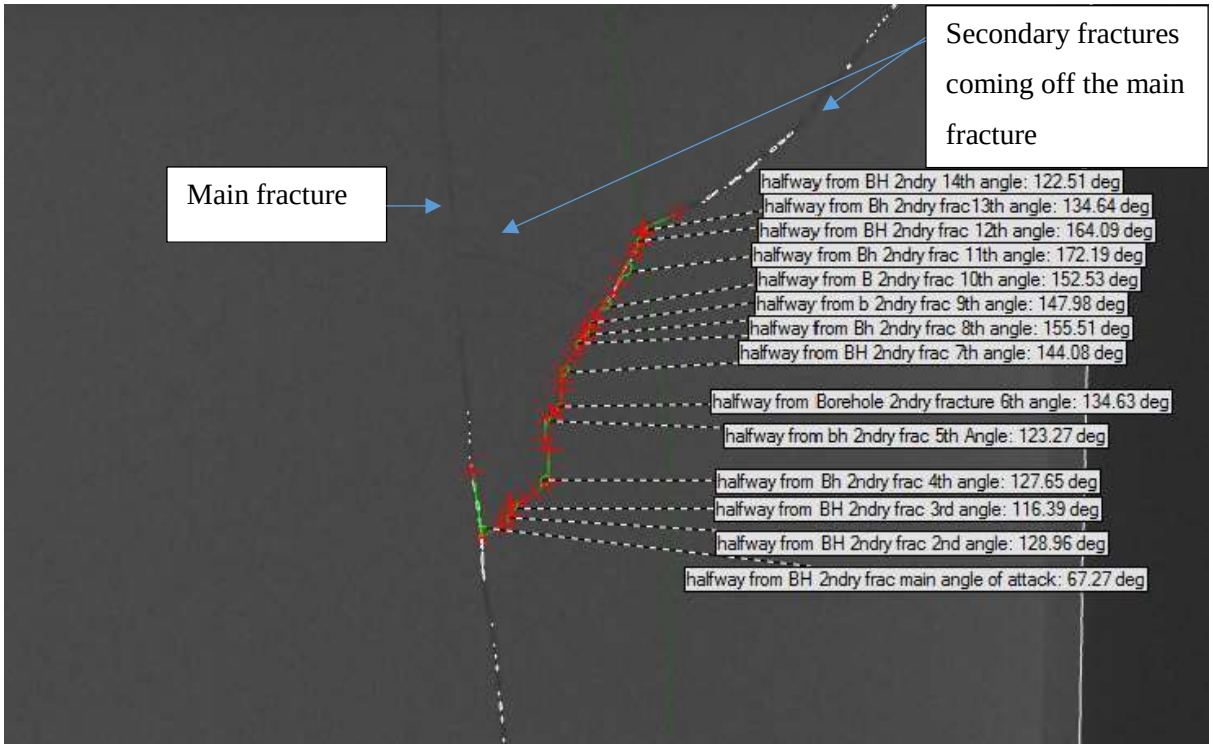

Figure 5-64: ½ distance along fracture half-length increase of the tortuosity.

Figure 5-65 is where the measurements are taken 39.42mm from the borehole. The intersection area of the secondary fracture suffers from 18 deviations from the straight path with angles ranging from 107.94º to 158.54º. The angle between the main and secondary fracture has also increased to 87.41º.

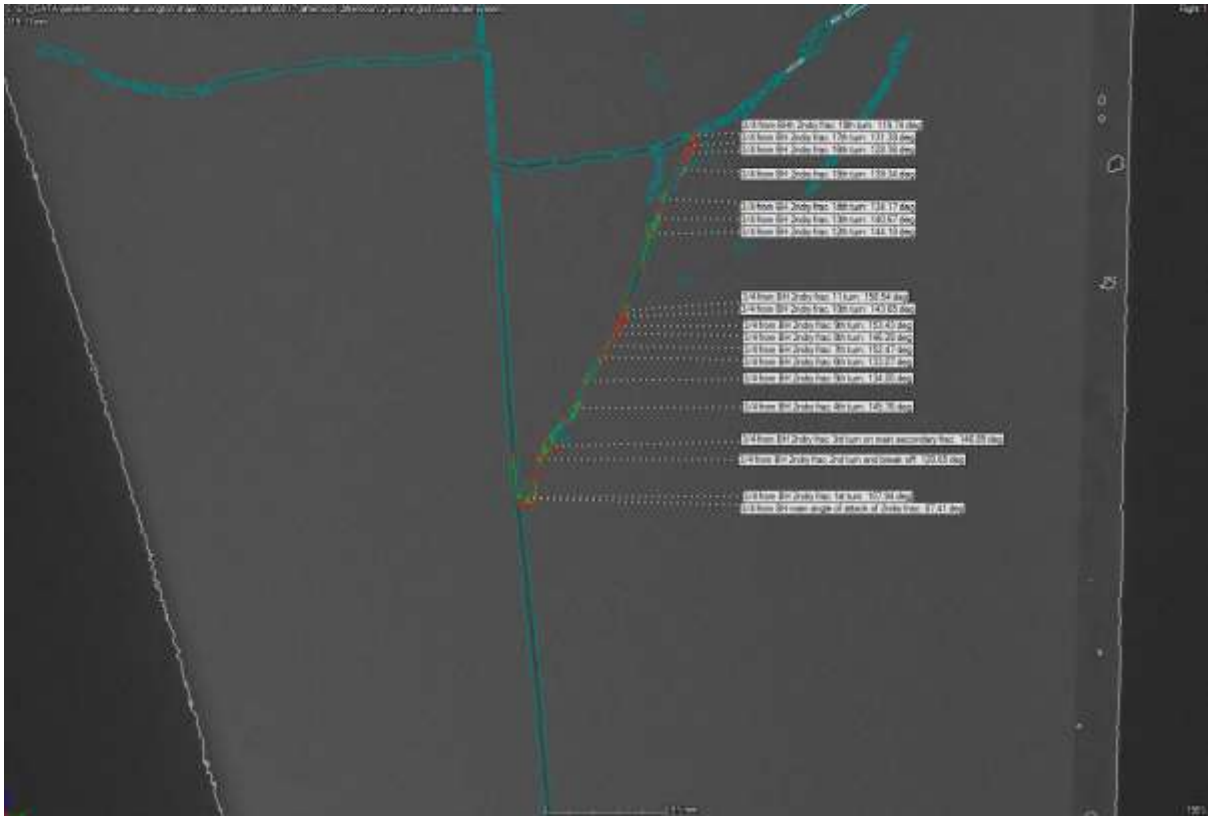

FIGURE 5-65: Edge of the sample showing increased tortuosity of the fracture angle.

As the fracture progresses to the edge of the sample and the energy dissipates over a wider area, areas of greater strength within the sediment are too strong for the energy in the fracture to overcome, forcing the fracture to find the weaker path. Though, as has been noted by Griffin (1920) and Irwin (1951) the fracture will follow a straight path, this leads to the levels of tortuosity seen near the intersection of the main and secondary fracture. While this intersection area of the two fractures shows a great deal of complexity, further up the secondary fracture the main line of propagation is shown to be similar throughout the progression of the fracture, although the length along the secondary fracture which suffers from this tortuosity also increases the further away from the borehole the fracture is analysed.

From this sample it can be surmised that there are two main areas associated with induced fractures joining each other; The intersection area, which shows a propensity towards an increased tortuosity as the fracture gets further away from the point of inducement and the second area; the main line of attack of the fracture tip point progression, is the section of the secondary fracture that lies further away from the intersection and follows a similar angle throughout its length. It is important to note that though this sample fractured during the drilling phase, it still gives an important understanding of how a fracture evolves when a shale sample is under pressure, whilst also showing the potential damage that can be caused whilst drilling. It appears that the fractures form mainly straight lines in order to find the shortest distance between the edges of the sample. The secondary angles show that a fracture can exhibit some tortuosity at its inception, but then the tortuosity of the fracture evolves to show a series of near right

angle fractures as the energy in the fracture finds areas of weakness in the sediment, this, in the shale, being the bedding plane.

AMS2 The dimensions of the fractures are presented in Table 5-6 & terms are explained previously in Figure 5-51 & Figure 5-52.

Sample name: AMS2											
Position to Borehole	Distance from borehole (MM)	Fracture length (mm)	Distance from Max width to the 10% max width at the top (mm)	Distance from maximum width to the 10% max width at the bottom (mm)	Maximum width (mm)	Top narrowing width (mm)	Bottom narrowing width (mm)	30% max width top	30% max width bottom	Distance from max width to 30% max top	Distance from max width to 30% max bottom
Half-length 1											
At the borehole	0	47.96	8.02	12.01	0.36	0.04	0.04	0.12	0.12	2.76	10.08
Near Borehole	6.83	96.40	13.89	46.45	0.32	0.03	0.03	0.09	0.09	10.83	21.49
Halfway from borehole	14.14	96.40	13.89	-	0.32	0.03	0.03	0.09	0.09	10.83	21.49
Three quarters way from borehole	30.14	97.20	35.81	-	0.25	0.03	-	0.09	-	31.87	-
Half-length 2											
At the borehole	0	50.65	13.15	16.66	0.22	0.02	0.02	0.06	0.06	5.83	10.36
Near borehole	8.70	98.95	-	-	0.28	-	-	0.09	0.09	8.55	27.28
Halfway from the borehole 1	18.59	99.11	-	45.73	0.19	-	0.02	0.06	0.06	16.97	9.74
Three quarters way from the borehole	28.33	100.00	44.33	50.61	0.19	0.02	0.02	0.06	0.06	14.47	33.31

TABLE 5-6: AMS2 Fracture Half-length dimensions.

The relative positions of the fracture are shown in Figure 5-52.

At the borehole fracture half-length 1 recorded a wide middle section that would account for the fact that the fracture was closest to its point of initiation. As the results in Table 5-6 show the middle section of the fracture had a maximum width of 0.32mm where distance between the max width and the 10% max width at the top and bottom was 8.02mm and 12.01mm respectively, though, with an overall height of 47.92mm. This accounts for only a small part of the fracture indicating that the fracture does indeed comprise of a wide body shape. However, a large section of the fracture has a thin cross section, less than 10% of the maximum width of the fracture, whilst an even smaller proportion of the fracture could be considered the wide body fracture (i.e. one that is wider than 30% of the max width).

With a total height of 47.96mm the section with a width greater than 10% of the maximum width accounted for 20.03mm of this. This amounts to 41.8% of the fracture height being of greater width than 10% of the maximum width, while the percentage of the fracture wider than the 30% of the maximum width of the fracture was only 26.7%. Further away from the borehole the fracture cross section did not narrow to a point that was 10% of the maximum width, though it did narrow to 30% of the max width. Thus, this gave a total area of the wide body of the fracture of 11.1% and a fracture height of 32.32mm against a total fracture height of 96.40mm. It should be noted that the widest section of the fracture was found to be much closer to the top narrowing point than the bottom making the shape less of an oval and more like an upside-down tear drop.

Approximately half way from the borehole to the side of the sample the fracture profile changed once again. The maximum width increased from 0.32mm recorded at the near borehole location to 0.36mm. The proportion of the wide section of the fracture had increased as a proportion of the total fracture height compared to what was recorded near the borehole. The fracture stayed wider as it propagated further away from the borehole and it did not narrow to 30% of the max width at the bottom of the fracture. Looking at the results of the fracture at the halfway point it becomes clear that this result does not follow the normal model with the widest point here being greater than those measurements taken near the borehole. In addition, a greater proportion of the entire fracture is part of the wide section. This is perhaps due to an existing weak bedding plane or an existing weakness in the sample.

Approximately three quarters the way along the half-length, the furthest section from the borehole, measurements were also made. A maximum width of 0.25mm compared to 0.36mm at the half way point, whilst the height of the fracture is comparatively similar the measurement of 97.22mm at ¾ compared to 96.44mm halfway along the fracture half length.

The second fracture half-length was also analysed to see if there were any similarities. At the borehole the fracture height was 50.65mm, increasing to 98.95mm at ¼ distance along the fracture length, 99.11mm at ½ way and 100.00mm at ¾ distance from the borehole. In this fracture half-length the max

width again showed the same feature noted on fracture half-length 1 in that the maximum width increased from 0.22mm at the borehole to 0.28 at ¼ distance along the fracture half-length before decreasing to 0.19mm at both the halfway and three-quarter distance.

On fracture half-length 2 the width did not narrow to 10% of the max width at all locations across the fracture length but it did narrow to 30% at both the top and the bottom of the fracture. At the borehole the height of the wide section measured 16.19mm out of a total fracture height of 50.65mm, only 32.0%, whilst at ¼ distance the wide part of the fracture accounted for 35.83mm out 98.95mm, 36.2% of the overall height of the fracture and by ½ way along the half-length the widest part of the fracture measured 26.71mm but the proportion of the fracture height being part of the widest section had decreased to 27.0%. Though by ¾ of the half-length the widest part of the fracture had increased dramatically and accounted for 47.78mm out of a total fracture height of 100mm giving a proportion of the wide section at 47.8%. So even though each fracture half-length appeared to have anomalous results the trend still suggests that the width of the fracture decreases further away from the borehole whilst the proportion of the fracture that is within 30% of the maximum width increases.

An image of the progress of the fractures for each fracture half-length is shown, Figure 5-66 and Figure 5-67, while the measurements taken in the planar view of the fracture that make up the labelling of these figures are presented in Figure 5-52.

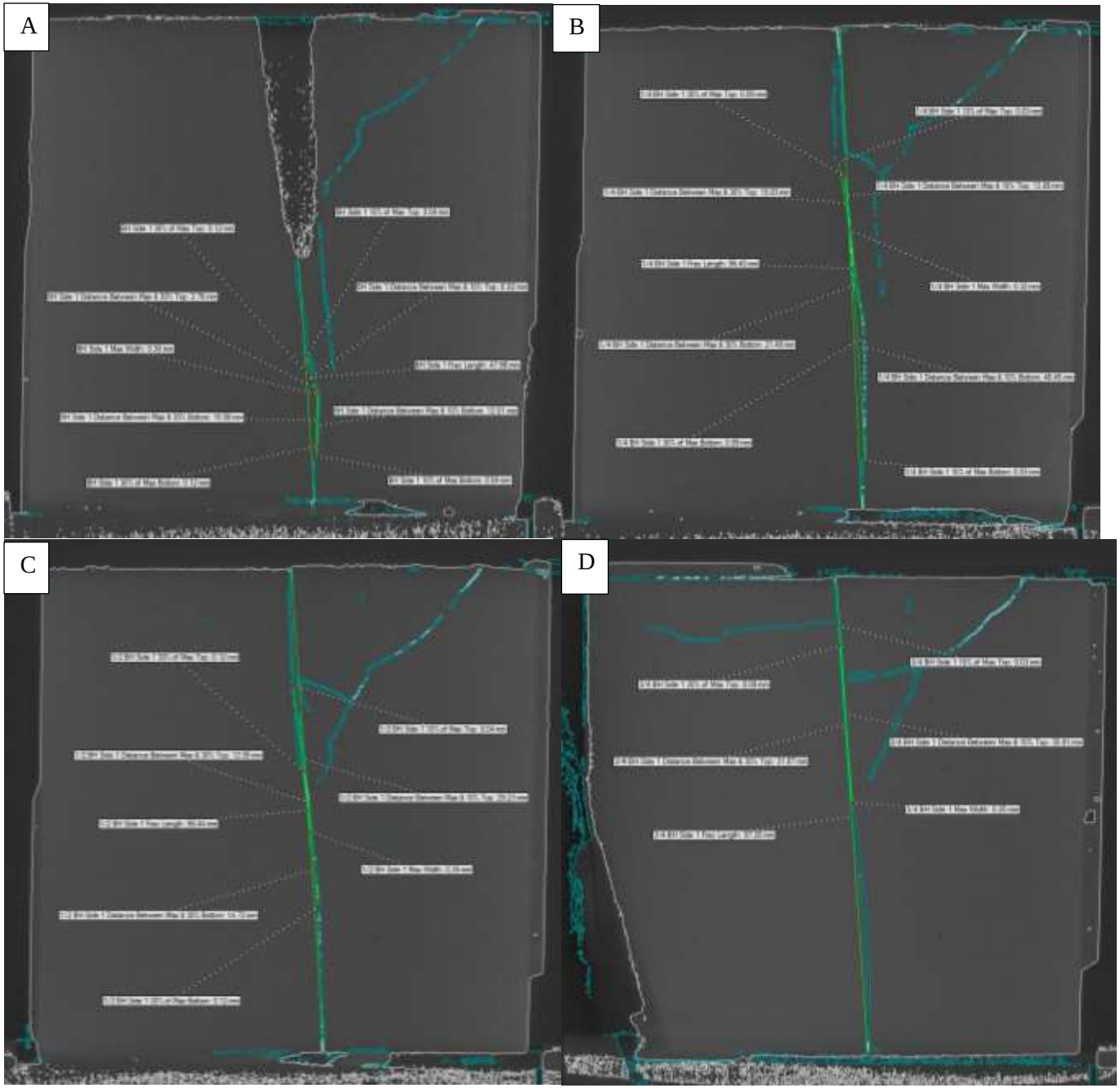

FIGURE 5-66: AMS2 Fracture Half-length 1, A) At the borehole, B) Near the borehole, C) Halfway along the half-length, D) ¾ along the half-length.

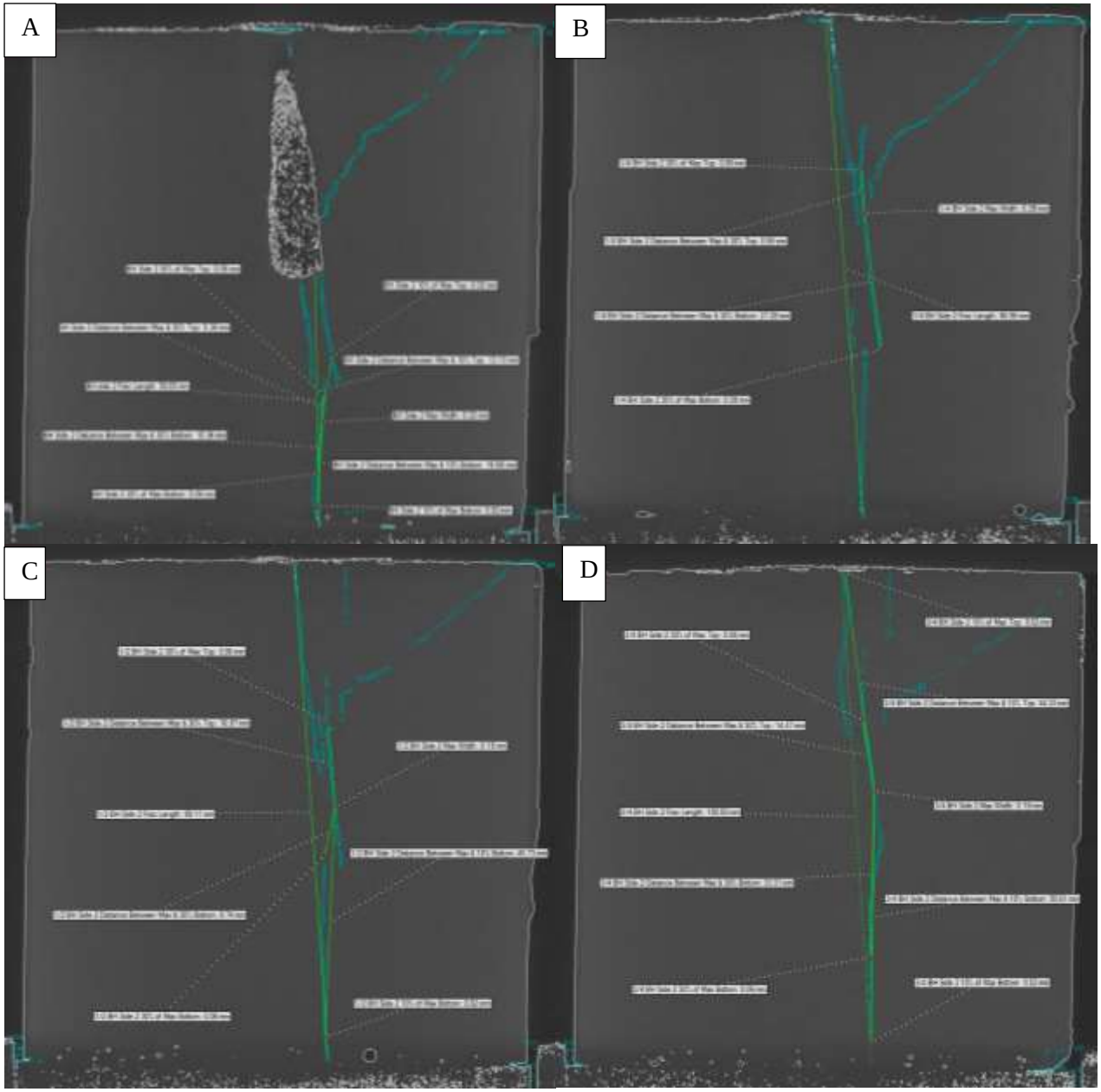

FIGURE 5-67: AMS2 Fracture Half-length 2, A) At the borehole, B) Near the borehole, C) Halfway along the half-length, D) ¾ along the half-length.

WESTBURY SHALE

The Westbury shale samples are higher in organic content and therefore much weaker than the Accrington Mudstone, due to a lower level of clay. A number of these samples were tested but most crumbled as soon as pressure was applied or during drilling. For this reason, only two samples remained cohesive enough to be scanned after fracture inducement was attempted, during the bi-axial part of the investigation. One sample that had bi-axial stress applied and one that had tri-axial stress applied were not actually fractured due to crumbling prior to fluid injection.

5.5.1.3 WBS1

The WBS1 sample crumbled when drilling was attempted, but the sample was still scanned in case any useful information could still be determined when investigating how the sample crumbled. The sample reconstruction is presented below in Figure 5-68 to Figure 5-70.

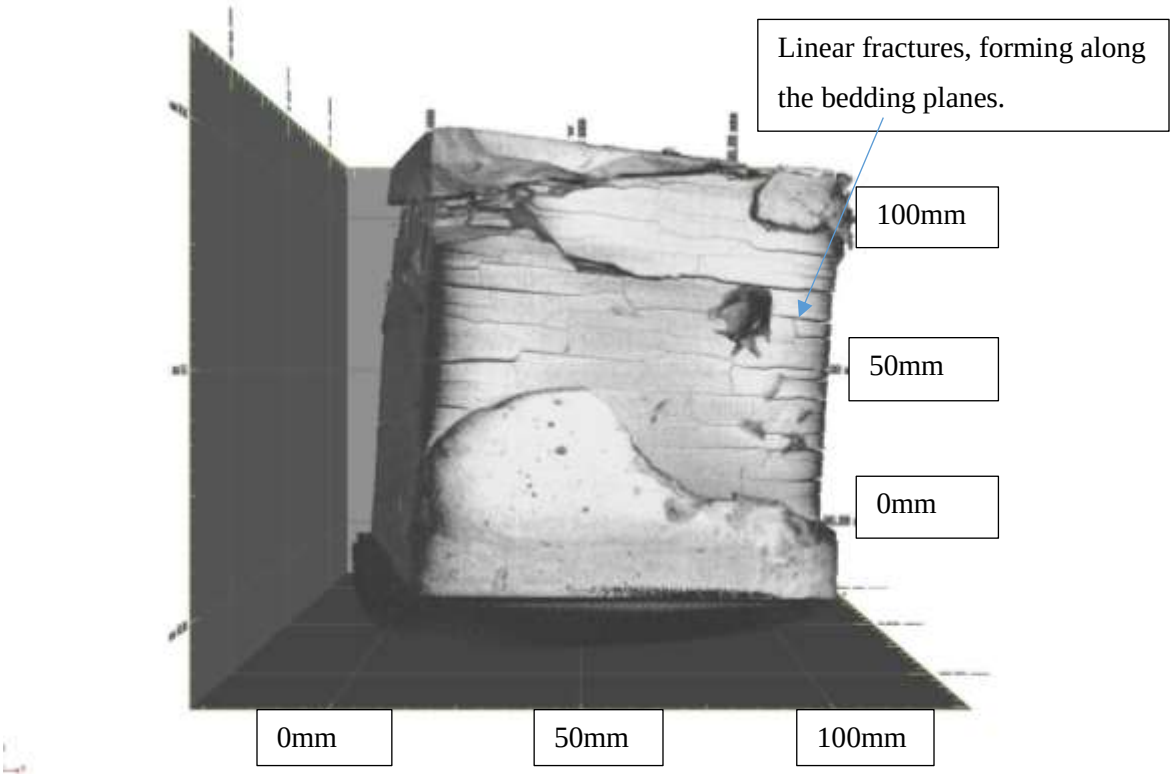

FIGURE 5-68: WBS1 Side view 1.

As can be seen in Figure 5-68, the cracks are parallel to the bedding plane, the cracks follow alongside the weakest planes on the sample, as also seen in Figure 5-69.

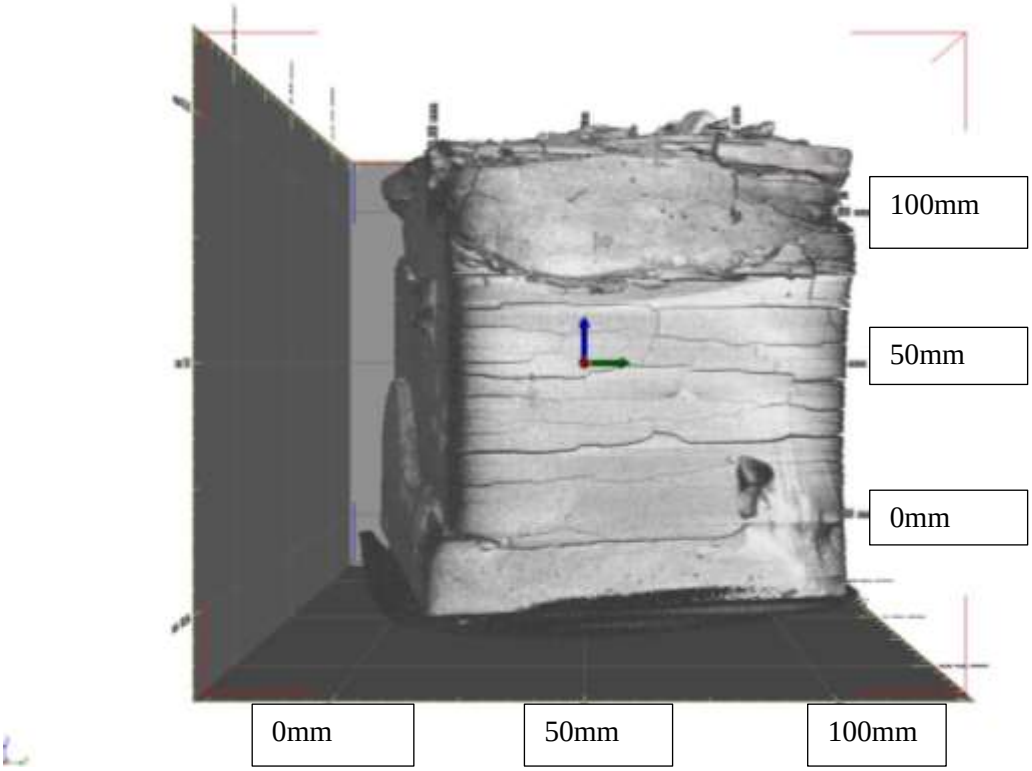

FIGURE 5-69: WBS1 Side view 2.

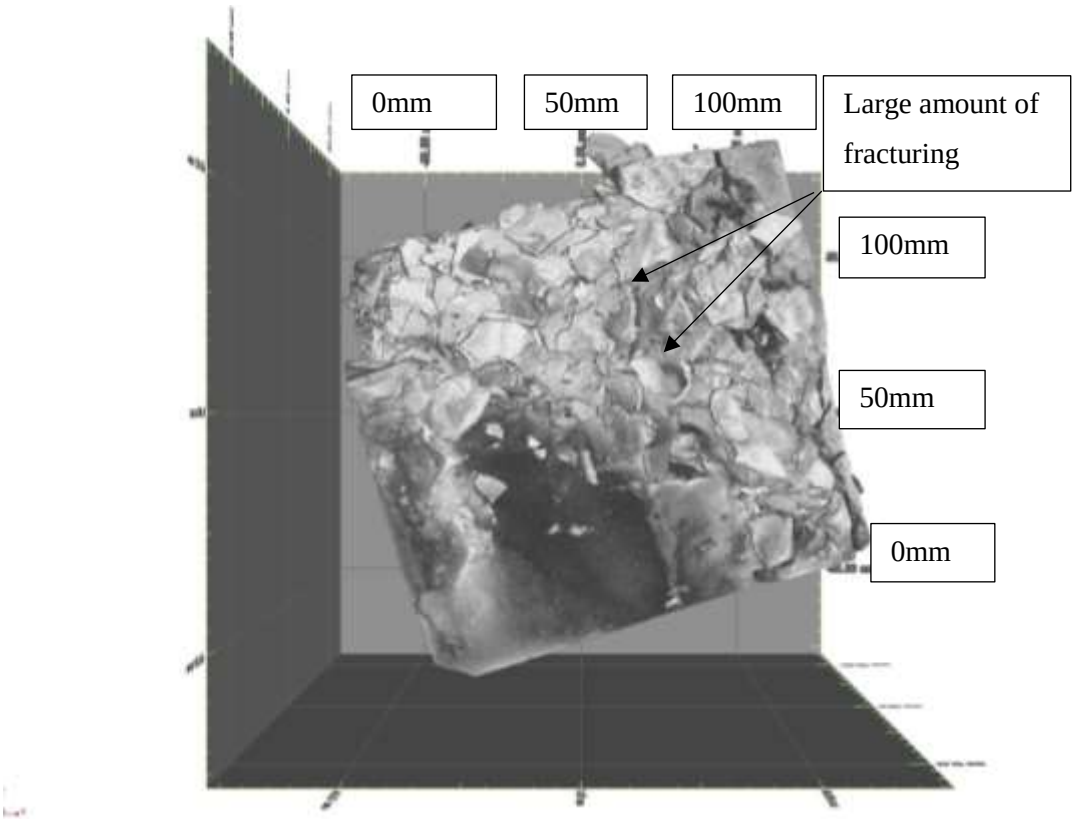

FIGURE 5-70: WBS1 plan view.

This sample has fractured along the bedding planes of the shale, a pre-existing area of weakness, so when pressure was applied, combined with the damaging effects of the drill, this created a great deal of instability which caused the fractured chippings that can clearly be seen in Figure 5-70. Figure 5-70 is the planar view of the scan.

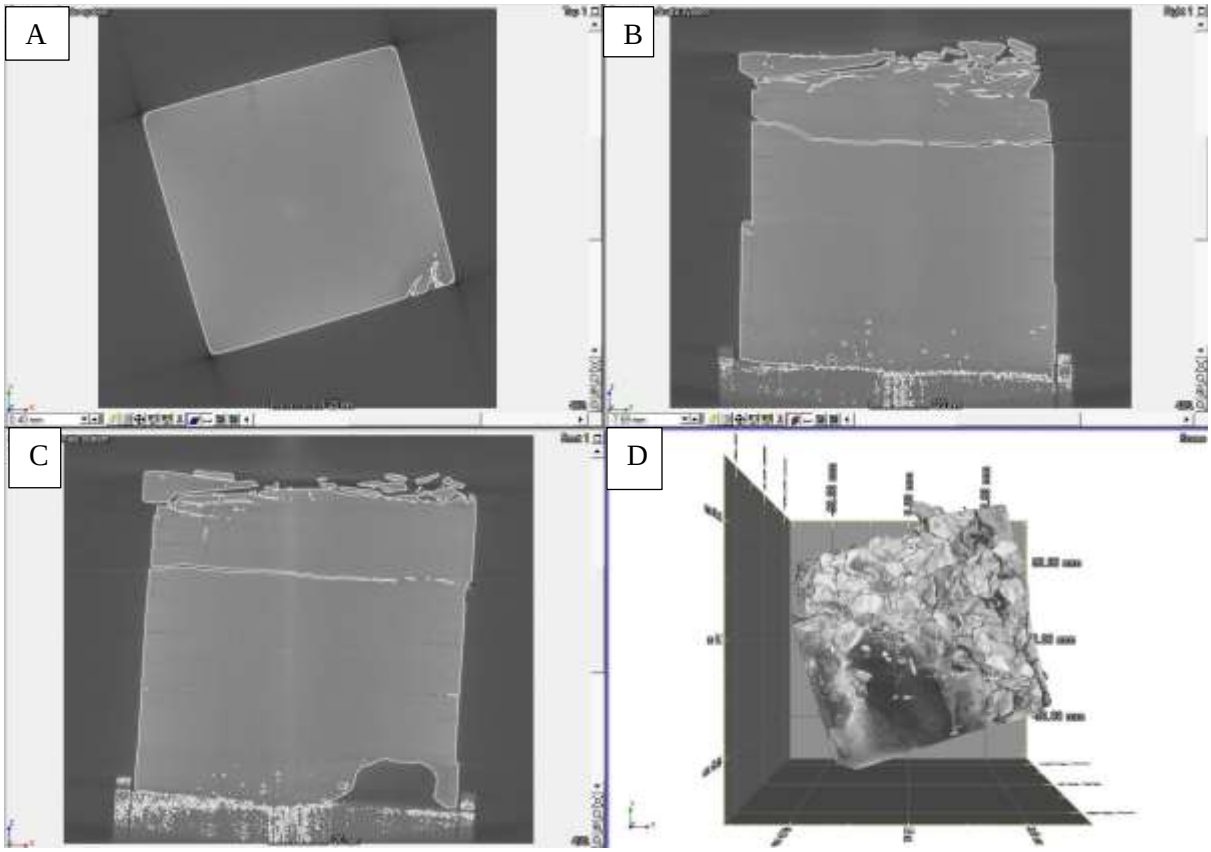

FIGURE 5-71: Planar X ray views of shale sample A) Overview B) Sideview 1 C) Sideview 2 D) 3D.

As is evident in Figure 5-71, the sample has fractured heavily along its bedding planes, especially in the top quarter of the sample, where a large portion of that quarter has been broken up as the drilling was attempted. This suggests that even when under pressure organic rich shale is still at great risk of fracturing and breaking, leading to complex fracture patterns, as can be seen in Figure 5-71.

5.5.1.4 WBS2

The WBS2 sample did fracture during inducement, creating one simple vertical fracture and two simple horizontal fractures, as shown below in Figure 5-72 to Figure 5-74. Figure 5-72 shows that this sample has one simple vertical fracture that has grown between two horizontal fractures. As the horizontal fractures clearly constrain the height of the vertical fracture, this indicates all three of the fractures occurred simultaneously. The dimensions of the fracture half lengths at different points, in relation to the borehole, are presented in Table 5-7 & terms are explained previously in Figure 5-51 & Figure 5-52.

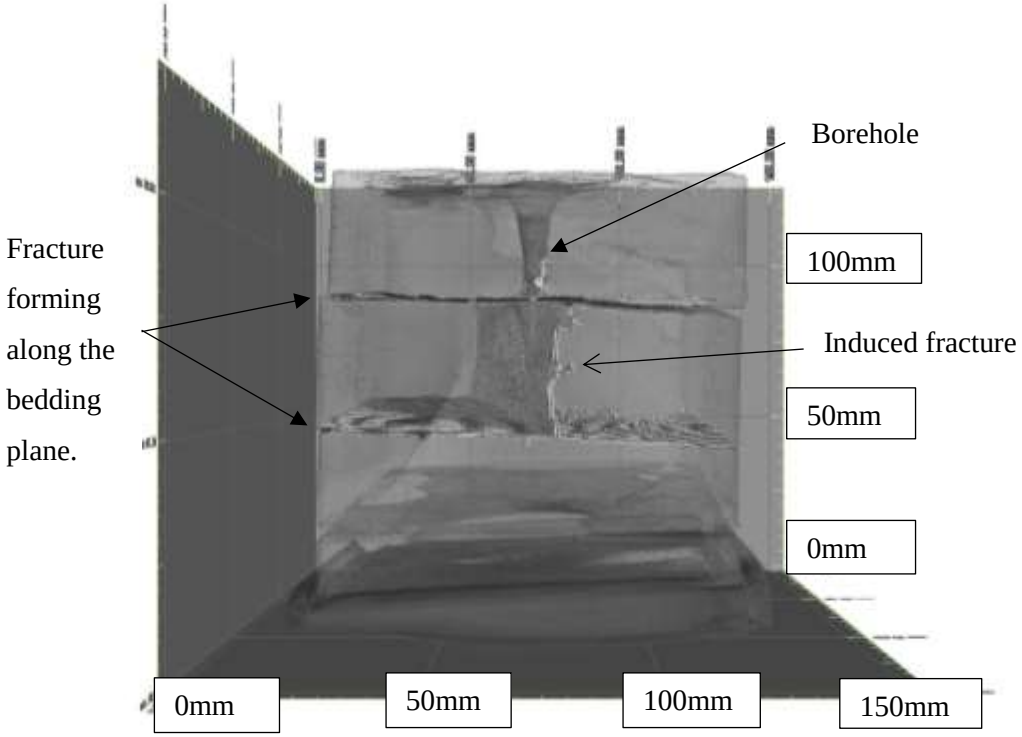

FIGURE 5-72: WBS2 Side view 1.

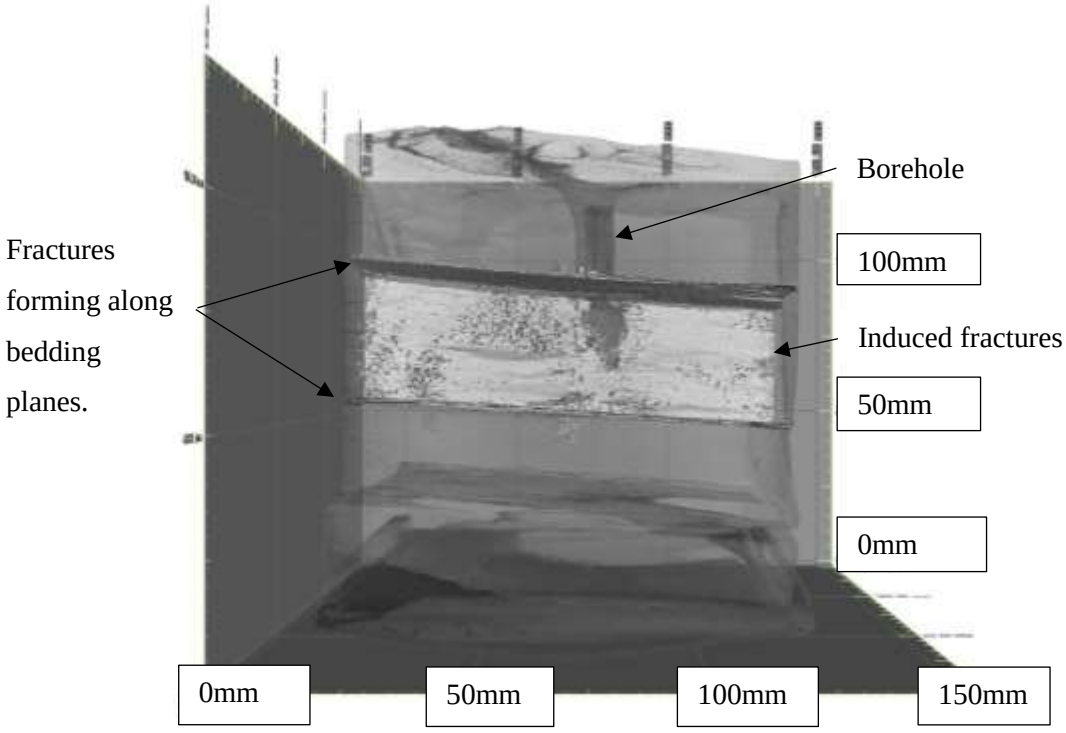

FIGURE 5-73: WBS2 Side view 2.

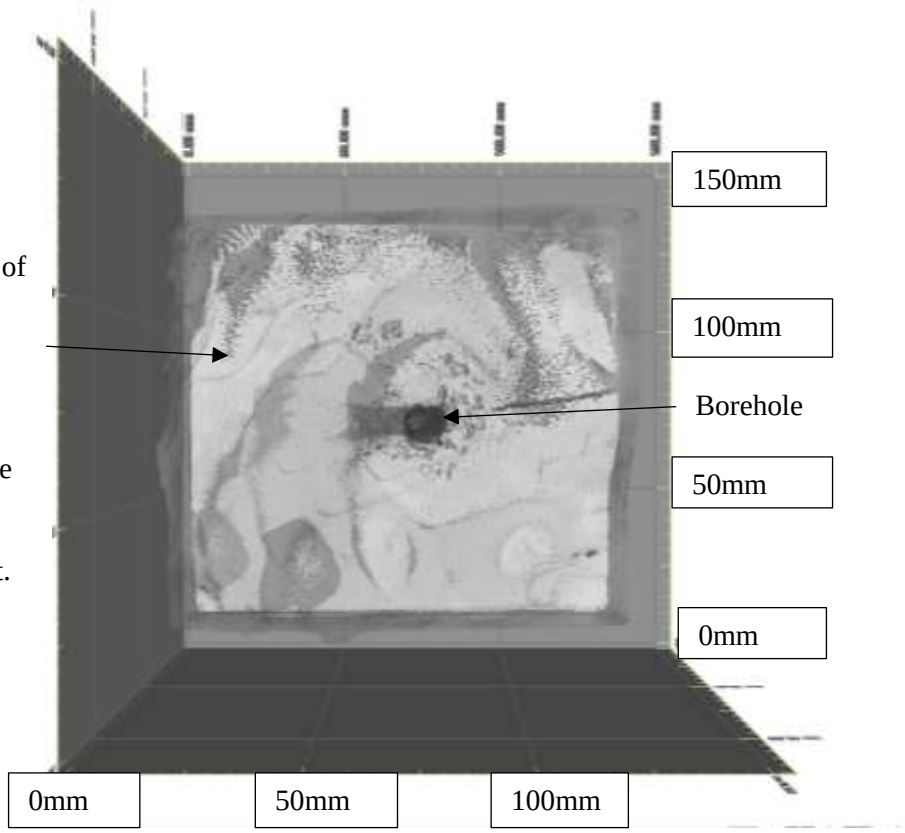

FIGURE 5-74: WBS2 Top view.

Sample name: WBS 2											
Position to Borehole	Distance from borehole (MM)	Fracture length (mm)	Distance from Max width to the 10% max width at the top (mm)	Distance from maximum width to the 10% max width at the bottom (mm)	Maximum width (mm)	Top 10% of max width (mm)	Bottom 10% of max width (mm)	30% max width top	30% max width bottom	Distance from max width to 30% max top	Distance from max width to 30% max bottom
Half-length 1	-										
At the borehole	0	31.42	-	-	6.25	-	-	-	-	-	-
Near Borehole	5.22	31.55	12.04	14.17	1.60	0.16	0.16				
Halfway from borehole	24.20	30.53			1.17	-	-	-	-	-	-
Three quarters way from borehole	36.60	30.74			01.27						
Half-length 2											
At the borehole	0	30.35			1.38						
Near Borehole	11.39	33.75			1.51						
Halfway from borehole	24.00	32.84			1.37						
Three quarters way from borehole	43.77	30.88			1.09						

TABLE 5-7: WBS2 fracture half-length dimensions.

The relative positions of the fracture are shown in Figure 5-52.

From the data in Table 5-7 it is clear that although there is a single vertical fracture, just as in the Accrington Mudstone, there is an important difference. This fracture is much smaller and is confined between two horizontal fractures. In this sample neither fracture half-lengths showed narrowing, except at the near borehole side of fracture half-length 1, though this narrowing has occurred so rapidly it has immediately reduced to 10% of the fracture width, with no gradual narrowing; hence why there is no 30% narrow point. This lack of narrowing of the fracture could perhaps be explained by the differences between the Westbury Shale and the Accrington Mudstone. In this sample the fracture has propagated vertically, though, simultaneously the fracturing fluid has also curtailed the fracture length by extending horizontal fractures that cut short the vertical fracture. The fluid pressure still retains a large pressure head from the injection needing to dissipate through this small fracture height. With a small area for the pressure head of fluid to dissipate the fracture width grows in proportion to the loss of the height in the fracture. Compare the near borehole distance on fracture half-length 1 in WBS2 and AMS2 the height of 31.55mm for WBS2 is 32.7% of the 96.40mm for AMS2, whilst the max width of 0.32mm of AMS2 is 20% of the 1.60mm recorded for WBS 2. This relationship between fracture height and width explains the wide fracture and lack of narrowing for WBS2. The lack of height means that there is no capacity for a slow dissipation of the pressure head. The pre-existing weakness of the bedding planes in the Westbury Shale has caused the shale to split when fracture propagation was occurring. This sudden break along weak planes took place simultaneously along the fracture half-length as the fluid discovered a weak plane. That weakened plane then became subjected to greater pressures and unable to withstand these pressures the bedding planes split allowing the fracturing fluid to dissipate the pressure head along these relatively thin fractures, this process is shown pictorially below in Figure 5-75.

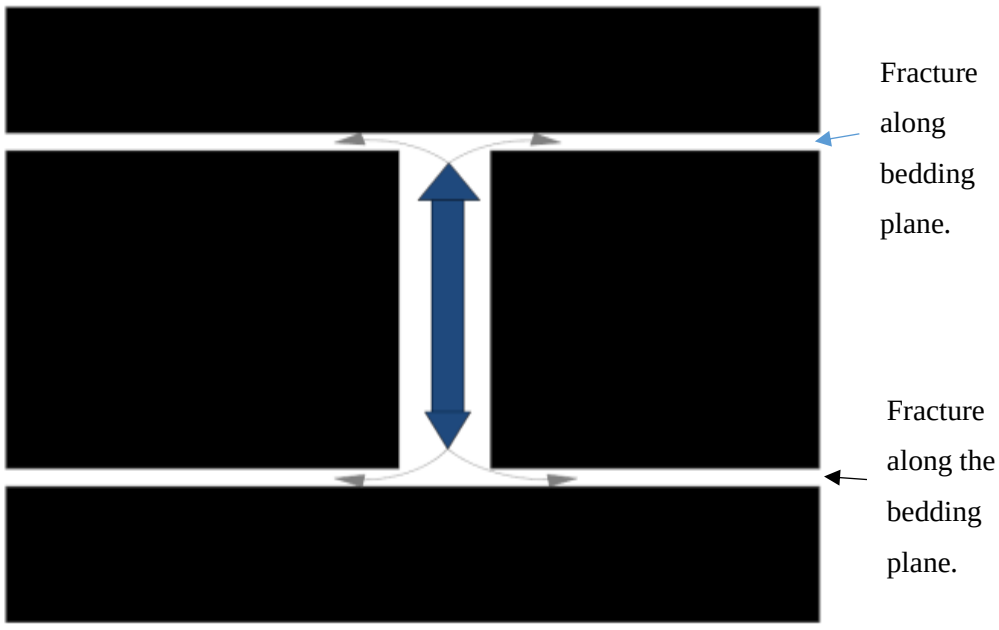

FIGURE 5-75: Dissipation of fracturing fluid pressure head along bedding planes.

The majority of the fracturing fluid travels along the fracture half-length thus most of the pressure remains within the propagated fracture whilst smaller volumes of the fluid break through the broken bedding planes allowing some dissipation of the pressure head. However, the continuance of a relatively wide max width from the borehole, ¼ borehole, ½ along & ¾ distance along the half-length of 6.25mm, 1.60mm, 1.17mm & 1.27mm respectively shows that only a small amount of the pressure head was dissipated. This is repeated along fracture half-length 2 with max width measurements of 1.38mm, 1.51mm. 1.37mm & 1.09mm.

A similarity between the Westbury Shale and the Accrington Mudstone is the increase in the tortuosity of the fractures the further away from the borehole the measurements are taken. On fracture half-length 2 at ¼ distance and ½ distance along the fracture half-length, the vertical fracture was noted to show some tortuosity along its height. Like the Accrington Mudstone the angles increased as the fracture propagated further away from the borehole. At ¼ distance on fracture half-length 2 the angles were 117.18^{o}, 119.59^{o}, 150.11^{o}, 135.31^{o} & 126.38^{o}. By the halfway mark the angles had increased to 162.44^{o}, 161,33^{o}, 163.24^{o}, 159.81^{o}, 168.72^{o}, 132.10^{o}, 130.16^{o}, 159.14^{o}, 162.55^{o}, 154.48^{o}. There is a clear increase in both the angle size and the number of twists which can only be explained by the dissipation of the fluid pressure further away from the borehole.

Closer to the borehole there is more fluid pressure and thus more energy to cut perpendicular to the bedding plane when traversing across areas of weakness greater than the inherent weakness in the bedding plane. The further fluid gets away from the borehole the less energy available to be expended. This loss of pressure head from the sample reduces the ability of the fracture to propagate through the sediment in the direction of the stronger orientation without coming across pockets of stronger cohesion in the rock, this forces the fracture to find a weaker area, surrounding this pocket of resistance, hence the tortuosity of the fracture. With this reducing force in the fracturing fluid, there will be a greater propensity to use the weakest part of the rock, the bedding plane to help navigate these pockets of resistance, which can be seen in the step effect of the fracture as shown in, Figure 5-76.

It is interesting to note that these samples do not follow the Accrington Mudstone exactly in that the tortuosity stops by the three quarters mark along the fracture half-length where the fracture has become relatively straight, albeit at an angle. This could be explained by the fact that the Westbury Shale is an inherently weak shale and that maybe it was only over this small area the fluid found any resistance whilst the Accrington Mudstone has a much greater clay content and would have a greater potential for areas of resistance along the half-length path. The X-ray planar view of the fractures and their measurements are shown in Figure 5-77 to Figure 5-78 (half-lengths 1 & 2 respectively).

The relative position of the fracture measurements, in relation to the positions distance from the borehole, are shown in Figure 5-51 while the measurements taken in the planar view of the fracture, that make up the labelling of these figures are presented in Figure 5-52.

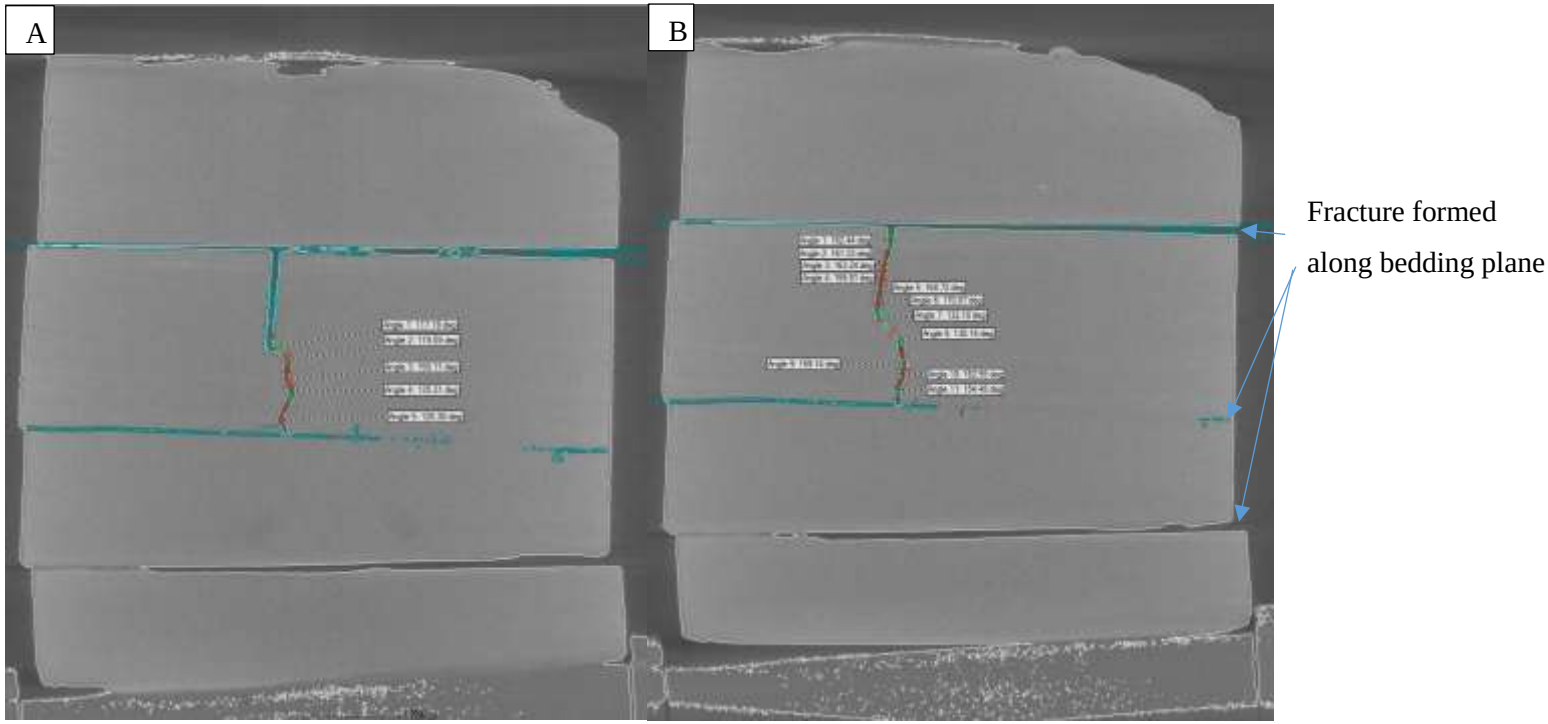

FIGURE 5-76: WBS2 Increasing tortuosity, A) Near the borehole, B) At the half way along the fracture half-length, side view.

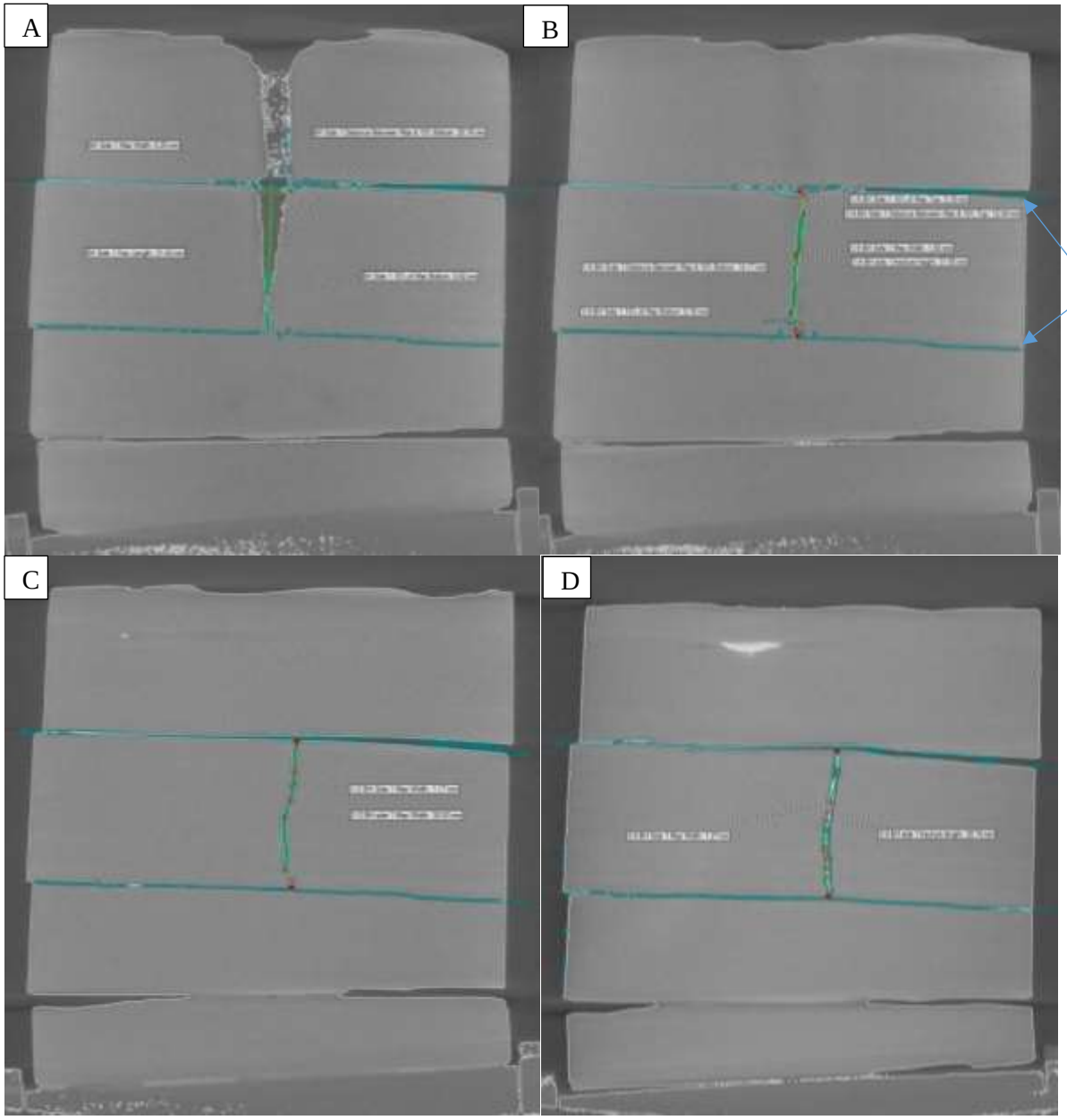

FIGURE 5-77: WBS2 Fracture half-length 1. A) At the borehole, B) Near the borehole, C) Halfway along the half-length, D) ¾ along the half-length, side view.

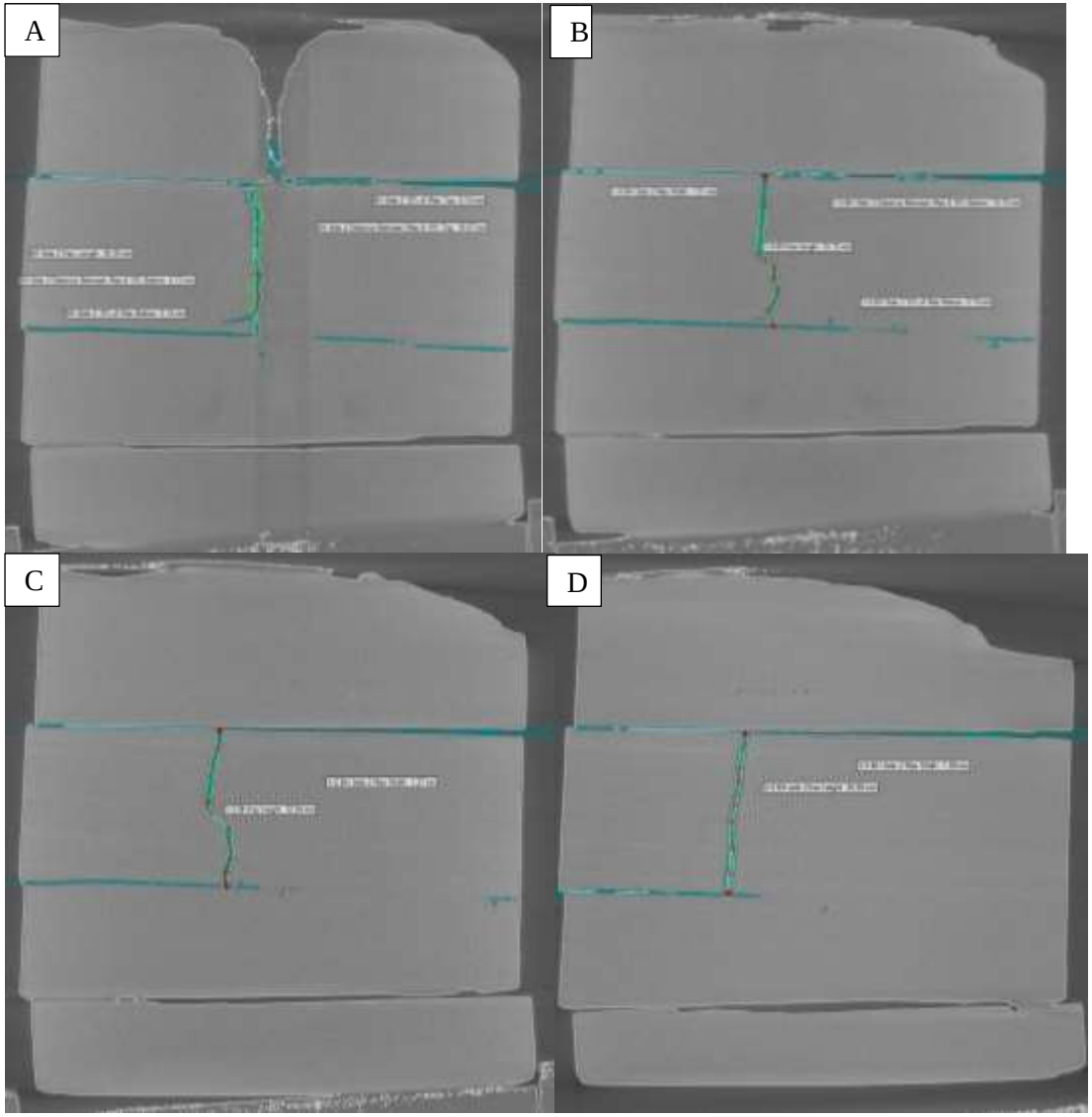

FIGURE 5-78: WBS2 Fracture half-length 2, A) At the borehole, B) Near the borehole, C) Halfway along the half-length, D) ¾ along the half-length.

5.5.2 Tri-axial fracture

5.5.2.1 AMS3

The AMS3 sample was subjected to tri-axial pressure with a σ^1 of 100 bar, σ^2 of 85 bar and σ^3 of 80 bar. The borehole was drilled off centre to avoid the pre-existing fracture discussed in section 5.3.1.3. The fracturing was induced at approximately 2,500 psi. The overhead view of the sample after fracture is shown in Figure 5-79; as shown the preliminary fracture goes from the borehole to the edge of the sample on one side. On the other side of the borehole the fracture meets the pre-existing fracture. A secondary fracture occurs parallel to the preliminary fracture that runs through the borehole.

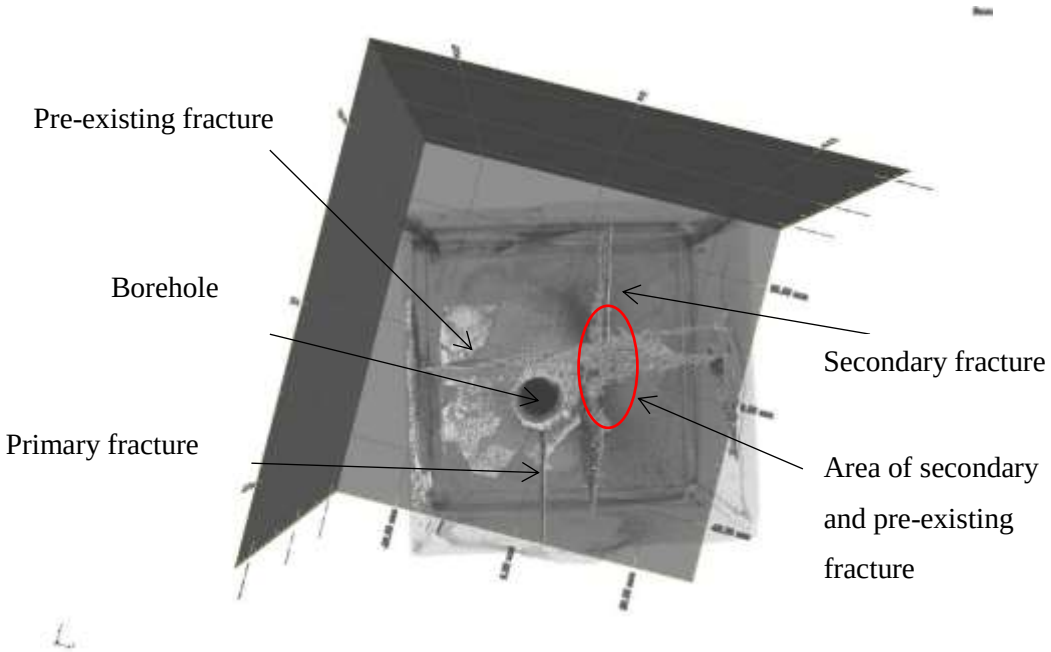

FIGURE 5-79: AMS3 overhead view.

The preliminary fracture intersects the pre-existing fracture at an angle of 77° and has a height of 52.83mm, the secondary fracture cuts across the pre-existing fracture at an angle of 105.91°, shown in Figure 5-79. The preliminary fracture deviates from the bottom of the borehole cutting down to the secondary fracture and joining it towards the bottom of the sample, (Figure 5-80 and Figure 5-80 to Figure 5-83). The deviation has a main angle of 155° but also consists of a number of small angle adjustments.

A possible explanation for the deviation from the preliminary fracture to the secondary fracture might be the small distance between the preliminary fracture and the pre-existing fracture. This distance is just too small to dissipate the pressure held in the fracturing fluid, though the pressure is too low to cut across the pre-existing fracture, so the new fracture is forced to deviate through a weaker area of the specimen in order to find a weaker plane where there is enough pressure in the fluid to cut through the pre-existing fracture.

The area around the base of the borehole has suffered from damage due to the drilling and therefore offers a weaker plane for the fracture to deviate through. It is notable that this deviation only occurs within the small gap (5.87mm) between the borehole and the pre-existing fracture. This deviation does not occur along the fracture from the borehole to the edge of the sample. This is because the fracture was not interrupted as it travelled to the extremities then as soon as it reached the edge the pressure behind the fracturing fluid was dissipated as the fluid flowed out. Whereas the pre-existing fracture would dissipate the fluid pressure, but due to the thin gap the pressure could not be dissipated enough so the backlogging of fluid at the intersection creates a build-up of pressure that the weaker plane cannot contain.

OBSERVATIONS DURING THE DRILLING.

Drilling the initial borehole was a lot harder under tri-axial pressures than when samples were under biaxial stress. To drill a 10mm depth under a tri-axial arrangement took roughly 45mins whilst under biaxial stress the same depth would take approximately 5 minutes.

It was also noted that although the same drill bit had been used to drill the samples that were under biaxial stress the injection nozzle used to inject the fracturing fluid did not fit into the boreholes drilled under tri-axial pressure. This meant that the hole had to be re-drilled to enable the nozzle to fit inside.

It was also observed that when fracturing sample AMS3 the fluid did not start flowing from the pre-existing fracture for least 30 seconds after fluid was flowing out of the preliminary and secondary fractures. The measurements of the fractures are presented in Table 5-8 & terms are explained previously in Figure 5-51 & Figure 5-52.

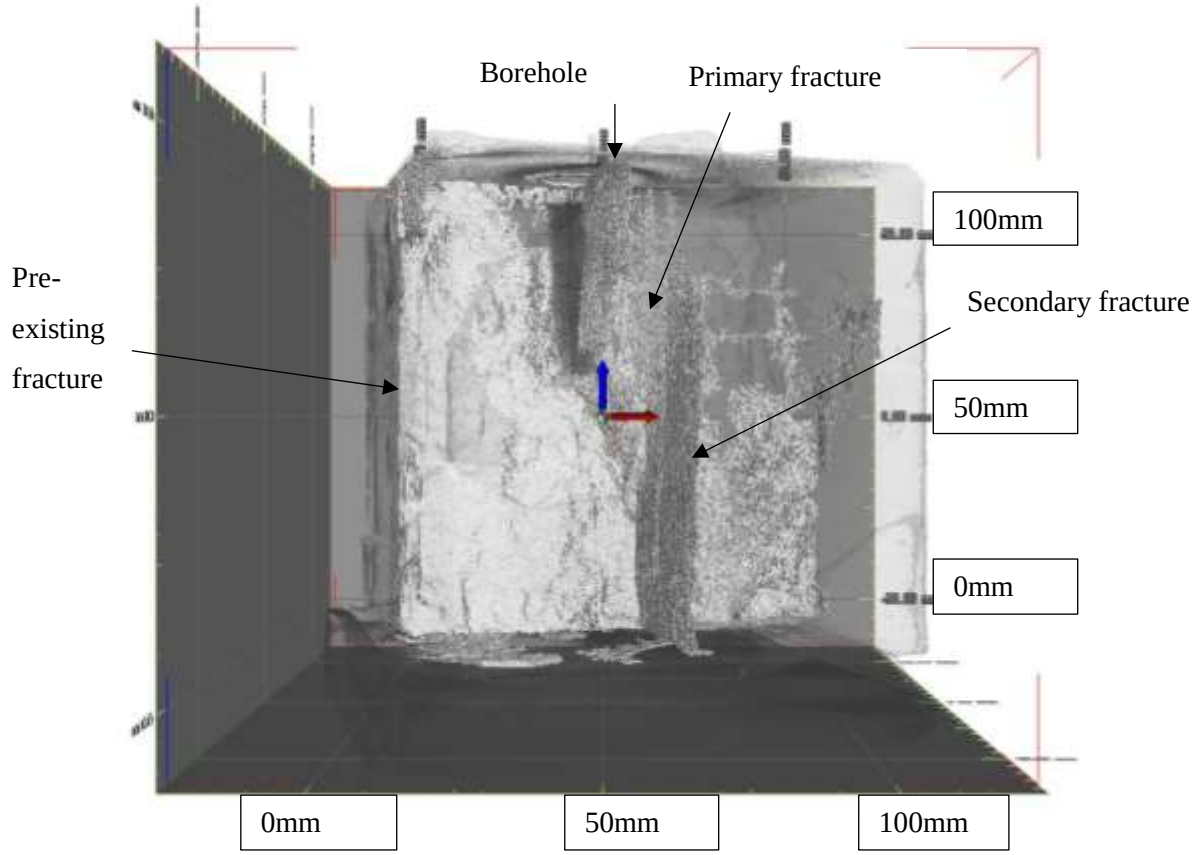

FIGURE 5-80: AMS3 Side view 1.

Sample name: AMS3											
Position to Borehole	Distance from borehole (MM)	Fracture length (mm)	Distance from Max width to the 10% max width at the top (mm)	Distance from maximum width to the 10% max width at the bottom (mm)	Maximum width (mm)	Top narrowing width (mm)	Bottom narrowing width (mm)	30% max width top	30% max width bottom	Distance from max width to 30% max top	Distance from max width to 30% max bottom
Half-length 1											
At the borehole	1.58	34.60		17.46	0.36		0.04		0.11		13.06
Near Borehole	12.36	34.08		12.08	0.34		0.03		0.102		7.54
Halfway from borehole	12.36	34.08		13.62	0.26		0.03		0.08		13.58
Three quarters way from borehole	30.89	22.11	3.96	16.74	0.30	0.03	0.03		0.09		14.05
Half-length 2											
At the borehole	0	105.95	33.21	18.37	0.32	0.03	0.03	0.10	0.10	32.35	17.56
End of the fracture	2.32	101.21			0.23						
Secondary side 1											
At the borehole	4.10	81.30			0.18						
Near Borehole	14.50	73.58			0.27						
Halfway from borehole	26.31	71.43			0.16						
Three quarters way from borehole											
Secondary fracture Side 2											
Halfway from BH	15.81	54.92			0.29						
End of fracture	32.58	24.64			0.44						

TABLE 5-8: AMS3 fracture dimensions along the fracture half-length.

The relative positions of the fracture are shown in Figure 5-52.

The sample data as shown in Table 5-8 deviates from the previous sample fractures, whilst still observing some similarities. The preliminary fracture, the one that extends from the borehole, narrows at the bottom and continues as a thin fracture; however, the widest part of the fracture is near to the top of the fracture. The dorsal side of the fracture does not show any narrowing, however as seen on both fracture half-lengths side 1 and 2 of the preliminary fracture the fracture height does decrease further away from the borehole.

The Fracture half-length 1 decreases gradually from 34.60mm to 22.11mm. While fracture half-length 2 decreases from 105.95mm through to 101.21mm. The excess pressure caused by the preliminary fracture striking the pre-existing fracture causes the fracture on half-length 2 to deviate and form a secondary fracture. This secondary fracture, on both sides, does not narrow as the preliminary fracture does, or like previous samples. This secondary fracture is reasonably thin compared to the preliminary fracture, the widest point level with the borehole is 0.18mm whilst the same corresponding points at the preliminary fractures are 0.36mm and 0.32mm for half-lengths 1 and 2 respectively.

Where the preliminary fracture breaks away to form the secondary fracture there are a number of sharp angular turns and the further away from the borehole the fracture travelled the more numerous the deviations in its path (shown on Figure 5-82).

The change in the fractures characteristic is shown in, Figure 5-81 through to Figure 5-84, which clearly show the preliminary fracture migrating into the secondary fracture, which allows it to propagate through the pre-existing fracture. The scans also show that at the point the pre-existing fracture has been crossed the secondary fracture height reduces steadily, Figure 4-79, with the fracture rapidly closing up to the dorsal side of the sample.

The relative position of the fracture measurements, in relation to the positions distance from the borehole, are shown in Figure 5-51 while the measurements taken in the planar view of the fracture, that make up the labelling of these figures are presented in Figure 5-52.

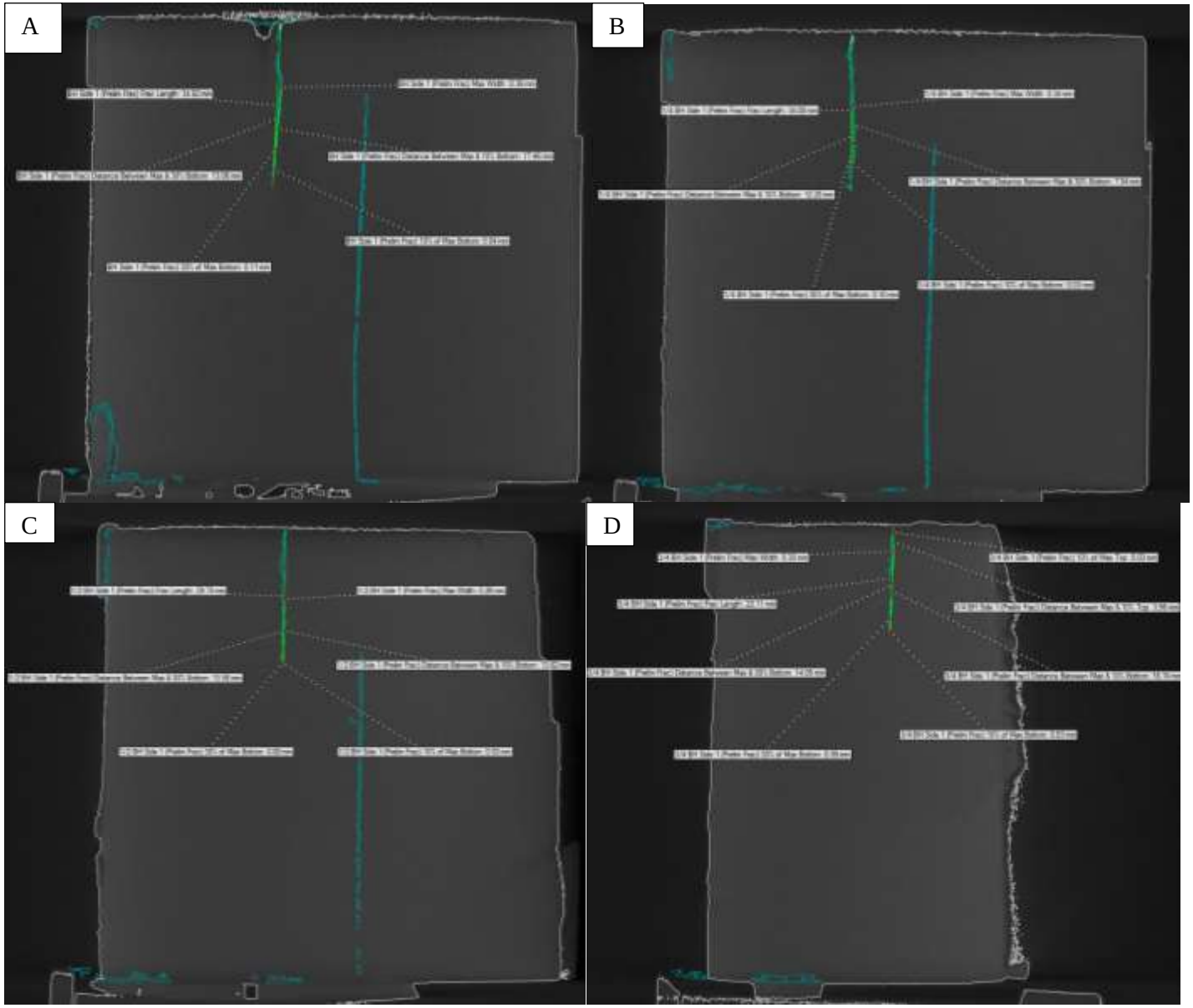

FIGURE 5-81: AMS3 Fracture half-length 1, preliminary fracture, A) At the borehole, B) Near the borehole, C) Halfway along the half-length, D) ¾ along the half-length.

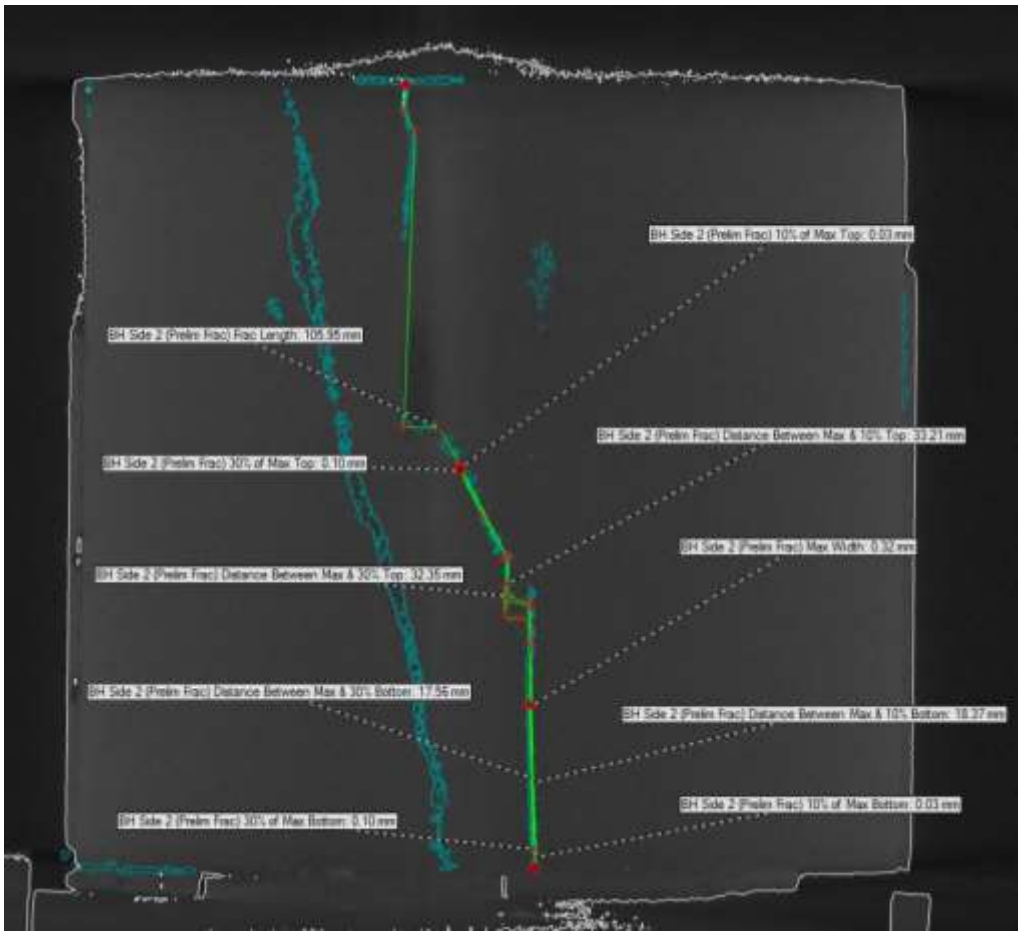

FIGURE 5-82: AMS3 Preliminary fracture side 2 at the borehole.

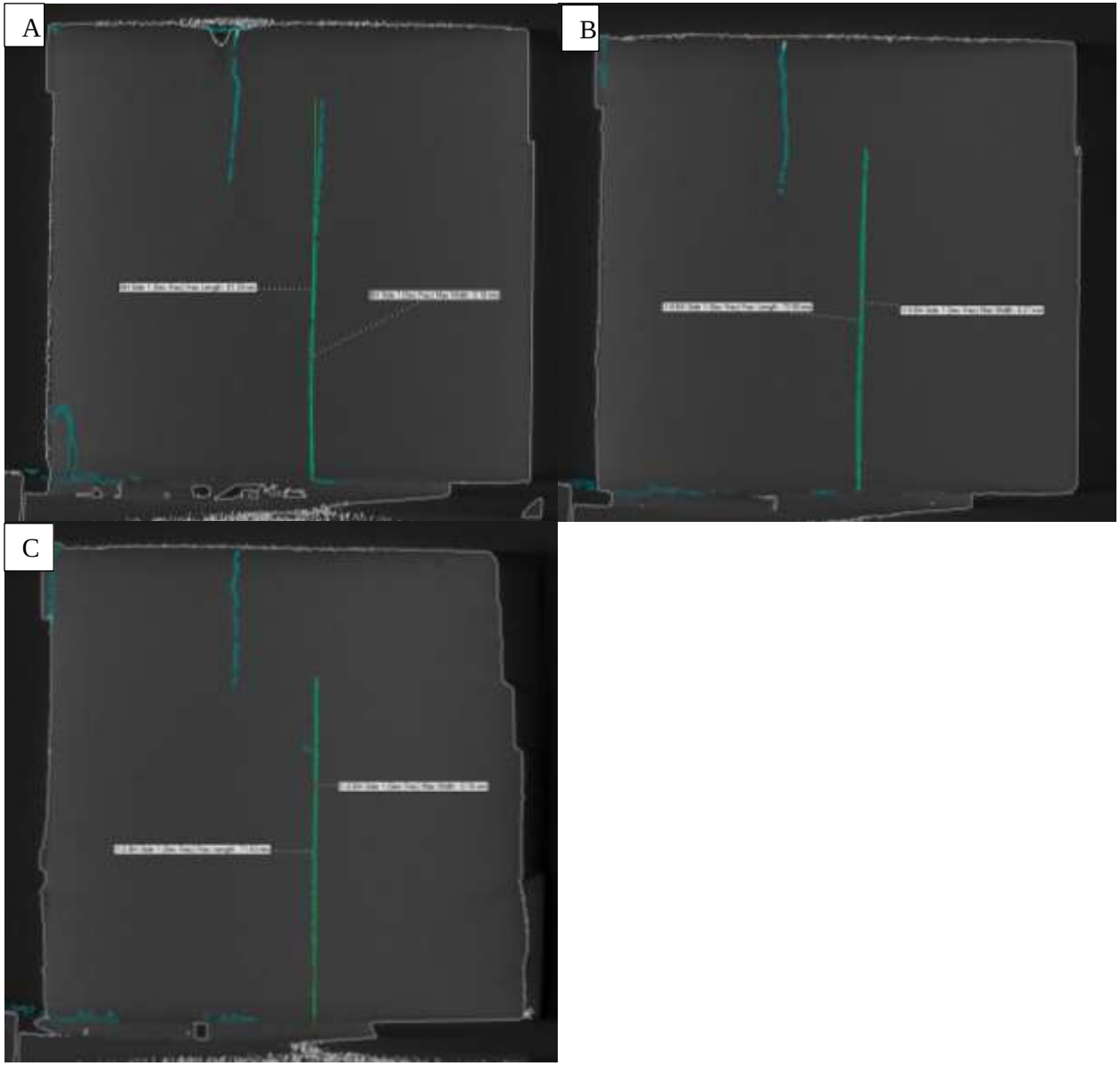

FIGURE 5-83: AMS3 secondary fractures side 1, A) At the borehole, B) Near the borehole, C) Halfway along the half-length.

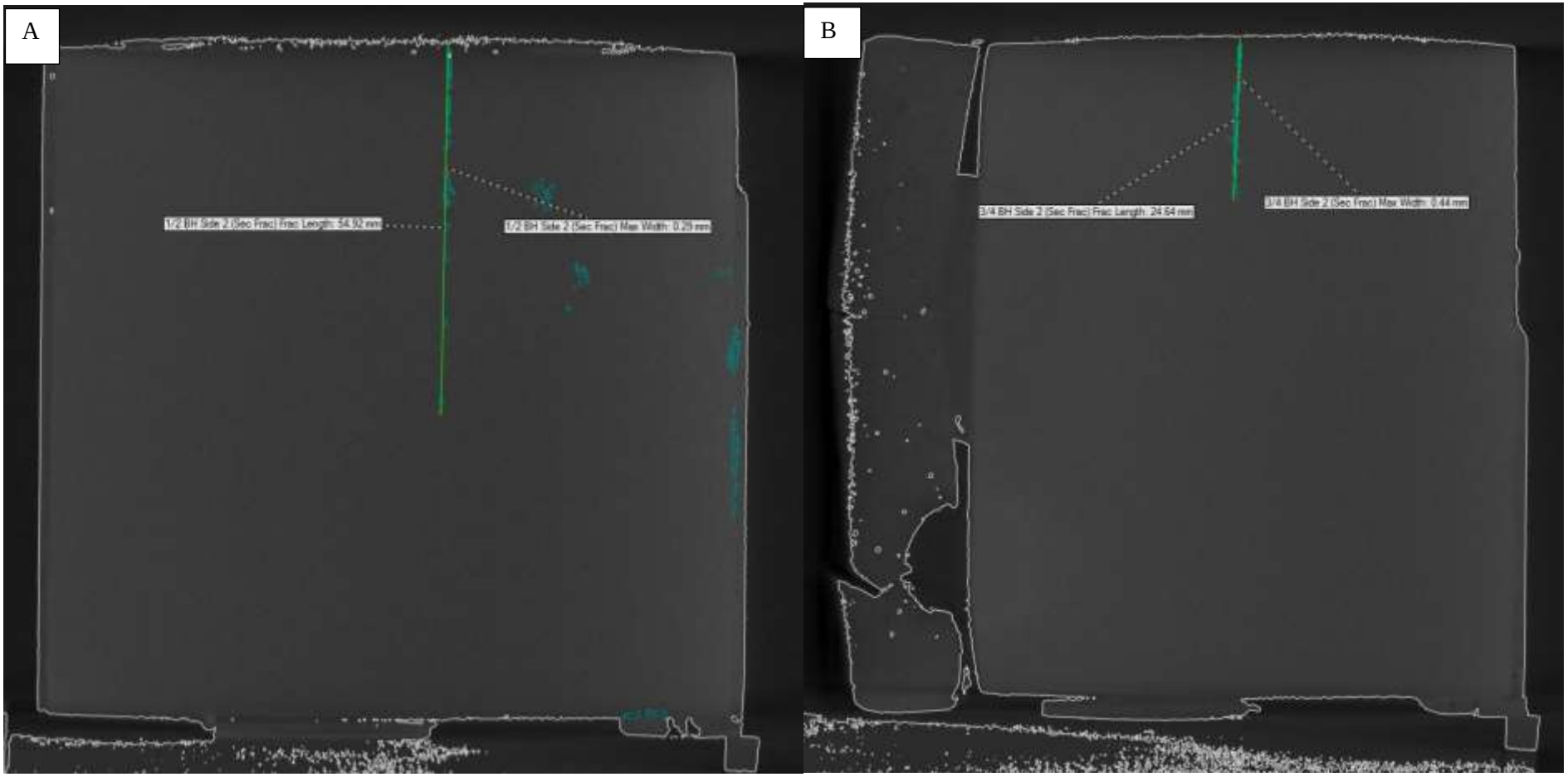

FIGURE 5-84: AMS3 Secondary fractures side 2 A) Halfway along the half-length, B) ¾ along the half-length.

5.5.2.2 AMS4

This sample was fractured under tri-axial conditions, the detected fractures are presented below in Figure 5-85 to Figure 5-87.

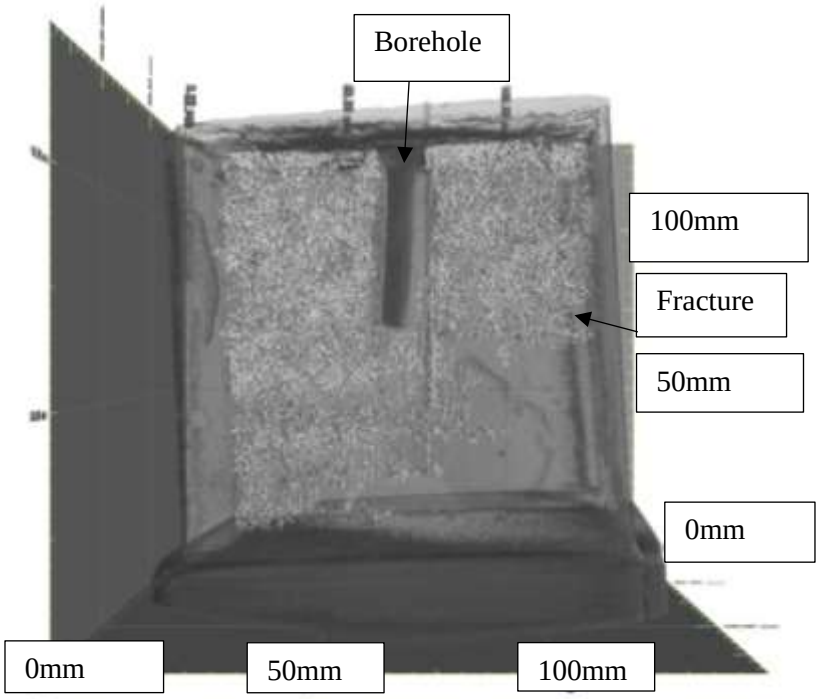

FIGURE 5-85: AMS4 side 1 View.

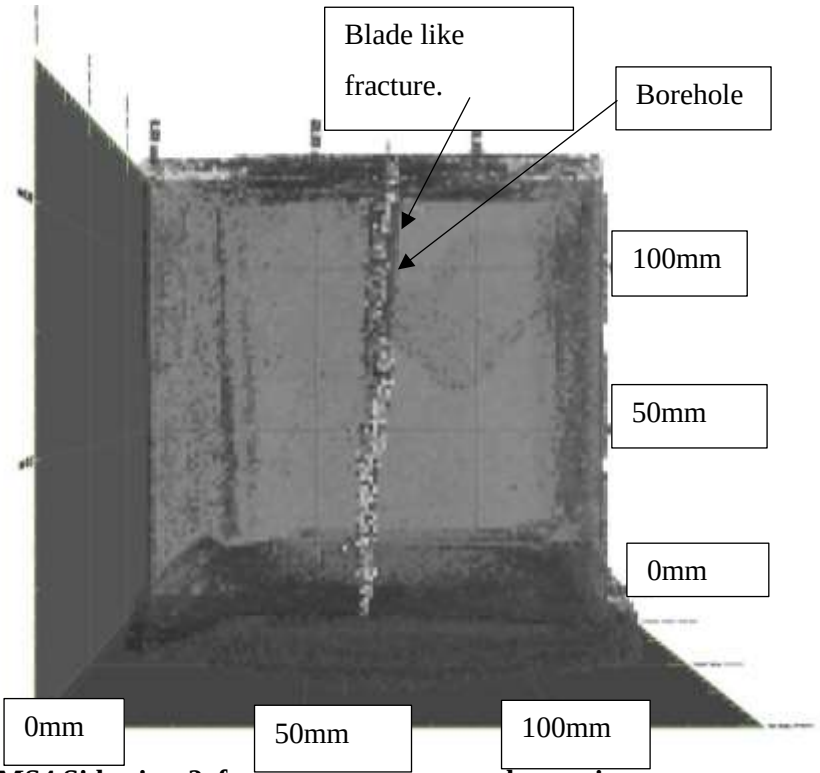

FIGURE 5-86: AMS4 Side view 2, fracture appears as a planar view.

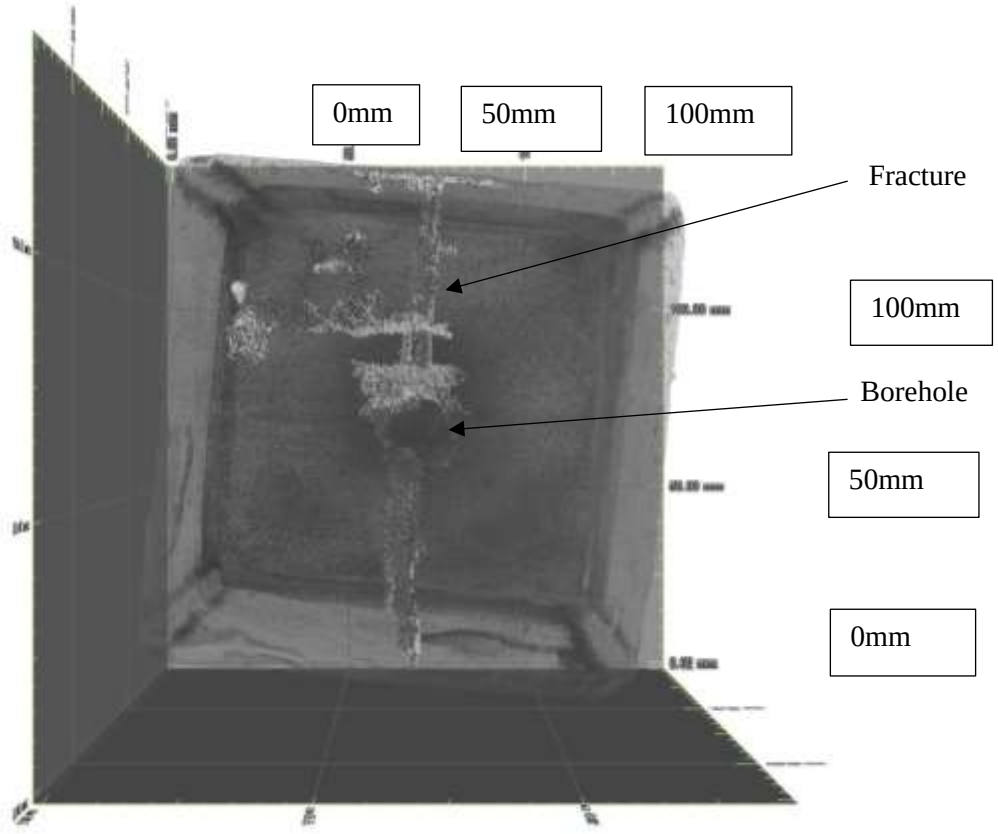

FIGURE 5-87: Sample AMS4 reconstruction of fracture C overhead view.

The AMS4 sample had one fracture that emanated from the borehole and finished at the edge of the sample. Rather like sample AMS1 fracture half-length 1 increases in height further away from the borehole but half-length 2 decreases in height towards the sample edge. However, in this sample it is interesting to note (Figure 5-87) that as fracture half-length 1 extends below the borehole it joins with fracture half-length 2, which rapidly losses height just after a ¼ distance along the fracture half-length before it then remains at a relatively steady height of roughly the same depth of the borehole. The dimensions for the fracture are presented in Table 5-9 below & terms are explained previously in Figure 5-51 & Figure 5-52.

Sample name: AMS4											
Position to Borehole	Distance from borehole (MM)	Fracture length (mm)	Distance from Max width to the 10% max width at the top (mm)	Distance from maximum width to the 10% max width at the bottom (mm)	Maximum width (mm)	Top narrowing width (mm)	Bottom narrowing width (mm)	30% max width top	30% max width bottom	Distance from max width to 30% max top	Distance from max width to 30% max bottom
Half-length 1											
At the borehole	0	94.28	17.26	52.87	0.45	0.05	0.5	0.14	0.14	16.64	50.80
Near Borehole	8.37	100.88	14.94	67.90	0.52	0.05	0.05	0.16	0.16	10.07	58.63
Halfway from borehole	16.66	100.82	52.77	38.50	0.33	0.03	0.03	0.10	0.10	52.62	33.03
Three quarters way from borehole	31.59	101.86	46.06	-	0.30	0.03	-	0.09	0.09	45.68	47.82
Half-length 2											
At the borehole	0	76.54	8.09	25.51	0.71	0.07	0.07	0.21	0.21	7.63	24.77
Near borehole	8.17	79.61	-	31.07	0.71	-	0.07	-	0.21	-	23.27
Halfway from the borehole 1	18.02	52.45	-	46.67	0.38	-	0.04	-	0.11	-	43.93
Three quarters way from the borehole	39.20	53.33	-	43.07	0.34	-	0.03		0.10	-	39.19

TABLE 5-9: AMS4 Fracture half-length dimensions.

The relative positions of the fracture are shown in Figure 5-52.

The AMS4 sample has behaved similarly to sample AMS1 in that the fracture half-length 1 increases in height to take up the entire sample length, while half-length 2 decreases in height, however, there is one important difference, in this sample the fracture continued to propagate below the borehole joining half-length 1 and 2 together. This is something that has not been seen in the other Accrington Mudstone samples.

Half-length 1; the fracture height at the borehole is 94.28mm, almost reaching the bottom of the sample. By a ¼ of the way along the half-length the height has reached 100.88mm, the bottom of the sample, going on to record 100.82mm at ½ distance (a slight decrease caused only by chipping of the sample edges during the fracturing process) and by ¾ of the distance the fracture had grown to 101.86mm. However, this fracture half-length starts underneath the borehole with a height of 40mm, only when it passes the borehole does it rapidly increase in height to 94.28mm. This continuation of the fracture below the borehole is probably due to a weakness in the bedding further exacerbated by damage during the drilling.

Removal from the rig after compression causes some distortion in the samples so that the initial dimensions of $100mm^3$ have increased/decreased along certain faces of the cube. Furthermore, the lack of a lid on the mould when the plaster is added during sample preparation also caused some minor discrepancies (± 2mm) in the sample size.

The fracture width increases from the borehole (BH) with 0.45mm to 0.52mm at the quarter point then decreases in width at the ½ and ¾ points to give 0.33mm and 0.30mm respectively. This then compares quite favourably to the widths measured for fracture half-length 1 of sample AMS1 of 0.27mm, 0.44mm, 0.25mm and 0.23mm at the BH, ¼ the way, ½ way and ¾ the way along the fracture half-length respectively.

Fracture half-length 1 followed the pattern of the other propagated fractures in that the cross section is ellipsoid in shape with a wide middle and thin, relatively straight, tips extending above and below the wide middle section. This is illustrated by the proportion of the fracture that is made up of the wide section compared to the overall fracture length as follows.

At the BH the fracture greater than 10% of the maximum height measured 70.13mm compared to an overall fracture height of 94.28mm giving the proportion as 74.3%. The section that made up the wide section of the fracture, greater than 30% of the maximum width, was 67.44mm giving a proportion, of the entire fracture, of 71.5%. At ¼ along the fracture half-length the measurements were 82.84mm out of 100.82mm giving a proportion of 82.1% for 10% of the maximum thickness while the measurement of the wide section was 68.7mm giving a proportion of the fracture greater than 30% of 68.1%. By ½ way along the fracture length the height greater than 10% of the fracture is 91.27mm giving a proportion of 90.5%, whilst the fracture above 30% measures 85.65mm giving a proportion of 85.0%. At the ¾

mark the fracture does not narrow to below 10% of the maximum width at the bottom but the wide section of the fracture measures 93.5mm out of 101.86 giving a proportion of 91.8%.

It is of interest to note that in both AMS1 and AMS4 fracture half 1, the half-length where the height of the fracture increased, there was a large increase in the maximum width ¼ way along the fracture half-length before slowly decreasing, and there is also a big jump in the proportion of the fracture that makes up the wide middle section from the halfway point. As in AMS1 fracture half-length 1 shows a slight, but clear, negative correlation. Shown in Figure 5-88, as the fracture height increases there is a corresponding decrease in the fracture width. This trend line gives the equation of y=51.667x +117.59. Again like AMS1 there is one anomalous result but the similarity with AMS1 shows the reproducibility of the experiment and gives credence to the results.

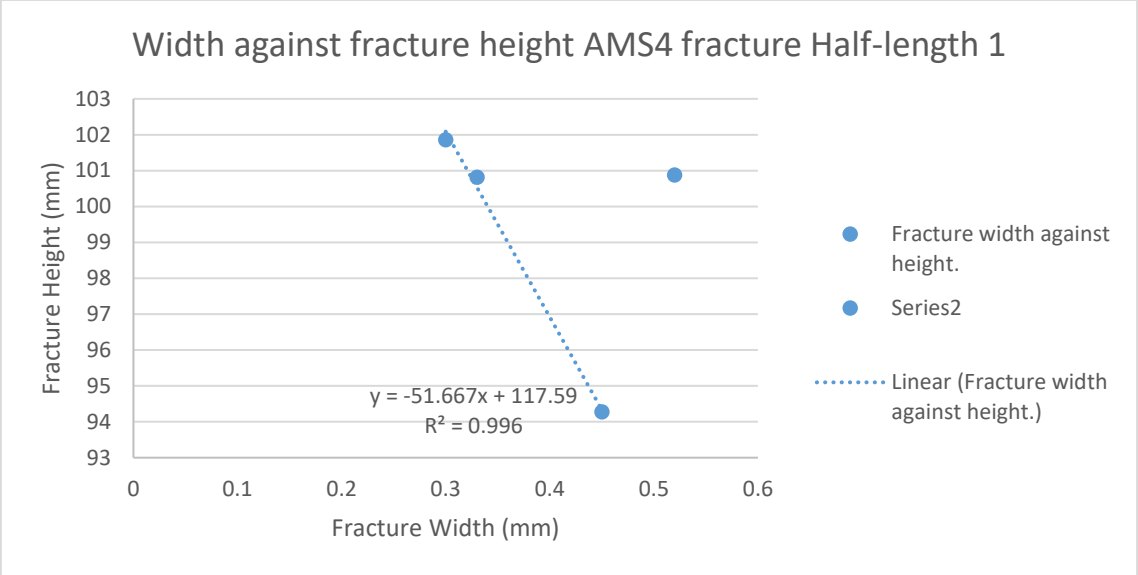

FIGURE 5-88: Graph showing the width against fracture height fracture half-length 1

Fracture half-length 2 shows a similar pattern to AMS1 half-length 2. Slight increases in the height of the fracture from the BH to ¼ distance along the fracture half-length from 76.54mm to 79.61mm. Followed by a rapid decrease in the height by ½ way along the fracture half-length to 52.45mm followed by a slight increase at the ¾ point to 53mm, which could also be construed as the height remaining constant. There was a slight difference between this sample and AMS1 in that the fracture widths started out much wider than normal at 0.71mm and stayed at 0.71mm by ¼ distance along the fracture half-length before dropping by the ½ mark to 0.38mm and slowly levelling at the ¾ mark to 0.34mm. Unlike the other plots there are no anomalous results shown in this graph; Figure 5-89 shows a clear well-fitting positive correlation. As the height of the fracture decreases the fracture width also decreases along the fracture half-length from the borehole.

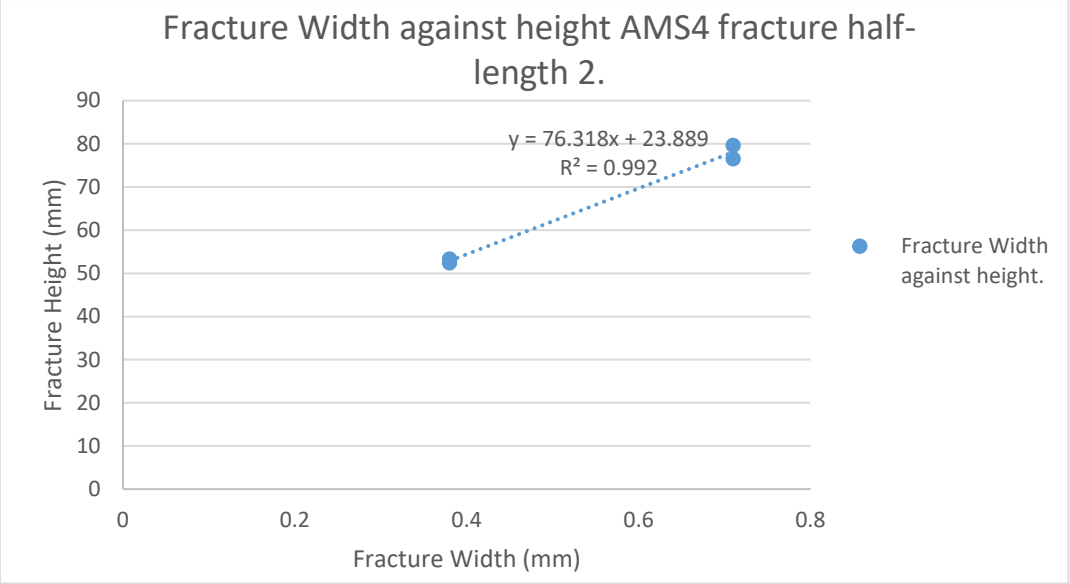

FIGURE 5-89: Graph shows showing the width against fracture height fracture half-length 1

This loss in height combined with the greater than normal maximum width suggests that there is a correlation between the fracture width and height implying that the greater the width of the fracture the greater the loss in fracture height. Dissipation of the head of pressure in the fracturing fluid is the driving force of the fracture, the coherence of the bedding in the rock will determine whether the fracture will open disproportionally wide and thus decreasing in height or a fracture that is more proportional which grows in height away from the borehole.

As with sample AMS1 the similarities suggest that this could be a reasonably common occurrence in fracture patterns. The repeatability of the pattern gives credence to the experimental procedure and the rig design. The planar view of each section of the fracture half-length that was measured is shown in Figure 5-90 & Figure 5-91.

The relative position of the fracture measurements, in relation to the positions distance from the borehole, are shown in Figure 5-51 while the measurements taken in the planar view of the fracture, that make up the labelling of these figures are presented in Figure 5-52.

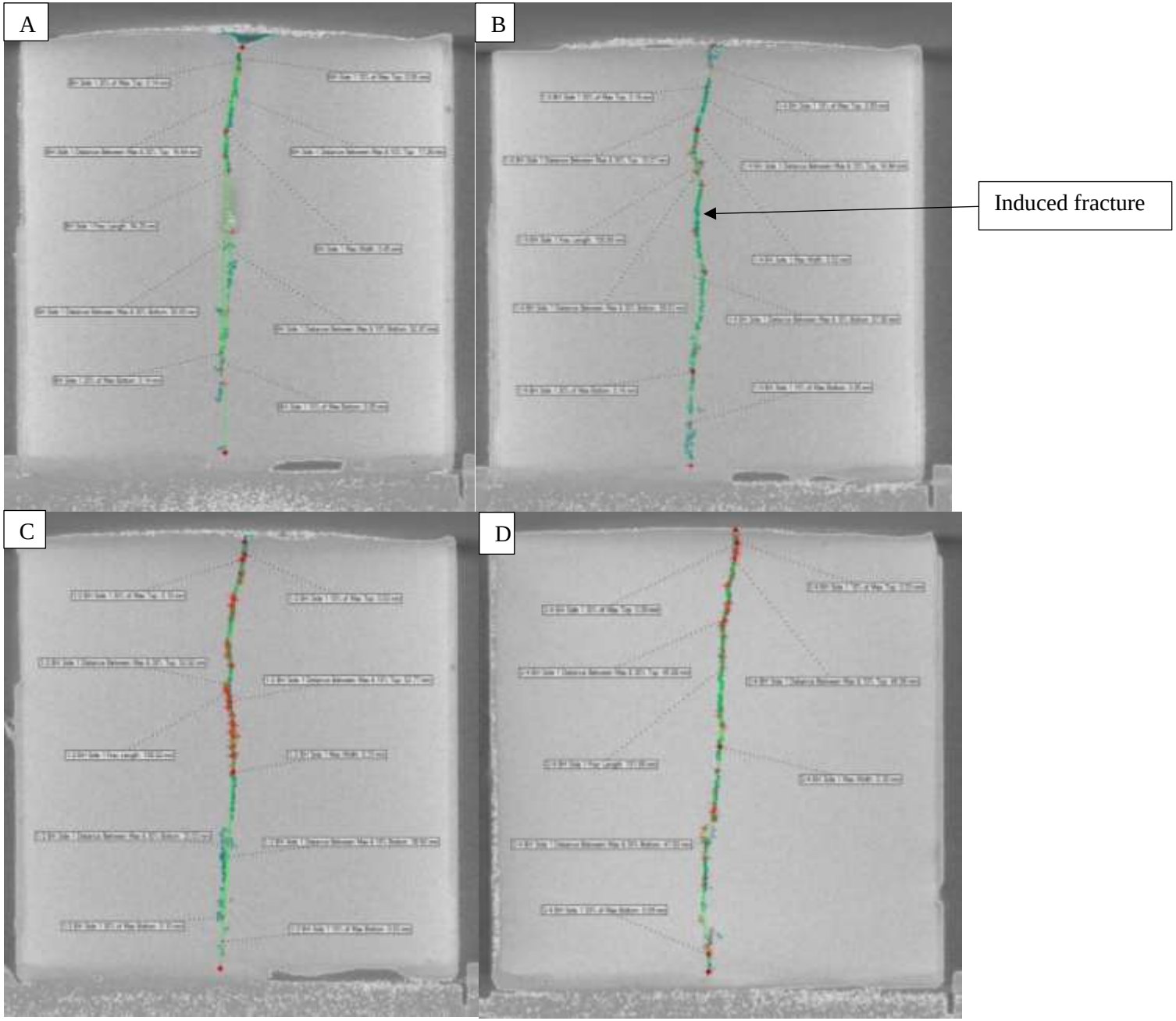

FIGURE 5-90: AMS4 fracture half-length side 1, A) At the borehole, B) Near the borehole, C) Halfway along the half-length, D) ¾ along the half-length.

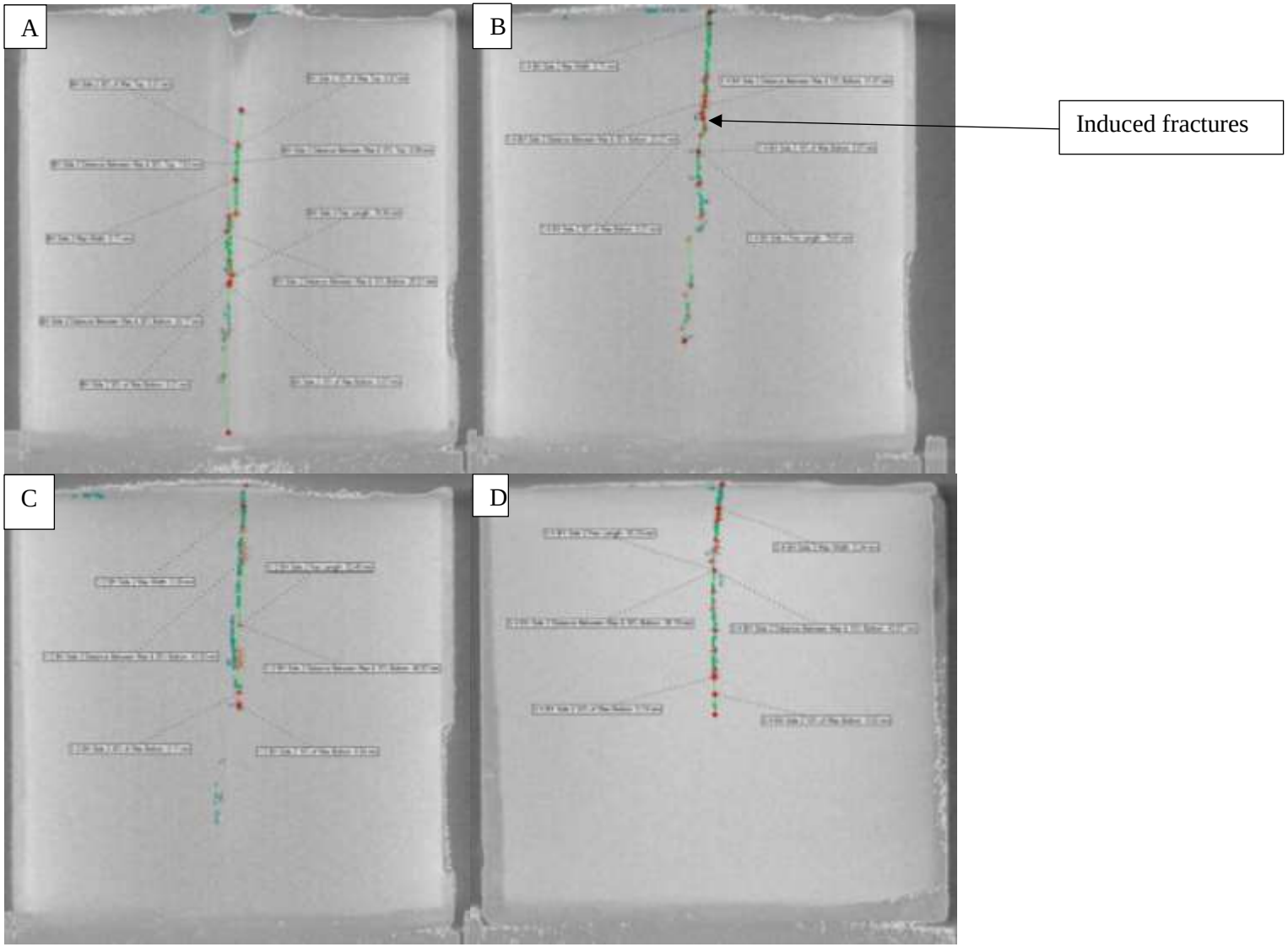

FIGURE 5-91: AMS4 fracture half-length side 2, A) At the borehole, B) Near the borehole, C) Halfway along the half-length, D) ¾ along the half-length.

5.5.2.3 WBS3

Westbury Shale samples fractured under a tri-axial load behaved very differently from the Accrington Mudstone samples and the Westbury Shale that was fractured under the bi-axial arrangement. When fractured, WBS3 sample fractured heavily along its bedding planes combining numerous thin fractures to form complex fractures induced from the borehole. The following CT reconstructions, Figure 5-92 through to Figure 5-94, show the sample after fracture.

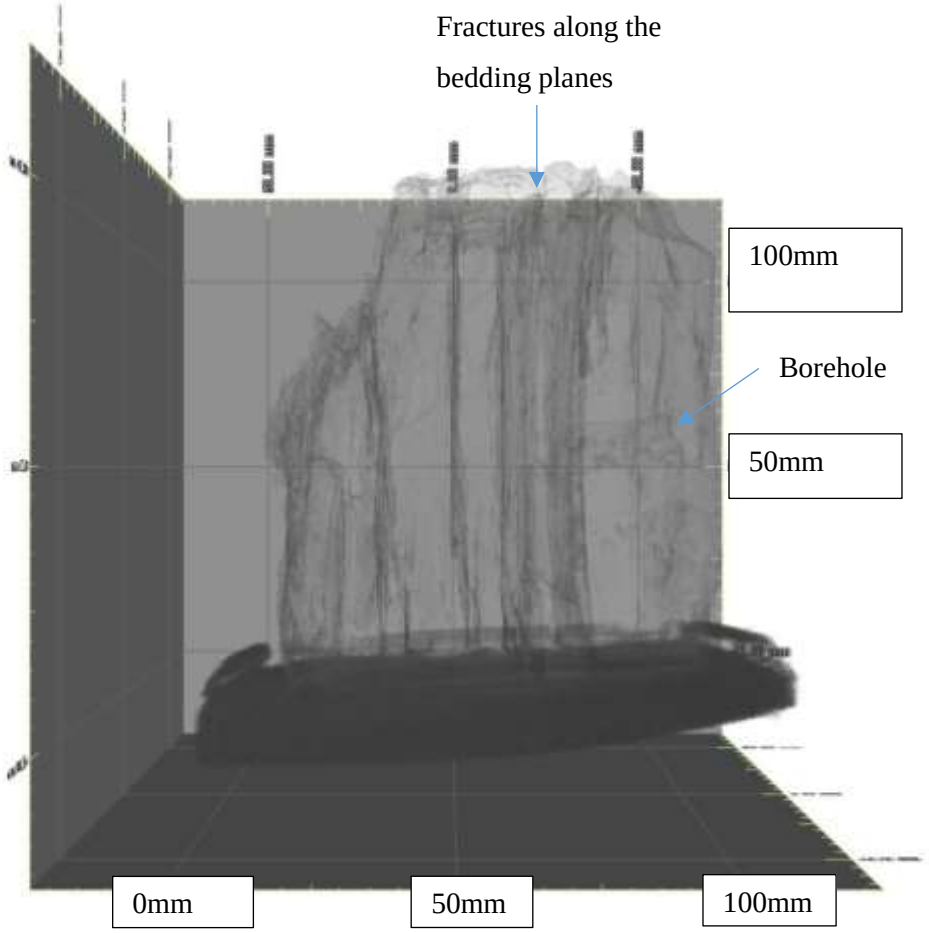

FIGURE 5-92: WBS3 CT reconstruction side 1.

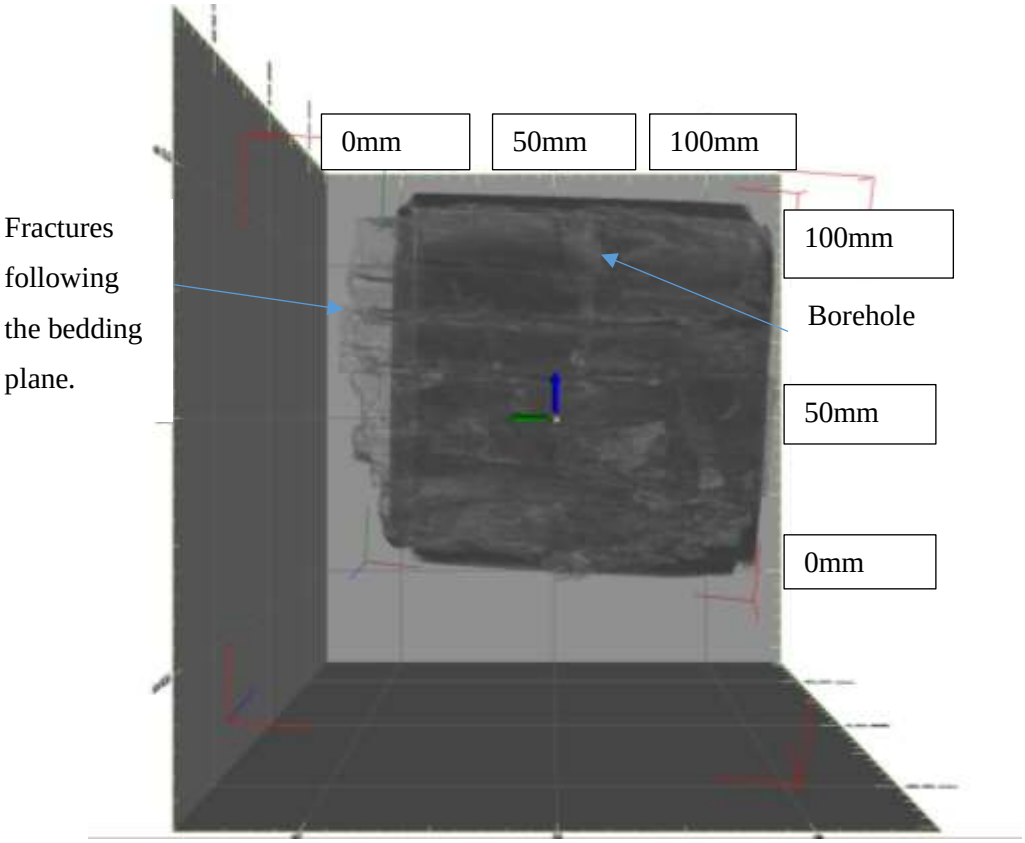

FIGURE 5-93: WBS3 CT reconstruction side view 2.

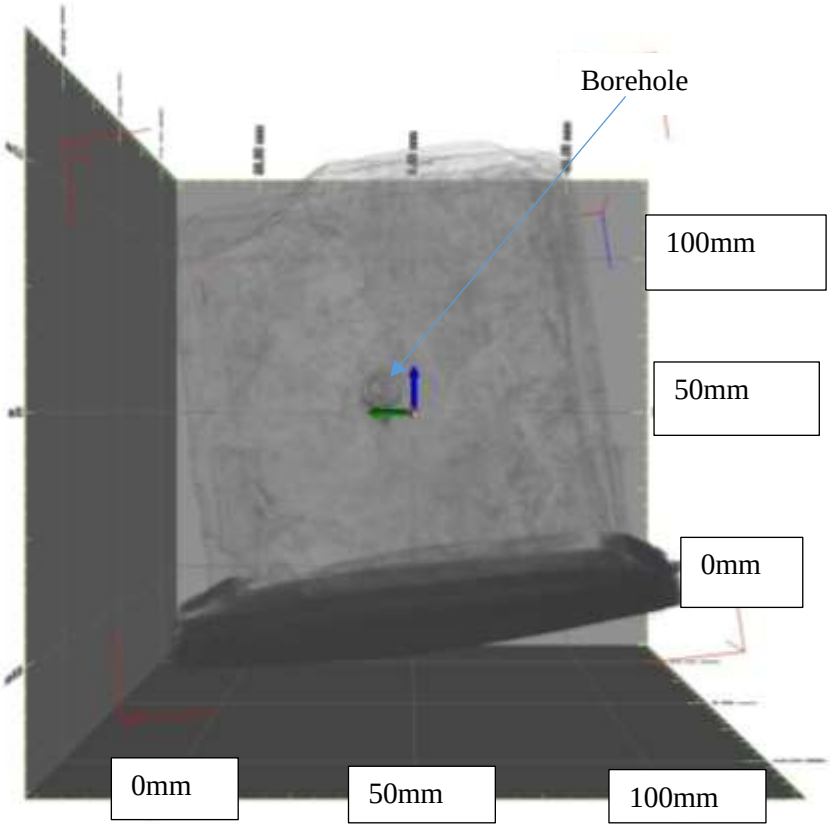

FIGURE 5-94: WBS3 CT reconstruction overhead view.

As shown in the reconstruction Figure 5-92 to Figure 5-94 there are a number of fractures running along the bedding planes throughout the total height of the sample. These fractures are connected to a series of complex fractures emanating from the borehole. Compared to what was seen in the Accrington Mudstone, these fractures emanating from the borehole are less uniform, being more undulating rather than a straight vertical fracture. They also have numerous small branches radiating from the two main fractures. In order to compare like with like when measuring the fracture half-length dimensions, the measurements have been taken from the main fracture emanating from the borehole. The fracture dimensions are presented in Table 5-10 & terms are explained previously in Figure 5-51 & Figure 5-52.

Sample name: WBS3											
Position to Borehole	Distance from borehole (MM)	Fracture length (mm)	Distance from Max width to the 10% max width at the top (mm)	Distance from maximum width to the 10% max width at the bottom (mm)	Maximum width (mm)	Top narrowing width (mm)	Bottom narrowing width (mm)	30% max width top	30% max width bottom	Distance from max width to 30% max top	Distance from max width to 30% max bottom
Half-length 1											
At the borehole	0	87.34	44.92	-	0.46	0.05	-	0.14	0.14	4.71	10.12
Near Borehole	8.98	87.80	29.57	-	0.31	0.03	-	0.09	0.09	28.78	8.57
Halfway from borehole	16.93	89.30	28.32	45.97	0.32	0.03	0.03	0.09	0.09	28.78	45.07
Three quarters way from borehole	24.61	75.92	35.66	37.22	0.35	0.04	0.04	0.12	0.12	32.86	36.15
Half-length 2											
At the borehole	0	74.45	49.46	-	1.13	0.11	-	0.33	0.33	43.69	4.93
Near borehole	8.59	86.32	-	-	1.05	-	-	-	0.32	78.17	-
Halfway from the borehole 1	15.65	108.44	92.16	-	1.26	0.13	-	-	0.38	56.13	-
Three quarters way from the borehole	28.01	106.62	105.69	-	1.06	0.11	-	-	0.32	99.78	-

TABLE 5-10: WBS3 dimensions of fracture half lengths.

The relative positions of the fracture are shown in Figure 5-52.

In the WBS3 sample there is a clear divergence between fracture half-length 1 and fracture half-length 2 although there are still some similarities between the two half-lengths such as the maximum width decreasing at the quarter distance mark before increasing again. In fracture half-length 1 the maximum width at the borehole was 0.46mm. By the quarter distance the width had decreased to 0.31mm, a decrease of 32.6%. In fracture half-length 2 the maximum width at the borehole was 1.13mm and decreased to 1.05mm by the quarter distance mark, a decrease of 7.1%.

In fracture half-length 1 the measurements increased from 87.34mm at the borehole to 87.80mm at the quarter mark (a 0.6% increase), increasing further to 89.30mm at the halfway mark (1.7% increase) before decreasing to 75.92mm at the ¾ mark (a 14.9% decrease). In the same order fracture half-length 2 increased from 74.45mm, 86.32mm to 108.44mm before decreasing at the three quarters mark to 106.62mm (an increase of 13.7% and 20.4% then a decrease of 1.75%).

The most noticeable divergence between the two half-lengths was the incredibly large difference in the width of the fracture. At fracture half-length 1, at the borehole, the maximum width was 0.46mm while in half-length 2 the maximum width was 1.13mm. It is also notable that in fracture half-length 2 the maximum width is recorded at the bottom edge of the fracture where the fracture opens up and doesn't narrow towards a tip. On fracture half-length 2 there was a thinning of the fracture to 10% at the top of the fracture for three of the four points measured along the distance of the half-length but not at the ¼ mark.

Figure 5-95 & Figure 5-96 show the fractures at the different distance points. This example shows a different pattern to that seen in the previously tested Westbury samples. The fracture forms a long meandering line, the main attack angle of the fracture is vertical ranging from 65^{o} to 80^{o} from a straight line from the borehole, which may be the product of the weaker nature of these shales. As the fracture propagates towards the top and bottom of the sample, for large periods of the propagation the fracture travels along the bedding plane. The fracture does cut across the bedding plane but due to the weak nature of shales, this cross cutting of bedding planes occurs over a wider area. Compared with the fractures carried out in rock samples with a higher clay content, where the fracture extends in a vertical manner, here the overall trend of the Westbury shale fracture is closer to a diagonal, following a line of least resistance.

The relative position of the fracture measurements, in relation to the positions distance from the borehole, are shown in Figure 5-51 while the measurements taken in the planar view of the fracture, that make up the labelling of these figures are presented in Figure 5-52.

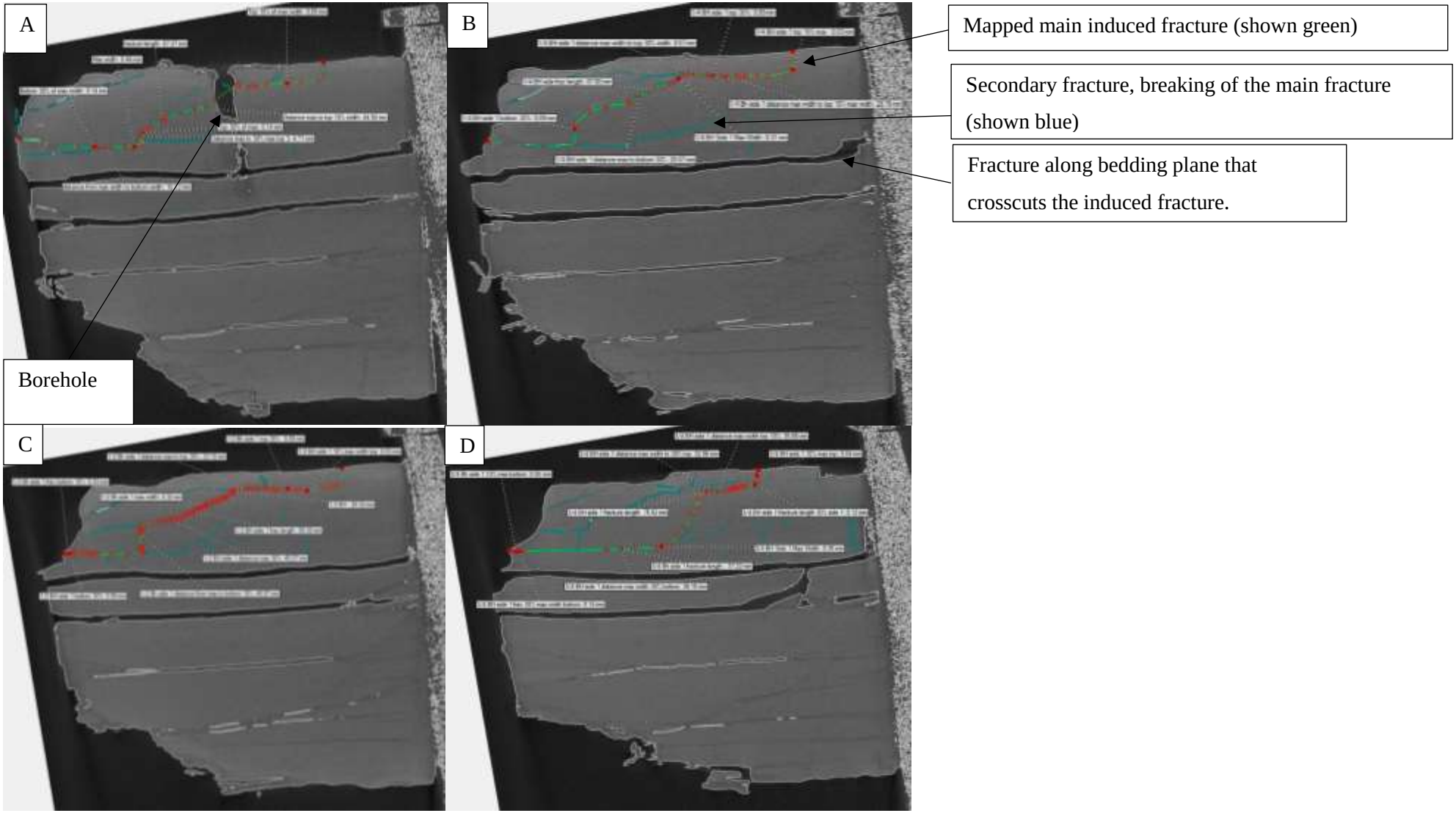

FIGURE 5-95: WBS3 Fracture half-length side 1 A) At the borehole, B) Near the borehole, C) Halfway along the half-length, D) ¾ along the half-length.

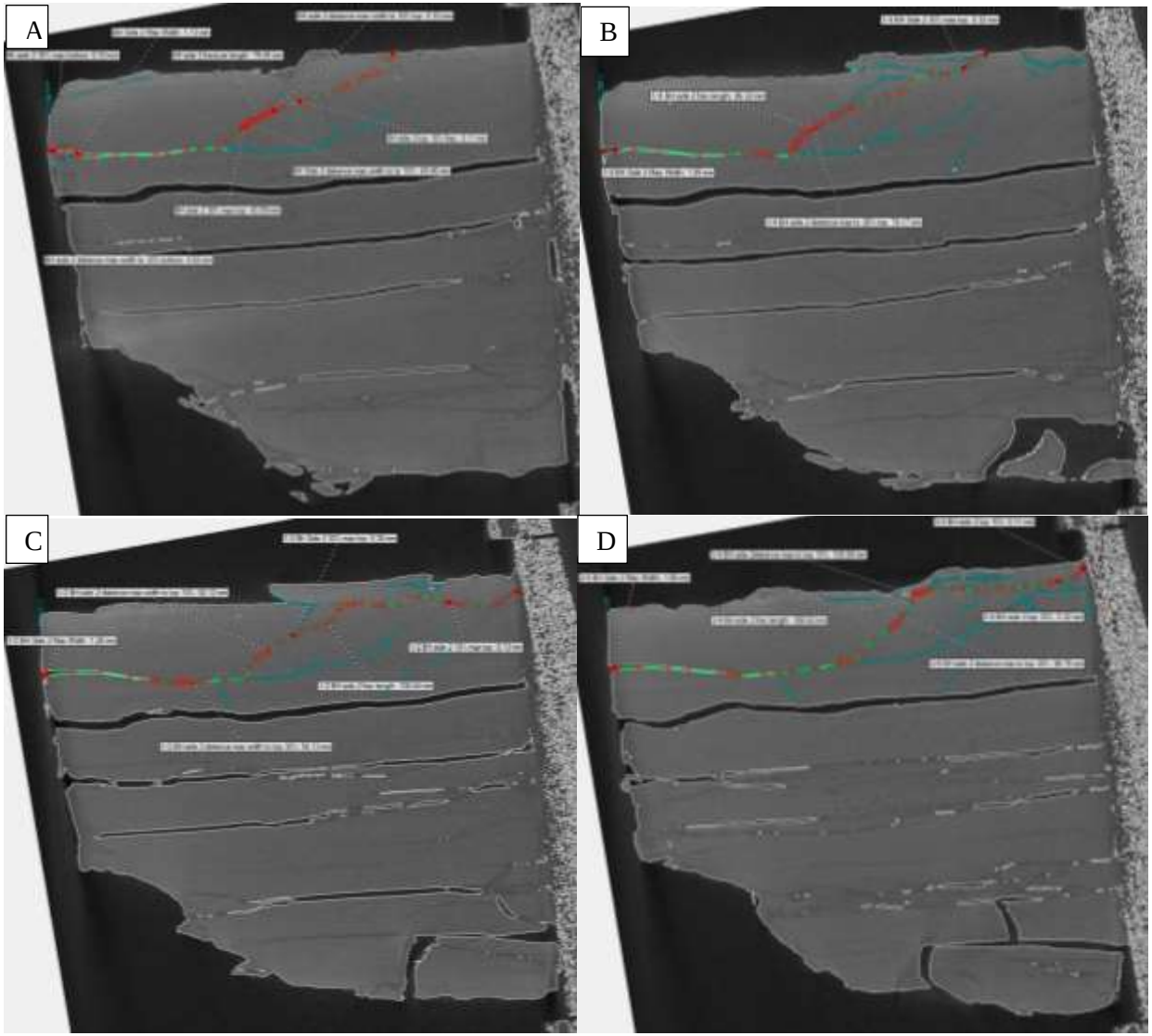

FIGURE 5-96: WBS3 Fracture half-length side 2, A) At the borehole, B) Near the borehole, C) Halfway along the helf-length, D/ ¾ along the half-length.

5.5.2.4 WBS4

For the WBS4 sample, a fracture was initiated in this sample but, unfortunately, the CT scanner broke during the scan which resulted in the sample drying out before it could be successfully re-scanned. As it was moved a number of more friable sections broke away which meant that any measurements taken of the fractures would now be incomparable. For that reason, the scan was only carried out to assess the shape of the fractures and the degree of fracture penetration, but no measurements were taken. The scan reconstructions are shown in Figure 5-97 to Figure 5-99. The sample was still included in this study as it was felt that meaningful observations could still be gained from studying the after effects of the compression.

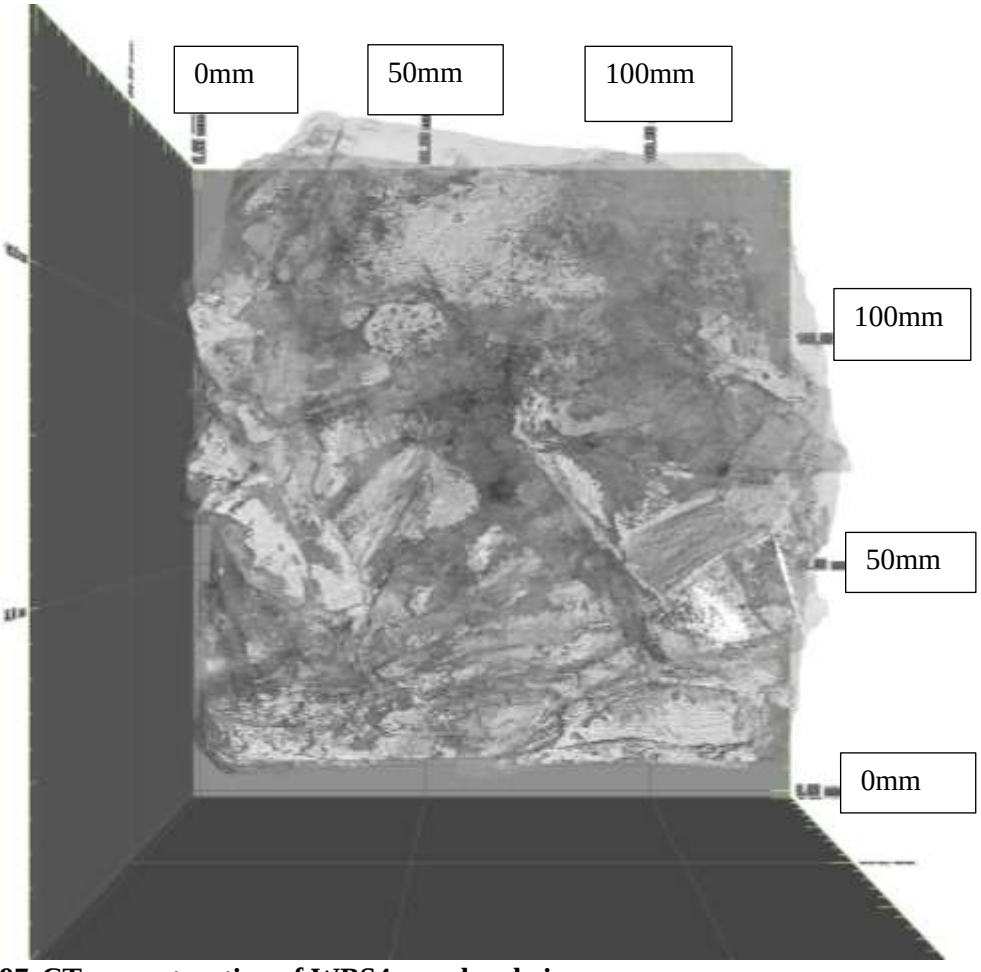

FIGURE 5-97: CT reconstruction of WBS4, overhead view.

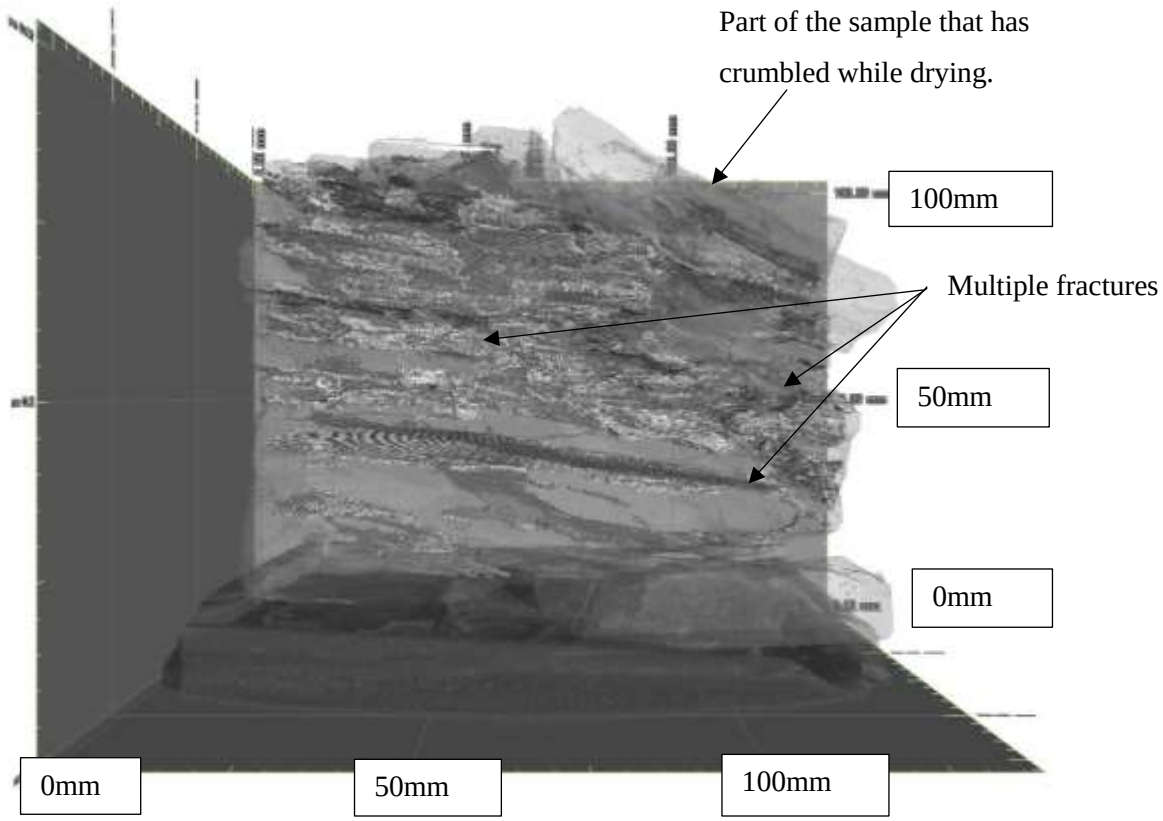

FIGURE 5-98: WBS4 CT reconstruction side view 1.

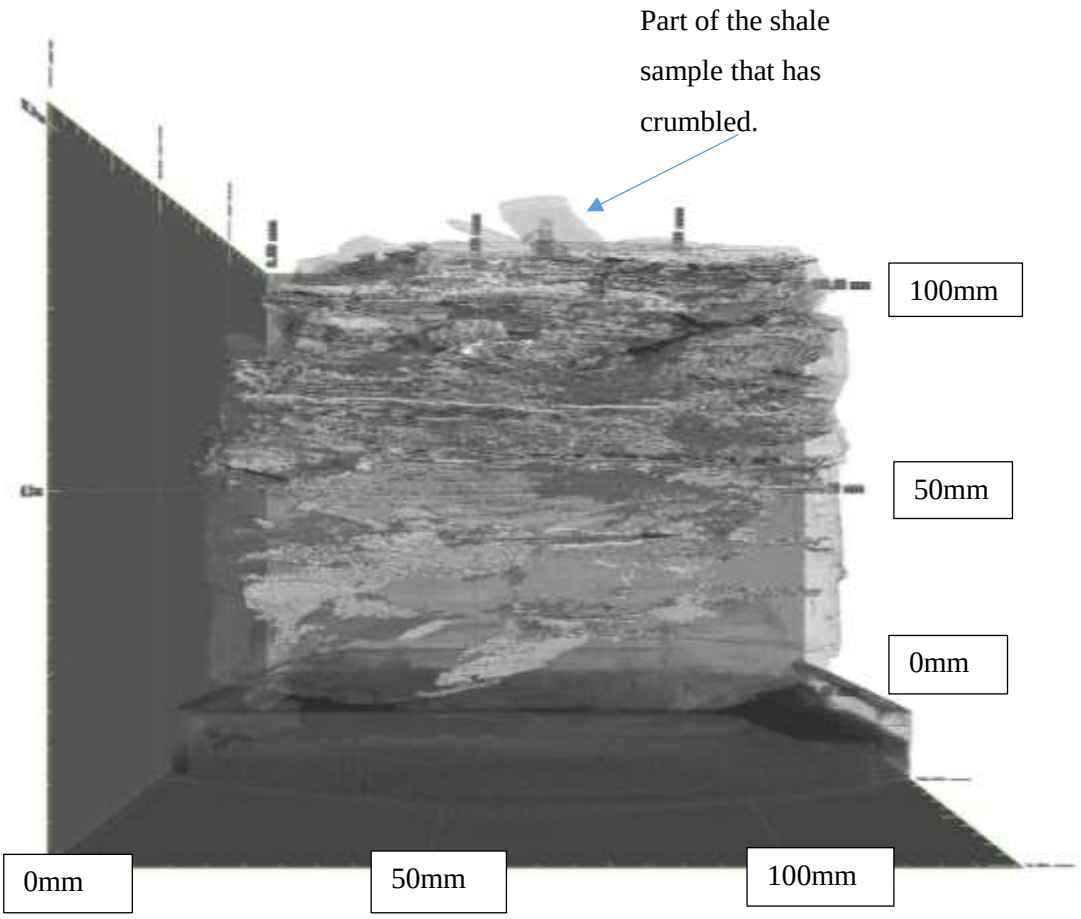

FIGURE 5-99: WBS4 CT reconstruction side view 2.

The scans (Figure 5-98 and Figure 5-99) show that there are numerous fractures in the top part of the shale sample, in fact, the shale follows the same configuration as that seen in WBS3 in that the initiated fracture follows a convoluted path, travelling in a diagonal line from the top corner to the bottom corner on the opposite side. This main induced fracture cuts across the many fractures that have opened up along the bedding planes.

Although a large section of the fractured sample has moved during the breakdown of the CT scanner, it is still noticeable that the heavily fractured area closely follows the area where the induced fracture propagated from. As with the other Westbury Shale samples that were fractured in a tri-axial arrangement, the volume of fractures along the bedding plane reduces in the lower half. This suggests that the bedding plane fractures are the natural consequence of inducing a fracture in such a weak shale.

While the induced fracture carries enough of a pressure head to cut across the bedding planes, the weak state of the shale, particularly in the direction of the bedding, means that fractures open up in the direction of the bedding. However, there is obviously still enough force left in the pressure head to break through the shale along its stronger axis, the axis perpendicular to the bedding plane, though still relatively weaker than the more structurally coherent rocks like the Accrington Mudstone, but not containing enough pressure to break across the bedding plane in a straight line. The introduction of these complex fractures has the unintended benefit of involving an increased number of fractures in the shale with the potential to release more fluid. However, this increase in fractures will also cause an increased number of fracture intersections which means that there will be a greater propensity of the fluid, released by the creation of the fractures, to back up into those junctions causing a potential reduction in the efficiency of the fluid flow but increasing the amount of fluid available to the wellbore.

5.5.2.5 WBS5

The WBS5 sample was successfully scanned and the main induced fracture was mapped. Similar to the previous Westbury Shale samples that were fractured under tri-axial conditions, there were numerous fractures following the bedding planes and the horizontal fracture followed a meandering pattern rather than a straight one. The CT reconstructions of the sample post fracture are presented below in Figure 5-100 to Figure 5-102;

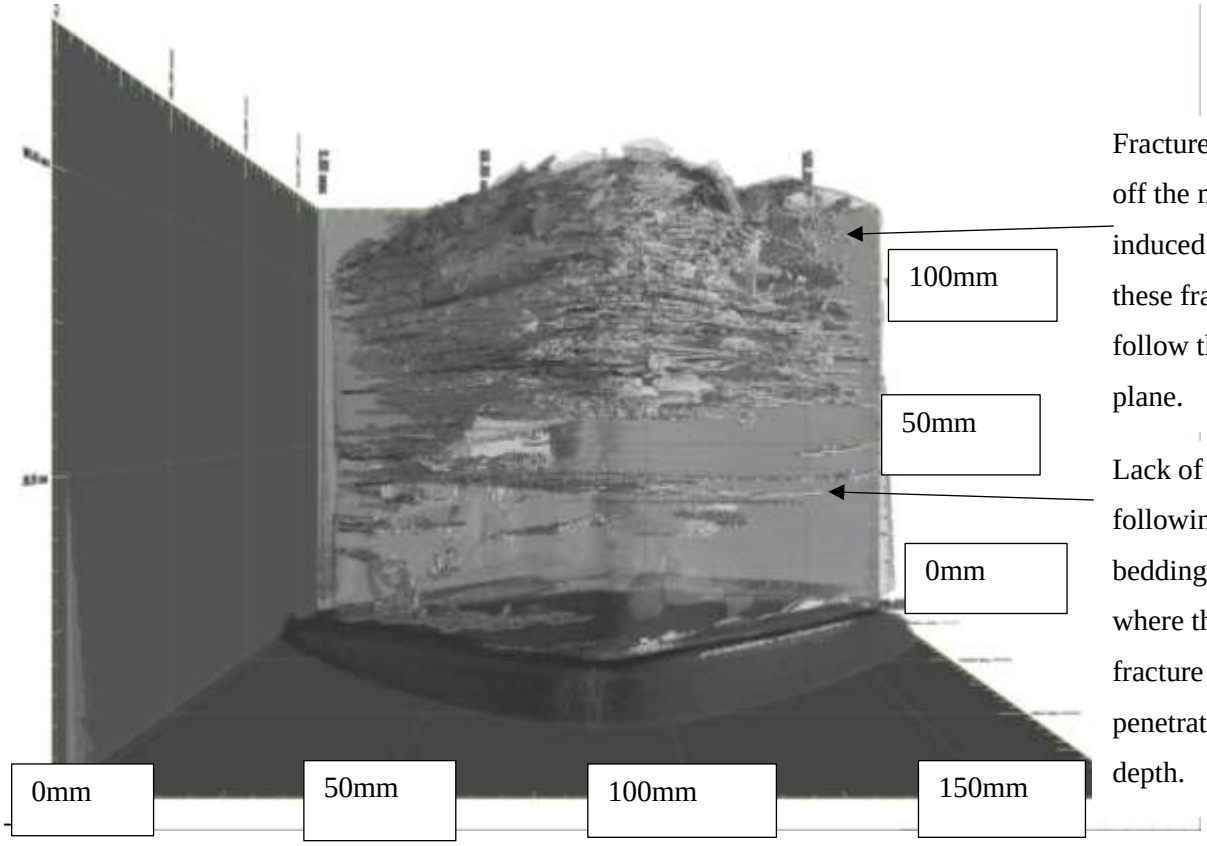

FIGURE 5-100: CT reconstruction WBS5 side view 1.

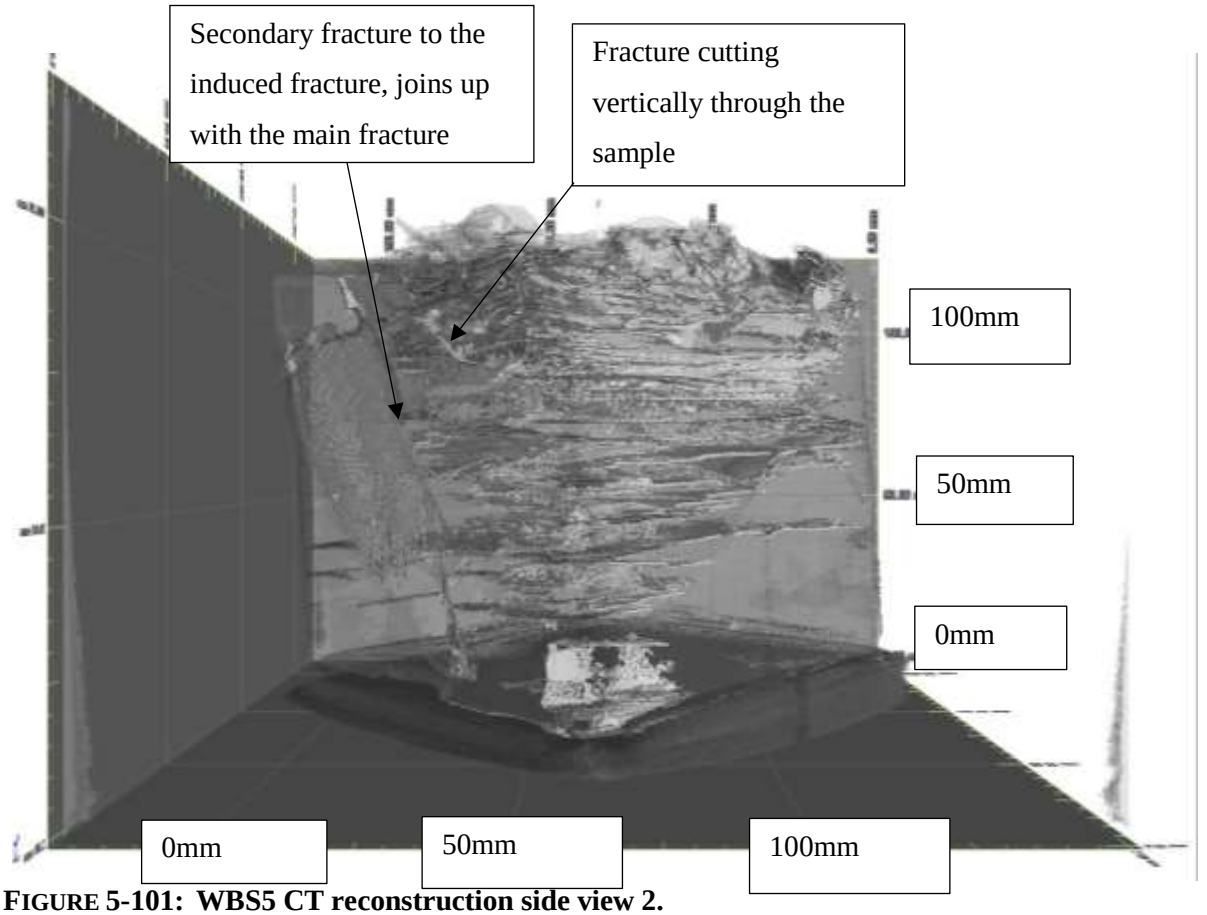

FIGURE 5-101: WBS5 CT reconstruction side view 2.

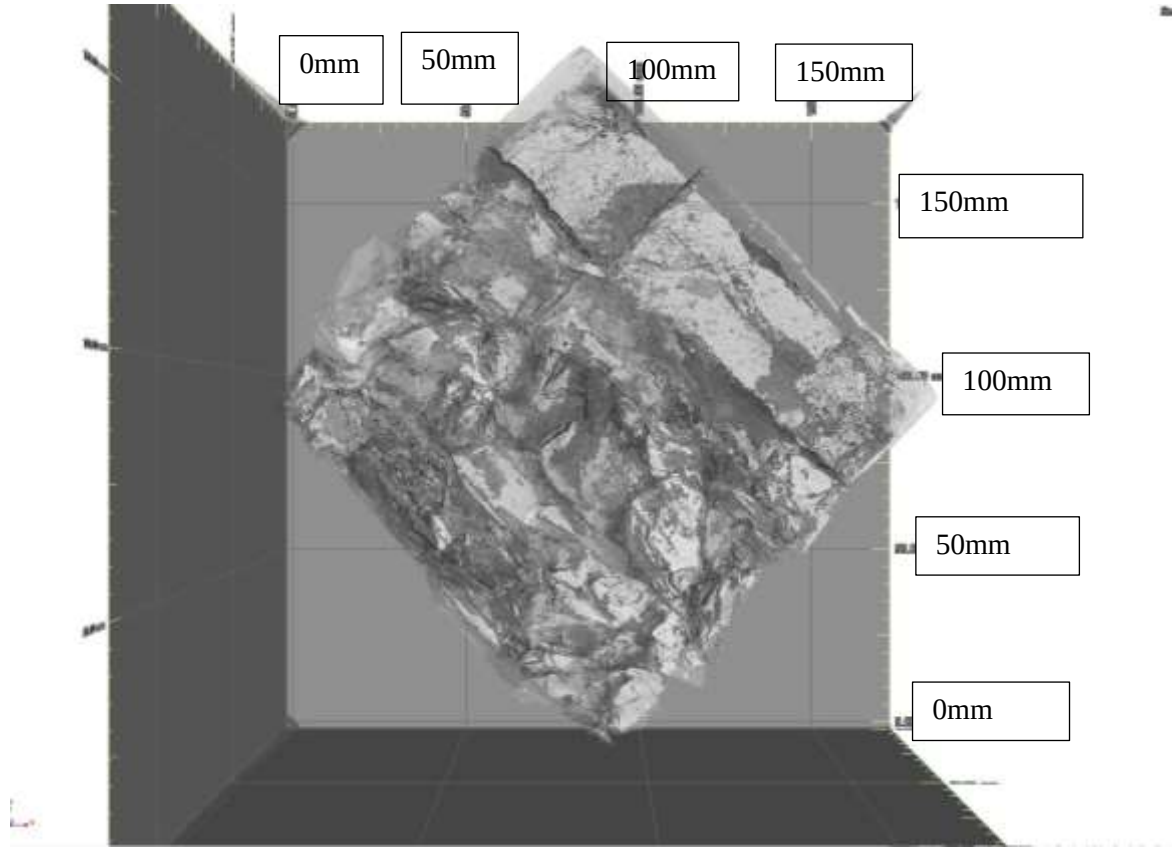

FIGURE 5-102: WBS5 CT reconstruction overhead view.

The measurements of the fracture along both half-lengths are presented below, Table 5-11 & terms are explained previously in Figure 5-51 & Figure 5-52;

Sample name: WBS5											
Position to Borehole	Distance from borehole (MM)	Fracture length (mm)	Distance from Max width to the 10% max width at the top (mm)	Distance from maximum width to the 10% max width at the bottom (mm)	Maximum width (mm)	Top narrowing width (mm)	Bottom narrowing width (mm)	30% max width top	30% max width bottom	Distance from max width to 30% max top	Distance from max width to 30% max bottom
Half-length 1											
At the borehole	3.64	55.520	0.32	-	0.03	-	33.40	0.1	0.1	4.62	19.41
Near Borehole	8.55	60.59	1.79	0.17	0.17	13.13	17.86	0.51	0.51	4.69	12.47
Halfway from borehole	20.77	76.94	1.01	0.10	0.10	14.67	60.79	0.30	0.30	11.89	25.1
Three quarters way from borehole	27.51	77.49	1.09	-	0.11	-	70.69	-	0.33	-	42.05
Half-length 2											
At the borehole	0.21	46.61	0.78	0.08	0.08	14.40	21.83	0.23	0.23	13.36	14.83
Near borehole	4.90	53.19	3.29	0.33	0.33	5.83	24.45	0.99	0.99	5.55	6.89
Halfway from the borehole 1	17.45	56.16	2.55	-	0.26	-	6.26	0.78	0.78	1.87	2.41
Three quarters way from the borehole	24.75	31.28	1.54	-	0.15	-	12.79	-	0.45	-	11.69

TABLE 5-11: WBS5 fracture half-length dimensions.

The relative positions of the fracture are shown in Figure 5-52.

The height of fracture half-length 1 followed the simple form of gradually increasing further away from the borehole, starting at 55.52mm at the BH and growing to 60.59mm at the ¼ point. At the ½ way point the fracture had grown by 16.35mm to 76.94mm but at the ¾ mark the fracture had only grown 0.55mm to 77.49mm, suggesting that the fracture height had reached the optimum level until it could start to decrease.

Fracture half-length 2 did not follow this same pattern. The fracture did indeed grow in height from the BH position to the ½ way mark from 46.61mm to 56.16mm but then decreased to 31.28mm. As has been noted for samples AMS1, 3 and 4, where the height of one fracture half-length is significantly smaller than the height for the other half-length at the near borehole position, the half-length that undergoes either smaller growth or reduces its size by the ¾ position along the fracture half-length has the smaller fracture height. This can only be explained by the fact that the fracture half-length with the reduced height is unable to take as much fracturing fluid, the larger proportion and thus the greater amount of pressure head flows through the half-length with the increased height at the borehole position. Thus, the fracture half-length with the shorter height is subjected to less fluid and hence less force for fracture inducement and thus the fracture starts to reduce in height.

As shown in the images of the measured plane (Figure 5-103) the fracture is not exactly vertical, the constant opening up of the fractures along the bedding plane diverts the induced fracture from a normal straight vertical. Again, this is caused by the fracturing fluid following the path of least resistance but still retaining enough of a significant pressure head to overcome the strength needed to break the cross-bedding strength of the rock, thus a vertical fracture becomes a meandering fracture.

It is interesting to note that on both fracture half-lengths there is a potential rise in the effective permeability of the reservoir due to the main induced fracture constantly crossing over the bedding plane fractures. With this increased connected permeability of the reservoir than would be expected if the rock was stronger and more coherent, the weaker shale thus gives a greater potential return than simulation software would allow for as the models are designed to mimic just one fracture. The constant crossing of the fractures also affects the maximum width recorded in the fractures, as displayed in the planar images (Figure 5-103 and Figure 5-104 respectively), the maximum widths are frequently found on the junction areas of the fracture, which means that when comparing the sizes of other samples, the 10% and 30% of maximum thickness are relatively large.

The attack angle of the fracture is mainly vertical ranging from 5^{o} to 20^{o} from a straight line from the borehole. Towards the edge of the sample the main angle decreases to approximately 125^{o} to 130^{o}. This decrease in the angle occurs only where intersecting bedding fractures have increased (as shown in Figure 5-103 & Figure 5-104) thereby reducing the pressure head in the fracturing fluid forcing the fracture to meander more as it only has the pressure to cut through the weaker parts of the rock.

The relative position of the fracture measurements, in relation to the positions distance from the borehole, are shown in Figure 5-51 while the measurements taken in the planar view of the fracture, that make up the labelling of these figures are presented in Figure 5-52.

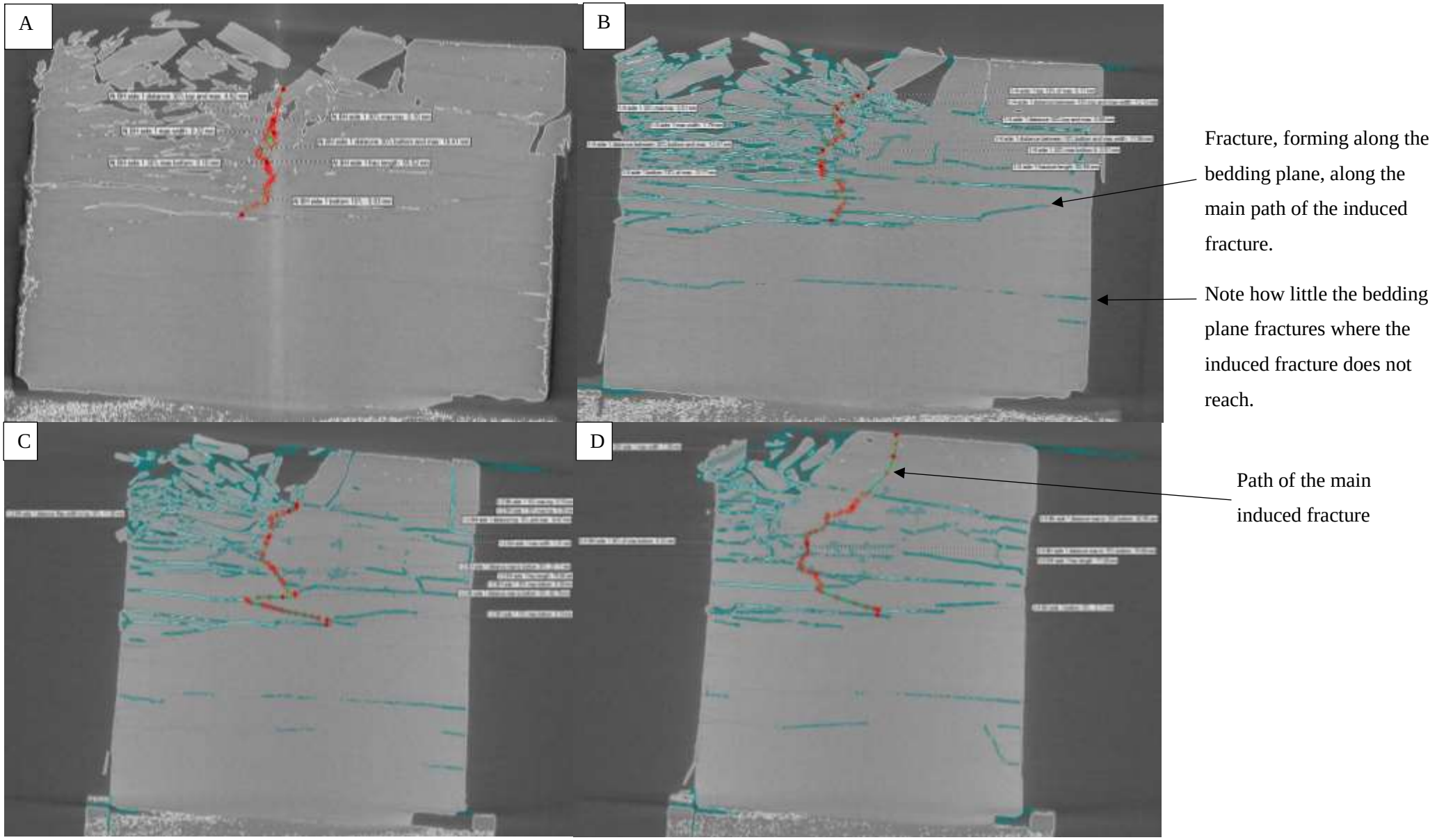

FIGURE 5-103: WBS5 Fracture half-length side 1 A) At the borehole, B) Near the borehole, C) Halfway along the half-length, D) ¾ along the half-length.

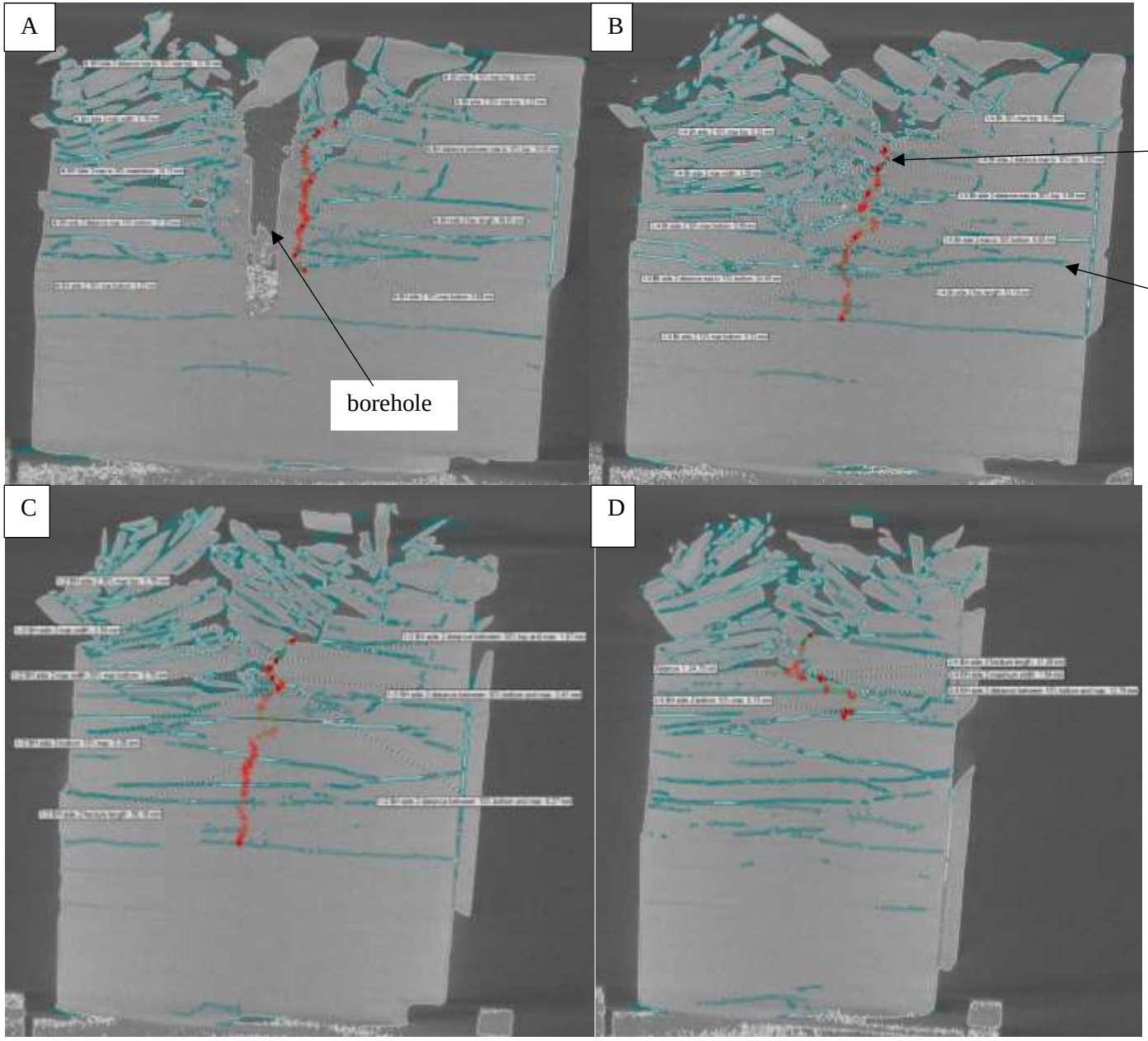

FIGURE 5-104: WBS5 Fracture half-length side 2 A) At the borehole, B) Near the borehole, C) Halfway along the half-length, D) ¾ along the half-length .

5.5.2.6 WBS6

Although the WBS6 sample was fractured under tri-axial conditions, the pressures were lower than for previous samples due to audible cracks being heard whilst pressure was being applied to the flat jacks. This sample showed similarities with the other Westbury Shales under tri-axial conditions. The induced fracture meandered aided by multiple fractures following the bedding planes, which occurred mainly in the upper half of the sample where drilling had taken place. The CT reconstructions of the side and overhead views are presented in Figure 4 100 & Figure 4 102. The measurements are presented in Table 4 12 & as explained previously in Figure 4 50 & Figure 4 51.

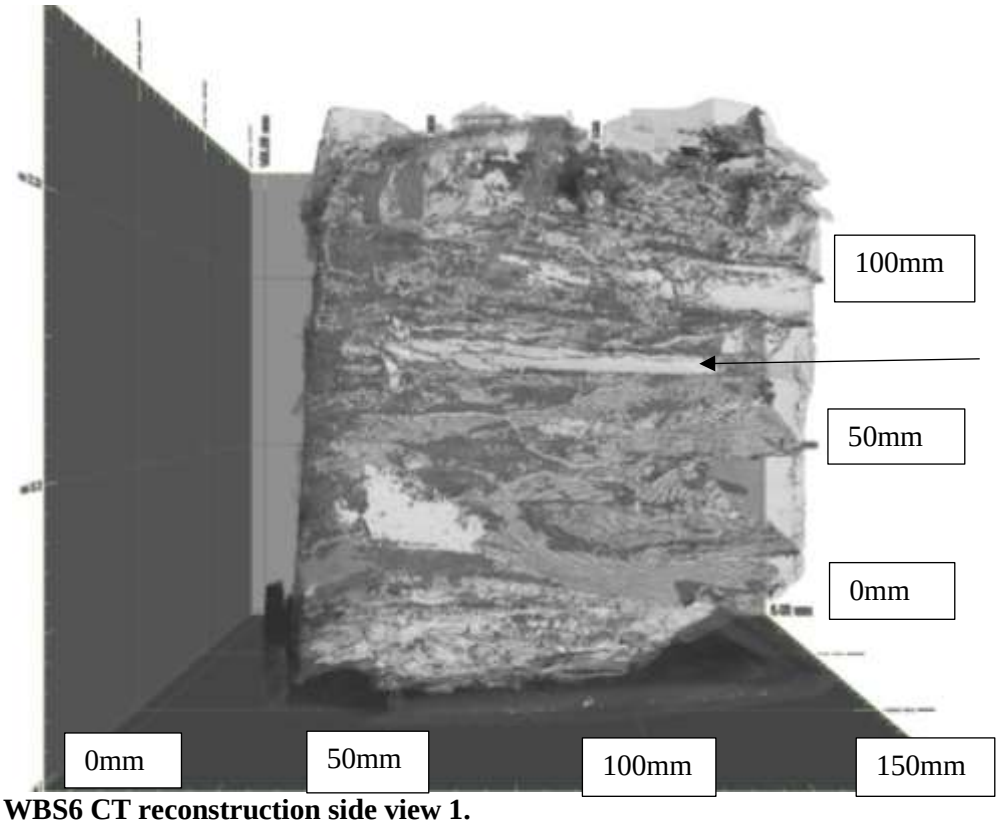

FIGURE 5-105: WBS6 CT reconstruction side view 1.

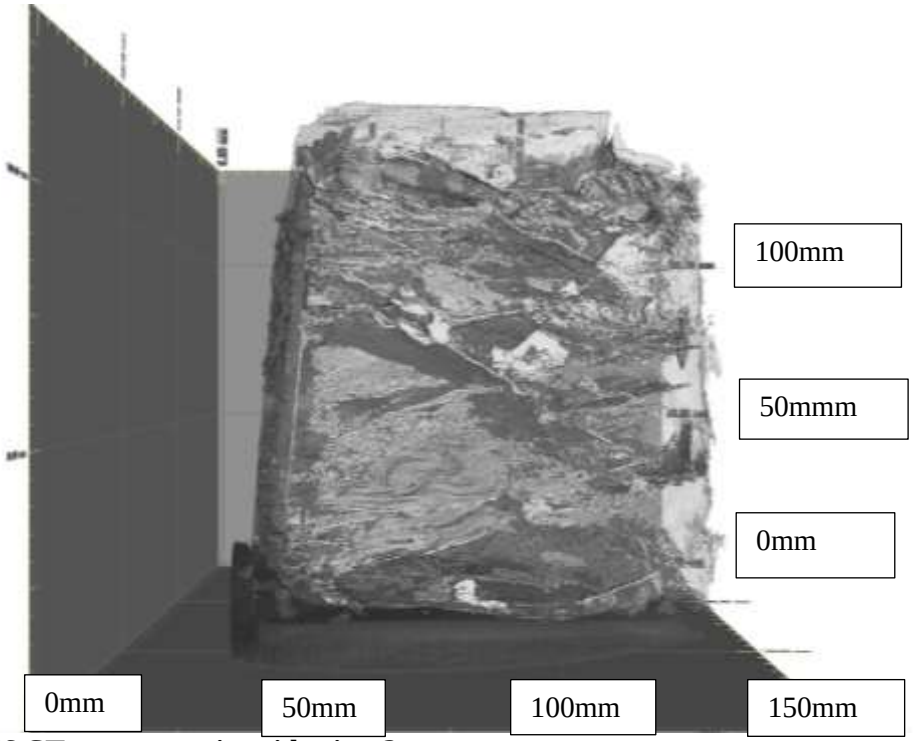

FIGURE 5-106: WBS6 CT reconstruction side view 2.

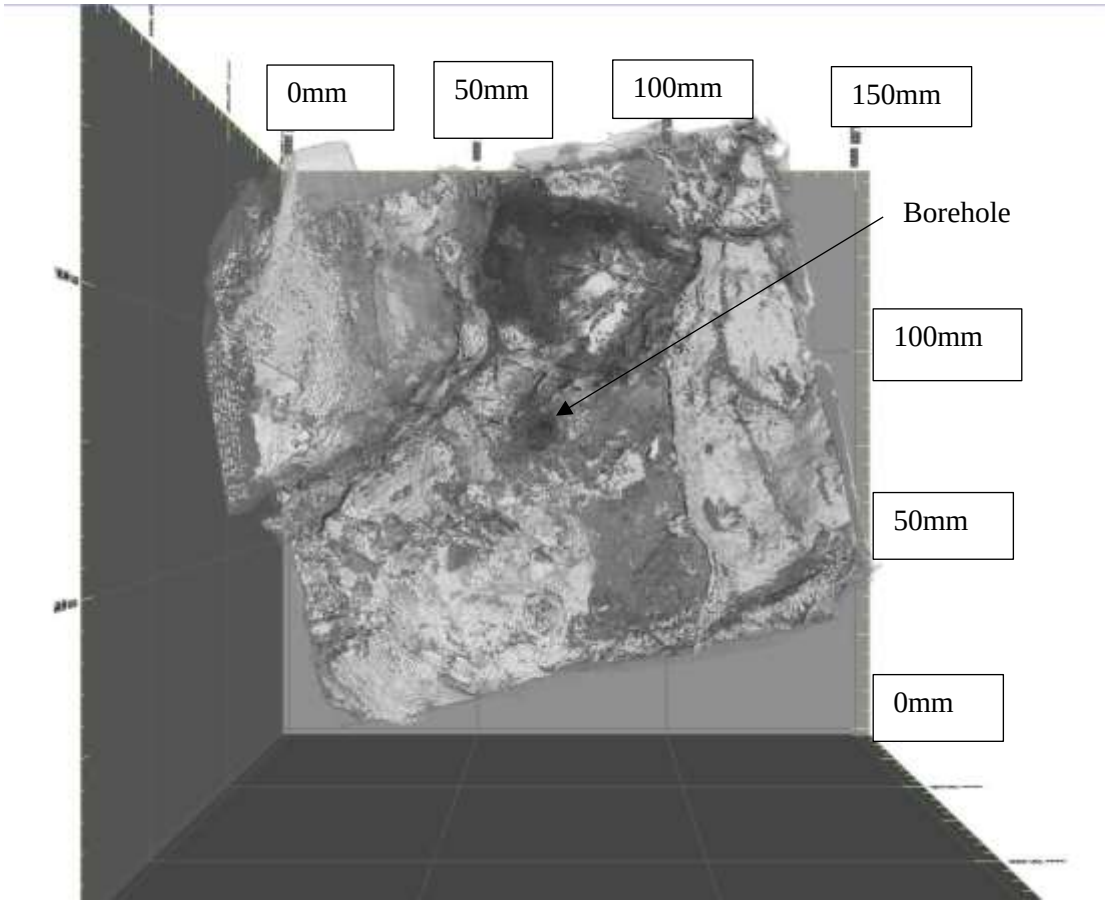

FIGURE 5-107: WBS6 CT reconstruction overhead view.

Sample name: WBS6											
Position to Borehole	Distance from borehole (MM)	Fracture length (mm)	Distance from Max width to the 10% max width at the top (mm)	Distance from maximum width to the 10% max width at the bottom (mm)	Maximum width (mm)	Top narrowing width (mm)	Bottom narrowing width (mm)	30% max width top	30% max width bottom	Distance from max width to 30% max top	Distance from max width to 30% max bottom
Half length 1											
At the borehole	0.61	46.68	1.06	-	0.10	-	8.85	0.30	0.30	26.63	2.10
Near Borehole	10.04	67.55	0.61	0.06	0.06	15.07	51.39	0.18	0.18	11.89	46.06
Halfway from borehole	24.92	93.71	0.56	0.06	0.06	13.14	69.00	0.17	0.17	6.93	68.04
Three quarters way from borehole	39.24	134.88	1.04	0.10	0.10	35.80	89.93	0.31	0.31	23.47	69.45
Half length 2											
At the borehole	2.22	43.65	0.43	0.04	0.04	3.66	40.04	0.13	0.13	3.27	39.49
Near borehole	10.33	62.78	0.47	0.05	0.05	38.20	15.70	0.14	0.14	36.56	15.67
Halfway from the borehole 1	19.21	72.35	0.58	0.06	0.06	16.11	58.22	0.17	0.17	15.29	58.14
Three quarters way from the borehole	31.11	93.90	0.48	0.05	0.05	43.71	49.41	0.14	0.14	42.24	49.21

TABLE 5-12: WBS6 fracture half-length dimensions.

The relative positions of the fracture are shown in Figure 5-52.

The WBS6 sample shows some similarities to those recorded for sample WBS3 to WBS5 and that of the Accrington Mudstone samples. As with the Westbury samples the maximum width does not follow the normal pattern of decreasing as it moves further away from the borehole. At the borehole the max width starts at 1.06mm and 0.43mm for half-length 1 & 2 respectively, before decreasing in size in half-length 1 to 0.61mm and increasing in size to 0.47mm in half-length 2. Half-length 2 max width then stays constant until it reaches the ¾ point at 0.48mm. Whereas in half-length 1 the maximum width decreases again from the ¼ mark (0.61mm) to the ½ mark (0.56mm) before increasing at the ¾ point to 1.04mm. Part of this can be explained by the volume of horizontal fractures that follow the bedding planes and which intersect with the induced fracture. As the fracturing fluid is slowed down by these junctions the build-up in pressure seems to help create larger openings to help dissipate the pressure head in the fluid.

The planar views for this sample show that the fractures do deviate from a straight vertical line, but rather less so than WBS 3 and 5. This lack of deviation and thus a lack of resultant pressure loss can explain why the fracture height on each fracture half-length increases the further away from the borehole it travels.

The resultant large variation in fracture width has led to a great variation of distance between the maximum width point and the 10% and 30% of the maximum width points, which will have an effect on the modelling equation for the fracture growth. The inherent weakness of the Westbury Shale formation and due to the chance and randomness of fractures opening up along the bedding planes as an induced fracture causes the random opening up of the weaker planes will make an accurate prediction particularly difficult. The image of each plane that was measured is presented overleaf in Figure 5-108 & Figure 4-104.

The main attack angle of the fracture is mainly vertical ranging from 5^{o} to 10^{o} from a straight line from the borehole.

The relative position of the fracture measurements, in relation to the positions distance from the borehole, are shown in Figure 5-51 while the measurements taken in the planar view of the fracture, that make up the labelling of these figures are presented in Figure 5-52.

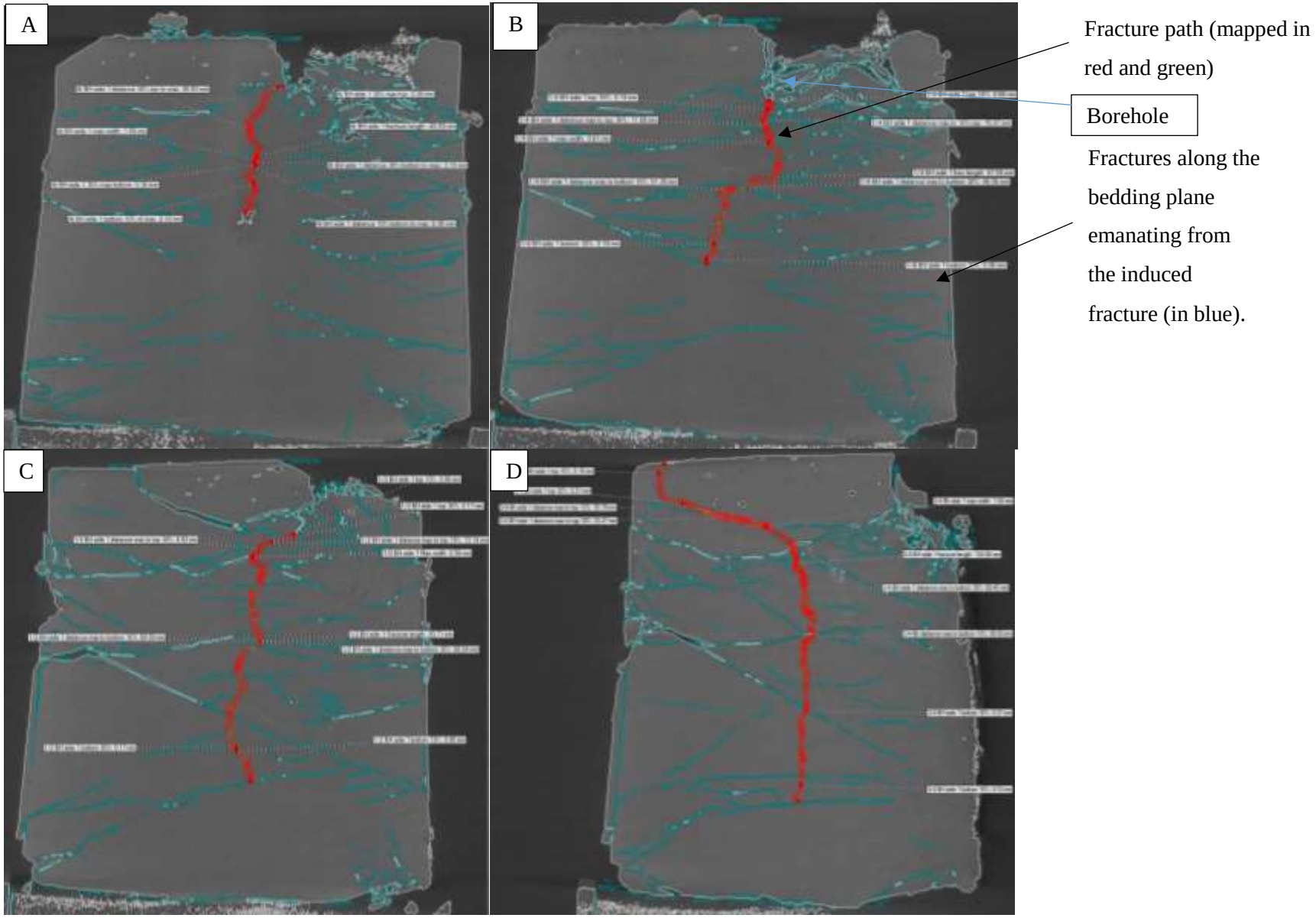

FIGURE 5-108: WBS6 Fracture half-length side 1 A) At the borehole, B) Near the borehole, C) Halfway along the half-length, D) ¾ along the half-length.

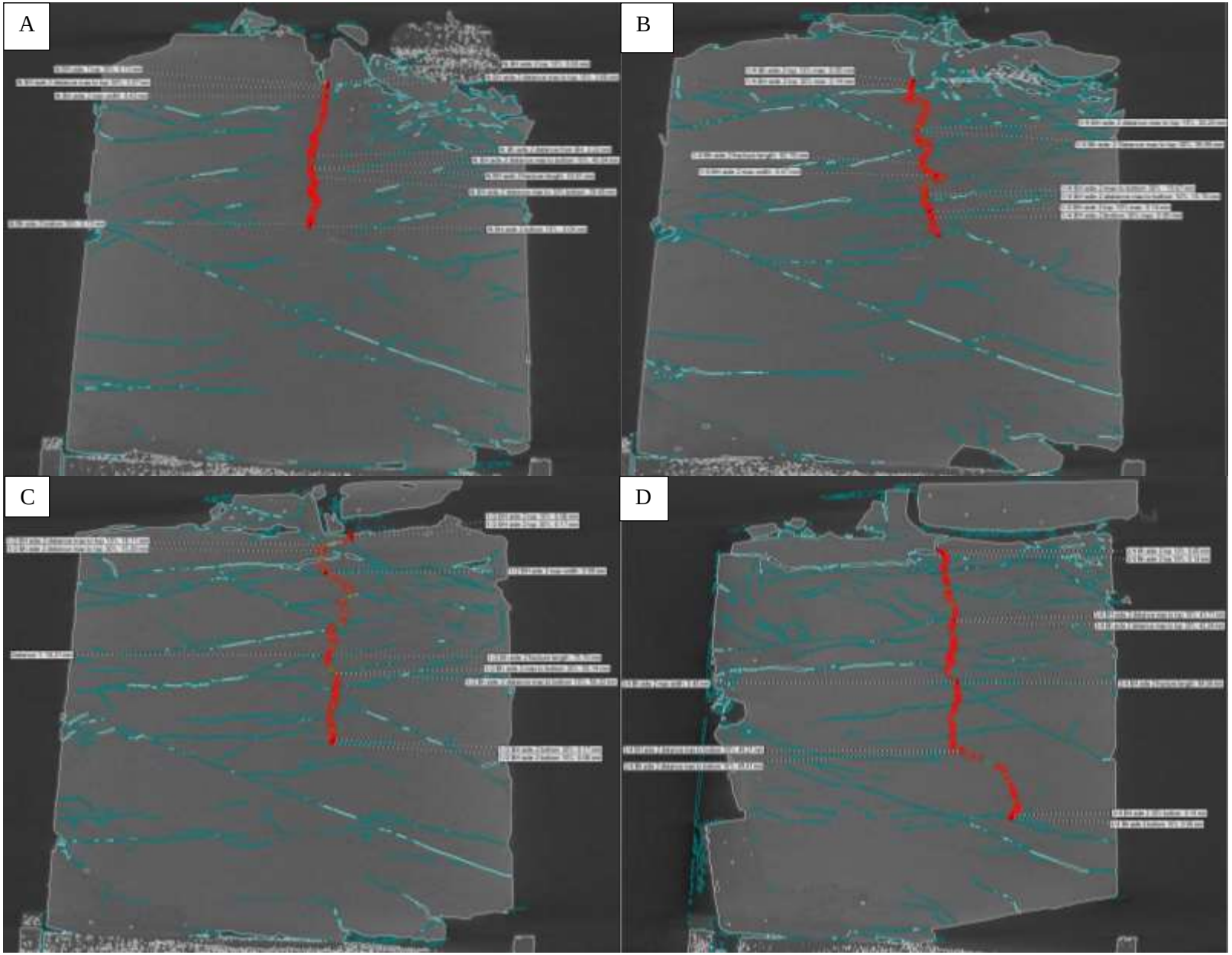

FIGURE 5-109: WBS6 Fracture half-length side 2 A) At the borehole, B) Near the borehole, C) Halfway along the half-length, D) ¾ along the half-length.

5.6 CT scanning summary

The main points taken away from the results presented in relation to the CT scanning are as follows:

- The Accrington Mudstone fractures neatly with two neat fracture half lengths, only with the fracture cutting through a pre-existing fracture does the induced fracture in an Accrington Mudstone become more complex. This is mainly due to the mudstone being more coherent than the weaker HOC shale. An example of the straight fracture is shown in Figure 5-58 compared to the more complex Westbury fracture shown in Figure 5-103.
- There is a correlation with fractures that increase in size the further they get from the borehole, generally, the thinner the fracture gets. Whilst the fractures that decrease in size generally stay wider, this is seen in AMS4 (pictures Figure 5-85 to Figure 5-91)
- The Westbury Shale shows a more meandering pattern, though they generally fracture in a near vertical pattern. This is due to its inherent weakness.
- This inherent weakness also causes the shale to open up along the weaker bedding planes, perpendicular to the induced fracture. This creates more complex fractures than models have suggested, seen in WBS5 and WBS6 (Figure 5-103 & Figure 4-103 respectively).

5.7 Acoustic Data

The following section presents the data obtained for each sample from the acoustic software. To demonstrate how this part of the system was developed each sample will be shown separately along with the details of how the arrangements and preparations were changed to improve the data and get more accurate results. This will prove the synopsis that the acoustics in a 3D arrangement can be used in both the laboratory and the field to help map induced fractures.

The data is presented in a series of 3D graphs; the first set is an X, Y, Z location graph showing the spatial location of the events. These events are shown as red dots, giving the exact location of the events recorded. The events are linked to the hits, the actual acoustic emissions detected, the events where the software can get all the sensors to agree a position of the emission. A low event to hit ratio does not necessarily mean a low accuracy. If the majority of the sensors are recording the same emissions it could mean the location is repeatedly in the same place or a large number of the hits are related to each other. The other 3D graphs show various representations of the signal strengths, signal durations, reverberations and energy. Thus, revealing if there is unique pattern or signal to the shale fracturing, compared with other emissions.

After analysing the data from the commissioning phase (discussed in Section 5.2.1), it was noted that there was too much data over too large an area. To make the data more readable and useful it was decided that the drilling of the samples would be kept to 10mm intervals where possible. The drilling

data is presented for each 10mm interval from 100mm at the dorsal (top) side to the 50mm depth of the borehole at the centre of the sample. As the conditions of each sample change when drilling i.e. a bigger hole etc. then there will be accompanying changes to confining stresses which in turn means the wave velocity will change at each interval. The velocity for each interval is presented in Table 3-1.

5.7.1 Biaxial

5.7.1.1 AMS1

DRILLING

In the AMS1 sample the acoustic hits were not recorded between 100 and 80mm. It was found that the sensors had become detached from the shale surface, this necessitated the reattachment of the acoustic sensors to the edge of the sample. Below the data from 80 to 50mm is discussed.

80-70MM

The acoustic location data and graphs are presented in Figure 5-110 to Figure 5-112.

4884 hits were recorded by the sensors but this only converged into three events as shown in Figure 5-110. This suggests that although there are acoustic events being detected something is distorting the events between the wave being emitted and being detected by the sensors. Out of the six sensors, four sensors picked up data, each with a range in amplitude. However, the three events, although reasonably centred height wise, were at a depth ranging from 66mm to 53mm, which is below the height expected. It would be reasonable to expect events between the depths of 80 to 70mm as well as those below 70mm which would reflect the damage done by the drill head just below the point of drilling. However, the fact that only three events were placed suggested that there was still a problem with the sensors detecting the acoustic waves in the sample. The plates and sensors were checked, and it was confirmed that each sensor was in firm contact with the surface of the sample. The lack of events corresponding to hits can only be explained by the process that was used to present a sharp flat face to the acoustic contact.

The sample was cut just short of 100mm and placed in a mould where high density plaster was added to surround the sample meaning that the two separate mediums would have different densities. When testing deep water sonar and an acoustic wave hits a medium with a differing density, that wave is distorted, the principle of which is shown below in Figure 5-113. This means that multiple sensors are detecting reverberations that have been distorted so much that they are unable to fix them accurately into one source location.

Figure 5-112 shows the energy released and the signal strengths and duration. This graph shows that most of the energy emitted by the acoustic wave only lasts for a small duration in time and gives the weakest signal, this will be weak rebounding signals. The largest amount of energy, >100,000 J, is given for a signal strength that lasts for just less than 3,500μsecs. The low energy signal strengths of short duration will not likely give a 3D placement, instead it will be the stronger signals that give a

greater chance of the software calculating an accurate 3D placement. The graph showing the reverberations displays continued small energy reverberations of less than 10,000 J but lasting between 2,000 to 3,000µsecs. This gives credence to the two different densities of the two mediums (the shale and high strength plaster) in the sample distorting the frequencies and causing reverberations that affect the readings.

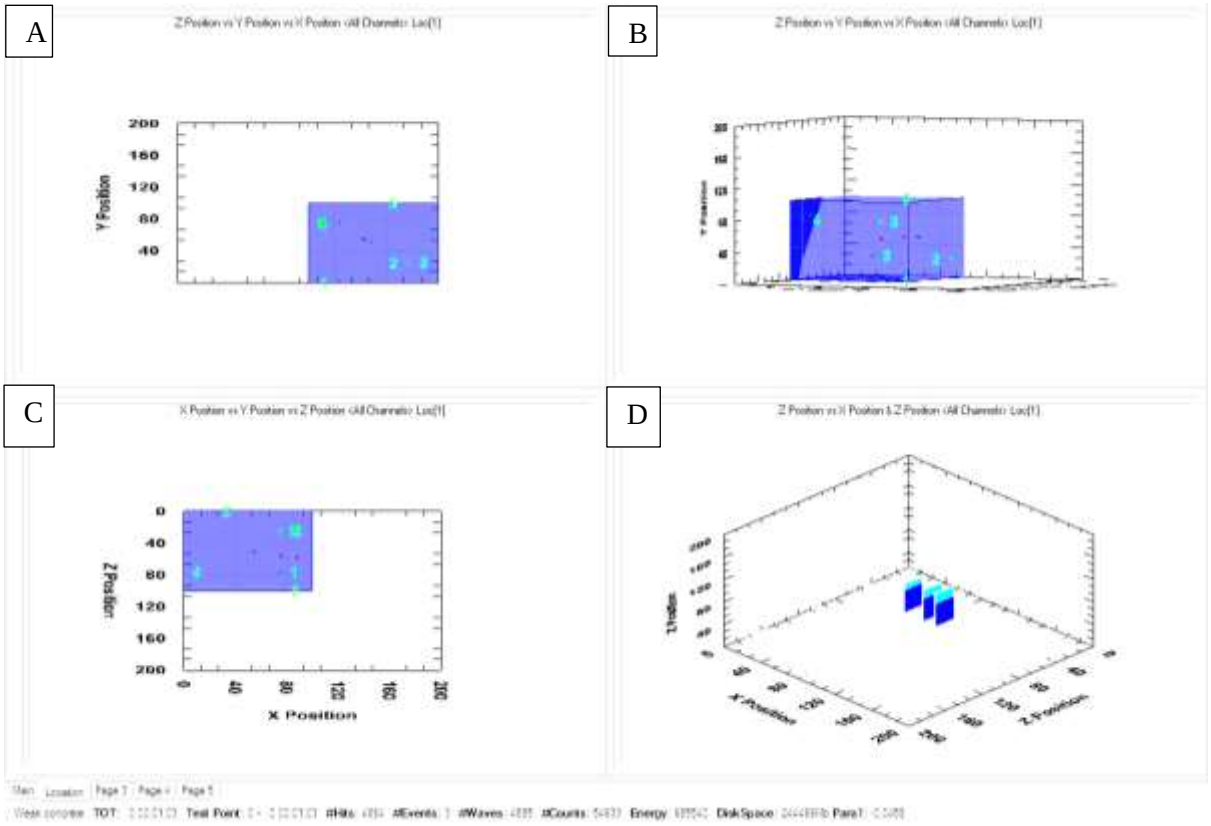

FIGURE 5-110: AMS1 Location Graphs between 80mm to 70mm A) Depth view, B) 3D view, C) Overhead view, D) Actual positioning spots.

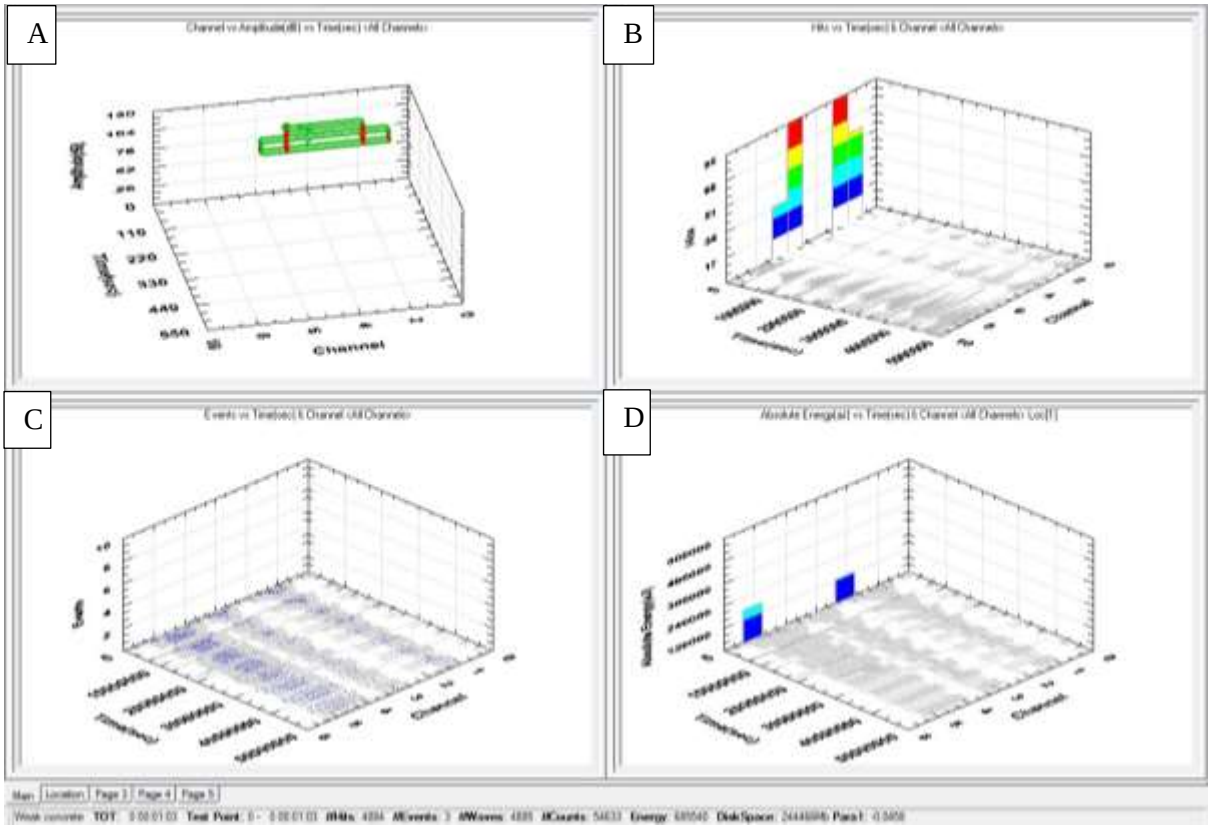

FIGURE 5-111: AMS1 Sensor graphs 80mm to 70mm, A) Acoustic signals detected by each channel, B) Hits Vs Time, C) Events Vs time, D) Absolute energy Vs time.

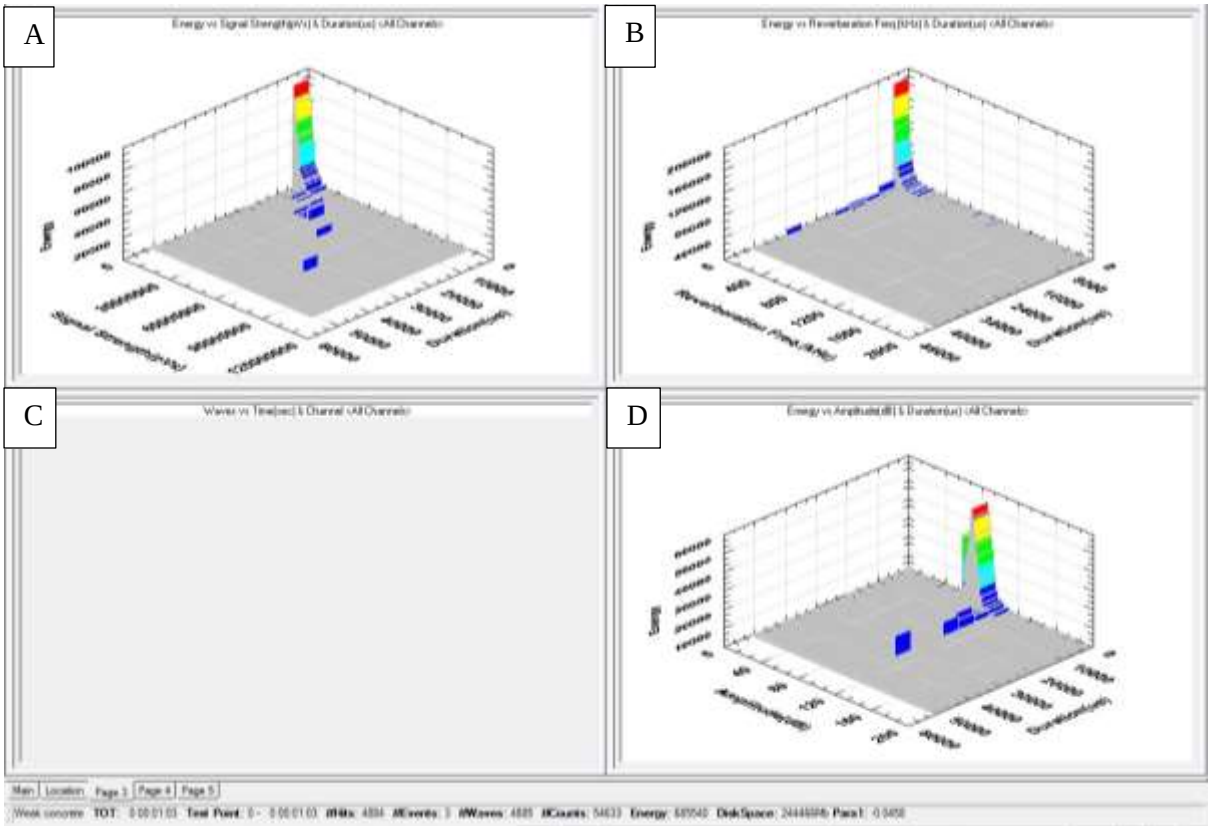

FIGURE 5-112: AMS1 Energy, duration and signal strength graphs 80mm to 70mm, A) Energy Vs signal strength, B) Energy Vs Reverberation, C) Empty, D) Energy Vs Amplitude.

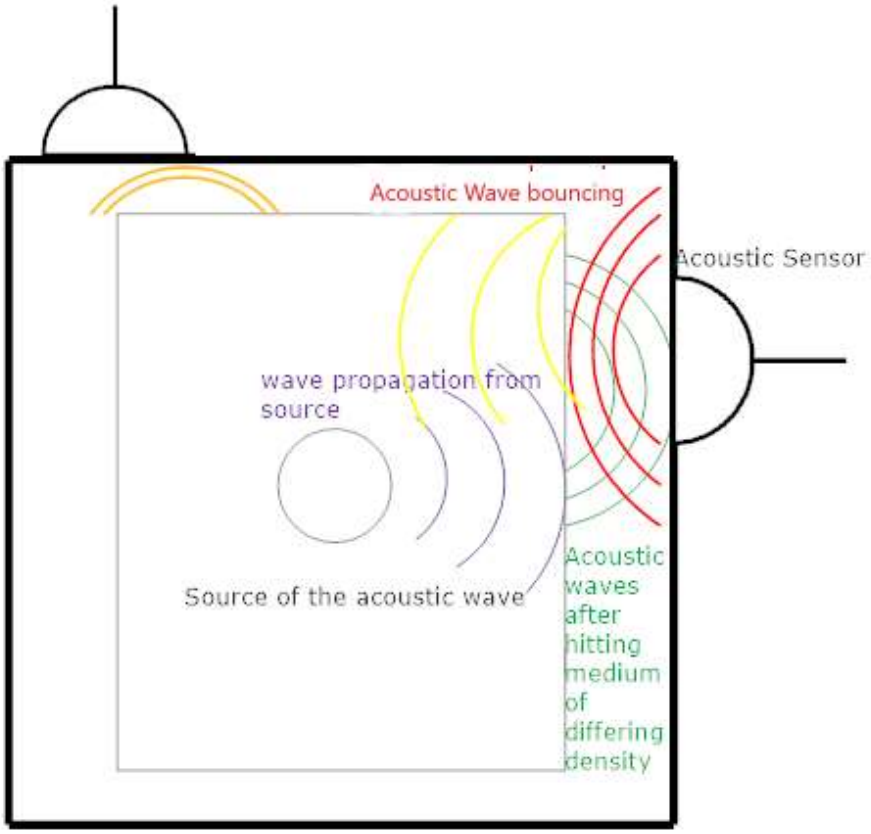

FIGURE 5-113: Principle of waves bouncing off different mediums of different densities.

60 TO 55MM

A similar pattern was noted in the acoustic signals to those acquired between 80 to 70mm. The plots of the 3D acoustic settings are shown in Figure 5-114 to Figure 5-117.

There were 5430 hits which translated into just 4 events. Figure 5-114 and Figure 5-117 show that these events were detected closer to the 60mm interval than the events detected at 80 to 70mm interval. Again, such a small number of events linked to a large volume of hits suggested that constant distortions of acoustic waves were affecting the ability of the sensors to place the acoustic emissions.

Figure 5-115 shows a large grouping of events however some sensors were not picking up signals that were being detected by other sensors so events were being grouped together (the green banding) but were not strong enough to give the event placement location. Though the closer placement of acoustics and closer grouping, Figure 5-114, suggests that the further down into a sample the drill travels, the closer to equalisation of each length of the two mediums the waves travel through, therefore, causing less distortion. Although this can only be surmised until this can be confirmed with more data.

Figure 5-116 shows the continued reverberation of less than 50Khz of low energy signals less than 10,000J, giving continued strong evidence that these signals are causing the lack of recorded events. It is also important to note that there is an improved signal strength, the majority of the energy, approximately 110,000J, is recorded for a signal strength of less than 1,000ρVs though unlike the 80mm

to 70mm interval there is a larger abundance of signal data from 300,000 to 900,000ρVs with energy typically of 10,000J.

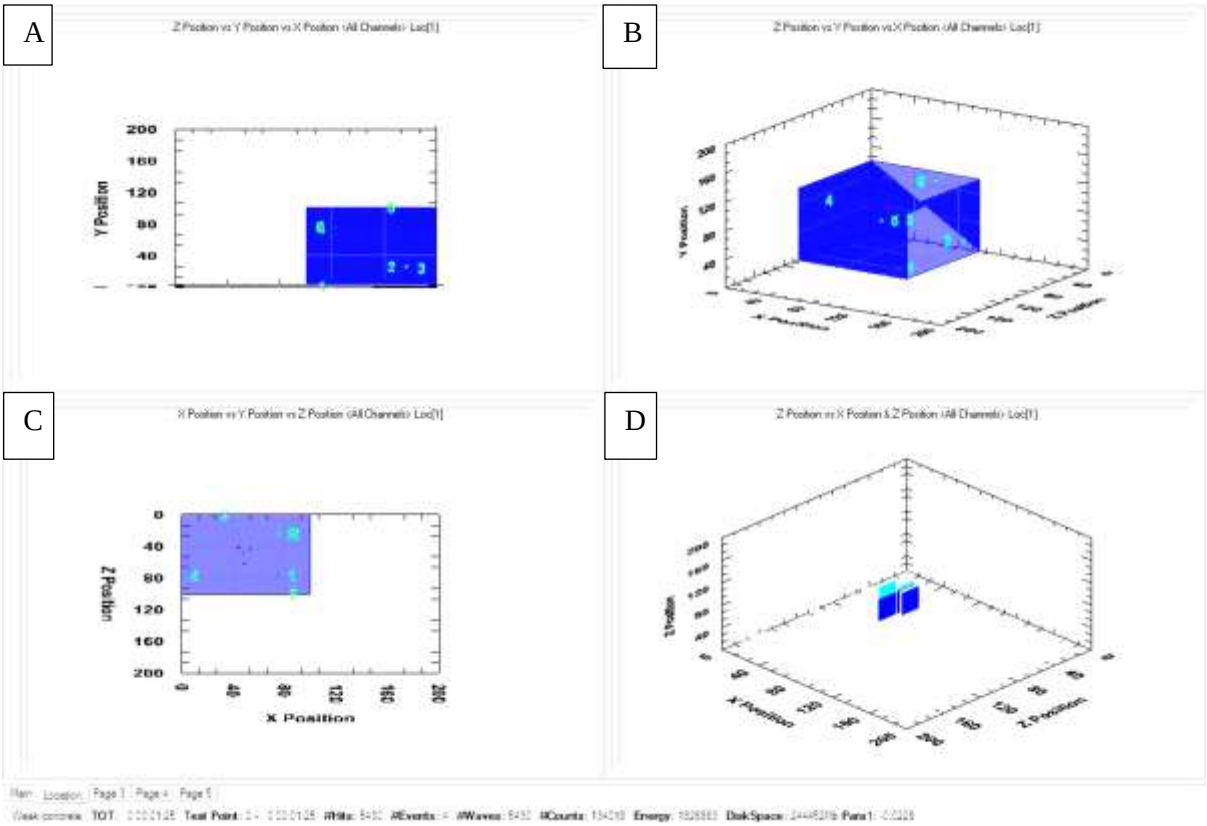

FIGURE 5-114: AMS1 location graph 60mm to 55mm, A) Depth view, B) 3D view, C) Overhead view, D) Actual positioning spots.

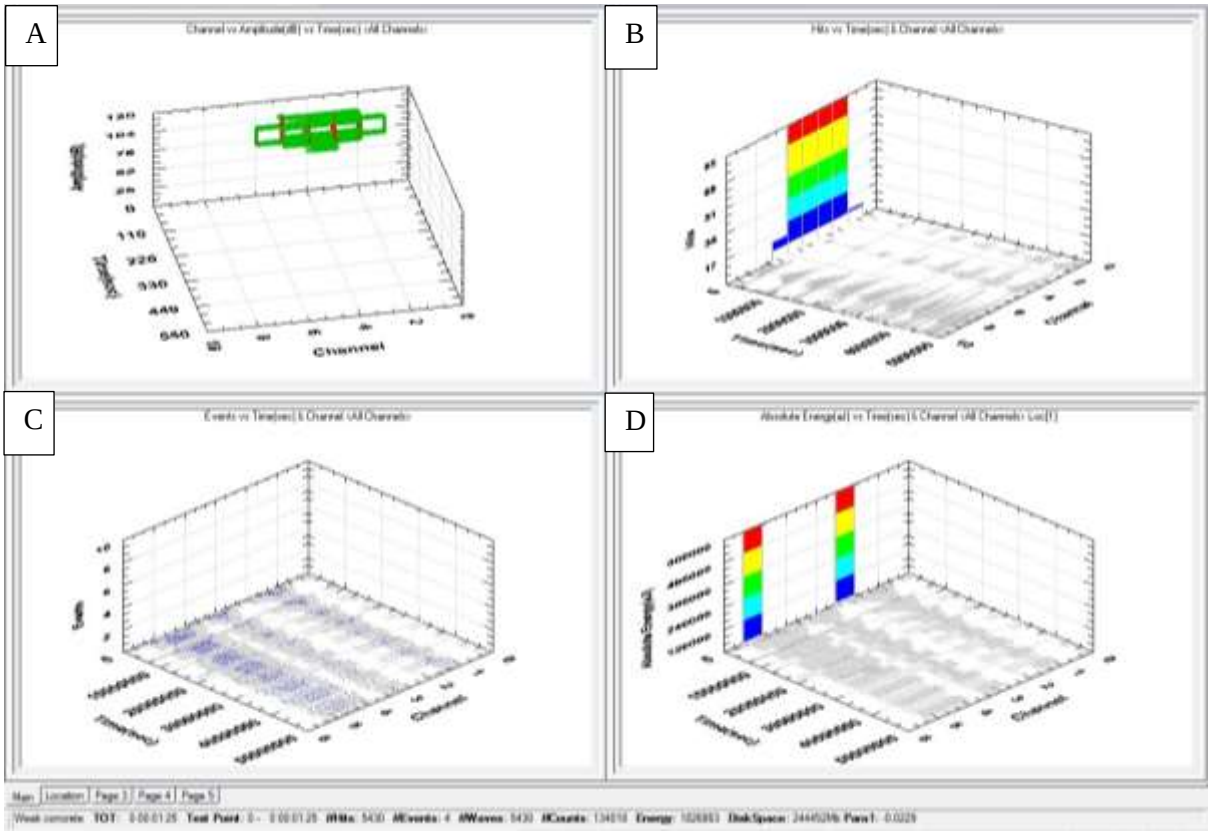

FIGURE 5-115: AMS1 sensor graphs 60mm to 55mm, A) Acoustic signals detected each channel, B) Hits Vs Time, C) Events Vs time, D) Absolute energy Vs time.

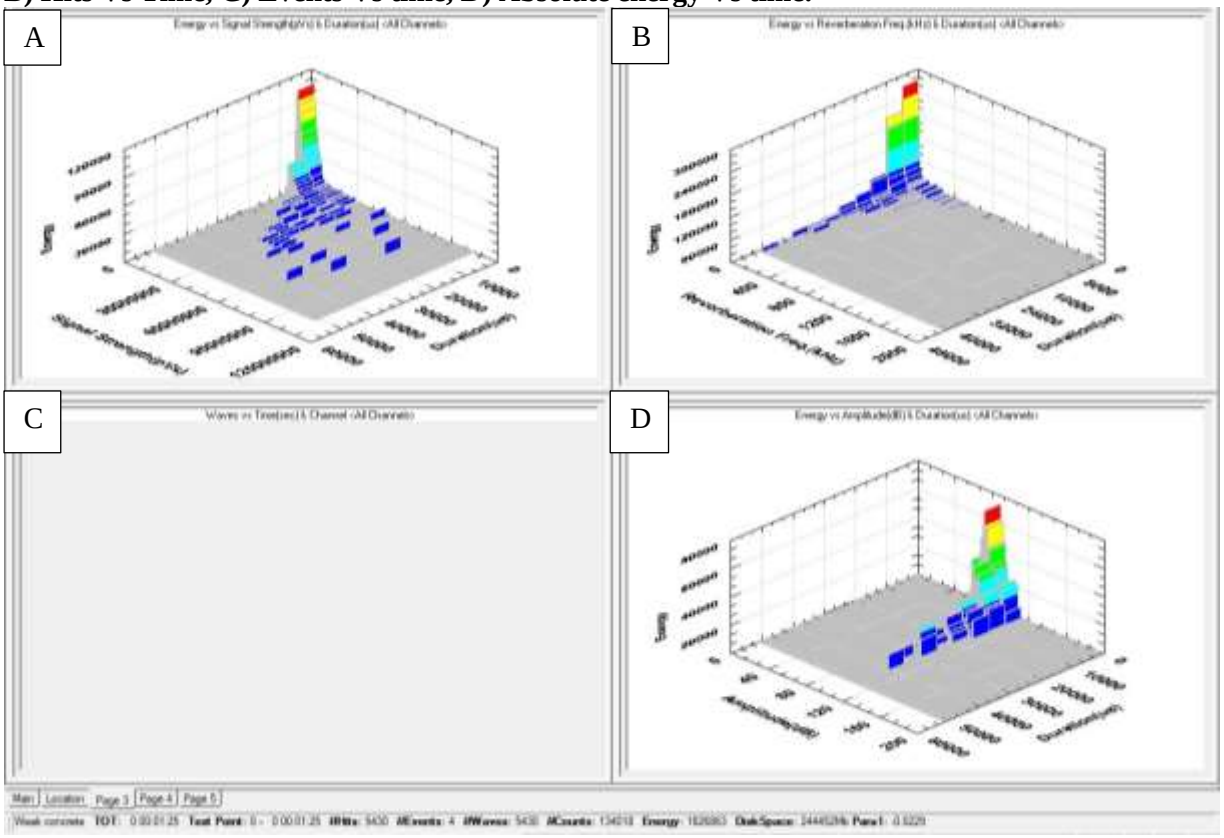

FIGURE 5-116: AMS1 Energy, duration and signal strength graphs 60mm to 55mm, A) Energy Vs signal strength, B) Energy Vs Reverberation, C) Empty, D) Energy Vs Amplitude.

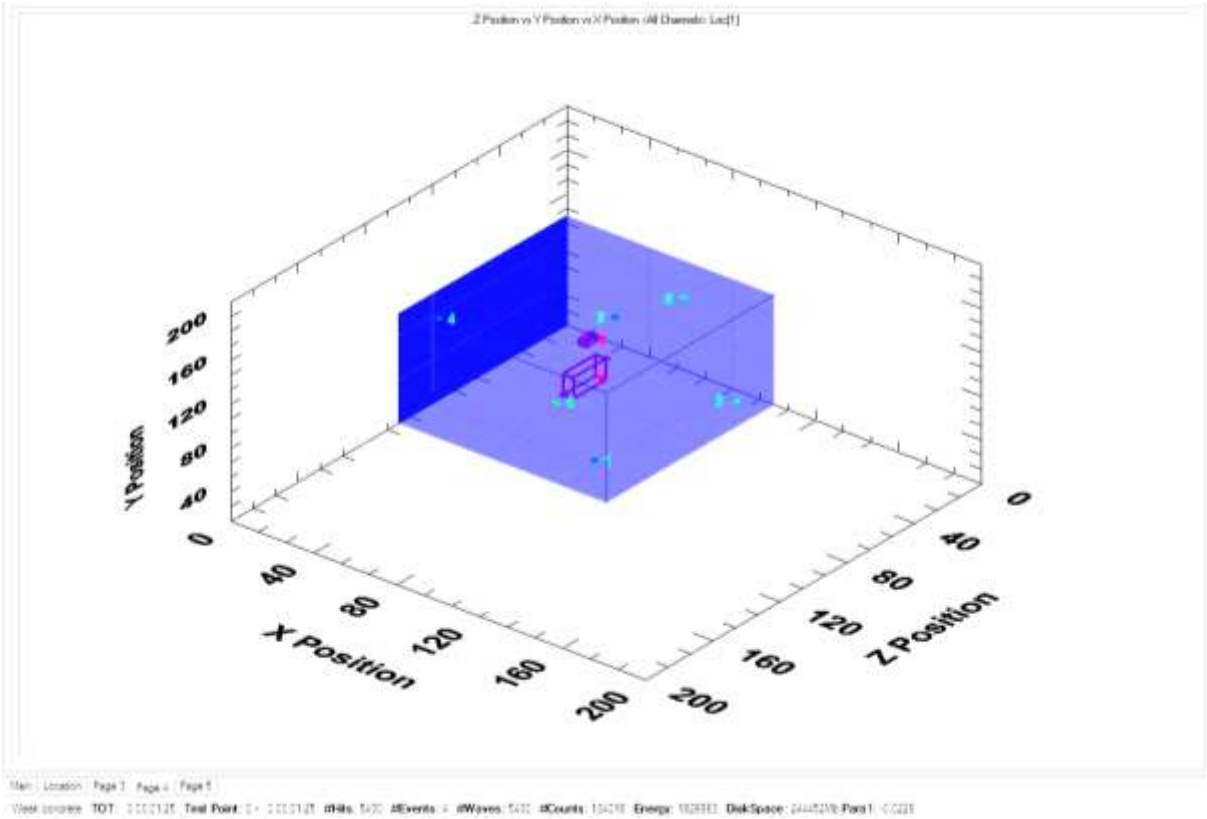

FIGURE 5-117: AMS1 3D graph of events grouped 60mm to 55mm.

55MM TO 50MM

The data of the acoustic placings and the emissions detected are presented in Figures 4-87 to Figure 4-90.

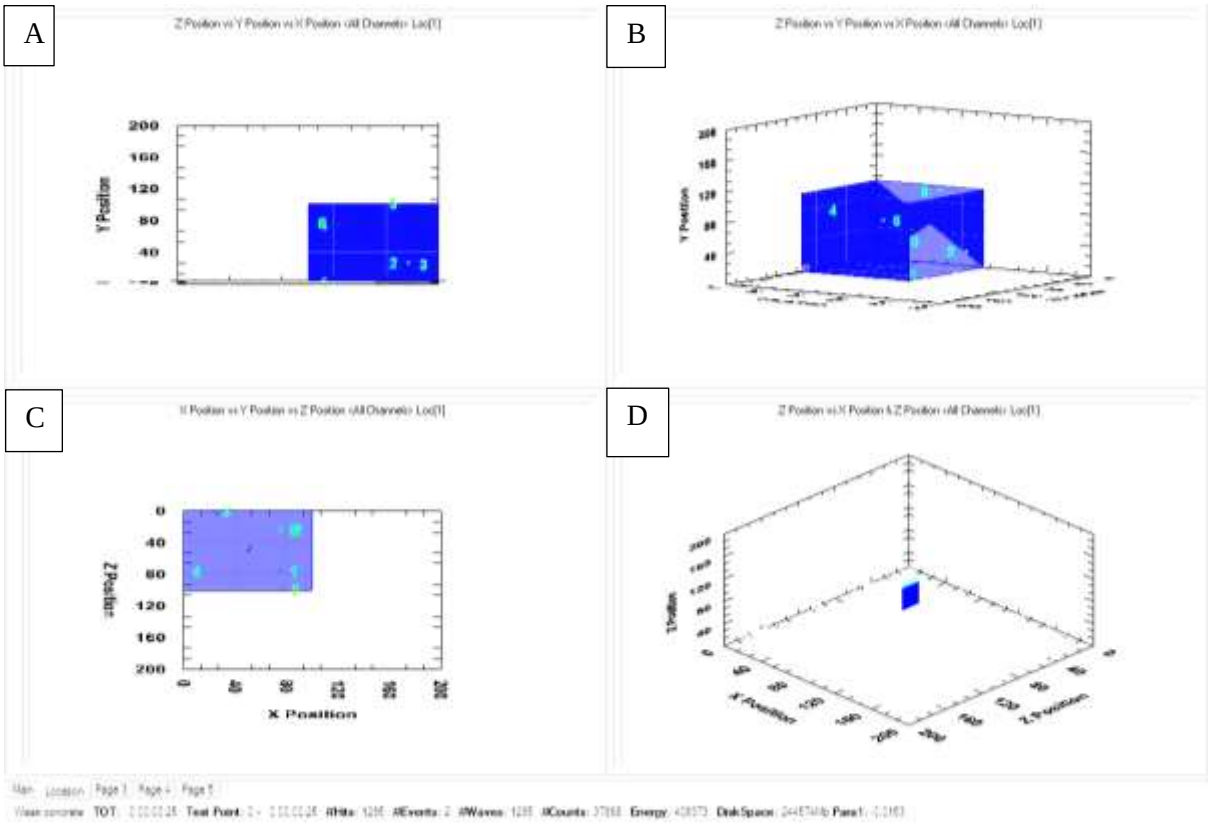

FIGURE 5-118: AMS1 Location graphs 55mm to 50mm, A) Depth view, B) 3D view, C) Overhead view, D) Actual positioning spots.

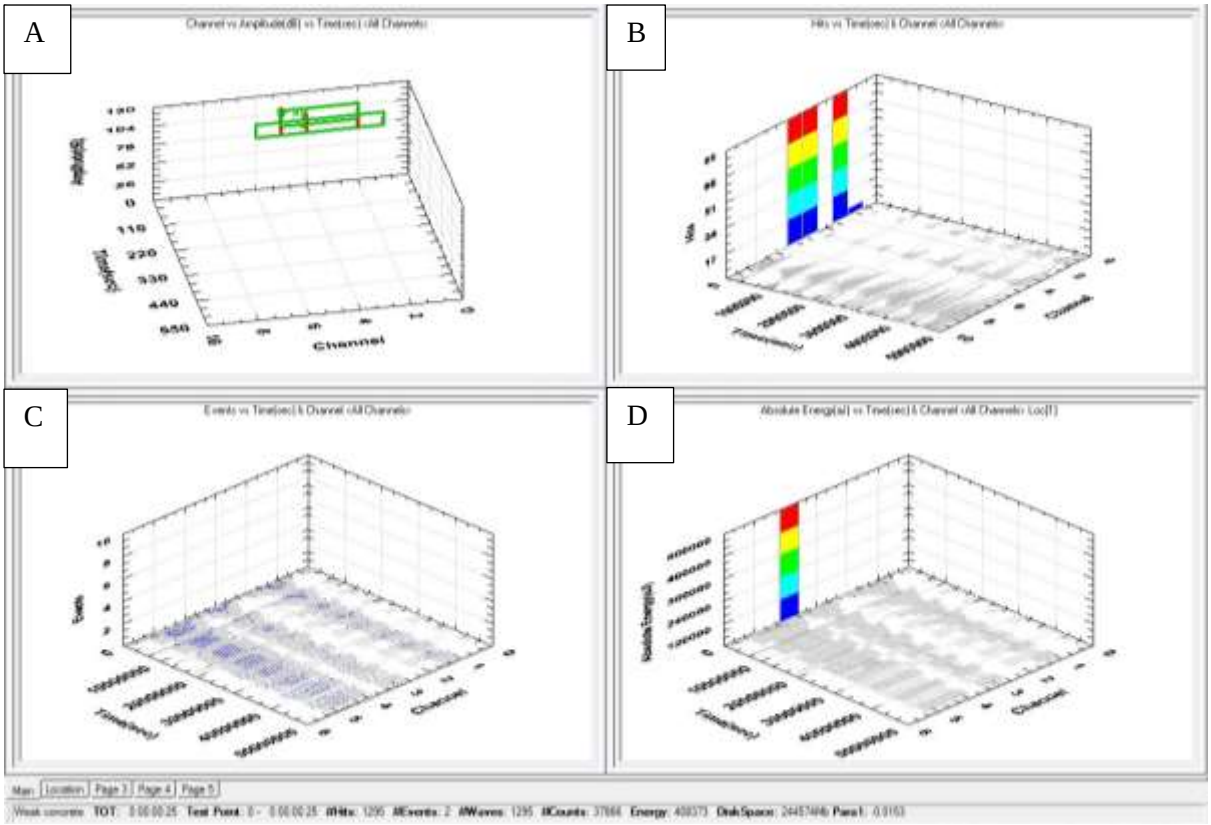

FIGURE 5-119: AMS1 Sensor graphs 55mm to 50mm, A) Acoustic signals detected each channel, B) Hits Vs Time, C) Events Vs time, D) Absolute energy Vs time.

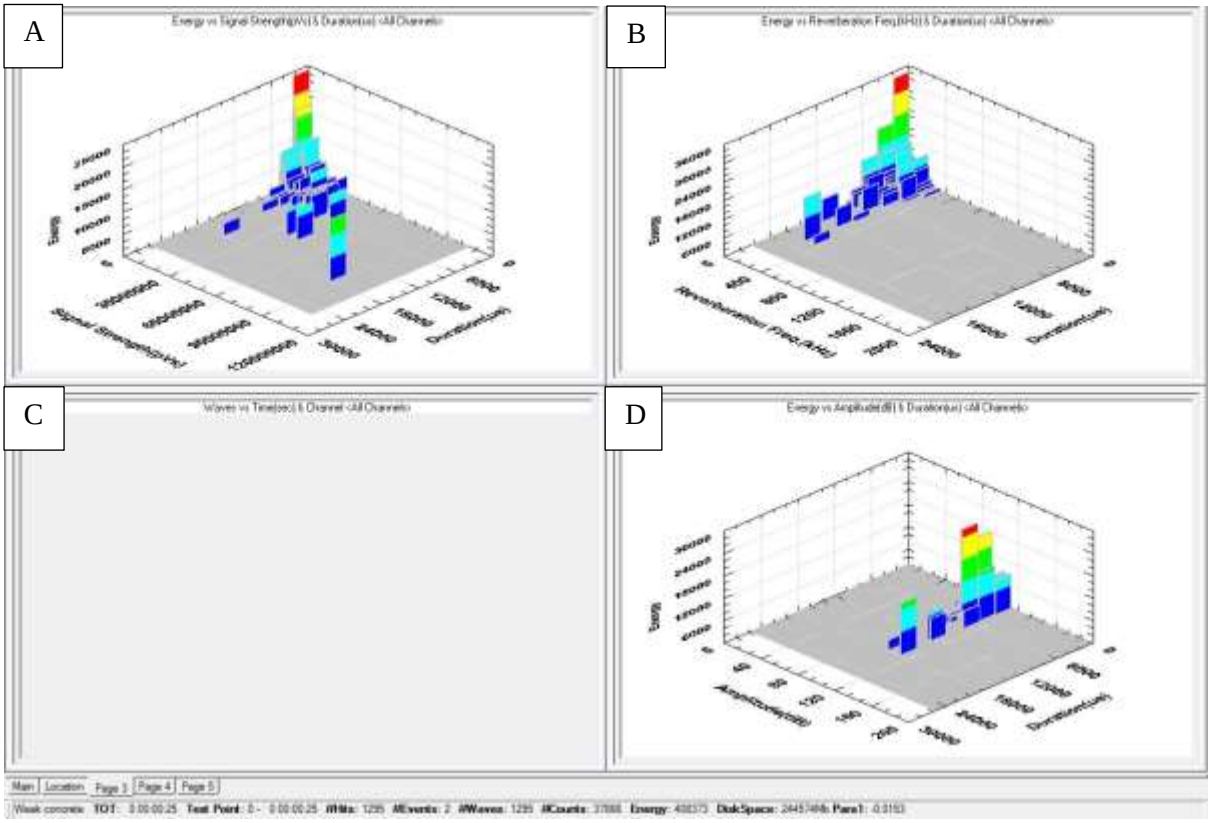

FIGURE 5-120: AMS1 Energy, duration and signal strength graphs 55mm to 50mm, A) Energy Vs signal strength, B) Energy Vs Reverberation, C) Empty, D) Energy Vs Amplitude.

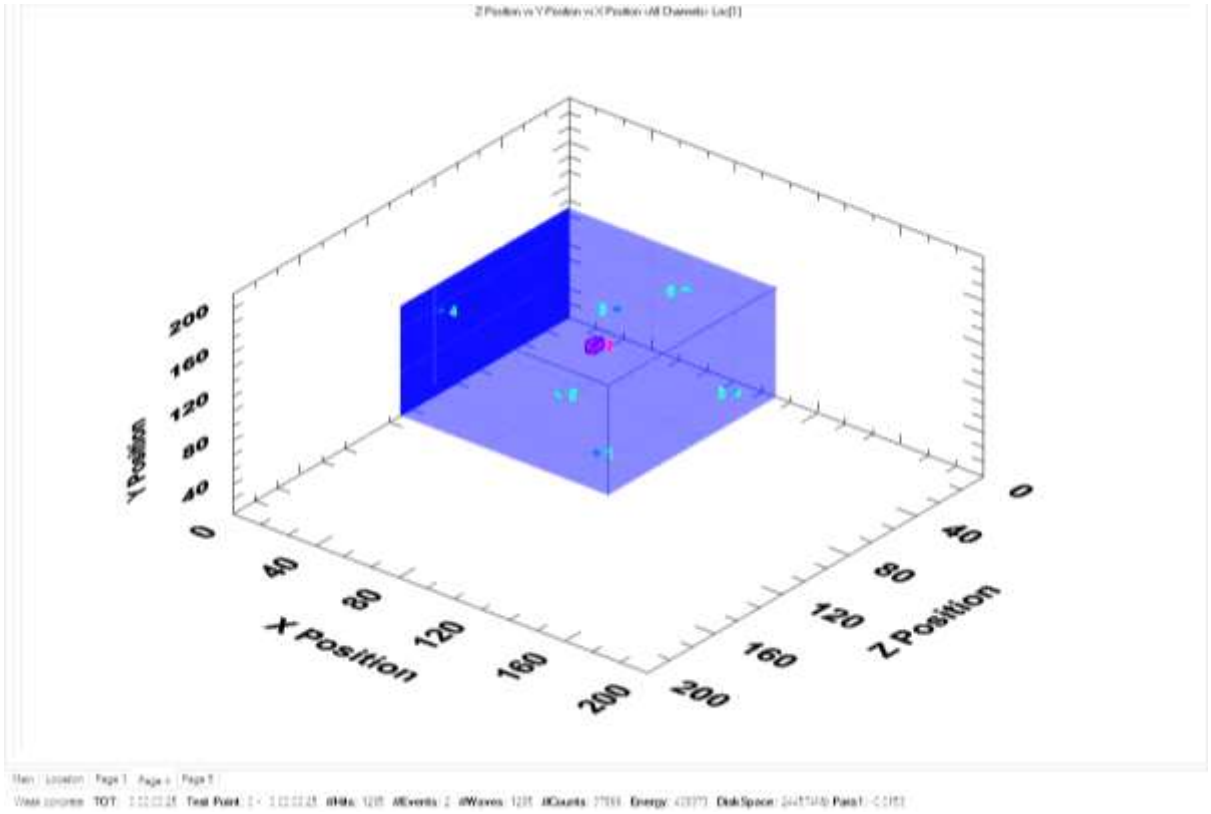

FIGURE 5-121: AMS1 3D graph of events grouped 55mm to 50mm.

In the last 5mm of drilling 1295 hits were detected assigned to two events. This is a much larger proportion of events to hits with no real change in the shale sample. The placement of the two events equates closely to the actual location of the end of the drill bit at approximately 50mm on both the Y and X axes, shown in Figure 5-118 and Figure 5-121. Thus, there is a continued improvement in placement of the events as the drill extends further into the sample. This can be only explained by the fact that there is an equal amount of material of both densities surrounding the drill bit, the source of the acoustic emission, when the drill bit is in the middle of the sample. This means there are waves hitting the different medium at approximately the same time, Figure 5-119. Although this will still cause distortions, the distortions will be much smaller. This is further validated in Figure 5-120, which shows that the main energy peak (approximately 280,000J) is still at the lowest signal strength of approximately 5ρVs with a duration of less than 1,000μsec. However, despite the weak signal strength the energy recorded at an upper signal strength is approximately 890,000ρVs at a duration of approximately 18,000μsecs. This is greater than any of the other energies recorded in the previous drilling intervals of AMS1.

POINT OF FRACTURE

The data for the acoustic placings and the emissions detected for the fracturing process are presented in Figure 5-122 to Figure 5-124.

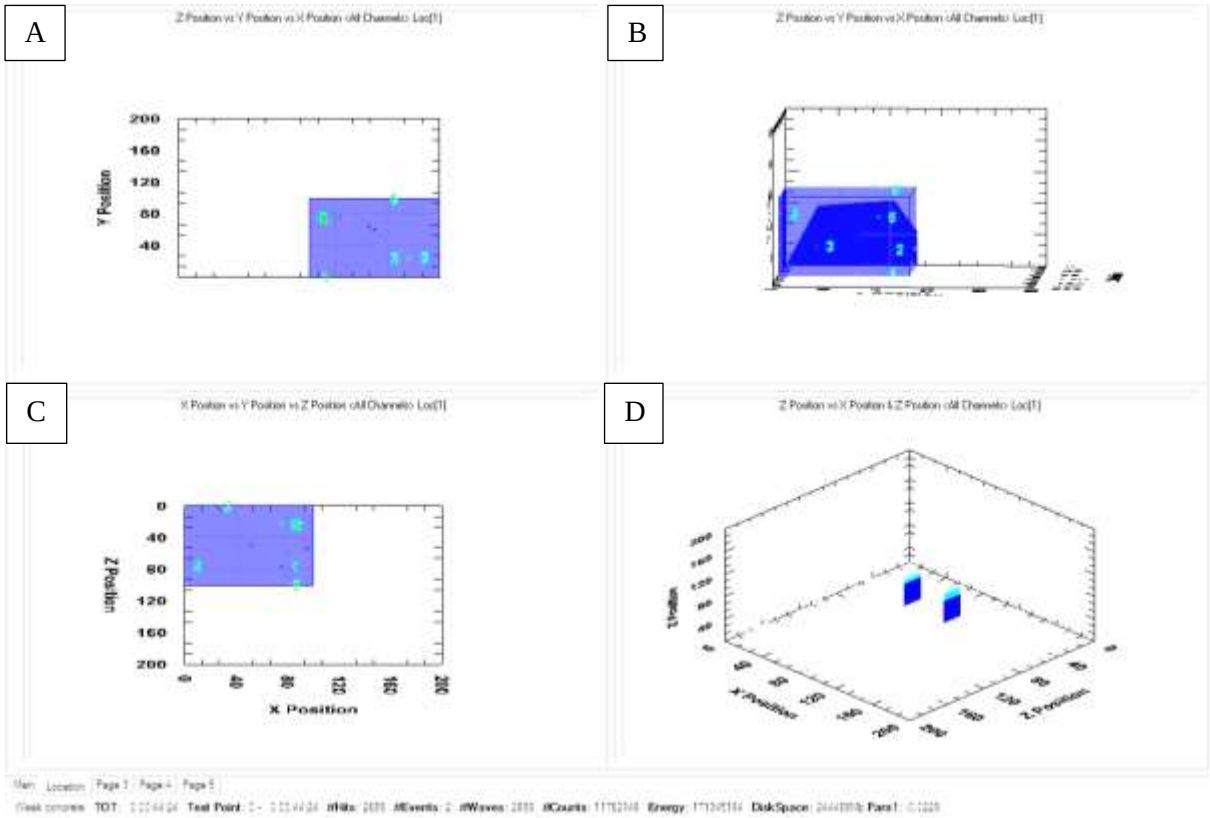

FIGURE 5-122: AMS1; Location graphs point of fracture, A) Depth view, B) 3D view, C) Overhead view, D) Actual positioning spots.

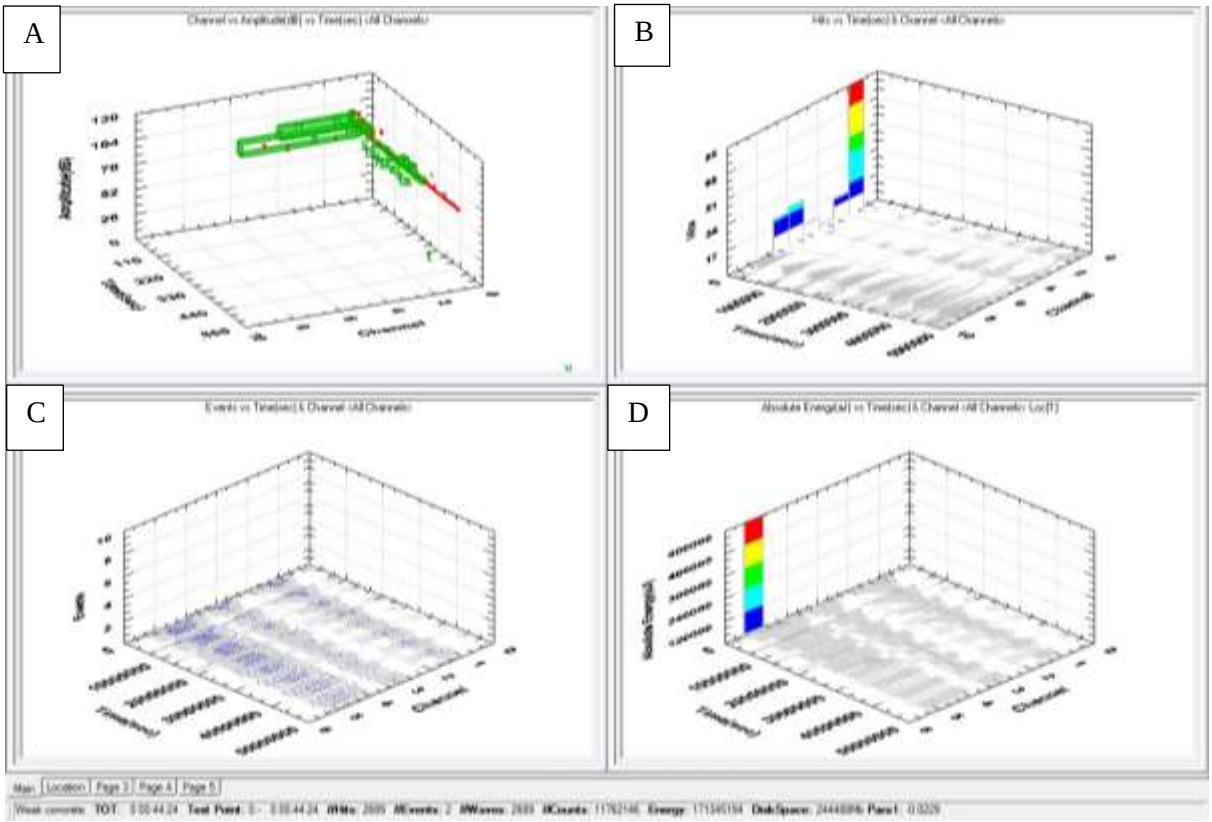

FIGURE 5-123: AMS1 Sensor graphs point of fracture, A) Acoustic signals detected each channel, B) Hits Vs Time, C) Events Vs time, D) Absolute energy Vs time.

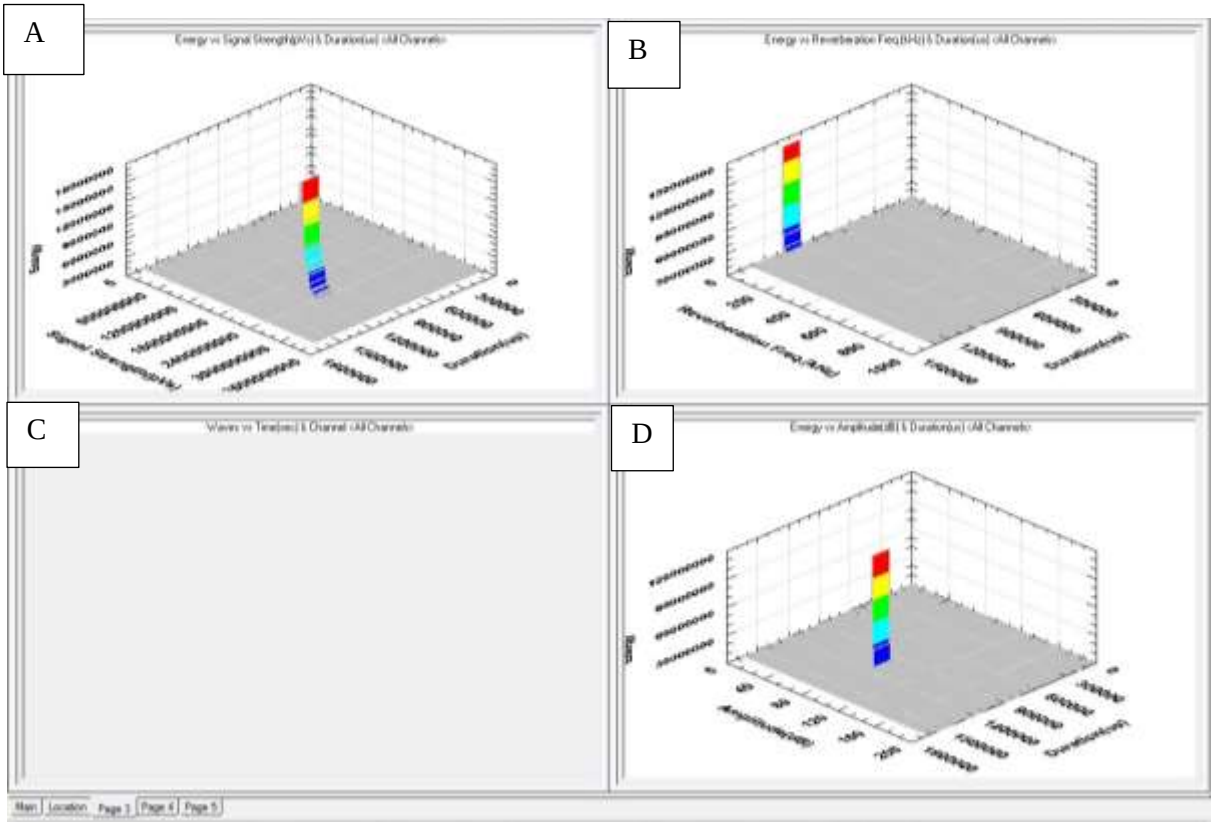

FIGURE 5-124: AMS1 Energy, duration and signal strength graphs point of fracture, A) Energy Vs signal strength, B) Energy Vs Reverberation, C) Empty, D) Energy Vs Amplitude.

As shown in Figure 5-122 2689 hits were recorded which produced 2 events, Figure 5-122 & Figure 5-123, one at the point of the initiation of fracture and another in the direction of the fracture. Although it does not give a complete picture of the evolution of the fracture, the short space between the timings of the two points show that the fracture was instantaneous. Although the hits did not transpose into more events, the data provided important information about the energy being released by the fracture. Signal strength, Figure 5-124, did not go below 210,000ρVs and had a maximum energy release of 150,000j. While the groupings of the duration indicate that the entire fracturing process took 1,200,000μsecs, with little reverberation and the quality of the signal strength along with the two hits following the observed direction of the fracture suggests that the fracture is being accurately mapped by the acoustic software. The lack of events provides important indications on how to improve the experiment to increase the likelihood of getting decent data for the next sample.

5.7.1.2 AMS2

For the AMS2 sample the areas where the acoustic sensors would be placed were scoured to ensure that the sensor would be in direct contact with the shale so that the signals would not have to pass through two different mediums. Despite this the sensors did not pick up any acoustic waves in the 100mm to 80mm drilling range. This is probably due to the fact that the drill bit was still drilling through the plaster and not the shale.

80MM TO 70MM

The data and plots from the acoustic software is presented below in Figure 5-125 to Figure 5-128.

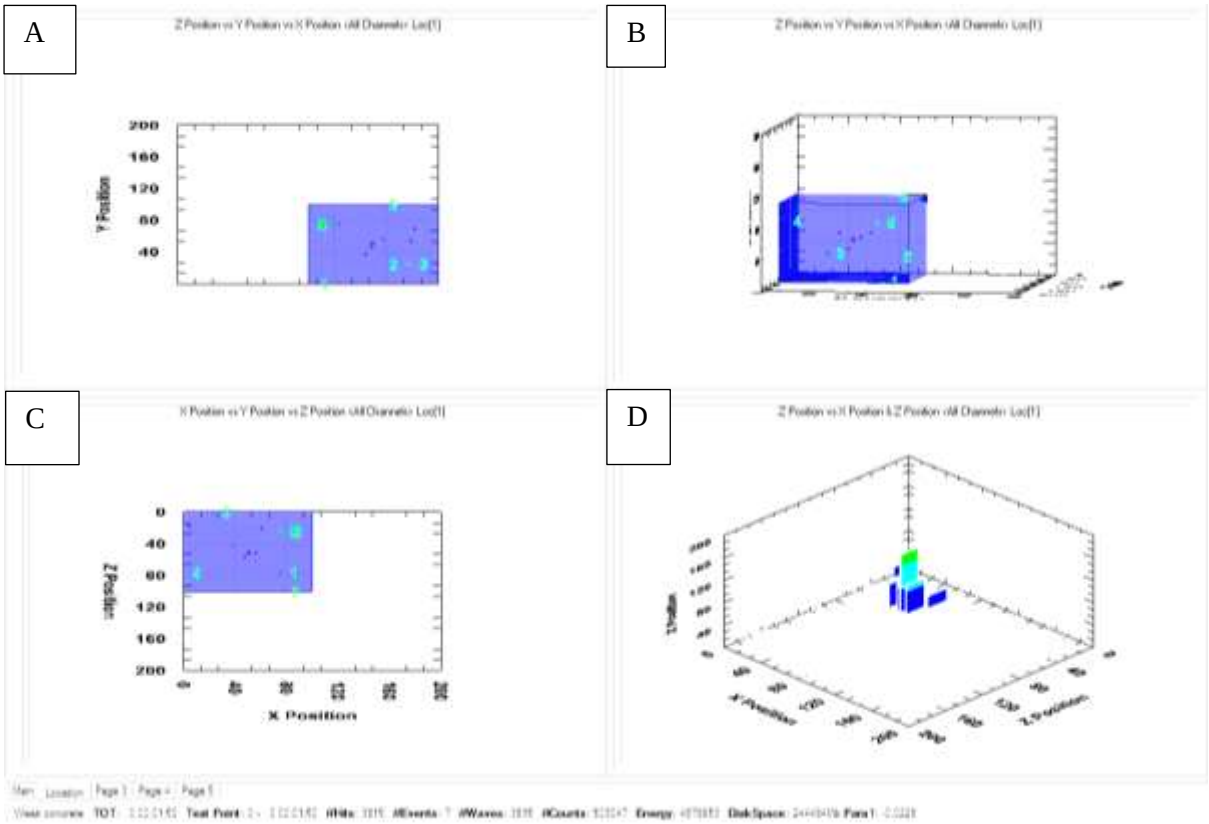

FIGURE 5-125: AMS2 location graphs 80mm to 70mm, A) Depth view, B) 3D view, C) Overhead view, D) Actual positioning spots.

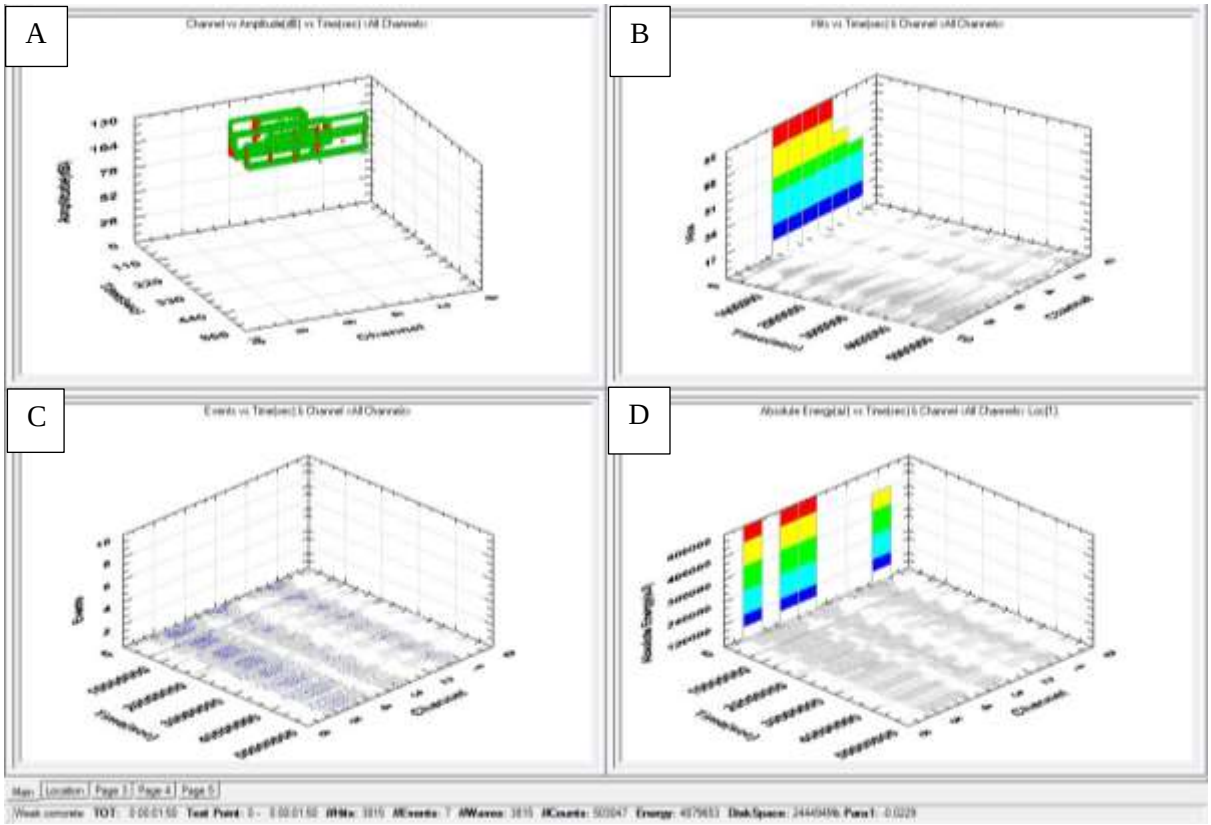

FIGURE 5-126: AMS2 Sensors graphs 80mm to 70mm, A) Acoustic signals detected each channel, B) Hits Vs Time, C) Events Vs time, D) Absolute energy Vs time.

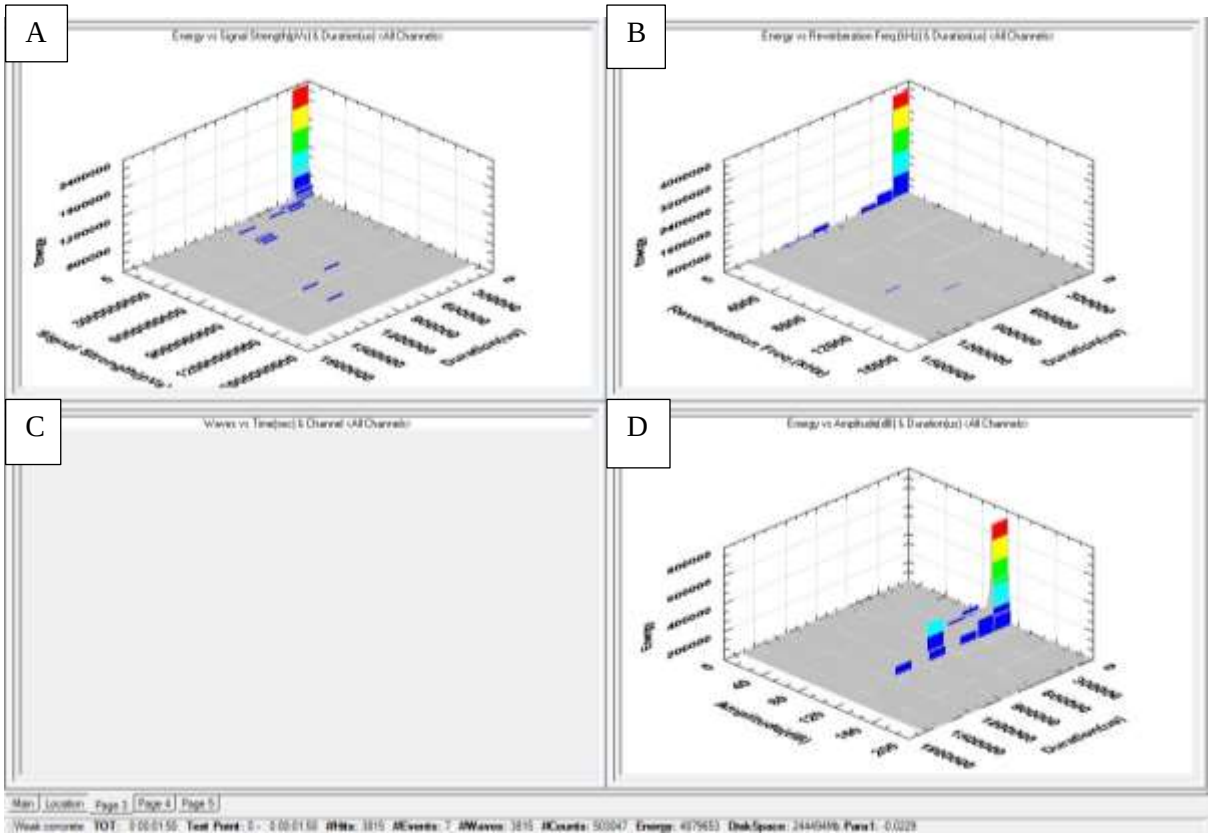

FIGURE 5-127: AMS2 Energy, duration, signal strength graphs 80mm to 70mm, A) Energy Vs signal strength, B) Energy Vs Reverberation, C) Empty, D) Energy Vs Amplitude.

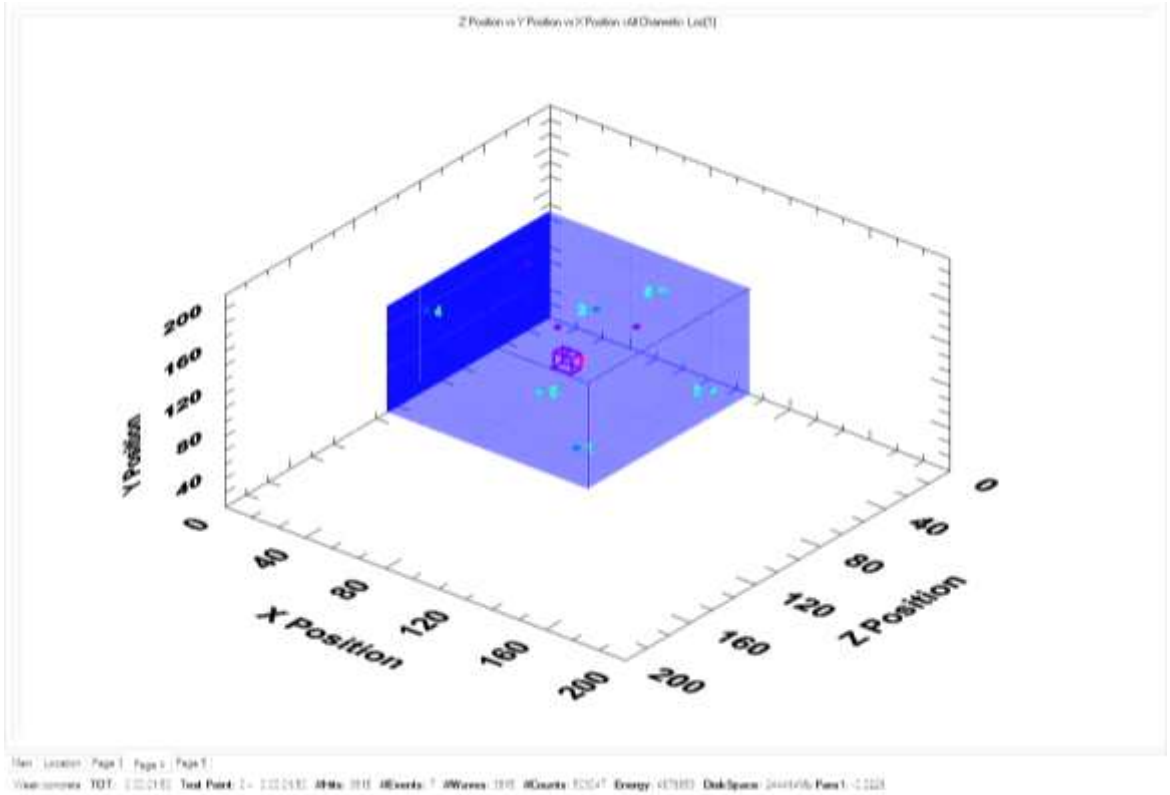

FIGURE 5-128: AMS2 3D graph grouped 80mm to 70mm.

Figure 5-125 & Figure 5-126 show that 3815 acoustic hits were recorded which gave 7 events. A big improvement on the data recorded for AMS1. Four of the events ranged from approximately 65mm to 70mm with one located at 39mm. The overhead view, Figure 5-125, shows that most were centred in the middle, again confirming the observation made in the commissioning phase that damage during drilling seems to be concentrated below the drill bit and down the sides of the drill as would be expected. This is further substantiated when the four most centred events, ranging from a height of 39mm to 65mm, all grouped together in one form and the other three can be seen in line with where the sample fractured during drilling at the 60-50mm mark. This could potentially indicate early signs of damage to the rock in the area where the fracture occurred, Figure 5-125 & Figure 5-128.

The total energy emitted by the acoustic emissions was 4879653J. Figure 5-127 shows that this energy 366,000J had a duration of less than 100,000μsecs with a reverberation of approximately 5kHz and a signal strength of less than 100,000,000ρVs. The range was significantly lower than recorded in any drilling interval for sample AMS1 and so provides greater confidence that the acoustic data is spatially mapping the locations of the fractures.

70 TO 60MM

The data collected by the acoustic software is presented in Figure 5-129 to Figure 5-132.

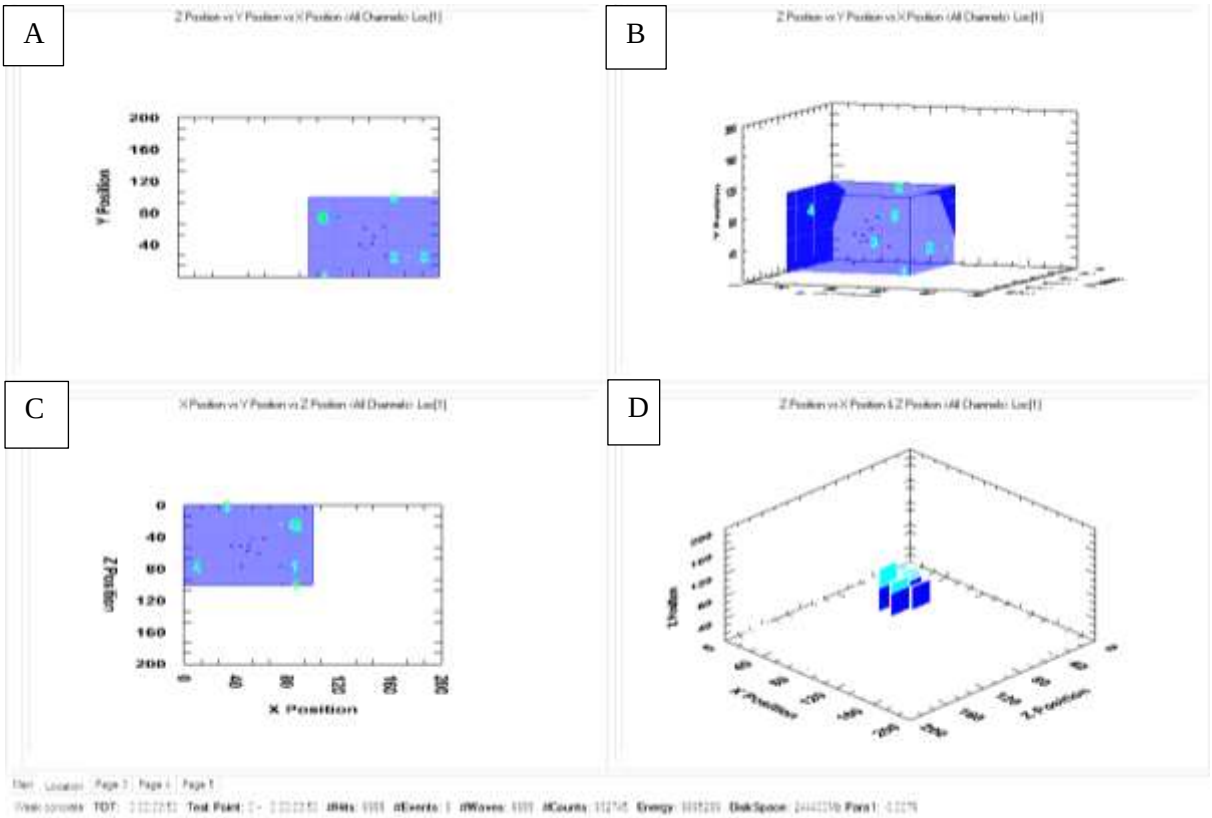

FIGURE 5-129: AMS2 location graphs 70mm to 60mm, A) Depth view, B) 3D view, C) Overhead view, D) Actual positioning spots.

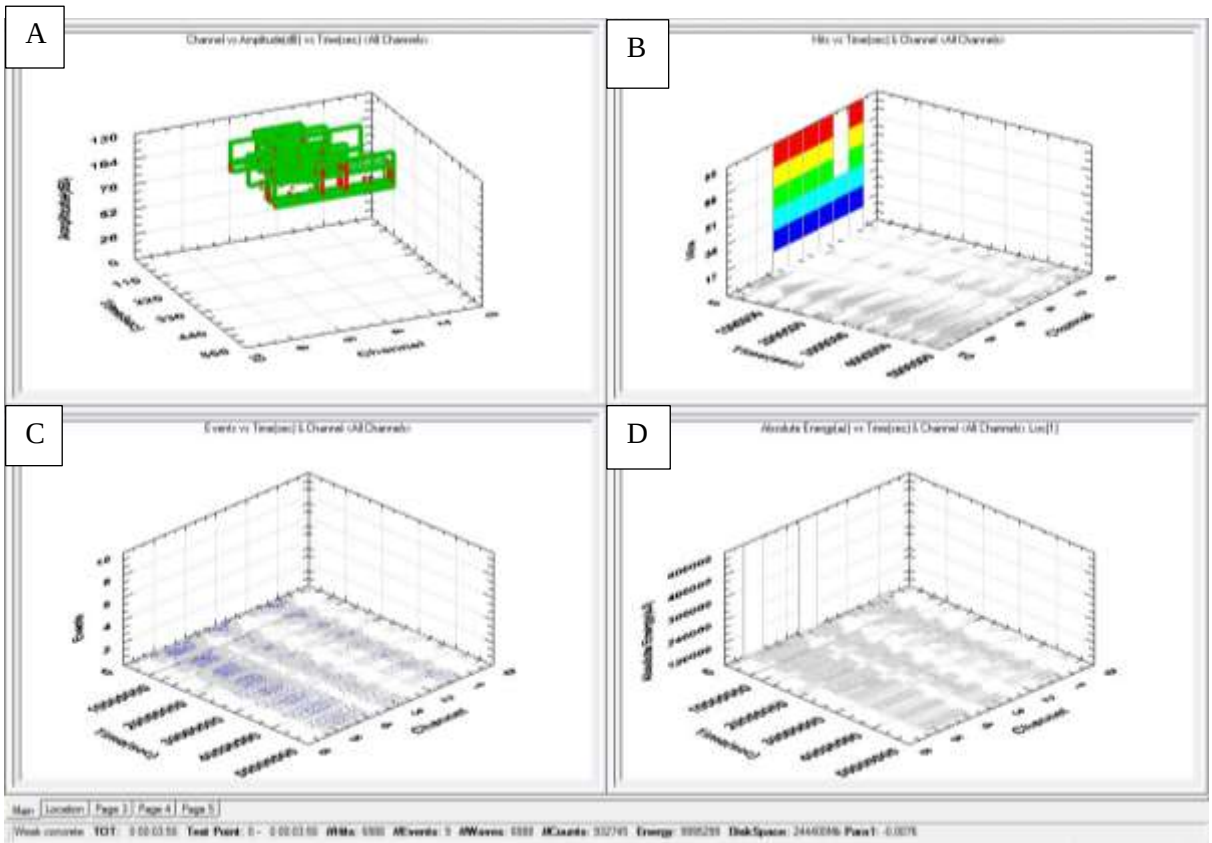

FIGURE 5-130: AMS2 sensors graphs 70mm to 60mm, A) Acoustic signals detected each channel, B) Hits Vs Time, C) Events Vs time, D) Absolute energy Vs time.

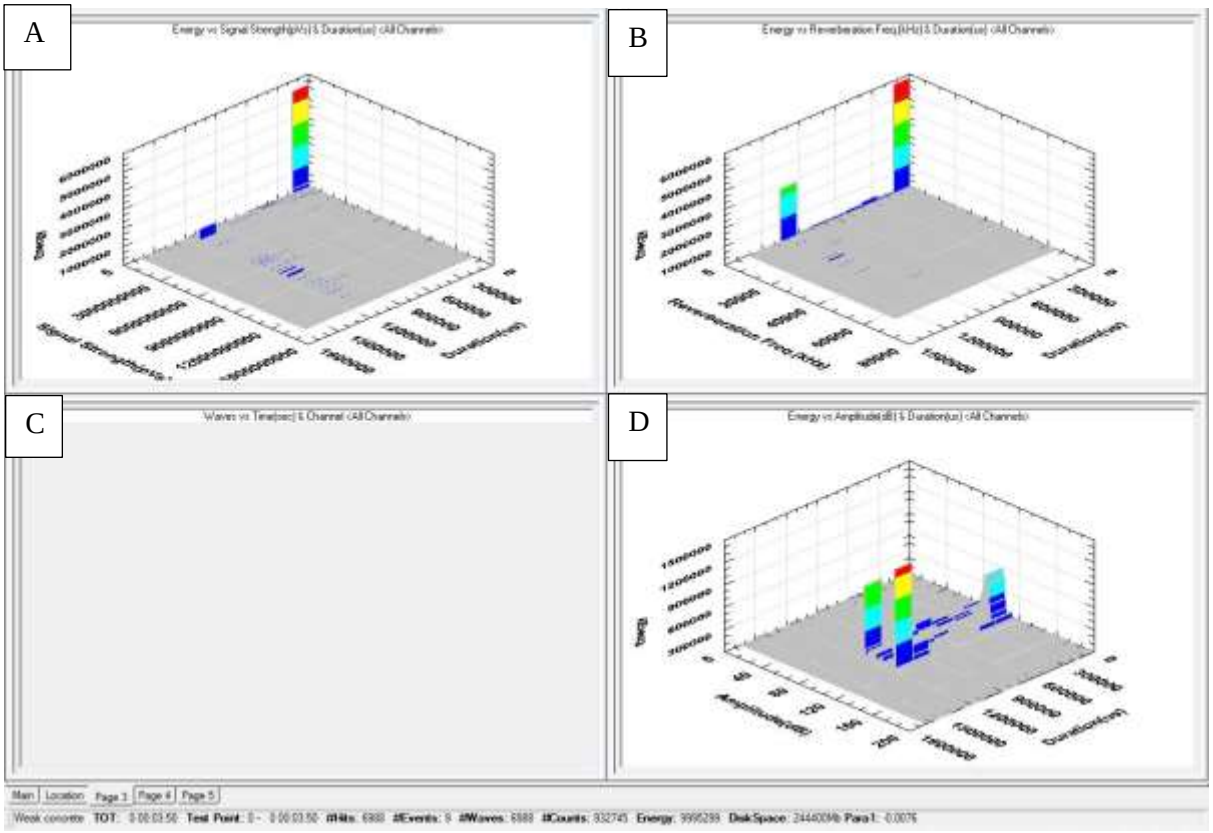

FIGURE 5-131: AMS2 Energy, duration and signal strength 70mm to 60mm, A) Energy Vs signal strength, B) Energy Vs Reverberation, C) Empty, D) Energy Vs Amplitude.

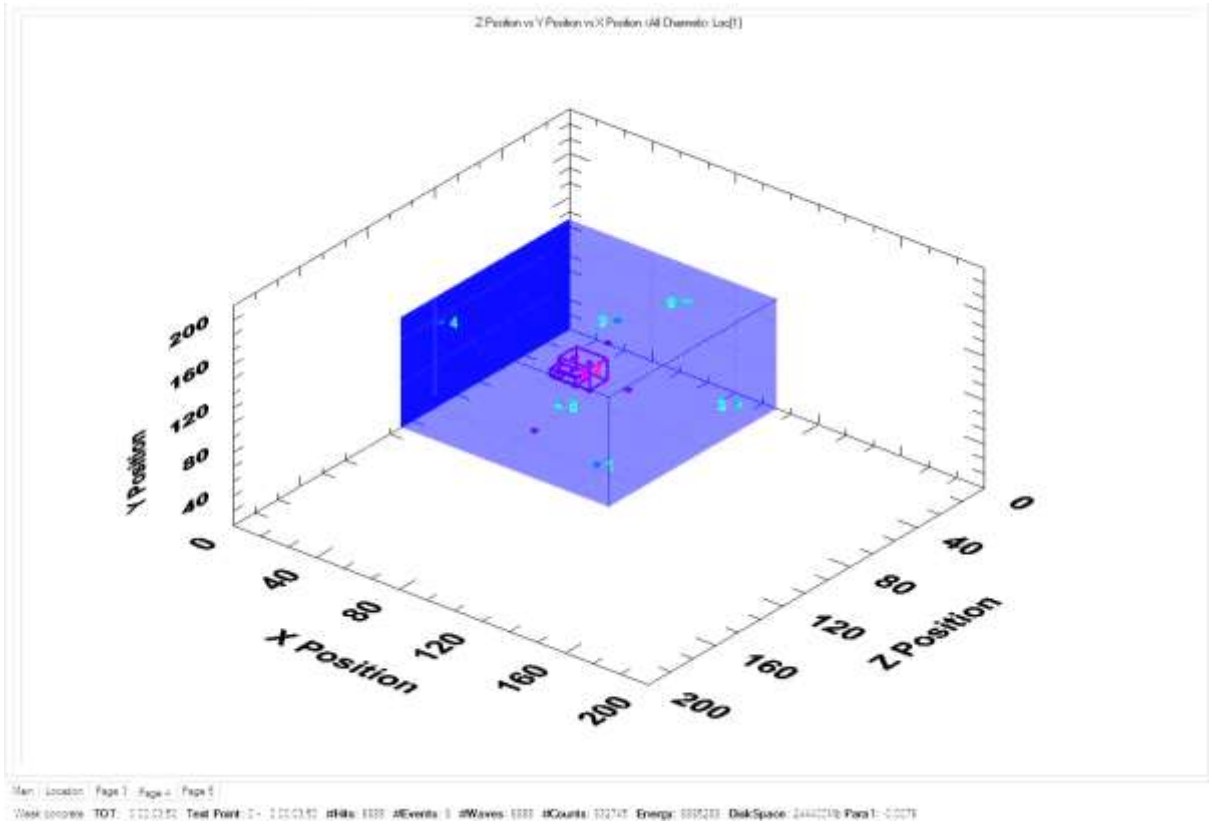

FIGURE 5-132: AMS2 3D graph Events grouped 70mm to 60mm.

Figure 5-129 & Figure 5-130 show 6988 hits were recorded giving 9 events, this was a reduction in the proportion of hits to events, however, the majority of the hits are well centred on the overhead view. Four of the events are at the base or just below the base of the drill bit 62mm to 35mm, with 2 at the side of the borehole and probably representing damage to the drill scraping the inside of the borehole, but as expected for a smooth rotary movement there is less damage compared to the drill bit which is actually forcing apart the solid sediment. One event lies well below the others at a height of 26mm along the Y axis and 40mm along the X axis and approximately 65mm on the Z axis. As noted in the 80 to 70mm drilling interval this event follows the line of the observed fracture that occurred during drilling through the 60 to 50mm interval. This means that accidental fractures in reservoir rocks are not as instantaneous as those recorded in induced fractures but that the growing damage causes a break down in the inherent strength of the rock until it is not able to withstand the pressures caused by the drilling creating a large fracture.

The sensors recorded a total energy of 99,952,999J as shown in Figure 5-131. Figure 5-131 also shows there was less reverberation and the majority of the energy 6,000,000J was of a low duration <10,000µsecs with reverberation of less than 5kHz and a signal strength of 100ρVs. Again, like the 80 to 70mm drilling interval there was a much reduced spread unlike AMS1, Figure 5-132, which continues to further confirm the theory that recording acoustic waves through two distinct mediums will affect their signals.

60 TO 50MM AND FRACTURE

The acoustic and plot data of this drilling interval and fracture is shown in Figure 5-133 to Figure 5-136.

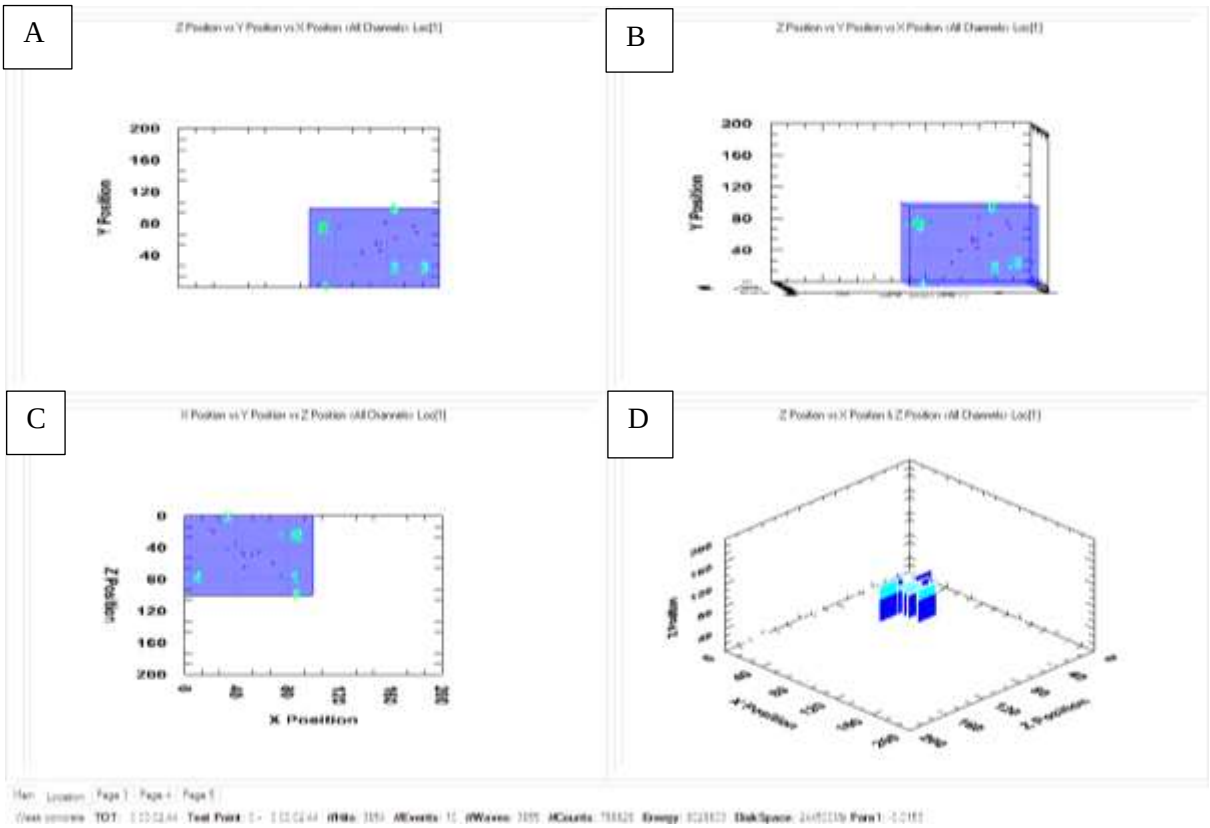

FIGURE 5-133: AMS 2 Location graphs 60mm to 50mm, A) Depth view, B) 3D view, C) Overhead view, D) Actual positioning spots.

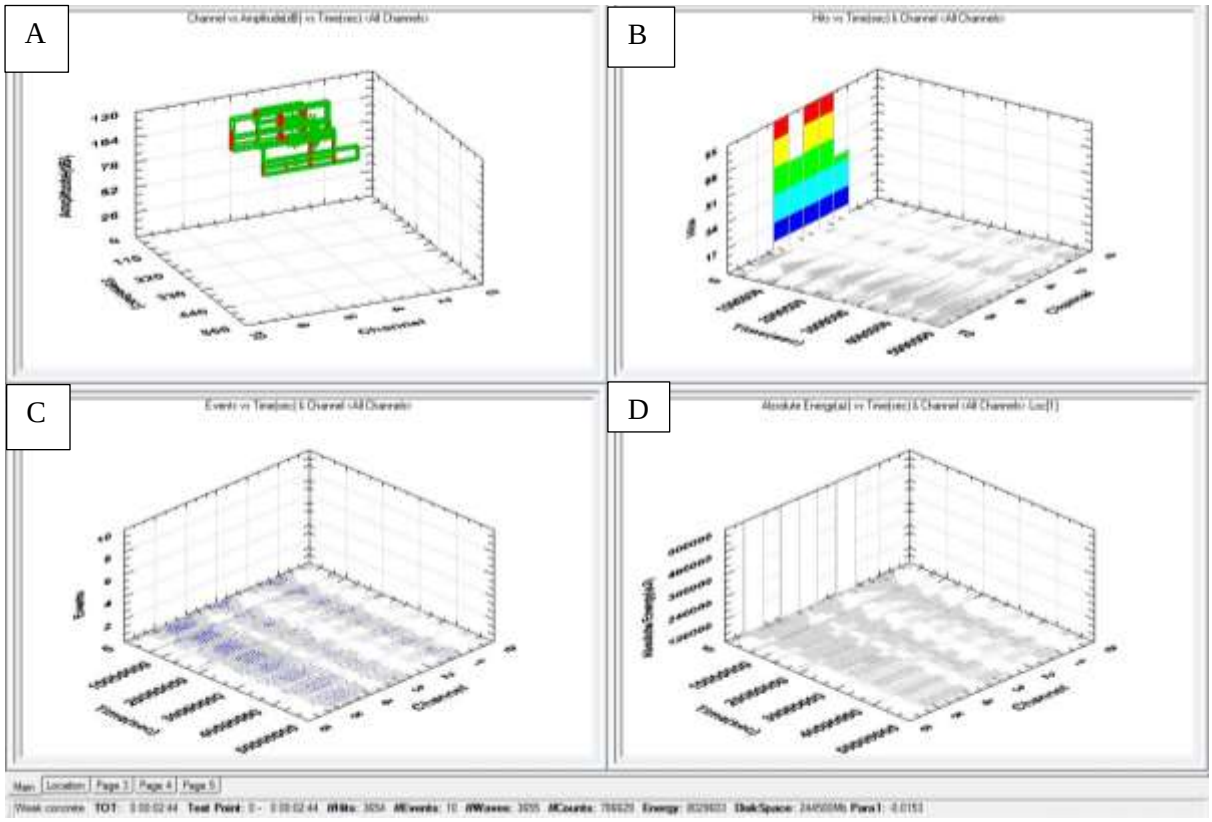

FIGURE 5-134: AMS2 Sensor graphs 60mm to 50mm, A) Acoustic signals detected each channel, B) Hits Vs Time, C) Events Vs time, D) Absolute energy Vs time.

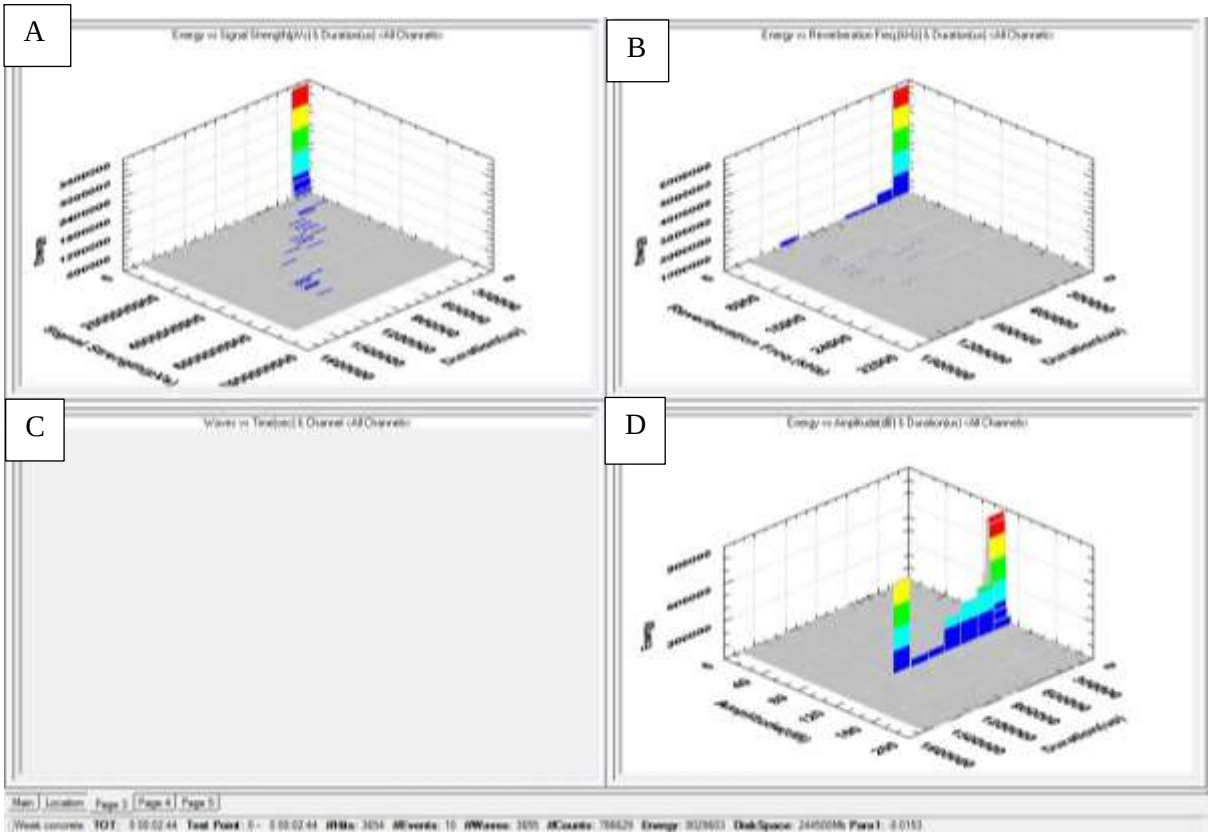

FIGURE 5-135: AMS2 Energy, duration, signal strength graphs 60mm to 50mm, A) Energy Vs signal strength, B) Energy Vs Reverberation, C) Empty, D) Energy Vs Amplitude.

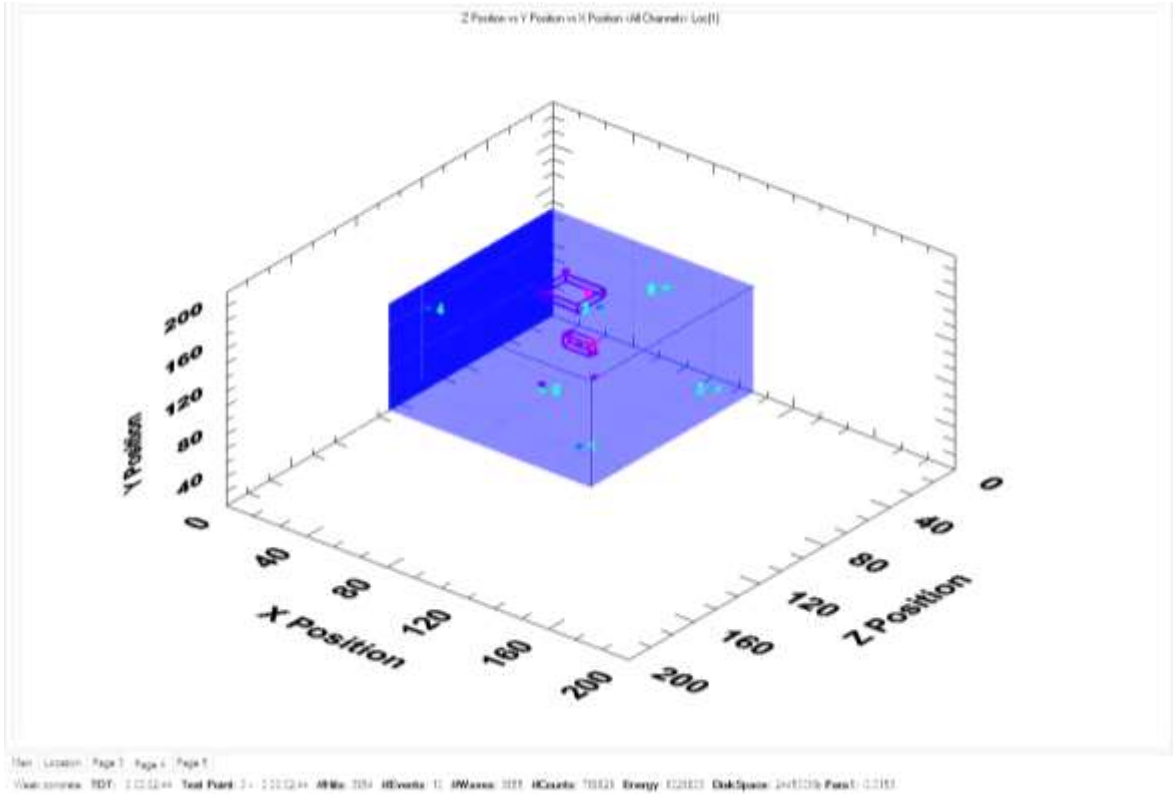

FIGURE 5-136: AMS2 3D graph of events grouped 60mm to 50mm.

Figure 5-132 to Figure 5-133 shows 10 events for a total of 3654 hits. This is a much improved proportion of events to hits, it is also important to note that the majority of the hits are within the drilling depth and are centred in both the side view and horizontal view. What is of interest, though, are the events that cut across the side view and the overhead view in Figure 5-133. These events mirror the fracture pattern that the drilling induced just as the drill bit reached 50mm in the Y scale. Although not many in number, events following the line of fracture that appeared at the same time are a good indication that the acoustic sensors picked up the fracture event and that the nature of these events being recorded at the same time indicate the fracture again was instantaneous. The total energy of the event was 8,029,603j as seen in Figure 5-135 the duration of most samples was <than 10,000µsecs, >7,500,000j which had a reverberation of less than 5Khz. This lack of reverberation could explain the ability of the acoustics to pick up a more accurate line of the fracture.

5.7.1.3 WBS1

This sample crumbled repeatedly for the first 20mm of drilling, however, the acoustic data and graphs for this sample are presented in Figure 5-137 to Figure 5-139.

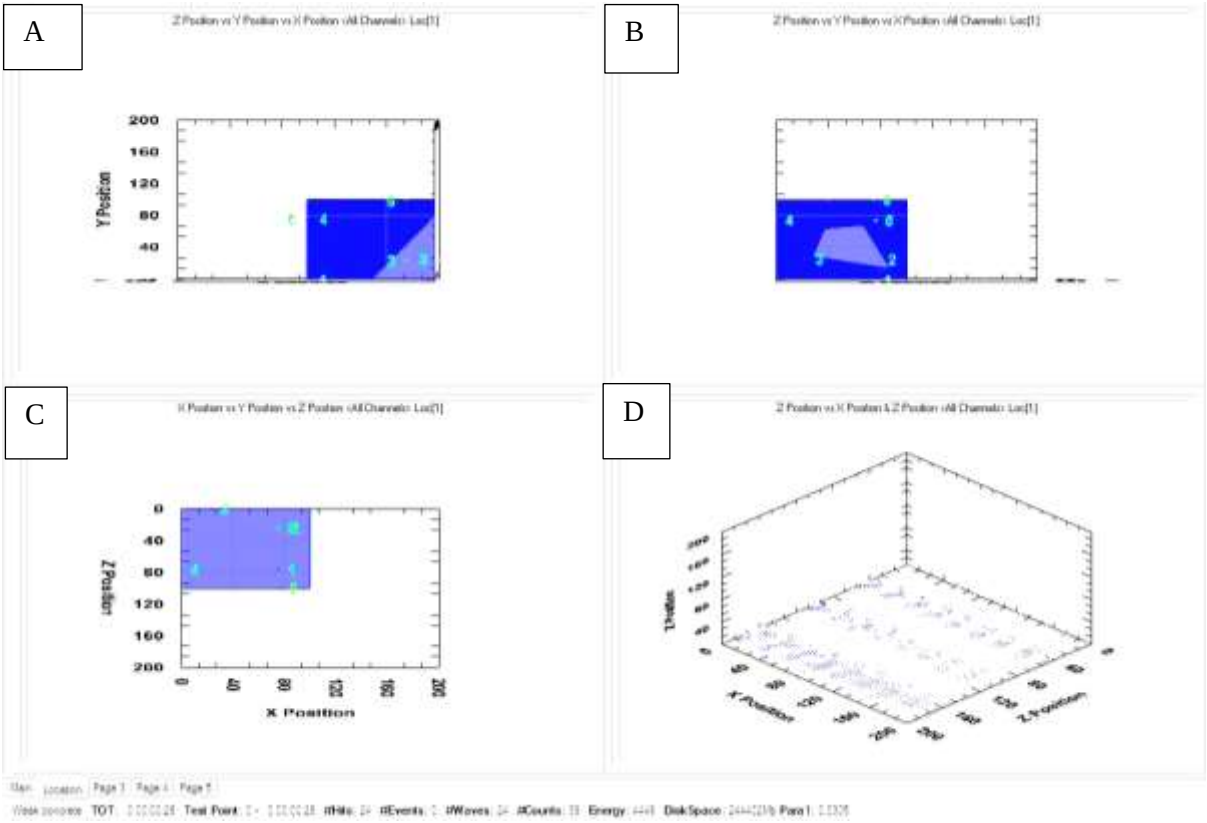

FIGURE 5-137: WBS1 location graphs 100mm to 80mm, A) Depth view, B) 2nd depth view, C) Overhead view, D) Actual positioning spots.

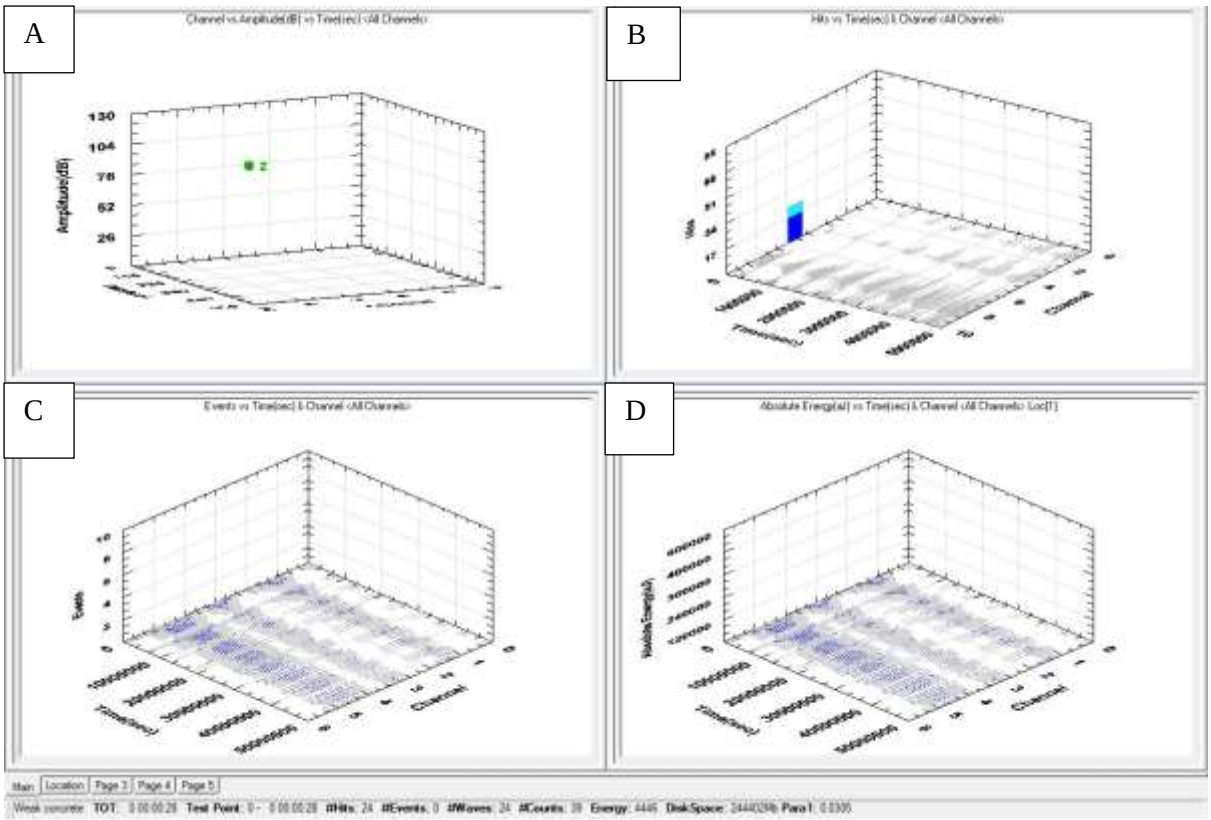

FIGURE 5-138: WBS1 Sensor graphs 100mm to 80mm, A) Acoustic signals detected each channel, B) Hits Vs Time, C) Events Vs time, D) Absolute energy Vs time.

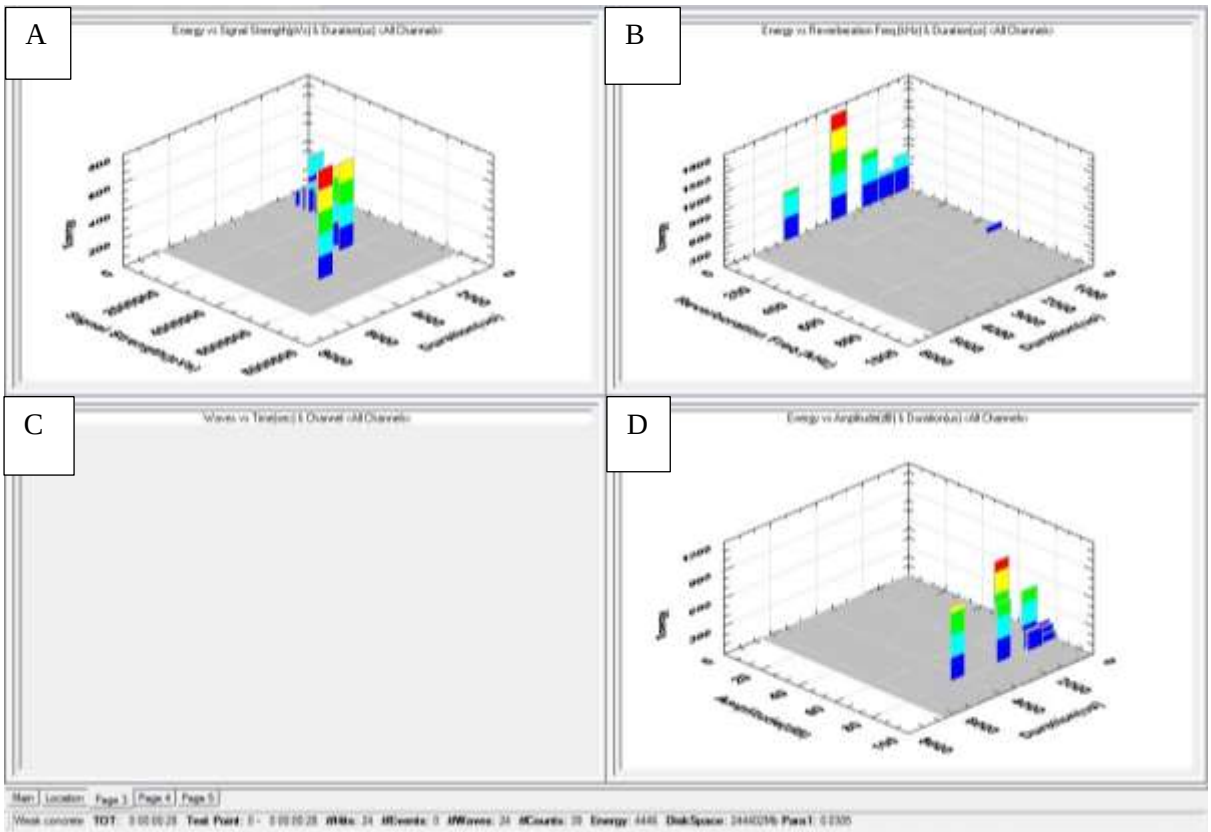

FIGURE 5-139: WBS1 Energy, duration and signal strength 100mm to 80mm, A) Energy Vs signal strength, B) Energy Vs Reverberation, C) Empty, D) Energy Vs Amplitude.

The main location image, Figure 5-137, shows that there were 24 hits detected by the sensors and no events. The constant crumbling of the sample meant even though the sensors had been attached to the shale by sealant, detached and distorted blocks of shale meant that the acoustic waves were not coming through the shale. Indeed it was found upon removal of the sample that sensors 5 and 6 were not attached to the main body of the shale but only to small fragments, thus, explaining the lack of any signals seen in Figure 5-138. The break between the medium and the sensor means that there is a change in medium thus causing a lack of acoustic activity being detected, Figure 5-138 & Figure 5-139.

This data has been included to show the limitations of acoustics and their associated issues that may affect their application in the field. Too much damage to a sample or a reservoir may render unsuitable detection of signals.

5.7.1.4 WBS2

The WBS2 sample was fractured and produced one clean fracture. The drilling was exceptionally soft and instead of recording in 10mm intervals, as intended, the drilling overshot to a 30mm interval.

100MM TO 70MM

The location and graph data collected during the drilling interval, between 100 to 70mm is presented below in Figure 5-140 through to Figure 5-143.

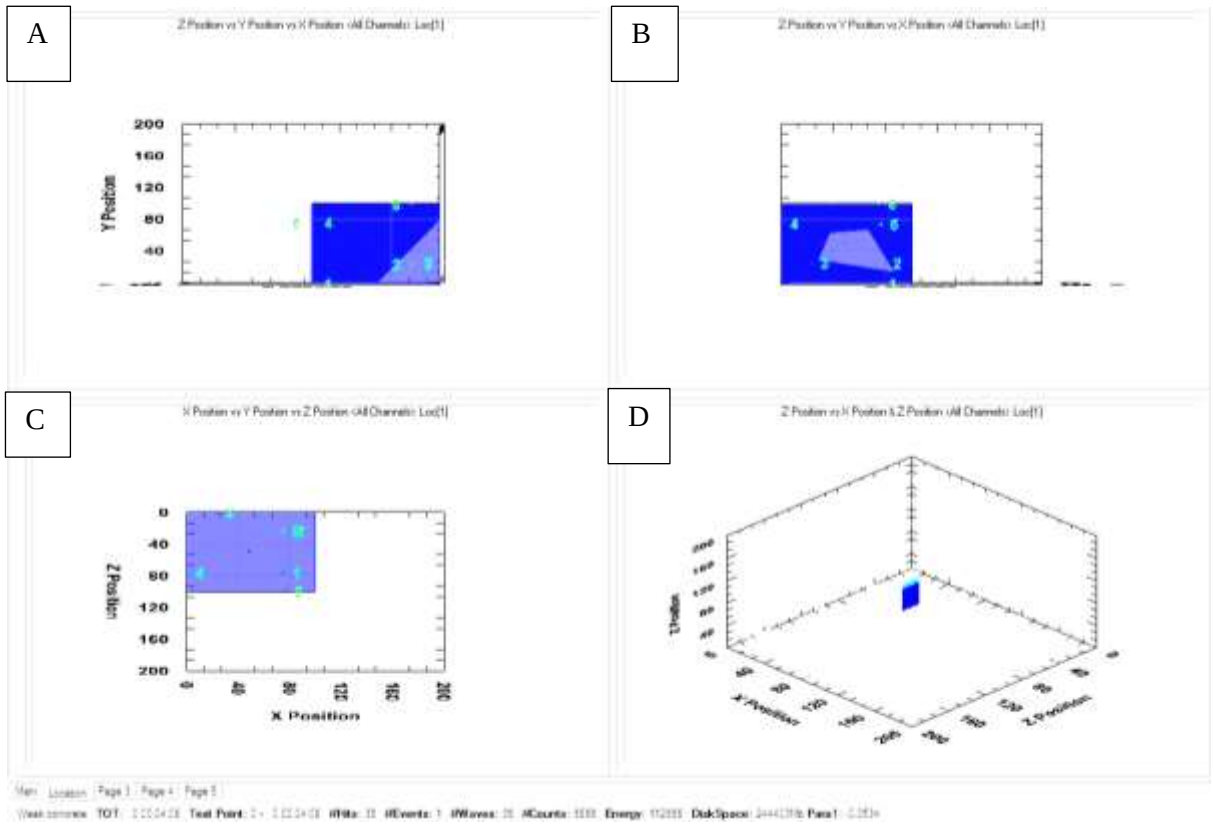

FIGURE 5-140: WBS2 location graphs 100mm to 70mm, A) Depth view, B) 2nd side view, C) Overhead view, D) actual positioning spots.

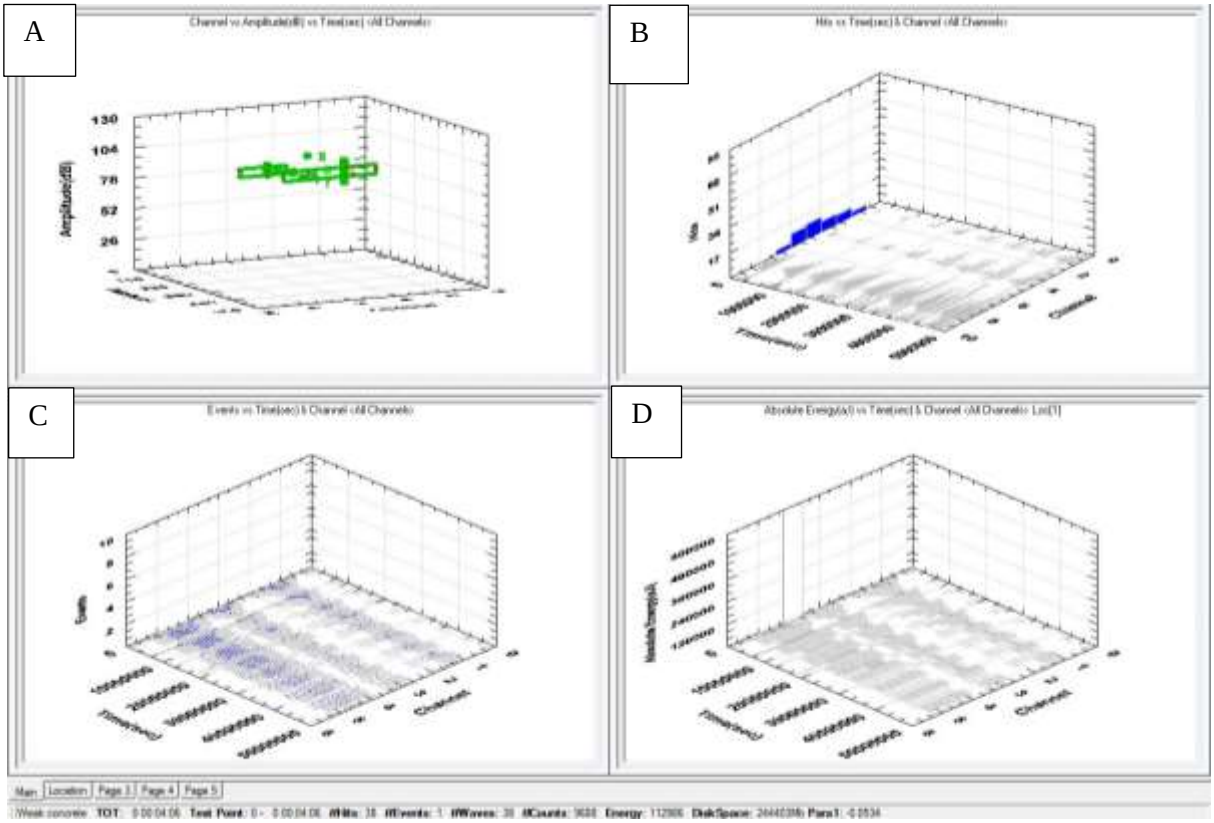

FIGURE 5-141: WBS2 sensor graphs 100mm to 70mm, A) Acoustic signals detected each channel, B) Hits Vs Time, C) Events Vs time, D) Absolute energy Vs time.

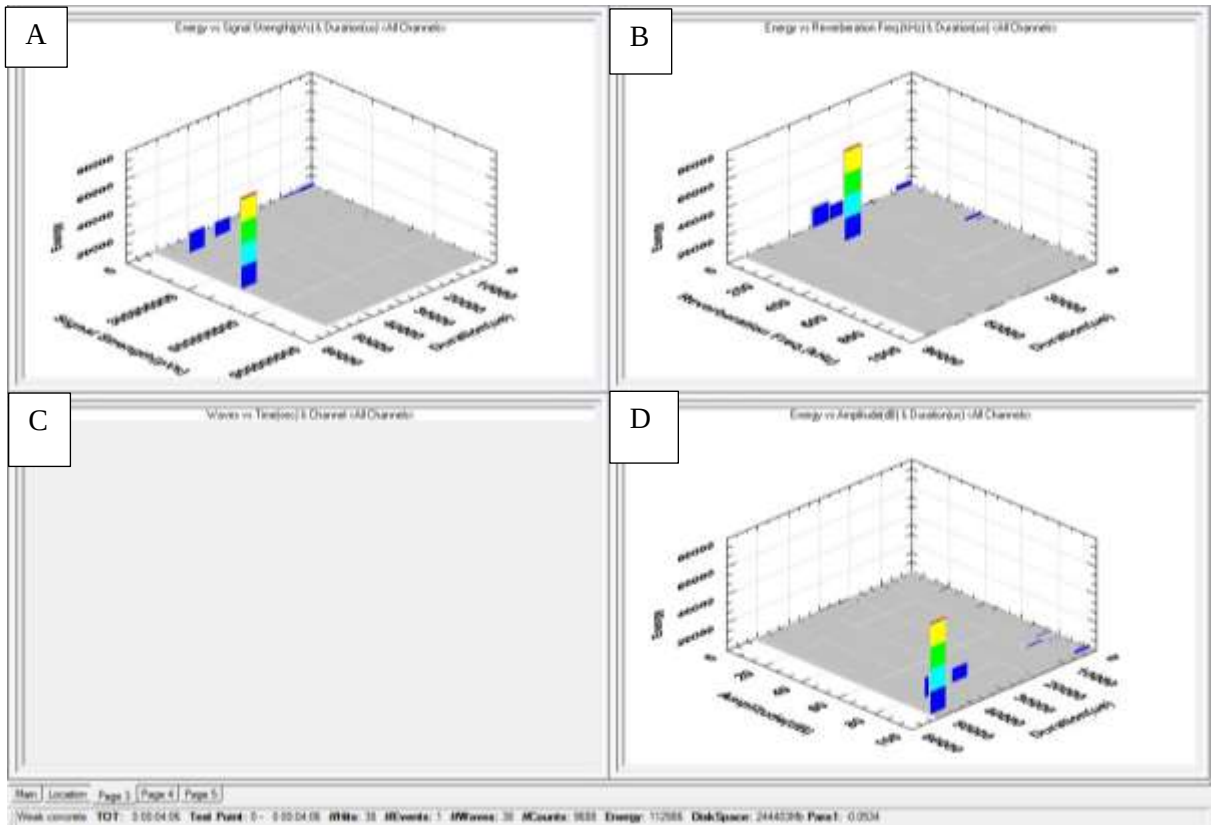

FIGURE 5-142: WBS2 Energy, duration, signal strength 100mm to 70mm, A) Energy Vs signal strength, B) Energy Vs Reverberation, C) Empty, D) Energy Vs Amplitude.

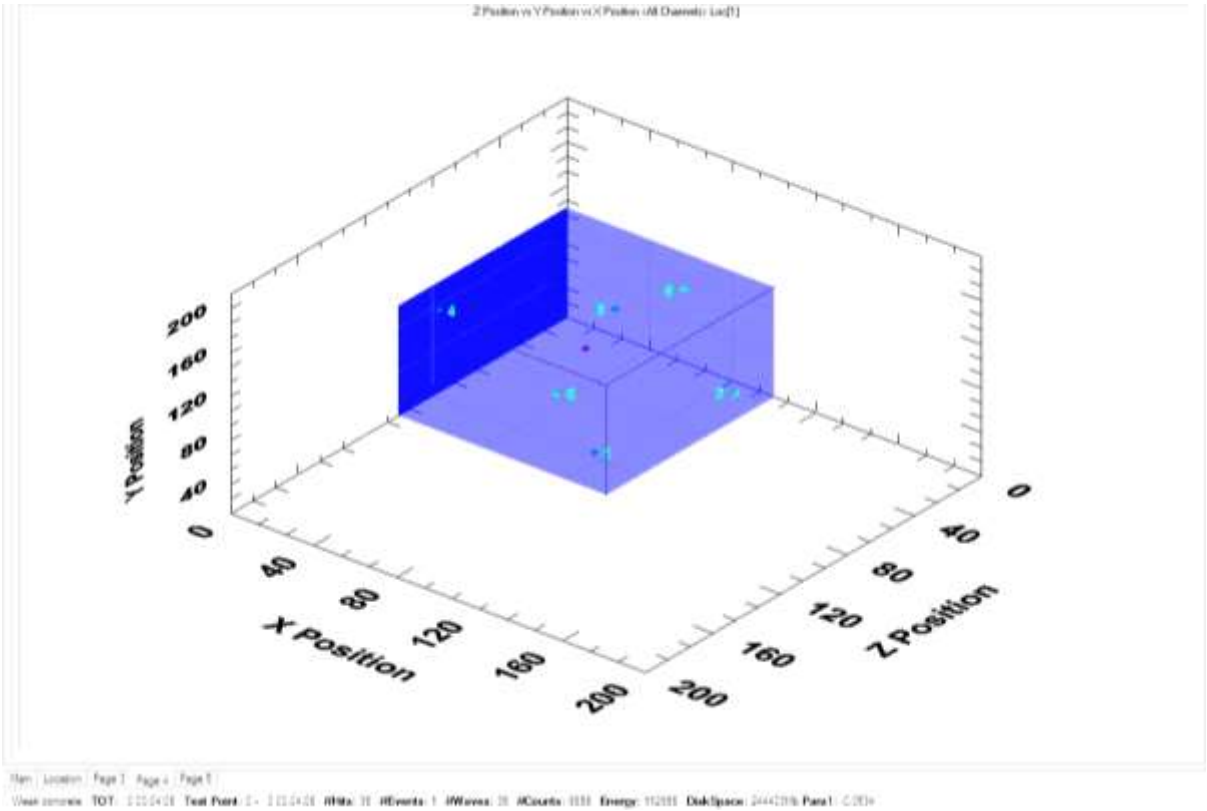

FIGURE 5-143: WBS2 3D graph events grouping 70mm to 500mm to fracture.

As can be seen in Figure 5-140 & Figure 5-141 the sensors picked up 38 hits which translated into just 1 event. Clearly the results of this experiment are not the most promising although the drill clearly shot through the shale with a lot more ease than was expected. The sensors did not pick up much, despite being in direct contact with the shale. With only one event detected, not much can be gained from analysing the results or the inability of the sensors to pick anything up. With only 38 hits the energy itself, Figure 5-142, was low at only 112,986J and there is little in the way of the data to actually locate a source area.

70MM TO 50MM AND FRACTURE.

Again, similar to the previous drilling run, there were very few returns picked up during the drilling of the sample between 70mm to 50mm. The sensors were kept on to include the fracturing of the rock as there had been no events placed during the drilling. The acoustic and graphic data is presented in Figure 5-144 to Figure 5-147.

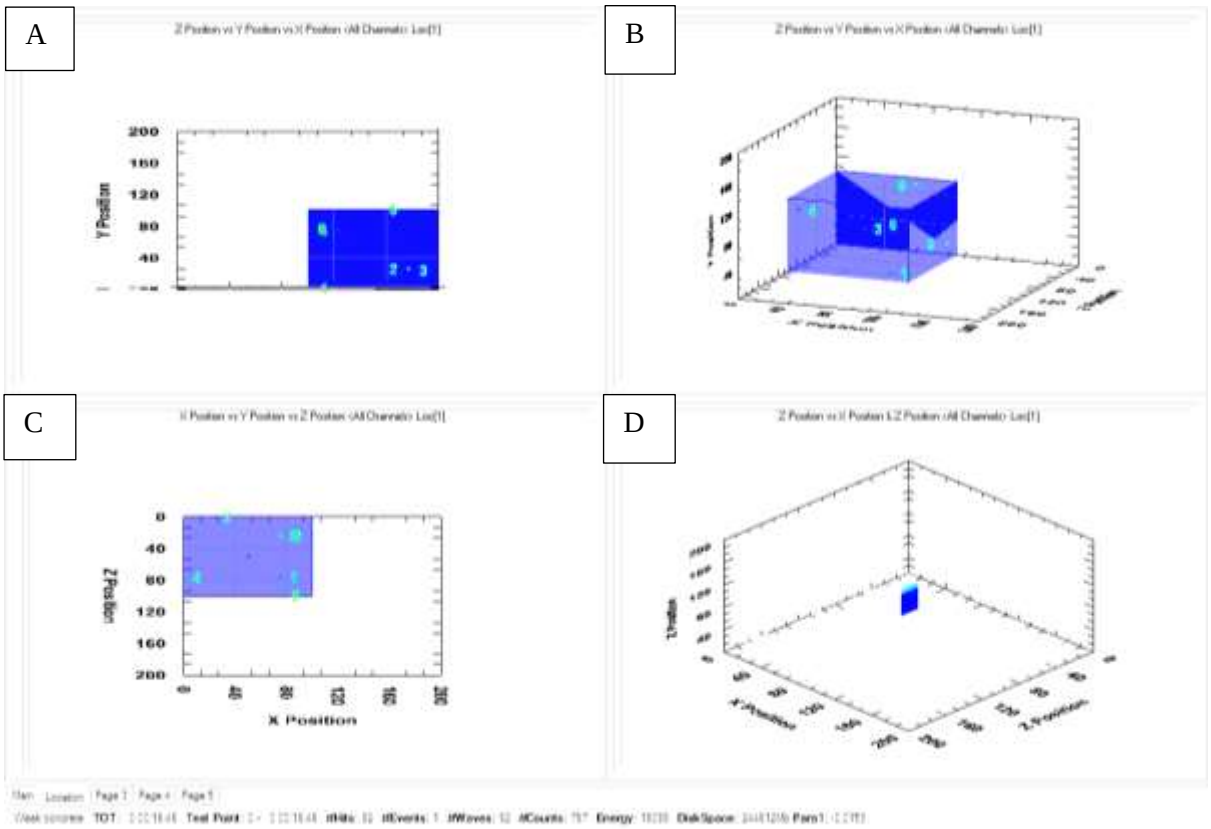

FIGURE 5-144: WBS2 location graphs 70mm to 50mm to fracture, A) Depth view, B) 3D view, C) Overhead view, D) actual positioning spots.

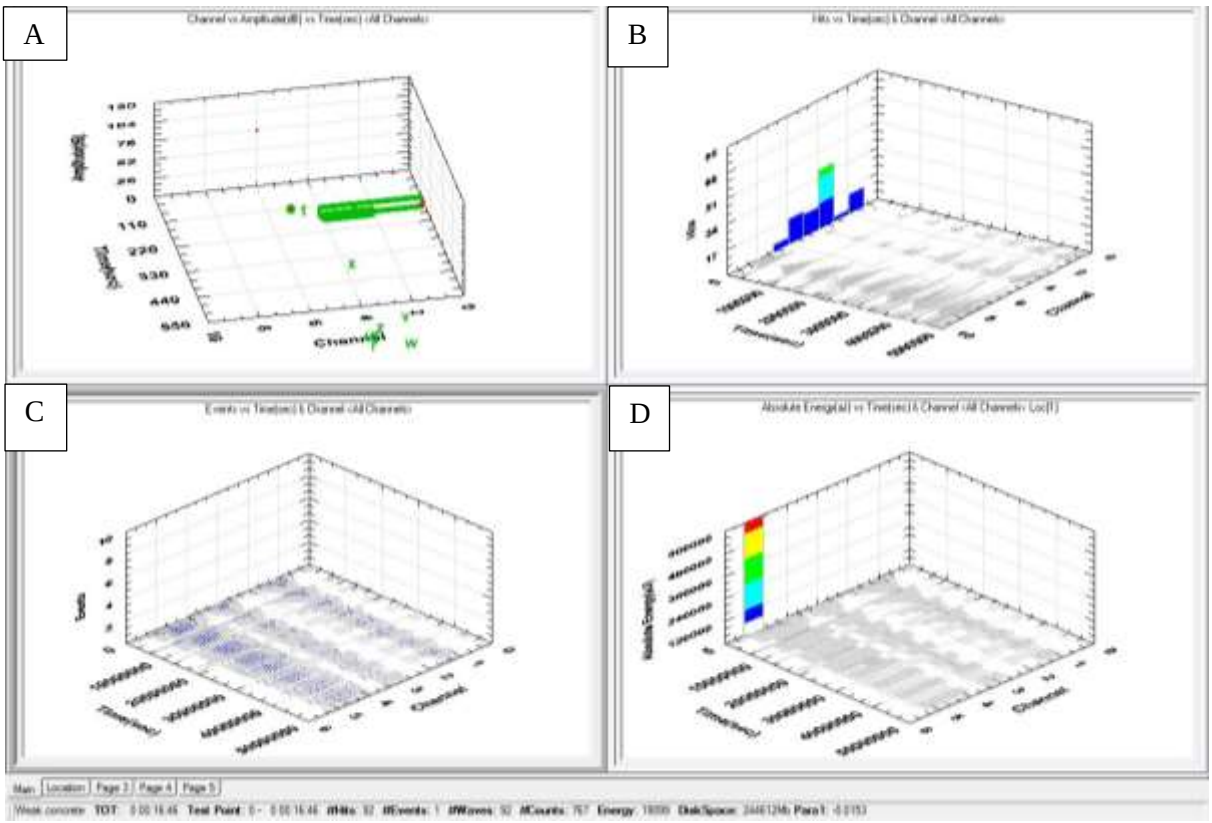

FIGURE 5-145: WBS2 Sensor graphs for 70mm to 50mm to fracture, A) Acoustic signals detected each channel, B) Hits Vs Time, C) Events Vs time, D) Absolute energy Vs time.

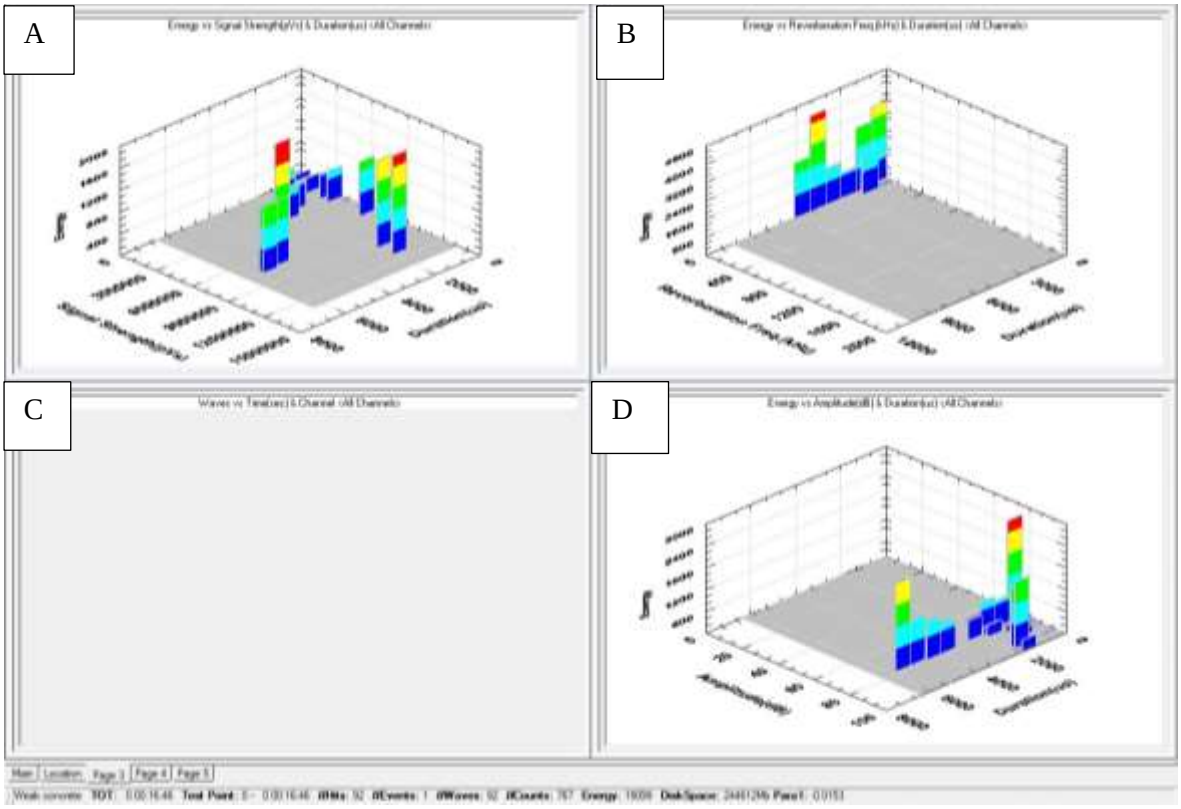

FIGURE 5-146: WBS2 Energy, duration and signal strength graphs 70mm to 50mm and fracture, A) Energy Vs signal strength, B) Energy Vs Reverberation, C) Empty, D) Energy Vs Amplitude.

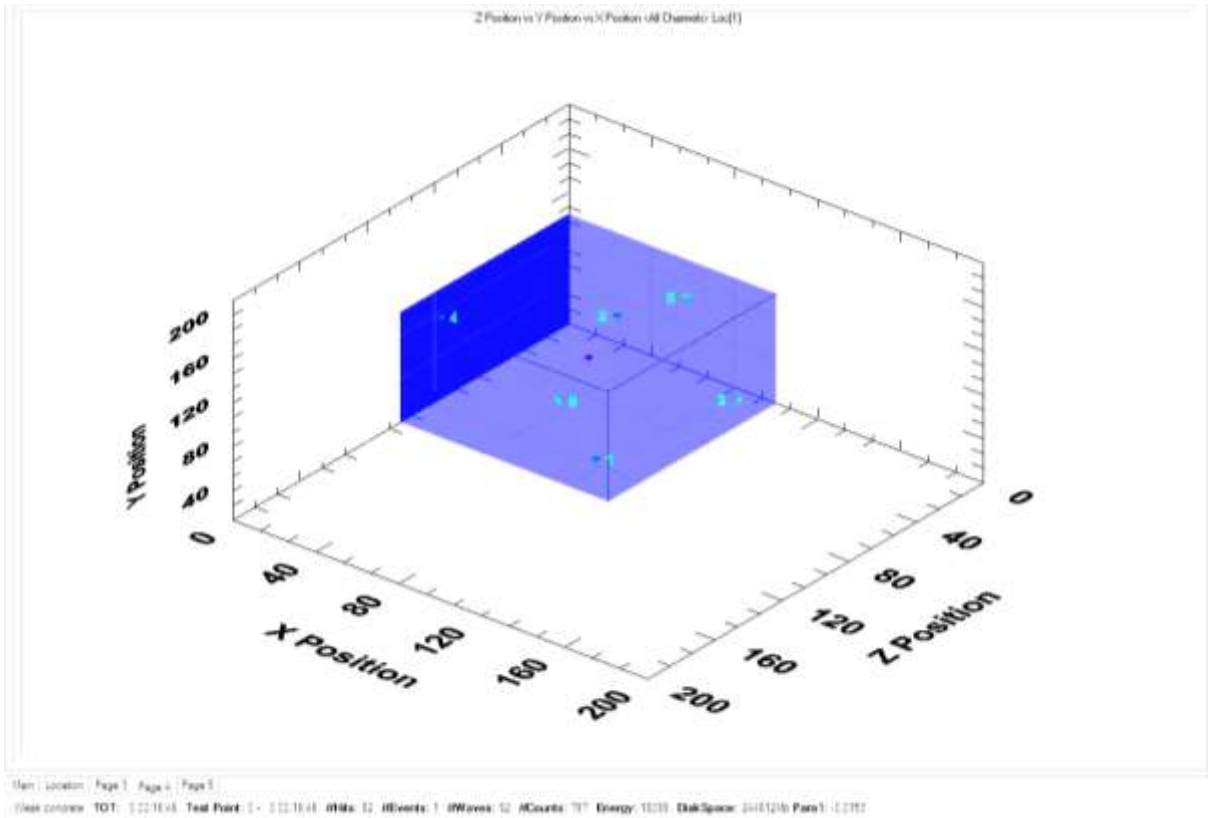

FIGURE 5-147: WBS2 3D graph events grouped 70mm-50mm & fracture.

One event of 92 hits was recorded, Figure 5-145, which corresponded to the location of the fracture shown in Figure 5-144 & Figure 5-145. The event that was recorded gave the point of fracture initiating at the base of the borehole. The lack of other events placed in the sample provides less confidence to the finding, though the one event does suggest that the fracture is instantaneous.

The lack of results was investigated to ensure that better results would be obtained in future analyses. When the sensors were removed it was immediately evident that they had been pushed well above the metal plate which houses them suggesting that the sensors had been extended too far and were not in close and level contact with the shale itself, hence the lack of acoustic data. To guarantee that this would not be repeated the decision was made to cut the sample as close to $100mm^3$ as possible, to ensure that the sensors would be in complete contact with a flat surface and not have a noticeable gap between the sensor and the surface of the shale. The sensors were still attached by sealant but given that there was a slight gap between the sensor and the surface of the shale the acoustic emissions at this point were only travelling through a band of sealant thus affecting the readings.

5.7.2 Tri-axial Data

The following samples were subject to the tri-axial conditions, which are listed in Table 5-4. These being Accrington Mudstone samples AMS3 and AMS4 and the Westbury Samples WBS3 to WBS6

5.7.2.1 AMS3

100MM TO 90MM

The acoustic and graph data is presented in Figure 5-148 to Figure 5-151.

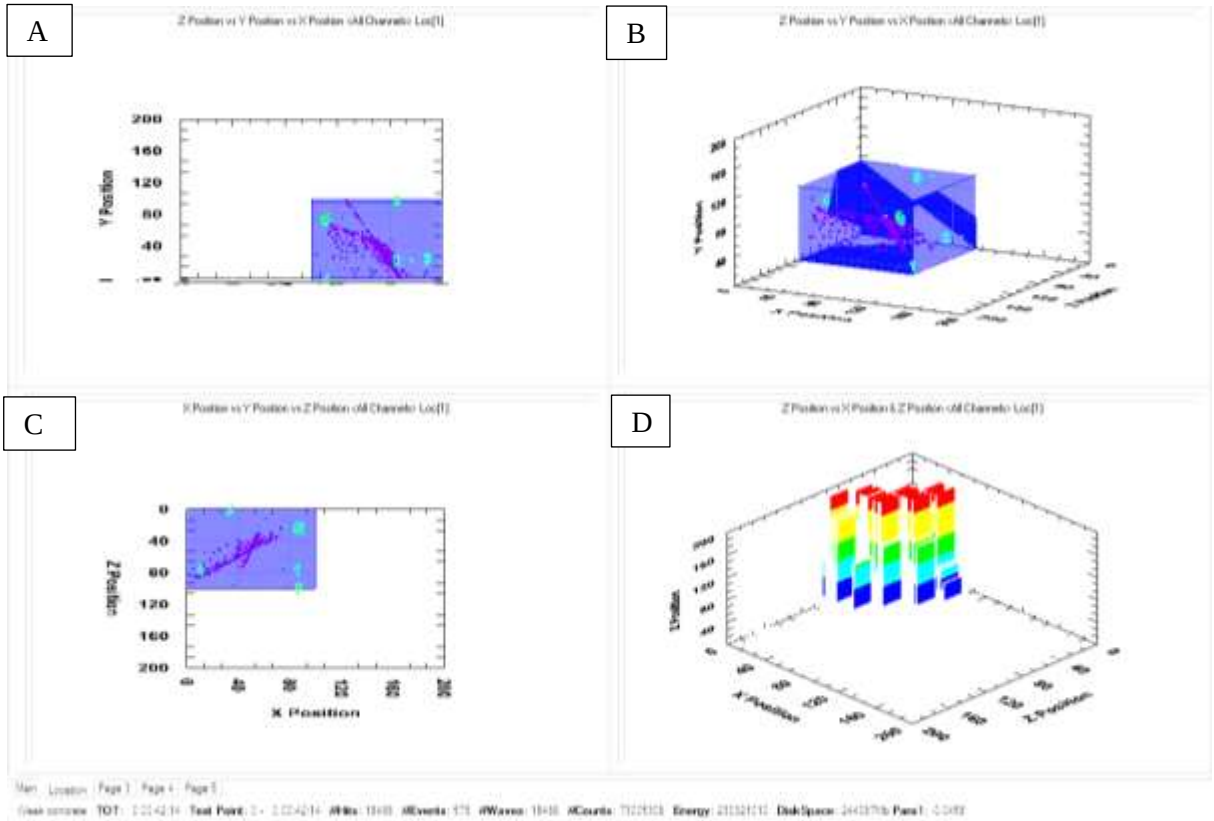

FIGURE 5-148: AMS3 location graphs 100mm to 90mm, A) Depth view, B) 3D view, C) Overhead view, D) actual positioning spots.

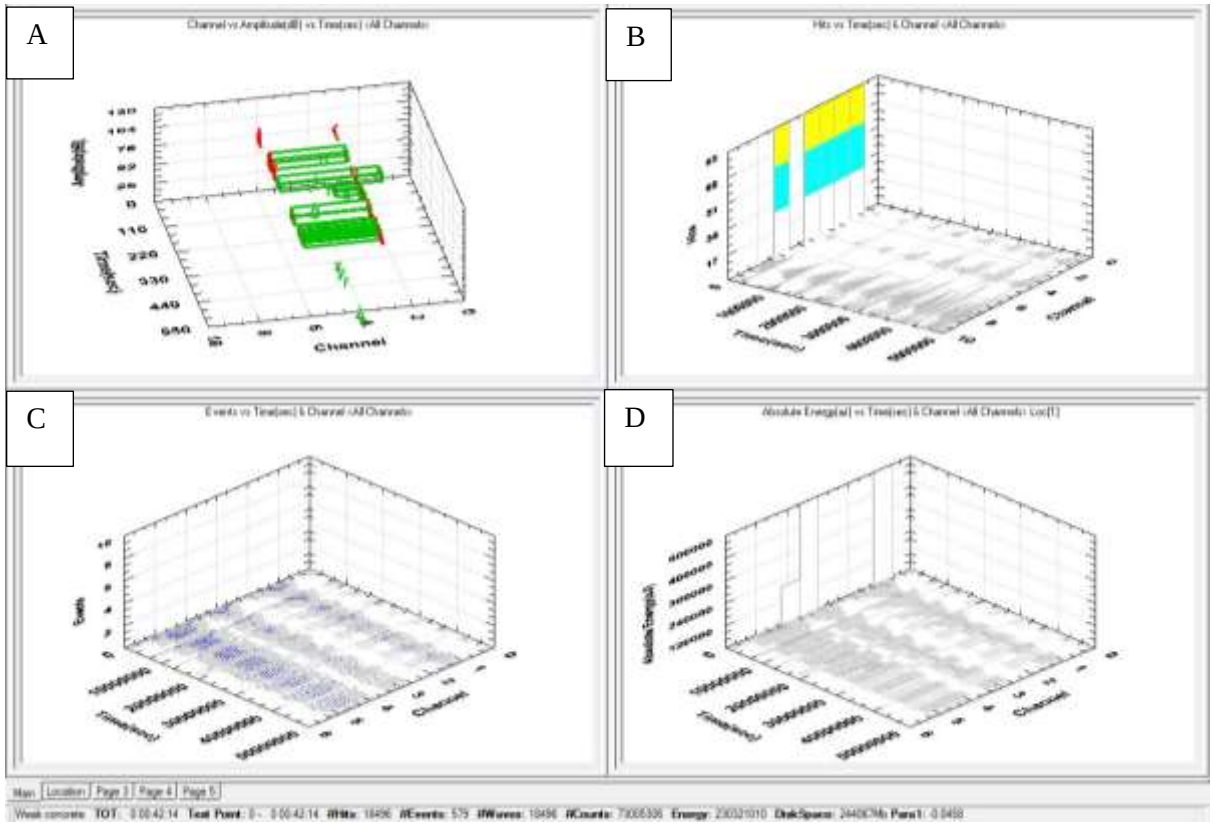

FIGURE 5-149: AMS3 sensor graphs 100mm-90mm, A) Acoustic signals detected each channel, B) Hits Vs Time, C) Events Vs time, D) Absolute energy Vs time.

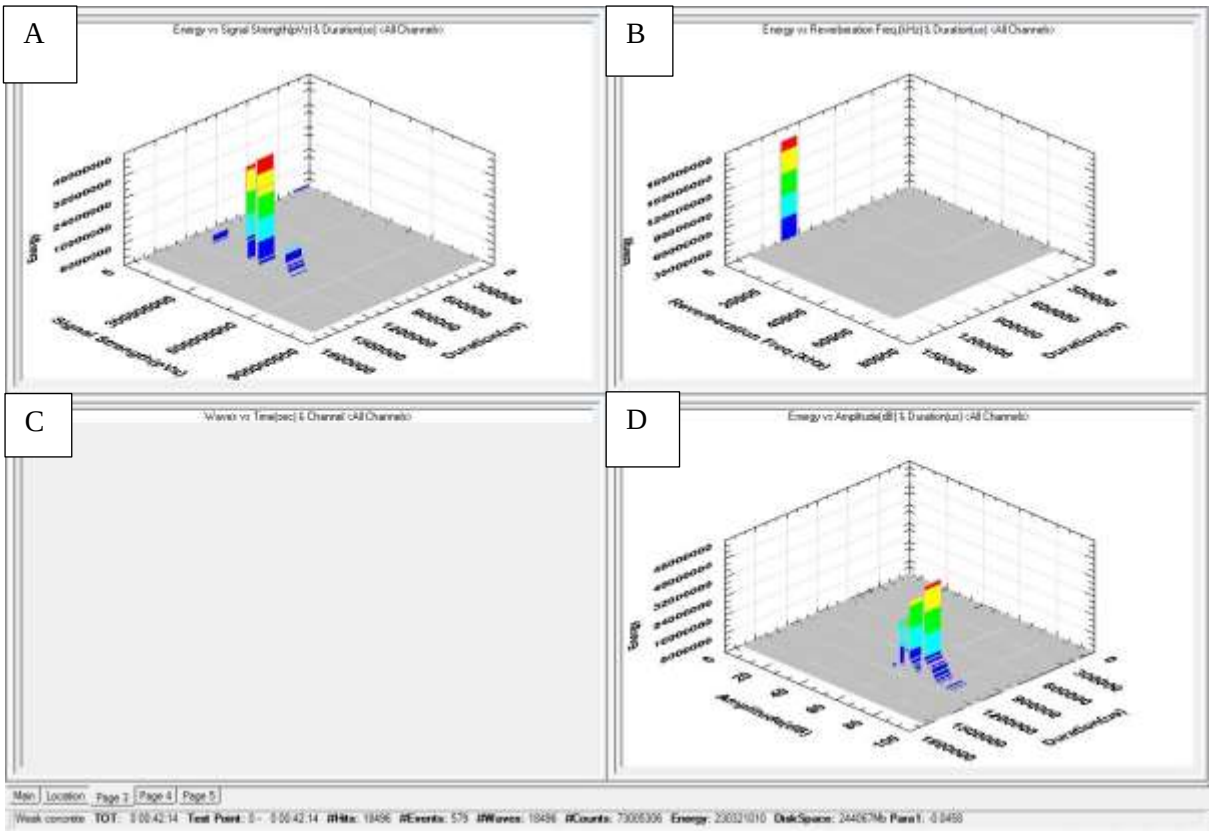

FIGURE 5-150: AMS3 Energy, duration and signal strength graphs 100mm - 90mm, A) Energy Vs signal strength, B) Energy Vs Reverberation, C) Empty, D) Energy Vs Amplitude.

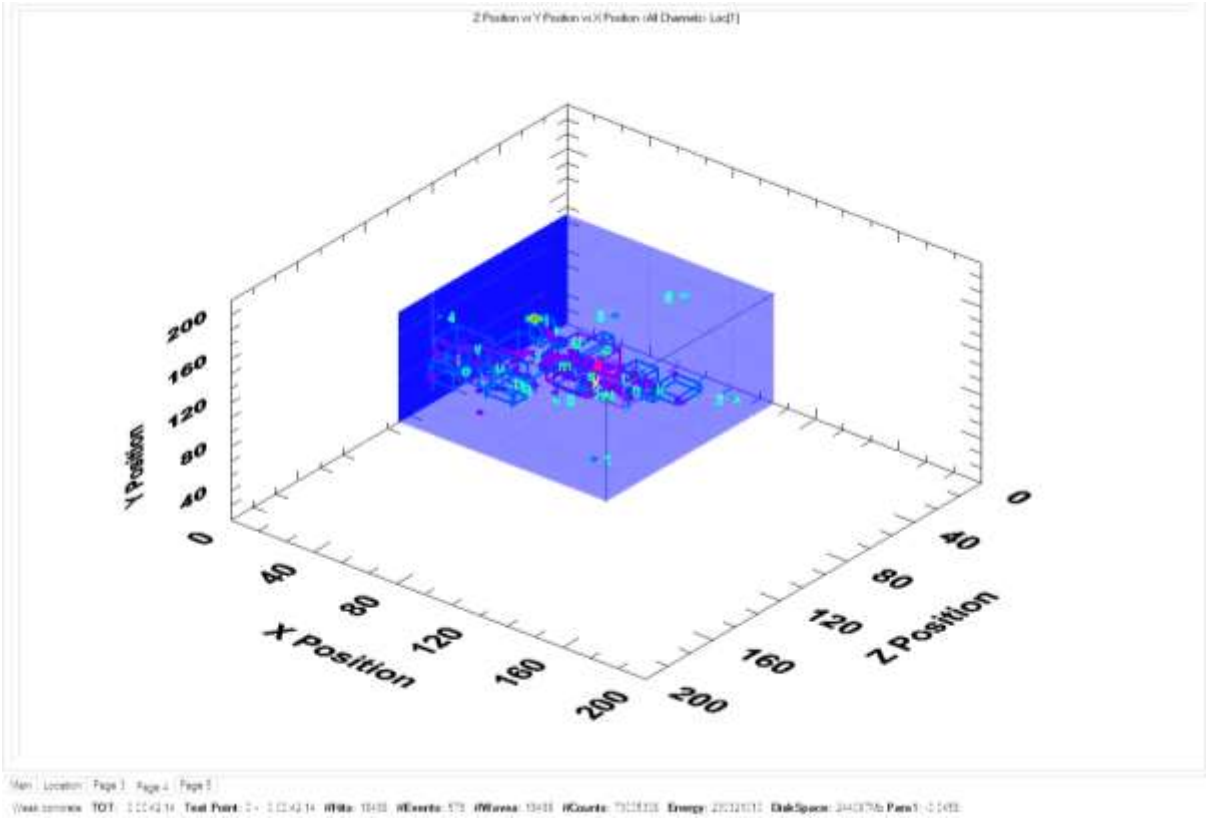

FIGURE 5-151: AMS3 3D graph showing events grouped 100mm-90mm.

The results for the first interval of 100mm to 90mm were very much improved on those from previous samples, with all the sensors showing similar patterns and signal detections, Figure 5-149. This gives greater confidence that the events shown are accurate. This sample had a pre-existing fracture and a further two fractures induced by the fracturing fluid caused by the main induced fracture hitting the pre-existing fracture. The spatial view in Figure 5-148 shows a line of events following a similar, but not exact path of the pre-existing fracture, whilst also showing an accurate determination of the drill bit location. The overhead view in Figure 5-148 shows the off centred location of the borehole (to avoid the pre-existing fracture) and a series of events tracking the borehole to 90mm. These events continue in a diagonal line, past the 50mm mark to the area where the primary fracture and the secondary induced fractures meet. This does indeed seem to show that most of the damage done to a formation whilst drilling is not at the tip of the drill bit but a small distance below the drill bit. The fact that events are linked along a vector similar to the pre-existing fracture can only be explained by the drilling near to the fracture causing the pre-existing fracture to vibrate giving off its own acoustic emissions. Furthermore, this will also contribute to potential damage to the existing fracture as new micro-fractures are opened up leading from the pre-existing fracture, hence the longer chain of acoustic emissions that followed from the drilling panel.

18496 hits gave 579 events, producing very good detection rates and had signal strengths ranging from $2{,}900x10^{6}\rho Vs$ to $5{,}250x10^{6}\rho Vs$ and reverberations of less than 5kHz, Figure 5-150. This increase in signal strength along with a huge increase in detected hits and placed events improves the degree of confidence in the acoustic performance in addition to the acoustics detecting pre-existing features. It would appear that acoustics can be used not only to track pre-existing damage in a formation but also to describe formation damage due to drilling.

90MM TO 80MM

The acoustic and graphic data, collected by the acoustic software is presented in Figure 5-152 to Figure 5-155

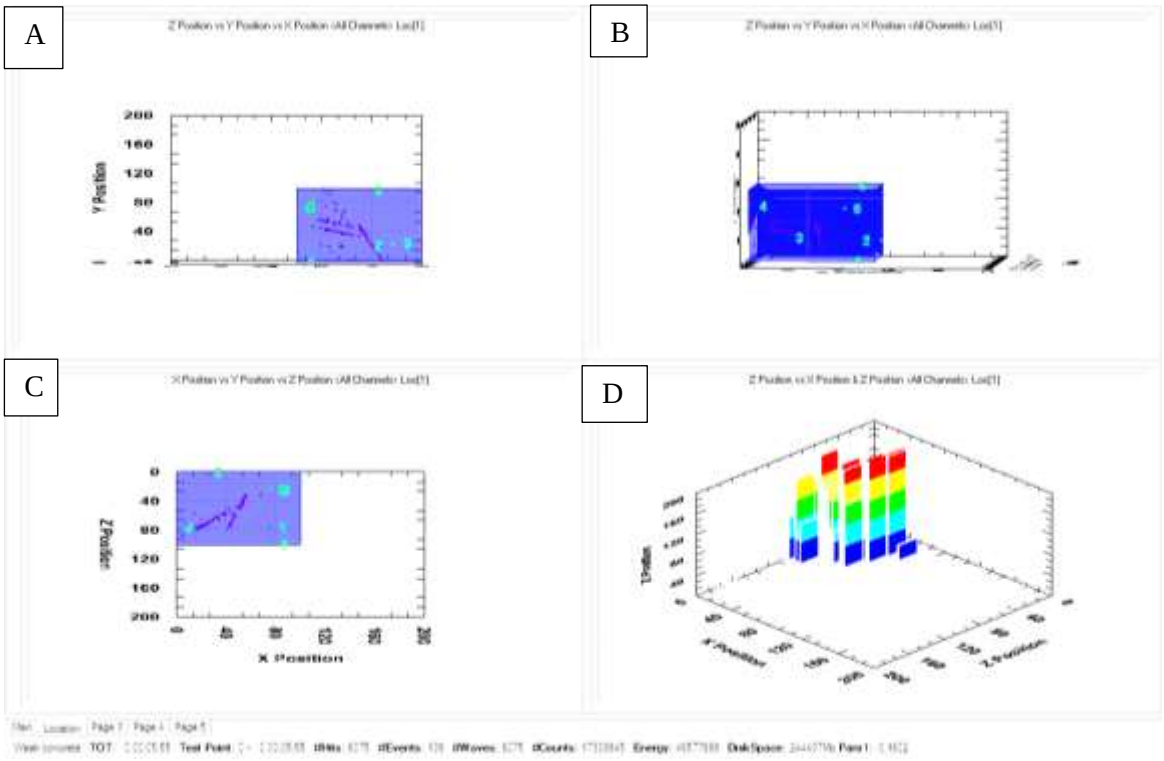

FIGURE 5-152: AMS3 Location graphs 90mm to 80mm, A) Depth view, B) 3D view, C) Overhead view, D) actual positioning spots.

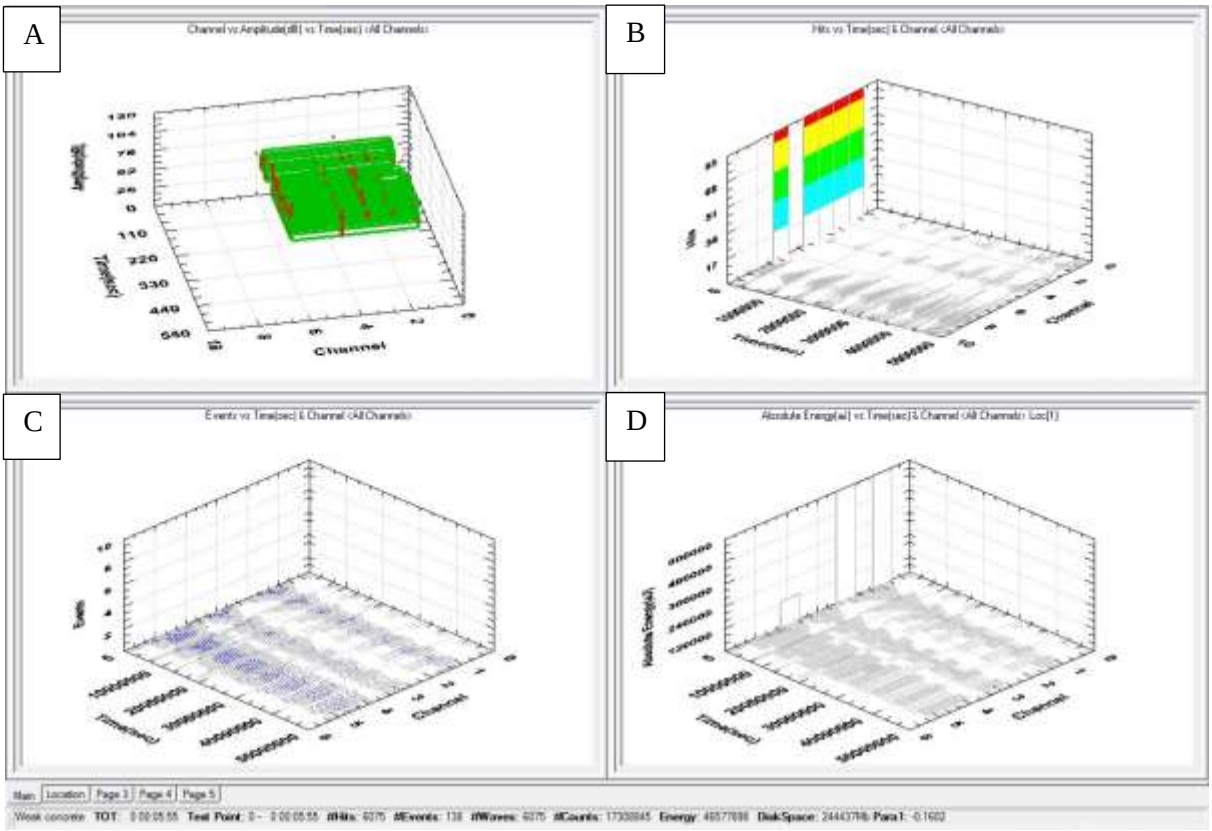

FIGURE 5-153: AMS3 Sensor graphs 90mm to 80mm, A) Acoustic signals detected each channel, B) Hits Vs Time, C) Events Vs time, D) Absolute energy Vs time.

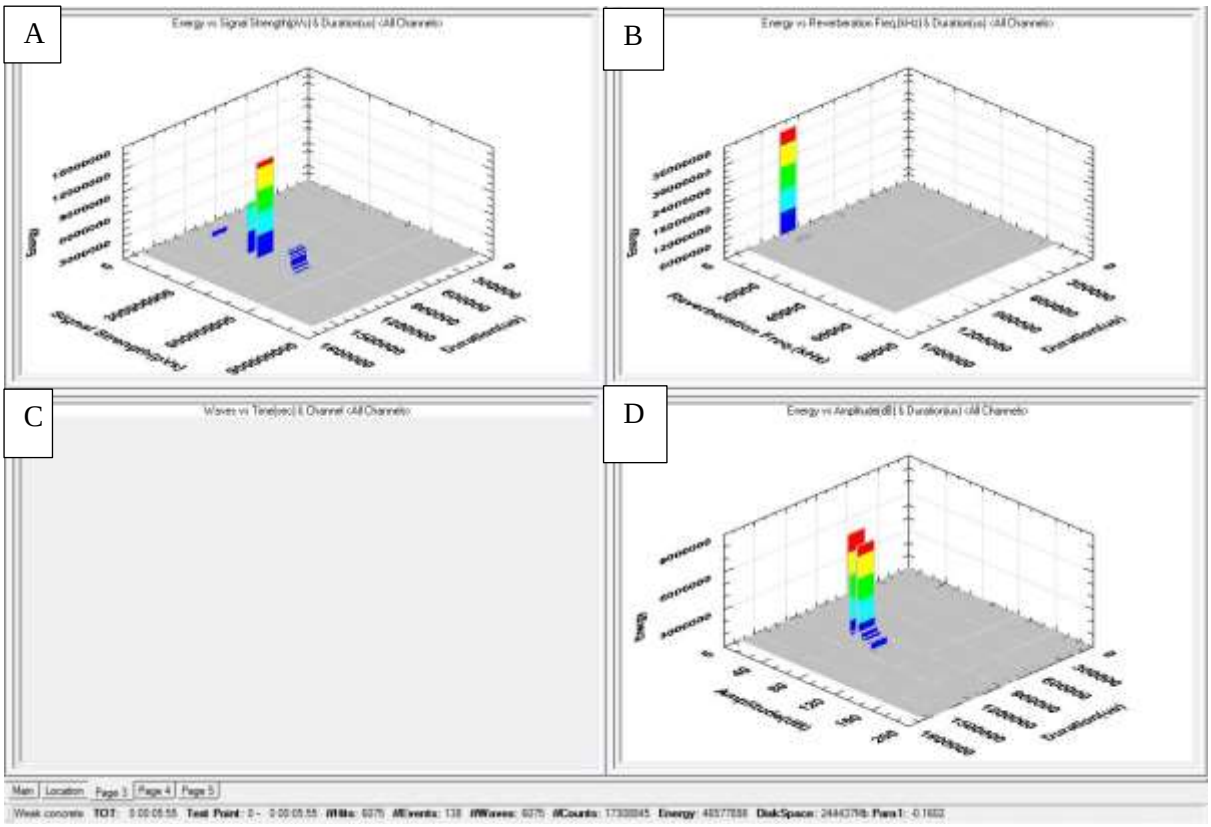

FIGURE 5-154: AMS3 Energy, Duration and Signal Strength Graphs 90mm – 80mm, A) Energy Vs signal strength, B) Energy Vs Reverberation, C) Empty, D) Energy Vs Amplitude.

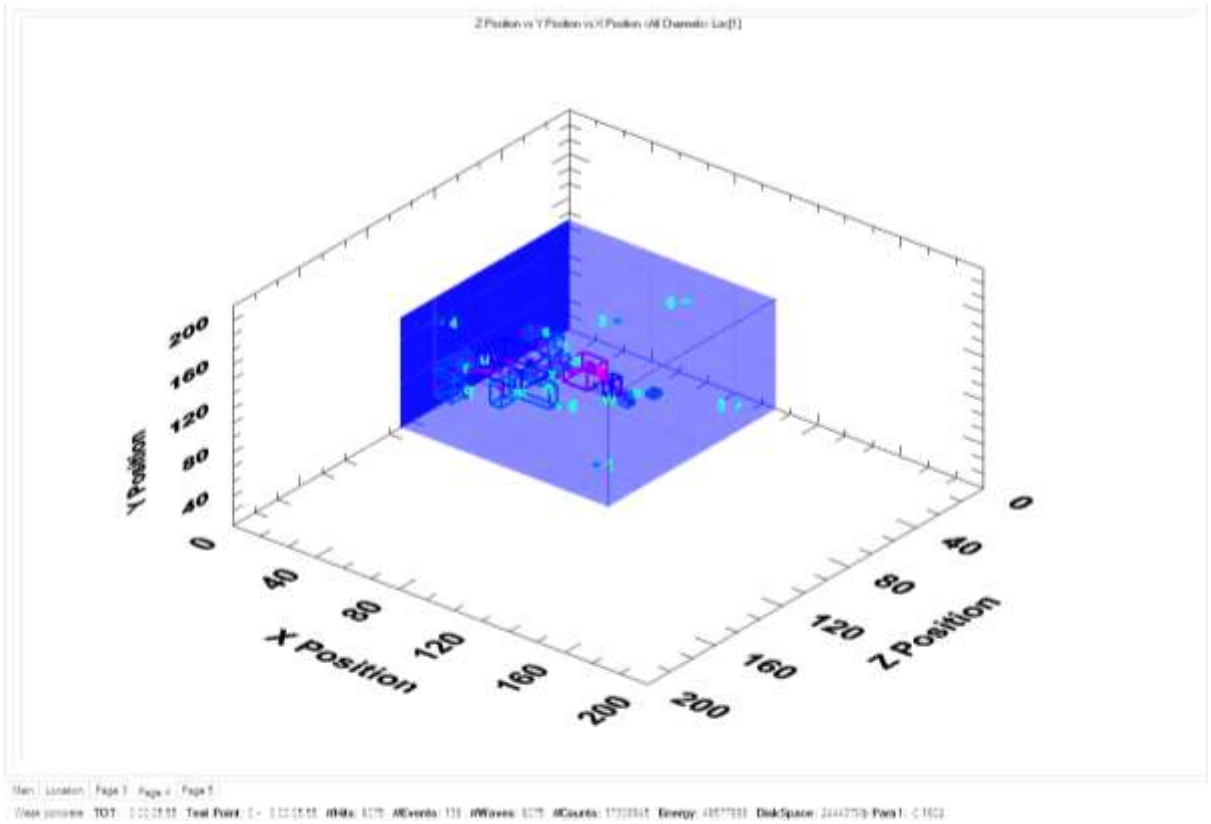

FIGURE 5-155: 3D graph events grouped 90mm - 80mm.

Figure 5-152 shows a clear progression of the borehole from 90mm to 80mm whilst still showing a number of events trailing below the borehole. However, the trail from the borehole is not as strong as the events recorded during the 100mm to 90mm interval, which would suggest that most of the damage was done during the initial drilling phase. The pre-existing fracture is still traceable and shows that the drilling will continue to cause the pre-existing fractures and micro-fractures to vibrate and occasionally grow, thus giving off more acoustic emissions.

In this drilling interval 6075 hits were detected giving 138 events and shown in Figure 5-153. This is still a large volume of hits and events but a clear decrease from the 100mm to the 90mm interval, this suggests that the greatest amount of damage is at the start of the drilling and as the drilling continues the events are mainly a continuation of damage and further opening up of existing micro-fractures.

Energy for this interval was recorded as 46,577,898J while the signal strength was the same as the 100mm to 90mm with durations between 1,000,000µsec 1,200,000µsec, Figure 5-154. Again, with a large signal strength and little reverberation the confidence levels with the acoustics are increased.

80MM TO 70MM

The acoustic and graph data from this interval are presented in Figure 5-156 to Figure 5-159

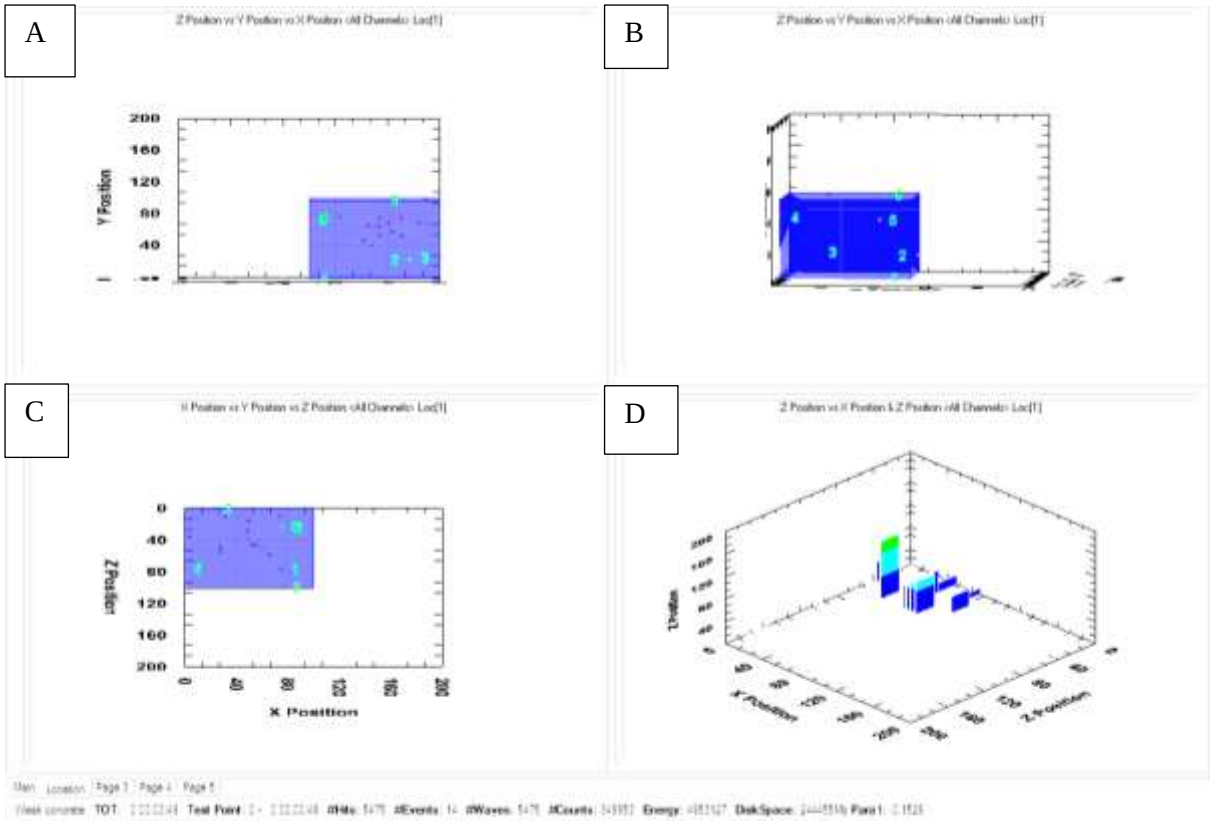

FIGURE 5-156: AMS3 Location graphs 80mm to 70mm, A) Depth view, B) 3D view, C) Overhead view, D) Actual positioning spots.

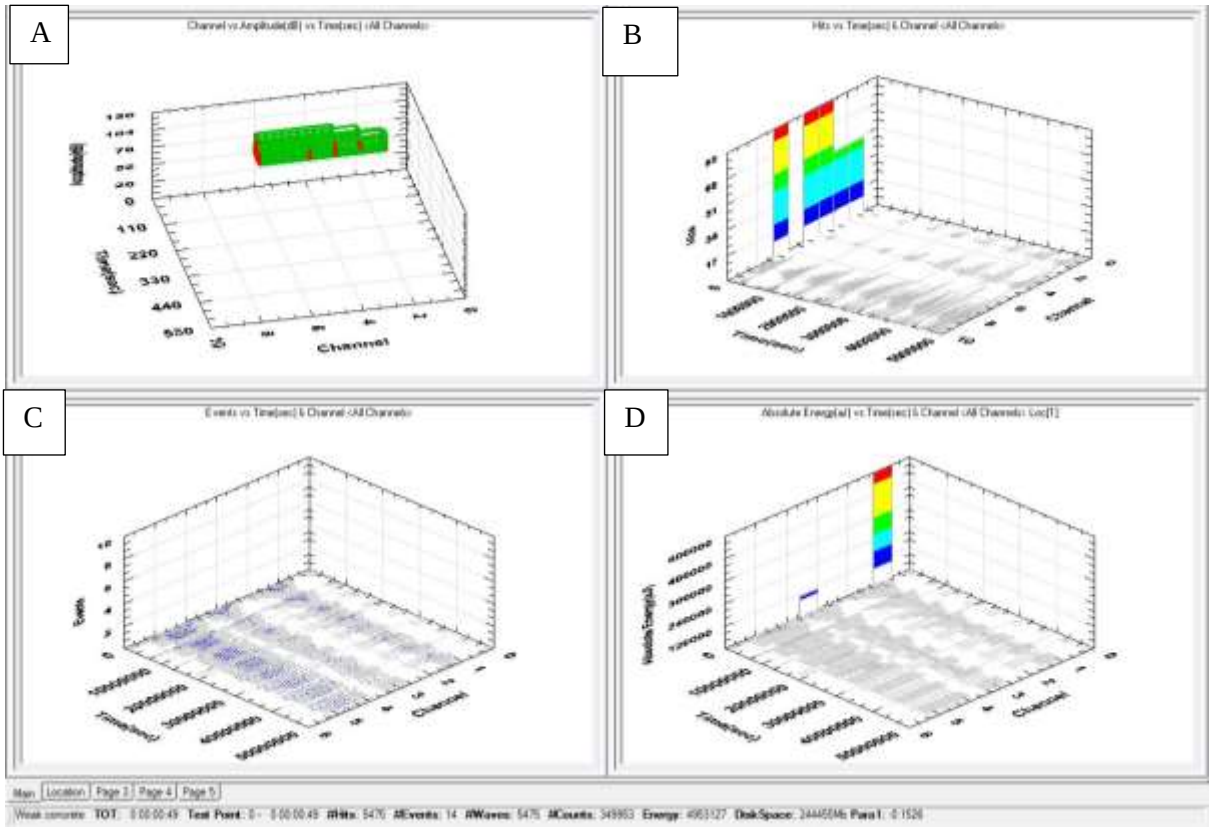

FIGURE 5-157: AMS3 sensor graphs 80mm - 70mm, A) Acoustic signals detected each channel, B) Hits Vs Time, C) Events Vs time, D) Absolute energy Vs time.

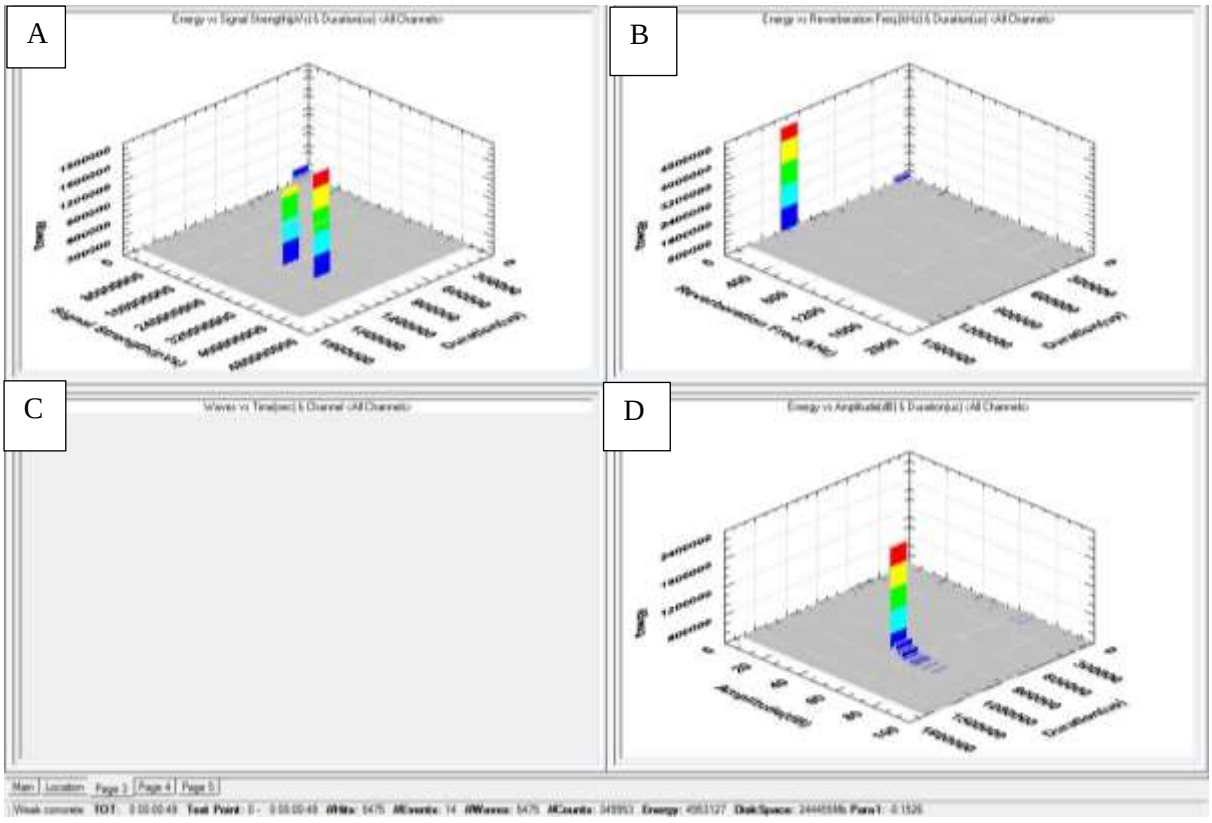

FIGURE 5-158: AMS3 Energy, duration and signal strength graphs 80mm – 70mm, A) Energy Vs signal strength, B) Energy Vs Reverberation, C) Empty, D) Energy Vs Amplitude.

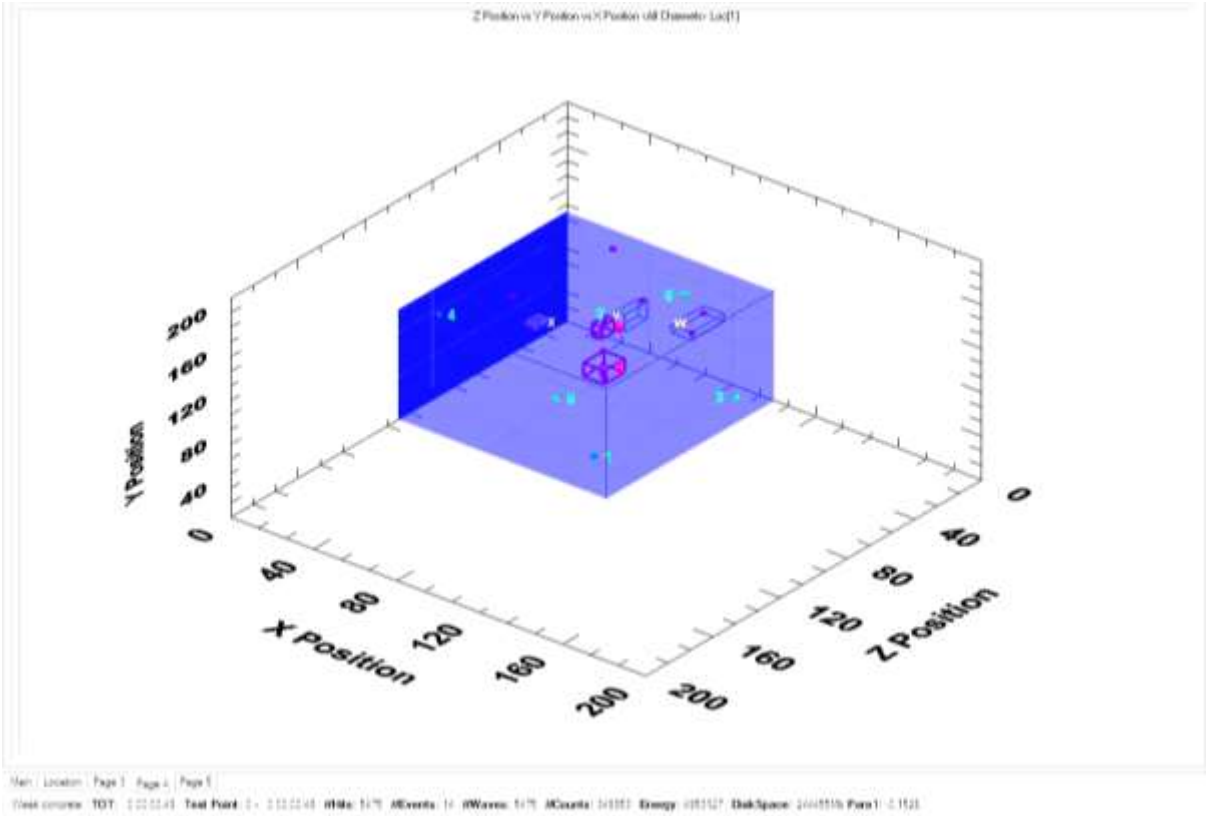

FIGURE 5-159: AMS3 3D Graph events grouped 80mm - 70mm.

In the location view in Figure 5-156 to Figure 5-159 it is clear that there are fewer events and yet the number of hits have not noticeably decreased, this can also be seen in the detection rates against the sensors in Figure 5-157. Whilst it is clear that there is still a progression working from the borehole from just below 80mm again the majority of the events are located below where the drilling is taking place, with a couple close the edges of the borehole which will be picking up the rotation of the drill. A couple of other events follow the same two lines of the pre-existing fractures or the area where the primary and secondary fractures converged. It was found that 5475 hits transcribed as 14 events. With signal strength being between $249x10^6\rho Vs$ and $320x10^6\rho Vs$ and duration of approximately 1,000,000µsecs, Figure 5-158 gives credence to the results. The results indicate that the longer the drilling continues so the growth of micro fractures in pre-existing fractures, or in areas of weakened planes (like the area of convergence of the primary and secondary induced fractures) slows. The majority of these micro fractures open up within the first part of drilling, with just occasional growths recorded. As this growth is gradual and in close proximity it would explain the lack of events as the number of acoustic hits will be next to each other and for all intents and purposes will inhabit the exact same location especially on the scale that the software works on. The area around the borehole still shows damage predominantly below the drill bit. That this event is shown repeatedly in all the acoustic profiles obtained further strengthens the argument that most of the damage occurs at the base of the drilling area.

The acoustic log for this drilling interval seems to record similar ‘event’ to ‘hit’ ratios as those seen in the previous Accrington Mudstone samples, with the larger number of events in the drilling intervals between 100mm to 80mm explained as belonging to micro-fractures opening up in areas of pre-existing fractures or areas of weakness. Thus, a lower number of hits would be expected when drilling an undamaged sample. With the same principle, lots of hits would indicate continuations of the same micro-fractures opening in the same location. The principle of which is shown below in Figure 5-160.

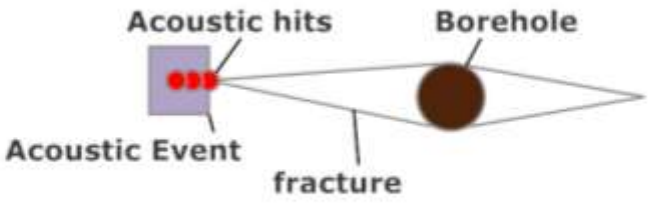

FIGURE 5-160: Principle of event location against sensor hits.

70MM TO 60MM

The acoustic and graph data of this drilling interval is presented in Figure 5-161 to Figure 5-164.

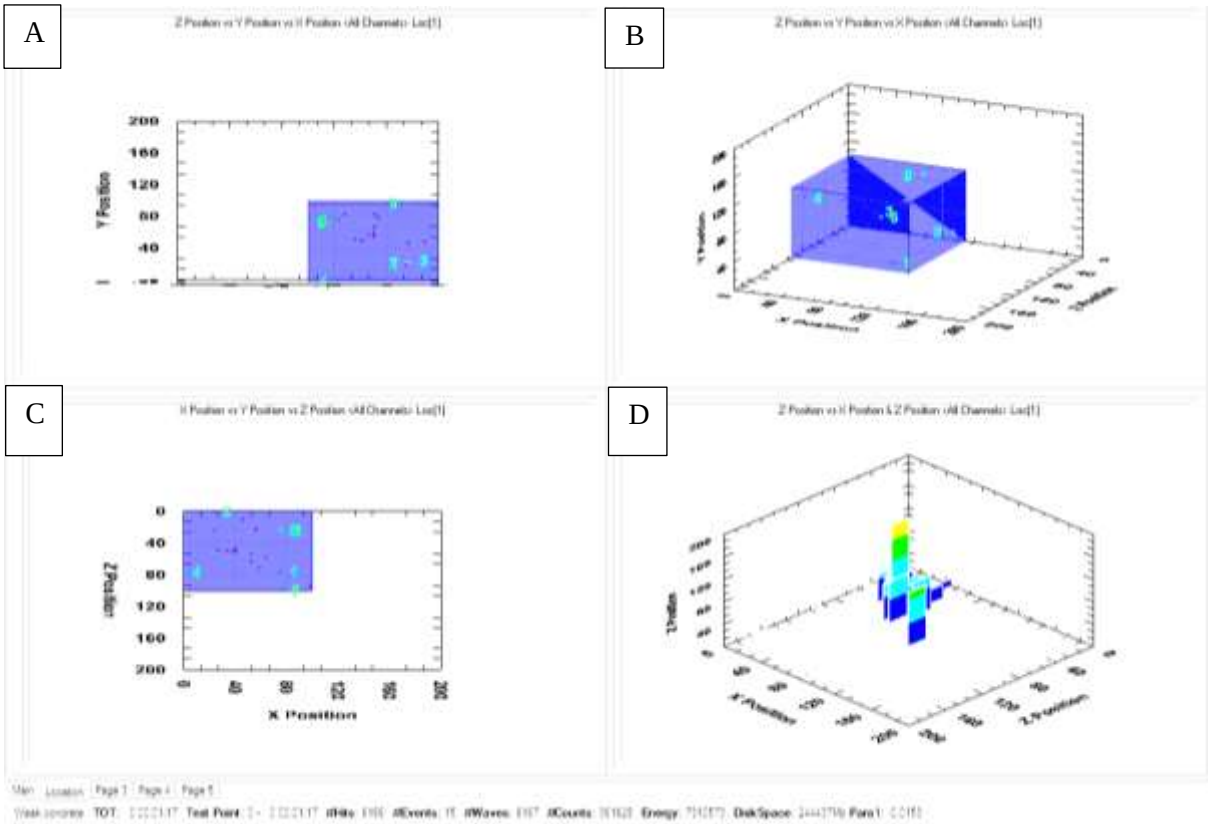

FIGURE 5-161: AMS3 location graphs 70mm to 60mm, A) Depth view, B) 3D view, C) Overhead view, D) Actual positioning spots.

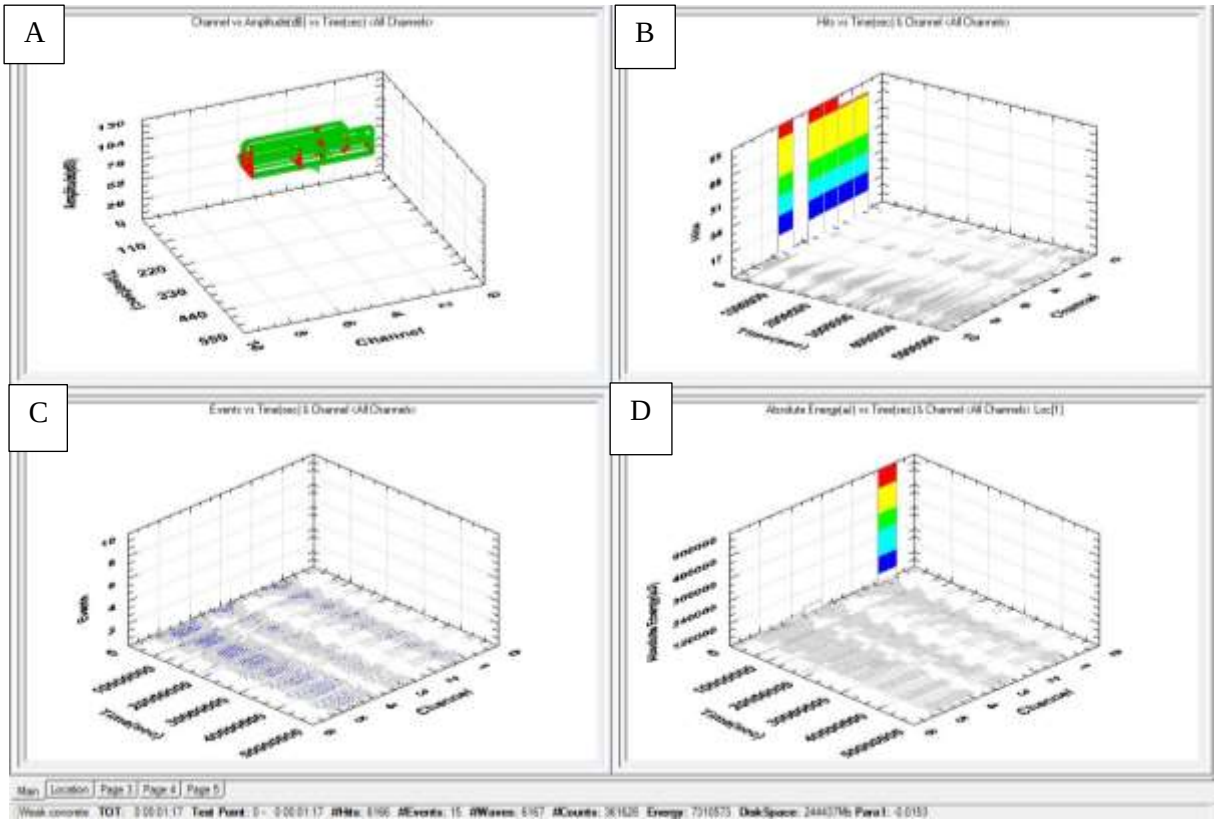

FIGURE 5-162: AMS3 Sensor graphs 70mm - 60mm, A) Acoustic signals detected each channel, B) Hits Vs Time, C) Events Vs time, D) Absolute energy Vs time.

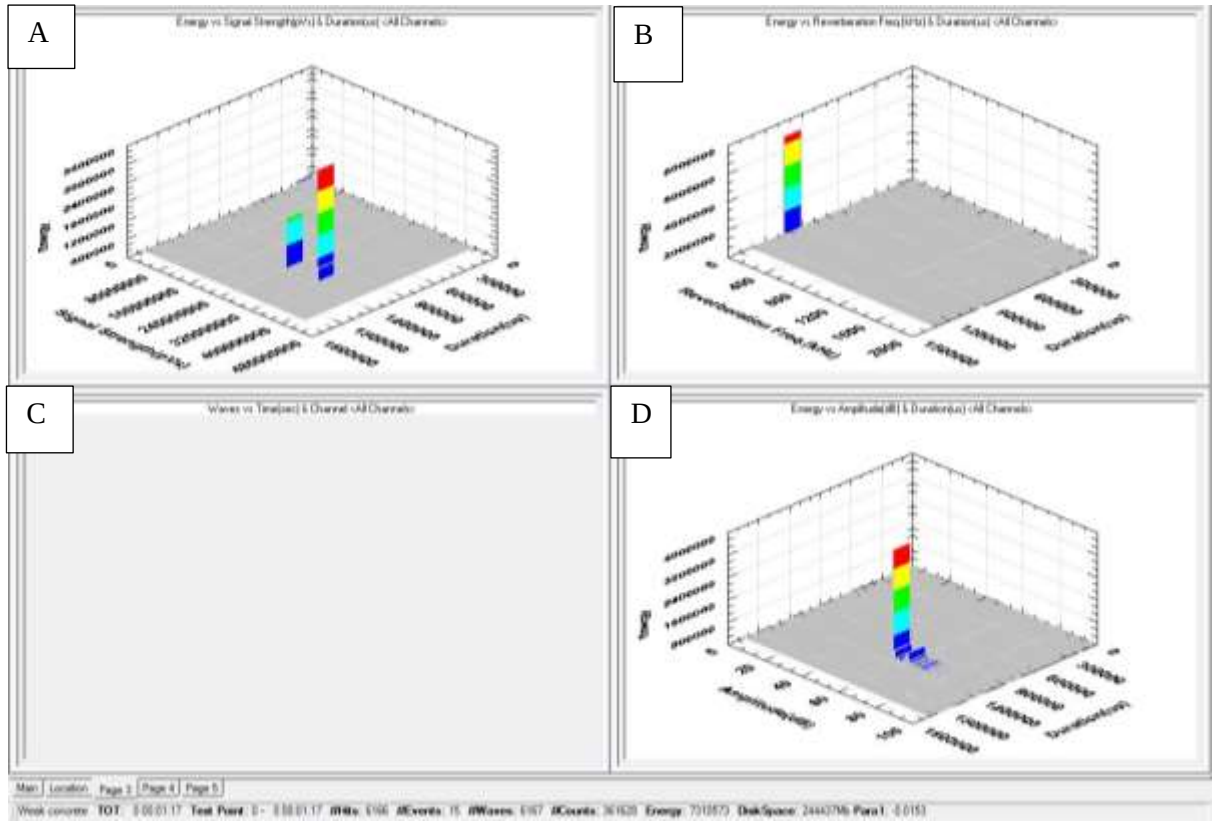

FIGURE 5-163: AMS3 Energy, duration & signal strength 70mm - 60mm, A) Energy Vs signal strength, B) Energy Vs Reverberation, C) Empty, D) Energy Vs Amplitude.

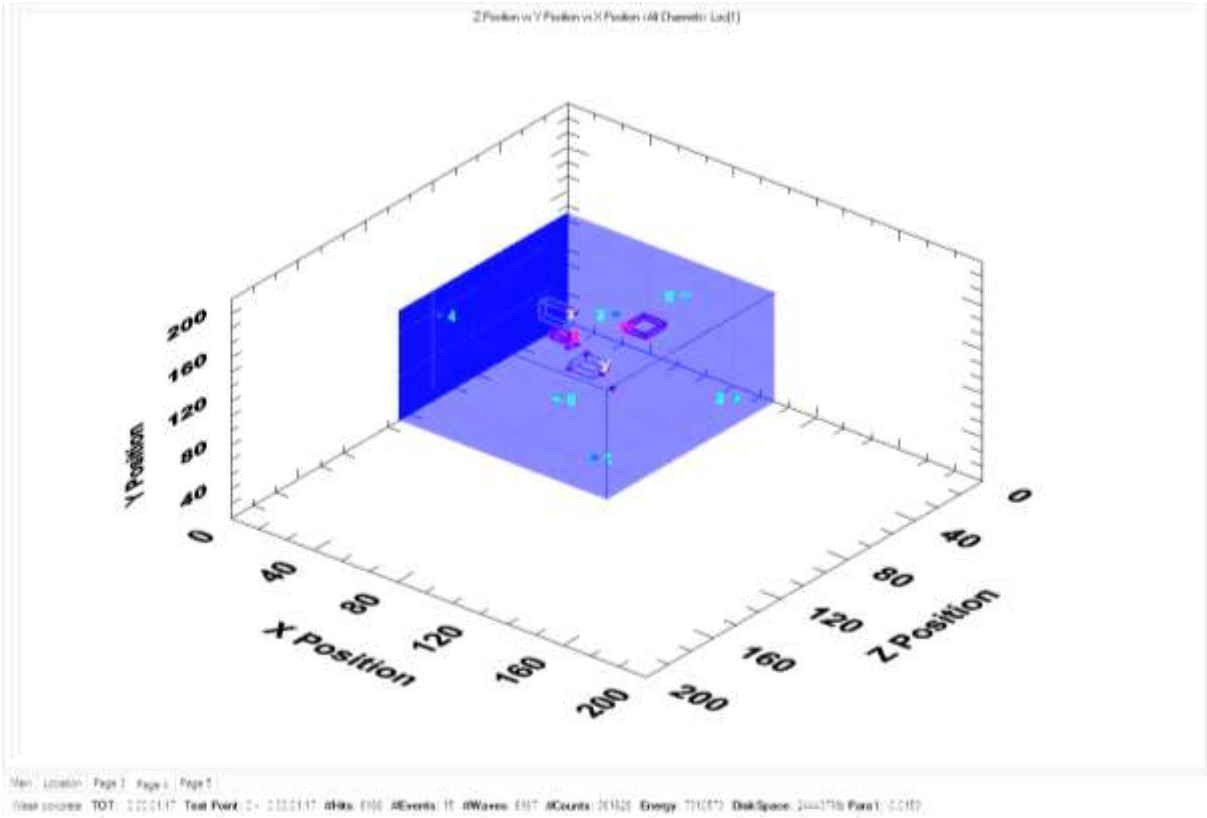

FIGURE 5-164: 3D Graph events grouped 70mm to 60mm.

Figure 5-161 shows a similar image to that seen in Figure 5-156 representing the 80mm to 70mm interval. There are some events clearly along the pre-existing fracture line and around the area of weakness in the sample and then there are the events linked to the borehole. These are displayed as slightly off centred events (on the overhead view in Figure 5-161), where they are picked up at roughly 66mm and progress further down to around 53mm along the Y axis. Again, a couple of events are linked to the side of the borehole further up the Y axis at around 80 to 82mm. This would fit with the drill spinning against the side of the borehole at this point, especially as this borehole is slightly angled. 6166 hits have given 15 events and following on from the previous acoustic data from this sample, Figure 5-162, strengthens the argument that once the majority of the damage is done to weakened and pre-damaged samples a low number of recorded events is to be expected.

Energy recorded in this drilling interval was 7310573J, the majority of that energy was reverberating at less than 5kHz and between $240x10^6\rho Vs$ & $320x10^6\rho Vs$, Figure 5-163.

60MM TO 50MM

The drilling interval again follows the same pattern as the previous one, with fewer events placed. The acoustic and graphic data is presented in Figure 5-165 to Figure 5-167.

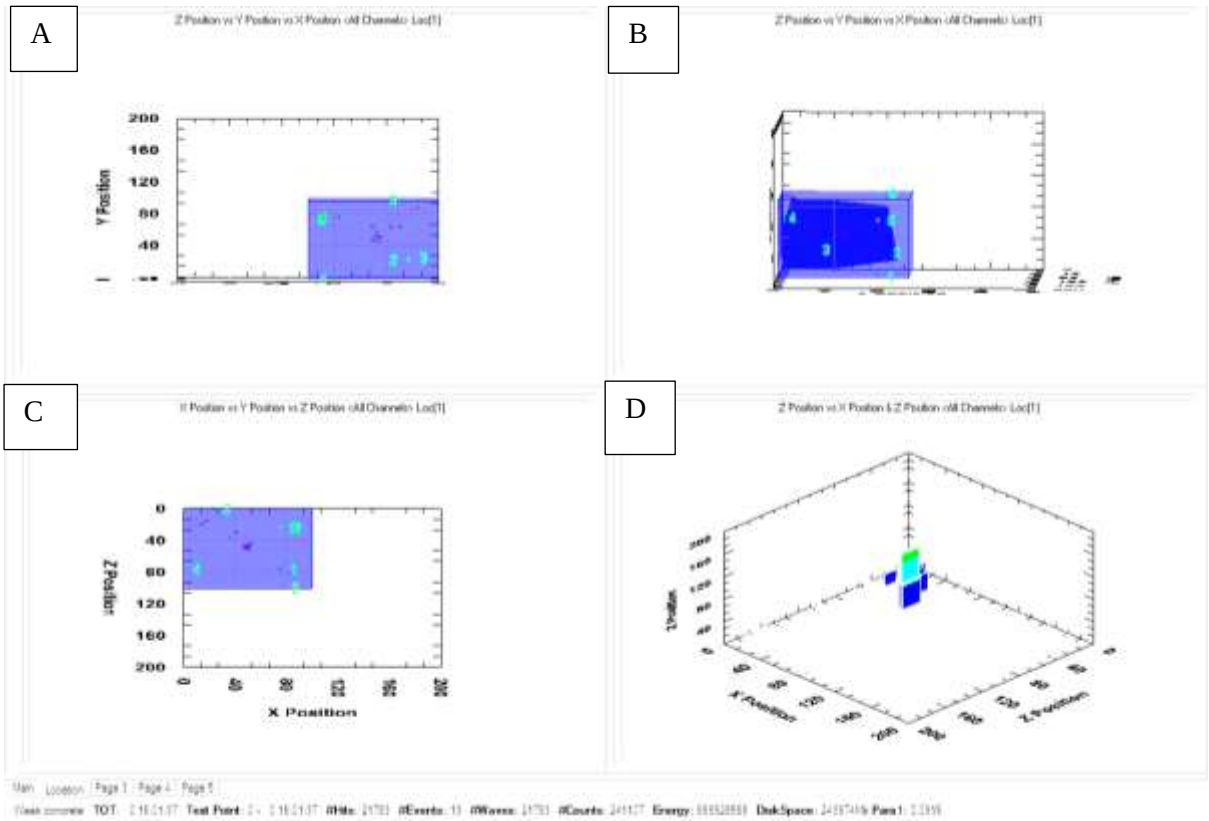

FIGURE 5-165: AMS3 Location view 60mm - 50mm, A) Depth view, B) 3D view, C) Overhead view, D) Actual positioning spots.

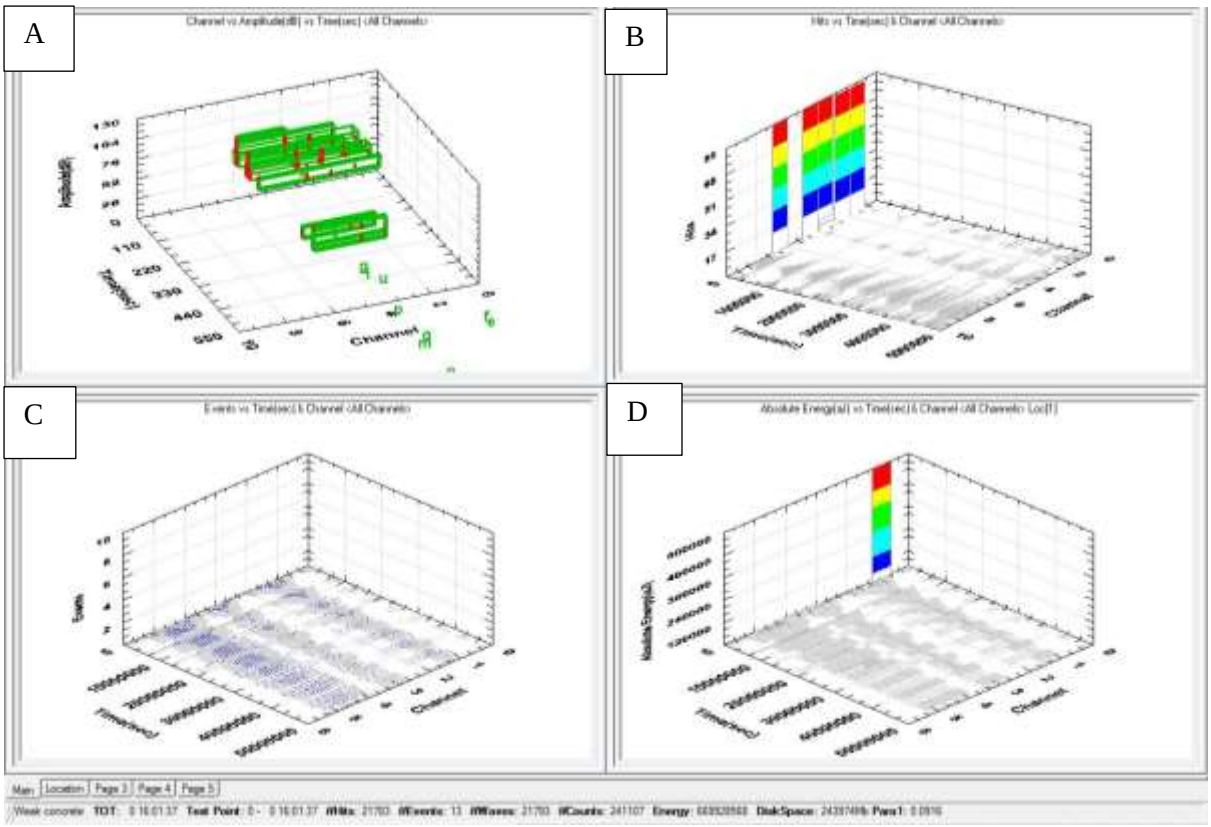

FIGURE 5-166: AMS3 Sensor Graphs 60mm – 50mm, A) Acoustic signals detected each channel, B) Hits Vs Time, C) Events Vs time, D) Absolute energy Vs time.

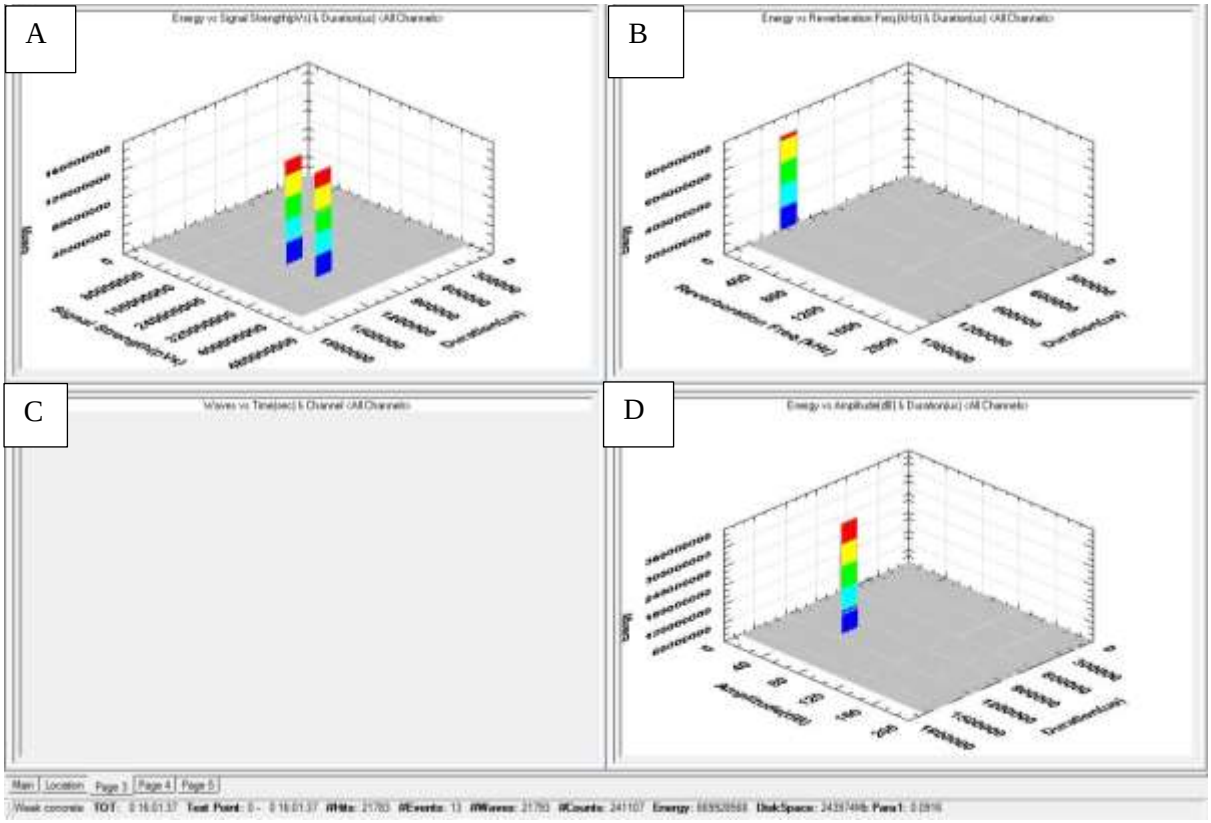

FIGURE 5-167: AMS3 Energy, duration and signal strength graphs 60mm to 50mm, A) Energy Vs signal strength, B) Energy Vs Reverberation, C) Empty, D) Energy Vs Amplitude.

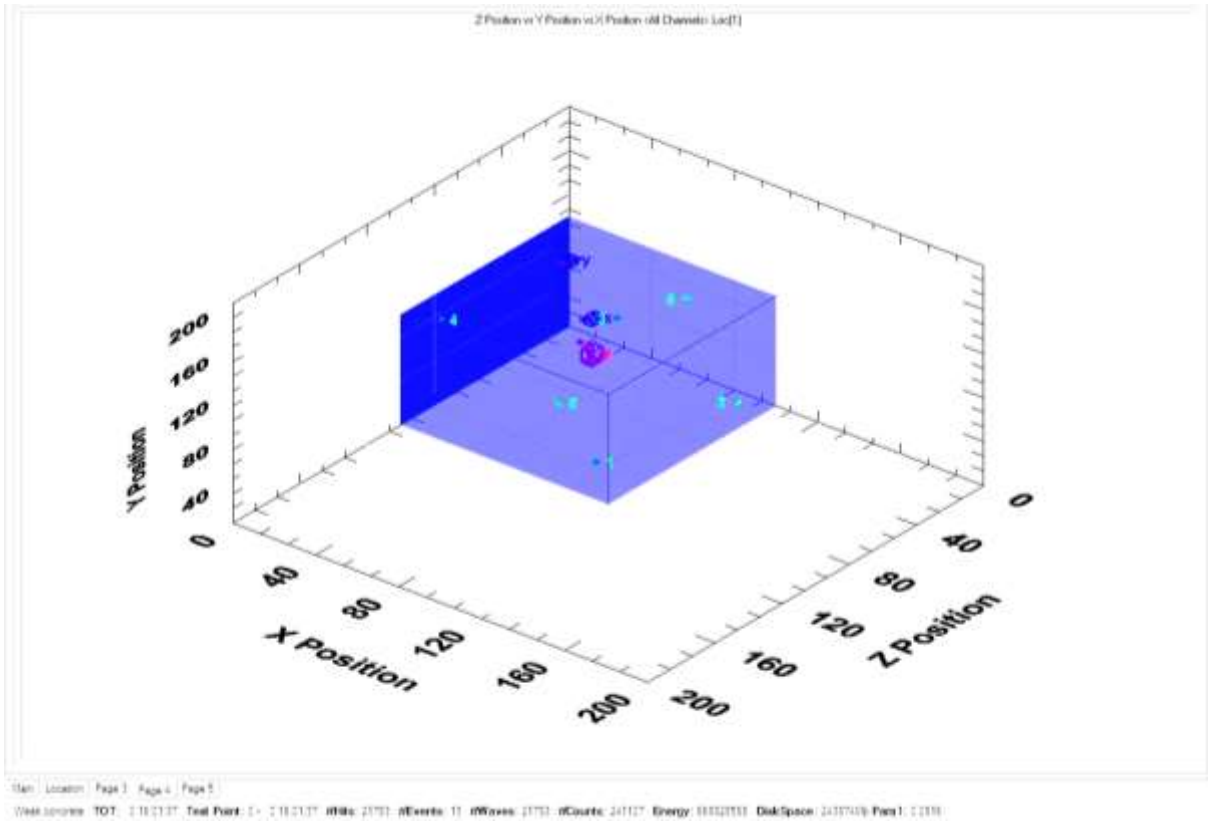

FIGURE 5-168: 3D Graph events grouped 60mm to 50mm.

It was noted that 13 events were transcribed from 21783 hits with all the sensors showing similar groupings as shown in Figure 5-166. This is except for later in the run when the drill bit was being taken out of the borehole, knocked the top sensor plate and made small acoustic hits as it scraped along the borehole. Figure 5-165 & Figure 5-168 shows that there is a clear grouping, in the overhead view, where the borehole is. These hits are recorded as striking just above 60mm all the way to approximately 48mm, showing a clear progression of acoustic events at and just below the drill bit progression. The rest of the acoustic events are detected in two main groupings that move towards the surface heading to the side of the sample that holds sensor three. These events can be described as other areas of weaknesses as the borehole reaches the halfway point of the sample. As the sample is already damaged with a pre-existing fracture and clearly a plane of weakness has been detected in the drilling intervals of 100 to 80mm then this will put excess strain on the sample creating more planes of weakness.

Figure 5-167 shows the high signal strength of the majority of the energy and the low reverberations, again this points to a greater level of accuracy than seen in the samples that were tested under the bi-axial conditions.

POINT OF FRACTURE.

The acoustic and graphic data of the software is presented in Figure 5-169 to Figure 5-172

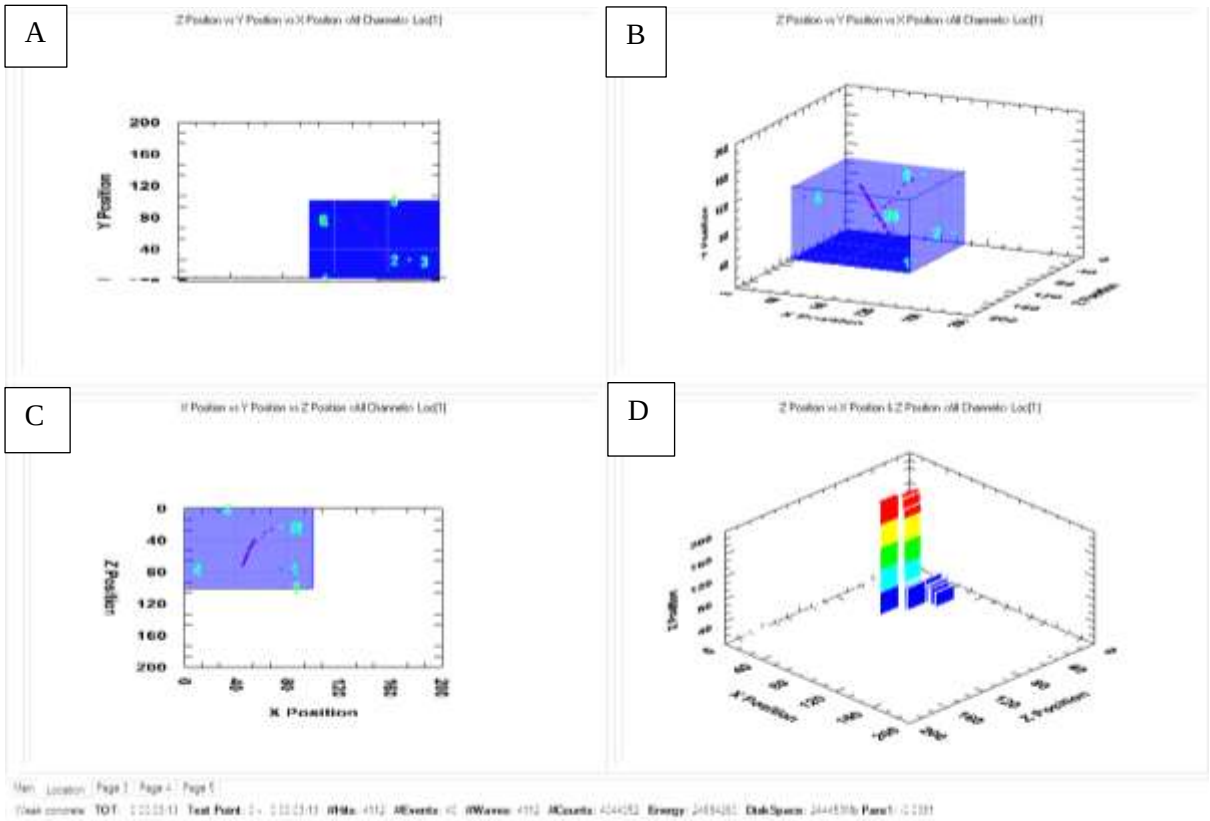

FIGURE 5-169: AMS3 Location graphs Point of fracture, A) Depth view, B) 3D view, C) Overhead view, D) Actual positioning spots.

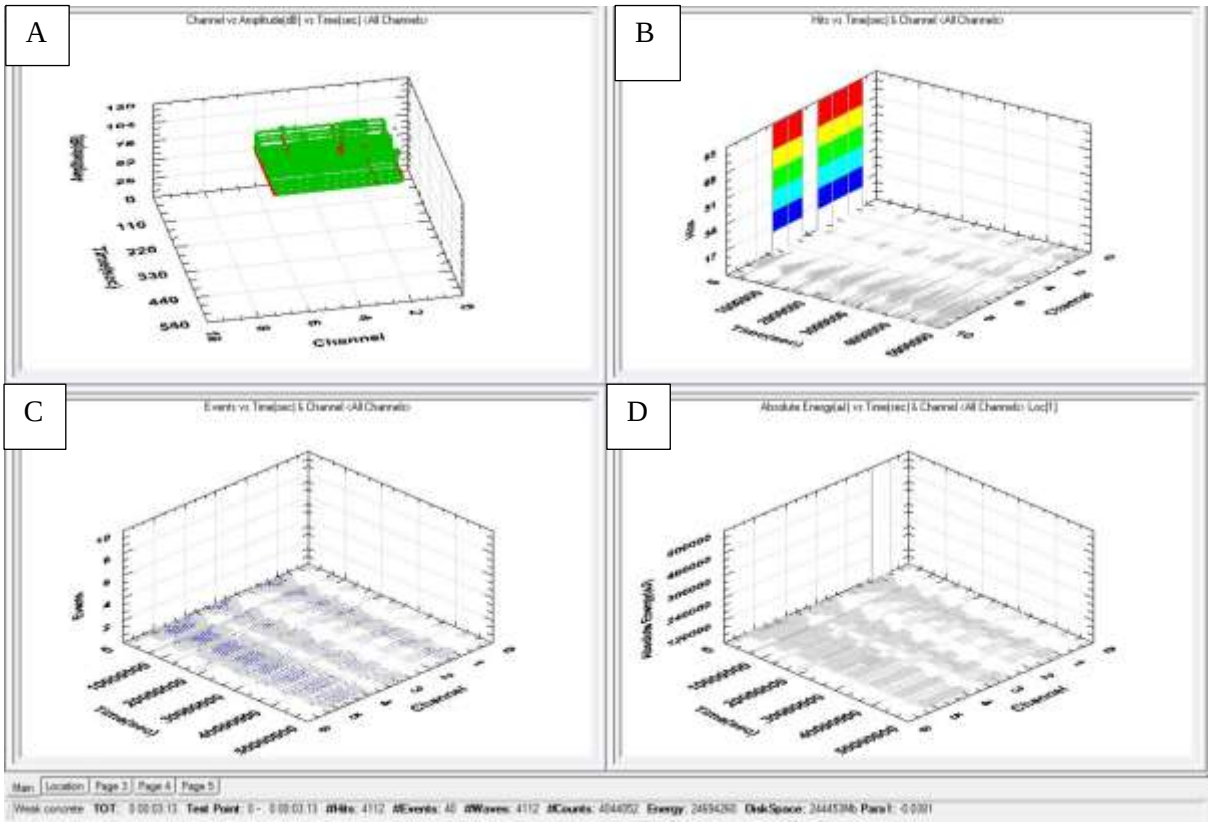

FIGURE 5-170:AMS3 Sensor Graphs Point of Fracture, A) Acoustic signals detected each channel, B) Hits Vs Time, C) Events Vs time, D) Absolute energy Vs time.

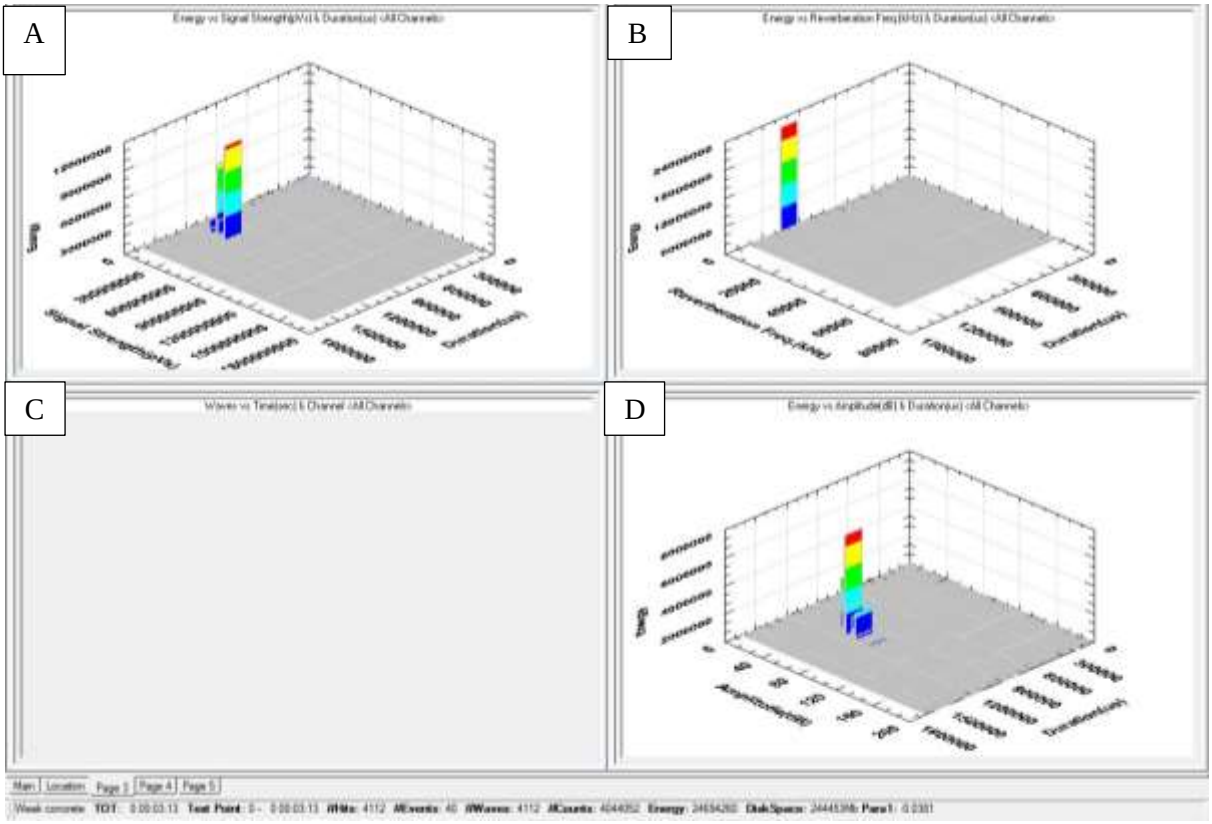

FIGURE 5-171: AMS3 Energy, duration and signal strength graphs Point of fracture, A) Energy Vs signal strength, B) Energy Vs Reverberation, C) Empty, D) Energy Vs Amplitude.

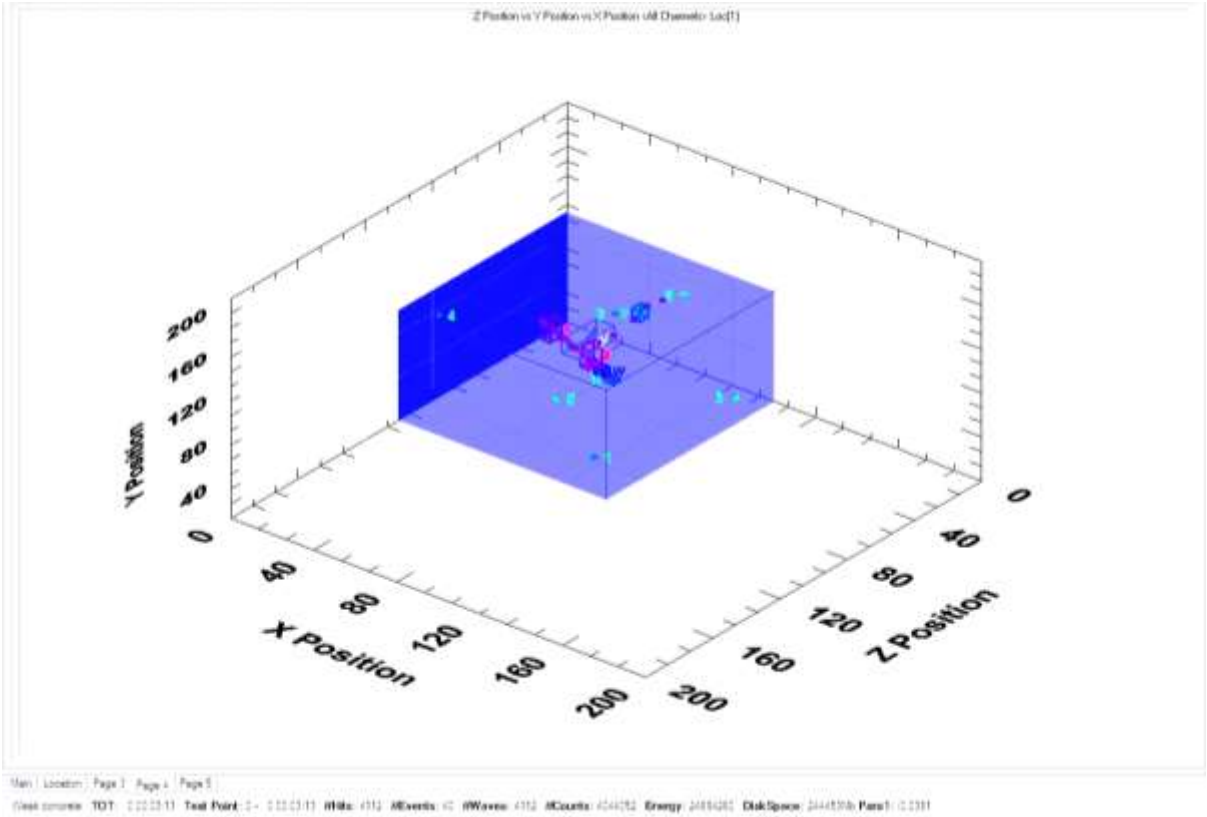

FIGURE 5-172: AMS3 3D graph events grouped Point of Fracture.

In Figure 5-169 & Figure 5-172 a trail of acoustic events has been plotted from the borehole following a diagonal vector that corresponds to the area of weakness that was found in drilling interval 100mm to 80mm; and which corresponds to the area of convergence between the primary fracture and the secondary fracture, the scan of which is shown in Figure 5-79 circled. While the events at the borehole represent the short primary fracture opening up, the lack of multiple different events suggests that this fracture was instantaneous. This is further corroborated when looking at the constant near identical trail of signals picked up by each sensor in Figure 5-170. The constant line from the borehole following the secondary fracture and the areas of weakness show that these fractures were not instantaneous but grow as the fluid was being pumped in to the sample. The weakened state of the rock was not able to withstand the pressure head of the fracturing fluid. The events follow the secondary fracture as it broke through the existing fracture but then seemingly trails off, which could be due to the ebbing motion of the fracturing fluid at the junction between the pre-existing fracture and the secondary fracture. This can cause 'echo's' which then get confused when similar frequency sounds hit the sensors. Indeed, this is a frequent occurrence in passive sonar when a number of contacts are made, sensors can be temporarily confused leading to the initial data being slightly out in distance and trajectory.

Looking at Figure 5-171 most signals were of amplitudes of around 50 to 90kHz with durations of 90,000 to 100,000µsecs the majority of the entire energy of 24694260J was of a reverberation of less than 5kHz. As expected the signal strength is not as strong as during the drilling but still the majority

of the entire energy had a signal strength of $150x10^6\rho Vs$ & $300x10^6\rho Vs$. This is still a relatively strong signal and therefore provides a high confidence rating of the readings of the acoustics.

5.7.2.2 AMS4

The AMS4 sample was the last Accrington Mudstone sample tested. Sensor 1 was not receiving any signals, probably due to the distance of the sample from the edge of the plaster. The programme was re-run with sensor 1 switched off so that this would not affect the result.

100MM TO 90MM

The acoustic location and graph data from the software is presented in Figure 5-173 to Figure 5-176.

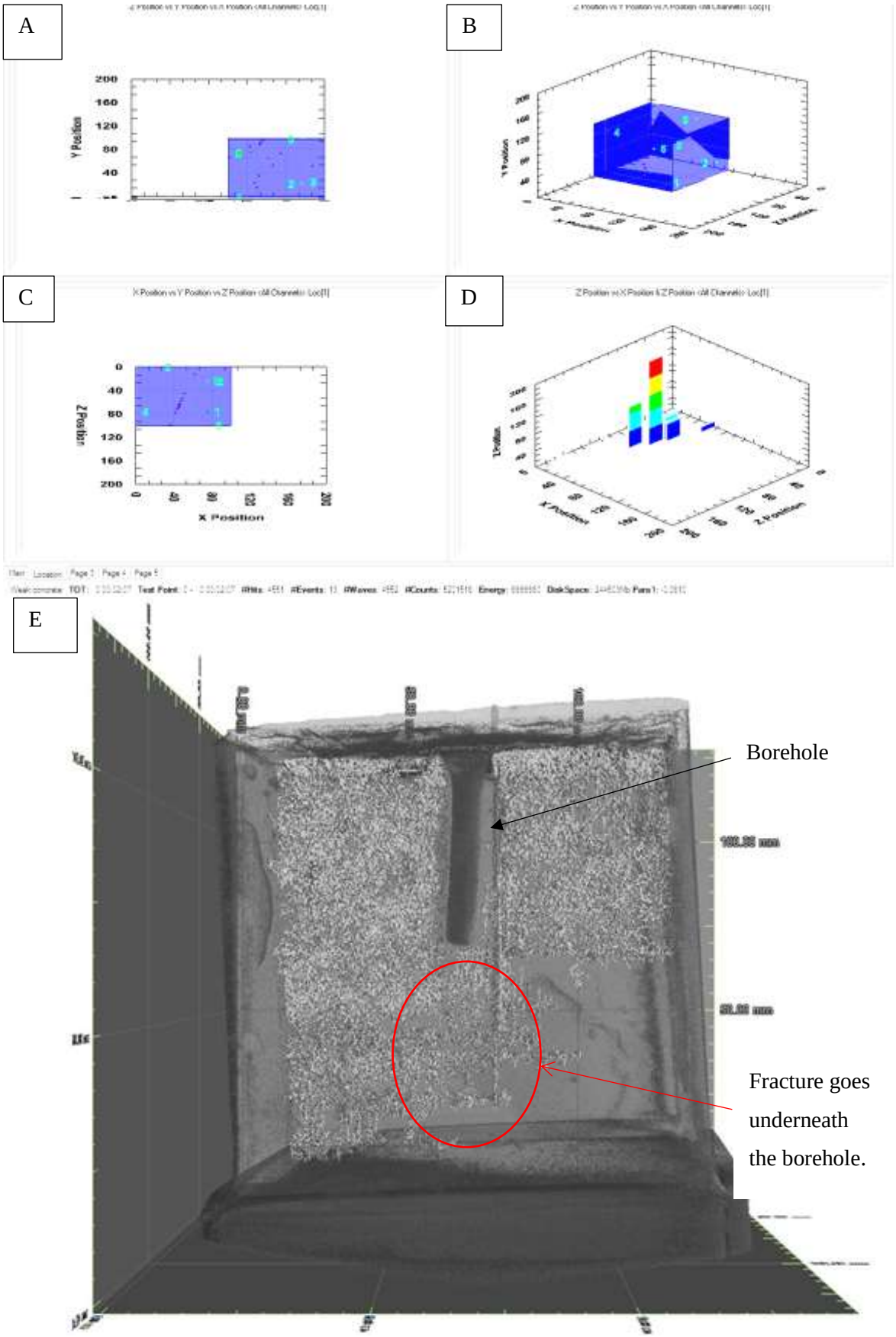

FIGURE 5-173: AMS4 Location graphs 100mm - 90mm & scan showing fracture below the borehole, A) Depth view, B) 3D view, C) Overhead view, D) Actual positioning spots. E) 3D reconstruction.

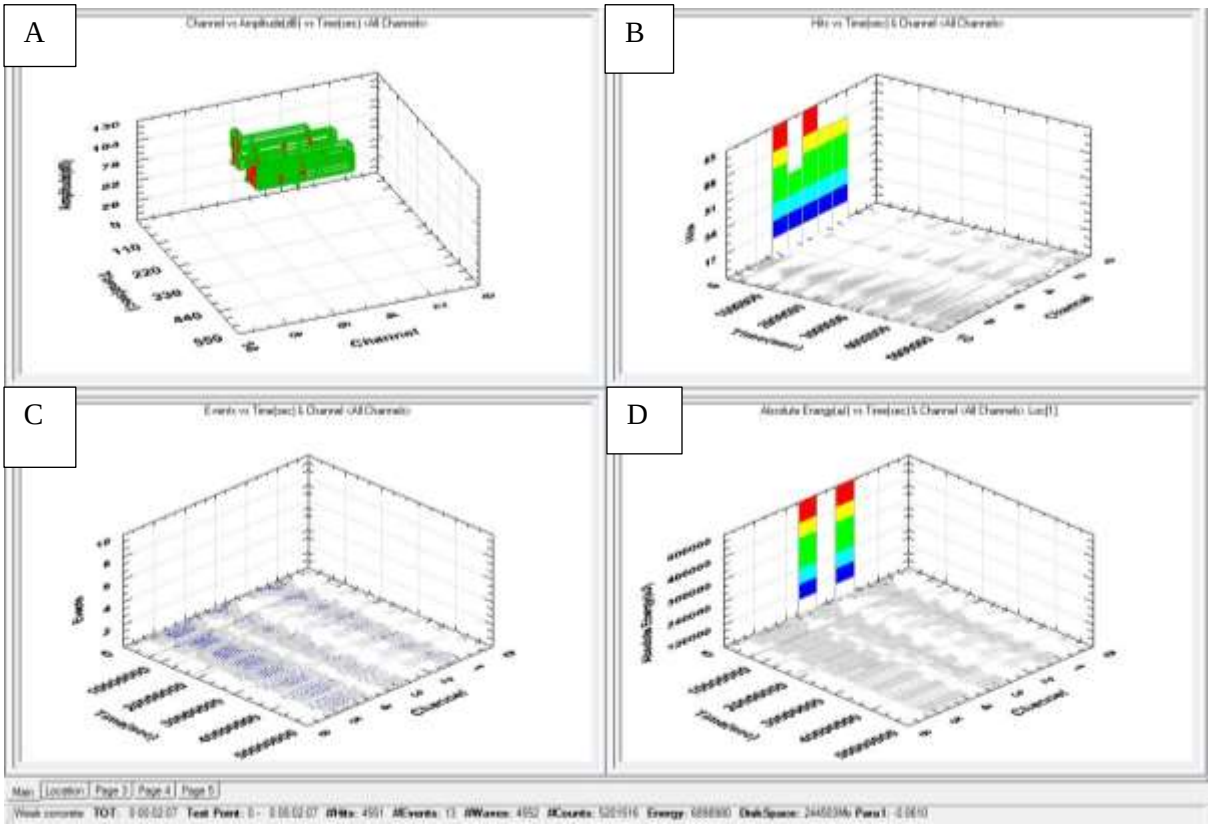

FIGURE 5-174: AMS4 Sensor Graphs 100mm - 90mm, A) Acoustic signals detected each channel, B) Hits Vs Time, C) Events Vs time, D) Absolute energy Vs time.

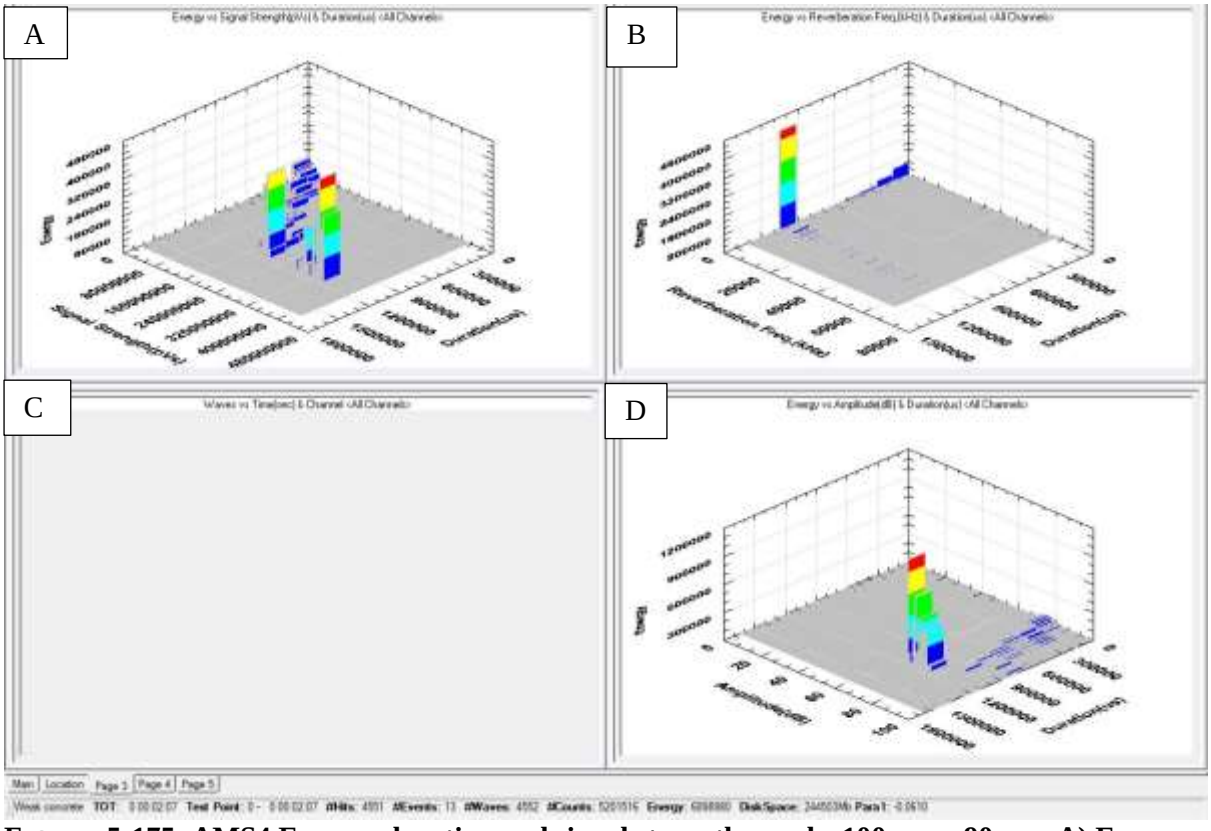

FIGURE 5-175: AMS4 Energy, duration and signal strength graphs 100mm – 90mm, A) Energy Vs signal strength, B) Energy Vs Reverberation, C) Empty, D) Energy Vs Amplitude.

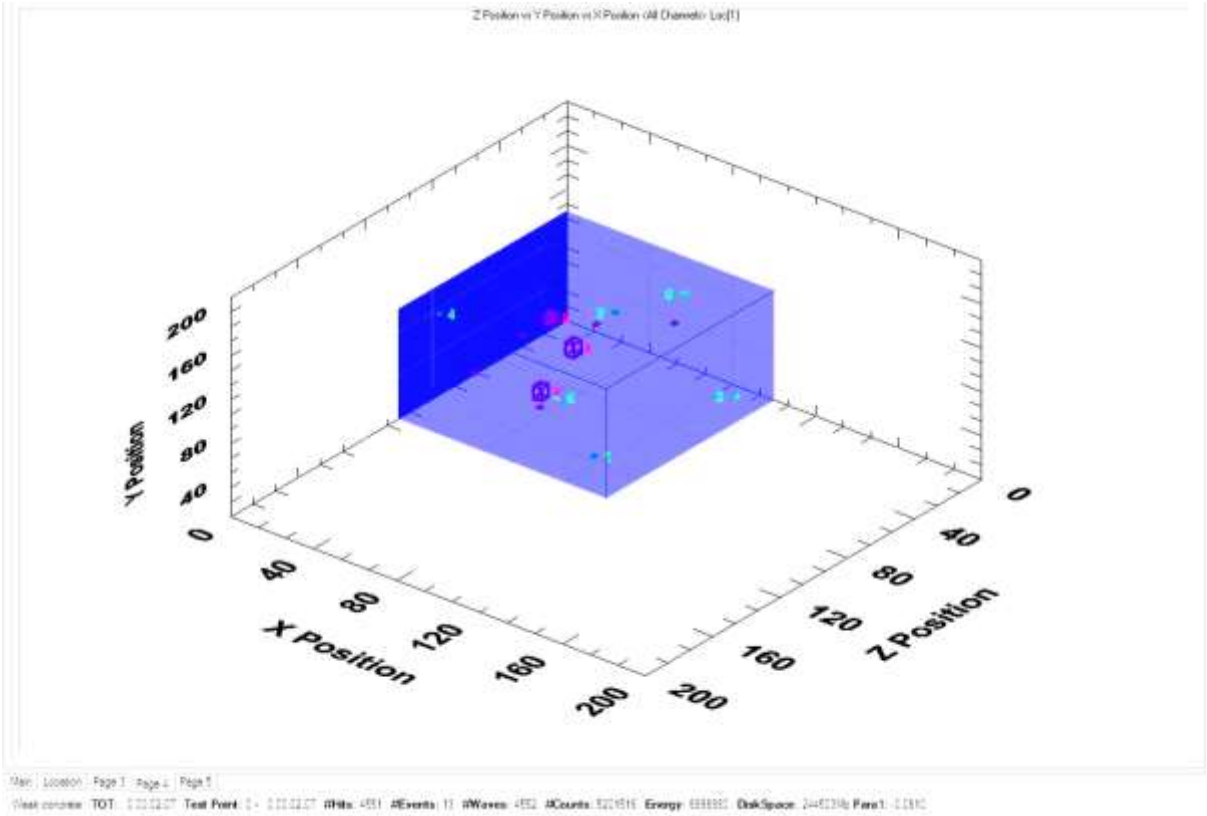

FIGURE 5-176: AMS4 3D Graph Event Grouping 100mm to 90mm.

Figure 5-173's Overhead view and side view shows the events being picked up close to the centre just below the top surface of the sample. Figure 5-176 shows that this area, close to the centre, has been grouped together. There is a clear grouping of events near the centre from approximately 99mm on the Y axis down to approximately 88-89mm. There is a collection of two other main groupings of placed events visible in Figure 5-176 with two other hits that have not been placed in groupings. These two groupings are found mid-way through the sample and towards the bottom of the sample, slightly off centre, respectively. These acoustic events are probably due to damage being done by drilling. Closer inspection of the post fracture scan (Figure 5-173), shows that there is a difference in this sample due to the fracture continuing beneath the borehole, this is highlighted in the red circle. In all other samples the fracture has radiated out from the borehole, either increasing or decreasing in height as it travels away from the borehole but not actually propagating underneath. This would suggest that there was some damage done to the sample during drilling towards the bottom of the sample hence its unusual fracture pattern, this corresponds to the acoustics groupings during the drilling.

4551 hits gave just 13 events, this shows that the acoustic activity was happening in just in a small defined area, as shown by Figure 5-174 and in relatively close groupings. Entire energy transmitted was 6898990J, the majority of the energy was transmitted in a signal strength of 160,000,000ρVs 350,000,000ρVs all with a duration of 90,000 and 120,000μsecs, Figure 5-175. With large amounts of energy transmitted with such a strong signal the confidence of the acoustic placings is high.

90MM TO 80MM

The acoustic and graph data provided by the software are presented in Figure 5-177 to Figure 5-180

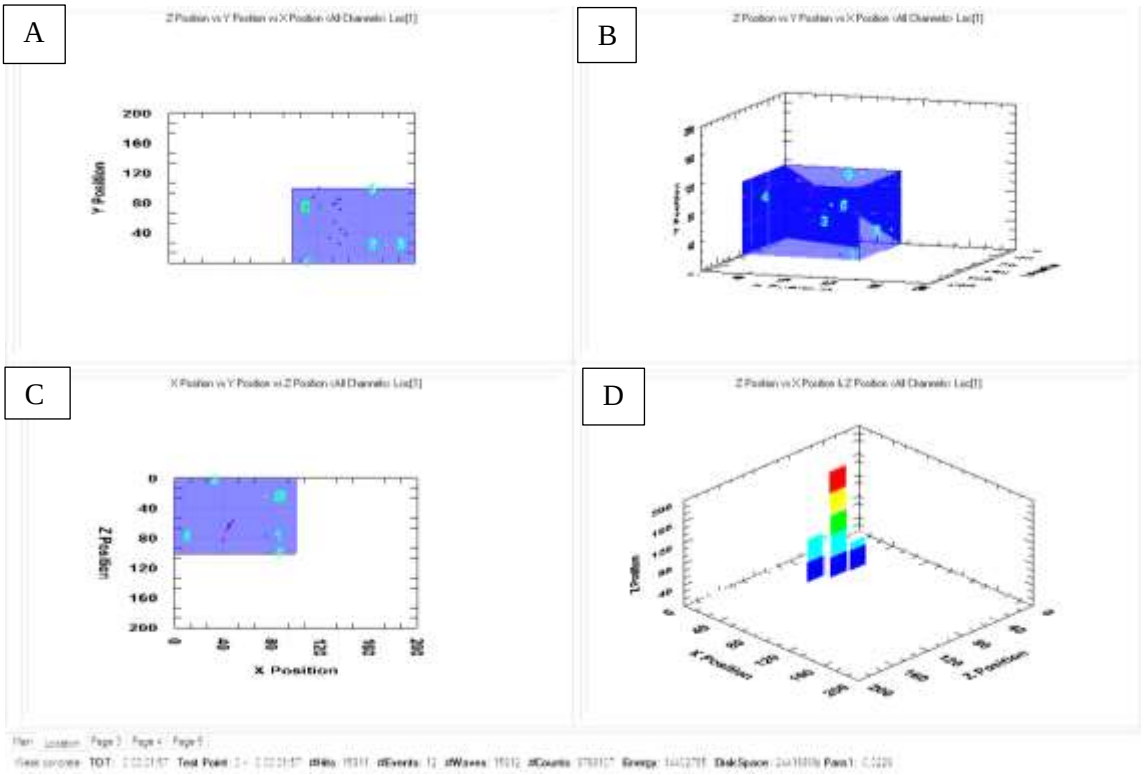

FIGURE 5-177: AMS4 location graphs 90mm to 80mm, A) Depth view, B) 3D view, C) Overhead view, D) Actual positioning spots.

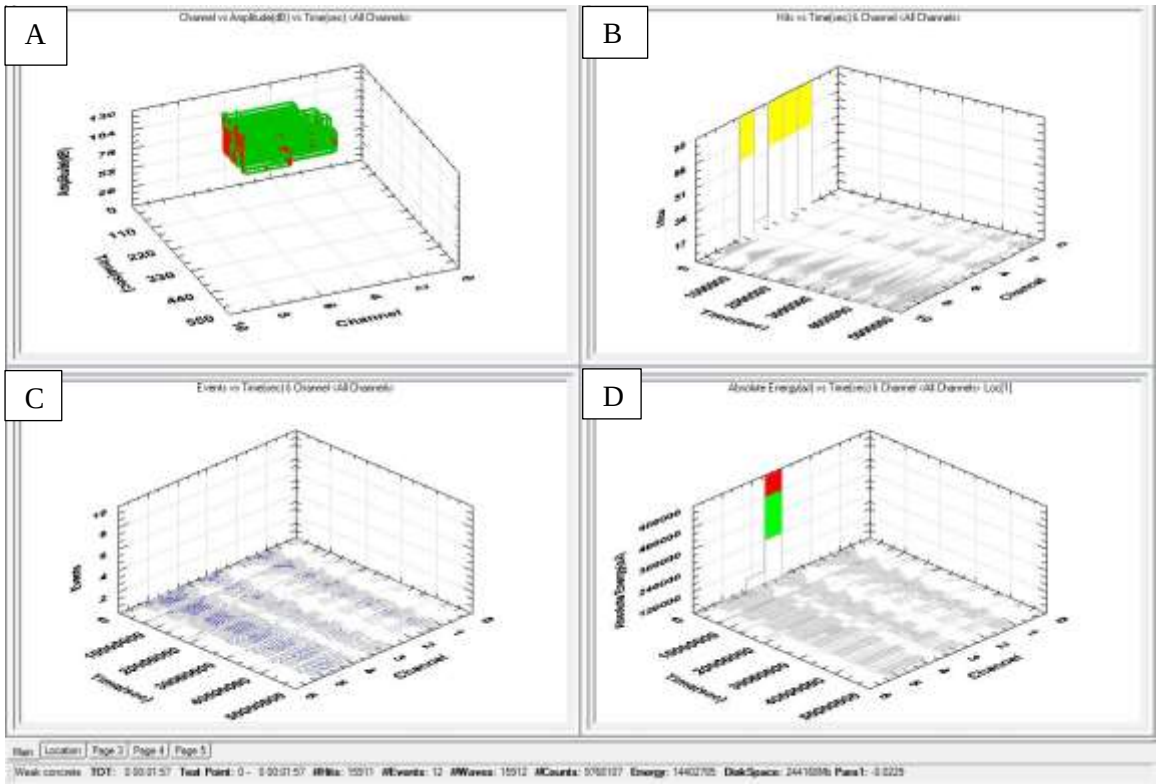

FIGURE 5-178: AMS3 Sensor graphs 90mm - 80mm, A) Acoustic signals detected each channel, B) Hits Vs Time, C) Events Vs time, D) Absolute energy Vs time.

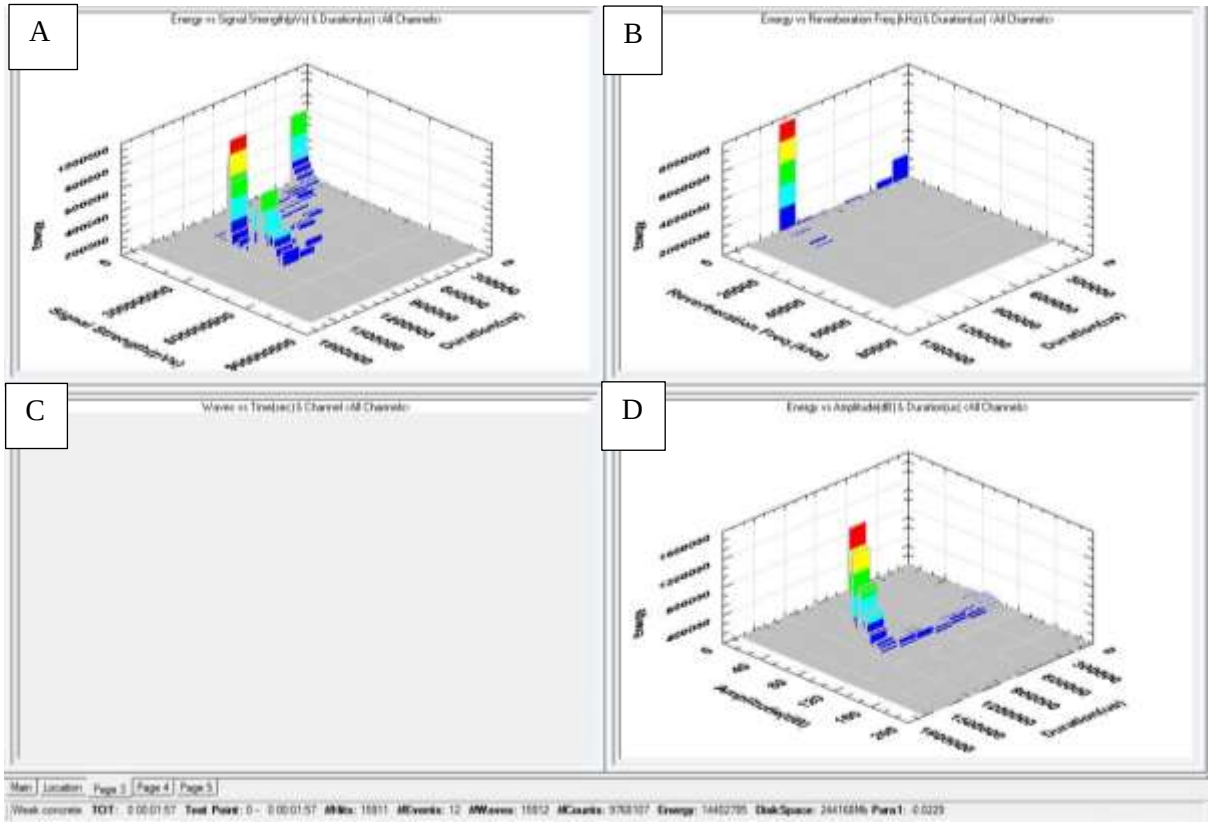

FIGURE 5-179: Energy, duration and signal strength graphs 90mm - 80mm, A) Energy Vs signal strength, B) Energy Vs Reverberation, C) Empty, D) Energy Vs Amplitude.

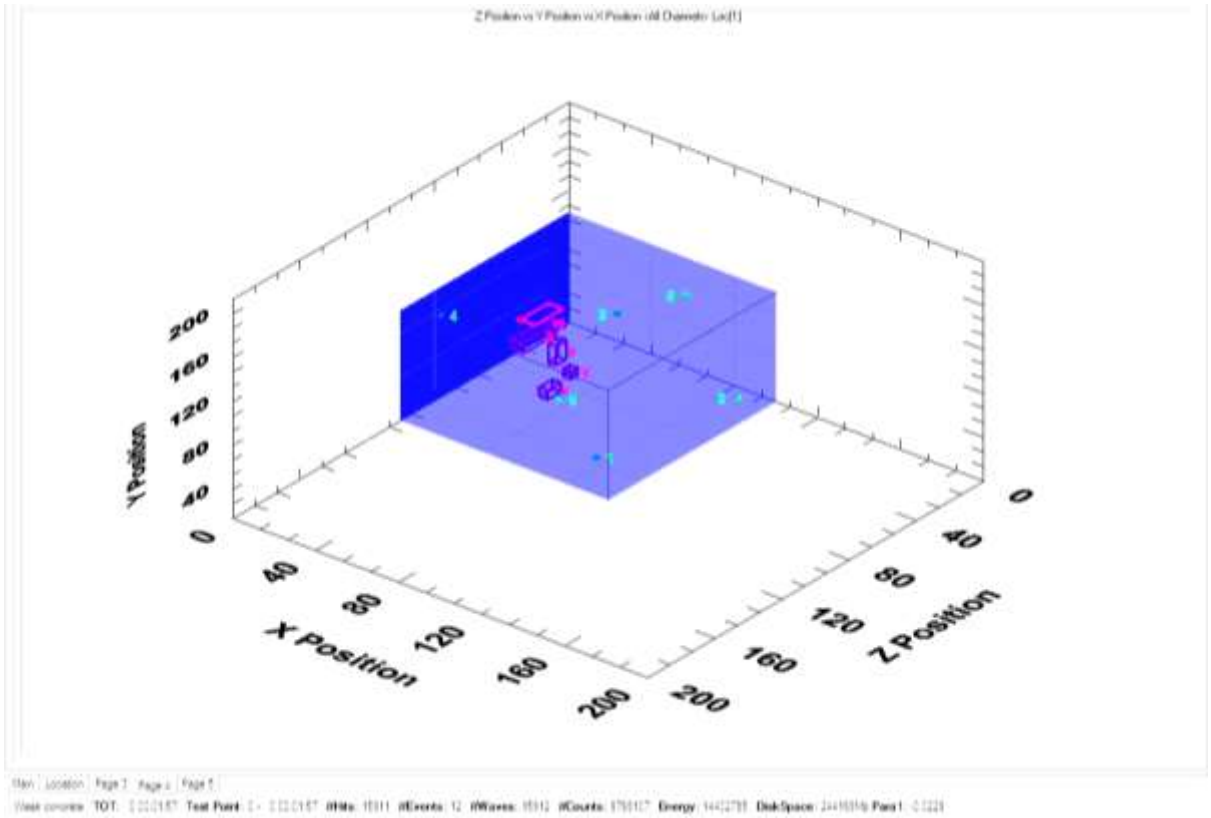

FIGURE 5-180: AMS4 3D Graph Events grouped 90mm to 80mm.

Figure 5-177 shows data similar to the 100mm to 90mm drilling interval in that the acoustics have picked up the drilling at just below 90mm (where the drill head was located). five events are linked working gradually down to around 80mm. The accuracy of the acoustics was confirmed when an event was placed linked to where the drill bit was accidentally dropped on to the sample, the acoustics picked this event up on the surface of the sample. The sample has a group of events placed three quarters of the length of the sample on the Y Axis. This suggests that there could be a plane of weakness towards the base of the sample and the continued drilling has started to open microfractures in this area.

Figure 5-180 shows events forming two groupings towards the base of the sample, indicating that there are two distinct areas of weakness with growing microfractures, this is evidence that acoustic events are placed along the route of where the fracture formed, when a fracture was induced, the fracture has followed the same area of weakness. Twelve events were linked for 15,911 acoustic hits which suggests that damage to the formation, due to areas of weakness from drilling and microfracture growth, is occurring in very confined parts of the sample. The similarity to the signals picked up by the sensors, in Figure 5-178, with sensor 6 having a spike, no doubt due to the close proximity of the drill to its holding plate and the sensor itself, suggest that there is a high confidence factor in the events where they are placed.

Energy was measured at 14402785J, with the main peaks being detected at signal strength of between $250x10^6$ρVs and $525x10^6$ρVs. It is interesting to note, though, that 600,000J had a minimum signal strength of less than 100ρVs whilst approximately 150,000J, in total, had a signal strength of less than $100x10^6$ρVs as shown on Figure 5-179. As this seems separate from the other signal strength groupings this looks like it could be the acoustic signal of the drill bit being dropped. This could account for its lack of signal strength as this was outside of the sample and not actually inside the sample.

80MM TO 70MM

The acoustic data and graphs are presented in Figure 5-181 to Figure 5-184

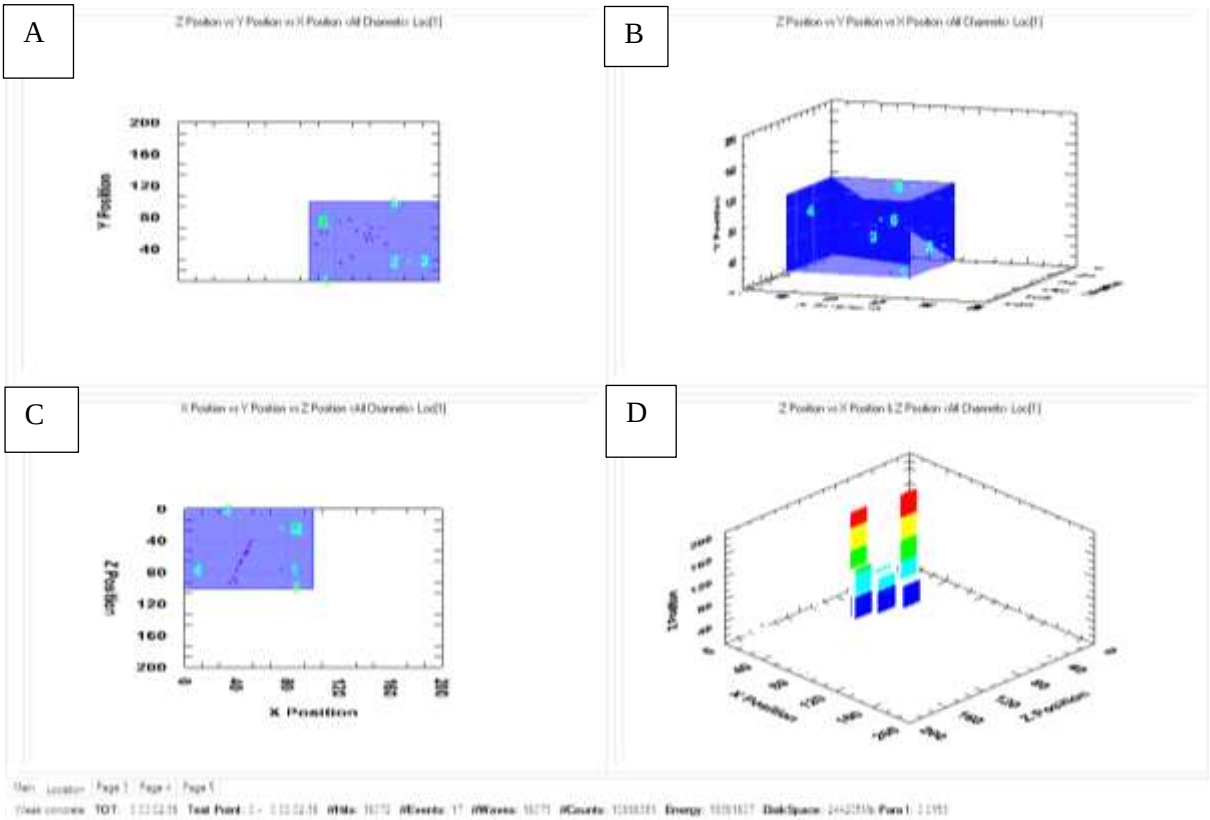

FIGURE 5-181: AMS4 Location graphs 80mm - 70mm, A) Depth view, B) 3D view, C) Overhead view, D) Actual positioning spots.

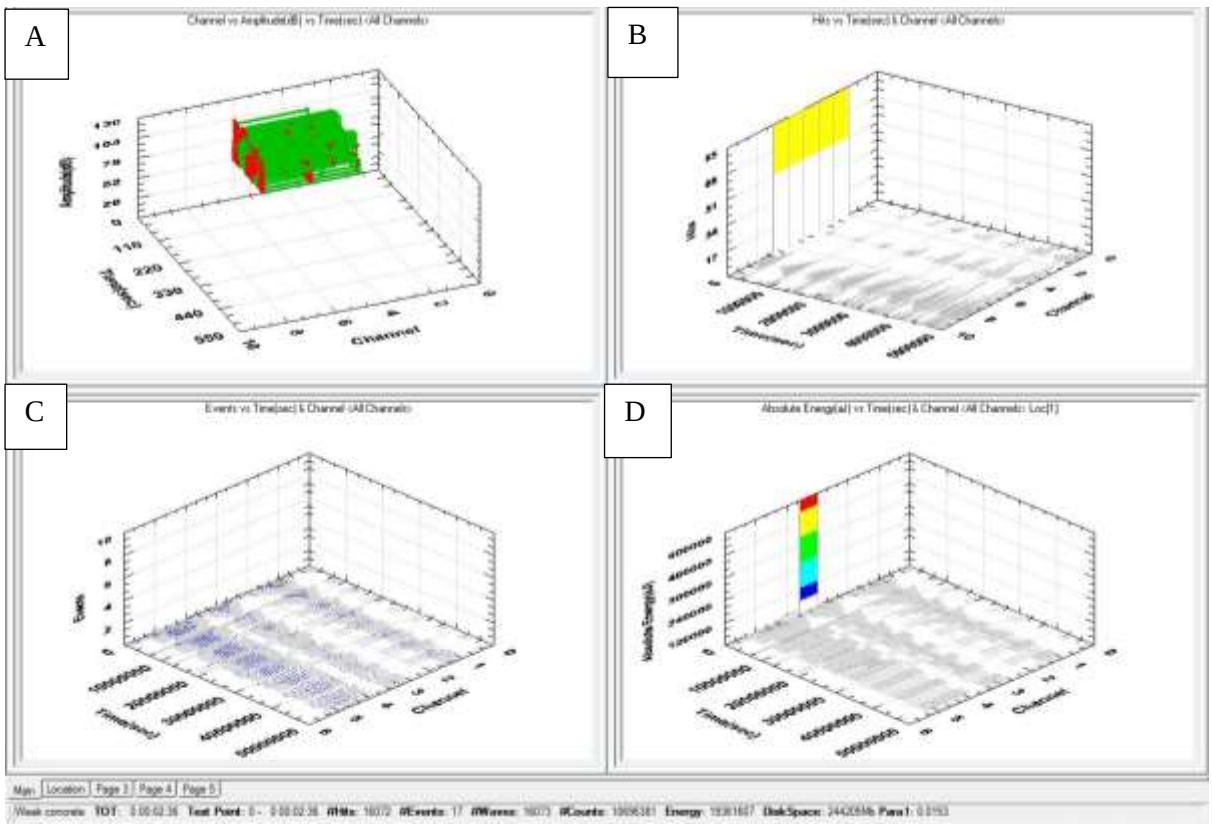

FIGURE 5-182: AMS4 Sensor Graphs 80mm - 70mm, A) Acoustic signals detected each channel, B) Hits Vs Time, C) Events Vs time, D) Absolute energy Vs time.

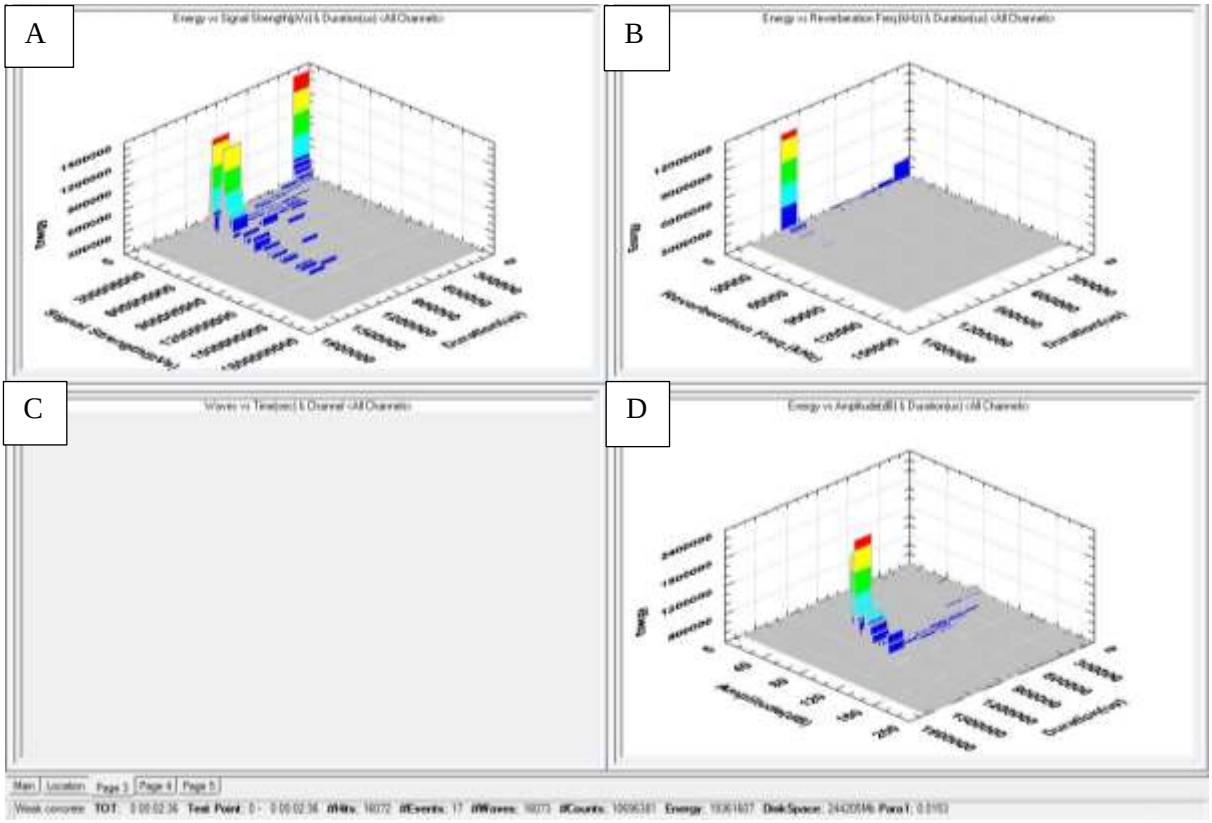

FIGURE 5-183: AMS4 Energy, duration and signal strength graphs 80mm - 70mm, A) Energy Vs signal strength, B) Energy Vs Reverberation, C) Empty, D) Energy Vs Amplitude.

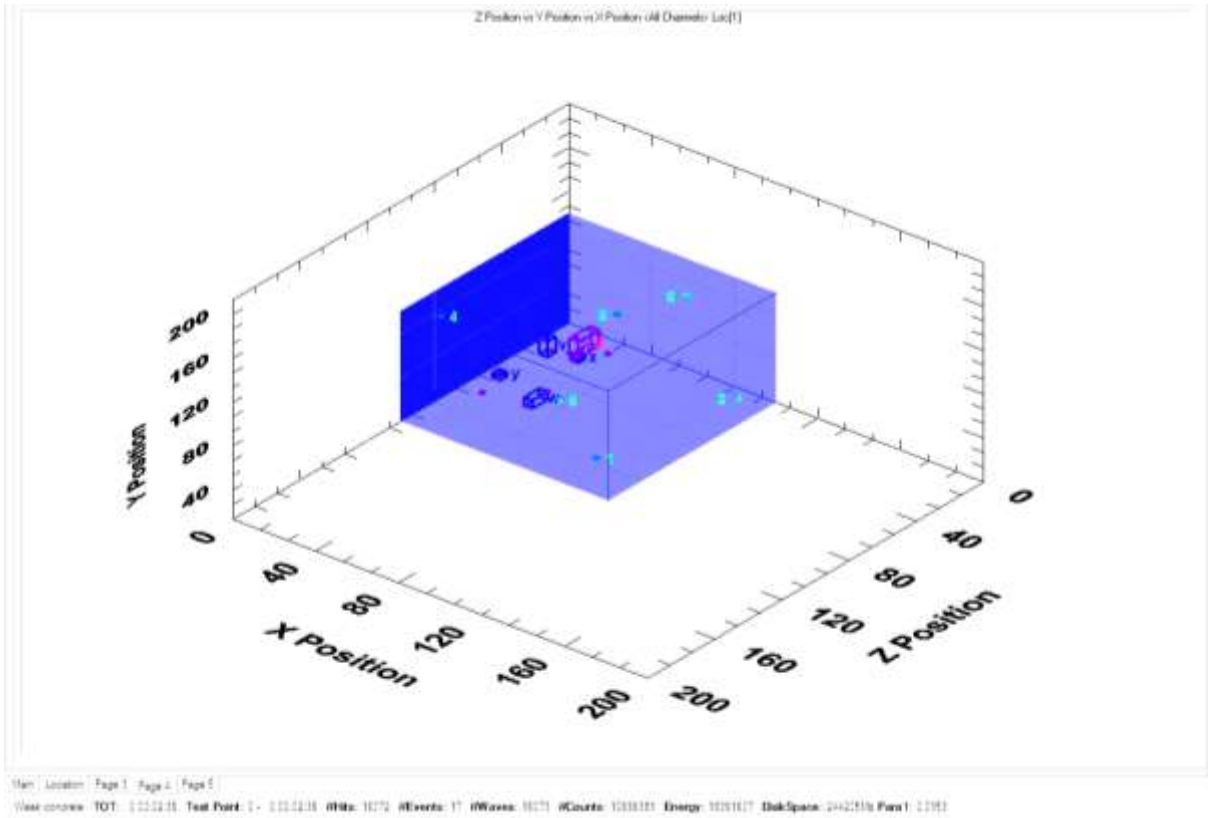

FIGURE 5-184: AMS4 3D graphs Events linked 80mm - 70mm.

Figure 5-181 shows the events are located lower on the Y axis starting at around 80mm down to approximately 65mm, though, there are also a number of groupings representing the events linked to extending the borehole. There are events moving down to the base of the sample, as in the previous drilling intervals. Figure 5-184 shows two groupings on the right of the sample, seen also in Figure 5-181, showing that there is damage being done to the sample in this section. Looking again at Figure 5-87, the sample with the side now recording hits has an unusually wide fracture that has extended from the bottom of the borehole. These acoustic events may be linked to previous areas of weakness, where microfractures have already opened up, and which have now placed strain on other parts of the sample. Unable to withstand these increased pressures two small areas have suffered damage in the form of micro fracture growth.

16072 hits were recorded and signals detected by the sensors were comparable (Figure 5-182). This transcribed into 17 events, with the placing of these events suggesting that acoustic activities are occurring in close succession and proximity. Figure 5-183 shows that the typical signal strength (as seen previously) for the main band of energy is recorded at between $300x10^6\rho Vs$ and $550x10^6\rho Vs$, however, small bands of lower energy were recorded up to $1{,}200x10^6\rho Vs$. These increasing small bands of localised energy groupings account for the increase in the events recorded and the detection of further damage done in the right-hand side of the sample, shown in the side view of Figure 5-181. 95% of the energy recorded has a reverberation of less than 5 kHz and a duration of between 900,000μsecs and 1,200,000μsecs.

70MM TO 60MM

The data for this drilling interval is presented in Figure 5-185 to Figure 5-188

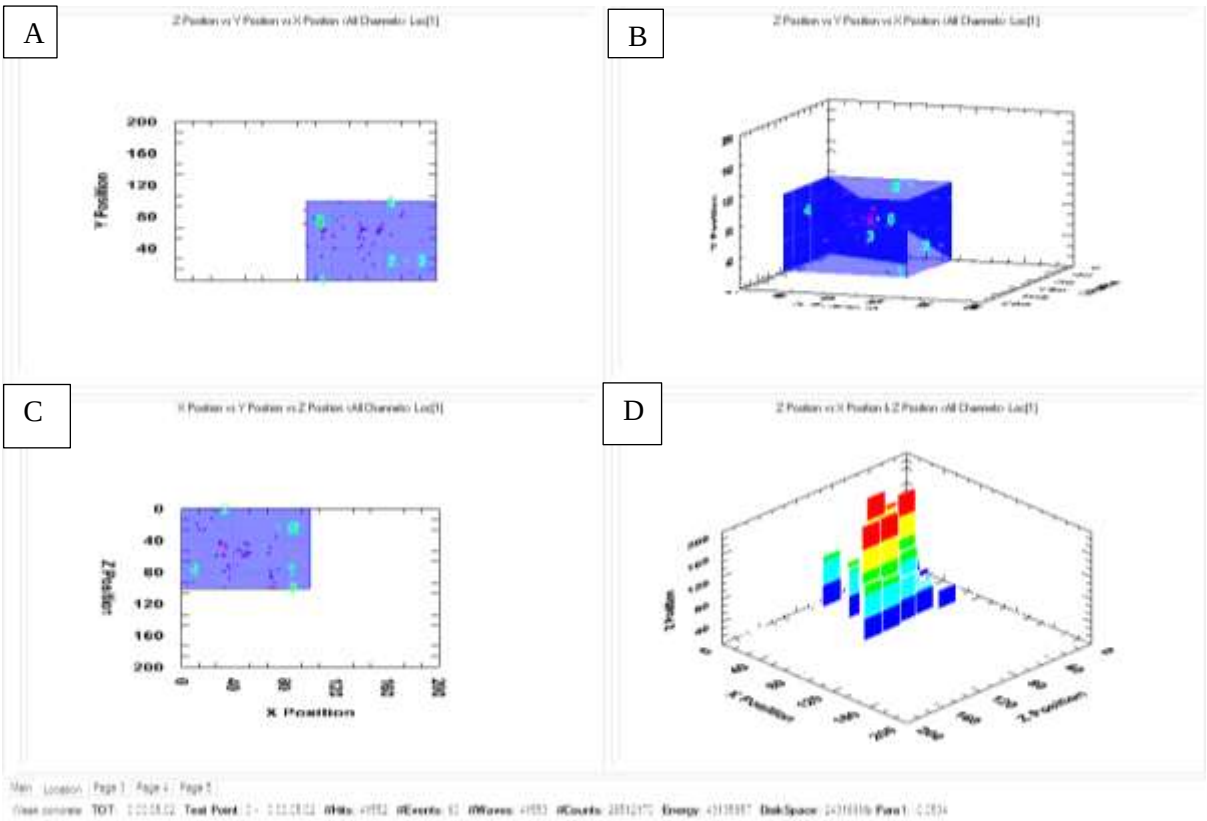

FIGURE 5-185: AMS4 location graphs 70mm-60mm, A) Depth view, B) 3D view, C) Overhead view, D) Actual positioning spots.

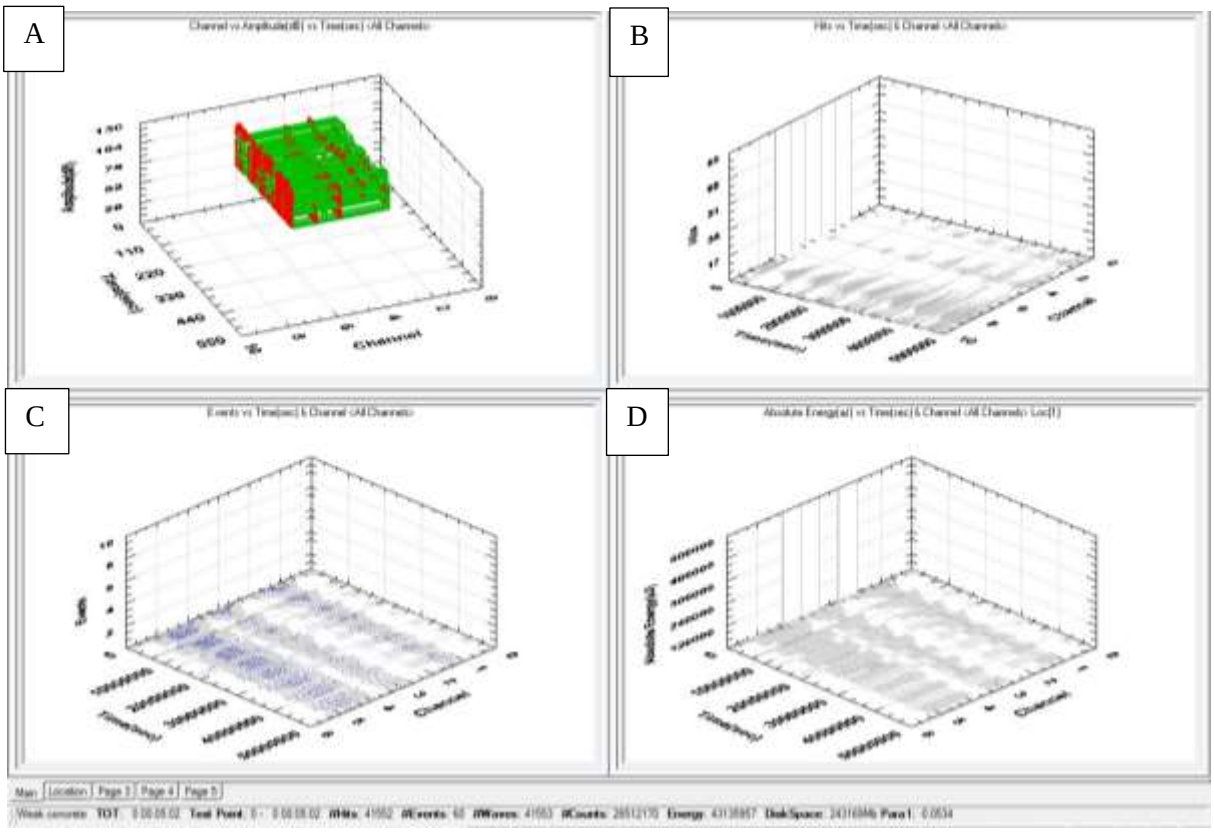

FIGURE 5-186: AMS4 Sensor Graphs 70mm - 60mm, A) Acoustic signals detected each channel, B) Hits Vs Time, C) Events Vs time, D) Absolute energy Vs time.

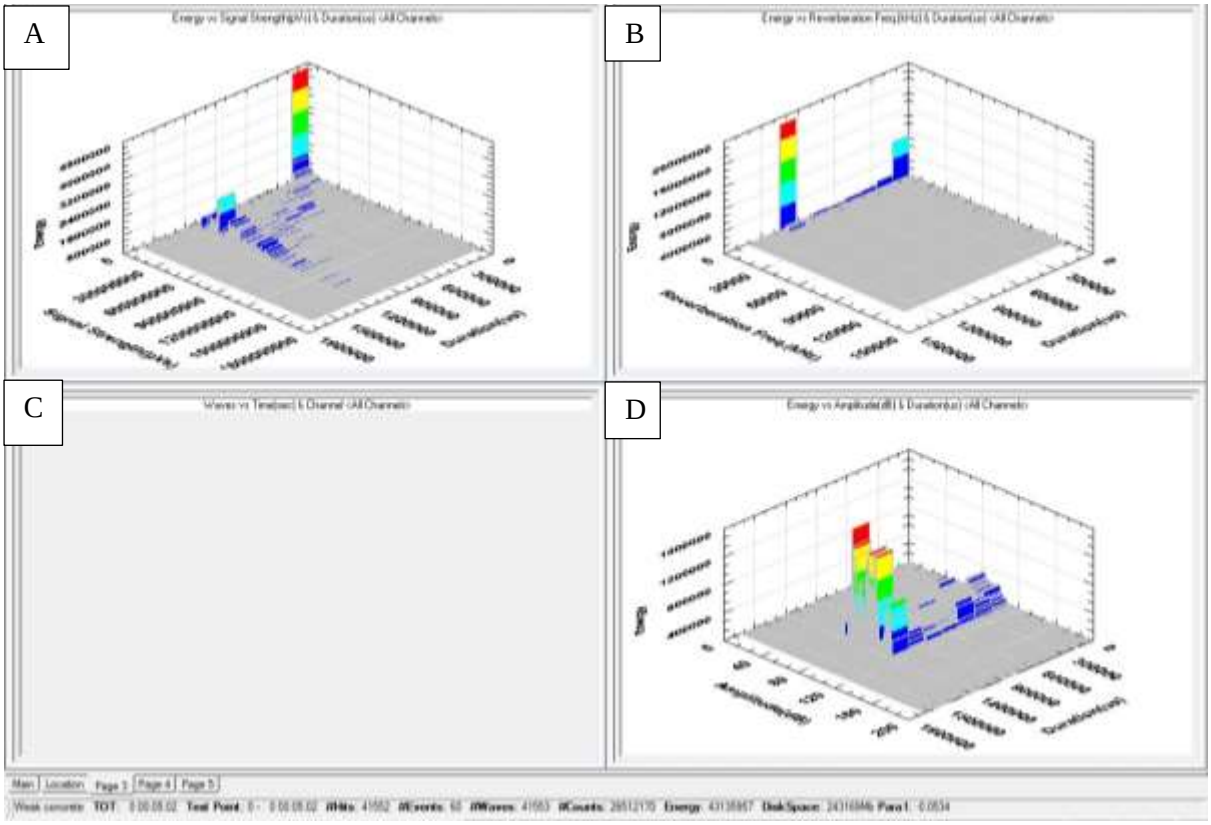

FIGURE 5-187: AMS4 Energy, duration and signal strength graphs 70mm - 60mm, A) Energy Vs signal strength, B) Energy Vs Reverberation, C) Empty, D) Energy Vs Amplitude.

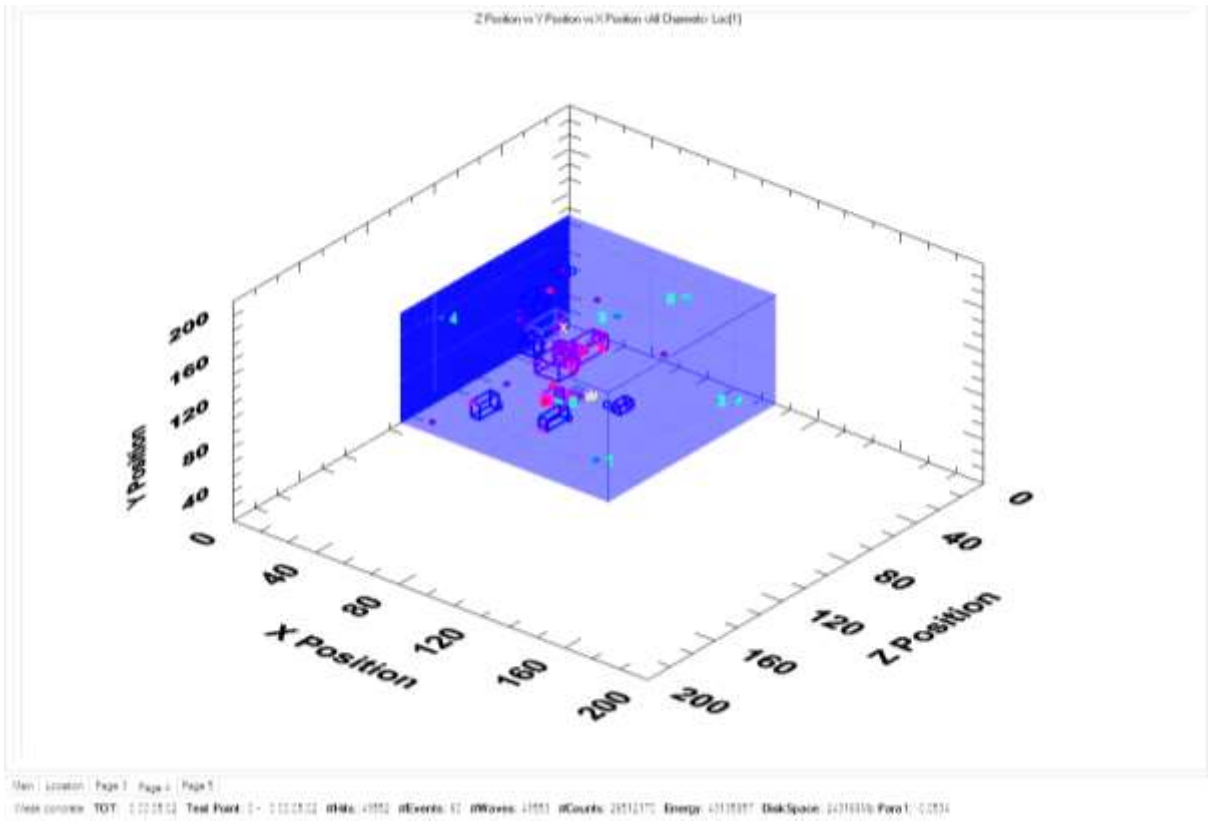

FIGURE 5-188: AMS4 3D Graph Events Grouping 70mm – 60mm.

Figure 5-185 & Figure 5-188 shows a large number of groupings predominately forming to the right of the sample, following on from the 80mm to 70mm interval, which shows further evidence of an increase in acoustic activity in the right hand side (when viewing from the side view in Figure 5-185). Again, this would suggest that as the sample is under stress and micro fractures have opened up in small weakened areas, other slightly more coherent areas are now unable to take the additional strain. There are even acoustic events occurring on the surface of the sample and this would tally with the observations noted of the plaster breaking during this interval. Signal strength, though still strong, was more scattered, with more individual hits measuring lower energy, at between $300x10^6\rho Vs$ and $600x10^6\rho Vs$, as seen in Figure 5-187. The signals picked up by the sensors are still analogous to previous samples, Figure 5-186, and the similar signal strengths and timings are recognised by the software and allow the placing of the events, giving a high confidence factor to the graphs.

60MM TO 50MM

The collected data is presented in Figure 5-189 to Figure 5-192.

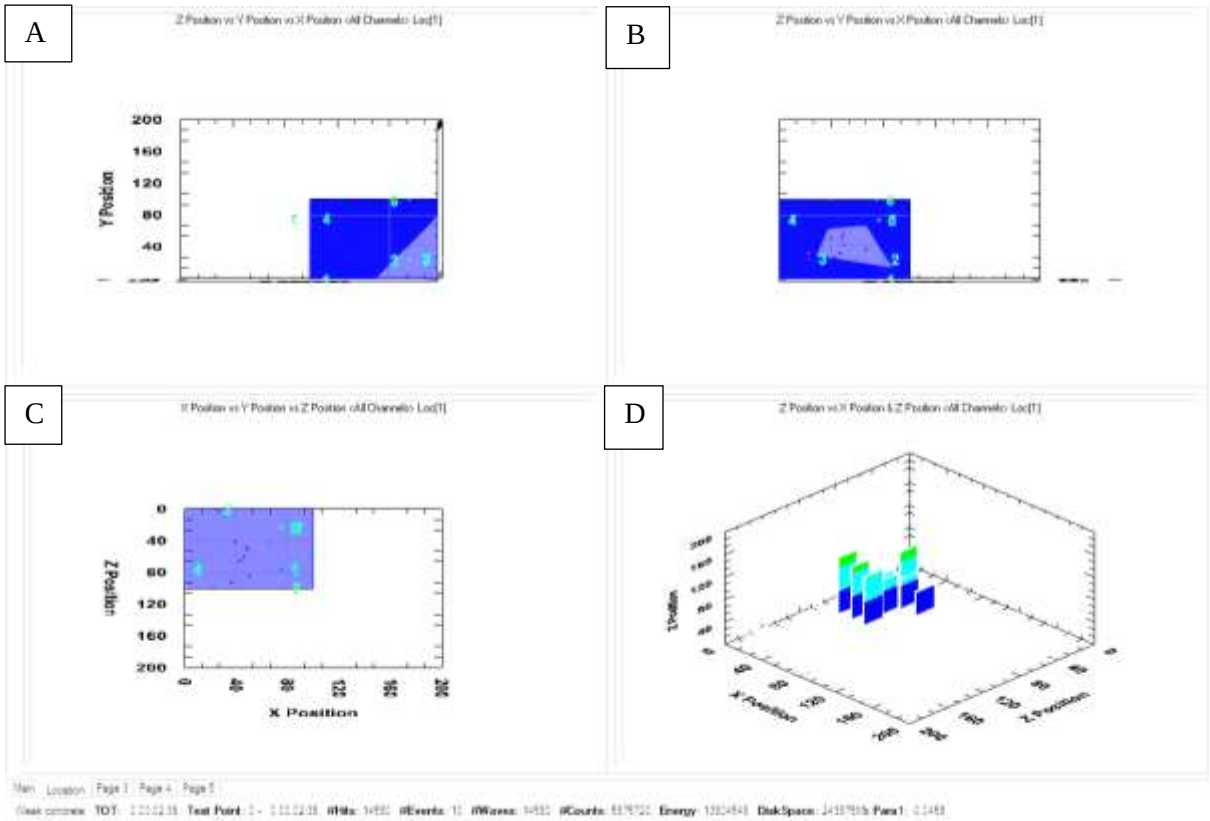

FIGURE 5-189: AMS4 Location Graphs 60mm to 50mm, A(Depth view, B) 3D view, C) Overhead view, D) actual positioning spots.

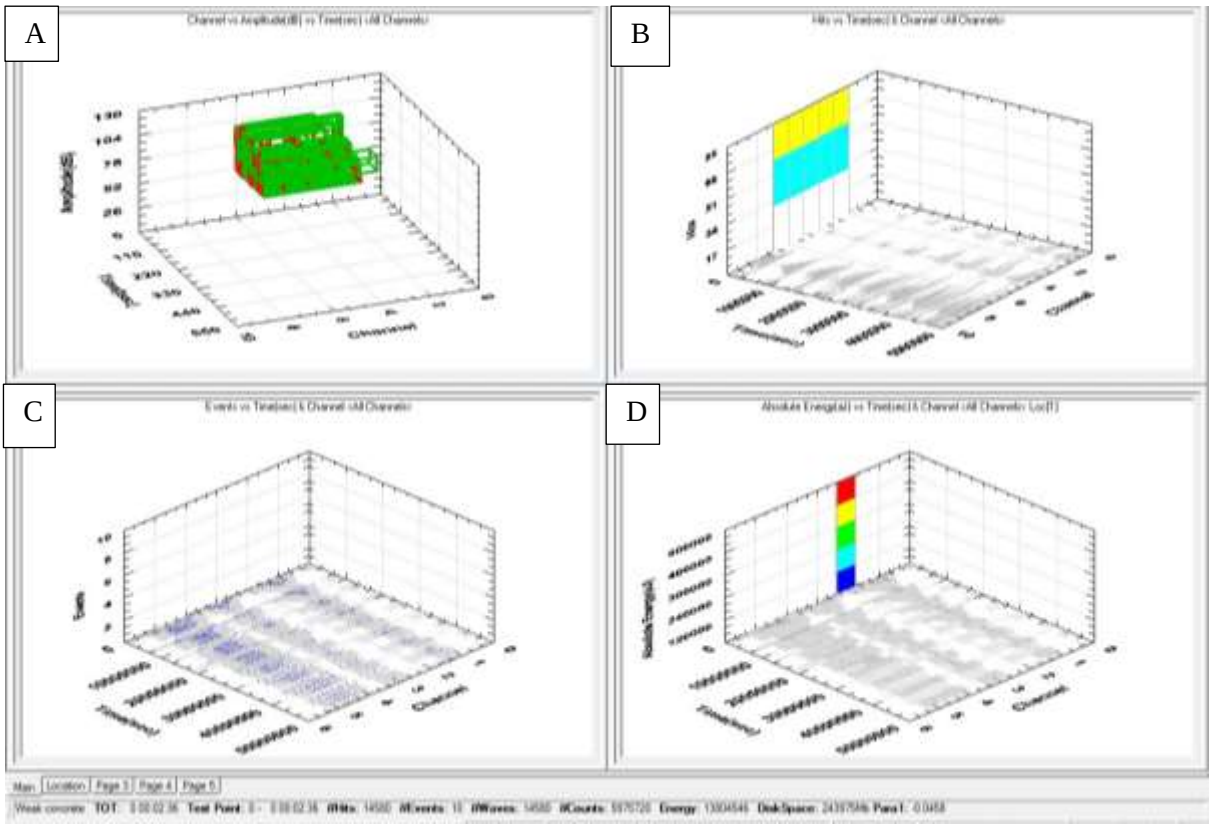

FIGURE 5-190: AMS4 Sensor Graphs 60mm-50mm, A) Acoustic signals detected each channel, B) Hits Vs Time, C) Events Vs time, D) Absolute energy Vs time.

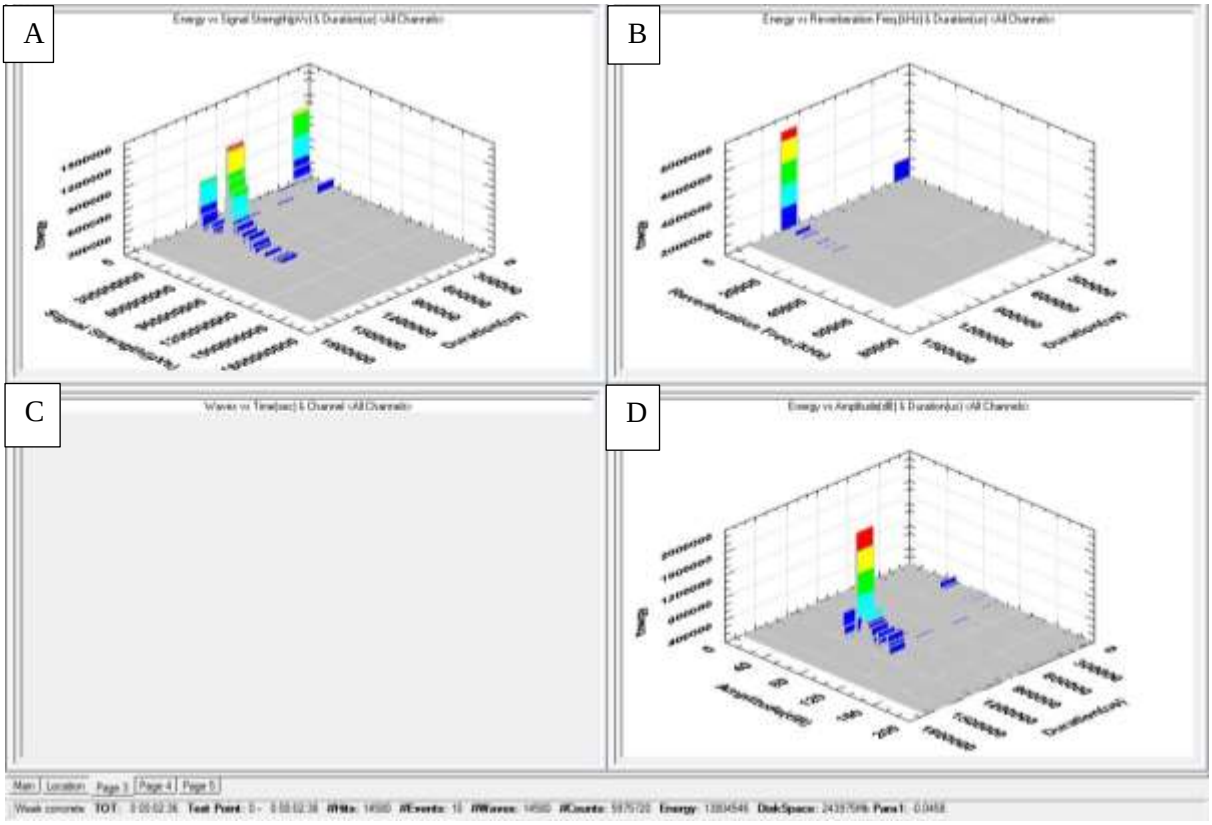

FIGURE 5-191: AMS4 Energy, duration and signal strength 60mm-50mm, A) Energy Vs signal strength, B) Energy Vs Reverberation, C) Empty, D) Energy Vs Amplitude.

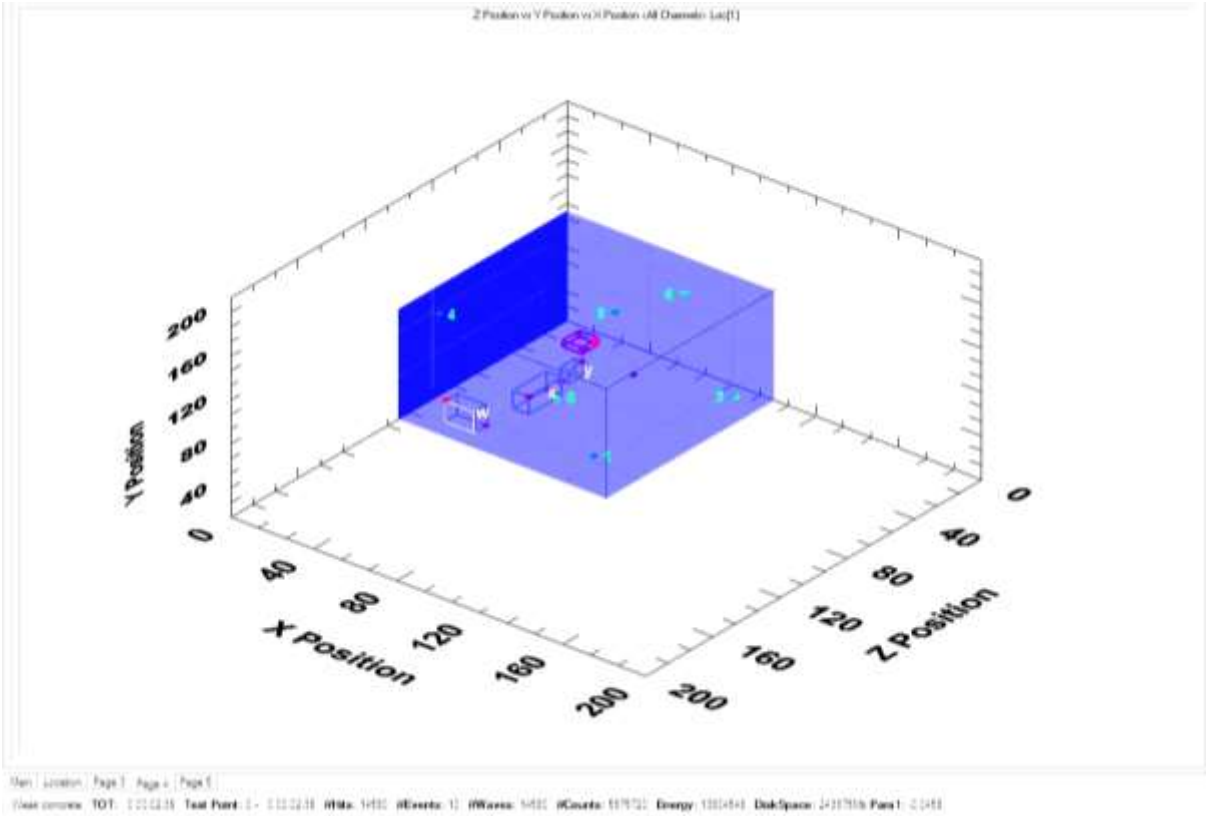

FIGURE 5-192: AMS4 3D Event Grouping 60mm-50mm.

As shown in Figure 5-189 and Figure 5-192 there are two centralised groups of events. One is picked up at approximately 60mm down to 45mm and corresponds to the drilling and the damage done to the sample directly under the drill bit. The second is beneath the first group registering at around 25 to 35mm. Again, this would suggest that there are areas directly under the borehole that are undergoing some damage as the drilling progresses. On this sample, as in the previous drilling intervals, there are still a number of events linked to the right side of the sample, again related to the damage done to this side and which would explain the unusual fracture pattern seen in the CT scan (Figure 5-87).

Figure 5-191 shows that although the signal strength is still strong the grouping starts at approximately $150x10^6$ρVs as opposed to the previous sample where the grouped signals, with a duration of between 900,000 and 1,200,000μsecs, had a signal strength starting in the region of $300x10^6$ρVs. Although weaker, it is still a relatively strong signal for the sensors. Figure 5-190 also highlights the correlating signals received by the sensors, with the top right graph showing the amplitude and timings of the signals.

POINT OF FRACTURE.

The acoustics did not record the point of fracture in this sample, but the location and energy graphs are presented in Figure 5-193 & Figure 5-194.

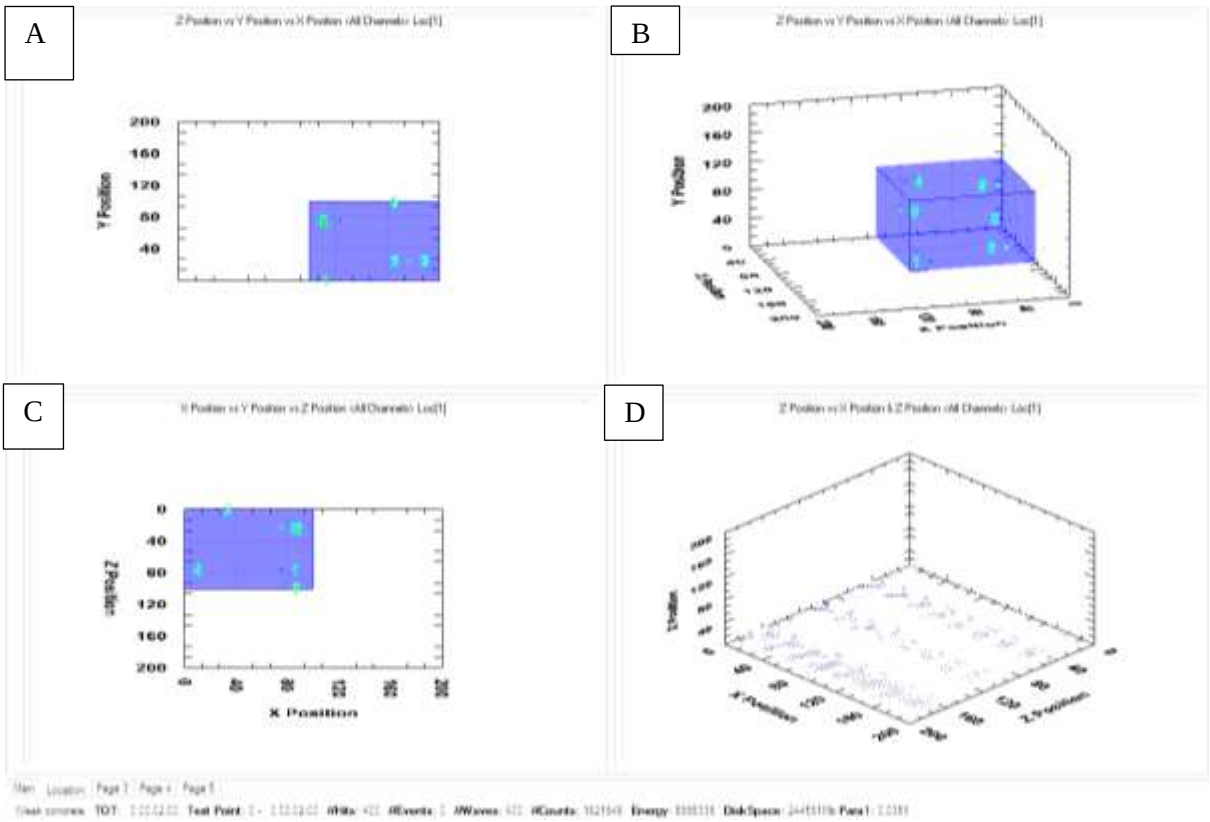

FIGURE 5-193: AMS4 Location graphs point of fracture, A) Depth view, B) 3D view, C) Overhead view, D) Actual positioning spots.

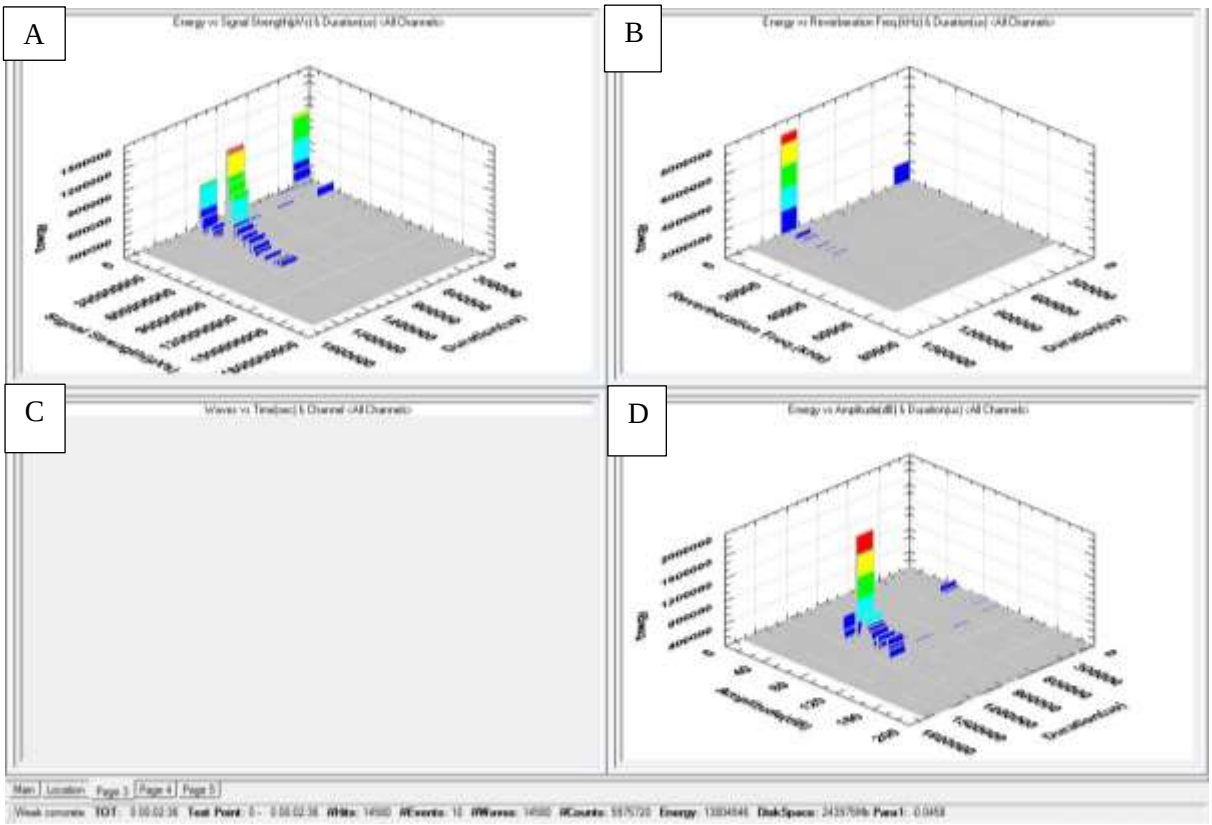

FIGURE 5-194: AMS4 Energy, Duration and Signal Strength Point of Fracture, A) Energy Vs signal strength, B) Energy Vs Reverberation, C) Empty, D) Energy Vs Amplitude.

Figure 5-193 shows that no events were placed even though the sensors detected 14580 hits. This is despite the low reverberation and high signal strength as shown in Figure 5-194 and can only be as a result of the previous damage done to the formation. The fracturing fluid had large areas to fill, each creating their own acoustic readings and echoes, over such a small instantaneous point in time during fracturing. The software has been unable to place the hits due to conflicting hit placements. It is possible that if sensor 1 had been operating the software might have been able to obtain sufficient data to differentiate the signals better, i.e. the software would have had more sensor information to aid placement calculations. This proves the importance that when further work is continued in this area it is vital that more acoustics are used.

WESTBURY SHALE.

The following four samples tested are from the Westbury shale formation. This organic rich shale is very weak due to the lack of clay content and is difficult to prepare without breaking. Hence some of these samples were contained in slightly more plaster than would be ideal.

5.7.2.3 WBS3

During the drilling of the WBS3 sample, the acoustic reader suffered a malfunction from 100mm to 70mm, which was subsequently found to be a loose connection in one of the wires that prevented the results from three sensors being received by the software. The connection was replaced by the time the 70mm drilling interval was started.

70MM TO 60MM

The acoustic and graph data is presented in Figure 5-195 to Figure 5-197

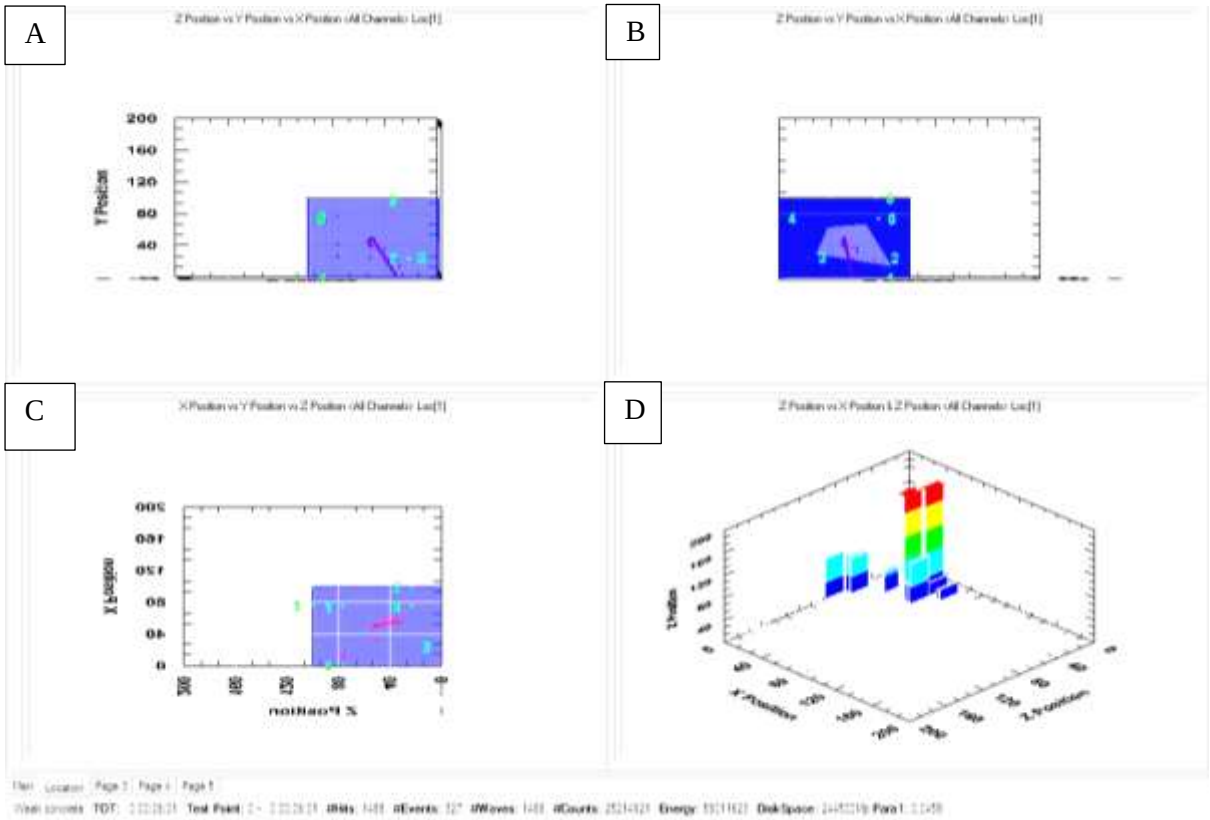

FIGURE 5-195: WBS3 Location Graphs 70mm-60mm, A) Depth view, B) 3D view, C) Overhead view, D) Actual positioning spots.

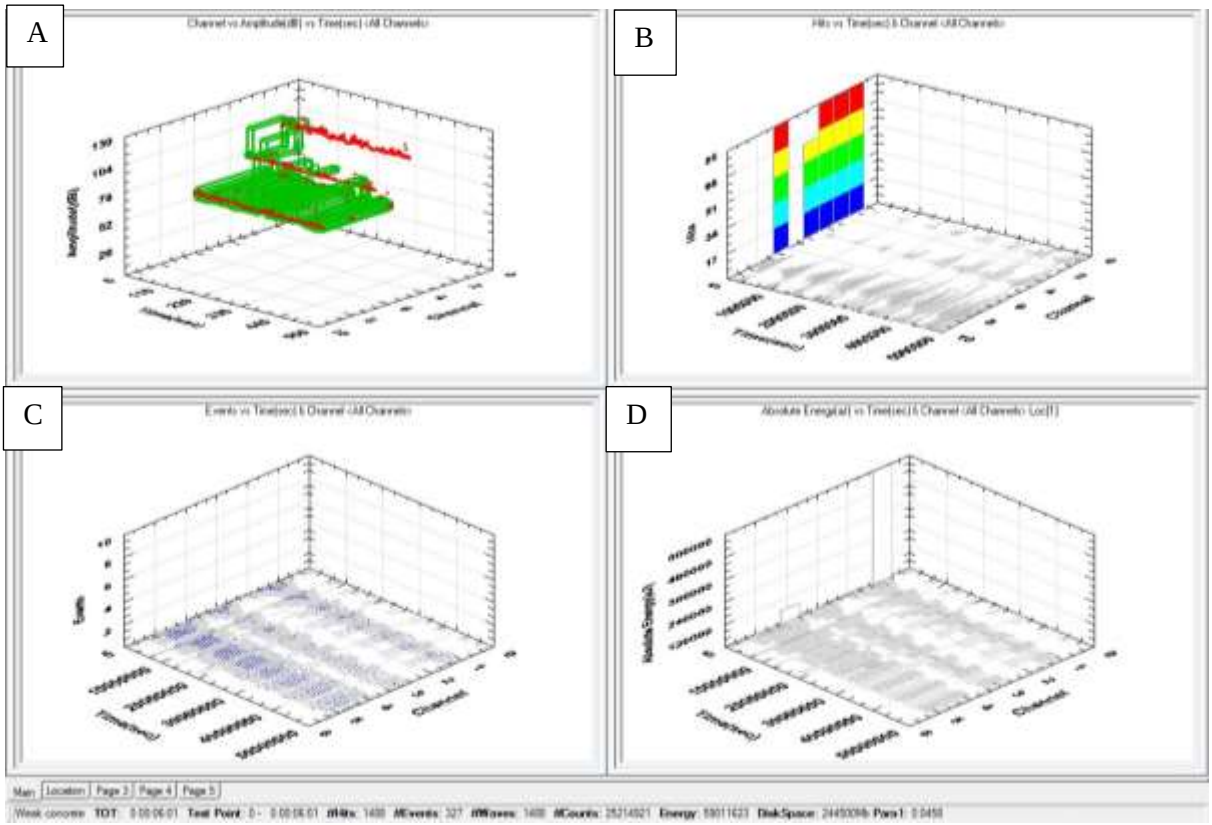

FIGURE 5-196: WBS3 Sensor graphs 70mm-60mm, A) Acoustic signals detected each channel, B) Hits Vs Time, C) Events Vs time, D) Absolute energy Vs time.

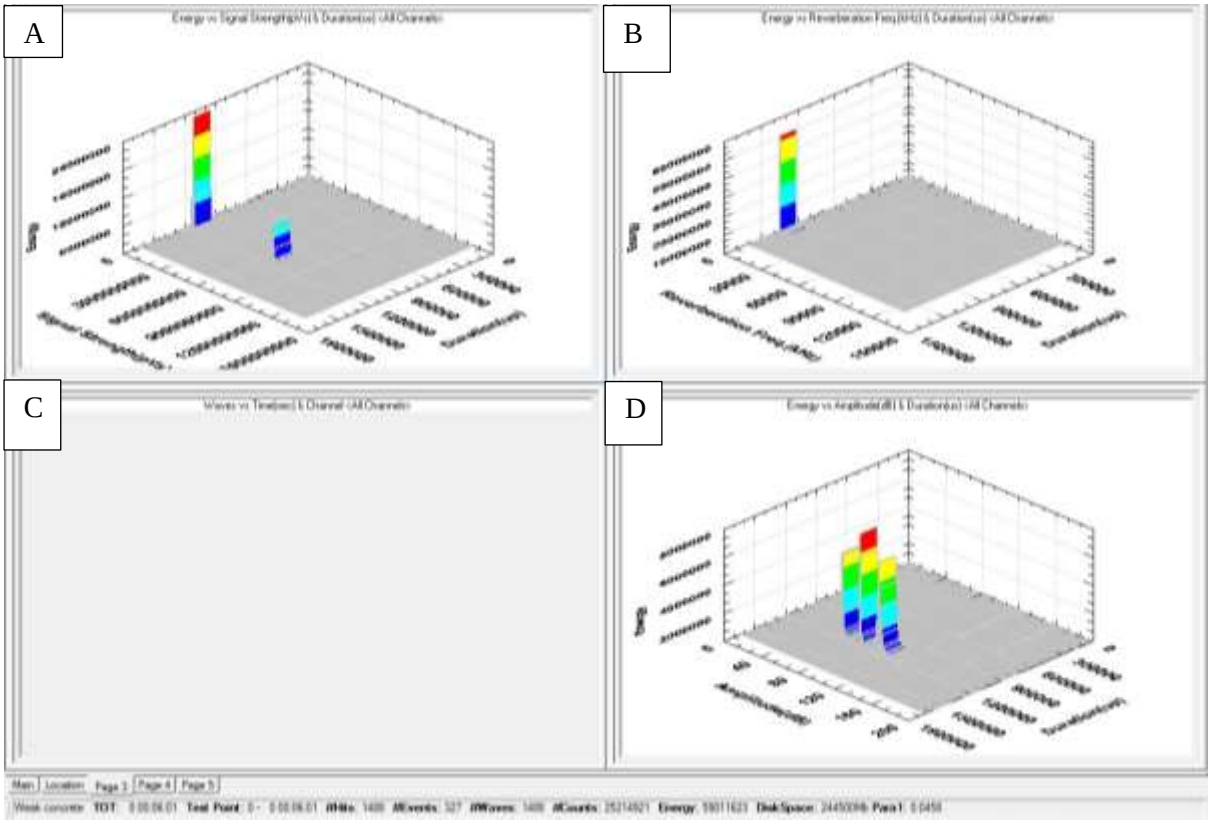

FIGURE 5-197: WBS3 Energy, duration & signal strength 70mm-60mm, A) Energy Vs signal strength, B) Energy Vs Reverberation, C) Empty, D) Energy Vs Amplitude.

Figure 5-195 & Figure 5-196 show multiple events (327) linked to just 1488 hits. There is a clear 'hook' like series of events that is shown from approximately 68mm to 59mm. This represents the drill bit being detected and the damage done to the formation just below the drill bit. A number of events also travel steeply down, slightly diagonally, from the point of drilling to the base of the sample, this would follow the pattern of the diagonal fractures seen in the WBS3 CT scan. This shows numerous fractures opening up along the bedding planes adjoining fractures diagonally crossing the bedding planes.

Looking at the events and their placements display a clear progression from the borehole to show that this damage to the formation is due to the drilling. Looking at the increase in hits compared to the Accrington Mudstone, it is quite clear that the weaker formation is subjected to a lot more damage during drilling which is what would be expected given the difficulty in preparing these samples at the outset. This weakness will affect the dimensions of the fracture, as seen on the CT scans (Figure 5-92 to Figure 5-94), the undulating fracture recorded which travels diagonally down towards the bottom of the sample, implies that this pattern of damage recorded by the acoustics is indeed correct.

The signal strength, Figure 5-197, was generally a lot weaker than that recorded for the Accrington Mudstone samples, the energy recorded was 59011623J shown as two peaks at $10x10^6\rho Vs$ and $90x10^6\rho Vs$ which is significantly weaker than the Accrington Mudstone. Although approximately

12,000,000J was recorded at 6,500x10^{6}ρVs which is significantly higher than the average signal strength of the Accrington and would suggest that this larger signal corresponds to the drilling, while the weaker signals are created by micro fractures forming away from the borehole, the weaker coherence of the material giving a weaker signal when damaged.

60MM TO 50MM

The data collected during this drilling interval is presented below in Figure 5-198 to Figure 5-201

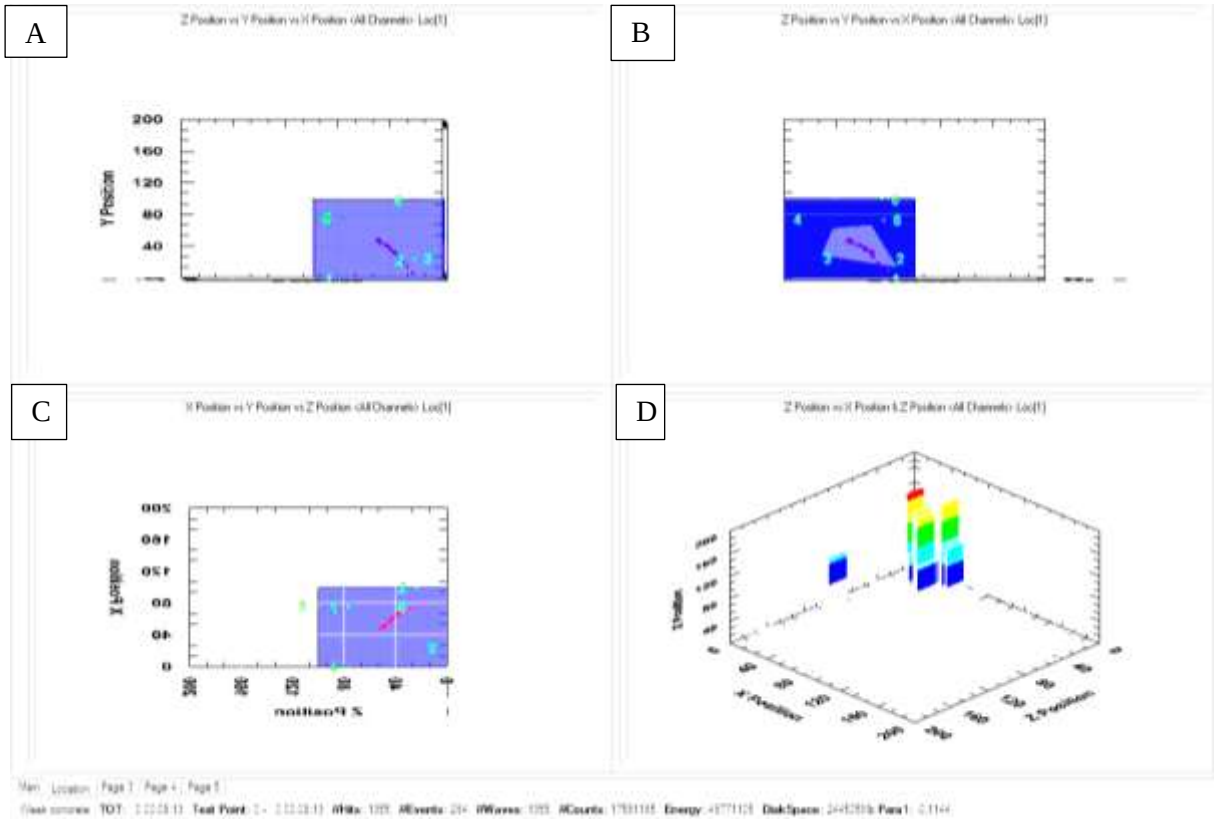

FIGURE 5-198: WBS3 Location Graphs 60mm-50mm, A) Depth view, B) 3D view, C) Overhead view, D) Actual positioning spots.

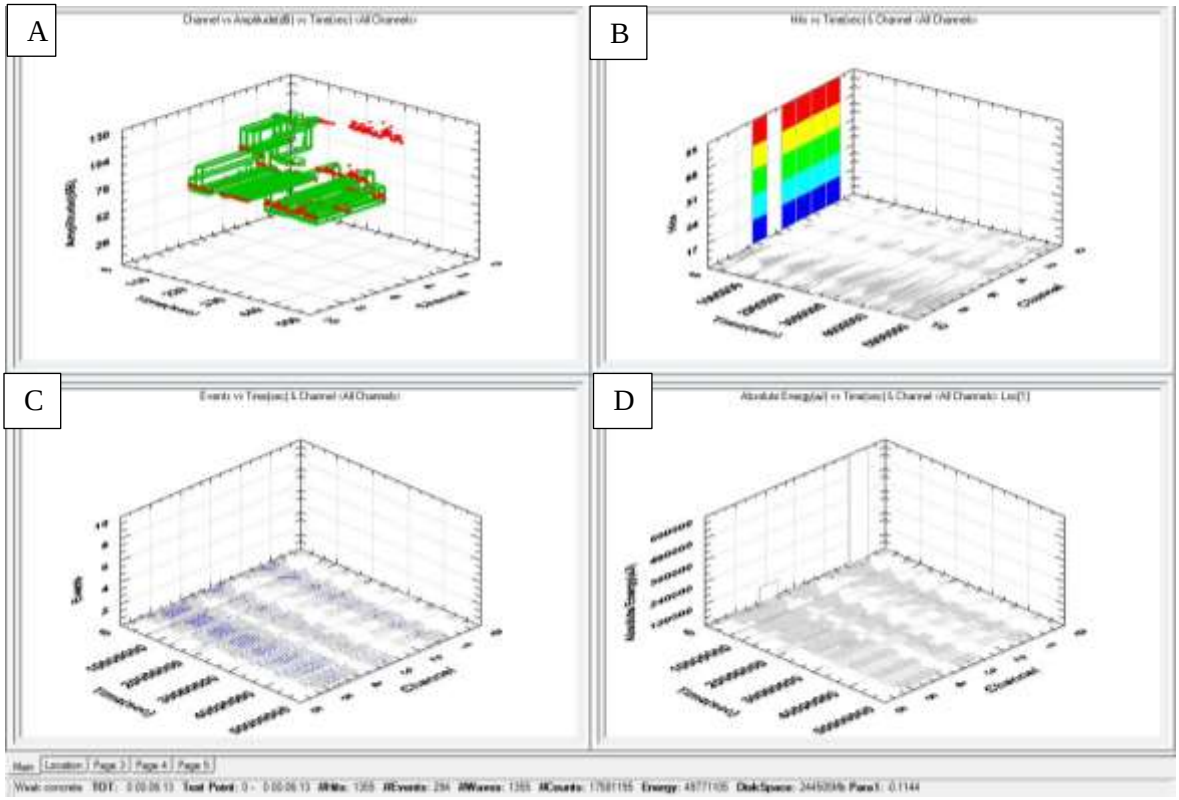

FIGURE 5-199: WBS3 Sensor Graphs 60mm-50mm, A) Acoustic signals detected each channel, B) Hits Vs Time, C) Events Vs time, D) Absolute energy Vs time.

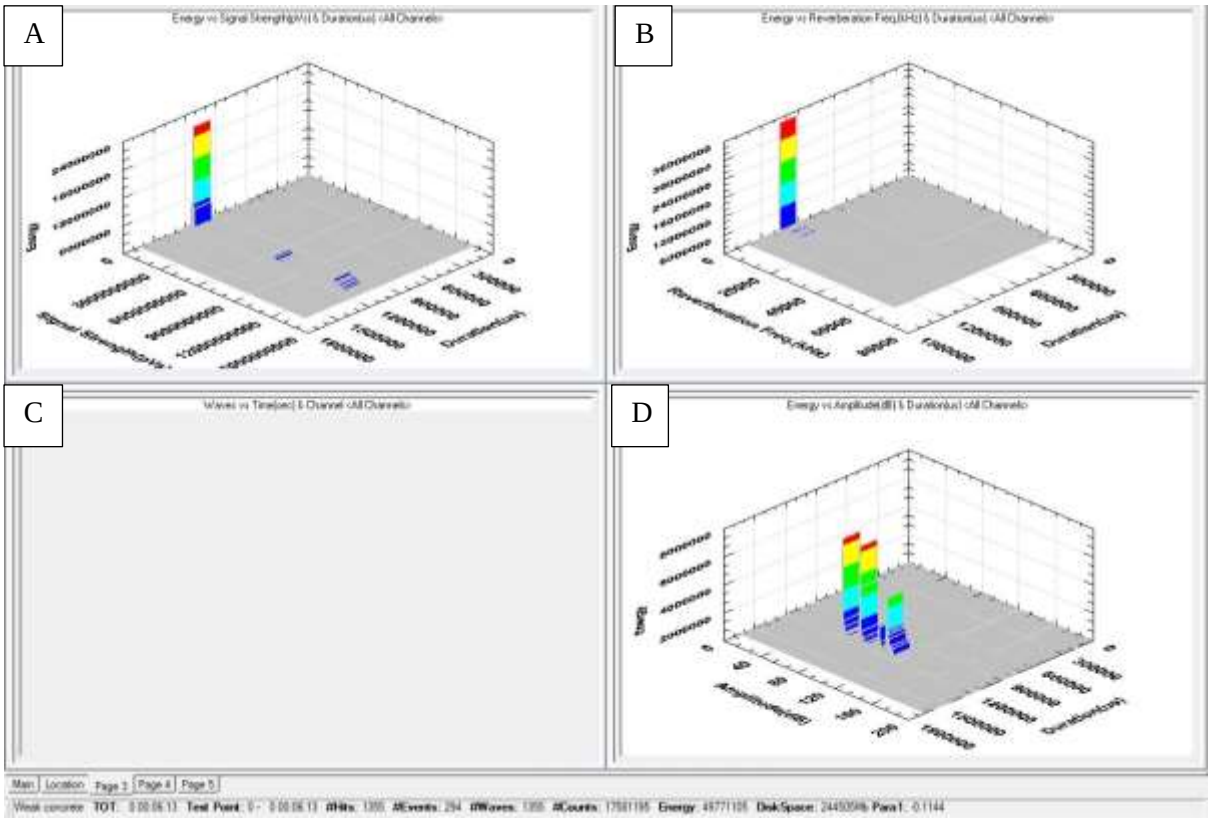

FIGURE 5-200: WBS3 Energy, duration & signal strength 60mm-50mm, A) Energy Vs signal strength, B) Energy Vs Reverberation, C) Empty, D) Energy Vs Amplitude.

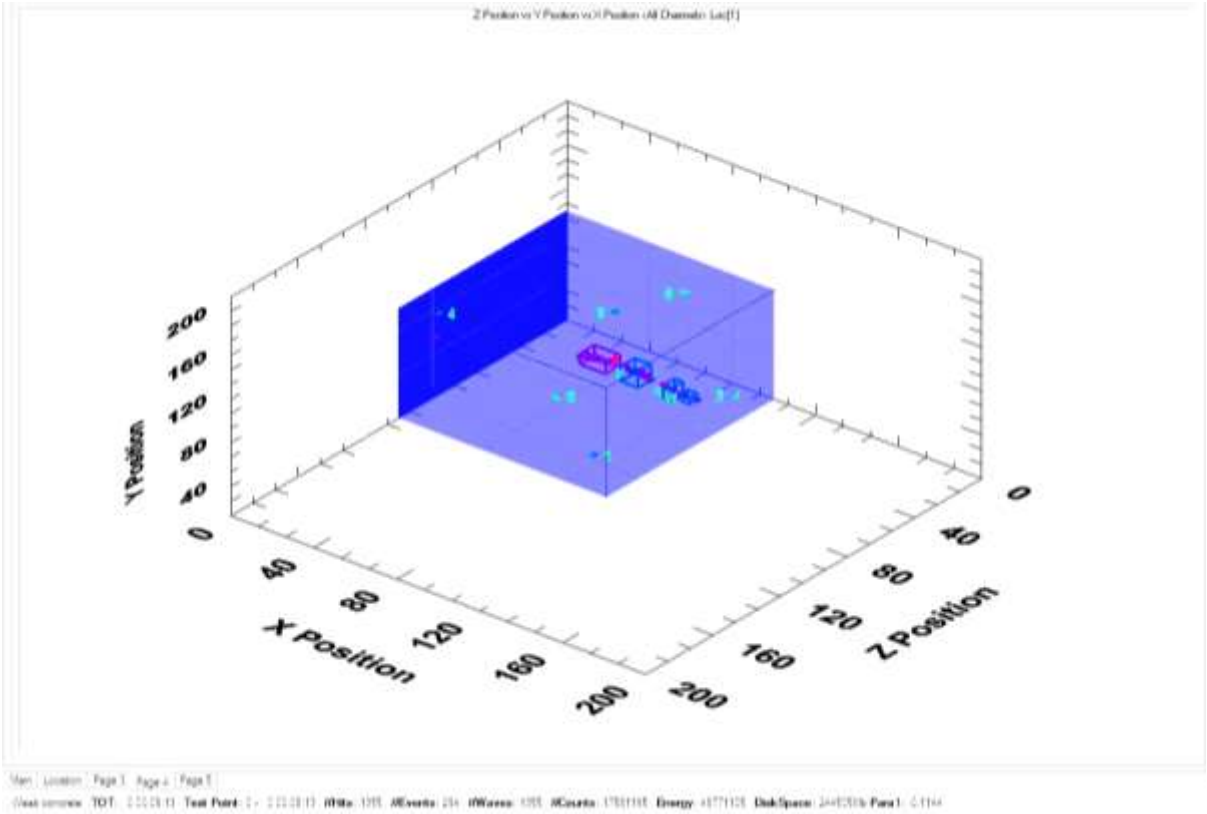

FIGURE 5-201: WBS3 3D Graph Events Grouped 60mm-50mm.

Figure 5-198 shows an almost similar pattern to that of the 70mm to 60mm drilling interval. Figure 5-201 shows the highest grouping represents the area being drilled with hits being recorded at around 58mm to around 48mm again indicating that a large amount of damage occurs during drilling; i.e. with microfracture growth, just below the drill bit. Other groupings are shown travelling straight down, again showing the same pattern of damage to the sample as seen previously. Only a small number of hits 1355 gave 294 events as the structurally weaker shale suffer more breaks in larger areas and thus more events than the Accrington Mudstone. The sensors show comparable signals received, Figure 5-199, except for a long chain received in sensor 1. However, as no other sensor picked up these signals the software did not group them and excluded them from event placement. The similarity of the other sensors gives a high confidence value to these results. The superfluous results from sensor 1 could be due to the drill pressing down on the shale, causing micro vibrations on the bottom of the sample.

In Figure 5-200 it is noticeable that energy peaks were recorded at 49,771,105J, though signal strength was of a reasonable duration 900,000µsec and 1,200,000µsec, it was weaker at less than $100x10^6$ρVs. Again, the events away from the borehole (weaker signals), represent the damage down further down, while the stronger signal strengths represent the area directly around the drilling, where signals were detected at $6,000x10^6$ρVs and $12,000x10^6$ρVs.

POINT OF FRACTURING

Data collected at this point is presented in Figure 5-202 to Figure 5-205

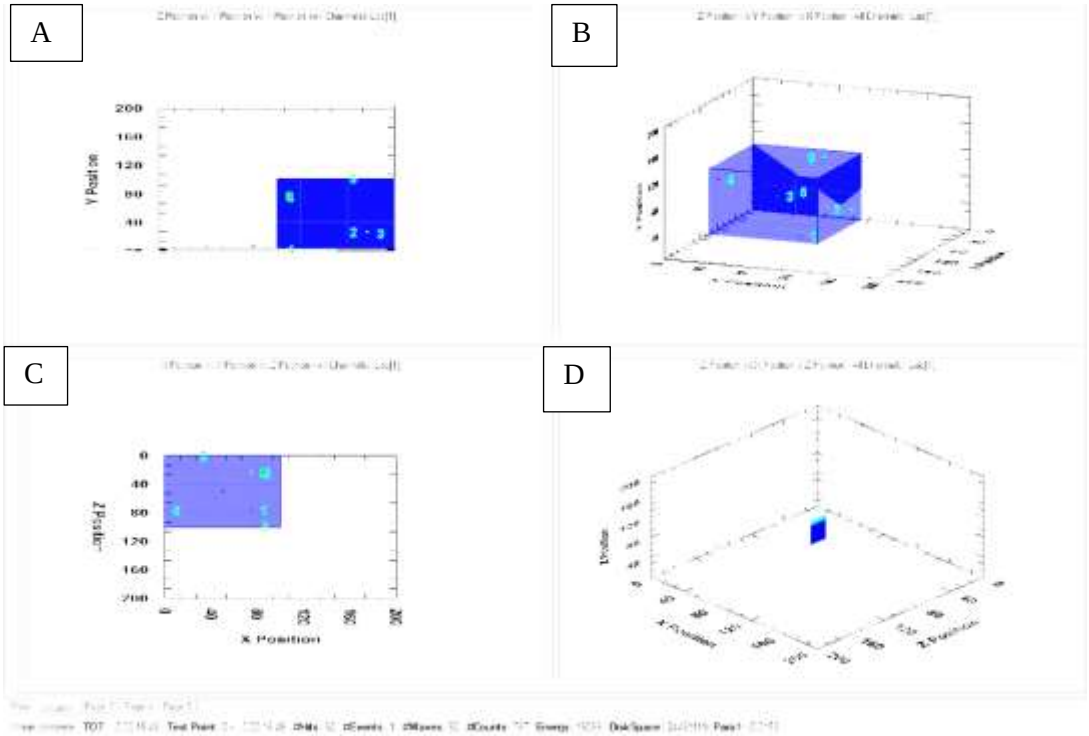

FIGURE 5-202: WBS3 Location Graph Point of Fracture, A) Depth view, B) 3D view, C) Overhead view, D) Actual positioning spots.

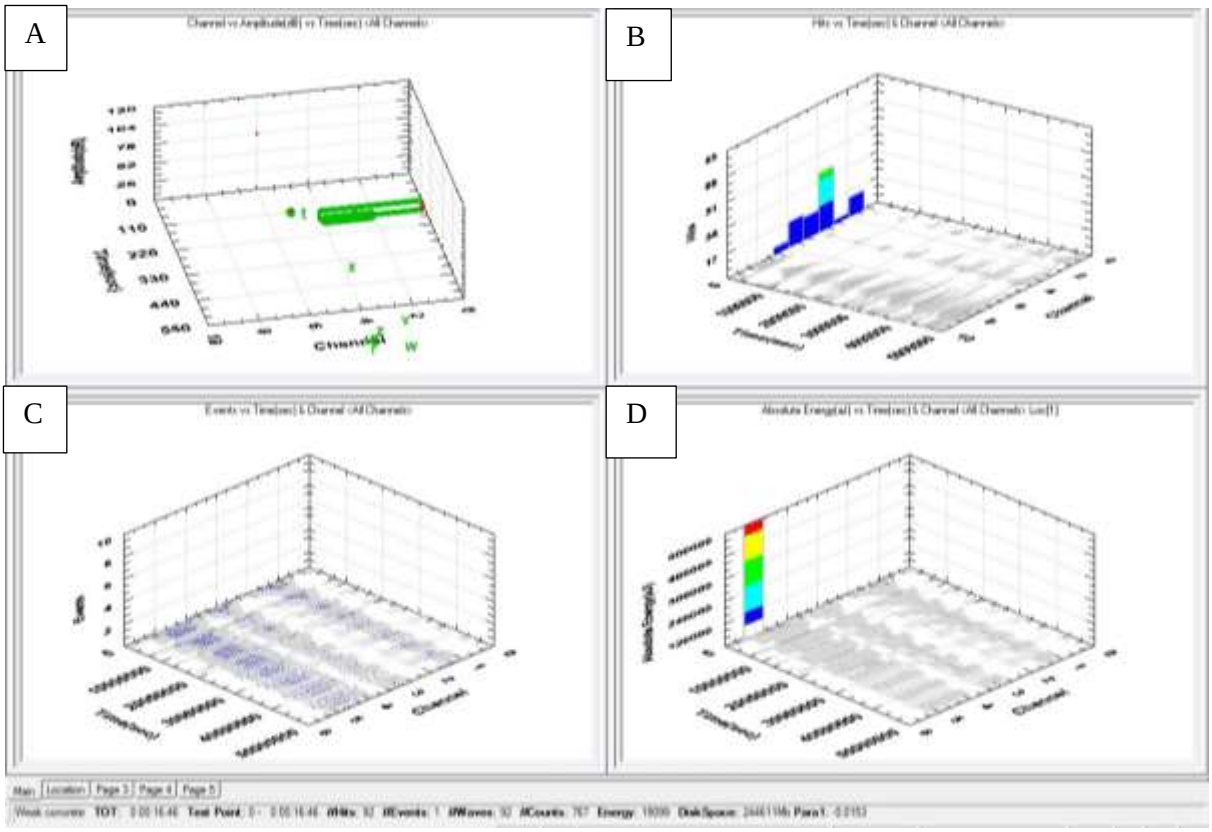

FIGURE 5-203: WBS3 Sensor Graphs point of Fracture, A) Acoustic signals detected each channel, B) Hits Vs Time, C) Events Vs time, D) Absolute energy Vs time.

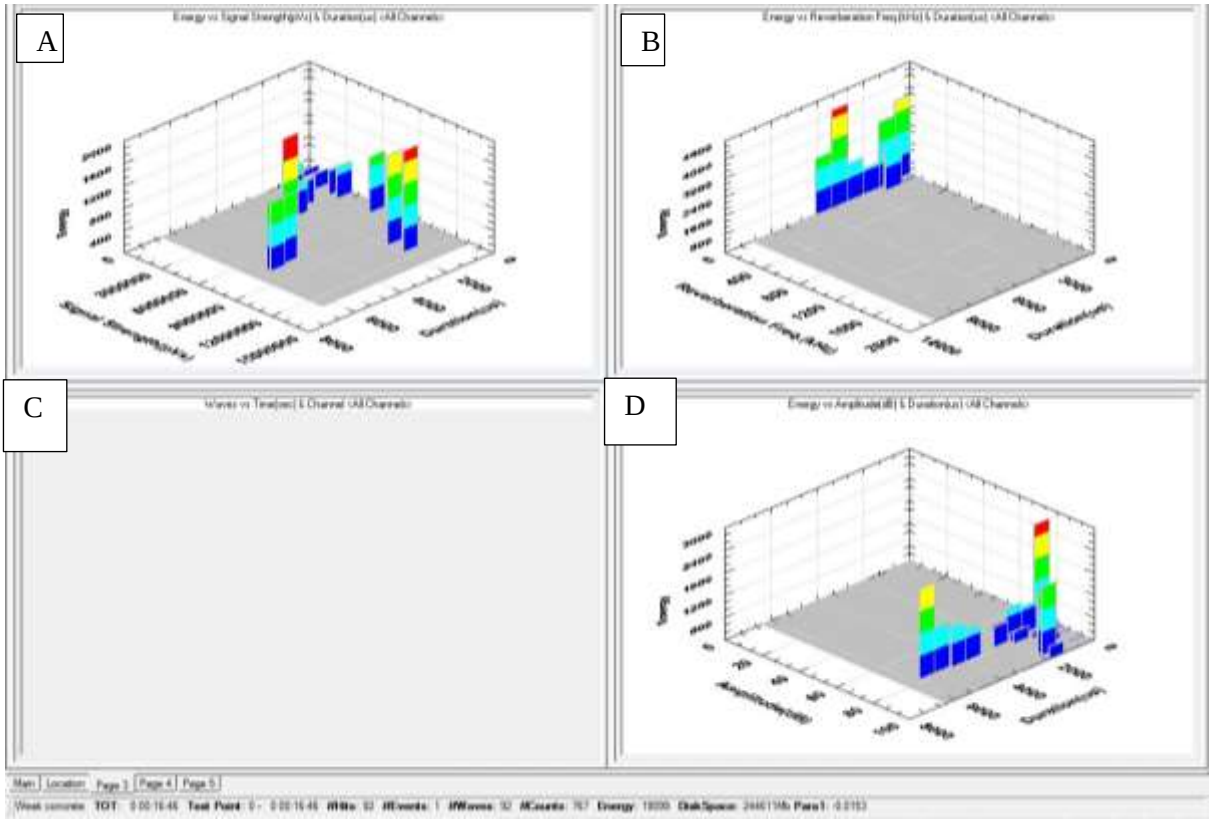

FIGURE 5-204: WBS3 Energy, duration & signal strength Point of Fracture, A) Energy Vs signal strength, B) Energy Vs Reverberation, C) Empty, D) Energy Vs Amplitude.

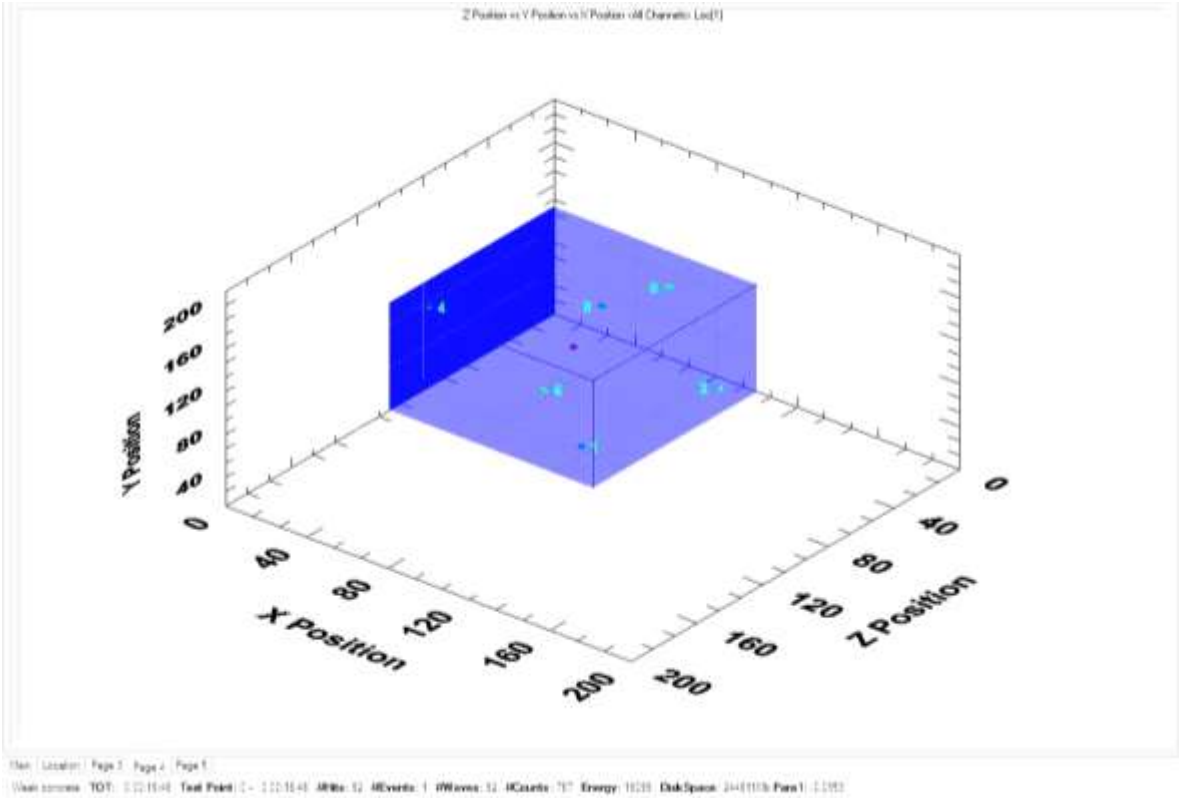

FIGURE 5-205: WBS3 3D Graph Events Grouped Point of Fracture.

Figure 5-202 & Figure 5-205 shows 1 event from 1355 hits, this was recorded at the break point of the fracturing fluid. After reaching pressure the pressure break event was recorded. The fact that this event is located at the base of the borehole indicates that this is recording the fracture point and the presence of only one event points to the fact that the fracture was instantaneous.

Signal strength ranged from $3x10^6\rho Vs$ to $11x10^6\rho Vs$ as seen in Figure 5-204, the weaker signals likely represent the fluid flowing into the borehole and pressure building up, while the stronger signal represents the point of fracture. The duration of the signal is also shorter than for the previous drilling intervals. This all points to the fracture being not only instantaneous but also short in duration, as seen by the small grouping and signals received in Figure 5-203.

5.7.2.4 WBS4

The WBS4 sample could not be scanned before it had started to dry out and crumble, thus affecting the fracture dimensions. This sample also caused issues when trying to take acoustic readings between 100mm to 80mm and 70mm to 60mm. The results that were obtained did not accurately reflect where the drill bit was located.

80MM TO 70MM

The location and graphic data is presented in Figure 5-206 to Figure 5-209.

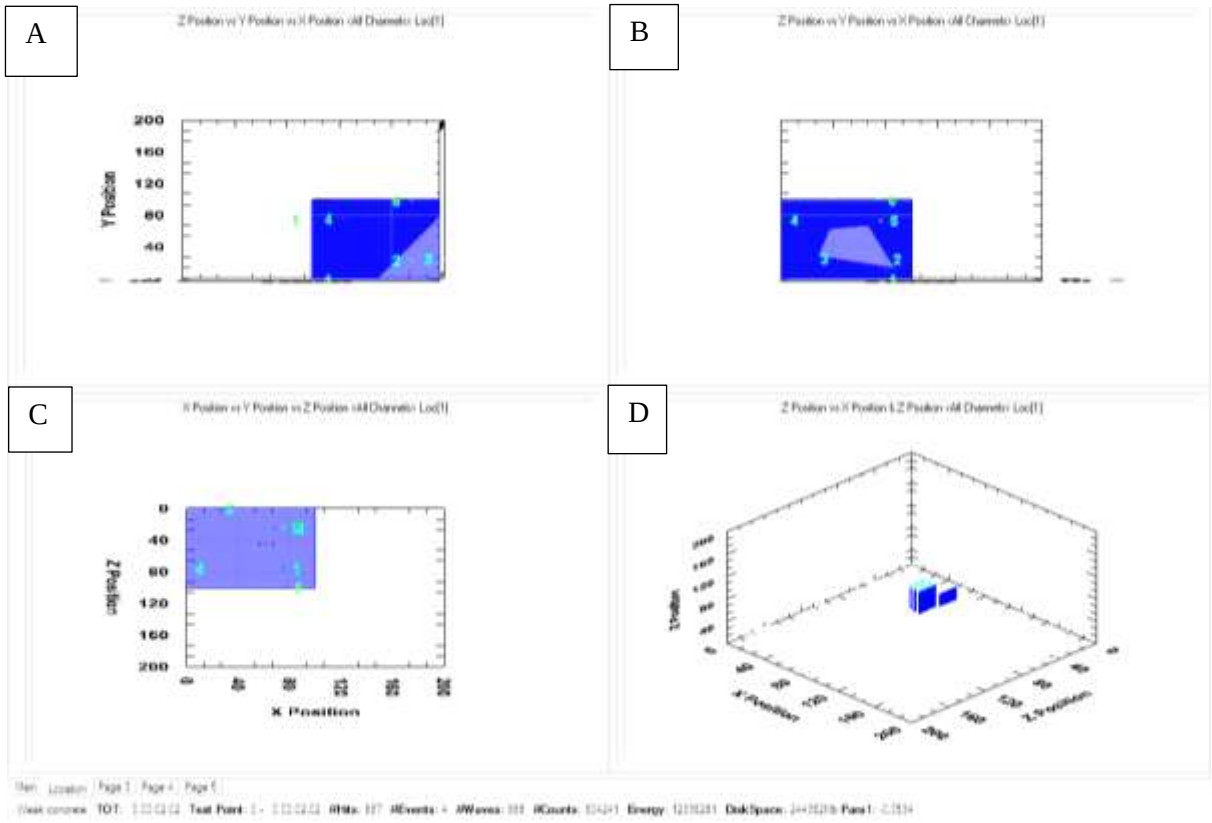

FIGURE 5-206: WBS4 Location Graphs 80mm-70mm, A) Depth view, B) 3D view, C) Overhead view, D) Actual positioning spots.

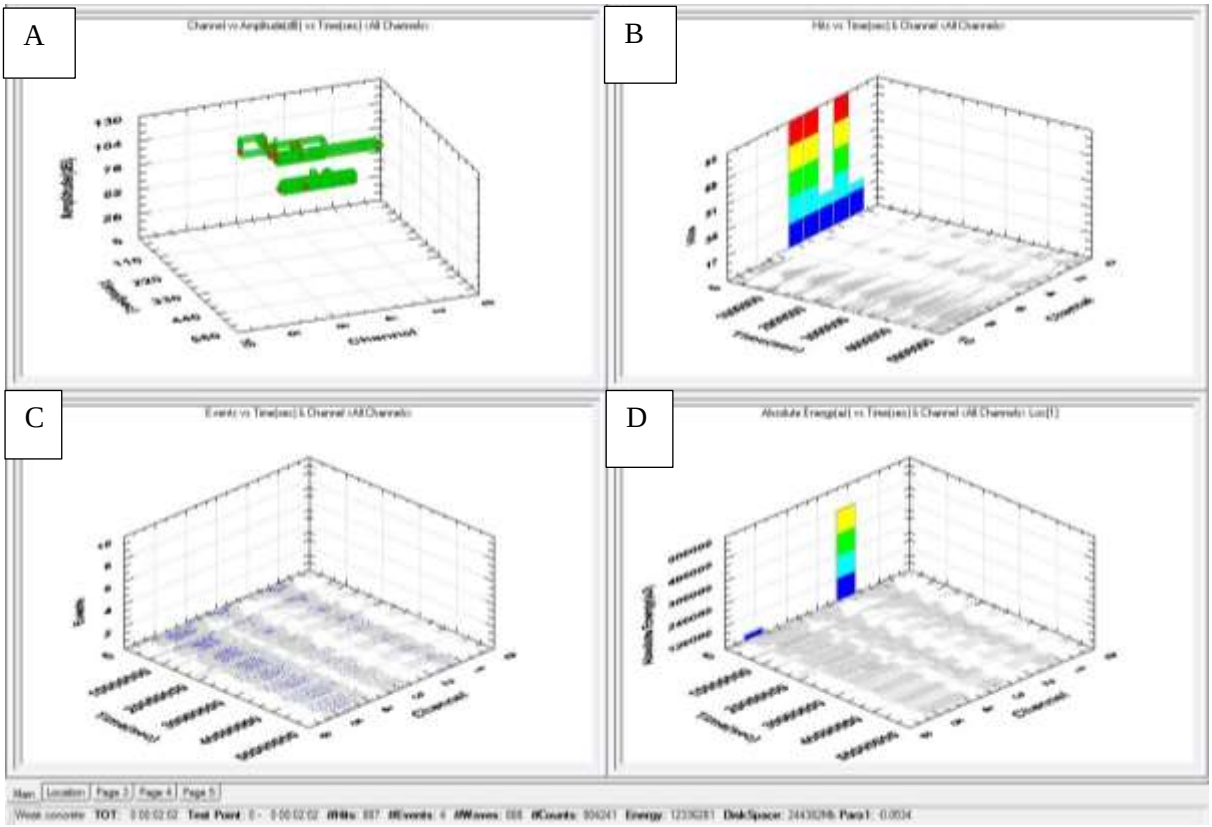

FIGURE 5-207: WBS4 Sensor Graphs 80mm-70mm, A) Acoustic signals detected each channel, B) Hits Vs Time, C) Events Vs time, D) Absolute energy Vs time.

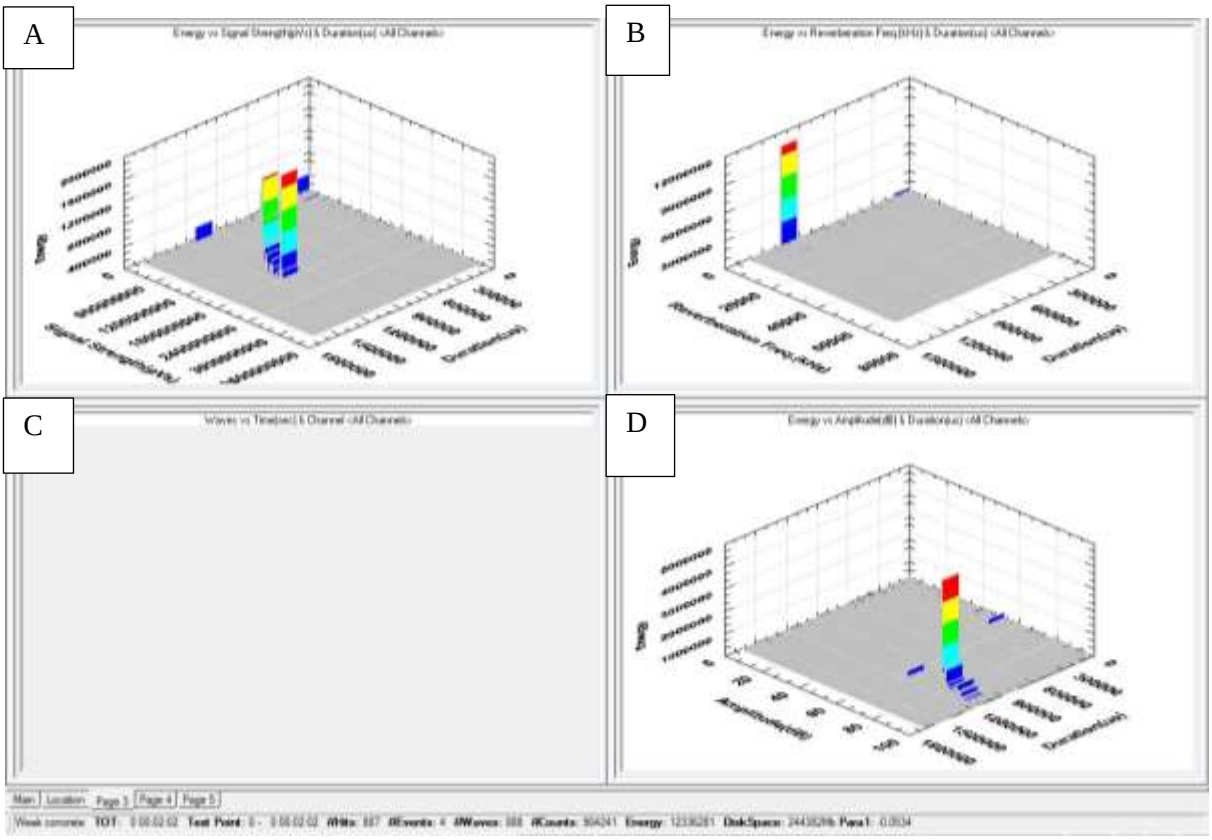

FIGURE 5-208: WBS4 Energy, duration & signal strength, A) Energy Vs signal strength, B) Energy Vs Reverberation, C) Empty, D) Energy Vs Amplitude.

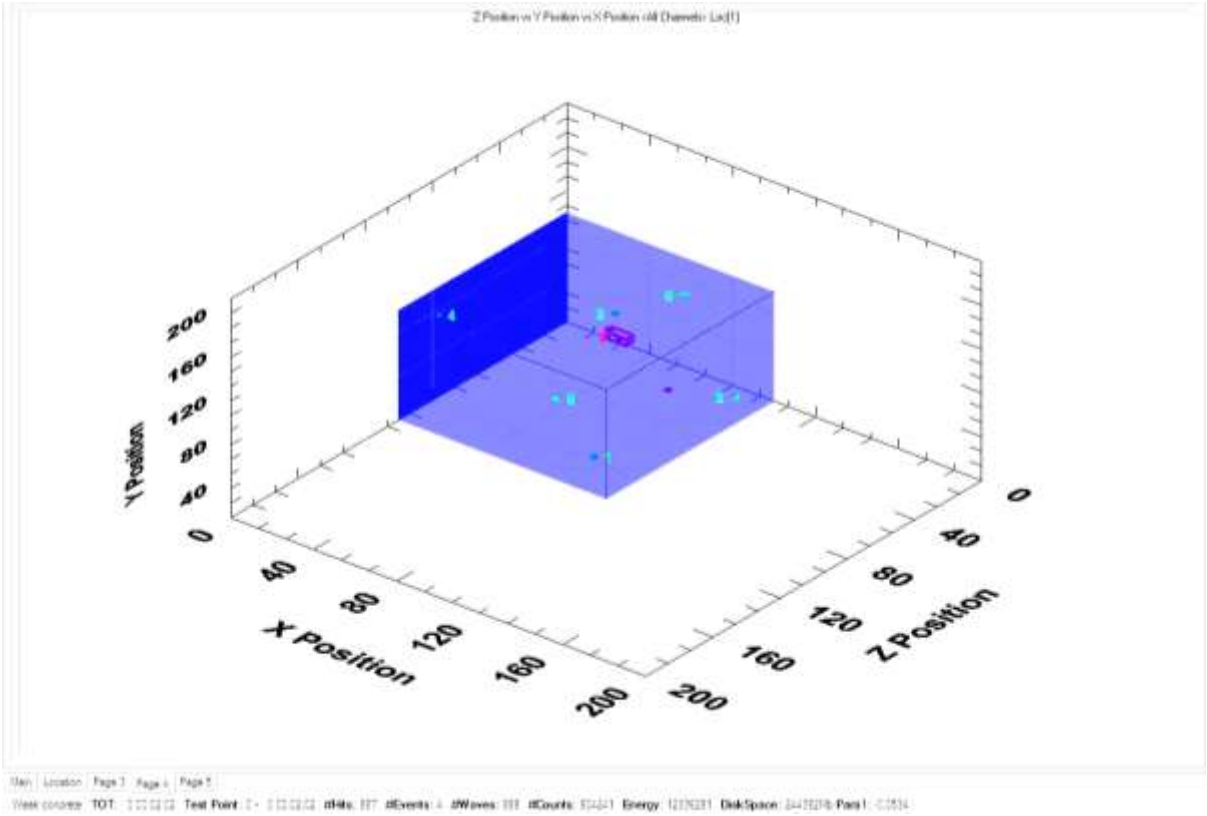

FIGURE 5-209: WBS4 3D Graph Events Grouped 80mm-70mm.

Four events were transcribed from 887 hits with all the hits being detected around the borehole at the depths below 50mm, Figure 5-206. The events are located close to the end placement of the drilling and there is a spread involving 3 hits. The fact that the events are located so far away from the drilling position shows that, although the signal strength is recorded as being relatively strong, Figure 5-208, problems can arise with the acoustics and slippage of the sensors will still produce hits but they will be off centred and away from where drill bit actually is positioned. This shows the importance of having sensors in contact with the medium to be drilled and of having an effective viscous medium joining the sensor to the sample being tested. Figure 5-207, shows how a number of sensors are not recording any signals which has affected the placement of the events.

60MM TO 50MM

The location data is presented in Figure 5-210

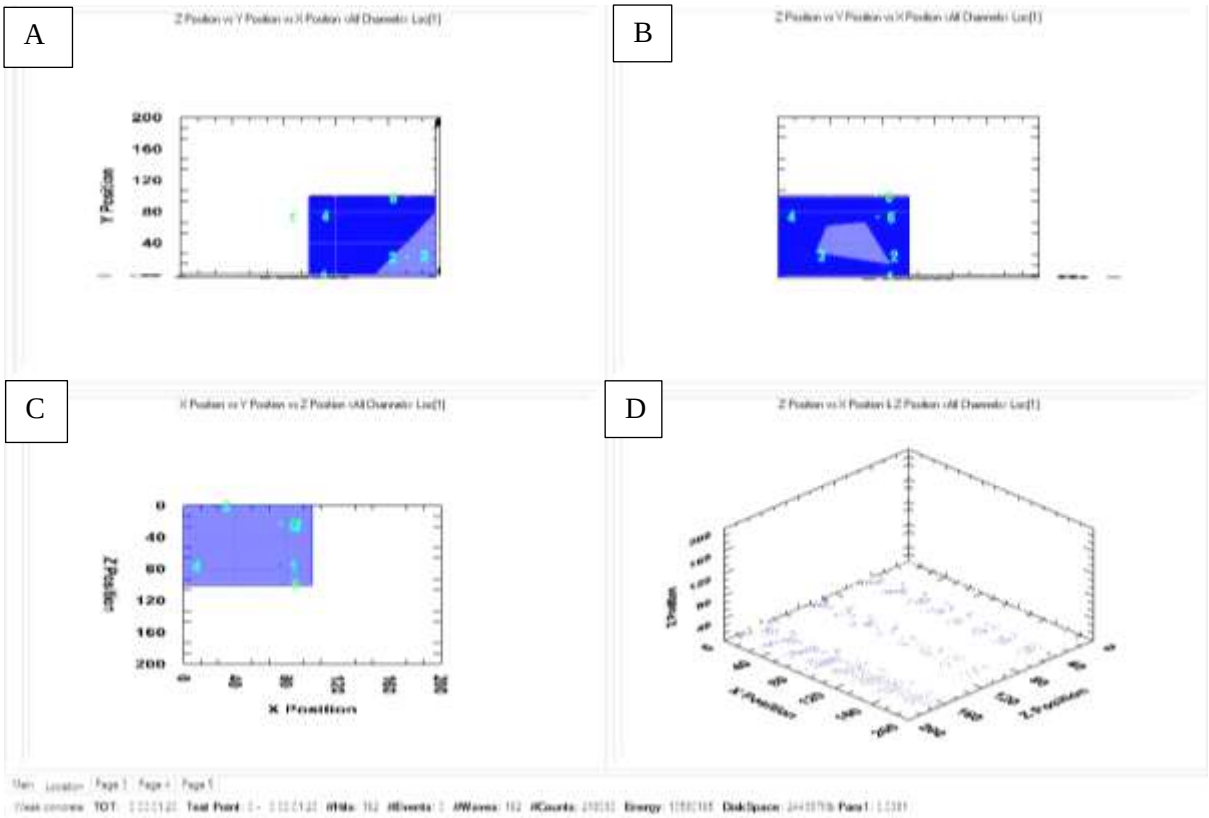

FIGURE 5-210: WBS4 Location graph 60mm-50mm, A) Depth view, B) 3D view, C) Overhead view, D) Actual positioning spots.

With no events linked to any of the 162 hits, Figure 5-210, and the number of hits being exceptionally low, would indicate that on this sample the acoustic data cannot be trusted.

POINT OF FRACTURE

The location data of this graph is shown below in Figure 5-211

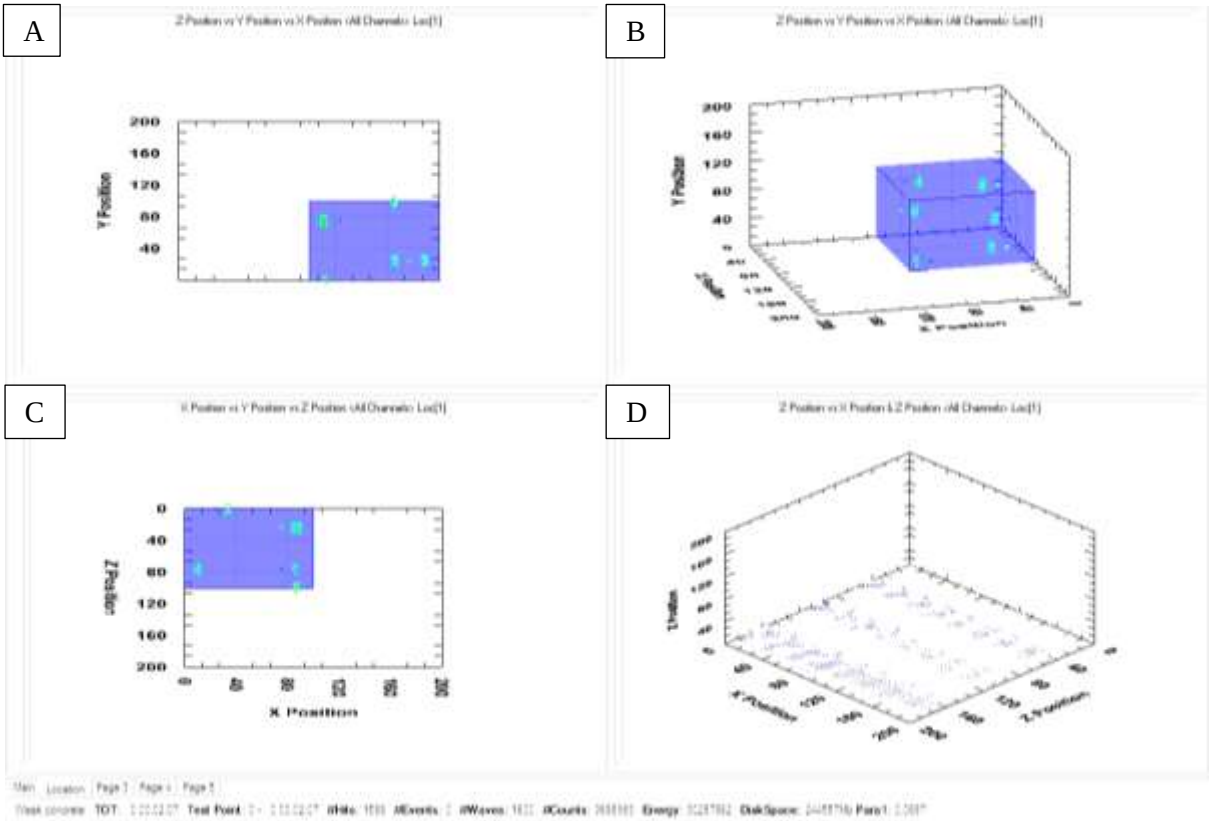

FIGURE 5-211: WBS4 Location Graph Point of Fracture, A) Depth view, B) 3D view, C) Overhead view, D) Actual positioning spots.

As shown above in Figure 5-211 there are only a small number of hits recorded, 1599, which have not been placed into any events. This meant that the point of fracture could not be located, again highlighting the importance of the secure placement of the sensors.

5.7.2.5 WBS5

In an effort to stop sensor slippage on sample WBS5 the metal plate holders were all glued together, to form a single structure. However, the sensors still could not place any events between the 90mm to 80mm interval, the 70mm to 60mm interval or the point of fracture. During flat jack pressure application, it was noted that the Westbury Shales continuously broke in places on the surface meaning that cracks kept preventing the uninterrupted placement of the sensors and the drill bit within the sample.

100MM TO 90MM

The location and graphic data of this drilling interval is shown in Figure 5-212 to Figure 5-215.

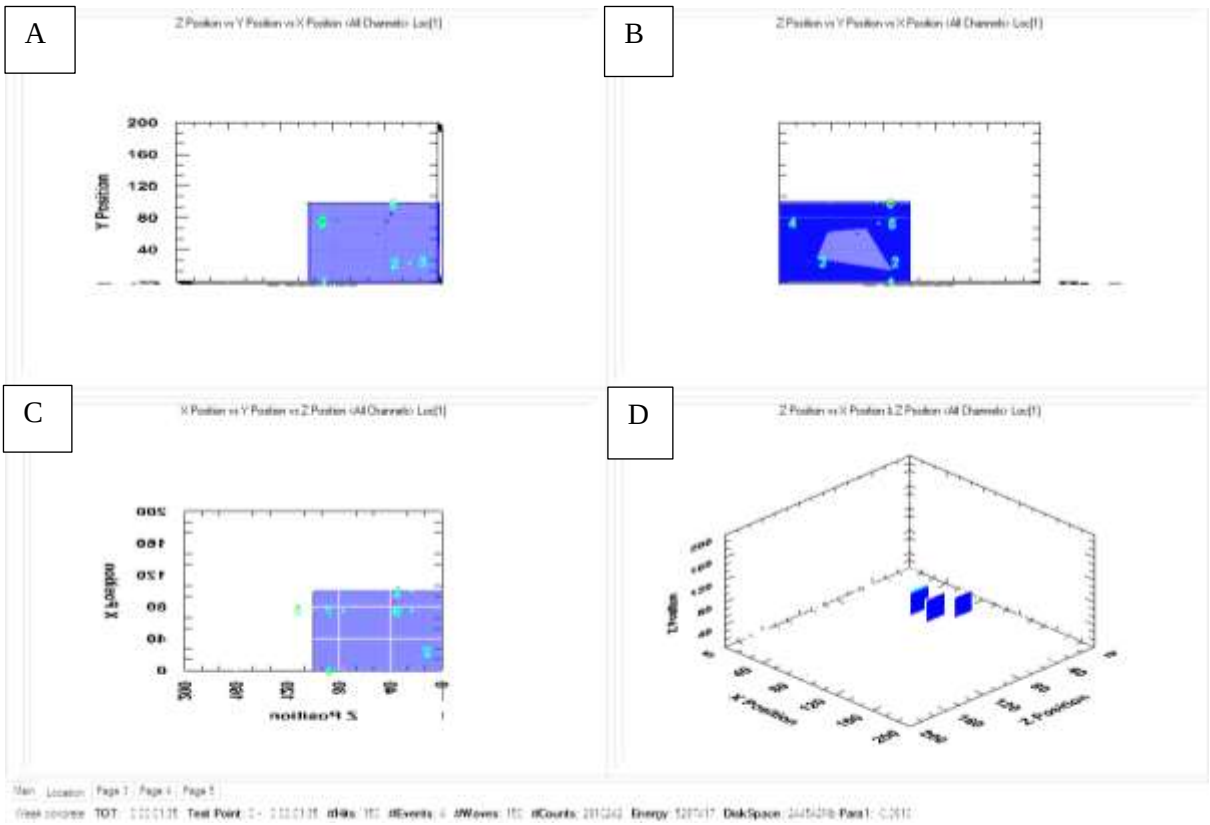

FIGURE 5-212: WBS5 Location graphs 100-90mm, A) Depth view, B) 3D view, C) Overhead view, D) Actual positioning spots.

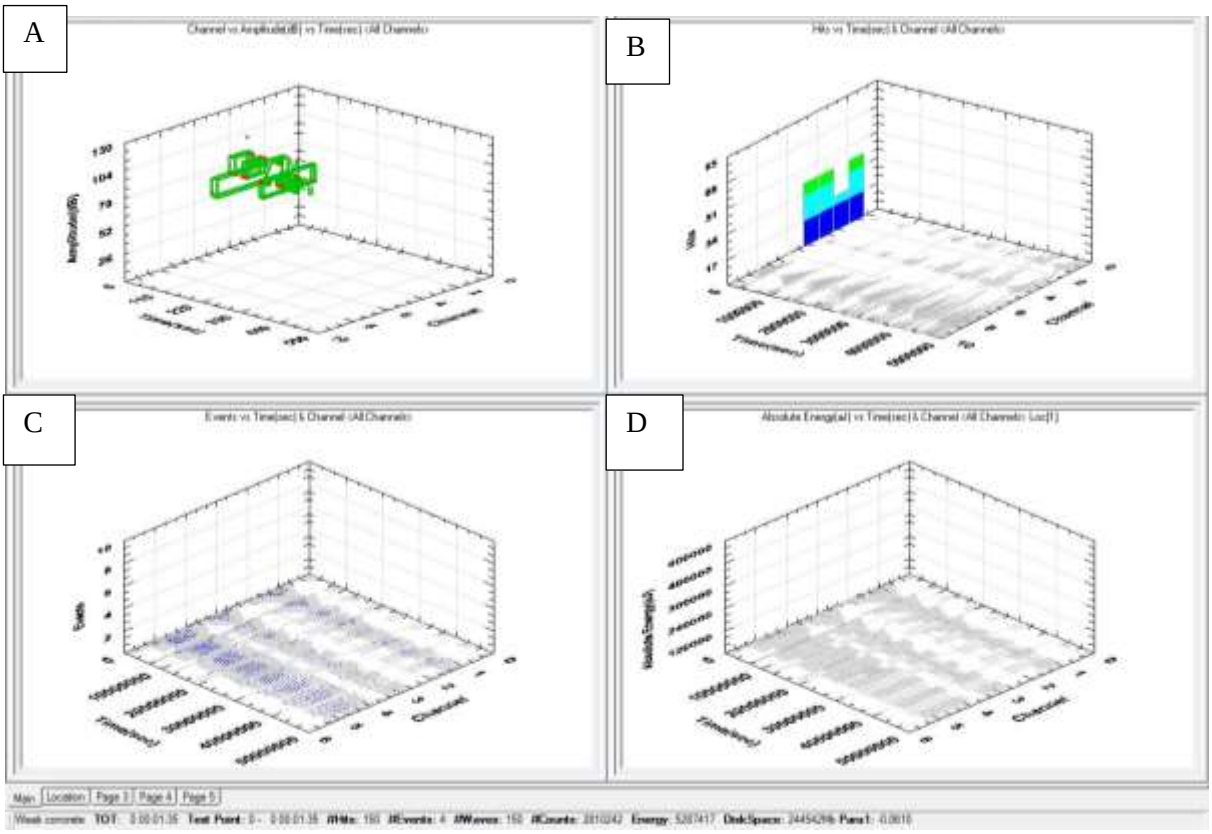

FIGURE 5-213: WBS5 Sensors Graphs 100mm-90mm, A) Acoustic signals detected each channel, B) Hits Vs Time, C) Events Vs time, D) Absolute energy Vs time.

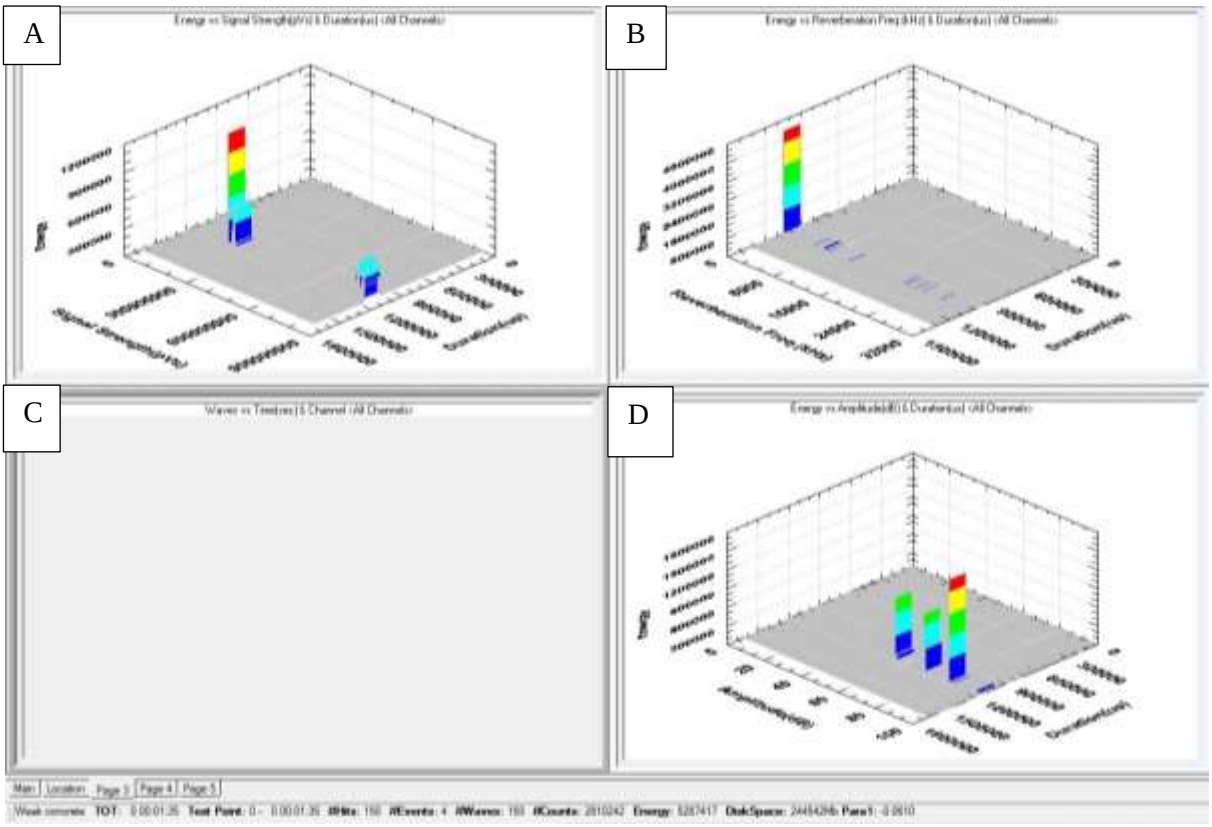

FIGURE 5-214: WBS5 Energy, duration and signal strength 100mm-90mm, A) Energy Vs signal strength, B) Energy Vs Reverberation, C) Empty, D) Energy Vs Amplitude.

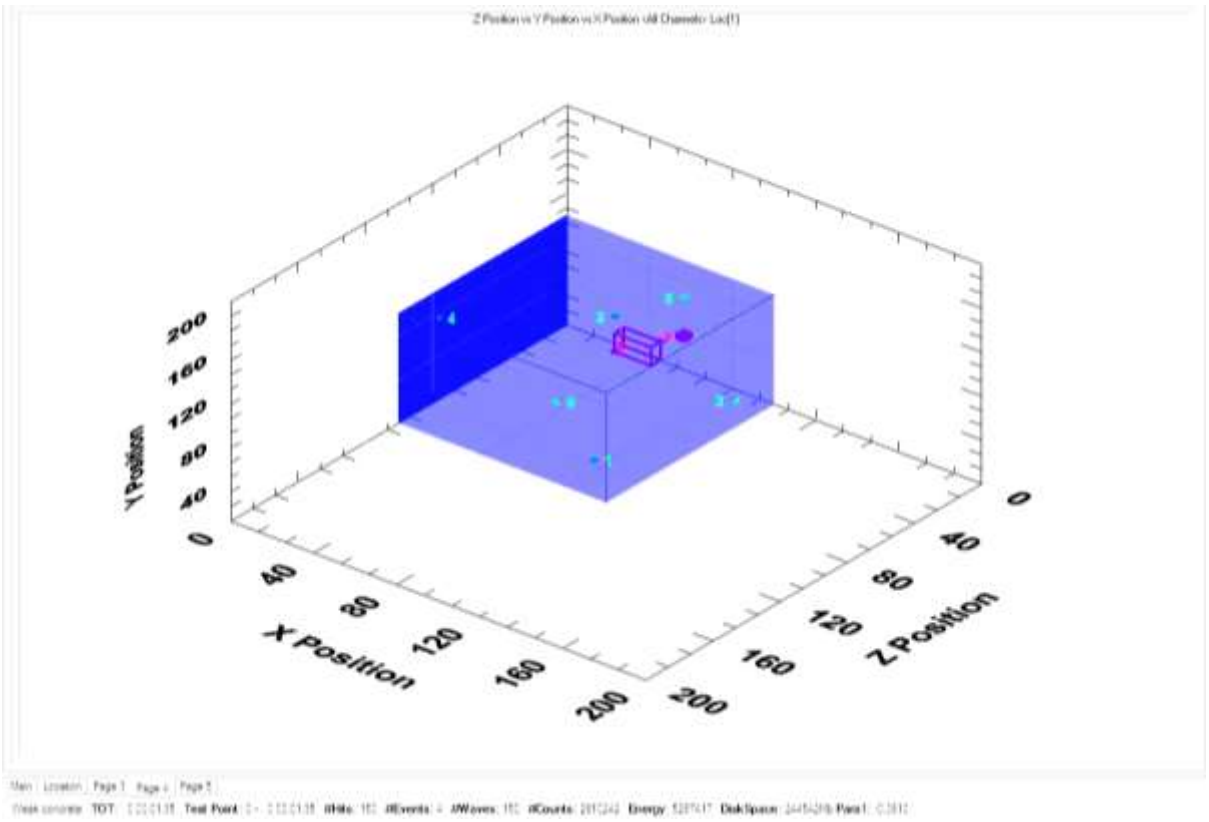

FIGURE 5-215: WBS5 3D Graph Events Grouping 100mm-90mm.

Figure 5-212 shows 4 events just off centre from around 95mm to 85mm. These four events are transcribed from just 150 hits, which is much lower than expected and shows the importance of ensuring direct contact between the sensor and the medium. However, the hits recorded had a strong signal with one band ranging from $150x10^6\rho Vs$ to $200x10^6\rho Vs$ and a smaller grouping recording an exceptionally strong signal of $850x10^6\rho Vs$ to $900x10^6\rho Vs$, shown in Figure 5-214. The sensors also indicate that all the signals received are comparable, Figure 5-213, leading to the small number of events placed by the software. Although there was an obvious break between sensor and sample a number of hits were still detected.

80MM TO 70MM

The location and graph data is presented in Figure 5-216 to Figure 5-219

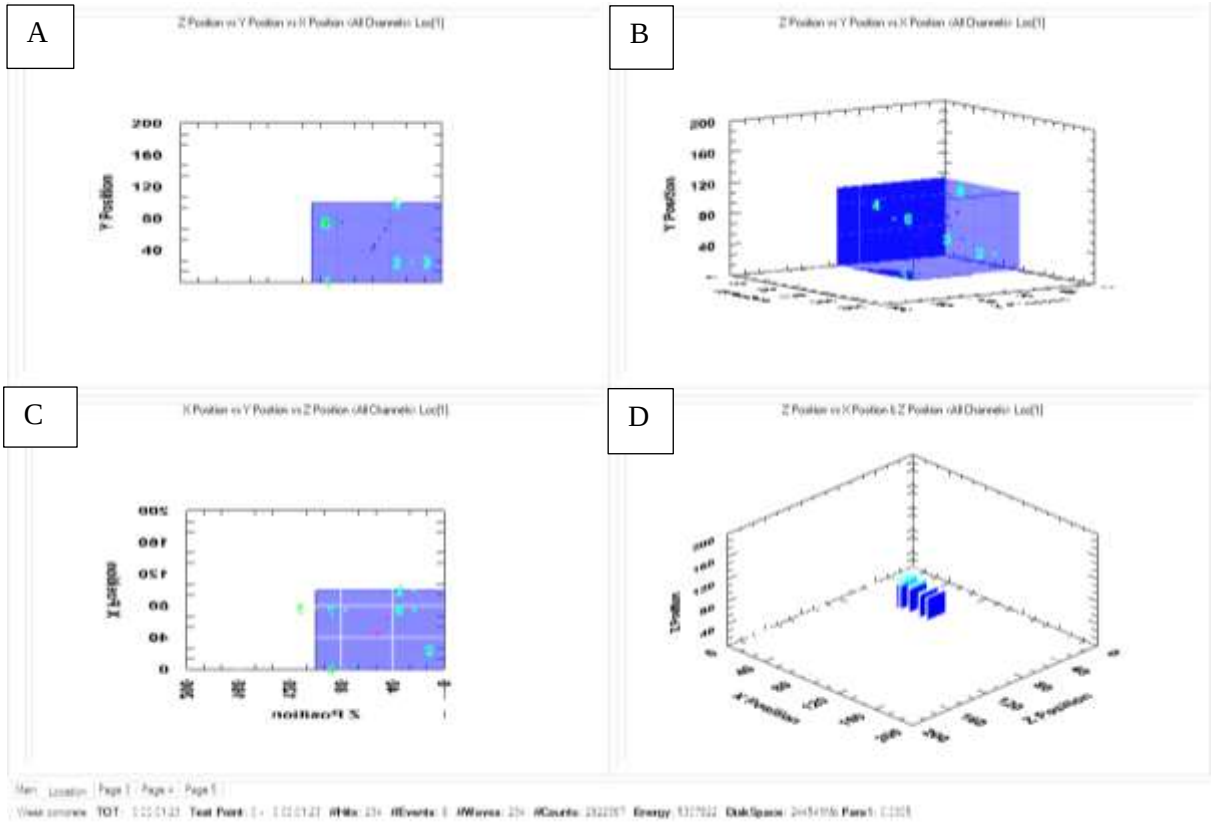

FIGURE 5-216: WBS5 Location Graphs 80mm-70mm, A) Depth view, B) 3D view, C) Overhead view, D) Actual positioning spots.

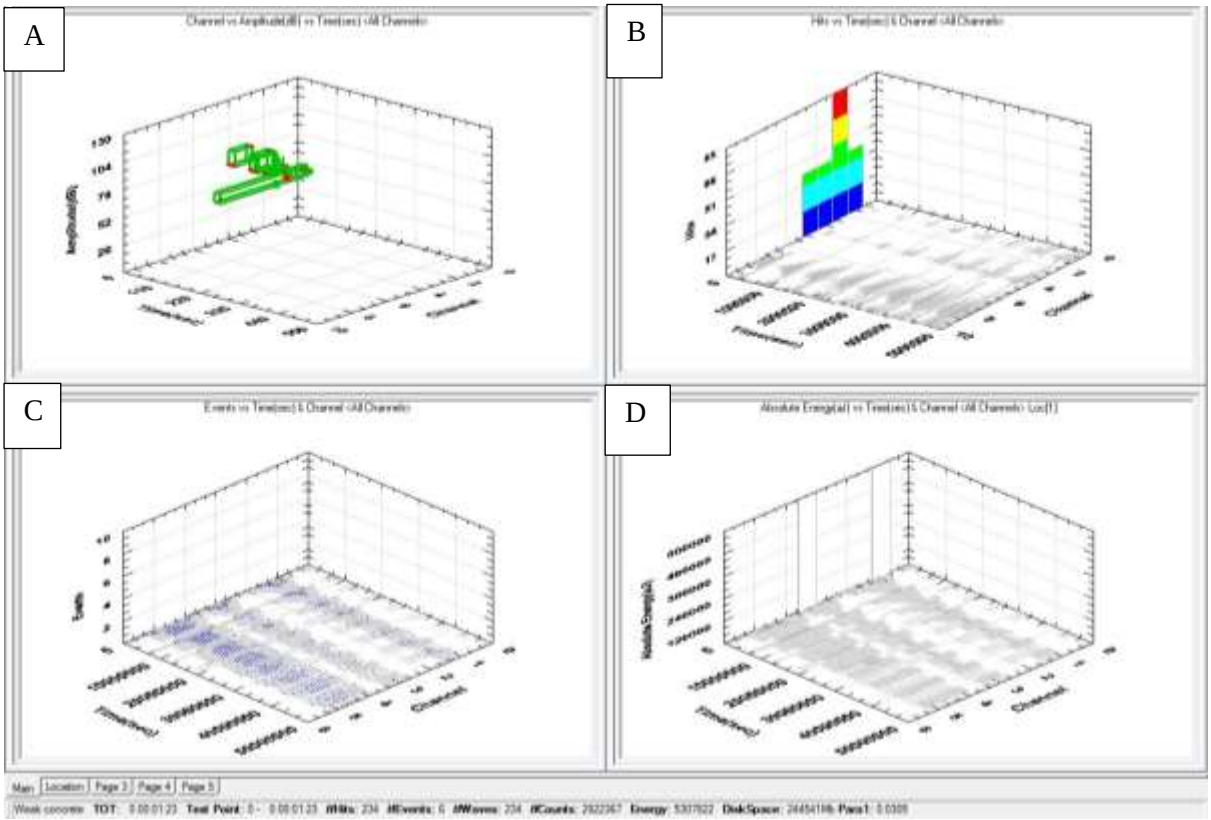

FIGURE 5-217: WBS5 Sensor Graphs 80mm-70mm, A) Acoustic signals detected each channel, B) Hits Vs Time, C) Events Vs time, D) Absolute energy Vs time.

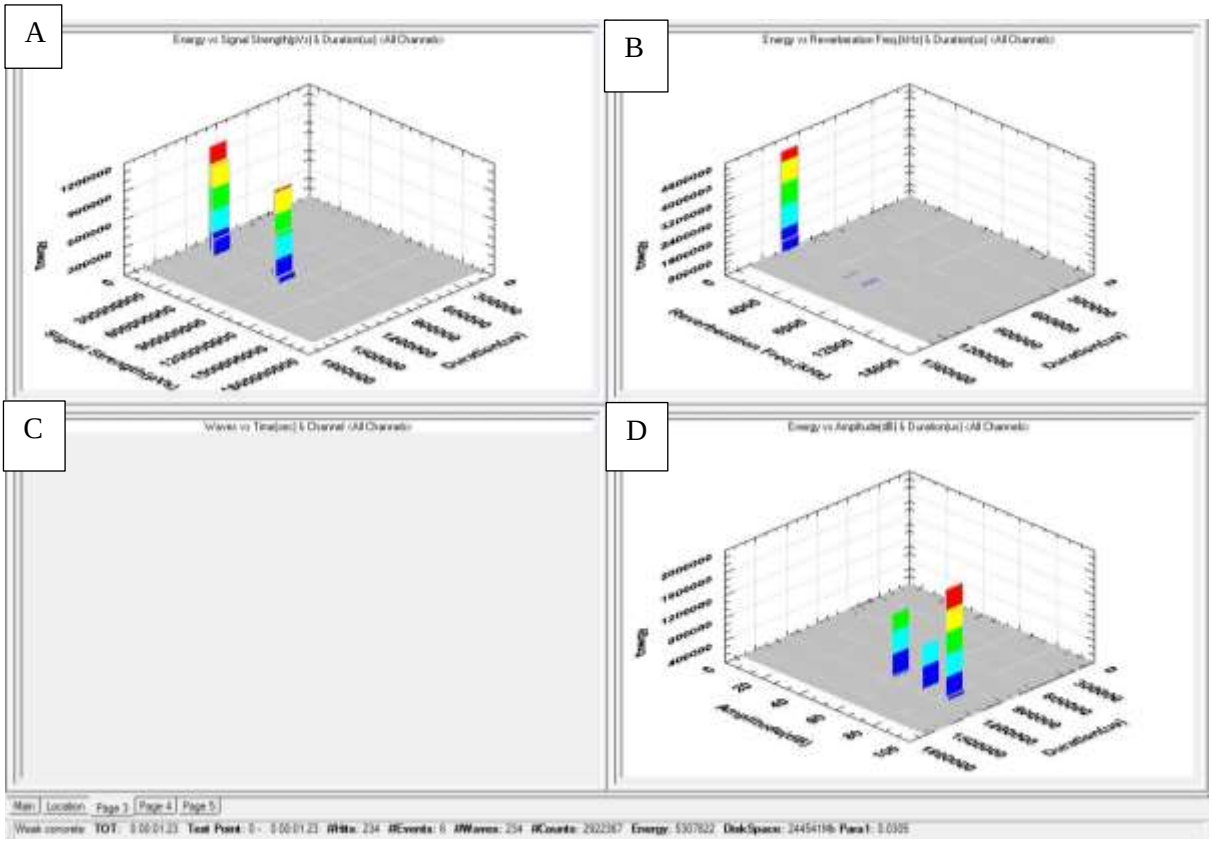

FIGURE 5-218: WBS5 Energy, duration & signal strength 80mm-70mm, A) Energy Vs signal strength, B) Energy Vs Reverberation, C) Empty, D) Energy Vs Amplitude.

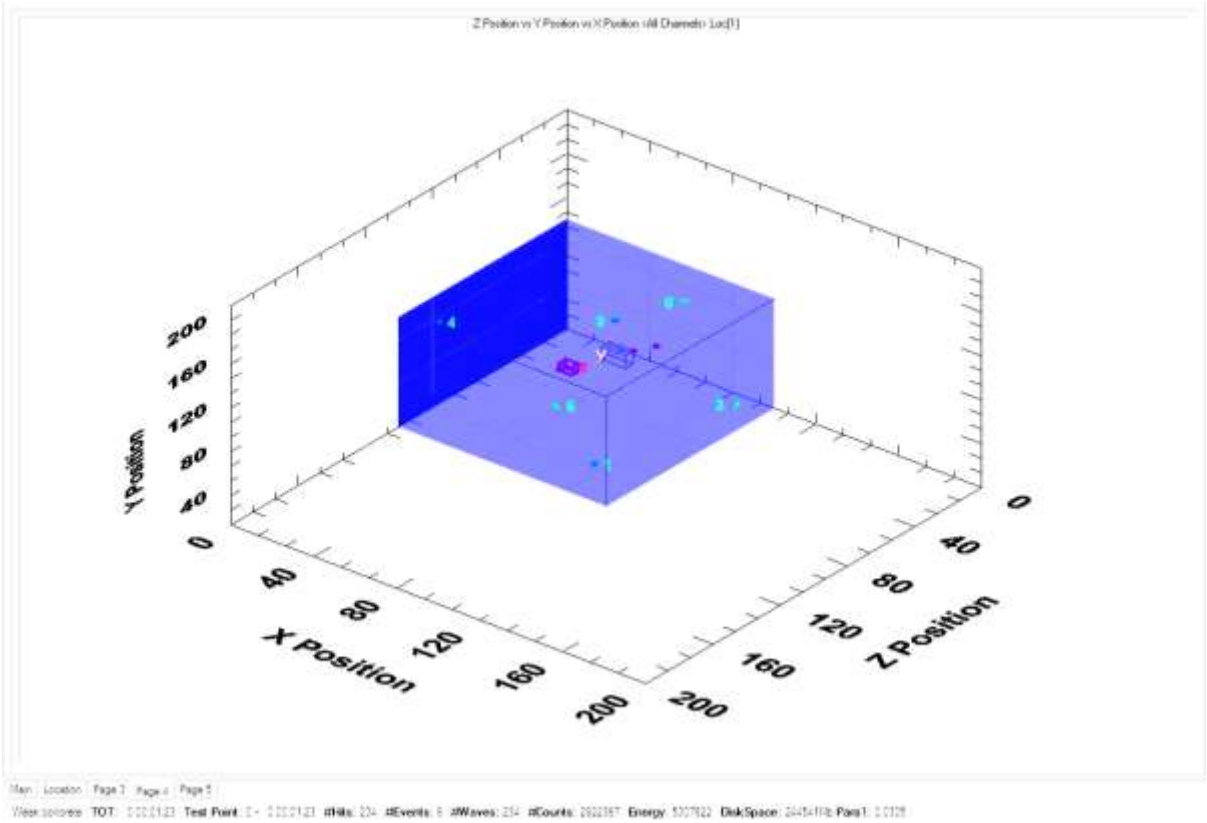

FIGURE 5-219: WBS5 3D Graph Event grouping 80mm-70mm.

Figure 5-216 shows that only 234 hits were recorded which transcribed to 6 events. Three of these events placed were between 79mm and 67mm and centralised as seen on the overhead view (Figure 5-216), giving an accurate placement of the borehole progression, again showing that acoustic events are placed just below the drill bit. The lack of hits can still be ascribed to the effects of cracking of the specimen removing the unbroken contact between the source of the acoustics and the sensors, the effects of which are shown in Figure 5-217.

This shows that although a small number of signals were received, most of the signals were similar in amplitude and arrived at the same time. Only sensors 2, 3 & 4 (Figure 5-127) have extra signals though they are similar and have been grouped, which could be indicative of damage to the formation. Some hits were received but compared to other Westbury Shales this hit rate is low meaning that some of the weaker emissions are not getting through. The only signals that are getting through have a duration between 900,000µsecs and 1,200,000µsecs (Figure 5-218). The weaker signals that typically sit in the corner of the graph shown in other samples are not present. This lack of background readings explains the low number of hits.

60MM TO 50MM

The location and graph data of the acoustics of this drilling interval are shown in Figure 5-220 to Figure 5-223

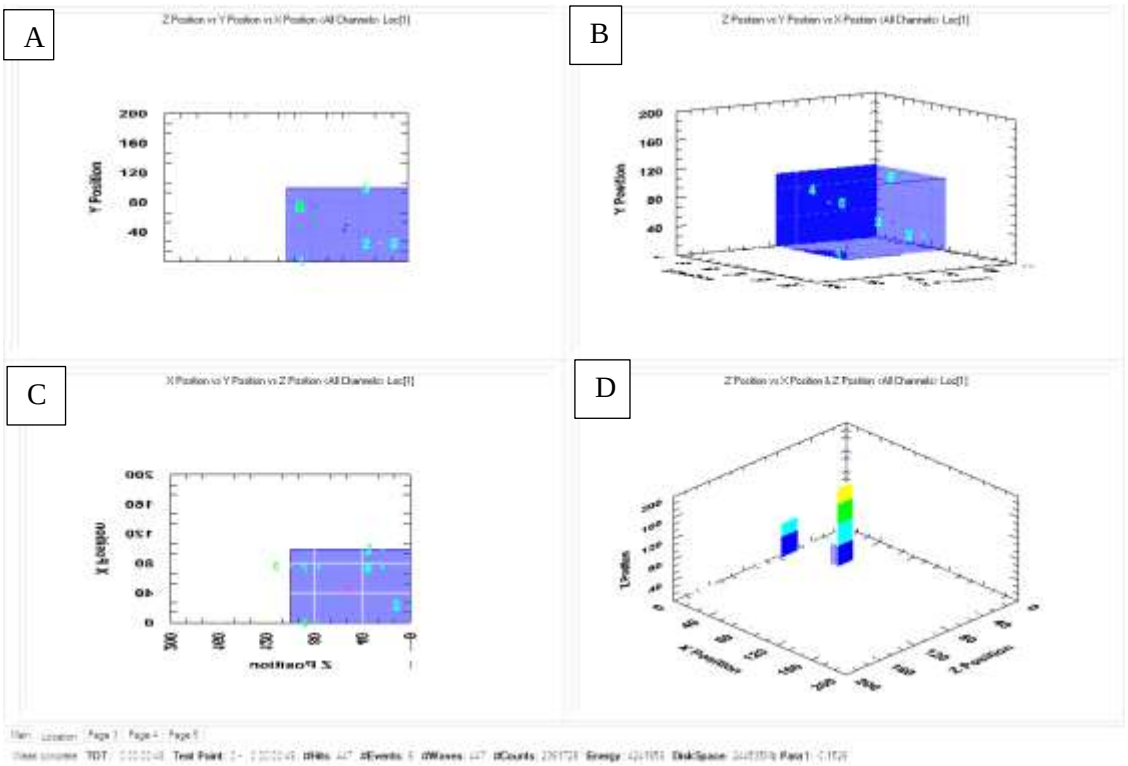

FIGURE 5-220: WBS5 Location Graphs 60mm-50mm, A) Depth view, B) 3D view, C) Overhead view, D) Actual positioning spots.

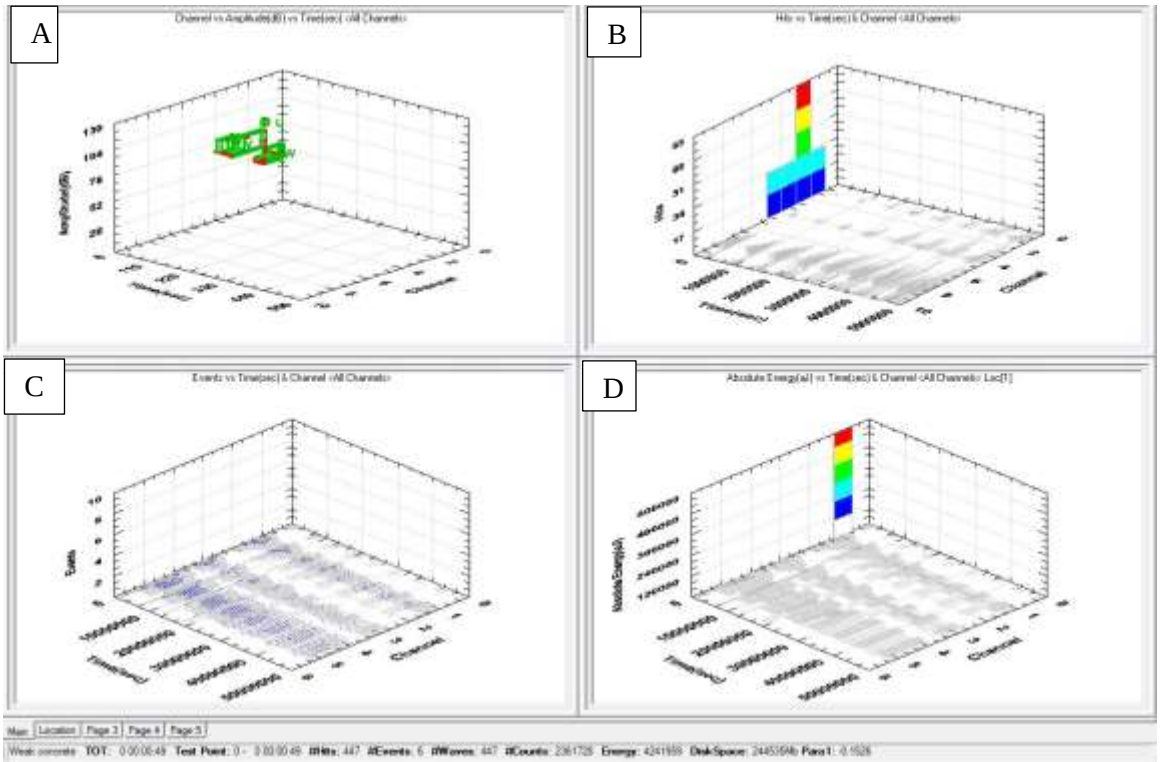

FIGURE 5-221: WBS5 Sensor Graphs 60mm-50mm, A) Acoustic signals detected each channel, B) Hits Vs Time, C) Events Vs time, D) Absolute energy Vs time.

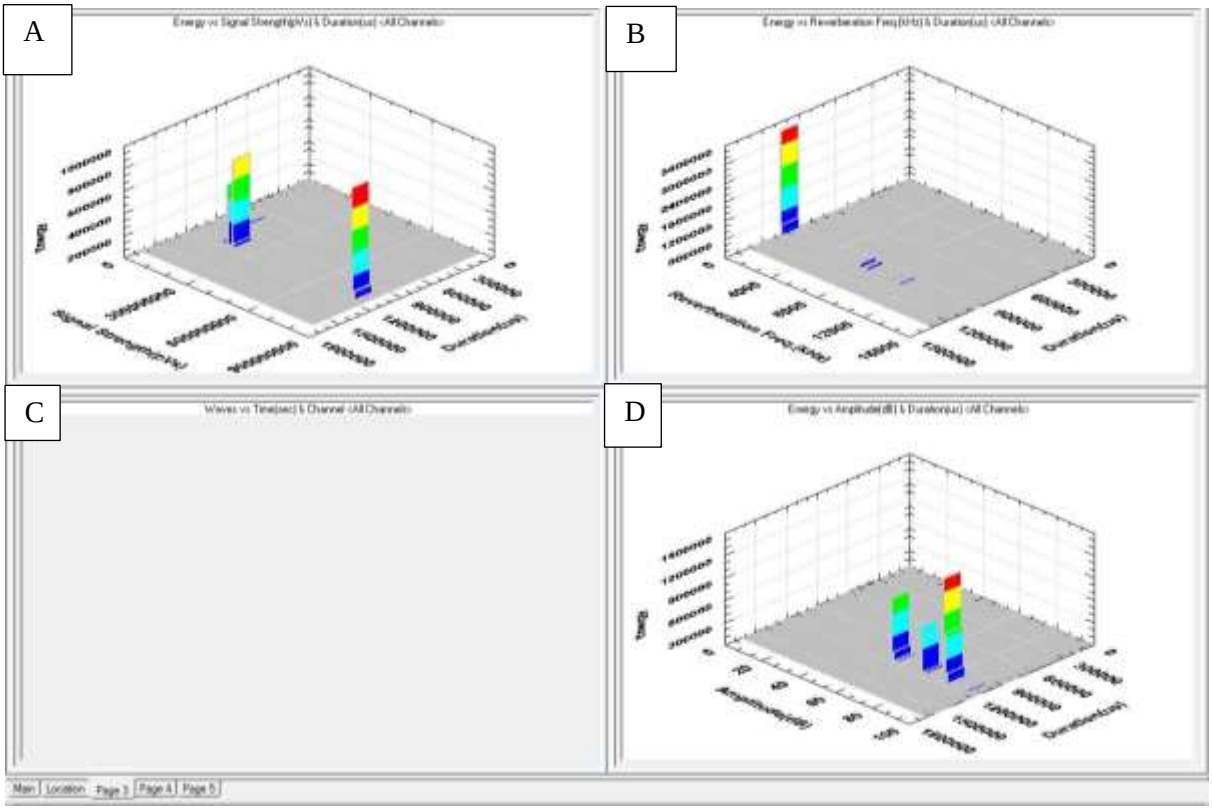

FIGURE 5-222: WBS5 Energy, duration and signal strength, A) Energy Vs signal strength, B) Energy Vs Reverberation, C) Empty, D) Energy Vs Amplitude.

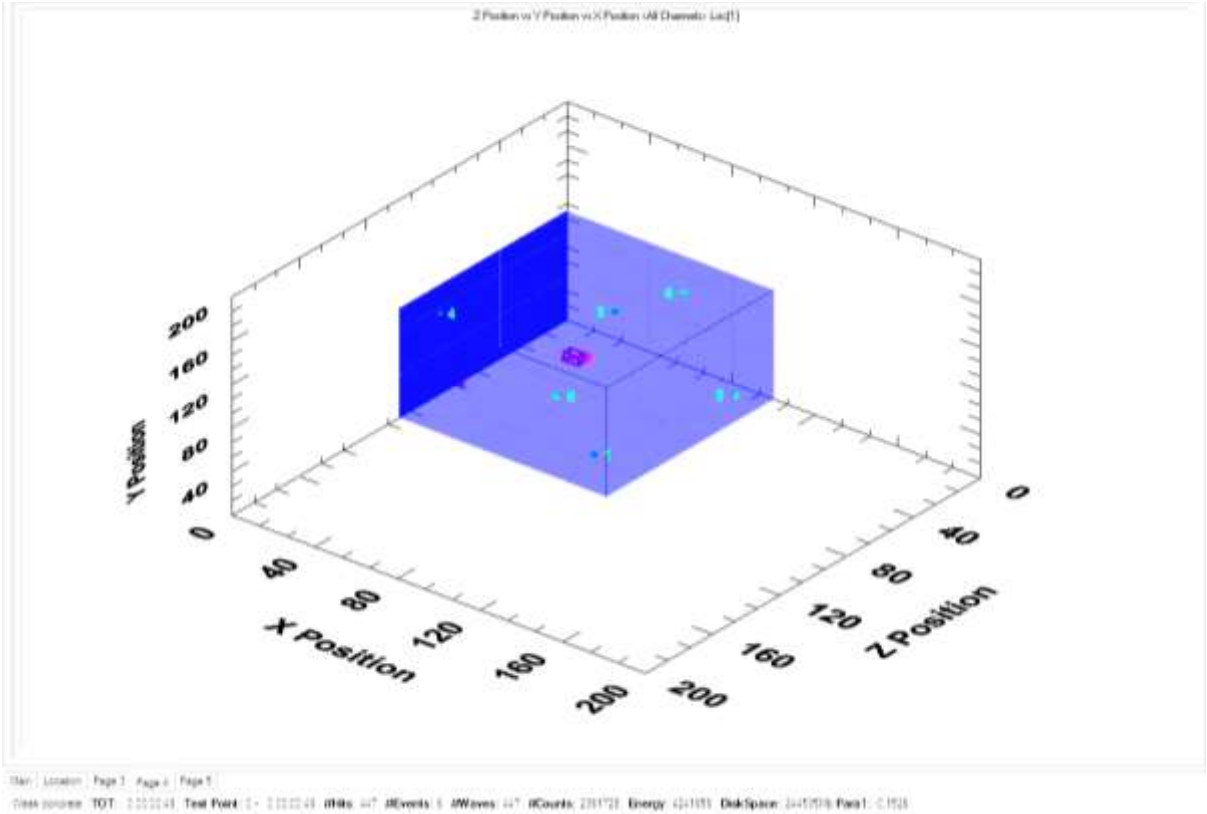

FIGURE 5-223: WBS5 3D graph Event Grouping 60mm-50mm.

As shown in Figure 5-220, the side view shows 6 events recorded from approximately 60mm to 45mm, all are well placed with the location of the drill as seen in Figure 5-223. The overhead view in Figure 5-220 shows that the events are centralised and in line with the borehole. This gives added confidence that the results accurately reflect the progression of the drilling and the induced fractures. Again, this result also shows that the main area of damage occurs underneath the drill bit.

During drilling 447 hits were detected, an increase from the previous sample, which is explained by the fact that as the drill bit progresses further down through the sample there are more unbroken paths to the sensors if cracking along the outer edges of the sample causes disruption from the source of the acoustic emission to the sensor. Again, the signal strength is split into two main peaks (Figure 5-222) with the signal strength of $150x10^6\rho Vs$ to $200x10^6\rho Vs$ for the first group and the second group registering between $850x10^6\rho Vs$ and $870x10^6\rho Vs$.

As seen in Figure 5-132 there is no clustering of weaker signals caused by background noise meaning there are fewer hits, though the sensors are still detecting the stronger, higher energy signals from the fractures and the damage occurring and are still able to accurately place it, compared to the other sensor graphs on the previous drilling intervals. Figure 5-221 shows a longer interval compared to the other samples while four of the six sensors are receiving similar signals.

This proves that it is still possible to use acoustics to accurately place the drilling and resultant damage to the sample even with some suppression of signals.

5.7.2.6 WBS6

WBS6 was the final sample tested in this investigation. To reduce the possibility of distorted acoustic readings the sample selected was as close as possible to $100mm^2$ to reduce the volume of plaster required to even out the flat surfaces and which could crumble and reduce contact/placement with the sensors. In order to retain the strength of the rapidly drying shale the sample was added to the plaster and was placed in the rig in as short a time as possible. In this case these particular labour-intensive efforts succeeded in ensuring high quality results throughout the drill run and fracturing of the sample.

100MM TO 90MM

The location and plot of the data is presented in Figure 5-224 to Figure 5-227

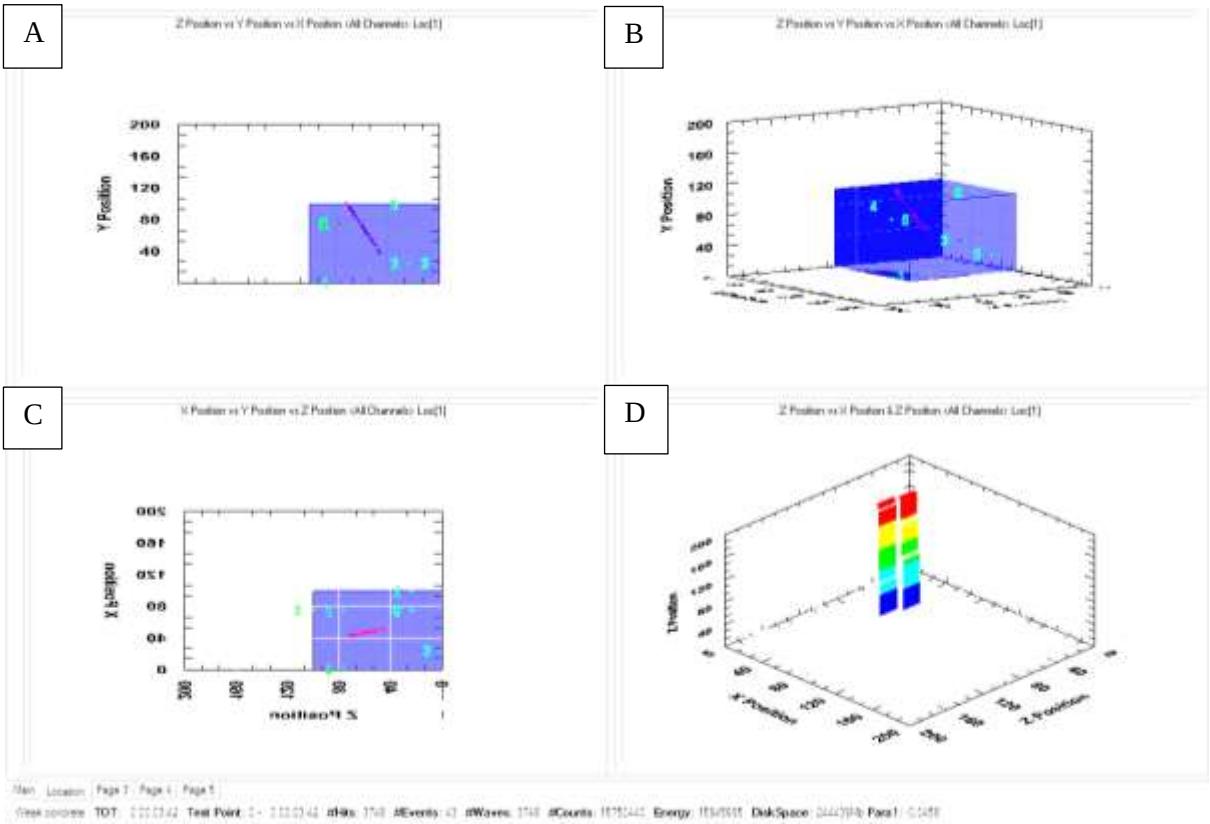

FIGURE 5-224: WBS6 Location graphs 100mm-90mm, A) Depth view, B) 3D view, C) Overhead view, D) Actual positioning spots.

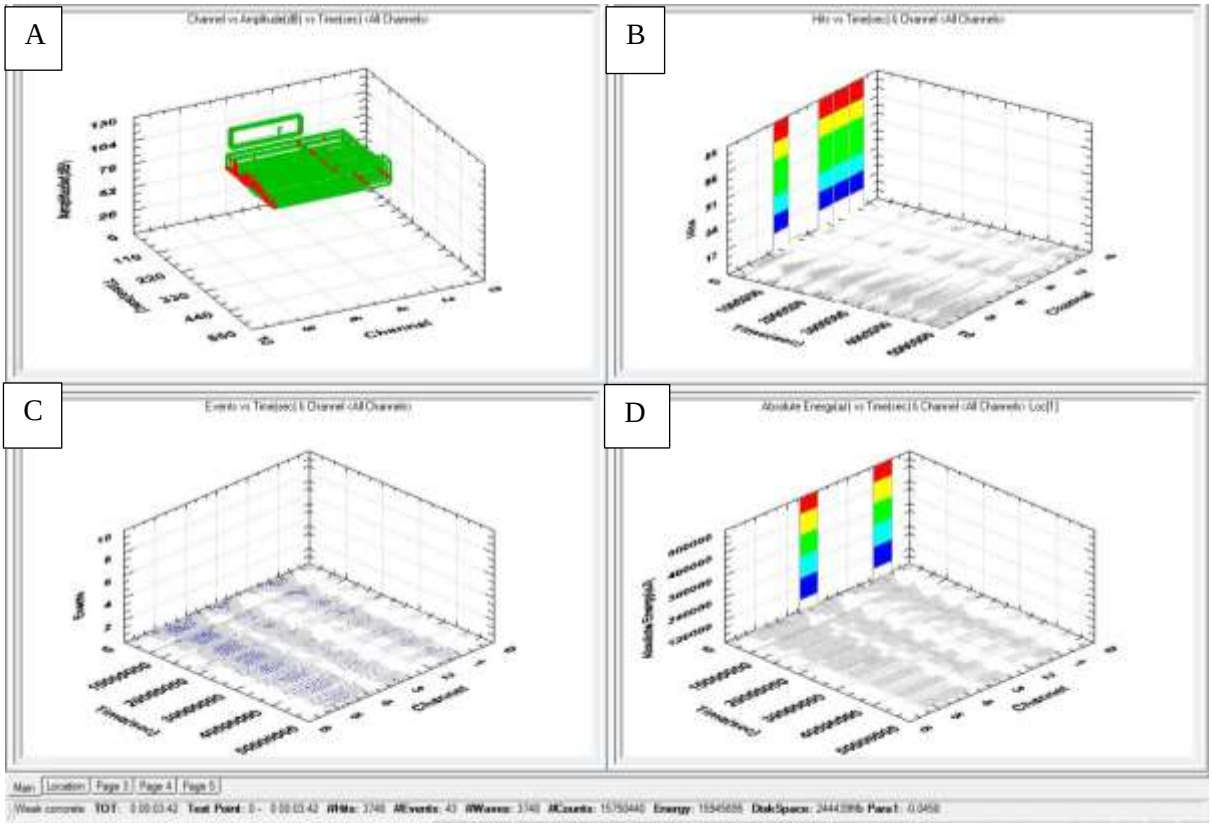

FIGURE 5-225: WBS6 Sensor Graphs 100mm-90mm, A) Acoustic signals detected each channel, B) Hits Vs Time, C) Events Vs time, D) Absolute energy Vs time.

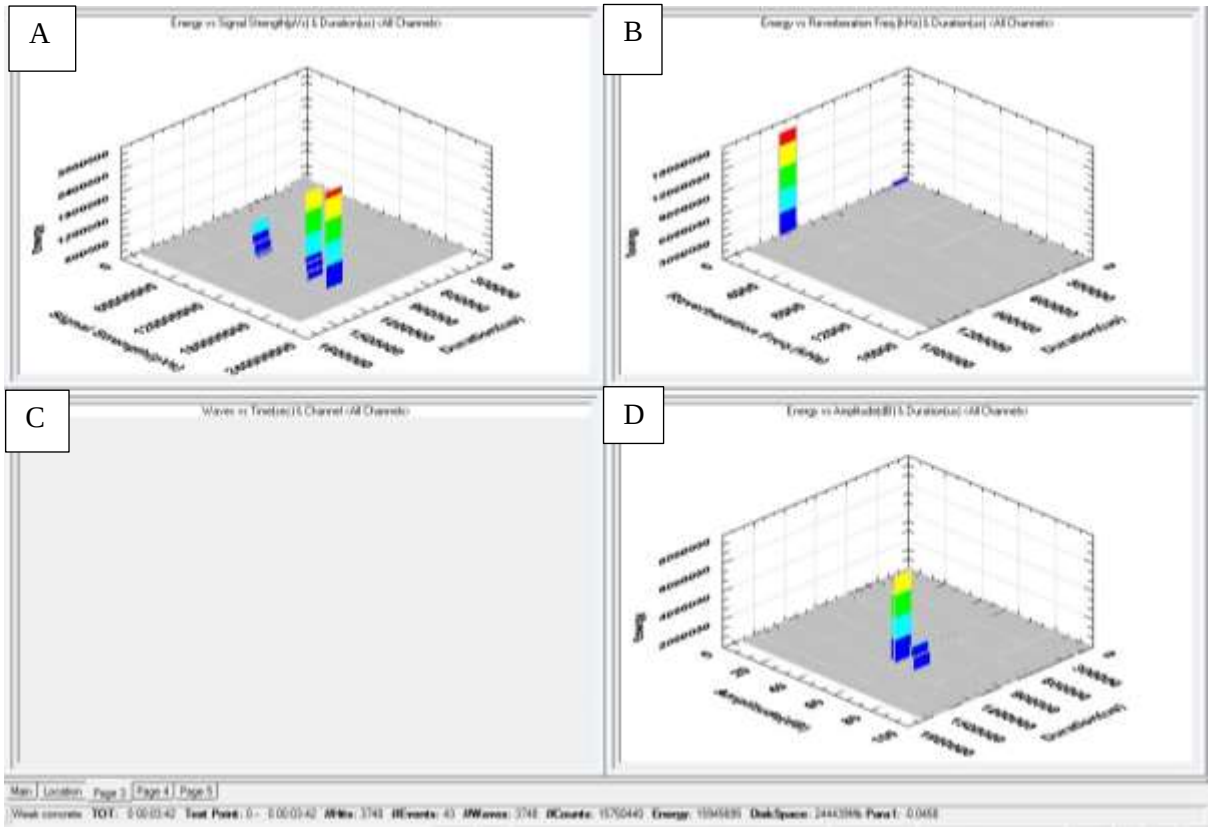

FIGURE 5-226: WBS6 Energy, duration and signal strength 100mm-90mm, A) Energy Vs signal strength, B) Energy Vs Reverberation, C) Empty, D) Energy Vs Amplitude.

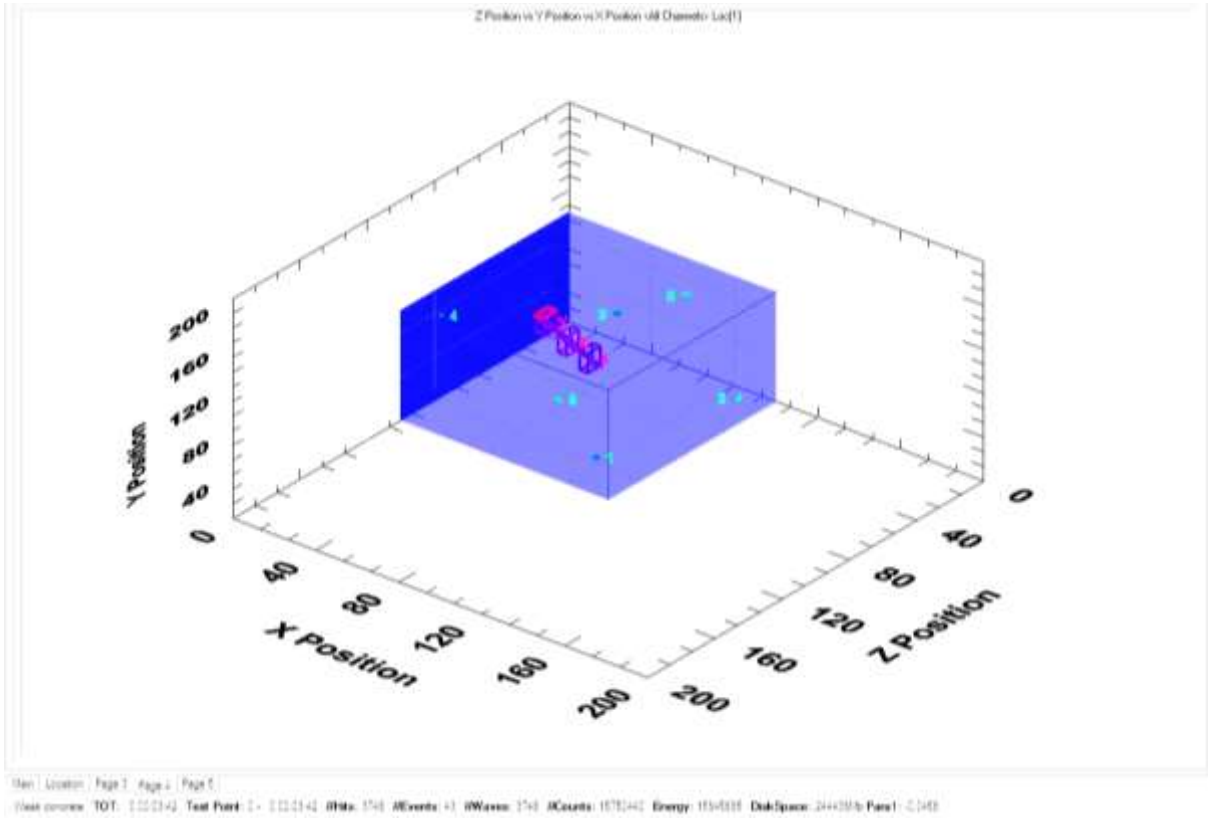

FIGURE 5-227: WBS6 3D Graph Event Grouping 100mm-90mm.

As shown in Figure 5-224 close examination of the side view reveals a number of events placed slightly off centre (in the overhead view) from 100mm to 89mm. This replicates the exact position of the borehole in the sample. A number of placements of acoustic emission trail from this location, these events are angled steeply and travel from the end of the borehole to approximately 42mm on the Y axis, thus locating the vector caused by the damage to the sample in the form of micro-fractures. This corresponds very well to the diagonal fractures that have merged with fractures that have opened up along the bedding plane as seen on the CT scans Figure 5-107 to Figure 5-109. It concurs that microfracture damage would occur along a diagonal vector as the damage evolves to combine with the weaker bedding plane fractures, this progression is seen in the grouping shown in Figure 5-227.

As seen in Figure 5-226 the duration is typical at between 900,000µsecs and 1,200,000µsecs, though the signal strength is significantly higher than seen for other Westbury samples. This sample has three distinct energy peaks, one with a signal strength of approximately $75x10^6$ρVs, one at $150x10^6$ρVs and a final grouping around $180x10^6$ρVs. There were also a small number of low energy signals of weak strength (<1,000ρVs) and short duration (<100,000µSec), these are typical back ground noises detected during the drilling. The ability of the sensors to pick up and differentiate a number of differing energy signals, Figure 5-225, including weak signals gives credence to the results and also indicates the problems previously seen in the last two Westbury samples have been overcome.

90MM TO 80MM

Data collected by the acoustic software is presented in Figure 5-228 to Figure 5-230

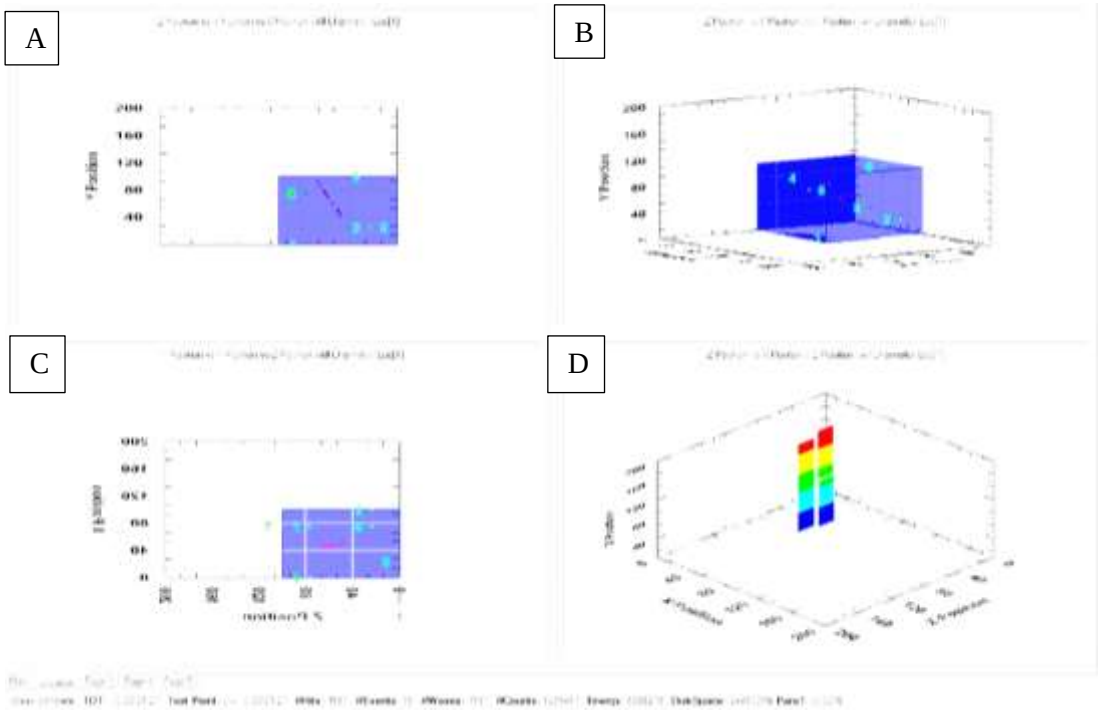

FIGURE 5-228: WBS6 Location graphs 90mm-80mm, A) Depth view, B) 3D view, C) Overhead view, D) Actual positioning spots.

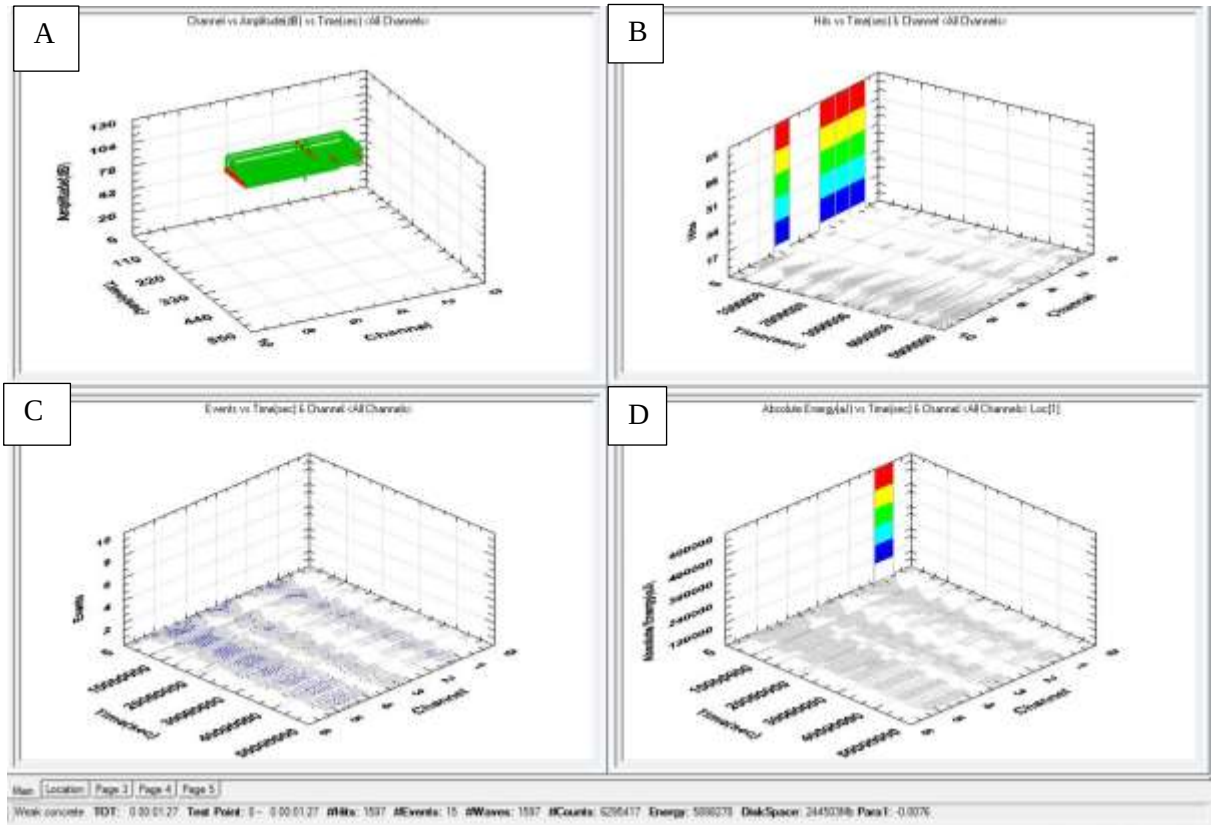

FIGURE 5-229: WBS6 Sensor Graphs 90mm-80mm, A) Acoustic signals detected each channel, B) Hits Vs Time, C) Events Vs time, D) Absolute energy Vs time.

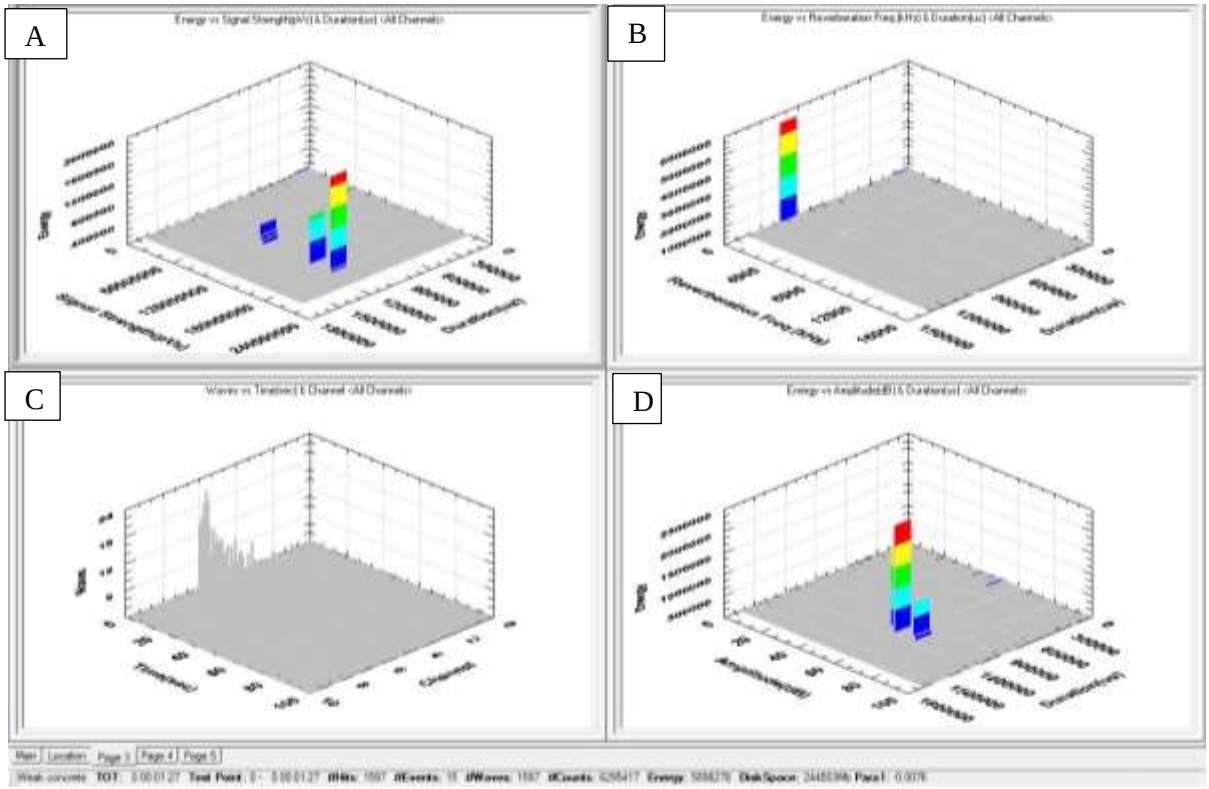

FIGURE 5-230: WBS6 Energy, duration & signal strength 90mm-80mm, A) Energy Vs signal strength, B) Energy Vs Reverberation, C) Waves Vs Time, D) Energy Vs Amplitude.

There were 1597 events detected in this drilling interval (Figure 5-229). This was down by half on the number of hits detected during the previous drilling interval. Figure 5-228 shows that some damage occurred diagonally from the bottom of the borehole. 15 events were placed, 13 of which worked downwards from the end of the borehole at 80mm, while 2 are placed between 90 and 80mm, slightly off centre in the overhead view which again accurately recreates the placement of the borehole. The accurate placement of the borehole and the capture of the events at the starting depth, midpoint and at the end signifies that the acoustic sensors are accurate thus, increasing confidence in locating areas of damage on the diagonal route from the borehole.

As shown in Figure 5-230, the total energy was 5,898,278J with approximately 5,800,000J recorded, as in the previous drilling interval, in three distinct bands of signal strength. The first and second groups peaking at strengths of $75x10^6$ρVs and $150x10^6$ρVs respectively and a final grouping around $180x10^6$ρVs. Each of these groups had a signal duration of between 900,000μsecs and 1,200,000μsecs. The remainder is composed of low strength, low duration background signals, which have been previously identified as the sides of the drill rubbing against the walls of the borehole and remnants of echoes.

80MM TO 70MM

The location and graphic data from the acoustic software is presented in Figure 5-231 to Figure 5-234

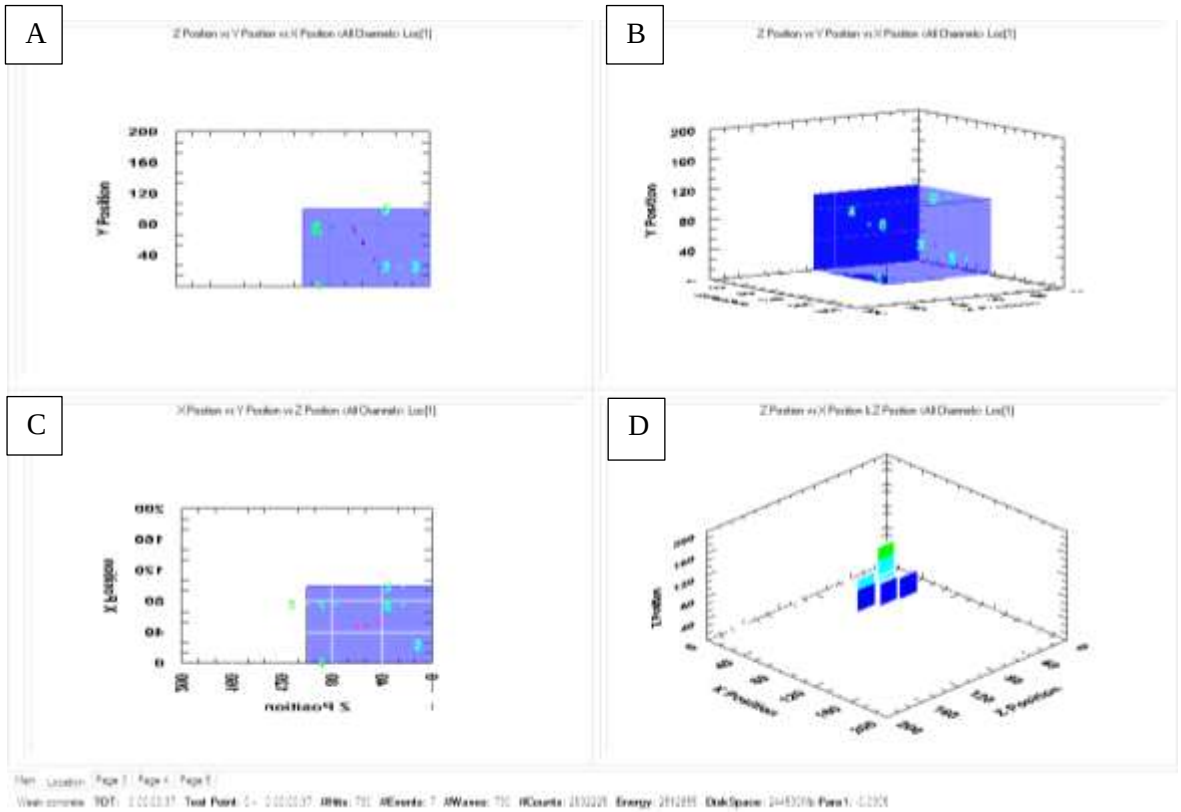

FIGURE 5-231: WBS6 Location Graphs 80mm-70mm, A) Depth view, B) 3D view, C) Overhead view, D) Actual positioning spots.

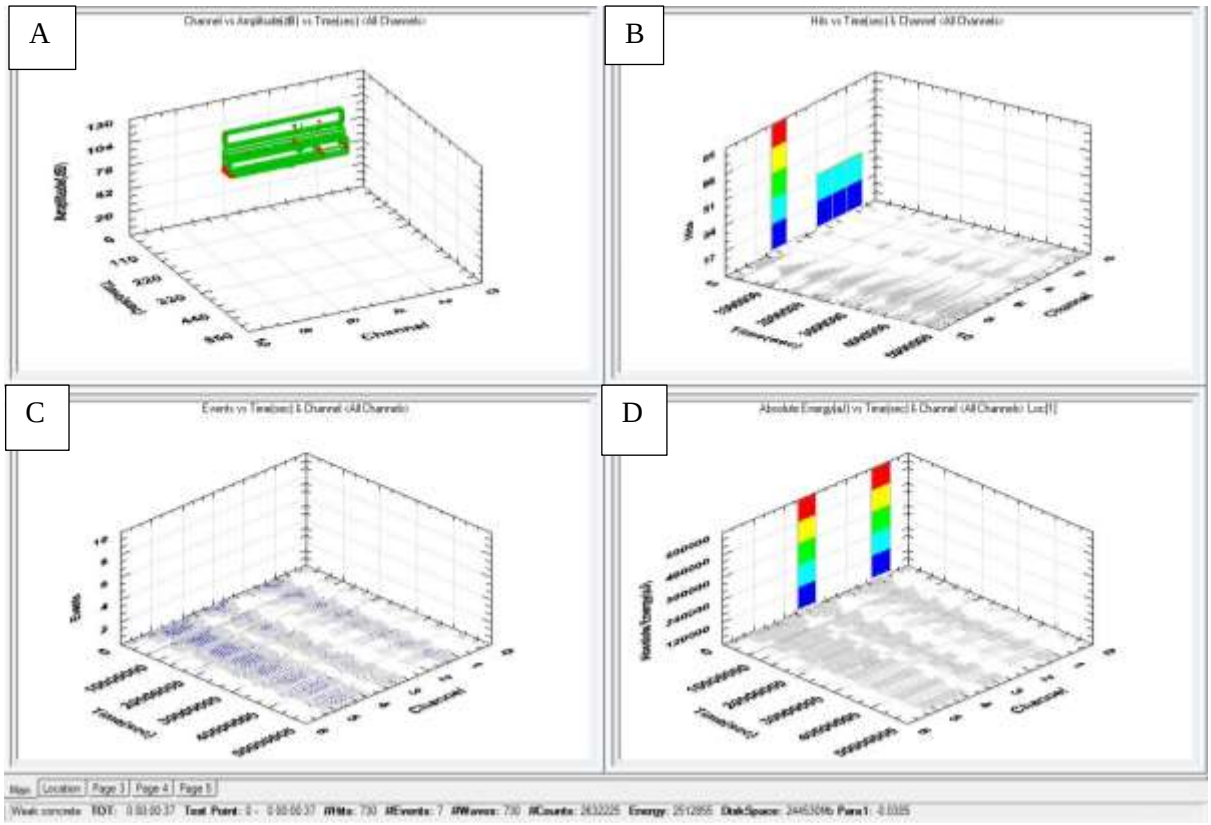

FIGURE 5-232: WBS6 Sensor Graphs 80mm-70mm, A) Acoustic signals detected each channel, B) Hits Vs Time, C) Events Vs time, D) Absolute energy Vs time.

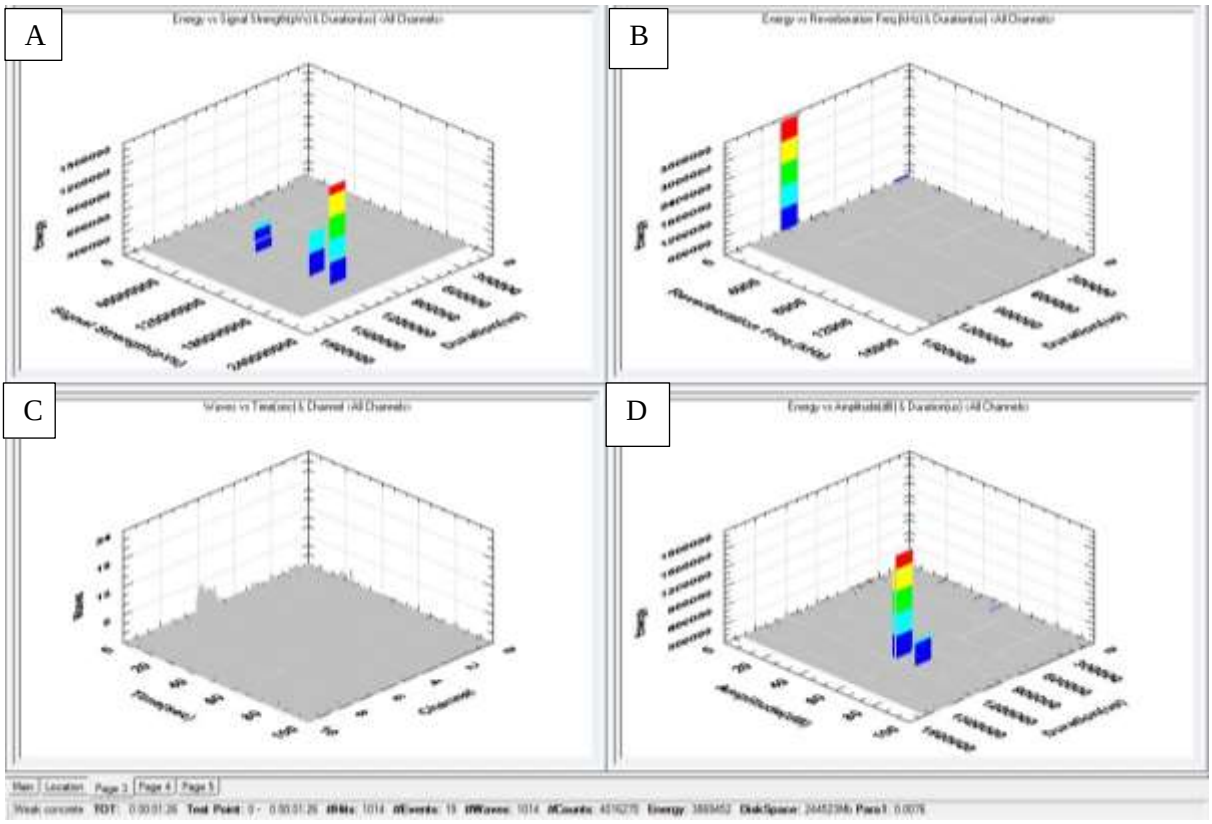

FIGURE 5-233: WBS6 Energy, duration & signal strength 80mm-70mm, A) Energy Vs signal strength, B) Energy Vs Reverberation, C) Waves Vs Time, D) Energy Vs Amplitude.

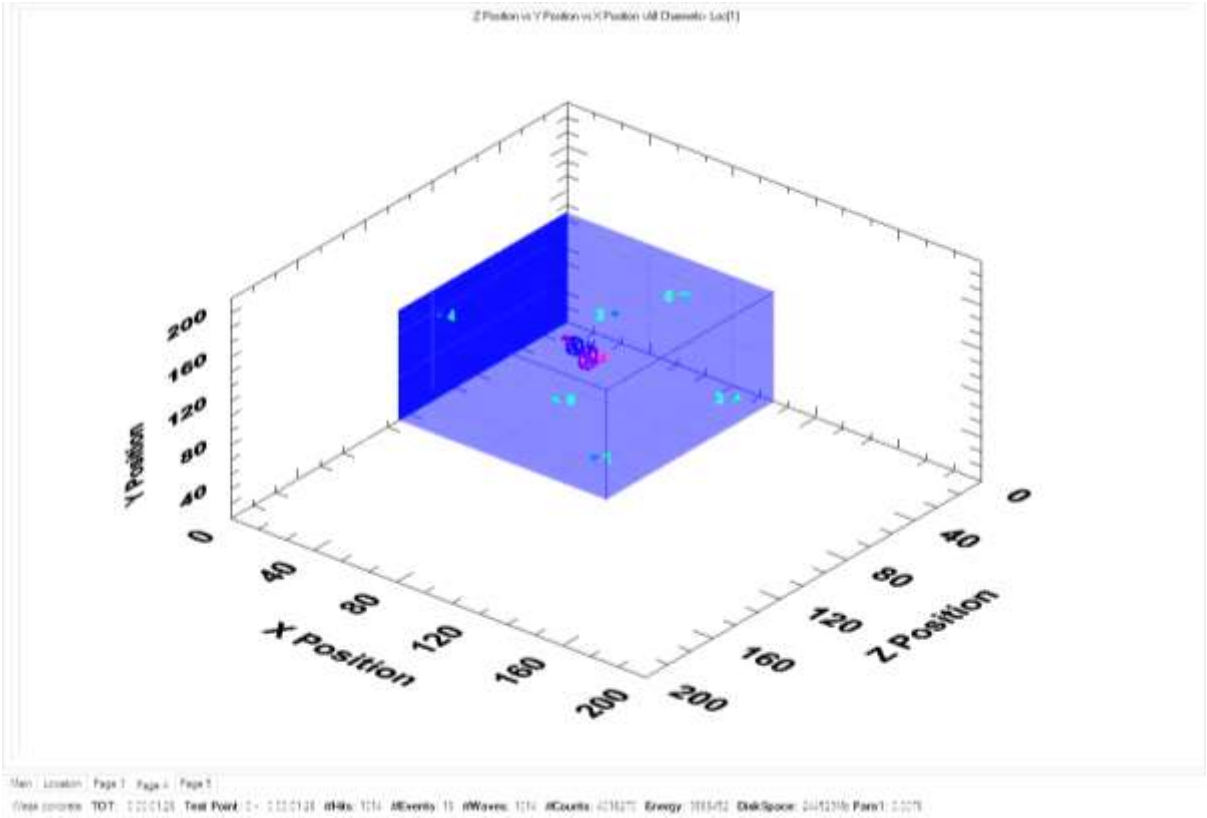

FIGURE 5-234: WBS6 3D Graph Events Grouped 80mm-70mm.

Figure 5-231 shows 19 events from 1014 hits, it is evident from all the Westbury samples, including the samples with poor acoustic returns, that the softer, weaker material returns fewer acoustic waves. Though the fact that the sensors still pick up signals and the software is able to place the events, the usefulness of acoustic positioning is still evident. Three events are placed off centre in the overhead view Figure 5-231, at 78mm on the Y axis with the lowest of the three being approximately 68.5mm in the Y axis. There is a slight slope to these three hits, which reflect the slight tilt that exists in the borehole.

The placement of the events just below the start and finish depths of the interval is further evidence that the majority of damage during the drilling, in the form of microfractures, occurs at a proportional distance below the drill bit. The remaining 16 events are grouped into two distinct bands as shown in Figure 5-234, the first group is located around the centre of the sample, again in a diagonal placement from the end of the borehole, while the bottom grouping extends to the bottom half of the sample. This shows that as the drilling progressed micro-fracture growth occurred. The signal strength and duration is almost a mirror image of the 90mm to 80mm drilling intervals, Figure 5-233 with a correlation shown by the signals detected in all the sensors, Figure 5-232.

70MM TO 60MM

The location data for this drilling interval is shown below, in Figure 5-235 to Figure 5-238.

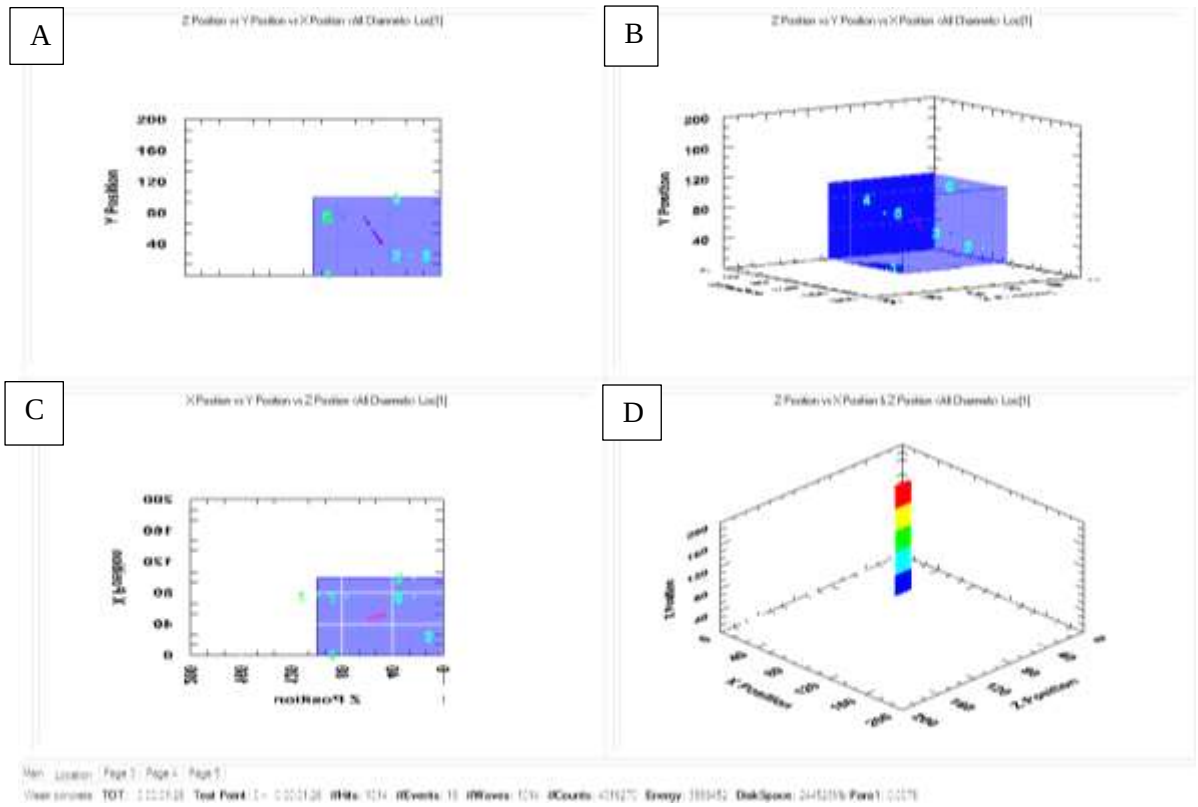

FIGURE 5-235: WBS6 Location Graphs 70mm-60mm, A) Depth view, B) 3D view, C) Overhead view, D) Actual positioning spots.

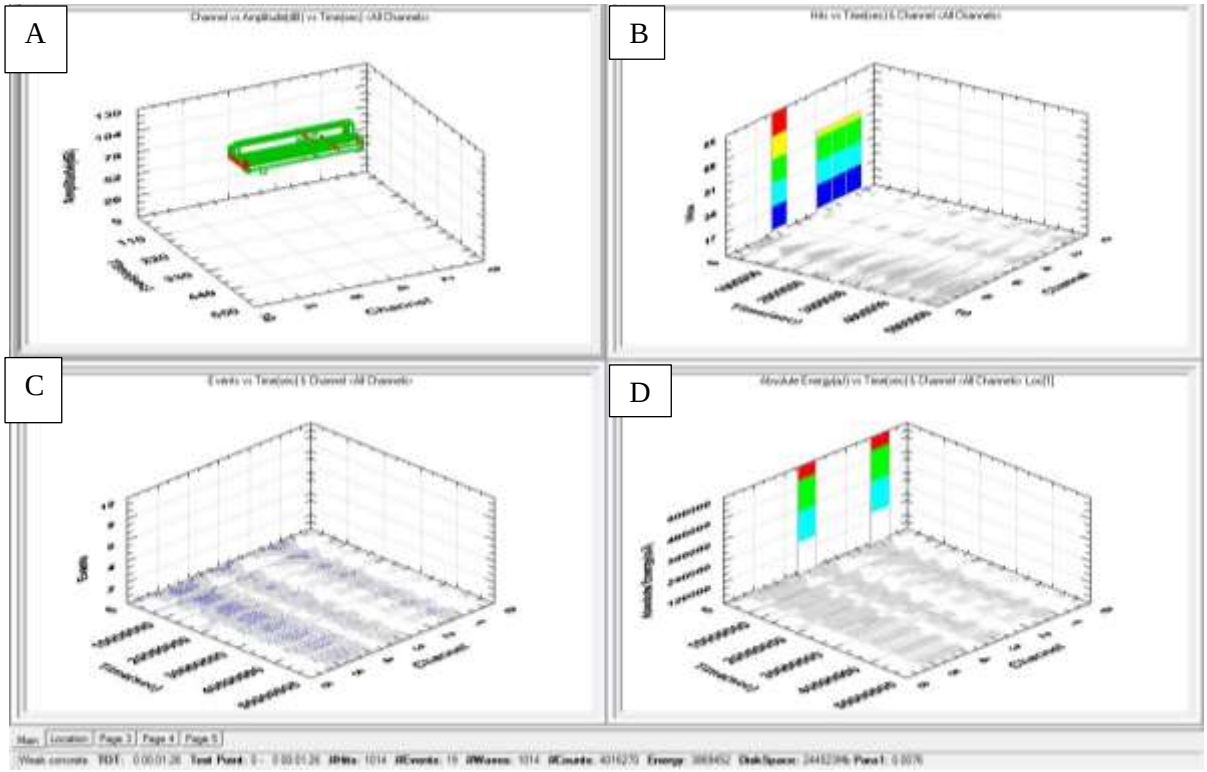

FIGURE 5-236: WBS6 Sensor Graphs 70mm-60mm, A) Acoustic signals detected each channel, B) Hits Vs Time, C) Events Vs time, D) Absolute energy Vs time.

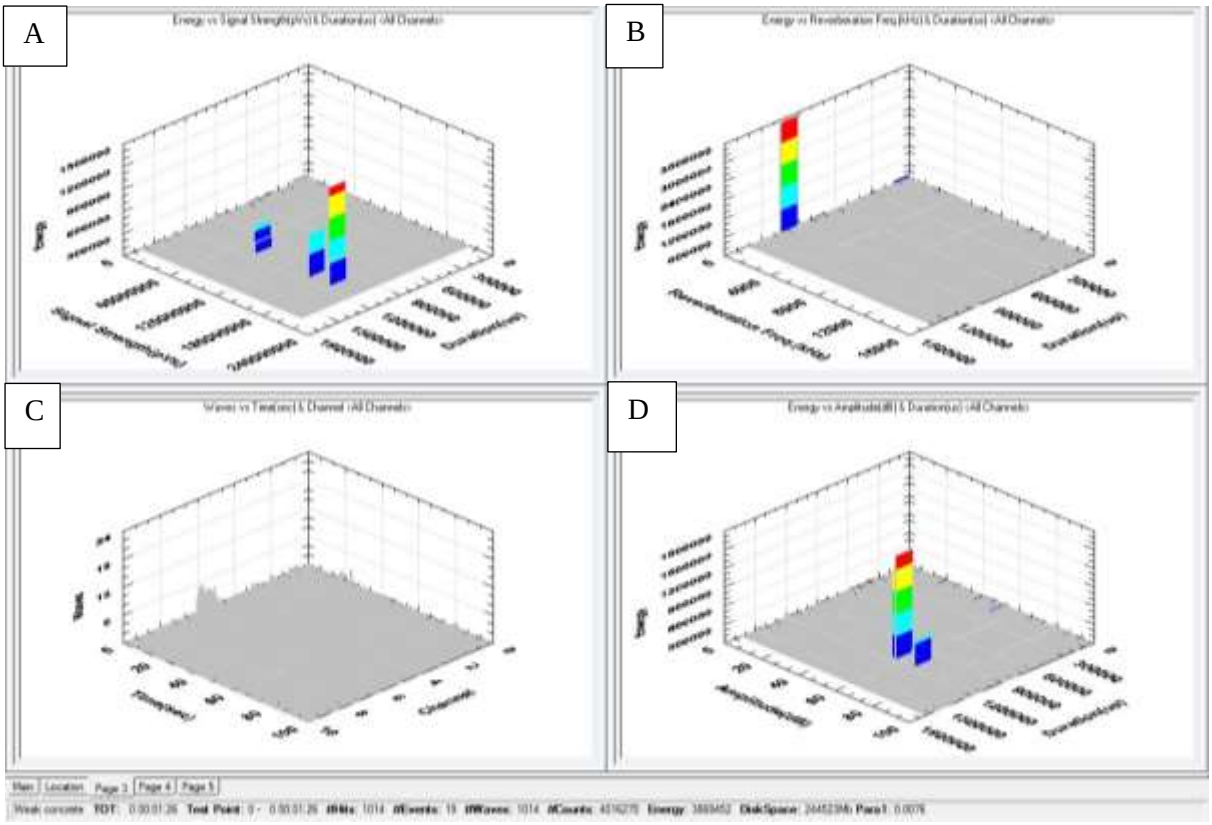

FIGURE 5-237: WBS6 Energy, duration and signal strength 70mm-60mm, A) Energy Vs signal strength, B) Energy Vs Reverberation, C) Waves Vs Time, D) Energy Vs Amplitude.

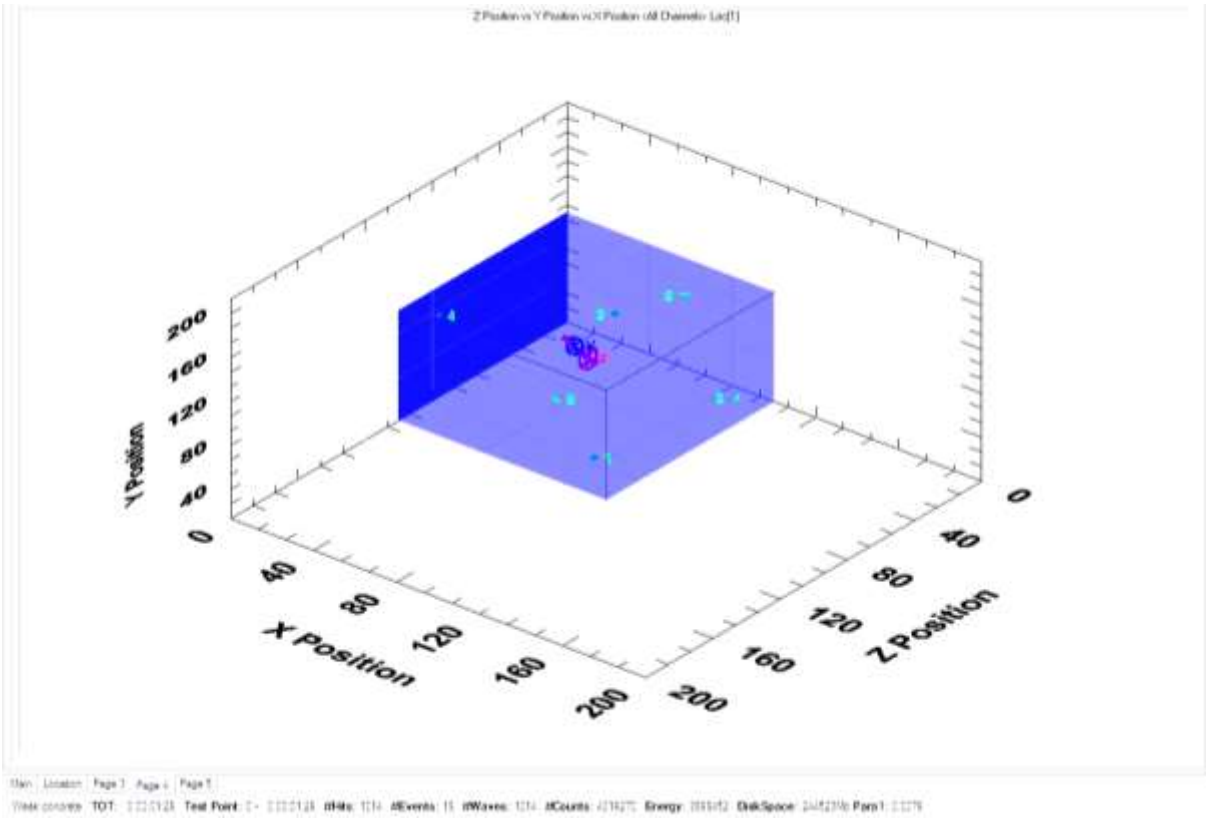

FIGURE 5-238: WBS6 3D Graph Events Grouped 70mm-60mm.

Figure 5-235 shows 19 events which are linked to 1014 hits, like the previous section, four of the events cover the borehole starting at approximately 69mm and ending at 58mm. The events start just below the drill bit which means that there is little damage to the side walls being done by the drilling action. Thus microfracture growth emanating from the side of the borehole, caused by the sides of the drill bit, seems to be a much rarer occurrence than microfracture growth emanating from the end of the drill bit, as evidenced by the lack of acoustic emissions detected that are positioned along the side of the borehole.

The other events, as in the previous drilling intervals, progress in a steep diagonal line down just below the borehole and form two specific groupings, as shown in Figure 5-238. The upper grouping is the smaller of the two, signifying that the majority of the damage in this area had occurred during previous drilling intervals. The main events are placed in the lower grouping, just as in the drilling interval of 80mm to 70mm where the events worked their way to the 40mm mark on the Y axis, so too has this drilling interval which can only mean that as the drilling progressed the line of damage has also increased. The fact that damage wasn't recorded this close to the bottom during drilling in the previous intervals shows that as microfracture growth has come closer to the lower grouping it has made this area weaker and thus more susceptible to fractures.

Like the previous samples the duration of the signals was between 900,000μsec and 1,200,000μsec, an optimum duration, and, like previous drilling intervals, the signal strength forms three distinct peaks. The first is around $75x10^6\rho Vs$, followed by $150x10^6\rho Vs$ for the second grouping and a final band around $180x10^6\rho Vs$ as shown in Figure 5-237. These strong signals, along with less than 10% of the total background energy giving weak strength short blast signals, gives credence to the results obtained. The sensors are picking up similar signals (strong signals of a long duration) at the same time allowing the grouping of these events, the similarity of the signals can be seen in Figure 5-236 and this allows for a greater degree of confidence in the placement of the events.

50MM TO 60MM

The location and acoustic data is shown in Figure 5-239 to Figure 5-242

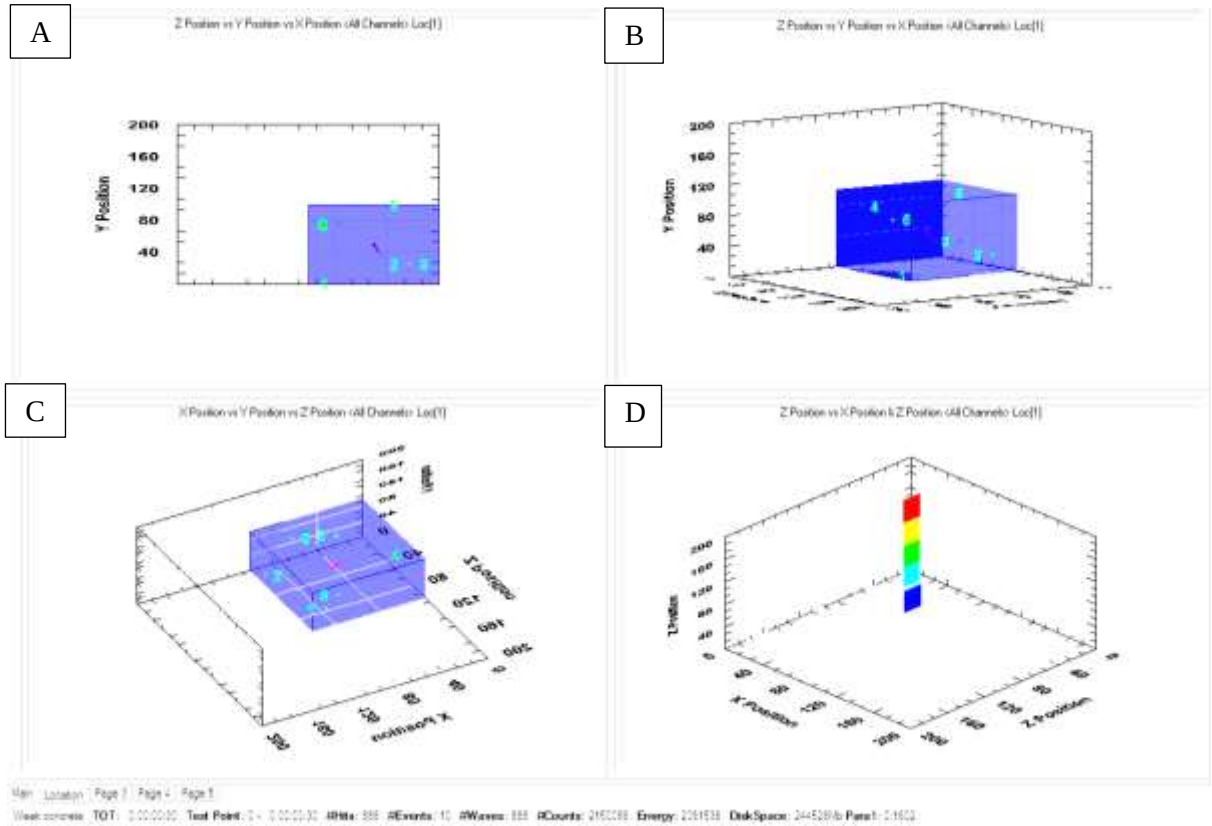

FIGURE 5-239: WBS6 Location Graphs 60mm-50mm, A) Depth view, B) 3D view, C) 2nd 3D reconstruction showing close grouping, D) Actual positioning spots.

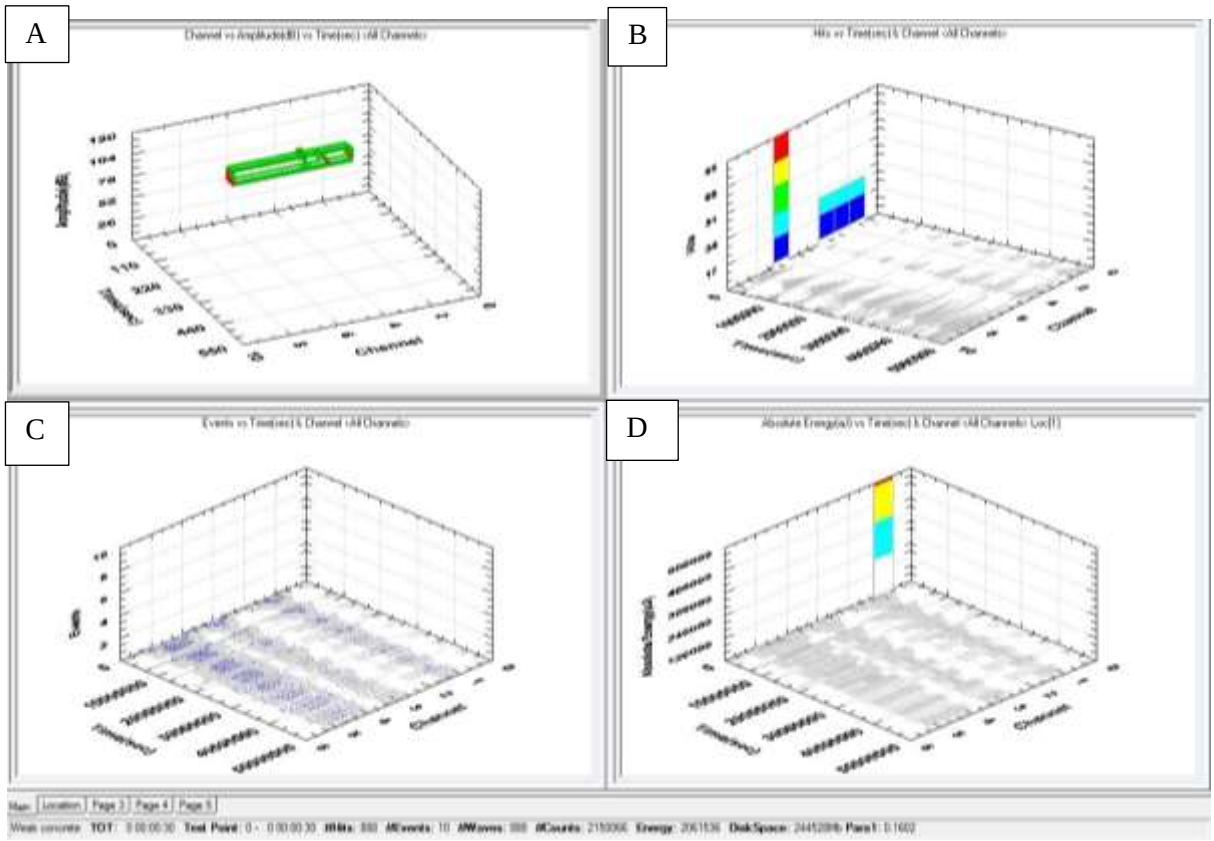

FIGURE 5-240: WBS6 Sensor Graphs 60mm-50mm, A) Acoustic signals detected each channel, B) Hits Vs Time, C) Events Vs time, D) Absolute energy Vs time.

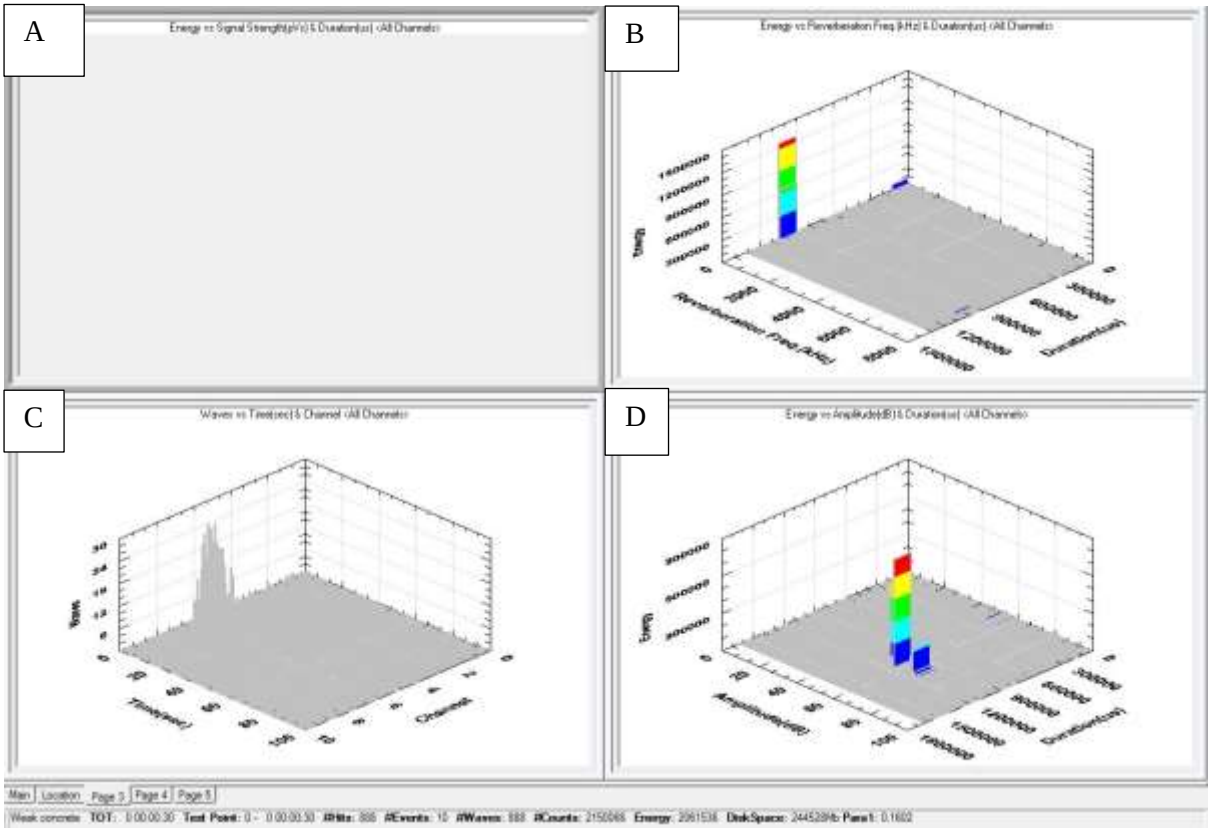

FIGURE 5-241: WBS6 Energy, duration and signal strength 60mm-50mm, A) Empty, B) Energy Vs Reverberation, C) Waves Vs Time, D) Energy Vs Amplitude.

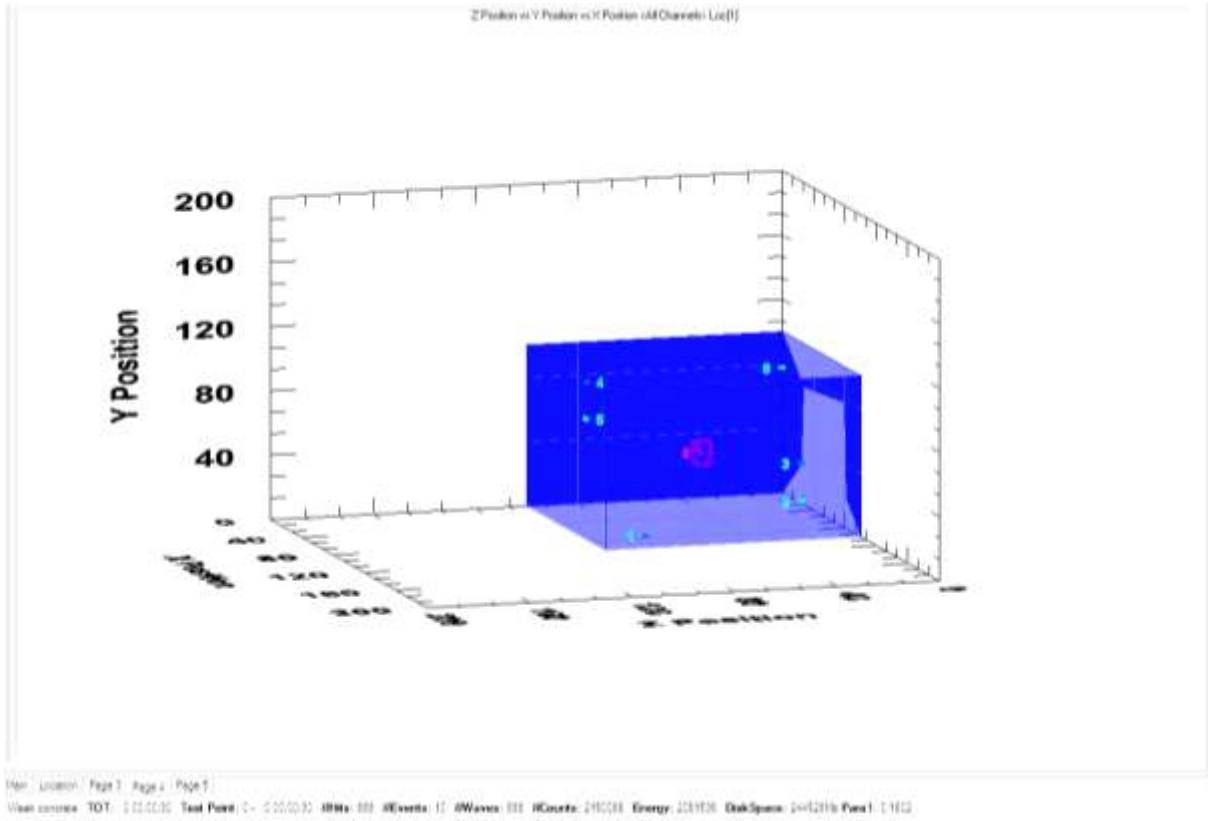

FIGURE 5-242: WBS6 3D Graph Event placement 60mm-50mm.

In this drilling interval 888 hits gave 10 events, nine of which are relatively closely spaced and recorded in areas that represent the borehole or the area directly underneath the borehole as seen in Figure 5-239. The events place between 60mm and 40mm, however, one event is placed diagonally away from the others at approximately 35mm along the Y axis. Figure 5-242 suggests that some damage has been done a little distance away from the drill bit, but the lack of more events suggests that long range damage during drilling has ceased.

The other events are associated with the borehole and thus account for the usual damage done around the immediate area beneath the drill bit. Energy and signal strength as shown in, Figure 5-241, is the same as seen in the previous drilling intervals in this sample.

Whilst four sensors are picking up signals identical to each other allowing events to be accurately placed, Figure 5-240 shows that two sensors were not in use during this drilling interval, however, this was not enough of an issue to prevent the software from making the placement of the events. Three sensors are sufficient to allow the software to locate the events. This shows the importance of maintaining contact between numerous sensors around a sample or when designing acoustics to be used in the field.

POINT OF FRACTURE.

The location and acoustic data derived from the point of fracture are shown in Figure 5-243 to Figure 5-246

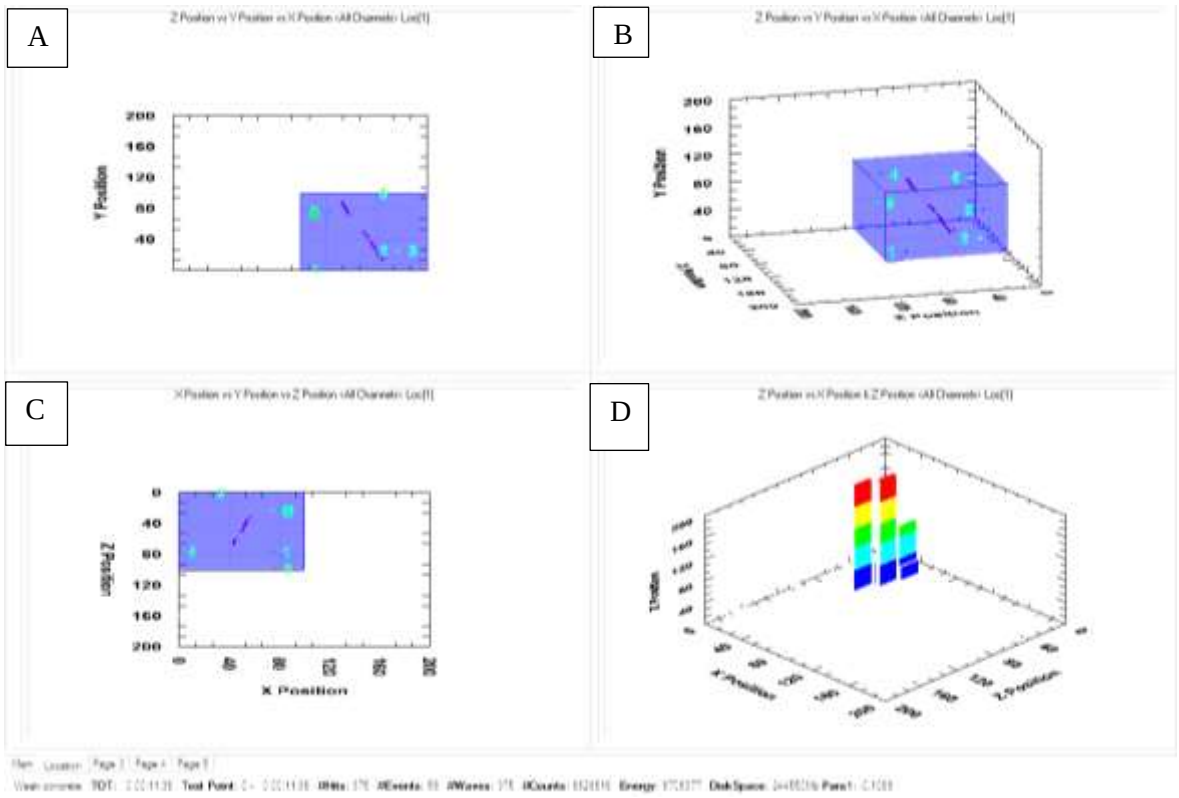

FIGURE 5-243: WBS6 Location Graphs Point of fracture, A) Depth view, B) 3D view, C) Overhead view, D) Actual positioning spots.

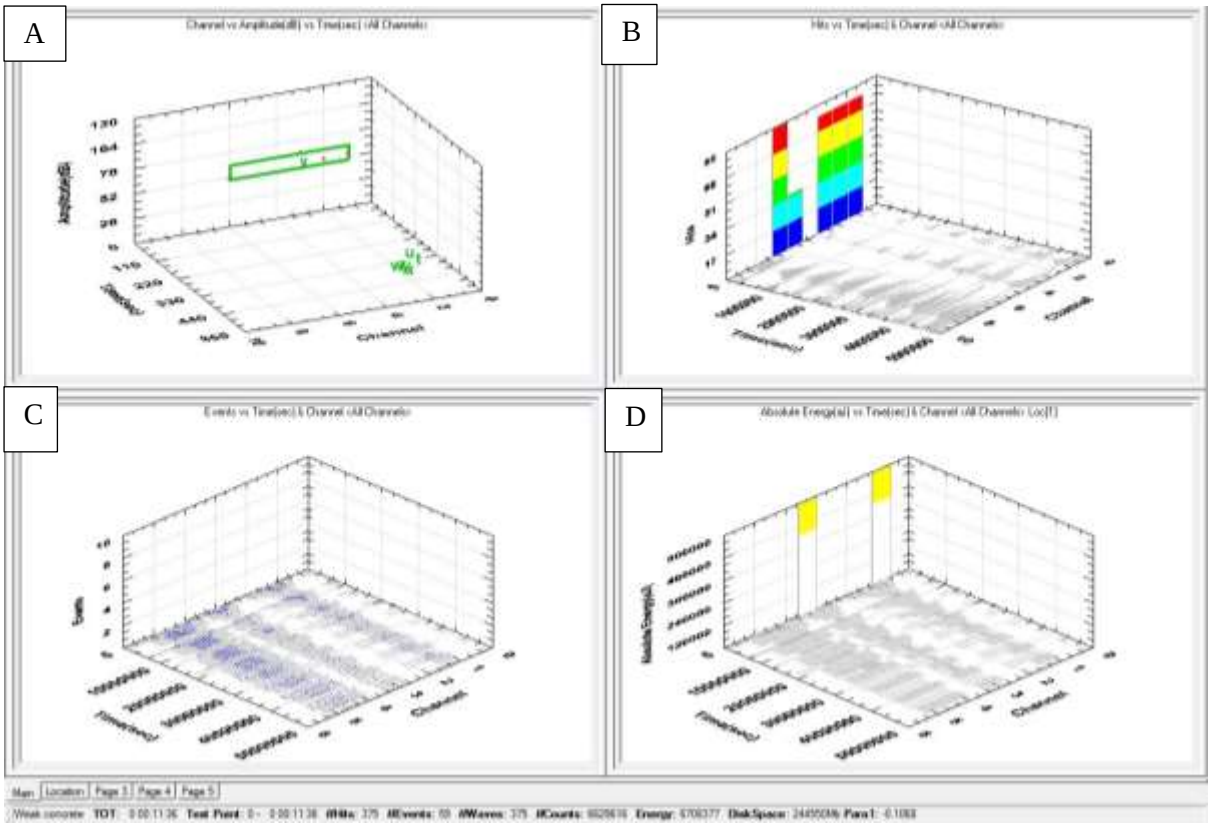

FIGURE 5-244: WBS6 Sensor Graphs Point of Fracture, A) Acoustic signals detected each channel, B) Hits Vs Time, C) Events Vs time, D) Absolute energy Vs time.

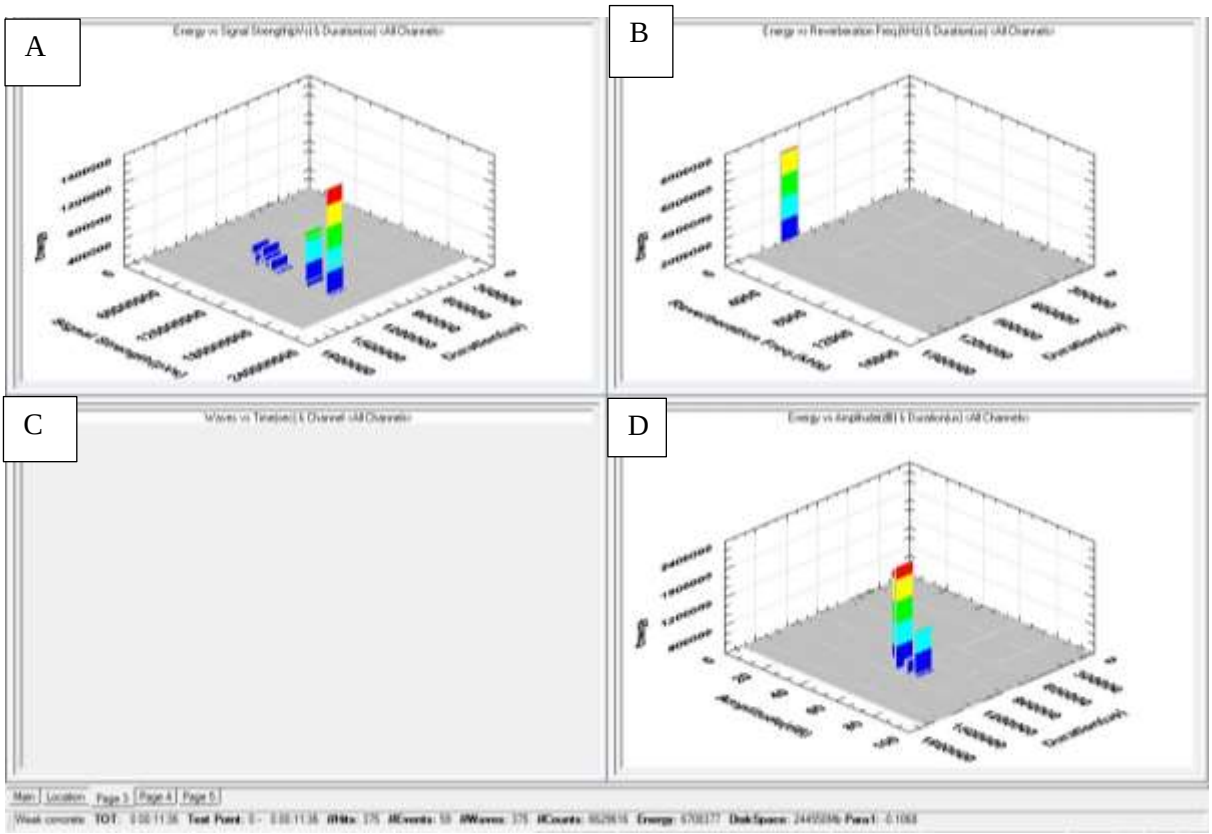

FIGURE 5-245: WBS6 Energy, duration, signal strength Point of Fracture, A) Empty, B) Energy Vs Reverberation, C) Empty, D) Energy Vs Amplitude.

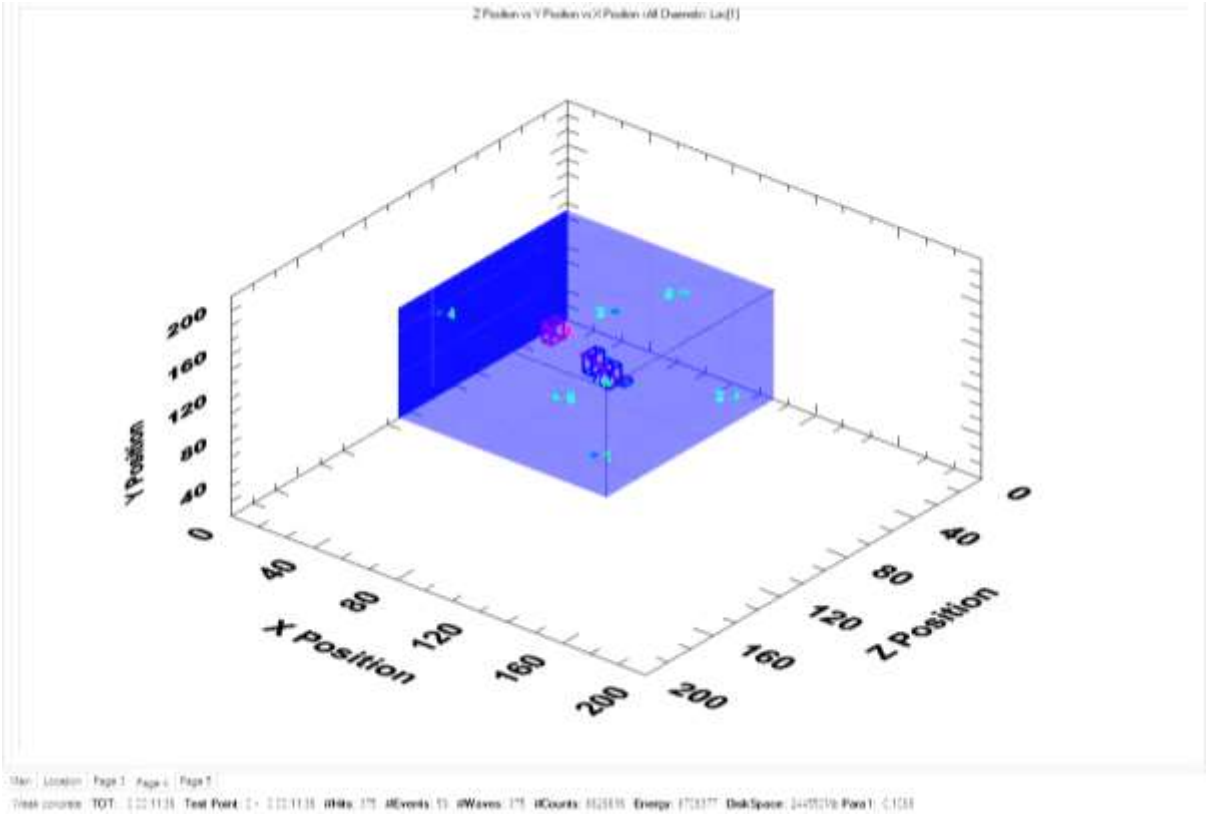

FIGURE 5-246: 3D Graphs Events Grouped Point of Fracture.

The fracture point raised 59 events from just 375 hits. The time plot of the signals per sensor, Figure 5-244, shows that the fracture was completed very shortly after starting. The constant hits in a diagonal path follow the meandering fracture that was shown in the CT scan shown in Figure 5-105 & Figure 5-106. The multiple events indicate that this fracture, although short lived, was not instantaneous. The induced fracture followed the path of micro fracture growth as seen in Figure 5-243 already documented in the drilling intervals of this sample.

The fracturing fluid opened up this weakened path as the fluid progressed, hence the progression shown in the placed events, Figure 5-246. This event worked outwards from the centre, following the progression of the fluid, which provides a greater confidence in the placement of the acoustic events. Figure 5-246 shows these events grouped into four distinct units all forming a distinct diagonal vector. However, the group with the largest peak of energy is the grouping in the top half of the sample, this would be the path that had the least amount of damage and thus required a greater amount of energy to further open up the microfractures caused by the drilling process.

The signal strength was similar to the 70mm to 60mm drilling interval with the exception that the first peak centred on signal strength of $70x10^6$ρsec had a wider grouping. In this grouping the signal strength extended from $70x10^6$ρsec to $110x10^6$ρsec. This could be explained by the fracturing fluid not only opening up the microfractures but also flowing through and filling the fractures. This has led to an increase in this signal strength grouping.

5.8 Summary of the acoustics results

The Results from the acoustics show a number of clear correlations;

- 3D acoustic location allows the accurate spatial location of the drill bit. The sensors consistently return acoustic data from just below the drill bit showing that damage during drilling occurs 2 to 3 mm ahead of the drill bit. A good example is shown in sample AMS2 in drilling interval 70-60mm, Figure 5-129.
- Pre-existing fractures and damage to a formation can be detected and mapped using acoustics; this is due to the vibrations from the drill bit causing reverberations within the damaged areas, as seen in AMS3 e.g. Figure 5-152.
- The more sensors detecting the acoustic emissions the more accurate the data collected and the source of the emissions spatially located. Breaking up of the sample could affect the ability of sensors to pick up acoustic emissions by breaking the line of travel from the source of the emission, as seen in WBS4's in Figure 5-213 & Figure 5-207.
- The mapping of damage during the drilling can also show the likely line of the induced fracture, as was seen in sample AMS3, where not only the pre-existing fracture was picked up but the lines of pre-existing weakness that eventually made up the path of the induced fracture, seen in Figure 5-152.

6 Conclusion and recommendations

This section deals with any correlations or differences noted across each single sample type, and those noted for both the Mudstone and the Shale. This conclusion takes into account the results and discussion from the CT scans, measurements of the fractures, acoustic emission data and the 3D view locations.

The results show a number of clear correlations in both the pattern of the fractures observed and the acoustic data. The Accrington Mudstone samples, in general, follow a very different relationship to the Westbury Shale samples.

6.1 Conclusions

6.1.1 Fracture patterns by sample type

There are important differences noted between the clay rich but organic poor Accrington Mudstones and the weaker organic rich Westbury Shales.

6.1.1.1 Accrington Mudstone

- The Accrington Mudstone samples have an ellipsoid fracture shape with elongated ends, with this elongated section leading up to the sample edge. This pattern was noted in samples subjected to both bi-axial and tri-axial pressures; biaxial loading samples; AMS1 pages 120 to 122, AMS2 pages 131 to 133 and tri-axial loading samples AMS3 pages 149 to 150 & AMS4 pages 157 to 159. The thin elongated fracture gives the potential for a greater reach into the sample than was previously thought, simulation software is predisposed to predict an ellipsoid with a sharp edge.
- This continuation of a fracture much further than the wide body proportion of the fracture opens up a larger area of the reservoir for exploitation, but the general thin structure could restrict fluid flow.

However, the samples of much weaker and more organic rich Westbury Shale show a different arrangement.

6.1.1.2 Westbury Shale

- In the Westbury Shales subjected to tri-axial pressures (WBS3 pages 165 to 166, WBS5 pages 174 to 175 & WBS6 Pages 180 to 181) the fracture pattern is more meandering with the induced fracture being diverted as the fracturing fluid helps open up fractures along the weaker bedding planes. These meandering fractures could cause problems with fluid flow purely because the fracture is providing so many junctions and complex fractures which might act as a ‘pinch point’ keeping fluid from flowing freely into the borehole. The result of which could mean the well would not be as productive as predicted.

- The reduction of fractures along the bedding plane past the point of the depth of the induced fracture, shows that with a weak shale the introduction of a fracturing fluid will not only induce a vertical fracture but will also open up fractures along the bedding plane, WBS3 Figure 5-92 page 175 Figure 5-95 page 180, WBS 4 Figure 5-98 page 183, WBS5 Figure 5-100 page 185 & WBS 6 Figure 5-105 page 192. This will have the added benefit of opening up more of the shale reservoir to the one borehole but could also seriously affect the pathway of the induced fracture; this meandering of the fracture could have a serious effect on predicting the final height of the fracture.
- There is no real objective method to measure the individual strengths of each bedding plane, thus there is little way of telling how many intersecting bedding planes will be created. Opening up a fracture along the bedding plane will also dissipate the pressure head of the fracturing fluid, which might also affect the height of the fracture.
- The Westbury Shales also show a large volume of complex fractures, not only fractures opening up along the bedding plane, but also smaller fractures running shorter distances and joining up parallel bedding fractures or joining with the induced fractures. All these facts serve to complicate the accurate prediction of the fracture pattern. However, the main induced fractures still follow the modelling predictions where the fracture is wider in the middle and then narrows. Occasional widening of the fracture at the end of the sample is possibly attributed to the effects of fluid forcing open the sample and washing away the weak shale where there is no continuation of the material, allowing chunks to break away giving a wider fracture.

6.1.2 Fracture patterns common to both sample types.

- One common detail of this investigation that was shared by both the Accrington Mudstone and the Westbury Shale was the change in the behaviour of fracture angles the further away the fracture half-length progressed from the borehole; AMS2 Figure 5-63 page 138 & Figure 5-64 page 139 and WBS2 Figure 5-76 page 155. If a fracture showed any tortuosity then the number of vector changes for a given area of the fracture would increase; i.e. there would be an increase in the amount of divergent turns in the planar view. This was also associated with the angles of the fracture increasing as the fracture attempted to 'right' itself. This effect is caused by the pressure head of the fracturing fluid dissipating. As the fluid contains less force, the fracture is less able to overcome the intrinsic strength of the sample, it cannot just force its way through as it is unable to break through stronger pockets of resistance. This, then forces the fracture to break through the weaker planes onto another path (in effect forcing the fracture to turn) if it comes across a pocket of greater resistance. This observed behaviour in both the Accrington Mudstones and the Westbury Shales could have the effect of reducing the efficiency of fluid flow from the reservoir into the borehole. It could also lead to the inefficient placement of

proppants; this tortuosity could affect the dispersal of the fluid causing the furthest parts of the fracture to be starved of the very product designed to open the fracture out further.

- The main angle of the fracture direction does show some variation between the organic rich Shale and the clay rich Mudstone. The mudstone, in both biaxial and tri-axial conditions, had near vertical fractures, giving an attack angle close to 0^o from a straight vertical line taken from the borehole. The shales were mainly vertical though showed more meandering. One sample (WBS3) did show a relatively low angle of attack of between 65^o to 80^o, whilst WBS5 and WBS6 had a fracture that meandered but the fracture was near vertical. The fracture angle of attack lowered only towards the edge of WBS5 when intersecting fractures from the bedding increased in numerousness. Thus, an induced fracture will rupture roughly vertically but this depends on the ability of the bedding to separate when the fracturing fluid is introduced.

6.2 Acoustic Emissions

- The acoustic data shows that whether the material is Accrington Mudstone or Westbury Shale the signals created by a fracture or drilling have similar properties, i.e. a duration of approximately 100,000μsecs. There was a difference between the signal strength with Accrington Mudstones recording approximately $300x10^6\rho Vs$ to $600x10^6\rho Vs$ during drilling and at the point of fracture, whereas in the Westbury Shale, 3 distinct signal strengths are seen at around $75x10^6\rho Vs$, $150x10^6\rho Vs$ and a final band around $180x10^6\rho Vs$. Again, these signal strengths are similar whether seen during the drilling phase or the fracture.
- Since events placed during the drilling seem intrinsically linked to micro fracture growth and damage to the sample, this leads to the conclusion that the acoustic signature of a fracture is the same whether it is micro growth caused by the drilling or the rapid propagation of a large fracture by the addition of fracturing fluid. The slight difference seen in the signal strength groupings between the Shale and the Mudstone leads to the conclusion that each different geological unit will have its own distinct acoustic profile. The weaker signal strengths in the Shale compared to those seen in the Mudstone formation suggest that the higher the organic content in the strata, thus a less coherent a rock, the weaker the signal will be which is in agreement with what would be expected.
- The 3D Acoustic Emission software showed the potential for its use to measure the progression of both the fracture and the drilling, or more accurately the progression of damage during drilling. It is important to note that there are some limits to its full potential; any change in density of the material will give a weaker reading. This is the same principle as in sonar, changes in density will affect the passage of a wave causing it to move. When a system relies on multiple sensors to pick up the same signal, anything that will distort or ‘bounce’ a signal will cause interference which will affect the readings and thus the placement of acoustic events.

- During the drilling it was noted that the placement of the acoustic events could be used to accurately locate the drill bit as the vast majority of the events placed were just below that location. In this case events were placed 2mm below the drill bit showing that damage that occurs to a formation during drilling arises, mainly, in an area directly underneath the drill bit.
- Acoustic monitoring during drilling can also highlight existing faults and areas of weakness within the rock formation which could be used to try to accurately predict the pattern of any fractures that are to be induced in a damaged formation.
- This investigation has also observed the relationship between an induced fracture and an existing fracture. The AMS3 sample showed that where a fracture is induced close to a pre-existing fracture, the pre-existing fracture will retard the development of the new fracture. This indicates that a fracture needs to be induced far enough away from an existing fracture in order to build up a rate of propagation sufficient to cross the boundary of the existing fracture. A fracture may still cross the boundary of an intersecting fracture; however, the new fracture will be diverted. The existing fracture will stop fluid from progressing forward but won't release the pressure head enough to stop the fracturing fluid. The fluid will then force a path through a weaker part of the formation, on the same side of the fracture, until the continued pumping of the fracturing fluid causes another fracture to open up at an appropriate distance away from the pre-existing fracture to build up sufficient pressure to eventually cross over the pre-existing fracture. This information combined with the ability of the acoustic emissions software to map existing structures can then be used to accurately determine where a fracture will be induced to ensure the most efficient way of planning the extraction of hydrocarbons.

6.3 Recommendations

There are a number of recommendations to be made following this investigation;

- The first of which is to carry out further study with this equipment using fluid in the void space to stimulate reservoir fluid. The fluid should be pressurised to 40 bars to mimic the behaviour of fractures at higher operating pressure.
- More shale samples from different shale formations should be tested to provide a larger, more encompassing collection of measurements of a greater selection of fractures so that an equation can be formulated to more accurately predict the evolution of a fracture during its propagation in the different rock types. This will also assist in building up a database of acoustic emissions to further understanding of the different rock formation behaviour.
- It is essential to test and confirm the concept of the correlation between the progression of the drill bit and the damage to formation picked up by the acoustic emission software. Perhaps with individual events separated with a shorter number of hits in order to work out a direct correlation between the actual depth of the drill bit and the recorded damage. This would improve our ability to work out critical damage to the boreholes and the formations.

- Different drill bit shapes, sizes and types should be used to see if they affect the depth of damage to the formation during drilling, and if so, a library of these differing effects can then be catalogued in order to provide more efficient borehole and reservoir management.
- Shale samples should be cut as close to the final size as possible, to within 2mm, a high strength plaster should continue to be used to ensure a straight edge on the sample, however, this layer should be as thin as possible and the areas where the acoustic sensors are to be placed should be calculated before the placement of the plaster, to ensure a gap in the plaster where the sensor is to be placed.

7 References

Adams, C. H., 1982. *Recommended Practice for accoustic Emission testing of fiberglass reinforced plastic tanks/Vessels.* s.l., s.n.

Alves, L. M. & De Lacerda, l. A., 2012. Fractal Fracture Mechanics Applied to Materials Engineering. *Applied Fracture Mechanics,* pp. 67-106.

Bhattacharya, 2011. *Optimal Fracture Spacing and Stimulation Design for horizontal Wells in Unconventional Gas Reservoirs.* Denver, Society of Petroleum Engineers.

Blanton, T. L., 1982. *An experimental Study of Interaction Between Hydraulically induced and Pre-Existing Fractures.* Pittsburgh, Society of Petroleum Engineers.

British Geological Survey, 2013. *Bowland Shale Gas Study: Geology and resource estimation.,* London: British Geological Survey.

Brown McFarlane, n.d. *BS 1501 161 430A and BS 1501 161 430B.* [Online]
Available at: http://www.brownmac.com/products/boiler-plate-steel/bs-1501-161-430a-and-bs-1501-161-430b.aspx
[Accessed 17 February 2016].

Chase & Dietrich, 1989. Compaction within the South Belridge Diatomite. *SPE Reservoir Engineering,* pp. 422-428.

ChemTerra International, n.d. *Resource Plays.* [Online]
Available at: http://www.chemterra.com/resource-play-consulting/
[Accessed 23 June 2014].

Clarkson, C., 2011. Integration off Raye-Transient and Microseismic Analysis for unconventional Gas Reservoirs: Where Reservoir Engineering Meets Geophysics. *Recorder - Official Publication of the Canadian Society of Exploration Geophysics.*

Crump, T. N. & Droge, M. A., 1979. Development of an Acoustic Emission Test for FRP Equipment. *Managing Corrosion with Plastics - Vol. IV. NACE.*

Darve, F., 1990. *Geomaterials: Constitutive Equations and Modelling.* New York City: EsevierApplied Science.

Ding, W. et al., 2012. Fracture Development in shale and its relationship to gas accumulation. *Geoscience Frontiers,* January Volume 3 Issue 1, pp. 97-105.

Elements, 2012. Water management Challenges Associated with the production of Shale Gas by Hydraulic Fracturing. *Elements.*

Environmental Engineering and Contracting, Inc, 2010. *A Brief History of Hydraulic Fracturing.* [Online]
Available at: http://www.eecworld.com/services/258-a-brief-history-of-hydraulic-fracturing
[Accessed 12 06 2014].

Farkas, P. D., 2000. Fracture Behaviour of Bulk Crystalline Material. *Philosophical Magazine,* Feburary, 8(6), pp. 1425-1444.

Finol, A. & Farouq Ali, S. M., 1975. Numerical Simulation of Oil Production with Simultaneous Ground Substance. *Society of Petroleum Engineers Journal,* pp. 411-424.

Geertsma, J. & F. De Klerk, 1969. A Rapid Method of Predicting Width and Extent of Hydraulic Induced Fractures. *Journel of Petroleum Technology,* pp. 1571-1581.

Gidley, J. l., Holditch, S. & Nierode, D., 1989. Three-dimensional Fracture Propagation Models. *Recent Advances in Hydraulic Fracturing,* p. 95.

Griffith, A. A., 1921. The Phenomenon of Rupture and Flow in Solids. *Royal Society Philosphical Transactions,* 221(Series A), pp. 163-198.

Halcomb, D. J. & Costin, L. S., 1986. Detecting Damage Surfaces in Brittle Materials Using Accoustic Emissions. *Journal of Applied Mechanics.*

Heffer, K. J. et al., 1992. *The Influence of Natural Fractures, faults and Earth Stresses on Reservoir Performance - Geomechanical ANalysis by Numerical Modelling.* Trondheim, Kluwer Academic, pp. 201-211.

Howard, C. & Fast, C. R., 1957. Optimum Fluid Characteristics For fracture Extension. *API Drilling & Production,* p. 261.

Irwin, G. R., 1957. Analysis of Stresses and Strains near the End of a Crack Traversing a Plate. *Journel of Applied Mechanics,* pp. 361-364.

Irwin, G. R., 1960 . *Proceedings of the 7th Sagamore Ordance Materials Research Conference.* Syracuse, Syracuse University Research Institute, pp. IV-63.

Isida, M., 1966. Stress Intensity Factors for the Tension of an Eccentrically Cracked Strip. *Transactions of the ASME Applied Mechanics Section Volume 88,* p. 94.

Kaiser, J., 1950. *Untersunchung uber das Auftreten von Gerauschen beim Zugversuch,* Munich: University of Munich.

Kishinouye, F., 1937. *Frequency-Distribution of theIto Earthquake Swarm of 1930,* Tokyo: Bulletin of the earthquake Research Institute, Tokyo Imperial University.

Koutsabeloulis, N. C. & Hope, S. A., 1998. *"Coupled" Stress/Fluid/Thermal Multi Phase Reservoir Simulation Studies Incorporating Rock Mechanics.* Trondheim, Society of Petroleum Engineers.

Kristianovic, S., 1955. *Formation of Vertical Fractures by Means of highly Viscous Liquid.* s.l., s.n., pp. 579-586.

Lagazette, A., 2001. *Natural Fracture Tyoes.* [Online]
Available at: http://www.naturalfractures.com/1.1.1.htm
[Accessed 13 June 2014].

Lamont, N. & Jensen, F. W., 1963. *The Effects of Exisitng Fractures in Rocks on the Extension of Hydraulic Fracturing.* Los Angeles, Society of Petroleum Engineers , pp. 203-209.

Li, Y. et al., 2012. *Optimizing Hydraulic Fracturing Design for Shale Gas Reduction through Numerical Simulations.*. Texas, SPE International.

Lorenz, J. C., 1999. Stress Sensitive Reservoirs. *Journal of Petroleum Technology,* 51(01).

Merle, H. A. & Kentie, C. J. P., 1976. A Composite Analysis of the behavior of a Compaction Drive/Solution Gas Drive Reservoir. *Journal of Petroleum Technology,* pp. 1107-1115.

Montgomery, C. & Smith, M., 2010. Hydraulic Fracturing: History of an Enduring Technology. *Journal of Petroleum Engineers,* 62(12).

Murakami, Y., Yamashita, H., Kita, T. & Yoshikawa, H., 1991. *Relation between Deformation Behavior and Acoustic Emission of Concrete subjected Freezing and Thawing.* s.l., 4th Domestic Conference on Subsurface and Civil Engineering AE, pp. 47-51.

Nolen-Hoeksema, 2013. Elements of Hydraulic Fracturing. *Oilfield Review,* Summer(25 No. 2), pp. 51-52.

Nordgren, R., 1972. Propagation of a Vertical Hydraulic failure. *SPE Journal Volume 12(4),* pp. 306-314.

Ohtsu, M., 1995. The History and Development of Accoustic Emission in Concrete Engineering. *Concrete Library of Japanese Society of Concrete Engineering,* 25 June, pp. 121-134.

Olson, J. E., Laubach, S. E. & Lander, R. H., 2007. Combining diagenesis and mechanics to quantify fracture aperture distributions and fracture pattern permeability. *Fractured Reservoirs,* pp. 101-115.

Parker & Son limited, 2016. *Universal beams 100 x 55 x 8.1KG S275JR IPE100.* [Online]
Available at:
http://www.parkersteel.co.uk/Product/0851124/European+Section/100+X+55+X+8.1KG+S275JR+IP

E100
[Accessed 1st July 2016].

Pollock, A. A. & Cook, W. J., 1976. *Acoustic Emission Testing of Aerial Devices.* New Orleans, s.n.

Potential Gas Committee, 2009. *Potential Supply of Natural gas in the United States.* [Online]
Available at: energyseminar.stanford.edu/sites/all/files/eventpdf/PGC%20slides.pdf
[Accessed 10 June 2014].

Potential Gas Committee, 2009. *Potential Supply of Natural Gas in the United States - Report of the Potential Gas Comittee,* Colorado: Potential Gas Comittee.

Rattia & Ali, M., 1981. *Effect of Formation Compacttion on Steam Injection Response.* San Antonio, Texas, SPE.

Rice, J. R., 1968. *Mathematical Analysis in the mechanics of Fracture,* New York: Academic Press.

Rooke & Cartwright, 1976. *Compendiu of Stress Intensity Factors,* London: HMSO Ministry of Defence, Procurement Executive.

Schlumberger, 2013. *Well Models.* [Online]
Available at: http://allaboutreservoir.blogspot.co.uk/2013/05/well-models.html
[Accessed 16 June 2014].

Schofield, B. H., 1963. *Acoustic emission under applied stress,* Alexandria, Virginia: Lessells & Associates Inc. Engineering & USAF.

Sesetty, V. & Ghassemi, A., 2012. *Modelling and Analysis of simulation for fracture Network generation.* Stanford, California, Stanford University.

Settari, 2000. *Coupled Fracture and reservoir Modelling.* Seattle, s.n.

Settari, A. & Price, H., 1984. Simulation of Hydraulic Fracturing in Low-Permeability Reservoirs. *Society of Petroleum Engineers Journal,* pp. 141-152.

Settari & Mourits., 1998. A Coupled Reservoir and Geomechanical Simulation. *SPE Journal,* pp. 219-226.

SPE, 2013. *Geomechanics in Reservoir Simulation.* [Online]
Available at: http://petrowiki.org/Geomechanics_in_reservoir_simulation#cite_note-r1-0
[Accessed 17 June 2014].

SPE, 2014. *Fracture propogation Models.* [Online]
Available at: http://petrowiki.org/Fracture_propagation_models
[Accessed 16 June 2014].

Stanchits, S. et al., 2011. *Hydraulic Fracture Propagation through Preexisitng Discontinuity Monitored by acoustic Emission and Ultrasonic Transmission.* s.l., AGU.

Stephansson, O., 1996. Coupled Thermo-Hydro-Mechanical Process of Fractured Media. In: *Developments in Geotechnical Engineering.* New York: Elsevier, p. 575.

Suare-Rivera, R. B. J. E. E. S. S., 2013. *Geomechanic considerations for hydraulic Fraacture.* San Francisco, s.n.

T. K. Perkins, &. K., 1961. Widths of Hydraulic Fractures. *The Journel of Petroleum Technolgy,* pp. 937-949.

Tang, C. & Hudson, J. A., 2010. *Rock Failure Mechanisms: Illustrated and Explained.* 1st ed. s.l.:CRC Books.

Tucker, M. E., 1991. Coal, Oil Shale and Petroleum. In: *Sedimentary Petrology Second Edition* . Cambridge: Univeristy Press, p. 207.

WalderHaug, 1994. Precipitation rates for quartz cement in Sandstones determined by fluid inclusion microthermometry and temperature history modelling. *journal of Sedimentary Research,* pp. 324-333.

Wang, H. F. et al., 1989. Thermal stress cracking in granite. *Journal o f Geophysical Research Atmospheres,* 10 February.

APPENDIX A

ORIGINAL CALCULATIONS FOR THE RIG

Appendix A

The original calculation

Radial stress at the inner radius

$$\frac{220^2 - 0.6 - 675^2 \cdot 0}{675^2 - 220^2} - \frac{(0.6 - 0) \cdot 220^2 - 675^2}{(675^2 - 220^2)\text{x } 220^2}$$

=0.6Nmm^{-2} or 6bars

At the outer radius

$$\frac{220^2 - 0.6 - 675^2 \cdot 0}{675^2 - 220^2} - \frac{(0.6 - 0) \cdot 220^2 - 675^2}{(675^2 - 220^2)\text{x } 220^2}$$

=0 Nmm^{-2} or 0bars

The 0 bars at the outer radius means there is no stress for the stress frame to dissipate out and the stress frame will be able to take any stress from any failure of the concrete.

Hoop Stress at the inner and outer radius is as follows;

Inner radius;

$$\frac{220^2 - 0.6 - 675^2 \cdot 0}{675^2 - 220^2} + \frac{(0.6 - 0) \cdot 220^2 - 675^2}{(675^2 - 220^2)\text{x } 220^2}$$

=0.743 N/mm-2 or 7.43 bars

Outer radius;

$$\frac{220^2 - 0.6 - 675^2 \cdot 0}{675^2 - 220^2} + \frac{(0.6 - 0) \cdot 220^2 - 675^2}{(675^2 - 220^2)\text{x } 675^2}$$

=0.143 N/mm^{-2} or 1.43 bars

Using a high strength concrete to cope with the high forces exerted by the flat jacks should ensure that the concrete will hold, however as there may be cracking due to natural compression of the concrete, a flexible membrane is to be placed around the internal surface of the void to offset any effect of this cracking and to allow the pressure in the reservoir to build up. Again the 0.143n/mm^{-2} is less than the stated yield stress of the metal.

Pressure on the top plate:

The top plate has a 150mm x 150mm flat jack exerting a pressure of 120 bar maximum. Using that gives a force of;

$$F = P \cdot A = 120 \cdot (150x150) = 270{,}000 \text{ N or } 270kN$$

The void is 440mm by 220mm and is subject to a liquid reservoir pressure of 40 bar

$$\text{Area subject to fluid pressure} = (440x290) - (150x150) = 105100mm^2$$

Fluid force works out to be:

$$4x\ 105100 = 4204kN$$

Leading to a total force of:

$$4204 + 270 = 4204.27kN$$

This shows that according to the calculations another metal plate of approximately 50mm thick of S35 grade would need to be placed on top of the concrete structure, underneath the lid of the stress frame

APPENDIX B

DRAWINGS

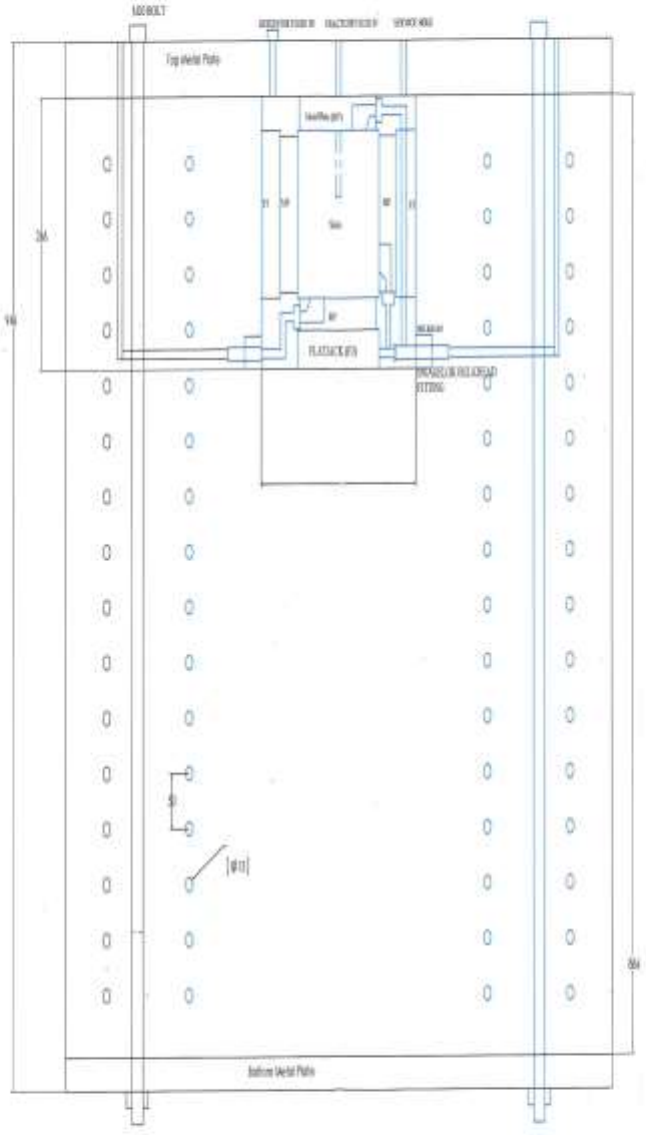

DRAWING 4.4: SIDE CROSS SECTIONAL VIEW OF REACTIONING ARK (CHICKEN)

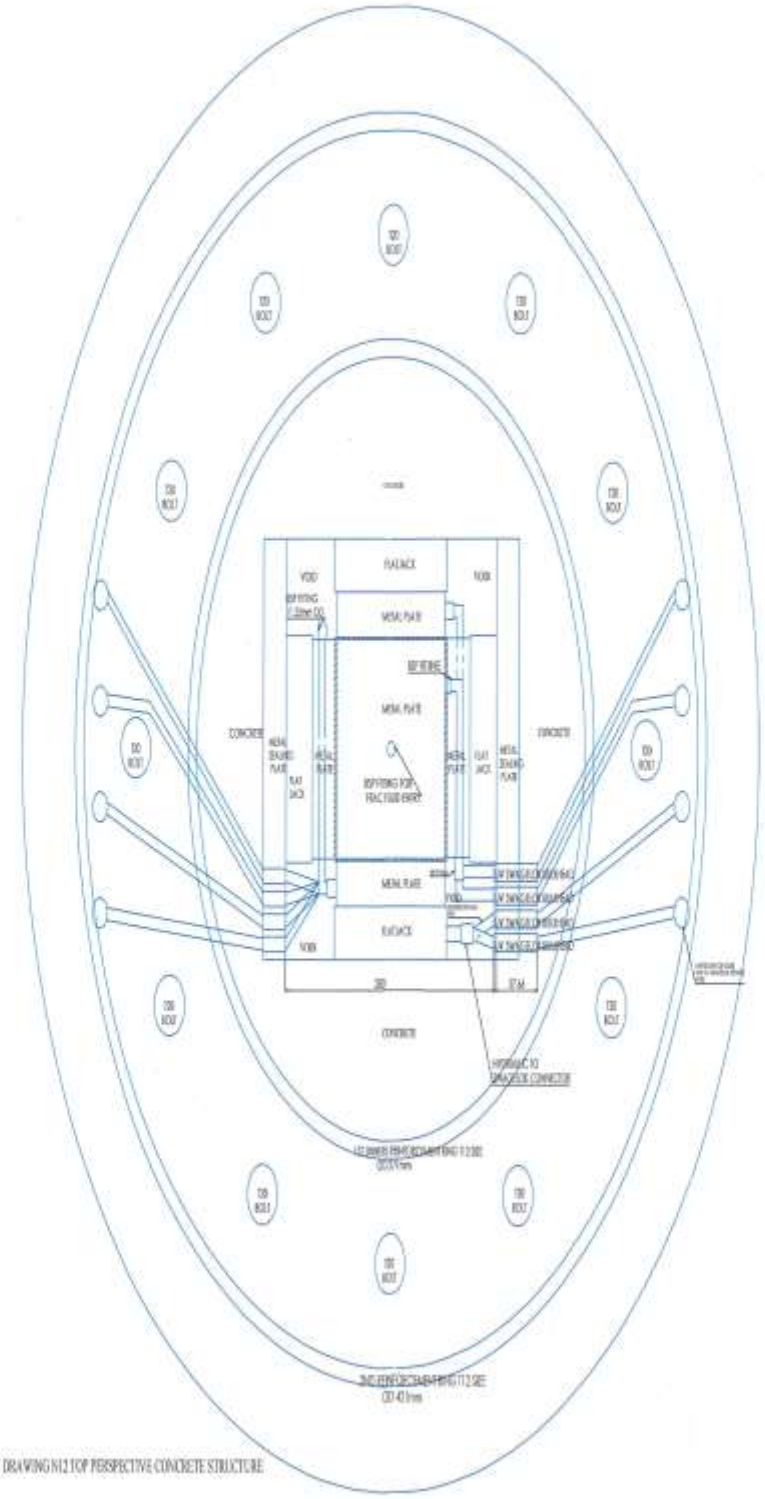

DRAWING NO.2 TOP PERSPECTIVE CONCRETE STRUCTURE

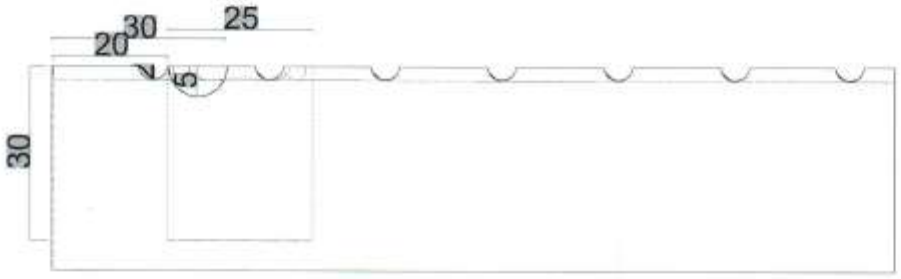

	Fracturing Shale Rig Project
Drawing No. & Title	8 B metal plate front view
Drawn By:	Stuart Penketh
	Concrete

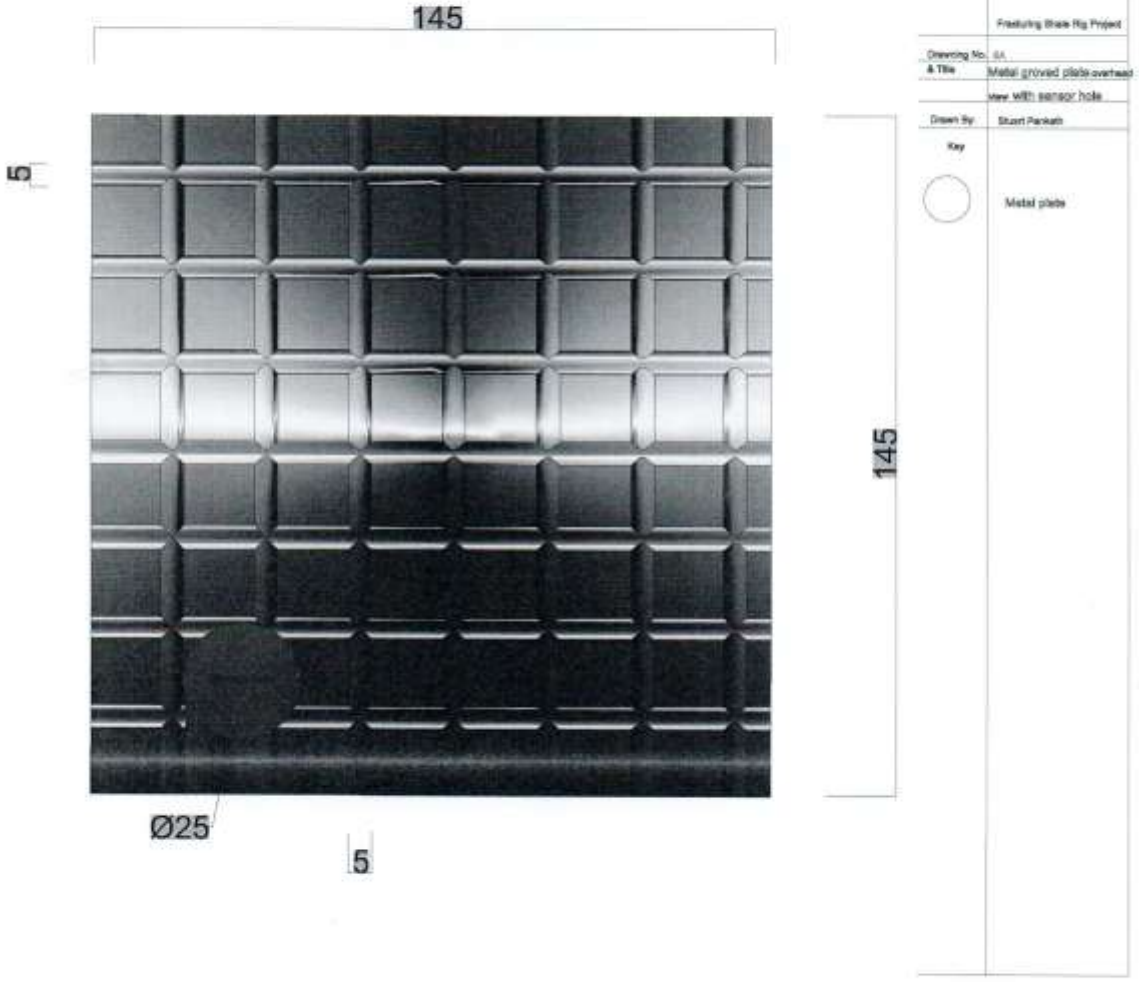
145
5
145
Ø25
5
Featuring Blade Rig Project
Drawing No. &
& Title
Metal grooved plate overhead
view with sensor hole
Drawn By
Stuart Pankeh
Key
Metal plate

Plan View

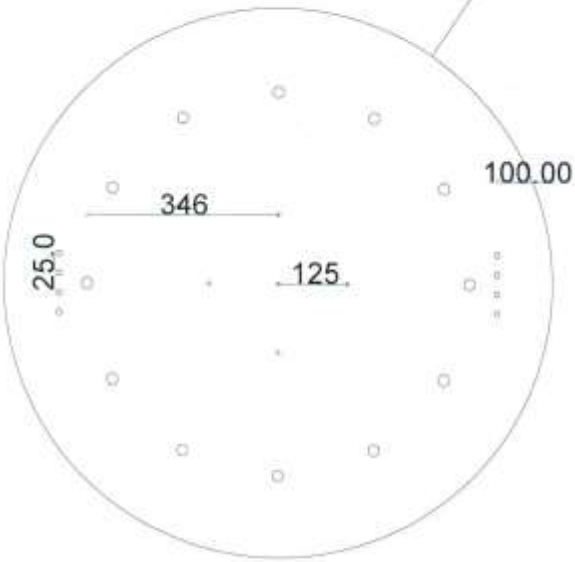

Drawing Number 16

Department Petroleum & Gas Eng.

Drawn By Stuart Penkath

Status Approved

Title Top Plate

3D Perspective

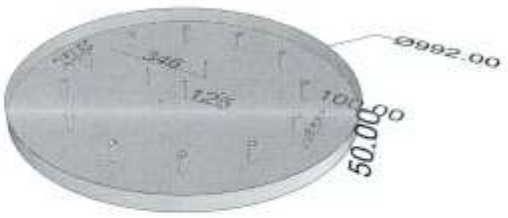

Side View

Plan View

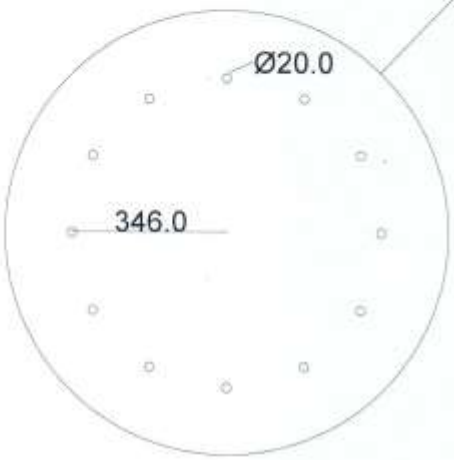

Drawing Number 17

Department Petroleum & Gas Eng.

Drawn By Stuart Penketh

Status Approved

Title **Bottom** Plate

3D Perspective

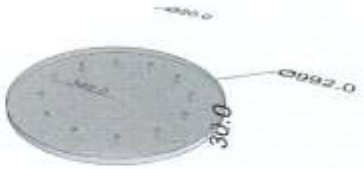

Side View

APPENDIX C

DR WEEKES FINAL STRUCTURAL CALCULATIONS FOR THE RIG

Triaxial Hydraulic Fraccing Project - Pressure Vessel Scoping Calcs and Design

A pressure container is required with an internal space (diameter) of 392mm and accomodation for 500~600mm outside radius. The internal surface of the pressure vessel will be subject to up to 40 bar pressure (4N/mm^2).

An RC circular 'disc' option is explored here. Firstly the radial and taangential stresses are examined using Lame's Thick walled cylinder calculations:

Factor of Safety $FOS := 1.5$

Internal Pressure $P_i := 40 \cdot bar \cdot FOS$ $P_i = 6 \cdot N \cdot mm^{-2}$

External Pressure $P_o := 0 \cdot bar$ $P_o = 0 \cdot N \cdot mm^{-2}$

Internal Radius $r_i := 196 \cdot mm$ External radius $r_o := 496 \cdot mm$

Calculate radial and tangential stresses using Lame's equations

$$\sigma_r(r) := \frac{r_i^2 \cdot P_i - r_o^2 \cdot P_o}{\left(r_o^2 - r_i^2\right)} - \frac{\left(P_i - P_o\right) \cdot r_i^2 \cdot r_o^2}{\left(r_o^2 - r_i^2\right) \cdot r^2} \qquad \sigma_\theta(r) := \left[\frac{r_i^2 \cdot P_i - r_o^2 \cdot P_o}{\left(r_o^2 - r_i^2\right)} + \frac{\left(P_i - P_o\right) \cdot r_i^2 \cdot r_o^2}{\left(r_o^2 - r_i^2\right) \cdot r^2}\right]$$

Concrete cylinder 300mm thick, check stresses at outer and inner radius

$\sigma_r(196 \cdot mm) = -6 \cdot N \cdot mm^{-2}$ $\sigma_\theta(196 \cdot mm) = 8.221 \cdot N \cdot mm^{-2}$

$\sigma_r(496 \cdot mm) = 0 \cdot N \cdot mm^{-2}$ $\sigma_\theta(496 \cdot mm) = 2.221 \cdot N \cdot mm^{-2}$

By inspection, the compressive stresses in the ring are ok, however there are tensile stresses of 8 N/mm^2 which will mean that the concrete could possibly crack. Rebar will be incorporated to help strengthen and share this stress. An FE model has been produced to examine this.

Figure 1 shows the tangential stresses across the radius in a concrete disc without reinforcement:

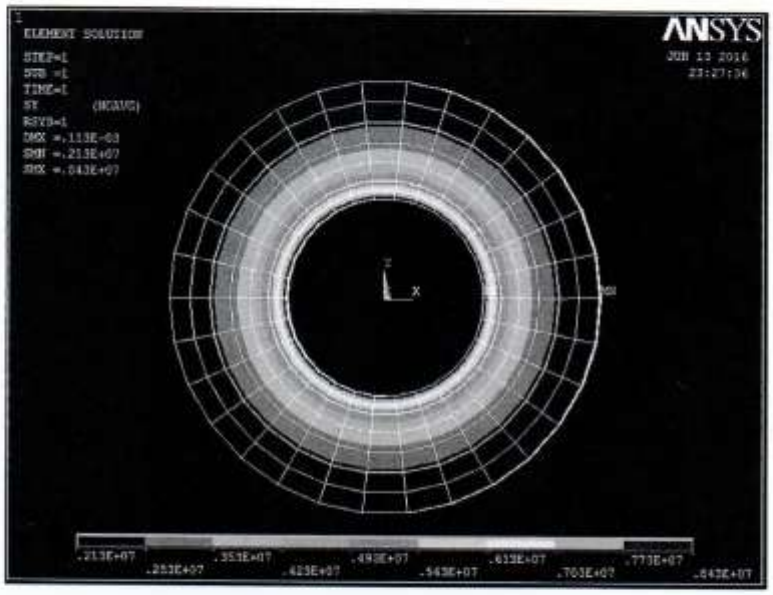

Figure 1 : Tangential stresses Plain Concrete

The next FE model incorporates 4 No circular profile rebars 12mm in diameter. These are placed with 2No. at a radius of 271mm and 2No. at a radius of 421mm, The tangential stresses are shown in Figure 2:

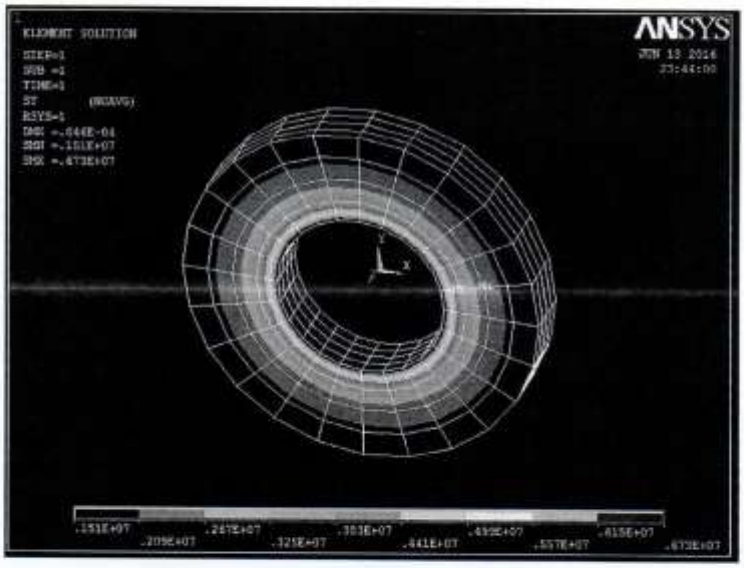

Figure 2: Concrete cylinder with 12mm dia rebar

The stresses have been reduced by about 1/5 however the modulus of rupture is still likely to be exceeded.

It is recommended that the cylinder is lined with a suitable impermeable membrane/layer on the inner radius. Also the rebar is spaced vertically at approximately 75mm, so it is recommended that rebar be placed at a spacing of 50~75mm vertically.

Top and Bottom Plates:

The stress to be applied to the top and bottom of the sample is 120 Bar with a sample size of 150x150mm. This equates to a top plate force of:

$F_{top} := 150 \cdot mm \cdot 150 \cdot mm \cdot 120 \cdot bar \qquad F_{top} = 270 \cdot kN$

In addition there is a pressure of 40 Bar on the remaining area of the plate exposed to the internal fluid pressure. This area is:

$Area := \pi \cdot (196 \cdot mm)^2 - (150 \cdot mm \cdot 150 \cdot mm) \qquad Area = 9.819 \times 10^4\ mm^2$

Hence the additional force is $F_{add} := 40 \cdot bar \cdot Area \qquad F_{add} = 392.75\ kN$

Total Force on plate $F_{top} + F_{add} = 662.75\ kN$

High Strength Friction Grip Bolts (HSFG) M20 have ultimate Load rating of 130kN Tension capacity

Try 6 No Bolts $6 \cdot 130 \cdot kN = 780\ kN \qquad FOS := \frac{780}{662} = 1.178$

Try 8 No Bolts $8 \cdot 130 \cdot kN = 1.04 \times 10^3\ kN \qquad FOS := \frac{1040}{662} = 1.571$ OK

In this situation the bolt forces could be amplified by prying. An FE plate model will be constructued to provide more accurate bolt forces and plate stresses to inform the thickness of the plate.

The FE model is shown in figure 3

From the FE model a Steel plate S355 thickness of 50mm is recommended to deal with the bending and shear stresses developed.

As expected, due to prying action, the bolt forces are elevated from the inital calculations. 12 No M20 bolts will experience 104kN a this load.

Figure 3: FE Model of End Plates with 12 No HSFG bolts

Check compressive stress through the concrete cylinder from the precompression of he HSFG bolts:

Assume working load of 104kN per bolt, applied compressive load:

$$F_{applied} := 104 \cdot kN \cdot 12 \qquad F_{applied} = 1248\,kN$$

Area of concrete cylinder

$$A_{cyl} := \pi \cdot (496 \cdot mm)^2 - \pi \cdot (196 \cdot mm)^2 \qquad A_{cyl} = 0.652\,m^2$$

Stress in Cylinder

$$\sigma_c := \frac{F_{applied}}{A_{cyl}} \qquad \sigma_c = 1.914\,N \cdot mm^{-2}$$

Therefore OK

Summary and Materials

- The diagrams of the vessel in plan and elevation are shown in figures 4 and 5
- Use a High strength Concrete min C50~60. The higher strength the better.
- The cylinder has an internal radius of 196mm and an outer radius of 496mm (This can be altered slightly to suit). The internal structure can be altered slightly to accomodate instrumentation (jacks etc)
- The cylinder will be reinforced with T12 rebar curved to two different radii. One will be 271mm and 421mm in RADIUS. The vertical spacing of the bars will be 50 to 75mm , and as many to suit the desired height of the cylinder.
- The top and bottom plates will be 50mm thick S355 steel 496mm in radius (or the desired outer radius of the concrete cylinder)
- 12 No HSFG M20 bolts will be used in clearance holes through the end plates and concrete cylinder, placed at 30 deg increments at a radius of approximately 346mm.
- Appropriate gasket material to be used between all mating surfaces.

Notes

- The HSFG bolts are 1 time use only. They will need to be renewed each time a new sample is tested.
- The vessel has not been designed in accordance with any pressure vessel codes of practice (usually vessels of this nature are specially designed and tested before commissioning). It is suggested that all precautions are taken to ensure personnel are not at risk in the unlikely event of sudden failure.

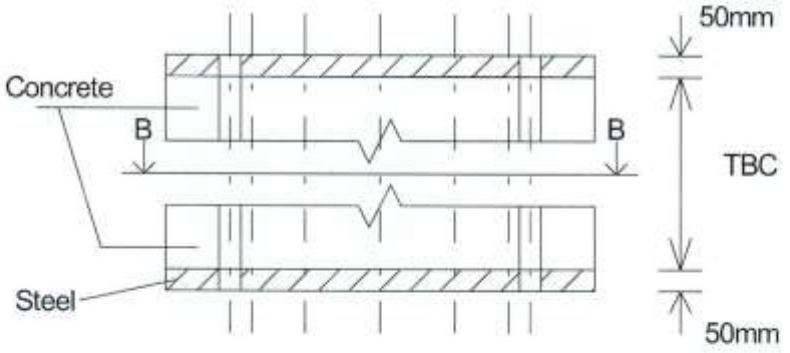

Figure 4: Elevation Section A-A

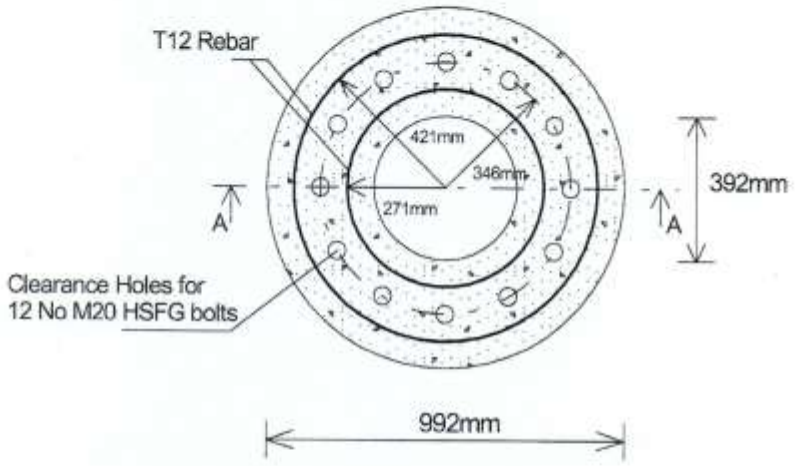

Figure 5: Plan Section B-B

APPENDIX D

FLAT JACK SPECIFICATIONS

Freyssinet Limited
Innovation House
Euston Way
Town Centre
Telford
TF3 4LT

Tel: +44 (0) 1952 201901
Fax: +44 (0) 1952 201753
Email: info@freyssinet.co.uk
Web: www.freyssinet.co.uk

FREYSSINET

QUOTATION COVERSHEET

TO:	Stuart Penketh	COMPANY:	University of Salford
VIA E-MAIL	S.Penketh@edu.salford.ac.uk	DATE:	07 September 2015
FROM:	Jayne Burgess	NO. OF PAGES:	6
CC:		REF:	PBD'8938 A,B,C & D

SUBJECT: SUPPLY OF FLAT JACKS

Dear Stuart

We thank you for your enquiry and have pleasure in submitting our revised quotations (split as requested) for the supply of Flat Jack, subject to the attached terms and conditions. All prices are given nett unless otherwise stated.

Our offer is valid for 30 days from the above date.

Please do not hesitate to contact us should any further information be required.

Regards,
FREYSSINET LIMITED

Jayne Burgess
Product Sales Co-ordinator

Prices quoted are based on quantities and descriptions attached.

FREYSSINET LTD
BRIDGE BEARINGS

FREYSSINET

PBD'8938A 07-Sep-15

Supply of Flat Jacks

ITEM NO.	CUSTOMER REFERENCE	BEARING	NO OFF	PRICE @ EACH	TOTAL PRICE
1	Flat Jack	15	4	£218.00	£872.00
		Total No.Off	**4**	**TOTAL PRICE**	**£872.00**

Notes:

Prices excludes transport and exclude VAT.

Our current delivery is 2/3 working days from your order

Note: To inflate Flat Jacks use Hydraulic Oil

Size	**15**	**42**
Max Load	**15**	**160**
Diameter mm	**150**	**420**
Closed Height mm	**32**	**32**
Max Stroke	**25**	**25**

FREYSSINET LTD	FLAT JACK LOADS (KN) AT HALF OPEN						FILE F'JACK		
Press. Bar	REF 07	REF 12	REF 15	REF 22	REF 25	REF 27	REF 30	REF 35	REF 42
1	0.13	0.53	1.01	2.58	3.47	4.21	5.33	7.41	11.40
5	0.67	2.63	5.03	12.88	17.35	21.05	26.65	37.03	57.00
10	1.33	5.25	10.05	25.75	34.70	42.10	53.30	74.05	114.00
15	2.00	7.88	15.08	38.63	52.05	63.15	79.95	111.08	171.00
20	2.67	10.50	20.10	51.50	69.40	84.20	106.60	148.10	228.00
25	3.33	13.13	25.13	64.38	86.75	105.25	133.25	185.13	285.00
30	4.00	15.75	30.15	77.25	104.10	126.30	159.90	222.15	342.00
35	4.67	18.38	35.18	90.13	121.45	147.35	186.55	259.18	399.00
40	5.33	21.00	40.20	103.00	138.80	168.40	213.20	296.20	456.00
45	6.00	23.63	45.23	115.88	156.15	189.45	239.85	333.23	513.00
50	6.67	26.25	50.25	128.75	173.50	210.50	266.50	370.25	570.00
55	7.33	28.88	55.28	141.63	190.85	231.55	293.15	407.28	627.00
60	8.00	31.50	60.30	154.50	208.20	252.60	319.80	444.30	684.00
65	8.67	34.13	65.32	167.38	225.55	273.65	346.45	481.33	741.00
70	9.33	36.75	70.35	180.25	242.90	294.70	373.10	518.35	798.00
75	10.00	39.38	75.37	193.13	260.25	315.75	399.75	555.38	
80	10.67	42.00	80.40	206.00	277.60	336.80	426.40	592.40	912.00
85	11.33	44.63	85.43	218.88	294.95	357.85	453.05	629.43	969.00
90	12.00	47.25	90.45	231.75	312.30	378.90	479.70	666.45	1,026.00
95	12.67	49.88	95.48	244.63	329.65	399.95	506.35	703.48	1,083.00
100	13.33	52.50	100.50	257.50	347.00	421.00	533.00	740.50	1,140.00
105	14.00	55.13	105.53	270.38	364.35	442.05	559.65	777.53	1,197.00
110	14.67	57.75	110.55	283.25	381.70	463.10	586.30	814.55	1,254.00
115	15.33	60.38	115.58	296.13	399.05	484.15	612.95	851.58	1,311.00
120	16.00	63.00	120.60	309.00	416.40	505.20	639.60	888.60	1,368.00
125	16.67	65.63	125.63	321.88	433.75	526.25	666.25	925.63	1,425.00
130	17.33	68.25	130.65	334.75	451.10	547.30	692.90	962.65	1,482.00
135	18.00	70.88	135.68	347.63	468.45	568.35	719.55	999.68	1,539.00
140	18.67	73.50	140.70	360.50	485.80	589.40	746.20	1,036.70	1,596.00
145	19.33	76.13	145.73	373.38	503.15	610.45	772.85	1,073.73	1,653.00
150	20.00	78.75	150.75	386.25	520.50	631.50	799.50	1,110.75	1,710.00

FLAT JACKS

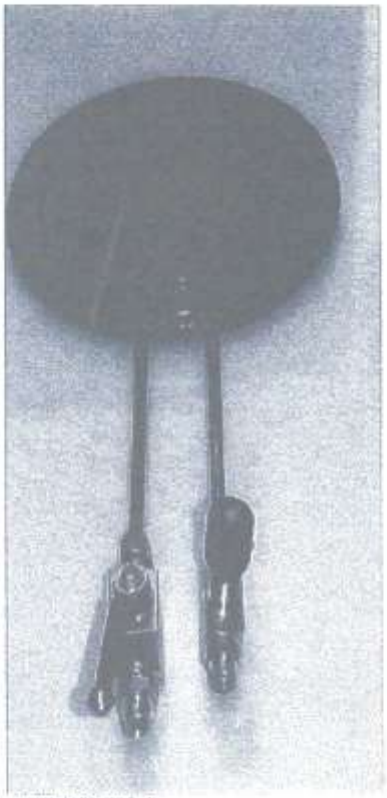

town Ref 50 Transfusion

A flat jack is a mild steel capsule, dished in shape, with an inlet & outlet pipe. They are supplied with two machined thrust plates. An inlet pipe is fitted with either a needle or ball valve depending on the fluid to be used, the outlet pipe is normally fitted with a plug.

Flat jacks are supplied to customer requirements, depending upon the application: Inflation with oil, water, resin, grout or grout transfusion, and can apply a temporary or permanent load.

A calibration chart is supplied which gives the applied load vs pressure.

The jacks can be filled with hydraulic oil and the load locked for a defined period.

They can also be filled with resin or grout for a permanent transfer.

As the units are low cost they can be left in position as part of the structure.

All flat jacks have the same closed height (32mm) and the same maximum stroke (25mm). The required access gap is 35 mm.

Sizes available:
Sz12 Diameter 120mm, 78KN @150bar
up to
Sz92 Diameter 920mm, 9405 KN @150bar

Resin/ Grout inflation cylinders, hoses, T pieces and calibrated gauges are also available.

APPENDIX E

PROPOSED PAPER ON CATEGORISING PRE-EXISTING DAMAGE TO SHALES & MUDSTONES

Characterisation of Westbury and Bowland shales and Pennine Lower Coal Measures Group Mudstones using X-ray Computed Tomography

S Penketh[1], G Nasr[1], M Burby[1], L Augusthus-Nelson[1], L Weekes[1], A Zuluaga Guerra[2]

[1]School of Computing Science and Engineering, University of Salford, United Kingdom

ABSTRACT

Hydraulic fracturing is set to become a major part of the UK's energy policy. Previous studies have looked at the problem of fracture optimisation to enhance recovery rates, however, these simulations are only educated approximations of the fracture that will be produced. They do not consider the potential for existing structures to affect fracture development which leads to inefficient extraction and increased costs during hydrocarbon production.

For any investigation into the evolution of an induced fracture, it's important to map the existing structures in the rocks. In this study, two shales (Westbury & Bowland) and one mudstone (Accrington Mudstone) were scanned using a high definition Computed Tomography (CT) scanner. it was found that the fractures are primarily located on the surface and associated with conchoidal fracturing where samples naturally cleaved from the parent unit.

These fractures can be grouped into four distinct trends, (families) although only family 1 is present throughout all the samples. The fracture pattern for family 1 follows the direction of the lamination, however fracture families 2, 3 & 4 all cut perpendicular to the bedding. Family 2 appears in some samples of all three rock types scanned and family 3 appears in only the shales, whilst family 4 occurs once only in the Accrington shale.

Fractures are grouped around conchoidal fracture patterns with little seen elsewhere. The heavier the conchoidal fracturing the larger the fracture parameters. All fractures were penetrating from the outside of the sample inwards, Penetration rate was typically around 2.5 to 5mm, some extended to 10mm, and one extended by 30mm. This indicated that although the samples are weak, the fractures found within the samples were associated with the worked, natural or non-natural cleaving from the parent unit.

Pores were heavily associated with the fractures and near to the surface and lacked interconnectivity. However, somewhat larger pores grouped around fossilised remains. Except surrounding the odd fossil no other patterns were discerned.

1. INTRODUCTION

With the discovery of shale oil and gas in the United Kingdom (UK), unconventional hydrocarbon production has the potential to become an important aspect of the UK's energy mix. In the Northwest of England (Andrews, 2013) the Bowland shale group forms the dominant shale play, primarily comprising of dark grey/black, finely laminated, fine-grained sediment, with a high total organic content (TOC) but low clay content. The Bowland shale has a permeability of <0.01mD, thus with a lack of interconnected porosity the high organic content is trapped within the rock making conventional methods of removal difficult. To access the oil and gas reserves the rock has to be fractured hydraulically, whereupon a small fracture is initiated, usually by an explosive charge, before a fluid is then pumped in at high pressure forcing the growth of the

fracture. This breaking of the sediment releases the trapped fluids allowing the hydrocarbons to travel through the reservoir to the borehole.

In the past it has been noted that there is a discrepancy between predicted simulation fractures and optimum fluid recovery. Saputelli et al. (2014) showed that various factors can affect the optimum recovery but it is the formation permeability and the stimulated reservoir volume that are the most important parameters for determining the optimum fracture length. Other investigators have looked for a more systematic approach to solve the problem of optimising multiple traverse fractures in a horizontal well employing the unified fracture theory and using a change in multiple dimensionless parameters to get an optimised fracture length (Guk, 2014). However, these studies have not looked at the existing faults/structures or fracture patterns that may exist in these shales to gain a more accurate understanding of how the fractures will interact. Therefore, existing fracture simulation software will only provide an approximation of the fracture that will be created. To improve on simulation modelling, it is important to map the evolution of the fractures and how they interact with pre-existing fractures or pores. One experimental technique that can be used to map a fracture is an acoustic emission sensor system similar to that used by Stanchits (2014) and Stanchits et al. (2012). These studies show the importance of rock properties to potentially affect the evolution of a fracture once induced in a shale, as (Li, et al., 2012) showed that a induced fracture will not cross an existing fracture until the pressure in the induced fracture is equal or lower than the pressure in the existing fracture.

Prior to undertaking computer simulation it is essential to establish the characteristics of shale with regard to categorising existing fractures and pores in the types of shales that are to be studied, as it has been shown previously how important existing fractures, faults and pore distribution are to arresting the development of the induced fractures (Lamont, 1963) & latter shown in (Sesetty & A. Ghassemi, 2012). It is thus, essential to know the existing fractures, fracture patterns and pore distribution in order to create an accurate assessment of the fracture parameters, whilst it has also been noted that the mineral content of a sediment can affect the structure and growth of a fracture (Ding, et al., 2011). The most widely accepted rock mechanic factor used to describe the propagation of a fracture is the Mohr-Coulomb single stress failure theory along with Griffith's (1921) generalised maximum tension stress strength theory shown in Price and Rhodes (1966).

High definition computer tomography scanning (CT) is already used on a micro scale in material science to evaluate internal structures and defects of solid materials (Withers, 2007) & (Singhal. A, 2013). Bearing in mind the importance of pre-existing faults, pores or structures within a sediment it is, therefore, essential to map and categorise these structures prior to fracture induction. To this end this study describes the mapping and characterisation of existing fractures within 15 samples using a CT scanner, to show what internal structures a typical shale formation may contain. Once these existing fractures and structures are mapped it is intended to examine their impact on induced fracture evolution under tri-axial stress loading. The results of the fracture induction experiment will be reported in a later paper.

The samples to be scanned are two dark organic rich shales (Bowland Shale Group and Westbury Shale Group) and a clay rich mudstone (Accrington Mudstone Group).

Using a high definition CT scanner, we have determined the natural fracture geometry and the porosity distribution of 15 different shale and mudstone samples from the three localities mentioned above. In this study, existing fractures are mapped and those that show a trend are then classified as families. A sample can have more than one fracture family and a family represents a fracture type that follows a certain characteristic, i.e. the angle in relation to the bedding planes, the depth that the fracture penetrates the sediment and how the different groups of fractures interact with each other. The porosity was calculated automatically by the CT software using the P201 porosity rules, which are dependent on the correct surface extraction being calculated. It is important to have a detailed understanding of porosity as, once calculated, this will show how the pores are distributed within the sample and can give a potential indication of areas of weakness as well as

the pore interconnectivity. Accurately categorising these structures will lead to more accurate models being able to predict a more precise and efficient fracture design.

2. SAMPLING & METHODOLOGY

2.1 Sample types

Two shales and one mudstone were sourced from quarries. The Westbury Shale (WS) samples were quarried from Newark where the shale overlays gypsum and anhydrite deposits. The Bowland Shale (BS) was quarried nearby to the town of Castleton in Derbyshire and the Accrington Mudstone (AM) was from the Accrington Pennine Lower Coal Measure Group which is interbedded with sandstones of the same formation and overlays the Bowland Shale. All samples were returned to the department upon being quarried and placed immediately in a bath of water to stop the shale drying and flaking.

2.2 Methodology

A total of 15 samples were chosen, five from each formation. All the Accrington Mudstone samples were cut mechanically as they were too well consolidated to naturally break into smaller samples due to a high clay content. This involved using a diamond tipped, water fed concrete cutter of variable speed set to the lowest speed to avoid introducing artificially induced fractures.

The Bowland & Westbury Shale samples were created by naturally cleaving them from the parent rock, all except for two samples (WS03 and BS09) which had some mechanical work done to break them into a size that would fit within the CT scanner. This mechanical work was carried out by use of a fine toothed junior hacksaw lubricated with water.

The sample sizes were varied to see if there was a difference in fracture propagation between the samples. The dimensions of each sample are listed in table 1.

Sample	Length (mm)		
	X Plane	Y Plane	Z Plane
WS001	120	145	25
WS002	160	90	65
WS003	45	143	61
WS004	155	104	87
WS005	75	123	20
BS006	60	137	70
BS007	108	129	32
BS008	67	16	32
BS009	86	32	27
BS010	89	139	5
AS011	75	105	22
AS012	85	155	18
AS013	120	147	20
AS014	85	125	60
AS015	45	90	35

Table 13: Sample dimension in each plane, in mm. Where BS = Bowland Shale, WS = Westbury Shale & AS = Accrington Mudstone

2.3 Equipment

This investigation relied on the use of a v|tome|x s CT scanner, from the GE Sensing & Inspection Technologies GmbH department (Singhal. A, 2013). . For this study the microfocus tube was used. This is a high-power tube which focusses at the micro scale and has a reflection target that can reach 300 kVp at 500W.

Once an image has been captured, the software; V.G StudioMAX 2.2 (Volume Graphics , 2012) is used to reconstruct the sample. Through careful examination of each plane of the scan each fracture was marked. The software also allows the P201 porosity file, (Verein Deutscher Giessereifachleute, 2002) to be used on an individual plane. For this investigation at least 100 random P201 scans in both the vertical and one horizontal planar views were carried out. Repeated application of this process through the individual planes enables the fracture planes in a sample to be mapped, whilst the porosity of individual planes can be analysed and calculated.

The settings of the CAT scanner used on each sample is presented in Table 2 below.

Sample	Voltage (V)	Current (Amps)	Power (W)
WS001	160	95	15.2
WS002	160	80	12.8
WS003	160	135	23.0
WS004	160	70	11.2
WS005	160	70	11.2
BS006	160	70	11.2
BS007	160	120	19.2
BS008	160	120	19.2
BS009	160	120	19.2
BS010	160	120	19.2
AS011	160	95	15.2
AS012	170	80	13.6
AS013	170	80	13.6
AS014	170	80	13.6
AS015	170	110	18.7

Table 14: CT scan parameters used for each sample; BS = Bowland shale WS = Westbury Shale & AS = Accrington Mudstone

3. RESULTS

The results of the pre-existing fracture patterns and pore distribution are discussed in this section.

3.1 Fracture Pattern and Distribution

The fractures were mapped using 3D reconstruction software, which produces a 3D image ~~distribution~~ of the fractures, as shown in figures 2 & 3. Four main fracture trends were found which were grouped together as families. Each family is described below and their angle of alignment is shown plotted in Figure 1. All of the fractures that were found emanated from the surface of the sample and penetrated only a short depth into the subsurface. For the Westbury Shale the fractures penetrated between 2 and 4mm into the sample, for the Bowland Shale, this increased up to 10mm from the surface, however, the fracture depths in the Accrington Mudstone varied between 1mm to 30mm. Whilst this suggests that these fractures were caused when the samples cleaved from their parent unit, it can also be seen that the three lithologies have responded slightly differently to the stress.

1. Family 1 consists of fractures that generally follow the direction of bedding or the laminations of the shale. The fractures are of a moderate length around 35-55mm on average (2 more at 60mm, one at 70mm and one at 90mm), an average width of 0.3mm and a penetration depth averaging around 2 - 3mm.
2. Family 2 is typified by cracks perpendicular to the lamination. The average fracture length is shorter than family one (at ~24mm) with an average penetration depth of 1.5mm and width of 0.1mm.
3. Family 3 fractures are not as common as the preceding two but again, like family 2, cuts across the lamination often converging with family 2 at an angle of between 70-110^{o} to the bedding. These fractures seem to follow existing conchoidal fracturing with an average depth of 2mm and width of 0.3mm.

4. Family 4 only occurs in one sample (WS005), where the fracture cuts across the lamination at around 45° with a penetration depth of 0.5mm and a width of 0.3mm.

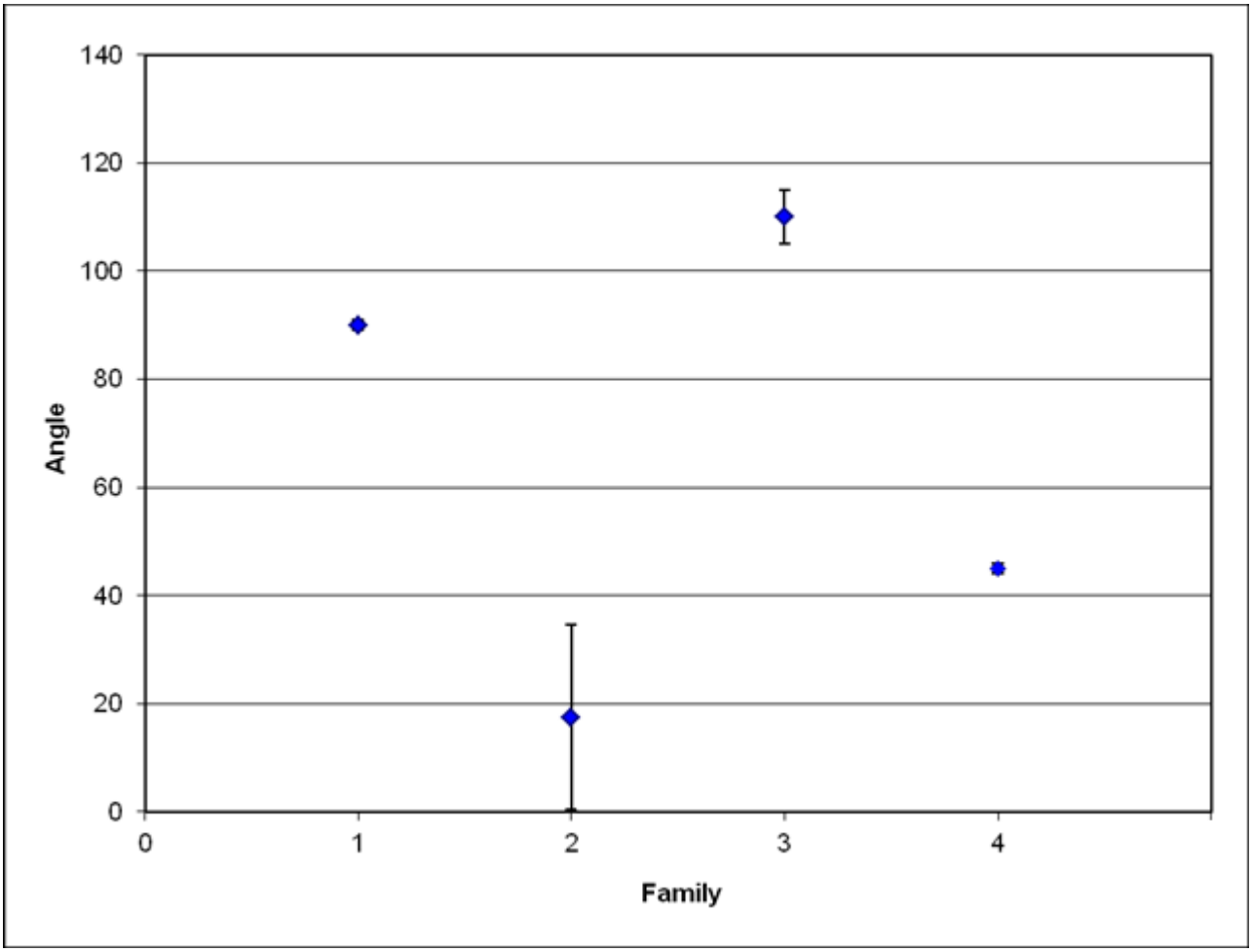

Figure 247: shows the fracture family types in relation to the angle in the shale samples Family 1 is generally parallel to the bedding/lamination. Family 2 fractures cut across the lamination lines at an angle of ~20°. Family 3 cut across the lamination at an angle of around 70 to 110° and are occasionally infilled. Family 4 lies at an angle 45° to the bedding plane.

Westbury Shale

The Westbury Shale is black with dark grey mottling and organic rich. The samples are all thinly laminated and easily cleave along this direction.

WS001, Figure 2: This sample shows marked fracturing in three directions (families). The first family with the longest fracture 30mm follows the shale lamination or crosscuts the lamination by 2-3°, and penetrates from the surface by 2-3mm. The second family is a curved fracture perpendicular to the lamination at around 25mm in length and also penetrates to 2mm depth from the surface. Finally, the third family penetrates by approximately 15-20mm from the surface and cuts perpendicular to the lamination but forming straight lines at 45 to 55° with family two.

WS002: Two fractures families have been identified, family 1 cross cutting the lamination at about 15° and family 2 cutting the lamination at 105-110°.

WS003: Again families 1 and 2 were identified with most of family 2 located on one side of the sample.

WS004: Family 1 cutting through the lamination at low angles between 2° to 7° and family 2, at an orientation of 100° to the lamination. However, there are also a number of other existing fractures in this sample with no

correlation which were mapped and have been included for completeness as they may be from previous damage or small unconformities and could still affect the propagation of an induced fracture.

WS005 is the only sample to contain all four fracture families, figure 6: Family 1 is orientated along the lamination, family 2 and 3 cut perpendicular to the first family and family 4 cuts through the lamination orientation at approximately 45°.

Bowland Shale

The Bowland Shale is very dark grey and mottled black in appearance with coal lenses indicating a very high organic content and traces of fossils are common. The shale is also very thinly laminated and very fissile on the surfaces. The sample is weakest along its lamination planes.

BS006: Contains families 1, 2 and 3. Family 2 and 3 converge with an angle of around 80°-90°. There are an additional number of small fractures that have been infilled, but these did not seem to correlate with any of the 4 families. Again, these have been mapped for completeness though not categorised

BS007: Family 1, 2 and 3 fractures are present. Family 2 are located almost exclusively around the borders of the sample. The third family is perpendicular to lamination and converges on family 2; the angle of convergence is between 100° and 110°. These fractures are infilled.

BS008: Family 1 and 2 identified. Family 2 cuts through the lamination planes at an angle of 75°. The fractures are not spread evenly but are densely packed and concentrated in the lower half of the sample.

BS009: Family 1 identified only. The fractures are very densely packed but evenly distributed throughout the sample. Most of these fractures are infilled.

BS0010: Again, only family 1 identified between 40-60mm in length with a penetration depth of ~4mm. There are in-filled lenses in this specimen with an average thickness of 0.5-1.0mm. In addition, two "V" shaped lenses cut the lamination at 7° and 10° with a thickness of 2mm. The fracture distribution and density is not homogeneous with the greatest concentration occurring on one side.

Accrington Mudstones

Accrington mudstone is typified as a homogeneous greenish-silty mudstone and thinly laminated. These samples are very well-cemented and compacted. There is a darker organic rich zone present as well as infilled lenses. Laminations within these samples are hummocky (not straight planes), as the fracture orientation is described with respect to the lamination plane, the reference for these samples was undertaken by orientation to the depositional flow orientation.

As this mudstone is well cemented and very strong the samples had to be machine worked, unlike the two shales which cleaved easily into smaller sub samples.

AS0011: Two fractures were found ~~so~~ with no real discernible trend ~~could be found~~. The first fracture is parallel to the direction of lamination, and, although the sample has a hummocky cross-lamination, the fracture is straight. The second fracture cuts the lamination at 15°.

AS0012: Again only two fractures were located, both of which are cutting the lamination plane at 90°, though the lamination in this sample is only weakly defined.

AS0013: Family 1 and 2 can be readily identified. Family 1 again follows the lamination pattern and family 2 is a single fracture orientated perpendicular to the first family but cutting across the thickness of the whole sample.

AS0014: Family 1 only.

AS0015: This sample is sparsely fractured but does show two readily identifiable fracture families. Two parallel fractures cut perpendicularly to the bedding. This family is complemented by a number of small fractures that fracture in the same direction. The deep penetration of the fracture can be discounted as this depth of penetration is not seen on the other mudstone samples.

The fracture families and their individual parameters from all the samples are presented in graphical form in figures 2 to 5. Figure 2 shows fracture length, figure 3 shows the fracture width and figure 4 shows the fracture penetration depth.

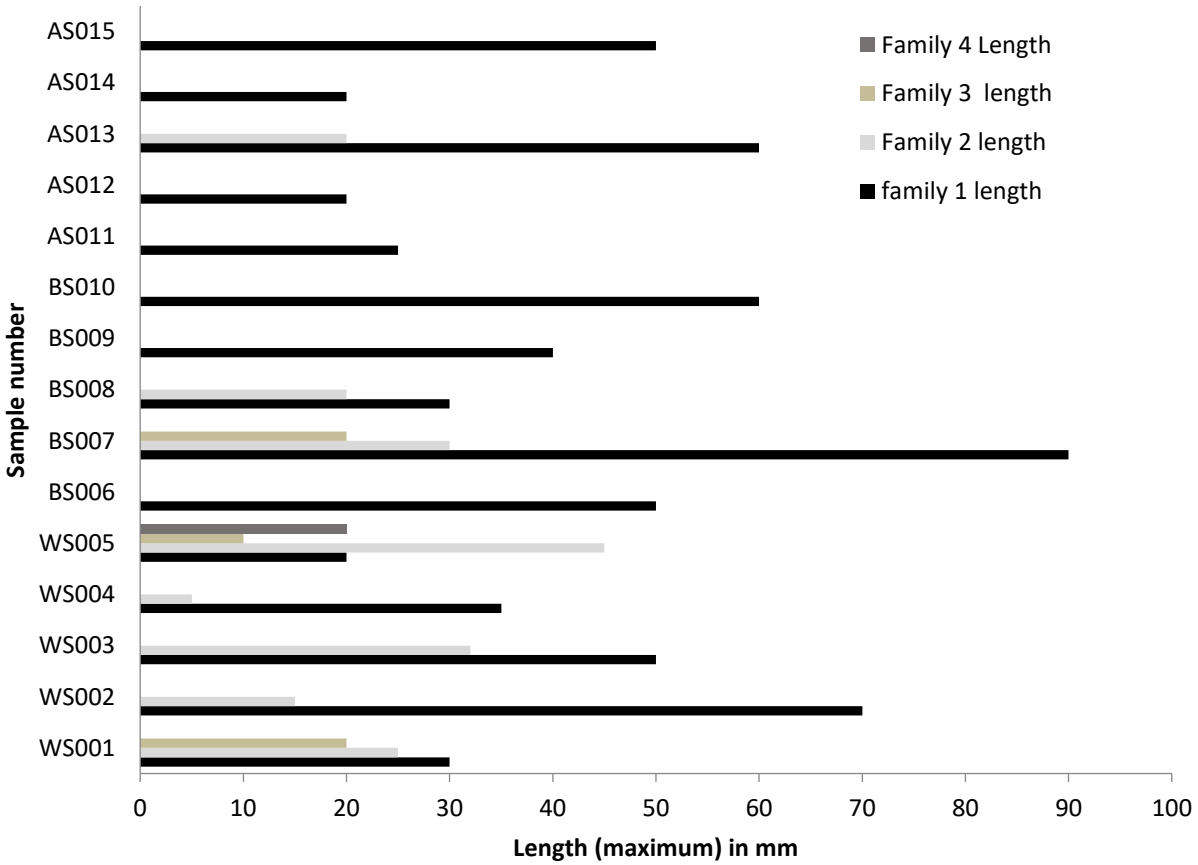

Figure 248: Graph showing maximum sizes (in mm) of each fracture family's length.

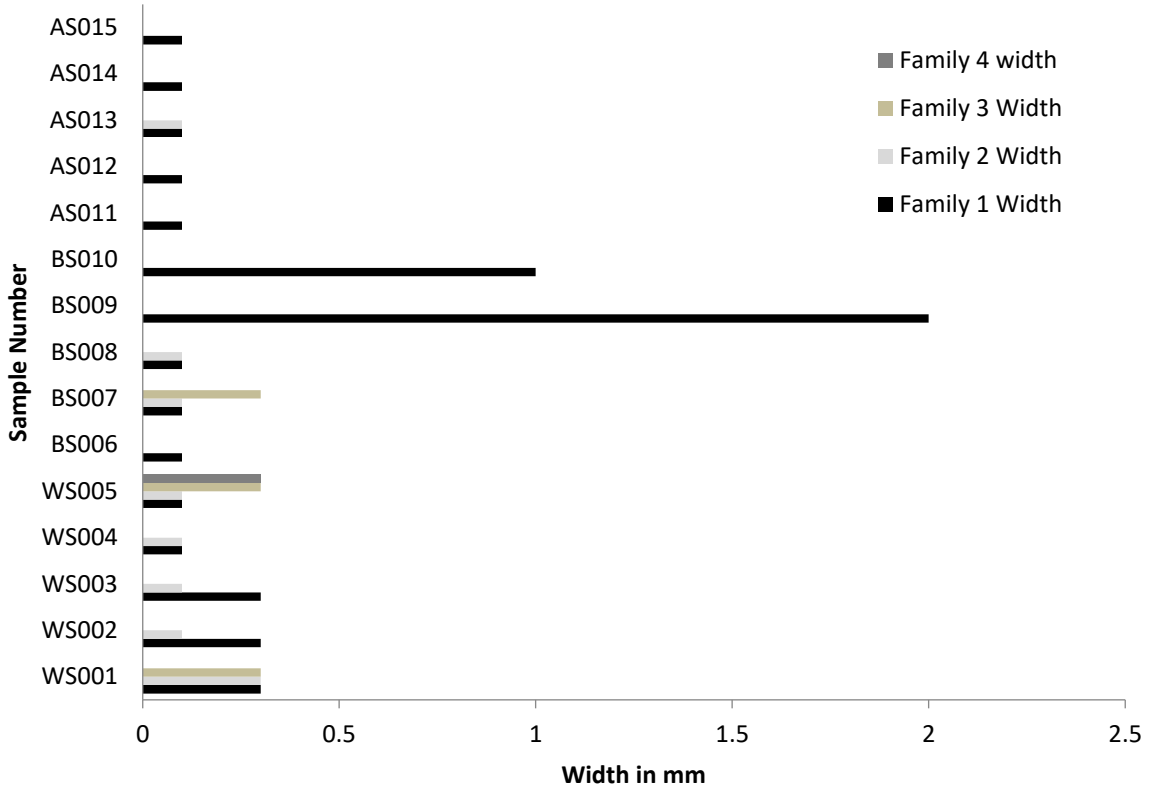

Figure 249:. Graph showing maximum sizes (in mm) of each fracture family's width.

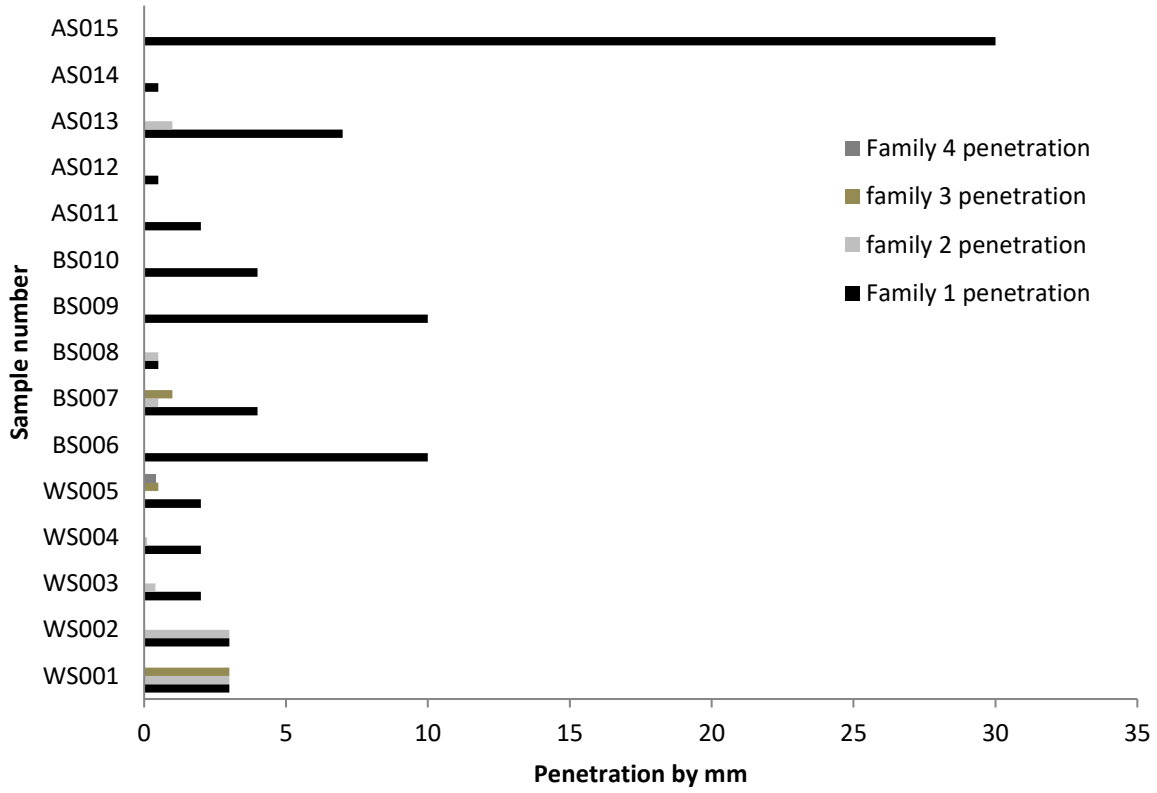

Figure 250: Graph showing the penetration (in mm) of the fracture into the shale

It is clear from Figures 2 to 4 that the Westbury Shale has the greatest propensity to fracture as all samples contain family one and family two fractures, two of the samples also contain family three and one sample contains all four fracture families. For the Bowland Shale all samples again contain family one fractures but only two samples contain families one and two, one sample contains families one, two and three and no samples contain family four. The formation type with the least propensity to fracturing is the Accrington Mudstone where all samples have family one fractures but only one sample also contains family two. None of the samples contain family three or four fractures. This confirms the observation that the Westbury Shale was more likely to cleave or crumble when being handled than either the Bowland Shale or the Accrington Mudstone.

Fracture length: Family one fractures are the longest across all formation types WS = 40mm, BS = 54mm and AM = 35mm. Family two is slightly shorter around 20 – 25mm for all three formations, family three is 15-20mm and family four is the shortest at 10mm, although this is only based on one example.

Fracture width: Family one; In the AM fracture width is a uniform 0.1mm across all samples, in the WS the average fracture width is 0.3mm, however, in the BS three out of the five samples have a fracture width of 0.1mm but the other two samples contain family one fractures at 1mm and 2mm wide. Family two fracture widths appear to be a uniform 0.1mm across all formations except for one WS sample which is 0.3mm wide. Family three and family four are 0.3mm wide across both the WS and BS.

Fracture depth: From visual inspection it is evident that all the fractures emanate from the surface of the samples and penetrate to generally shallow depths. Family one fractures penetrate the deepest in terms of fracture families and, in particular, within the AM where the fractures penetrate up to 30mm. In the BS the fractures penetrate up to 10mm however in the WS the fractures only penetrate between 2 and 3mm. Family two fractures penetrate between 0.5 and 3mm in WS, 1mm in BS and 1.5mm in the AM. Family three have depths of 1 – 3mm and family four is only 0.5mm so families two, three and four are similar.

However, in each case it must be borne in mind that there are only three examples of family three fractures and only one of family four, therefore any trends are sample biased.

3.2 Porosity Distribution

The VG studioMAX 2.2 reconstruction software package allows the user to select a planar slice so that the pores on that image can be traced. This same process can be used to work out the porosity of the sample in that particular plane. Therefore, to get a more accurate and representative porosity a number of slices on that same plane have to be selected. In this study between 65 to 165 planes have undergone a P201 scan to determine porosity.

Westbury Shale

WS001, Figure 7; pores are widely spaced apart with little connectivity, though there is a small densely packed area surrounding some fossilized organic material. The size of the pores ranges from 0.05mm to 5.15mm, with a typical diameter of around 0.1mm. Pores of greater than 1.5mm are found around the fossilized remains or at the edge of the sample and are rare. The remainder are randomly spaced with only a few on each plane.

WS002; In this sample there are very few pores except for those located on one of the edges of the shale sample, particularly around a conchoidal fracture. However, the few pores that do exist in the centre of the sample range from 0.01mm to 0.5mm in diameter, whilst the pores on the edges of the sample range from 0.5mm to 2.05mm in diameter. The blue lines in the figure show the relatively large distance between pores in each plane.

WS003; This sample is more indicative of a typical shale with a smaller volume of pores seen and a smaller average pore size. The pore sizes range from 0.03mm to 3.5mm with the average size being 0.4mm. However, again, as in WS002, the pores appear more concentrated near the edges and seem to be associated quite strongly with fracture family two which cuts across the lamination of the shale.

WS004; This sample, also like sample WS002, shows prominent conchoidal fracturing, though not as pronounced. The pores are small and well dispersed with diameters ranging from 0.07mm to 2.5mm, though the pores over 0.5mm are on the edge of the sample. The pore with the largest diameter recorded further into the sample is 0.37mm. The pores are reasonably interspersed with areas of greater volume around the edges.

WS005; Contains a small number of pores ranging from 0.06mm to 3.01mm and averaging about 0.2mm in diameter. Again, the largest pores are recorded by the surface, near the conchoidal fracture. The remainder of the pores are found deeper in the shale, do not have a diameter greater than 1.01mm and have low connectivity.

Bowland Shales

Bowland shales show some of the same characteristics as the Westbury Shales. Samples that show more pronounced conchoidal fracturing also show numerous large pores in the same vicinity, this is not seen in samples that do not show this type of fracturing on their faces.

BS006; Pores are very sparse in this sample with an average size of 0.04mm diameter, ranging from 0.03 to 0.06mm.

BS007; This sample exhibits some quite pronounced conchoidal fracturing and again the larger pores are found near the outer edges where the conchoidal fractures are most prominent. These pores tend to be over 1mm in diameter. Though the pore size remains relatively normal for a shale, ranging from 0.06-2.51mm, again the pores found towards the centre are smaller, rarely over 0.5mm in diameter. The pores seem to group but show little connectivity.

BS008; Shows sparse pore content and little connectivity. The average size of the pores is 0.01mm.

BS009; The pores are sparse with an average size of 0.04mm. The small connected line matches up with the infilled fracture.

BS010; Most of the voids found were surrounding infilled lenses and fractures and so were relatively large. The few pores that were found not associated with an infilled fracture were approximately 0.03mm in diameter.

Accrington Mudstones

The Accrington Mudstone samples had few pores.

AS011; Pores of approximately 0.04-0.9mm in size, though the majority were under 0.3mm in diameter; there was a lack of homogeneity in the concentration of pores in this sample, as most pores were located in the middle of the back edge of the sample. There are groupings of pores that are largely unconnected and poorly sorted and which are likely to be formed from decomposed organic matter,

AS012; Pore sizes range from 0.07-1.41 mm, with the average size being 0.1mm. The pores show no connectivity. Most of the pores are scattered in the lower half of the sample.

AS013, AS014 & AS015; No pores were found.

There are few pores present in the Bowland and Westbury Shale samples, and they lack connectivity. However, there are two areas associated with an increase in porosity, areas adjacent to conchoidal fracturing and areas associated with fossilised remains and soft organic material. The pores associated with the conchoidal fracturing are larger than the individual pores but still show no connectivity.

No pores were detected in three of the Accrington Mudstone samples and where they were present in the remaining two samples, they were infrequent and poorly sorted and pore sizes were typically small. Due to the high clay content that makes this sample a mudstone, there was a lack of conchoidal fracturing which could explain the lack of pores. As seen in the Bowland and Westbury shales the pores seemed to concentrate in areas of conchoidal fracturing or are associated with fossilized remains.

4. DISCUSSION

From the investigation there is a clear pattern of fracture behaviour forming one of 4 patterns, however, these families of fractures emanating from the edges of the sample and work into the sample. The samples that have shown conchoidal fracturing, where the sample has fractured away from the parent unit, show a great amount of these fracture patterns but again this fracture patterns are associated with areas of weakness where the shale has fractured away from the parent unit. So while there may well be areas of weakness that has led to these samples breaking from their parent unit. The samples themselves only show the fractures associated with the conchoidal fracture patterns. Whilst pores were sporadic there were isolated large pores that were associated around fossilised remains and probably are associated with the soft organic tissue which has decomposed. Although each shale group had their own defining characteristics, all three different sites were found to have similarities. Most of the three different shale/mudstone types had two readily identifiable fracture families. By far the most common fracture family was the one that followed the existing lamination. It was also short in length with only a small depth of penetration.

This shows that the fracture families are associated with the actions that separated the samples from their parent unit. Which is also supported by the clear conchoidal fractures seen on the shales. The 1st family grouping does seem to have the greatest penetration but like the other fracture families the majority of the penetration is below 5mm. This greater amount of penetration could also be partly explained that the other groupings are not present in each sample unlike family 1. Family 1 has 4 samples, two Bowland shales two samples from the Westland Shale which have a penetration of greater then 5mm but these penetrations are an outlier of one fracture belonging to that fracture having a greater depth of penetration then the rest of the fractures that belong to that family within the sample.

Still common, but not as numerous was a recognisable 2nd family that quite often cut perpendicular through the direction of the lamination. Though this family did show itself in samples from all three sample locations it was more prevalent in the shale samples. The 2nd fracture family was not common in the mudstone samples, however, it is important to note that even family one type fracturing was not as common in the mudstones. The shales appear to be quite similar whilst the mudstone is more slab-like. The mudstones contain a heavy clay content, which could explain its lack of propensity to fracture, which could be seen by the relative straight natural edges of the samples, as opposed to the conchoidal fracturing observed in the darker Bowland and Westbury shales. These shales are darker due to their organic rich and reduced clay composition and were found to cleave easily. Their ease at cleaving and splitting could explain the increased density of fractures in these shales.

In each sample pores are small and lack any connection, though, in the shale samples with high organic content there is a concentration of pores associated with fossilised remains. This would seem to be soft organic material that has been decomposed, as can be clearly seen in ATNS001 the pores surround the fossilised remains but still remain unconnected to other pores. Apart from these pores associated with organic remain remains all three sample groups had very small pore average size. The pores form an orb around the fossilized

remains and could be due to degradation of organic material. As the Accrington Mudstone contains less organic material, there is also less likely to be any soft organic material that will be able to decompose to leave pores.

5. CONCLUSIONS

The following conclusions could be made from analysing the existing fracture patterns:

- Fractures were found on the edges of the samples, specifically around the areas where the samples broke away from the parent units. Penetration depths were also shallow with families two, three and four having a maximum penetration depth of 3mm. This suggests that these fractures types are associated with areas of weakness in the shales and mudstones sampled. Fracture family one varied in length, depth and width in accordance with the fractures following the already weaker bedding planes or laminations.
- Most fractures and fracture families were located in the very organic rich Westbury Shale, fewer in the Bowland Shale and only those that followed the already weaker bedding planes in the Accrington Mudstone (with the exception of one sample).
- The presence of conchoidal fracturing in a sample seems to be an indicator of an increase in size and occurrence of pores, namely towards the outer edges of the sample. Samples that had conchoidal fracturing from the Westbury and Bowland Shales, namely WS002, WS004, BS007 and to a lesser extent WS001, all show an increased average pore density towards the outer edges, with these pores tending to be much larger than the pores detected towards the centre of the sample.
- The remaining pores are widely dispersed in the samples and show no connectivity at all. In a number of samples some pores seem to be grouped in clusters but these clusters still show no connectivity. Where pores are grouped together they seem to be associated with organic remains and it would seem sensible to assume that these pores are caused by the degradation of organic material and would be the oil and gas reservoirs of the shale. This was not evident in the organic poor Accrington Mudstone.
- The Accrington Mudstone samples were the only ones that had been machine worked and still showed fewer fractures or pores than those samples that had naturally cleaved from the parent unit. This would suggest that as long as due care and diligence are taken during transportation, storage and sample preparation the sample should not be affected by working.

Recommendations

Although this investigation has shown that fractures are not penetrative, they are shown to be associated with areas of weakness, therefore;

Large cubic samples should be prepared, pre-scanned and subjected to tri-axial pressures to have fractures induced.

Any resulting model should introduce these thin, shallow fractures to the calculations and compare and contrast the simulated models with actual field results.

6. ACKNOWLEDGEMENTS

The Authors would like to Acknowledge the Institute of Civil Engineers, whose help was invaluable to carry out this study.

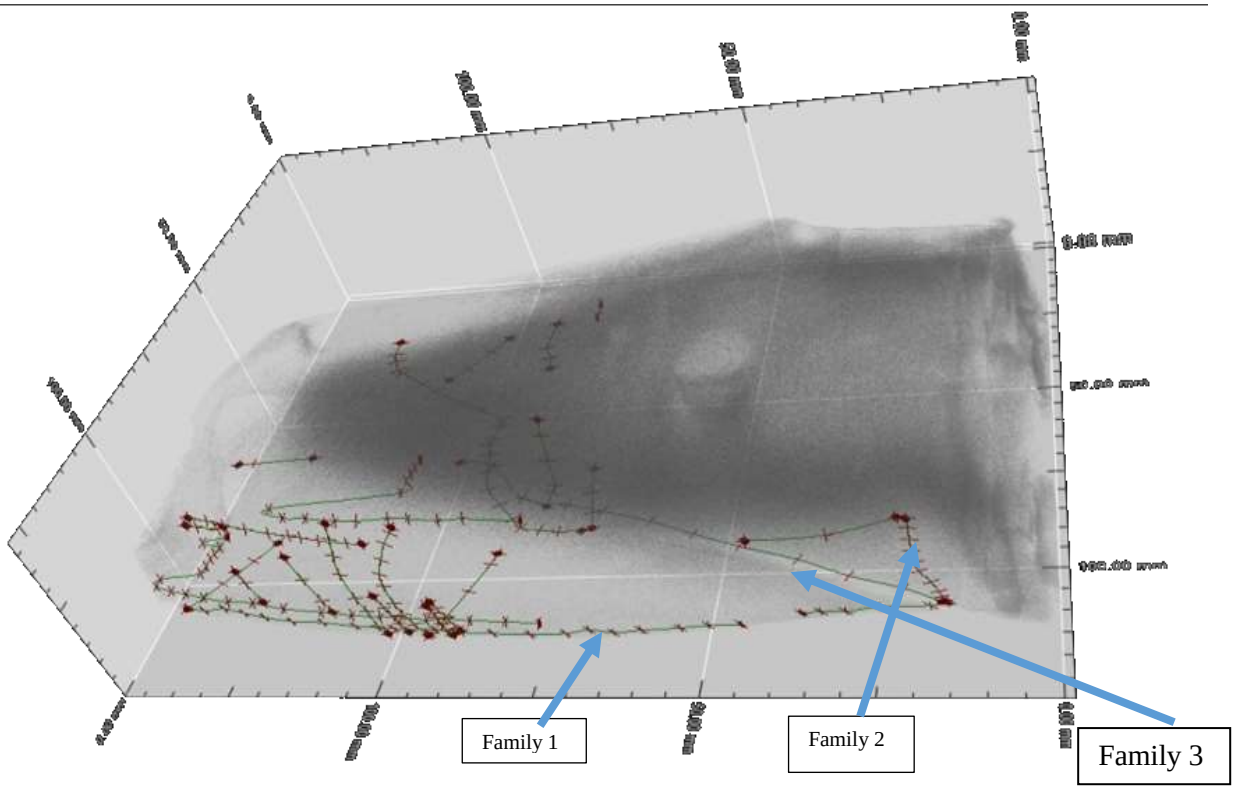

Figure 251:WS001 with 2 fractures families mapped

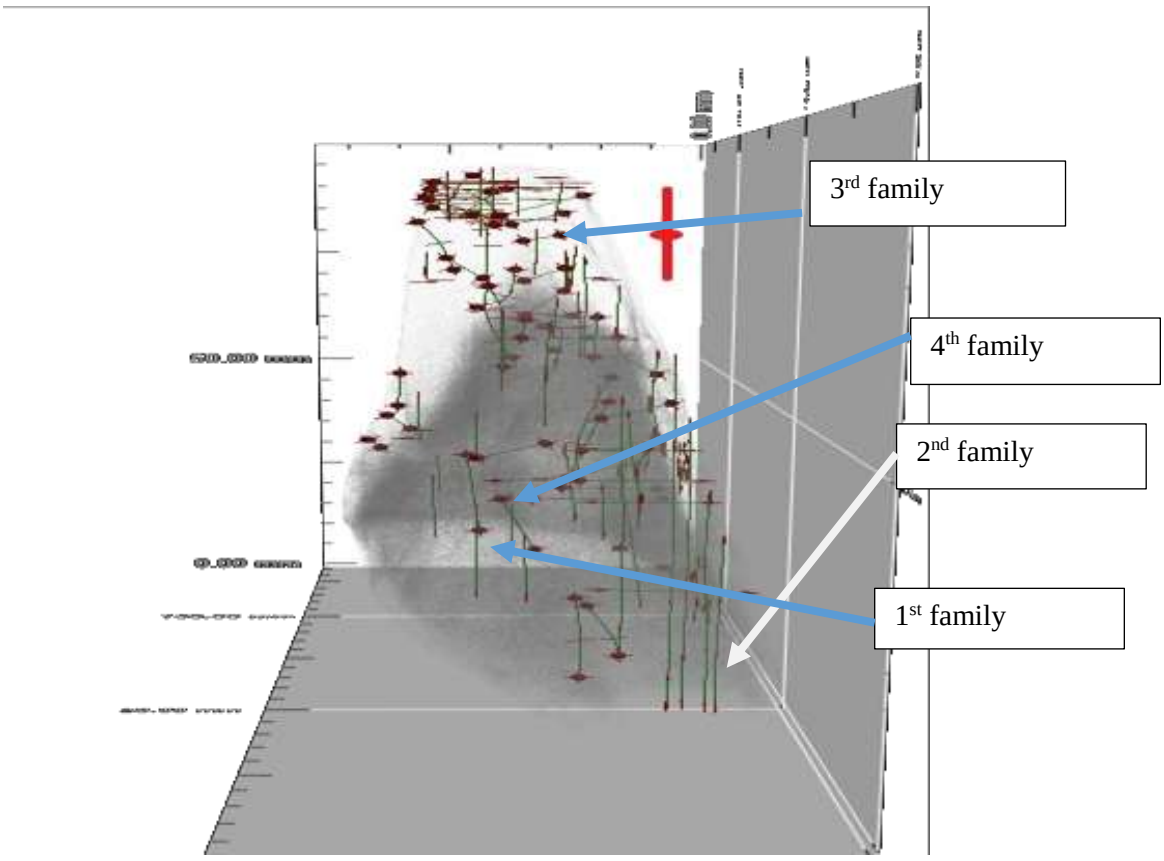

Figure 252: WS005 fractures families mapped.

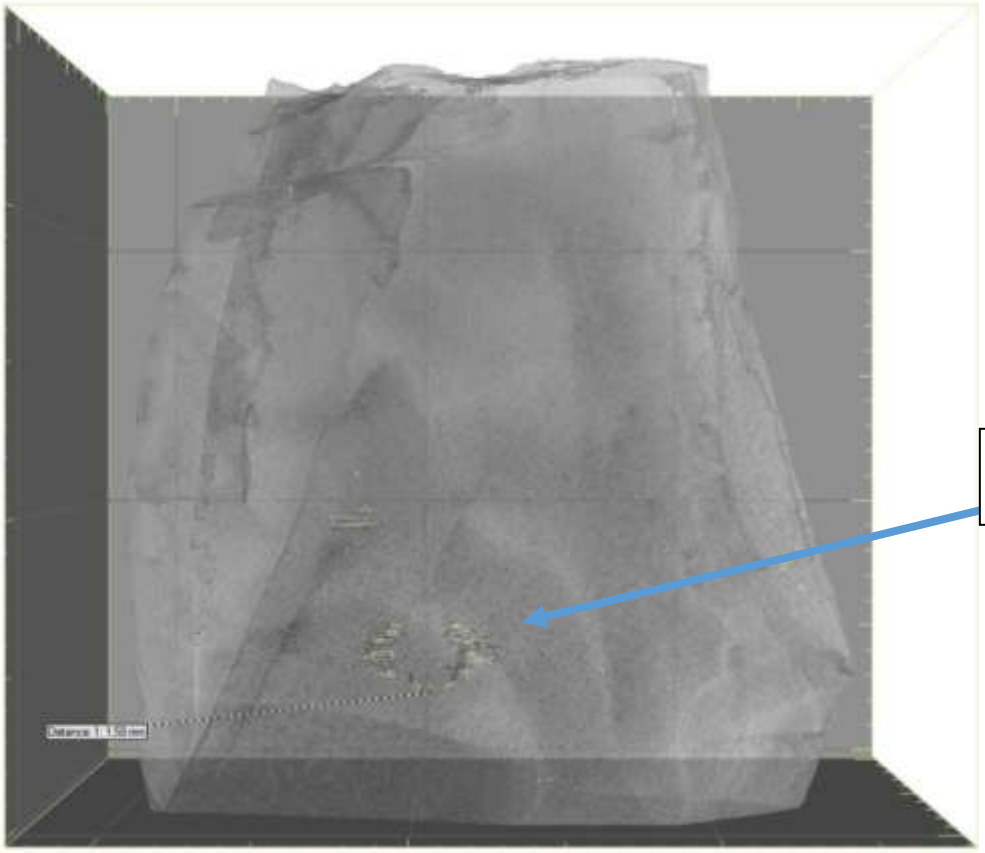

Figure 253: Pores mapped in Sample WS001 Transparency of the sample set to 40%

8 References

Andrews, I., 2013. *The Carboniferous Bowland Shale gas study:geology and resources estimation,* London, UK: British Geological Survey Foir the Department of Energy & Climate Change.

Ding, W. et al., 2011. Fracture development in shale and its relationship to gas accumulation. *Geoscience Frontiers,* III(1).

Griffith, A. A., 1921. The Phenomenon of Rupture and Flow in Solids. *Royal Society Philosphical Transactions,* 221(Series A), pp. 163-198.

Guk, V. B. M. W. D. E. M., 2014. *Reconciliation of fracture Performance and Fracture Geometry with Design.* Lousiana, SPE.

Lamont, N. J. F., 1963. *The Effects of Exisitng Fractures in Rocks on the Extension of Hydraulic Fracturing.* Los Angeles, 37th Annual Fall meeting of the SPE.

Li, Y. et al., 2012. *Optimizing Hydraulic Fracturing Design for Shale Gas Reduction through Numerical Simulations..* Texas, SPE International.

Price, N. & Rhodes, F., 1966. Fault and Joint Development in Brittle and Semi-brittle Rock.

Saputelli, L., Lopez, C., Chacon, A. & Soliman, M., 2014. *Design Optimization of Horizontal Wells With Multiple Hydraulic Fractures in the Bakken Shale.* Vienna, SPE.

Sesetty, V. & A. Ghassemi, 2012. *Modelling and Analysis of simulation for fracture Network generation.* Stanford, California, Stanford University.

Singhal. A, G. J. C. Z. Y., 2013. Micro/Nano-CT for visualisation of internal structures. Issue March.

Stanchits. S, B. J. S. A. E. E. S.-R. R., 2014. *Accoustic Emission Monitoring of hetorgenous ROck Hydraulic Fracturing.* Minneapolis, American Rock Mechanics Association.

Stanchits, S., Surdi, A., Edelman, E. & Suarez-Rivera, R., 2012. *Acoustic Emission and Ultrasonic Transmission Monitoring of Hydraulic.* Granada, 30th European Conference on Acoustic Emission Testing & 7th International Conference on Acoustic Emission.

Volume Graphics , 2012. *VG Studio Max - User manual 2.2.* s.l.:Volume Graphis GMBH.

Withers, P., 2007. *Materials Today.* s.l.:s.n.

APPENDIX F

TABLE OF ALL DIMENSIONS TAKEN

			Position to Borehole	Distance from borehole (mm)	Fracture length (mm)	Distance from Max width to the 10% max width at the top (mm)	maximum width to the 10% max width at the bottom (mm)	Maximum width (mm)	Top narrowing width (mm)	Bottom narrowing width (mm)	30% max width top	30% max width bottom	Distance from max width to 30% max top	Distance from max width to 30% max bottom
Accrington Mudstone	Bi-axial	AMS1	Half-length 1											
			At the borehole	1.69	34.72	23.03	7	0.27	0.03	0.03	0.09	0.09	22.95	3.67
			Near Borehole	6.83	65.83	31.11	11.35	0.44	0.04	0.04	0.12	0.12	35.16	6.41
			Halfway from borehole	17.98	78.49	26.83	22.96	0.25	0.03	0.03	0.08	0.08	25.41	18.17
			Three quarters way from borehole	29.8	94.97	27.46	43.78	0.23	0.02	0.02	0.07	0.07	27.44	42.63
			Half-length 2											
			At the borehole	0.51	26.74	12.82	7.14	0.41	0.04	0.04	0.12	0.12	12.66	5.34
			Near borehole	9.28	29.36	14.27	9.03	0.23	0.02	0.02	0.07	0.07	11.11	7.93
			Halfway from the borehole 1	15.88	25.1	11.13	9.82	0.23	0.02	0.02	0.07	0.07	11.05	9.8
			Three quarters way from the borehole	28.28	25.72	10.85	4.78	0.23	0.02	0.02	0.07	0.07	10.84	4.75
		AMS2	Half-length 1											
			At the borehole	0	47.96	8.02	12.01	0.36	0.04	0.04	0.12	0.12	2.76	10.08
			Near Borehole	6.83	96.4	13.89	46.45	0.32	0.03	0.03	0.09	0.09	10.83	21.49
			Halfway from borehole	14.14	96.4	13.89	-	0.32	0.03	0.03	0.09	0.09	10.83	21.49
			Three quarters way from borehole	30.14	97.2	35.81	-	0.25	0.03	-	0.09	-	31.87	-
			Half-length 2											
			At the borehole	0	50.65	13.15	16.66	0.22	0.02	0.02	0.06	0.06	5.83	10.36
			Near borehole	8.7	98.95	-	-	0.28	-	-	0.09	0.09	8.55	27.28
			Halfway from the borehole 1	18.59	99.11	-	45.73	0.19	-	0.02	0.06	0.06	16.97	9.74
			Three quarters way from the borehole	28.33	100	44.33	50.61	0.19	0.02	0.02	0.06	0.06	14.47	33.31
	Tri-axial	AMS3	Half-length 1											
			At the borehole	1.58	34.6		17.46	0.36		0.04		0.11		13.06
			Near Borehole	12.36	34.08		12.08	0.34		0.03		0.102		7.54
			Halfway from borehole	12.36	34.08		13.62	0.26		0.03		0.08		13.58
			Three quarters way from borehole	30.89	22.11	3.96	16.74	0.3	0.03	0.03		0.09		14.05
			Half-length 2											
			At the borehole	0	105.95	33.21	18.37	0.32	0.03	0.03	0.1	0.1	32.35	17.56
			End of the fracture	2.32	101.21			0.23						
			Secondary side 1											
			At the borehole	4.1	81.3			0.18						
			Near Borehole	14.5	73.58			0.27						
			Halfway from borehole	26.31	71.43			0.16						
			Three quarters way from borehole											
			Secondary fracture Side 2											
			Halfway from BH	15.81	54.92			0.29						
			End of fracture	32.58	24.64			0.44						
		AMS4	Half-length 1											
			At the borehole	0	94.28	17.26	52.87	0.45	0.05	0.5	0.14	0.14	16.64	50.8
			Near Borehole	8.37	100.88	14.94	67.9	0.52	0.05	0.05	0.16	0.16	10.07	58.63
			Halfway from borehole	16.66	100.82	52.77	38.5	0.33	0.03	0.03	0.1	0.1	52.62	33.03
			Three quarters way from borehole	31.59	101.86	46.06	-	0.3	0.03	-	0.09	0.09	45.68	47.82
			Half-length 2											
			At the borehole	0	76.54	8.09	25.51	0.71	0.07	0.07	0.21	0.21	7.63	24.77
			Near borehole	8.17	79.61	-	31.07	0.71	-	0.07	-	0.21	-	23.27
			Halfway from the borehole 1	18.02	52.45	-	46.67	0.38	-	0.04	-	0.11	-	43.93
			Three quarters way from the borehole	39.2	53.33	-	43.07	0.34	-	0.03		0.1	-	39.19
Westbury Shales	Bi-axial	WBS2	Half-length 1											
			At the borehole	0	31.42	-	-	6.25	-	-	-	-	-	-
			Near Borehole	5.22	31.55	12.04	14.17	1.6	0.16	0.16				
			Halfway from borehole	24.2	30.53			1.17	-	-	-	-	-	-
			Three quarters way from borehole	36.6	30.74			1.27						
			Half-length 2											
			At the borehole	0	30.35			1.38						
			Near Borehole	11.39	33.75			1.51						
			Halfway from borehole	24	32.84			1.37						
			Three quarters way from borehole	43.77	30.88			1.09						
	Tri-axial	WBS3	Half-length 1											
			At the borehole	0	87.34	44.92	-	0.46	0.05	-	0.14	0.14	4.71	10.12
			Near Borehole	8.98	87.8	29.57	-	0.31	0.03	-	0.09	0.09	28.78	8.57
			Halfway from borehole	16.93	89.3	28.32	45.97	0.32	0.03	0.03	0.09	0.09	28.78	45.07
			Three quarters way from borehole	24.61	75.92	35.66	37.22	0.35	0.04	0.04	0.12	0.12	32.86	36.15
			Half-length 2											
			At the borehole	0	74.45	49.46	-	1.13	0.11	-	0.33	0.33	43.69	4.93
			Near borehole	8.59	86.32	-	-	1.05	-	-	-	0.32	78.17	-
			Halfway from the borehole 1	15.65	108.44	92.16	-	1.26	0.13	-	-	0.38	56.13	-
			Three quarters way from the borehole	28.01	106.62	105.69	-	1.06	0.11	-	-	0.32	99.78	-
		WBS5	Half-length 1											
			At the borehole	3.64	55.52	0.32	-	0.03	-	33.4	0.1	0.1	4.62	19.41
			Near Borehole	8.55	60.59	1.79	0.17	0.17	13.13	17.86	0.51	0.51	4.69	12.47
			Halfway from borehole	20.77	76.94	1.01	0.1	0.1	14.67	60.79	0.3	0.3	11.89	25.1
			Three quarters way from borehole	27.51	77.49	1.09	-	0.11	-	70.69	-	0.33	-	42.05
			Half-length 2											
			At the borehole	0.21	46.61	0.78	0.08	0.08	14.4	21.83	0.23	0.23	13.36	14.83
			Near borehole	4.9	53.19	3.29	0.33	0.33	5.83	24.45	0.99	0.99	5.55	6.89
			Halfway from the borehole 1	17.45	56.16	2.55	-	0.26	-	6.26	0.78	0.78	1.87	2.41
			Three quarters way from the borehole	24.75	31.28	1.54	-	0.15	-	12.79	-	0.45	-	11.69
		WBS6	Half length 1											
			At the borehole	0.61	46.68	1.06	-	0.1	-	8.85	0.3	0.3	26.63	2.1
			Near Borehole	10.04	67.55	0.61	0.06	0.06	15.07	51.39	0.18	0.18	11.89	46.06
			Halfway from borehole	24.92	93.71	0.56	0.06	0.06	13.14	69	0.17	0.17	6.93	68.04
			Three quarters way from borehole	39.24	134.88	1.04	0.1	0.1	35.8	89.93	0.31	0.31	23.47	69.45
			Half length 2											
			At the borehole	2.22	43.65	0.43	0.04	0.04	3.66	40.04	0.13	0.13	3.27	39.49
			Near borehole	10.33	62.78	0.47	0.05	0.05	38.2	15.7	0.14	0.14	36.56	15.67
			Halfway from the borehole 1	19.21	72.35	0.58	0.06	0.06	16.11	58.22	0.17	0.17	15.29	58.14
			Three quarters way from the borehole	31.11	93.9	0.48	0.05	0.05	43.71	49.41	0.14	0.14	42.24	49.21